

**EXPERIMENTAL PERFORMANCE AND MODELING OF ASR  
AND DEF DETERIORATED STRUCTURAL CONCRETE BRIDGES**

A Dissertation

by

MADHU KARTHIK MURUGESAN REDDIAR

Submitted to the Office of Graduate and Professional Studies of  
Texas A&M University  
in partial fulfillment of the requirements for the degree of

DOCTOR OF PHILOSOPHY

Chair of Committee,  
Co-Chair of Committee,  
Committee Members,  
Head of Department,

John B. Mander  
Stefan Hurlbaas  
Mary Beth D. Hueste  
Mohammed E. Haque  
Robin Autenrieth

August 2015

Major Subject: Civil Engineering

Copyright 2015 Madhu Karthik Murugesan Reddiar

## ABSTRACT

Severe concrete cracking and ensuing deterioration caused by ASR/DEF expansion strains in bridge piers is a major concern for state transportation officials. A dual experimental and analytical modeling approach is used to determine the effects of severe ASR/DEF deterioration on concrete structures. A minimalist semi-empirical method is developed and validated to estimate ASR/DEF induced expansion strains in reinforced concrete structures. As part of the experimental study, expansion data are gathered from a large-scale C-beam specimen that is field conditioned for five years. The expansion model is then used to simulate the progression of ASR/DEF induced expansion strains in the C-beam specimens showing various degrees of deterioration. Considering the variability of the field recorded expansion data, the ASR/DEF expansion model simulates the expansion strains quite well. The severely damaged C-beam specimen is experimentally tested, and its overall and internal behavior are compared to previously tested C-beam specimens without and with ASR/DEF deterioration. Key improvements are made to the Compatibility Strut-and-Tie Method (C-STM) to better model the overall behavior of structures through failure. To incorporate the effects of ASR/DEF deterioration in the C-STM technique, cover and core concrete properties are modified. The expansion strains from the ASR/DEF model are inferred to estimate the prestressing forces to be applied to the C-STM to simulate the self-prestressing effects caused by the restraint offered by reinforcing steel to concrete core expansion. Although the appearance of the C-beam specimen was in poor condition, the experimental test did not show any reduction in the load carrying capacity of the structure, but compared to an undamaged benchmark specimen an overall increase in stiffness and decrease in ductility is evident. However, excessive cracking can cause accelerated hidden reinforcement corrosion which can be a cause of major concern, and in conjunction with ASR/DEF may affect the strength, stiffness and ductility of the structure. The displacement-based C-STM technique simulates the overall force-deformation and internal behavior of the concrete specimens without and with ASR/DEF deterioration well.



# **DEDICATION**

To My Father and Mother

## **ACKNOWLEDGEMENTS**

I wish to thank my committee chair, Dr. Mander, and committee co-chair, Dr. Hurlebaus, for their invaluable guidance and support throughout the course of my research. This work would not have been possible without their vision, thoughts, and advice. I am also deeply grateful to the Texas Department of Transportation and the Zachry Department of Civil Engineering for the financial support that I received during various phases of my stay at Texas A&M University.

I would also like to thank Dr. Hueste and Dr. Haque for serving on my advisory committee. Thanks also to Dr. Keating and the High-Bay laboratory technicians for their assistance during the experimental testing, and to the department faculty and staff for making my time at Texas A&M University a memorable experience. I would also like to especially thank my colleagues Mr. Kyle Wiegand, Dr. Shih-Hsiang Liu and numerous other friends at Texas A&M University for their constant help and support.

Last, but not the least, I would like to show my utmost gratitude to my father Dr. Murugesan Reddiar and mother Ms. Prabhavathy Murugesan, brother Mr. Anandh Kumar and good friend Ms. Ranjisha Kumar for making this exciting journey at Texas A&M University possible, and for their constant support, encouragement, patience, love and prayers.

# TABLE OF CONTENTS

	Page
ABSTRACT .....	ii
DEDICATION .....	iii
ACKNOWLEDGEMENTS .....	iv
TABLE OF CONTENTS .....	v
LIST OF FIGURES.....	x
LIST OF TABLES .....	xv
LIST OF SHEETS.....	xvi
1 INTRODUCTION .....	1
1.1 Research Motivation.....	1
1.2 Research Objectives .....	4
1.3 New Contributions and Significance.....	5
1.4 What Then is Particularly New in this Research? .....	7
1.5 Organization of the Dissertation.....	8
2 LITERATURE REVIEW OF PREVIOUS WORK, RESEARCH NEEDS AND QUESTIONS ARISING.....	11
2.1 Introduction .....	11
2.2 Concrete Deterioration over Time: The ASR Chemical Process .....	11
2.2.1 Review of Laboratory Experiments on ASR Deteriorated Reinforced Concrete.....	12
2.2.2 Review of Modeling ASR Induced Expansion Strains .....	19
2.3 Delayed Ettringite Formation: The DEF Chemical Process.....	26
2.3.1 Experimental Investigations on DEF.....	27
2.3.2 Review of Modeling DEF Induced Expansion Strains.....	32
2.4 Structural Deterioration due to ASR/DEF.....	34
2.4.1 TxDOT Project #12-8XXIA006.....	34
2.4.2 TxDOT Project #0-6491 .....	35
2.4.3 TxDOT Project #0-5722.....	36
2.4.4 TxDOT Project #0-5997.....	38

2.5	Historic Developments in Strut-and-Tie Modeling .....	46
2.5.1	Compression Field Theory and Softened Truss Model (Collins vs. Hsu) .....	46
2.5.2	Other Developments Contemporary to Compression Field Theory .....	48
2.5.3	Modified Compression Field Theory and Fixed Angle Softened Truss Model .....	49
2.5.4	Force Transfer Method .....	54
2.6	Evolution of Compatibility Strut-and-Tie Modeling .....	55
2.7	Research Questions Arising .....	62
3	DISPLACEMENT-BASED COMPATIBILITY STRUT-AND-TIE METHOD AND APPLICATION TO MONOTONIC AND CYCLIC LOADING .....	65
3.1	Summary .....	65
3.2	Introduction .....	66
3.3	Softened Concrete Model for Diagonal Concrete Struts .....	69
3.4	Implementation of Analysis in Displacement-Control .....	72
3.5	Monotonic Loading Modeling Validation: Bridge Bent-Cap .....	73
3.6	C-STM Results and Discussion .....	77
3.7	Cyclic Loading Modeling Validation: Coupling Beam .....	83
3.8	C-STM Results and Discussion .....	85
3.9	Closure and Key Findings .....	88
4	MODELING ASR/DEF EXPANSION IN REINFORCED CONCRETE STRUCTURES .....	89
4.1	Summary .....	89
4.2	Introduction .....	90
4.3	Modeling ASR/DEF Expansion in Saturated Prisms .....	91
4.4	Modifications to Account for Temperature and Moisture Variations .....	103
4.5	Validation of Proposed Model for ASR Related Expansion .....	106
4.6	Validation of Proposed Model for DEF Related Expansion .....	109
4.7	Application of Proposed Model to Post-Tensioned Reinforced Concrete Column Specimen .....	111
4.8	Discussion .....	119
4.9	Closure and Key Findings .....	120
5	DETERIORATION DATA OF LARGE-SCALE SPECIMEN WITH HEAVY ASR/DEF DETERIORATION .....	121
5.1	Summary .....	121
5.2	Introduction .....	122
5.3	Visual Inspections and Observations over Time .....	123
5.4	Surface Concrete Strains .....	129

5.5	Internal Concrete Strains .....	136
5.6	Reinforcing Steel Strains .....	138
5.7	Discussion and Comparison .....	143
5.8	Closure and Key Findings .....	146
6	APPLICATION OF PROPOSED EXPANSION MODEL TO ESTIMATE EXPANSION STRAINS IN C-BEAM SPECIMENS.....	147
6.1	Summary.....	147
6.2	Introduction .....	148
6.3	Parameters for Modeling Expansion in C-beam Specimen.....	150
6.4	Modeling ASR/DEF Expansion in C-beam Specimen.....	153
6.5	Expansion Modeling of Companion Tests .....	159
6.6	Discussion.....	164
6.7	Closure and Key Findings .....	165
7	EXPERIMENTAL FORCE-DEFORMATION BEHAVIOR OF LARGE REINFORCED CONCRETE SPECIMENS WITH HEAVY ASR/DEF DETERIORATION .....	167
7.1	Summary.....	167
7.2	Introduction .....	168
7.3	Experimental Investigation.....	169
7.3.1	Concrete Compressive Strength .....	169
7.3.2	Experimental Test Setup.....	169
7.3.3	Instrumentation.....	171
7.3.4	Experimental Testing Procedure and Loading History .....	175
7.3.5	Experimental Performance .....	176
7.3.6	Force-Displacement Behavior .....	176
7.3.7	Failure Assessment.....	177
7.4	Discussion and Comparison with Previous Tests.....	186
7.5	Key Findings from the Experimental Testing Program .....	189
8	FORCE DEFORMATION MODELING OF EXPERIMENTAL RESULTS .....	191
8.1	Summary.....	191
8.2	Introduction .....	192
8.3	Modified Material Properties to Account for ASR/DEF.....	193
8.3.1	Assessment of Deteriorated Cover Concrete Properties .....	194
8.3.2	Assess Concrete Core Confinement and Modify Concrete Properties .....	196
8.3.3	Prestressing Effect in Reinforcement Caused by Concrete Swelling .....	196
8.4	C-beam Structure.....	197
8.5	Preliminary Analysis .....	200

8.6	Strength and Deformation Capacity Using C-STM .....	201
8.6.1	C-STM Model .....	201
8.6.2	Results of C-STM Analysis.....	207
8.6.3	Interrogation of Internal Strains from C-STM and Comparison with Experimental Results .....	210
8.6.4	Failure Analysis.....	215
8.7	Discussion.....	219
8.8	Key Findings from C-STM Modeling.....	221
9	C-STM APPLICATION TO TEXAS BRIDGE PIERS .....	223
9.1	Summary.....	223
9.2	Introduction .....	224
9.3	Analysis Methods .....	225
9.3.1	ASR/DEF Expansion.....	225
9.3.2	C-STM Analysis.....	227
9.4	Analysis of Pier H19C.....	229
9.4.1	The Structure .....	229
9.4.2	Modeling Potential Free Expansion Strain due to ASR and/or DEF.....	232
9.4.3	Expansion Strain Modeling based on Experimental Evidence from C-beam Specimens .....	234
9.4.4	Expansion Strain Modeling based on Free Expansion Tests.....	248
9.4.5	Loading .....	251
9.4.6	The C-STM Model .....	258
9.4.7	C-STM Results and Discussion.....	264
9.5	Analysis of Pier I5C .....	269
9.5.1	The Structure .....	269
9.5.2	Expansion Strain Modeling due to ASR/DEF .....	271
9.5.3	The C-STM Model .....	283
9.5.4	C-STM Results and Discussion.....	289
9.6	Key Findings .....	293
10	SUMMARY, CONCLUSIONS, AND RECOMMENDATIONS.....	295
10.1	Summary.....	295
10.1.1	Deterioration Program .....	296
10.1.2	Destructive Load Testing .....	297
10.1.3	Analytical Modeling: ASR/DEF Expansion .....	298
10.1.4	Analytical Modeling: C-STM.....	298
10.2	Conclusions .....	299
10.2.1	Concrete Deterioration due to ASR/DEF .....	299
10.2.2	Observations from Destructive Testing.....	300
10.2.3	Observations from Analytical Modeling of ASR/DEF Expansion.....	301

10.2.4 Inferences from Code-Based Analysis .....	301
10.2.5 Observations from the C-STM Analysis .....	302
10.3 Recommendations and Future Work .....	303
10.3.1 Present Practice .....	303
10.3.2 Future Work.....	304
REFERENCES.....	305
APPENDIX A1.....	320
APPENDIX A2.....	343
APPENDIX A3.....	354
APPENDIX A4.....	363
APPENDIX A5.....	389

## LIST OF FIGURES

	Page
Figure 2-1: Prototype Reinforced Concrete Bridge Bents (Adopted from Mander et al., 2012).....	40
Figure 2-2: Reinforcement Details of Experimental C-beam Specimen. ....	41
Figure 2-3: Experimental Test Setup for Specimen 4. (Adopted from Liu, 2012).....	44
Figure 2-4: External Instrumentation Layout for C-beam Specimen 4. ....	45
Figure 3-1: Diagonal Concrete Web Elements. ....	71
Figure 3-2: Elevation and Cross Section of Selected Bent-Cap Specimens (Bracci et al., 2000).....	74
Figure 3-3: C-STM Model for Bent-Cap Specimen. ....	75
Figure 3-4: Cracked Reinforced Concrete Material Properties. ....	78
Figure 3-5: Comparison of Experimental and C-STM Results. ....	80
Figure 3-6: Comparison of Internal Member Strains Obtained from C-STM Analysis with Experimental (Bracci et al., 2000) Results. ....	81
Figure 3-7: Failure Analysis of Specimen 2A .....	82
Figure 3-8: Elevation, Cross-Section and C-STM of Coupling Beam 312. ....	84
Figure 3-9: Comparison of Experimental and C-STM Results for Coupling Beam 312. ....	86
Figure 3-10: Spatial Distribution of Strains along Coupling Beam Reinforcement. ....	87
Figure 4-1: Expansion Model for ASR/DEF Induced Expansion in Concrete.....	92
Figure 4-2: Stress-Strain Models for Components of Reinforced Concrete.....	94
Figure 4-3: Effects of Compressive and Tensile Loads on ASR/DEF Induced Expansion.....	98
Figure 4-4: Stress-Strain Models for Various Components.....	99
Figure 4-5: Variation of Characteristic Time with Relative Weight Increase. ....	105
Figure 4-6: Model Validation for ASR Expansion with Experimental Data in Reinforced Concrete. ....	108



Figure 4-7: Model Validation for DEF Expansion with Experimental Data (Bouzabata et al., 2012) in Reinforced Concrete.....	110
Figure 4-8: Reinforcement Details of Splice Column Specimen.....	112
Figure 4-9: Information Pertinent to Model Expansion Strains in Splice Column Specimens.....	114
Figure 4-10: Comparison of Experimental and Model Strain Propagation Results on Specimen Large Face—Longitudinal Direction.....	116
Figure 4-11: Comparison of Experimental and Model Strain Propagation Results on Specimen Large Face—Transverse Direction.....	117
Figure 4-12: Comparison of Experimental and Model Strain Propagation Results on Specimen Small Face—Transverse Direction.....	118
Figure 5-1: Deteriorated State of Specimen 3 at Texas A&M Riverside Campus.....	125
Figure 5-2: Crack Pattern over Time in Specimen 3.....	126
Figure 5-3: Final Crack Widths on Specimen 3.....	127
Figure 5-4: Progression of Cracks on Specimen 3 with Time.....	128
Figure 5-5: Horizontal Surface Concrete Strains from DEMEC Points on C-beam Top Face—Specimen 3.....	131
Figure 5-6: Vertical Surface Concrete Strains from DEMEC Points in Joint Region—Specimen 3.....	132
Figure 5-7: Vertical Surface Concrete Strains from DEMEC Points in Beam and Joint Region—Specimen 3.....	133
Figure 5-8: Diagonal Surface Concrete Strains from DEMEC Points in Beam and Joint Region—Specimen 3.....	134
Figure 5-9: Mid-Depth Concrete Strains Measured from Concrete Gages—Specimen 3.....	137
Figure 5-10: Longitudinal Reinforcing Steel Strains in Beam—Specimen 3.....	139
Figure 5-11: Longitudinal Reinforcing Steel Strains in Column—Specimen 3.....	140
Figure 5-12: Transverse Reinforcing Steel and U-bar Strains.....	141
Figure 5-13: Reinforcing Steel Strains in Compression Zone.....	142
Figure 5-14: Comparison of Surface Strains from DEMEC (DM) Points to the Internal Strains from Strain Gages (SG) and Concrete Gages (KM) for C-beam Specimen 3.....	144
Figure 6-1: Reinforcement Layout of C-beam Specimen.....	149

Figure 6-2: Information Pertinent to Model Expansion Strains in C-beam Specimen.....	151
Figure 6-3: Computation of Average Tensile Loads from C-STM in the C-beam Specimen due to Post-Tension Load.....	154
Figure 6-4: Observed and Computed ASR/DEF Induced Expansion Strains– Specimen 3.....	157
Figure 6-5: Observed and Computed ASR/DEF Induced Expansion Strains– Specimen 2.....	161
Figure 6-6: Observed and Computed ASR/DEF Induced Expansion Strains– Specimen 4.....	163
Figure 7-1: Comparison of Cured and Field Cylinders (at 1977 days). .....	170
Figure 7-2: Experimental Test Setup for C-beam Specimen 3.....	172
Figure 7-3: Experimental Setup for Specimen 3: Plan and Front Elevation View.....	173
Figure 7-4: External and Internal Instrumentation Layout. ....	174
Figure 7-5: Condition of Specimen 3 at Various Loads: Singly Reinforced Beam .....	178
Figure 7-6: Condition of Specimen 3 at Various Loads: Doubly Reinforced Beam. ....	179
Figure 7-7: Force-Displacement Behavior of C-beam Specimen 3.....	180
Figure 7-8: Internal and External Strains at Critical Regions of C-beam Specimen 3.....	181
Figure 7-9: Physical State of the Failed End after Load Testing of Specimen 3.....	183
Figure 7-10: Observed Out-of-Plane Strains in the Beam-Column Joint of C-beam Specimen 3. ....	185
Figure 7-11: Comparison of Force-Deformation Behavior of C-beam Specimens Subjected to ASR/DEF Deterioration.....	187
Figure 7-12: Corrosion and Post-Peak Load Damage at Failure: A Comparison of the Four C-beam Specimens at the Knee-Joint.....	188
Figure 8-1: Deteriorated Specimen Appearance, and the Modeled Transverse Strains in the C-beam Out-of-Plane Direction.....	195
Figure 8-2: Modified Stress-Strain Model for Steel to Account for Prestressing Effects due to ASR/DEF.....	198
Figure 8-3: Representative Structures, and Elevation and Cross-Section of the C-beam Specimens.....	199
Figure 8-4: Experimental, Code Based Predictions and C-STM Results. ....	203

Figure 8-5: Modeling the C-beam Specimens without and with ASR/DEF Damage. ....	205
Figure 8-6: Cracked Reinforced Concrete Material Properties. ....	206
Figure 8-7: Comparison of Experimental and C-STM Results for C-beam Specimens Subjected to ASR/DEF Deterioration.....	209
Figure 8-8: Failure Pattern Observed at the Beam-Column Joint of C-beam Specimen 1.....	211
Figure 8-9: Experimental (Mander et al., 2012) vs. C-STM Comparison of Internal Nonlinear Concrete and Steel Response for C-beam Specimens. ....	212
Figure 8-10: Experimental vs. C-STM Comparison of Nonlinear Concrete and Steel Response: Specimen 3. ....	213
Figure 8-11: Computed Sequence of Nonlinear Behavior Events.....	216
Figure 8-12: Comparison of Strains Parallel and Perpendicular to Crack in the Joint and Beam Region. ....	218
Figure 8-13: Force-Deformation Results for C-beam Specimens. ....	220
Figure 9-1: Model Representing the Maximum and Minimum Temperature Variations in a Year in San Antonio, TX.....	226
Figure 9-2: Cracked Reinforced Concrete Material Properties. ....	228
Figure 9-3: Layout and Reinforcement Detail of Pier H19C–Sheet 1 (Adopted from Mander et al., 2012). ....	230
Figure 9-4: Layout and Reinforcement Detail of Pier H19C–Sheet 2 (Adopted from Mander et al., 2012). ....	231
Figure 9-5: Modeling Free Expansion Results for Parameter Identification.....	233
Figure 9-6: Modeled ASR/DEF Induced Expansion Strains in Pier H19C based on Observations from Experimental C-beam Specimens. ....	247
Figure 9-7: Modeled ASR/DEF Induced Expansion Strains in Pier H19C based on Free Expansion Tests on Cores from H19C. ....	249
Figure 9-8: Distribution of Crack Widths Across Column Face. ....	250
Figure 9-9: Loads on Pier H19C.....	252
Figure 9-10: Bending Moment Diagram for Normal Service Regime of Pier H19C.....	254
Figure 9-11: Column Interaction Diagram with Different Load Cases. ....	256

Figure 9-12: Bending Moment Diagrams for (a) the Design Ultimate Strength and (b) for Overload at Incipient Mechanism Formation.....	257
Figure 9-13: C-STM Model for Pier H19C.....	259
Figure 9-14: Cracked Reinforced Concrete Material Properties for Pier H19C.....	266
Figure 9-15: Force-Deformation for Case 1 and Case 2 Live Load.....	268
Figure 9-16: Layout and Reinforcement Detail of Pier I5C (Adopted from Mander et al., 2012).....	270
Figure 9-17: Modeled ASR/DEF Induced Expansion Strains in Pier I5C based on Observations from Experimental C-beam Specimens.....	281
Figure 9-18: Modeled ASR/DEF Induced Expansion Strains in Pier I5C based on Free Expansion Tests on Cores from H19C.....	282
Figure 9-19: C-STM Model of Pier I5C.....	284
Figure 9-20: Cracked Reinforced Concrete Material Properties for Pier I5C.....	290
Figure 9-21: Force-Deformation of Pier I5C without and with ASR/DEF Damage.....	291

## LIST OF TABLES

	Page
Table 3-1: Material Properties, and Experimental Results for Bent-Cap Specimens.....	76
Table 6-1: Properties for C-beam Specimen.....	154
Table 6-2: Computation of Reinforcement Ratio and Maximum Expansion Strain for C-beam Specimen 3.....	156
Table 6-3: Computation of Reinforcement Ratio and Maximum Expansion Strain for C-beam Specimen 2.....	160
Table 6-4: Computation of Reinforcement Ratio and Maximum Expansion Strain for C-beam Specimen 4.....	162
Table 7-1: Concrete Material Properties of C-beam Specimen 3.....	170
Table 8-1: Material Properties, Stage 1 and 2 Analyses, and Experimental Results.....	202
Table 8-2: Prestrains in C-STM Members for C-beam Specimens.....	208
Table 8-3: Ultimate Load Capacity of C-beam Specimens.....	221
Table 9-1: Maximum Potential Crack Width in Pier H19C based on Modeled Transverse Expansion Strains.....	246
Table 9-2: Column Axial Load and Moment for Various Load Combinations.....	253
Table 9-3: Prestrains in the C-STM Members of Pier H19C.....	265
Table 9-4: Maximum Potential Crack Width in Pier I5C based on Modeled Transverse Expansion Strains.....	280
Table 9-5: Prestrains in the C-STM Members of Pier I5C.....	288

## LIST OF SHEETS

	Page
Sheet 9-1: Computation of Reinforcement Ratio $\rho$ and Maximum Expansion Strain $\varepsilon_{\rho}^{\max}$ for Pier H19C .....	235
Sheet 9-2: Expansion Model and Computation of Prestrains for the Various Members of the C-STM Model for Pier H19C .....	260
Sheet 9-3: Computation of Reinforcement Ratio $\rho$ and the Maximum Expansion Strain $\varepsilon_{\rho}^{\max}$ for Pier I5C.....	272
Sheet 9-4: Expansion Model and Computation of Prestrains for the Various Members of the C-STM Model for Pier I5C.....	285

# 1 INTRODUCTION

## 1.1 Research Motivation

The structural longevity of a large number of reinforced concrete bridge piers may have been compromised as a result of premature concrete deterioration. Alkali-Silica Reaction (ASR) and Delayed Ettringite Formation (DEF) are two material related issues that can lead to premature concrete deterioration. It is important to analyze structures that are subjected to such reactive deterioration to determine if a particular structure can perform in a safe manner for the remainder of its service life. By means of a dual analytical and experimental study, the research presented herein develops tools that are necessary to model the expansion strains caused by ASR/DEF deterioration in reinforced concrete, and to study the effects of ASR/DEF deterioration on the structural load-carrying capacity, ductility, and overall behavior.

The effects of ASR/DEF on plain concrete have previously been investigated extensively and documented by others. However, studies related to the effects of ASR/DEF expansion on reinforced concrete structures have been quite limited. Most of these studies have focused on small-scale ordinary reinforced concrete structures, while relatively few studies have been oriented towards studying the effects of ASR/DEF on complex large-scale structures. Additionally, the existing modeling techniques that simulate the expansion strains induced by ASR/DEF reaction in reinforced concrete are complex, and often require detailed finite element implementation to study their effects on the structure. Therefore, one of the primary goals of this research is to establish minimalist models to estimate the possible expansion strains and the resultant strength capacity of ASR/DEF deteriorated reinforced concrete structures.

Limited field data are available on external surface strains, and internal steel and concrete expansion strains in heavily ASR/DEF deteriorated large-scale concrete structures. To shed insight into the long term effects of ASR/DEF deterioration on reinforced concrete structures, a detailed laboratory program is designed to monitor the

damage caused by ASR/DEF deterioration and study the deterioration process in large-scale concrete structures.

ASR/DEF deterioration can impose severe cracking in reinforced concrete structures which may provide an appearance that these structures may be unsafe, both to inspecting engineers and members of the public. Therefore, it is also important to investigate the effects of ASR/DEF deterioration on the structural load carrying capacity of the structure. A laboratory based destructive testing of structures with significant ASR/DEF deterioration may shed light on how the load carrying capacity and the global force-deformation behavior of reinforced concrete structures are affected.

To extend the value of the experimental tests it is essential that the experimental results can be captured and replicated with rigorous mathematical or computational structural models, and analyze the strength and deformation capacity of the affected structures with respect to the imposed loads. Therefore, there is a need to develop effective and efficient analysis techniques that not only model the structural behavior of a sound structure, but also can take into account any effect of ASR/DEF deterioration.

Reinforced concrete structural members can be divided into two broad categories: beam regions and discontinuity regions, also known as the B-regions and D-regions, respectively. The Euler-Bernoulli beam theory including assumptions such as linear strain distribution, can be used to analyze B-regions with good accuracy. D-regions or disturbed regions exist due to geometric discontinuities at or near supports, member connections or where concentrated loads are applied. Beam theory is not strictly valid in D-regions. The complex internal stress and strain distribution and the interaction of flexure and shear make it extremely difficult to analyze cracked concrete structures with significant D-regions.

Strut-and-Tie (SAT) methods have gained prominence and may be used as an effective simple design method for structures with D-regions. The SAT method is a lower bound plastic truss, and as such does not provide a uniquely valid solution. Obtaining meaningful results from a SAT analysis depends on the judicious choice of a SAT model which can represent the actual flow of stresses in the structure as closely as



practicable. The principal shortcoming of classic SAT design solutions is that while they may provide approximations of required strength, there is no indication of deformability, including ductility if this aspect is required in design or assessment of structures. Moreover, a comprehensive insight into the evolution of the failure mechanism and strength hierarchy does not exist.

An alternative to the SAT approach is to use the finite element method (FEM) analysis. However, because structural concrete has highly nonlinear constitutive relations, to reliably represent system behavior a large number of elements are needed for a meaningful solution. Associated with a refined mesh is the large number of degrees of freedom, consequently leading to slow computer runtimes and greater computational resources, particularly for highly nonlinear behavior. Thus, while the FEM approach remains a valid research tool, it may not be sufficiently practical for solving routine design office analysis problems.

Recently it has been demonstrated by Scott et al. (2012a,b) that a good compromise between SAT and FEM is the Compatibility Strut-and-Tie Method – C-STM. Scott et al. claim C-STM as a minimalistic computational analysis technique based on rational mechanics that satisfies equilibrium and compatibility conditions while taking into account realistic nonlinear material behavior of reinforced concrete. They demonstrate that C-STM can be an effective tool in analyzing reinforced concrete structures, especially those with significant D-regions. Their approach was demonstrated to be efficient in modeling the force-deformation response and provides an insight into the structural behavior. However, certain shortcomings such as inability to subject the structure to loading and unloading cycles, and the inability to directly model the post-peak behavior and hence the final failure load and corresponding displacement have been identified and remain to be overcome; this is another motivation of the present research study.

Finally, the ASR/DEF expansion model is used in conjunction with the universally applicable displacement-based C-STM analysis to analyze reinforced concrete structures that may or may not be subjected to ASR/DEF deterioration.

## 1.2 Research Objectives

The major objectives of this research follow:

1. Advance and validate a minimalist analysis technique to model the expansion strains caused by ASR/DEF in reinforced concrete.
2. Monitor the deterioration caused by ASR/DEF effects on field exposed reinforced concrete C-beam specimen.
3. Apply the expansion model to simulate ASR/DEF induced expansion strains on the heavily deteriorated reinforced concrete C-beam specimen.
4. Perform destructive testing to study the effects of significant concrete deterioration caused by ASR/DEF on the load carrying capacity of the laboratory C-beam specimen.
5. Advance the C-STM analysis technique to implement a displacement-based strategy to permit loading and unloading cycles and concrete softening effects to be easily captured.
6. Validate the modified C-STM with experimental results for both monotonic and reverse cyclic loading.
7. Devise a method to implement the effects of ASR/DEF related concrete expansion and deterioration into the C-STM analysis.
8. Apply the modified displacement-based C-STM technique to the laboratory C-beam specimens to analyze the structures without and with ASR/DEF deterioration, and compare the overall and internal behavior of the structure with the experimental results.
9. Apply the developed transient expansion model and displacement-based C-STM technique to determine the behavior of large-scale bridge piers showing signs of ASR/DEF induced deterioration.

### 1.3 New Contributions and Significance

The contributions to the field of existing knowledge are as follows:

1. A minimalist semi-empirical method is developed to model ASR/DEF induced expansion strains in reinforced concrete. This expansion model is validated and applied to simulate the field expansion data gathered from the C-beam specimens.
2. External surface strains, and internal steel and concrete strains are gathered from a reinforced concrete C-beam specimen that is field conditioned for a total of five years and shows significant deterioration due to ASR/DEF induced expansion strains.
3. A destructive experimental test is performed on a reinforced concrete C-beam specimen that was exposed outdoors for five years and subjected to severe ASR/DEF deterioration.
4. The C-beam specimen was experimentally tested to investigate force-deformation behavior to failure. Results are compared to an undamaged control specimen and other deteriorated C-beam specimens that were tested by previous investigators. Conclusions are drawn on the effects of long-term ASR/DEF deterioration on reinforced concrete C-beam specimens.
5. Based on existing experimental data a softened concrete model that discriminates between softened confined and softened unconfined concrete is proposed that can be easily implemented into the C-STM analysis.
6. A displacement-based C-STM analysis technique is proposed in-lieu of the present force-based C-STM analysis technique, to enable modeling of reinforced concrete structures subjected to monotonic and reverse-cyclic loading.
7. The effects of ASR/DEF induced expansion strains on reinforced concrete structures are modeled into the C-STM analysis. The C-STM is then used to obtain the overall force-deformation and internal behavior, the failure mechanism, and the final mode of failure of both sound and ASR/DEF deteriorated C-beam specimens.

The above listed contributions are significant in the following ways.

The minimalist semi-empirical expansion model developed to simulate ASR/DEF induced expansion strains in reinforced concrete, is a rapid and relatively simple means of assessing the progression of expansion strains in a deteriorating structure. Based on this model, estimates can also be made on the total crack width that can be observed on the deteriorated structure.

The improvements to the C-STM technique makes the C-STM analysis rigorous and applicable to various loading and deformation scenarios. This technique can now equip researchers and practicing engineers alike with a more robust (than the force-based C-STM by Scott et al., 2012a,b) minimalistic analysis tool that can be used efficiently to determine the load-carrying capacity and the deformability of large concrete structures with significant D-regions. The C-STM also provides insight into the internal behavior of the structure, thus enabling better understanding of structural behavior. Based on the work presented herein it is now possible to know the final cause of failure of the structure. These characteristics of the C-STM are vital as this may assist engineers to devise the required strengthening or rehabilitation process for the structure.

The information from the expansion model may be used to assess the prestressing forces to be applied on the C-STM, which in conjunction with the modified concrete and steel material properties can be effectively used to model the force-deformation and internal behavior of ASR/DEF deteriorated structures. This will be an important analysis technique that may be helpful to state Department of Transportation (DOT) officials in evaluating structures showing signs of deterioration due to ASR/DEF.

The deterioration data collected from the C-beam specimen contributes to the limited pool of field data available on large-scale reinforced concrete structures showing severe damage due to ASR/DEF induced expansion strains. This sheds light on what one might expect to observe in terms of expansion strains and crack widths on structures severely affected by ASR/DEF deterioration.

The information from the destructive testing of the C-beam specimen promotes a more erudite understanding of the effects of severe ASR/DEF deterioration on reinforced

concrete structures. The experimental test results demonstrate the significance of how heavy ASR/DEF deterioration may affect the structural load carrying capacity, ductility and internal behavior of a structure. The experimental results contribute to the limited amount of data/information available on the effects of severe ASR/DEF on reinforced concrete structures.

#### **1.4 What Then is Particularly New in this Research?**

The deterioration of concrete structures due to the effects of ASR/DEF is of significance to structural engineers. Limited number of studies have been conducted on its effects on reinforced concrete structures, and there is not an efficient method to model these effects. This present research develops a minimalist semi-empirical model that can estimate the expansion caused by ASR/DEF in reinforced concrete. This can be used in conjunction with the C-STM to obtain the force-deformation behavior of ASR/DEF deteriorated reinforced concrete structures.

The C-STM model has proven to be an efficient minimalistic analysis technique to assess reinforced concrete structures with significant D-regions. Although it can give the force-deformation behavior of a structure, in its present state it is not capable of predicting the ultimate displacement. The current research will overcome this shortcoming and enable analysts to determine the entire force-deformation behavior of the structure including the final load and corresponding displacement at failure directly from the analysis. It will also enable analysts to infer the final cause of failure of the structure. Additionally, adaptations are also made to the C-STM to enable modeling of the structure subjected to reverse-cyclic loading.

Few earlier experimental studies have been conducted to study the effects of ASR/DEF on large-scale reinforced concrete structures. These studies have shown that slight to moderate amounts of ASR/DEF deterioration do not affect the load-carrying capacity of reinforced concrete structures. In fact, it was shown that structures affected by slight to moderate amounts of ASR/DEF deterioration showed slightly higher stiffness and a marginally higher load carrying capacity. However, the effects of severe ASR/DEF deterioration on reinforced concrete structures are still unknown. This present

research monitors and later tests a specimen that is subjected to severe ASR/DEF deterioration. This helps one to further understand the effects of significant concrete deterioration caused by ASR/DEF on reinforced concrete structures.

## **1.5 Organization of the Dissertation**

The dissertation is divided into ten sections. Following this introductory section, Section 2 presents a literature review which focuses on two broad topics. First, the historic developments in SAT modeling and the evolution of C-STM analysis technique. Second, a review of ASR/DEF phenomena, modeling ASR/DEF in concrete, and their effects on the performance of concrete structures.

Section 3 commences the main new work of this dissertation where computational tools are developed for structures that may or may not be affected by ASR/DEF induced deterioration. Section 3, in particular, presents the modifications to the force-based C-STM approach, to develop a more universal displacement-based C-STM which takes into account the concrete softening characteristics. The displacement-based C-STM approach is verified for both monotonic and cyclic loading with the results of large-scale experiments with respect to the overall and internal behavior.

Section 4 presents the development of a minimalist semi-empirical model to simulate the expansion strains caused by ASR/DEF expansion in reinforced concrete. First, the model is formulated to simulate expansion strains in reinforced concrete members that are cured under conditions of constant temperature and complete saturation, and validated against experimentally observed data. Following this, modifications are introduced into the model, to take into account the variation in temperature and humidity. This enables the model to be applied to reinforced concrete structures that are exposed to environmental conditions. The model is validated by simulating the field recorded expansion strains in reinforced concrete column splice specimens (Bracci et al., 2012).

Section 5 documents the visual observations recorded over the five year field exposure period leading to the severely deteriorated C-beam Specimen 3. Visual

observations, the surface strain measurements from DEMEC points on the concrete specimen, and concrete and steel strains obtained from the embedded instrumentation are also presented. Also presented in Section 5 are the progression of cracks at various ages of the specimen and the final crack widths that were measured on the specimen. Discussions are made based on the field observations.

Section 6 presents the application of the ASR/DEF expansion model developed in Section 4 to the field observations made for C-beam Specimen 3 presented in Section 5. Comparisons are made between the field observations and the expansion strains obtained from the predictive model. To demonstrate the repeatability of the model, the model is also applied to previously examined C-beam Specimens 2 and 4 expansion strains (Mander et al., 2012; Liu, 2012).

Section 7 presents the experimental test setup, the instrumentation details, and the experimental testing procedure for the heavily deteriorated C-beam Specimen 3. The performance, force-deformation behavior, and various other important observations made during the destructive testing of the heavily deteriorated C-beam specimen are discussed in detail. Comparison are made with the previously tested undamaged C-beam Specimen 1 and deteriorated Specimens 2 and 4 (Mander et al., 2012).

Section 8 presents the modifications that need to be made to the material properties to account for ASR/DEF damages in the structure. The preliminary analysis of the C-beam specimens using code-based methods are presented next. The application of the displacement-based C-STM analysis methodology to the C-beam specimens without and with ASR/DEF deterioration are also presented in this section. Finally, Section 8 studies the internal strains obtained from the C-STM model and the corresponding failure analysis results, in addition to modeling the overall force-deformation behavior of the C-beam specimens. All C-STM results are compared with the experimental results and differences discussed.

Section 9 presents case studies of two large-scale bridge piers that are part of the downtown San Antonio *Y* located along I-10 and I-35, that are subjected to ASR/DEF damage. This section presents the application of the expansion model, and the C-STM

analysis technique to these large-scale bridge piers. Finally, conclusions regarding the structural safety of the ASR/DEF deteriorated bridge piers are drawn accordingly.

Finally, Section 10 presents a summary of the dual experimental and analytical modeling program and the key findings from this study. Major conclusions from each of the sections are presented, and recommendations for future work are made.

In addition to the above mentioned ten sections, several appendices are presented. Appendix A1 presents an analysis schema for determining the structural capacity of cracked concrete bridge piers. The methodology is particularly useful for those portions of the bridge piers where disturbed regions may govern the behavior. Appendix A2 presents the computations for the preliminary analysis of the bent-cap specimens presented in Section 3. Appendix A3 shows the computation of reinforcement ratio and maximum expansion strains for simulating ASR/DEF induced expansion strains in C-beam Specimen 3. Appendix A4 presents the preliminary code-based computations for the analysis of all the four C-beam specimens presented in Section 8. Finally, Appendix A5 presents the computations for the C-STM analysis of the C-beam specimens. Additionally, calculations for the effective concrete material properties, and the prestrains to be applied on the C-STM model to simulate the effects of ASR/DEF into the analysis are also presented.



## **2 LITERATURE REVIEW OF PREVIOUS WORK, RESEARCH NEEDS AND QUESTIONS ARISING\***

### **2.1 Introduction**

This section presents a review of earlier work relevant to this study. First, a review of the earlier work related to ASR mechanism, laboratory experiments on ASR deteriorated reinforced concrete, and modeling ASR induced concrete deterioration are presented. This is followed by the DEF mechanism, and some relevant laboratory tests studying the effects of DEF in concrete. The effects of ASR/DEF deterioration in large reinforced concrete specimens is presented next. Finally, historic developments in the SAT modeling technique is presented, which is followed by the evolution of the C-STM.

### **2.2 Concrete Deterioration over Time: The ASR Chemical Process**

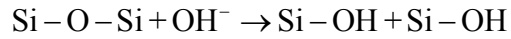
The expansion of concrete caused by the reaction between cement and aggregate was first reported by Stanton (1940). It is now well known that the reaction between alkalis in Portland cement and certain reactive silica in the aggregates can lead to what is called the Alkali Silica Reaction or ASR (Hobbs, 1988; Swamy and Al-Asali, 1988; Poole, 1992; among others). This can cause excessive cracking and deterioration of concrete structures (Multon et al., 2006; Deschenes et al., 2009; Bracci et al., 2012; Mander et al., 2012).

The overall process of ASR is still not fully understood. However, based on the present state of knowledge, ASR can be considered to be a multistage process, described as follows (Pesavento et al., 2012):

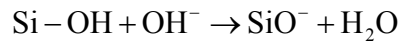
---

\* Previously published work is available to the public through National Technical Information Service. Mander, J.B., Karthik, M.M., and Hurlebaus, S. (2015). "Structural Assessment of "D" Region Affected by Premature Concrete Deterioration: Technical Report." *Report No. FHWA/TX-15/0-5997-2*, Texas A&M Transportation Institute, College Station, Texas, USA.

- The hydroxyl ions ( $\text{OH}^-$ ) in the pore solution react with silanol groups  $\text{Si}-\text{OH}$ , which cause the breakage of the siloxane bonds and the creation of additional silanol bonds (Bažant and Steffens, 2000; Kurtis, 2003).



- Silanol groups react with hydroxyl ions in the aggregate particle surfaces (Glasser and Kataoka, 1981; Bažant and Steffens, 2000), liberating more water.



Cations in the pore solution are attracted to the negatively charged group ( $\text{SiO}^-$ ).  $\text{Na}^+$  and  $\text{K}^+$  diffuse into the gel in sufficient numbers to balance the negatively charged group.

- After reaching the saturation point, a gel consisting of silica, alkalis, water, and other ions is created. The alkali-silicate gel has a higher specific volume than the reactants. The gel is hydrophilic, hence in the presence of water it expands causing a swelling process. The composition of the gel can vary a lot, thus making the prediction of its behavior quite difficult.

The extent of the damage induced by ASR depends on the magnitude and time-evolution of ASR induced strains. These in turn depend on several factors (Multon et al., 2006) such as the content of the reactive materials (alkali and reactive silica), environmental factors like temperature and humidity (Olafsson, 1986), water supply (Larive, 1998; Larive et al., 2000), stress conditions due to either mechanical loading (Larive et al., 1996; Gravel et al., 2000; Multon, 2004; Multon et al., 2004) or restraint provided to ASR expansion by steel reinforcement (Swamy and Al-Asali, 1989; Fan and Hanson, 1998; Monette et al., 2002; Multon et al., 2005).

### **2.2.1 Review of Laboratory Experiments on ASR Deteriorated Reinforced Concrete**

In this sub-section some of the relevant experimental studies that were conducted to study the performance of reinforced concrete affected by expansion due to ASR are reviewed.

Hobbs (1988) carried out tests on plain and reinforced concrete specimens and focused on axial strains measurements caused by ASR expansion. The concrete specimens were moist cured at a constant temperature of 20°C. Two series of tests were conducted, for Series I of the test the reactive particle size varied from 300–1200 µm whereas for Series II the particle size varied from 150–300 µm. The evolution of expansion strain over time was recorded. From the strain evolution data, researchers observed that as the reinforcement ratio in the reinforced concrete beam increased, the maximum expansion strain considerably reduced. It was also evident from the experimental results that irrespective of the amount of reinforcement present, the rise time, i.e., the time between the onset of ASR expansion until the final expansion was reached, was approximately the same. Hobbs observed that the reactive particle size had a considerable effect on the free expansion of ASR in plain concrete. Series I with larger reactive aggregate particles showed less expansion in plain concrete compared to Series II with finer reactive aggregates. The effect of the size of reactive particles in reinforced concrete was not as significant as observed in plain concrete.

Swamy and Asali (1989) conducted laboratory studies on the effects of ASR on the structural behavior of reinforced concrete beams. The beams ( $b \times d \times l = 75 \times 100 \times 800$  mm) were singly reinforced with shear reinforcement and two different reactive aggregates were used for the study. The specimens were placed in a fog room at 20°C and a relative humidity of 96 percent. The concrete expansion, cracking, and reinforcing steel strains were monitored. The researchers observed that the presence of tension face reinforcement subjected the beam to differential expansion. Due to the lack of compression face reinforcement the differential expansion caused a camber in the ASR affected beam specimens. Based on pulse velocity measurements, it was hypothesized that the ASR induced cracking was limited to the surface and did not always extend to the core of the beam. Load tests showed that the effects of ASR substantially reduced the stiffness of the beam, and beams affected by ASR did not appear to lose their ductility or capability to absorb large amounts of energy at failure. However, during the load tests, the ASR affected beams showed little sagging before failure as the loads were

insufficient to overcome the camber that was initially caused by the expansion. The irreversible strains caused by ASR accelerated the yield of the reinforcing steel under load tests and caused the beams to fail at lower loads compared to the reference sound beam.

Jones and Clark (1996) experimentally studied the effects of restraints on ASR expansion in reinforced concrete. The experimental program involved testing concrete cylinders ( $dia. \times l = 100 \times 200$  mm) with a single reinforcing bar running through the center of the cylinder, which were conditioned under different stresses and had various reinforcement ratios. Reinforced concrete beams ( $b \times d \times l = 100 \times 200 \times 2000$  mm) with two different reinforcement ratios, unreinforced prisms ( $200 \times 200 \times 100$  mm) and a concrete block ( $450 \times 300 \times 600$  mm) with reinforcement were also cast. After curing, most specimens were stored under water at 38°C. To study the effects of temperature on the expansion rate few specimens were also stored in water at 30°C and 20°C. The researchers observed that the applied stresses reduced ASR expansion, and even at higher applied stresses there was noticeable expansion. The increase in the reinforcement ratio caused a decrease in ASR expansion. However, observations also revealed that increasing the reinforcement ratios beyond 2 percent had minimal effect in decreasing the expansion caused by ASR. As observed earlier by Hobbs (1988), after the commencement of expansion, the expansion rate for all reinforcement ratios was constant until the final expansion was reached. Additionally, applied compressive stresses further decreased the expansion in reinforced concrete specimens, but beyond an applied stress of 2 MPa the reinforcement ratio made little difference in the expansion. Other important observations that were made in the experimental study was that the free expansion was dependent on the casting direction, size of the specimen appeared to have an effect on the expansion, rate of expansion had little effect on the relationship between restraint and expansion, the restraint did not significantly affect the expansion perpendicular to its direction, and with an increase in temperature there was an increase in the rate of expansion.

Fan and Hanson (1998) investigated the effects of ASR expansion on the structural behavior of reinforced concrete beams. The beam test specimens ( $b \times d \times l = 150 \times 250 \times 1500$  mm) were singly reinforced with different reinforcement ratios. Concrete cylinders ( $100 \times 200$  mm) were cast to study the effects of ASR on the mechanical properties of concrete. To simulate service load conditions, two beams (one reactive and one non-reactive) were preloaded until cracks of specific widths were observed on the tension side. The test specimens were placed in 0.5N alkali solution, and the solution in the tank was heated to 38°C. The tank was alternately heated to 38°C and cooled to 24°C for 5–7 days and two days, respectively. The expansion of the reactive specimen due to ASR started at about five months of immersion of the test specimens. The longitudinal expansion at the level of reinforcement was greatly reduced due to the restraint provided by the reinforcement. The difference in the reinforcement ratio did not cause any difference in the rate of expansion and cracking in the reactive beams. For the pre-cracked reactive beam, cracks were observed in the compression face after one year of conditioning. A substantial reduction in the compressive strength, splitting tensile strength and dynamic modulus were observed with the onset of expansion due to ASR. Results from the load tests on the beam specimens showed that the ASR expansion and cracking did not reduce the flexural load capacity of the reinforced concrete beams. The researchers hypothesized that the effects of ASR were limited to the beam surface or that since the beams were under-reinforced the reduction in concrete compressive strength made little difference to the beam flexural strength.

Ahmed et al. (1998) conducted experimental studies to investigate the effects of ASR on the static and fatigue strength of reinforced concrete. For the purpose of this study reactive and non-reactive (control) beams ( $b \times d \times l = 120 \times 100 \times 1300$  mm) were constructed with different reinforcement details, such as, with and without compression and shear reinforcement and with and without proper anchorage for the longitudinal reinforcement bars. The beams were stored for six months in a hot water tank at 40°C to accelerate ASR induced expansion. The expansion data showed that good anchorage of the longitudinal tension reinforcement is necessary for inhibiting the detrimental effects

of ASR expansion. Moreover, the addition of some compression reinforcement further reduced ASR induced expansion. The lateral expansion was also reduced with proper anchorage of longitudinal reinforcement and in the presence of shear reinforcement. As expected a rapid increase in the steel strain was observed with the commencement of ASR reaction. Ultrasonic Pulse Velocity tests further affirmed that the deleterious effects of ASR in concrete members can be reduced with good anchorage and with the presence of shear links. From the static test for shear, researchers observed that ASR increased the shear capacity of reinforced concrete beams with and without shear links, and the increase was greater in doubly reinforced beams affected by ASR. Fatigue tests demonstrated that neither the fatigue life nor the shear strength of beams were adversely affected by ASR, because of: (a) the prestress induced by the tensile reinforcement; (b) the beneficial effects of hydration of cement, which were greater than the detrimental effect of cracking; and (c) the ASR gel acting as a strong filler, which reduced the loss of tensile strength due to ASR reaction. The flexural stiffness of both the control and ASR affected specimens decreased significantly with increase in the number of cycles. The ASR affected beams also experienced lower deflections than the control specimens under repeated loading.

Monette et al. (2002) conducted experimental investigation on the effects of ASR expansion on reinforced concrete beams ( $b \times d \times l = 90 \times 120 \times 900$  mm) conditioned without loads and under sustained and cyclic loads. Concrete cylinders ( $100 \times 200$  mm) were used to monitor the concrete expansion and compressive strength, and concrete prisms ( $100 \times 75 \times 400$  mm) were used to monitor resonant frequency and concrete flexural strength. The major goals of this research were to examine the relationship between measured ASR expansions and visual observations of ASR on the beams and quantify the damage using Damage Rating Index (DRI), and make observations on the residual strength and stiffness of the beams under different conditioning loads. The reactive and non-reactive beams, respectively, were conditioned under one normal Sodium Hydroxide (NaOH) at 38°C for 147 days and 161 days and were air dried for 150 days and 60 days. The expansion data showed that the sustained and cyclic flexural

conditioning loads and the longitudinal reinforcement had significant restraining effects on ASR expansions. The DRI measurements were unable to differentiate between the mechanical cracks and the cracks caused by ASR expansion, and the expansion measurements better indicated the expansion due to ASR. The beams were load tested to failure under four-point bending. All the beams, both reactive and non-reactive, showed similar load-deformation behavior, even when conditioned under different loads. Tests on the mechanical properties of concrete revealed that ASR did not prevent the increase in concrete compressive strength with time; however, concrete cracking caused by ASR significantly reduced the stiffness of the reactive concrete cylinders. The dynamic modulus of elasticity was found to be less sensitive to ASR effects when compared to the static modulus of elasticity. Researchers also observed that the flexural strength of concrete reduced with ASR expansion and it was more sensitive to ASR expansion than the concrete compressive strength.

Mohammed et al. (2003) conducted an experimental investigation on how various restrained conditions provided by the embedded steel reinforcement in concrete could affect the strains induced on the concrete surface and the steel bars. For this study, plain and reinforced concrete prisms ( $b \times d \times l = 250 \times 250 \times 600$  mm) and cylinder specimens ( $100 \times 200$  mm) were cast with and without reactive aggregates, and then submerged in seawater at 40°C for a period of 200 days. The study was oriented in determining if the degree of restraint provided by the reinforcement, location of reinforcement, and the presence of stirrups had any effects on the concrete surface and steel strains. Eight different cases, which included plain concrete and concrete with different restraint conditions and reinforcement ratios, were considered. From the deterioration data, researchers observed that the degree of restraint had significant influence on the concrete surface strain and the strains in the bars. Additionally, the closer the reinforcement was to the concrete surface, less concrete surface strains and higher steel strains were observed. The presence of stirrups did not appear to have any significant effect on the lateral expansion or the longitudinal steel strain. Additionally, the strains in the lateral reinforcement were higher compared to their longitudinal bars.

However, the influence of lateral reinforcement was not fully established as only one configuration was tested and investigation of beams with more confinement by stirrups was necessary.

Multon et al. (2005) conducted experiments to study the effects of ASR on the structural behavior of concrete. The major scope was to study how moisture gradients in the structure affected the structure, as this could lead to differential ASR development and expansion. For this study, plain and reinforced concrete beams ( $b \times d \times l = 250 \times 500 \times 3000$  mm) were cast along with concrete cylinders ( $160 \times 320$  mm) and prisms ( $b \times d \times l = 140 \times 140 \times 280$  mm) to study the evolution of the mechanical properties of concrete. The bottom of the concrete beams was immersed in water and the upper face was exposed to air at 30 percent relative humidity. The side faces were covered with watertight aluminum sheets to ensure a vertical drying process. The beams were stored in an air-conditioned room with 30 percent relative humidity at 38°C. From the deterioration data collected for about 14 months of exposure, the following major conclusions were drawn. The ASR expansion was highly anisotropic and significant expansions occurred even without external water supply. Distribution of water within the reactive specimen induced large expansions in the transverse and vertical directions between depths of 170 mm to 500 mm from the top of the specimen, and shrinkage on the exposed drying face. As evident in the earlier tests, researchers noticed that the longitudinal reinforcement caused a large decrease in ASR expansion strain. However, the local effects on stirrups were hardly significant on the vertical and transverse deformations.

The experimental studies conducted by various authors on the effects of ASR expansion on reinforced concrete elements clearly established that the presence of reinforcement significantly decreases the expansion caused by ASR in the direction of the reinforcement. Additionally, to enable prediction of expansion strains in concrete, there is a need to model the expansion caused by ASR in concrete structures. Various authors proposed models to simulate the expansion caused by ASR in concrete. Models that are relevant to this study are briefly reviewed in the following sub-section.



### **2.2.2 Review of Modeling ASR Induced Expansion Strains**

This section concentrates on the relevant developments on modeling the expansion caused by ASR in plain and reinforced concrete.

Hobbs (1981) presented a model to predict ASR induced expansion in mortar. Hobbs assumed that ASR expansion was a two-stage process where, in the first stage the alkalis and reactive silica react rapidly until one of the reactants is depleted, and in the second phase the reaction product absorbs water and hydroxyl ions to form alkali-silica gel, which expands and causes cracking in the mortar. The author presented expressions that predicted the time to cracking and the expansion caused by ASR. However, the expressions had a few constant terms that were determined numerically from the experimental data. The proposed model was observed to be in general agreement with observed expansion behavior of mortar bars, which were stored under water at 20°C.

Groves and Zhang (1990) presented a dilation model for the expansion of silica glass in ordinary Portland cement mortar. This model was based on the observation that the main reaction product was a layer of C-S-H gel that was formed at the surface of the glass. The mortar expansion was predicted as the increase in the glass volume plus the reaction product layer, and was found to be in the same order of magnitude as the observed results.

Clark (1991) carried out studies in order to identify the main factors to be considered in modeling the effects of ASR on a structure. Clark found it necessary to consider numerous factors to efficiently model the effects of ASR on a structure, including: the proportion of reactive particles; particle size; porosity of the aggregate and concrete; curing conditions; rate of expansion; specimen size; reinforcing steel content; specimen shape; and casting direction, etc. Clark advised caution when extrapolating modeled results to prototype structures, as accelerated laboratory conditions may not be observed in the field. Clark's study provides a glimpse on how complex it is to model each of the interacting factors where ASR may adversely affect reinforced concrete behavior.

Charlwood et al. (1992) presented a phenomenological model in which the expansion was treated as an initial strain induced by temperature increase. The anisotropic expansion was dependent on the stress state and was defined as a function of the stress tensor. Although this model was simple and effective, it did not consider the detailed mechanism of ASR.

Furusawa et al. (1994) dealt with modeling the chemical reaction and the ensuing expansion in the case of ASR. They assumed that the rate of diffusion of hydroxyl and alkali ions into the aggregate determined the overall propagation rate of ASR. The researchers also assumed that there was a porous zone around the aggregate and expansion was initiated only after the reaction product exceeded the volume of this porous zone. From an analysis of powdered specimens at the end of mortar bar tests, a close agreement was found between the estimated and actual values of total amount of reaction products. The proposed model was able to capture certain characteristic features of ASR related expansion such as the initial incubation period, varying rates of expansion, and the shapes of expansion-time curves. However, the applicability of this model to reinforced concrete needed further investigation.

Pietruszczak (1996) proposed a continuum theory for the description of mechanical effects of Alkali Aggregate Reaction (AAR) in concrete. In the formulation of this phenomenological approach restricted to isothermal conditions, the progressive expansion of concrete due to ASR was coupled with the degradation of mechanical properties, which was described within the framework of elastoplasticity. They assumed a reduction in Young's modulus and the compressive and tensile strength of concrete due to ASR expansion. The rate of expansion however was assumed to depend on the available alkali content in the cement matrix. Other important factors like the variation of temperature and humidity effects on the rate of the reaction were not considered. Huang and Pietruszczak (1996) later made modifications to the model and included a parameter to control the rate of strain softening. The authors developed an implicit integration scheme for the implementation of the continuum model in a finite element analysis. An application of the numerical analysis to a powerhouse was also presented.

In a later development Huang and Pietruszczak (1999) assumed that the expansion rate depended on the alkali content, magnitude of confining stress, and the evolution of temperature. The authors discussed a mathematical formulation under nonisothermal conditions, describing the thermomechanical effects of ASR. The temperature of the concrete mass was assumed to affect both the rate of volumetric expansion and the degradation of mechanical properties. A notion of thermal activation time was introduced to formulate the evolution law for ASR induced expansion. The formulation presented focuses on the description of long-term degradation resulting from continuing ASR, and the influence of temperature fluctuations on the instantaneous values of material constants was neglected. A finite element model consisting of about 23,000 four-node tetrahedral elements was used for the analysis of a power plant consisting of gravity dams, powerhouse, and water intake structures. The analysis was carried under nonisothermal and isothermal conditions. The predictions based on the thermomechanical analysis were consistent with the field measurements. However, the continuum approach presented by these researchers is complicated to implement. Additionally, the analysis involves employing the non-unique complexity of finite element models to determine the effects of ASR on the structure.

Léger et al. (1996) presented a flowchart for the numerical simulation of concrete expansion in dams affected by AAR. The authors note that due to the complexity of ASR expansion, any simulation model has to be calibrated against the displacements recorded from the monitoring system and strains in rebars and concrete when possible. Normalized expansion factors for different zones of the dam considering confinement, temperature, moisture, and material reactivity were introduced into the numerical simulation. A calibration factor was also introduced to adjust the computed displacements to match the field measurements. This model was based on trial-and-error to match observed deformations and did not reflect the physical mechanism.

Bažant and Steffens (2000) proposed a mathematical model for a quantitative prediction of ASR expansion. The two problems to be dealt with were identified as the kinetics of the chemical reaction with the associated diffusion process and the fracture

mechanics of the damage process. The authors only address the kinetics of the reaction in this work. The study was done on ground waste glass used as an aggregate in concrete; the authors noted that it could be extended to cases where natural aggregates were used. Their model was developed by analyzing an idealized repetitive cubical cell with one spherical reactive particle. The radial growth of the spherical layer of basic ASR gel was assumed to be controlled by the diffusion of water through the gel layer toward the reaction front. Concrete, however, resists this swelling and a pressure is developed. Parametric studies on the numerical solutions clarified the effects of particle size. However, it is not clear how this model could be applied to concrete with natural aggregates, as waste glass consists entirely of silica and a radial growth can be assumed.

Ulm et al. (2000) proposed a chemoelastic model for ASR swelling in concrete from the level of macroscopic material modeling to the level of analysis for full-size concrete structures. This was a first-order engineering approach to capture the timescale and magnitude of ASR expansion. Two timescales, specifically (a) the latency time associated with the dissolution of reactive silica, and (b) characteristic time scale associated with ASR product formation, were required for a realistic prediction of structural effects caused by ASR. In the model, concrete is considered as a porous medium consisting of a solid matrix skeleton with ASR gel occupying the voids. In their analogue spring model, one spring modeled the gel (comprising of an expansion cell in series with a linear spring representing ASR gel expansion and gel compressibility, respectively) while the other modeled the concrete solid matrix. The researchers concluded that temperature played a major role in ASR expansion kinetics. However the effects of humidity and stress induced anisotropy of ASR swelling were not considered in this model. Additionally, the equations derived remain complex and not amenable for application by practicing engineers.

Capra and Sellier (2003) noted that due to the random distribution of reactive sites and the lack of complete understanding of the chemical reactions, it becomes difficult to model ASR. The authors presented a new approach, based on the probabilistic description of the main physical parameters of concrete and AAR, that

allowed simulation of the orthotropic swelling of concrete subjected to AAR. In order to perform structural computations, reactions were modeled within a phenomenological approach framework by taking into account the reaction kinetics, temperature, moisture, and stress state. Concrete was modeled as a damageable material having elastic and inelastic strains, whereas AAR was modeled by a global kinetics including temperature and humidity effects. Modeling of AAR also took into account the probability of cracking due to AAR and due to tensile and compressive stresses. A coupling between the mechanics and AAR was established by introducing damage coefficients and this made it possible to simulate tests carried out on concrete specimens. The model showed good agreement with the longitudinal and transverse swelling data of concrete specimens subjected to uniaxial loading.

Frangé et al. (2004) presented a macroscopic approach where the uncoupling between AAR and stress and the representation of anisotropic characteristic of chemical swelling was considered. In their constitutive model, Ulm et al.'s (2000) analogue model for concrete was modified by adding a cohesive joint element for modeling crack opening in tension, represented by concrete tensile strength. The proposed model was able to simulate laboratory tests concerning reactive concrete samples under constant uniaxial loading. For the case of free expansion, isotropic behavior was assumed, which led to an overestimation. Factors such as random distribution of reactive sites, temperature, and moisture conditions could be incorporated into the model to improve the modeling for free expansion. The model was able to represent adequately the unloading and loading behavior of AAR affected concrete. Further studies were recommended to study the coupling between stresses and AAR to extend the application of the model to structures under complex loading conditions and boundary conditions. One of the shortcomings of the model is that the gel and concrete properties and the characteristic parameters for gel kinetics are required as an input for the implementation of the model, which could be a difficult task in itself for existing ASR damaged structures. There could also be difficulty in implementation of this finite element approach for complex structures.

Fairbairn et al. (2005) presented a thermo-chemo-mechanical expansion model for ASR. In their model the stress induced anisotropy was represented by a classical smeared cracking model. The influence of temperature and humidity in ASR expansion was considered. Their model was an enhanced version of the model proposed by Ulm et al. (2000), to better capture the cracking of the concrete skeleton. The model was applied to a concrete dam affected by ASR through a finite element code, and a good agreement between the experimental and numerical data was observed.

Saouma and Perotti (2006) proposed a new thermo-chemo-mechanical model that was rooted in the chemistry (kinetics of the ASR reaction), physics (crack gel absorption, effect of compression), and mechanics of concrete. A few considerations that were taken into account in the proposed model were the kinetics and volumetric expansion of the ASR gel, temperature, constraining effects of compression on ASR expansion, effects of triaxial compressive state of stress and high compressive hydrostatic stresses on the ASR expansion, and reduction of tensile strength and elastic modulus due to ASR expansion. Anisotropy of the ASR induced expansion was accounted for by assigning weights to each of the three principal directions. The model was used in the analysis of a dam subjected to ASR deterioration. Extensive preliminary work was conducted to prepare the necessary initial data for the model. The results from this model were compared to the current state of the practice model proposed by Charlwood et al. (1992). The dam structure was subjected to the same final crest displacement using the two models. However, the internal field stresses were drastically different in the two models considered. The lack of stress redistribution in Charlwood's model led to an underestimation of the stress field.

Multon et al. (2006) noted that the major parameters to be considered for predicting the mechanical behavior of ASR-damaged structures are the concrete mixture, environmental conditions, water supply, the stresses due to mechanical loading, and the restraint to ASR expansion caused by the steel reinforcement. The analysis showed that steel reinforcement not only caused direct prestressing effects by restraining ASR expansion, but the compressive stresses due to local restraints by steel caused a

reduction in ASR expansion along the compressed direction. The study found that taking into account the elastic effects of reinforcing bars alone could not explain the structural behavior of reinforced beams subjected to ASR. ASR expansion was not only counteracted by compressive stresses, but it appeared to be largely prevented in the compressed direction. A reduction factor in the range of 0.45–0.30 was used to account for this effect. The model could, however, not be used for predictive purposes for the case of reinforced concrete. The authors conclude that the effect of compressive stresses on ASR expansions had still not been solved by predictive models using chemoelastic concepts.

Winnicki and Pietruszczak (2008) proposed a continuum approach for describing chemomechanical interaction in reinforced concrete. Mathematical formulations were derived for the mechanical degradation of reinforced concrete due to ASR. Based on Pietruszczak and Winnicki (2003), the material was treated as a composite medium consisting of the concrete matrix and two orthogonal families of reinforcement. The model was formulated in two stages: Phase I dealt with homogeneous deformation mode prior to cracking of the concrete matrix; and Phase II involved the localized deformation associated with formation of macrocracks. The numerical analysis was restricted to the material point level in order to validate the formulation against experimental data involving homogeneous stress states. The formulation was able to capture the basic trends in mechanical response of reinforced concrete subjected to ASR effects and external loading. However, the mathematical formulations may be considered rather difficult for implementation by practicing engineers. The validity of the formulation also needs to be verified for actual reinforced concrete structures, particularly reinforced concrete beams that are not under homogeneous stress states.

Many of the modeling approaches that have been briefly reviewed here are limited to ASR expansion caused in plain concrete, and almost all require a finite element implementation to predict the expansion caused in concrete. Very limited studies have been conducted in studying ASR related expansion in reinforced concrete. The various methodologies presented take into account different factors that affect ASR

related expansion, which is important in fully understanding the phenomena. However, this leads to more complex equations and difficulties may arise during its implementation on structures. In the present research a general strain-based approach is proposed as a minimalist, easy to implement, semi-empirical model for the analysis of swelling strains in reinforced concrete members where the reinforcement ratios are different in each of the three orthogonal axes.

### **2.3 Delayed Ettringite Formation: The DEF Chemical Process**

Delayed Ettringite Formation (DEF) is the formation of ettringite and associated expansion when the concrete is subjected to high temperature during its curing period. Experiments have shown that when mortar/concrete is subjected to high temperatures during the curing and hardening process, they tend to expand and crack when subsequently exposed to moisture. The chemistry/phenomenon behind DEF is explained in the following paragraph (Folliard et al., 2006).

Very early in the cement hydration process calcium aluminates ( $C_3A$  and  $C_4AF$ ) react with gypsum ( $C\hat{S}H_2$ ) to produce ettringite ( $C_3A.3CaSO_4.32H_2O$ ). After the completion of this reaction, if additional  $C_3A$  is available, calcium monosulphoaluminate ( $C_3A.CaSO_4.12H_2O$ ) or monosulphate forms. There is a general tendency for monosulphate to exist in higher proportions than ettringite, but it is not uncommon to find both hydrates in the hydrated cement paste. After a majority of the ettringite is formed, calcium silicate hydrate (C-S-H) gel fills in the bulk of the concrete matrix and provides much of the concrete strength. At elevated curing temperatures ( $>70^\circ C$ ) C-S-H gel production is accelerated when compared to ettringite. The accelerated formation rate of C-S-H gel physically traps some of the sulphates and aluminates in its layered structure before they can react to form ettringite (Older, 1980; Fu, 1996; Scrivener et al., 1999). At high curing temperatures, the trapping continues until the C-S-H gel becomes fully saturated with sulphates. Ettringite and then monosulphate are formed with the remaining sulphates as would occur in concrete cured in ambient temperatures. After the concrete has gone through the entire heat curing cycle, and is stored in a moist environment at ambient temperatures, the sulphates diffuse out of the C-S-H gel into the



pore solution. This provides an internal source of sulphate and triggers the reformation of ettringite in hardened concrete. This reformation of ettringite causes expansion and cracking of concrete. This delayed or secondary formation of ettringite in hardened concrete is widely known as Delayed Ettringite Formation.

### **2.3.1 Experimental Investigations on DEF**

A brief review of relevant past work with regard to DEF in concrete is presented in what follows.

Heinz and Ludwig (1987) investigated the causes of loss in strength and damages to structures that were precast units made of high strength concrete and heat treated during production. In particular, these damages occurred in structural components that were exposed to frequent moisture saturation for several years. The authors carried out an experimental investigation on mortar prisms, concentrating on the threshold temperature of damage, SO<sub>3</sub> content in cement, storage humidity, and the water-cement ratio. Heat treatment at temperatures above 75°C led to expansion linked with a decrease in strength. Temperatures below 75°C did not bring any damaging reaction in the specimen. The researchers suggested keeping the SO<sub>3</sub>/Al<sub>2</sub>O<sub>3</sub> molar ratio in cement to below 0.55 to minimize the contribution of SO<sub>3</sub> toward the deterioration of concrete. The samples that were stored under water showed early signs of the damage reaction and different water-cement ratios did not cause any variation in the swelling reaction.

Scrivener and Taylor (1993) tested cement paste samples that were cured at 80°C and examined them by scanning electron microscopy, X-ray microanalysis, and X-ray diffraction immediately or after storage in water for various periods at 20°C. The experiments showed that ettringite present in the cement paste was destroyed during curing in water for 16 hours at 80°C. After the heat treatment, aluminate and sulphate were largely present in the C-S-H gel. Ettringite formation, in the form of very small crystals thinly distributed in the C-S-H gel, started within a few days after the heat cured specimen was stored in water at 20°C. The ettringite recrystallized in cavities 5–10 μm in size, and there was no indication that this process disrupted the surrounding material in any way different from the surrounding empty but otherwise similar cavities. The

ettringite seen at aggregate interfaces in mortars and concretes expanded following recrystallization. From these observations the authors were of the view that the paste expanded, thereby creating spaces around the aggregate particles. The ettringite seen at the interfaces was a result of these expansions and was not what caused the expansion.

Based on field reports of damage associated with DEF in non-steam cured concrete (Pettifer and Nixon, 1980; Jones and Poole, 1986; Larive and Louarn, 1992), Diamond (1996) refuted the claim that DEF is confined to steam cured concrete that had been subjected to excessive temperatures during curing. The crack pattern observed were a network, with cracks running partly along the aggregate peripheries (rim cracks), generally connecting cracks running through the cement paste (paste cracks). This pattern reflected local and inhomogeneous crack propagation. In concrete affected by DEF, the crack network resulted in a severe loss of dynamic elastic modulus. Filling up of fine air voids by ettringite may also interfere with frost resistance.

Kelham (1996) studied the effects of cement composition and fineness on expansion associated with DEF. Kelham concluded that curing temperature was a dominant factor in determining the extent of expansion, while the expansion also increased with cement fineness, alkali, C<sub>3</sub>A, C<sub>3</sub>S, and MgO contents.

Hobbs (1999) conducted laboratory studies to investigate the factors that caused DEF in precast concrete and cast in-situ concrete structures that saw high temperatures during curing and were subsequently subjected to wetting and drying cycles. Hobbs observed that laboratory studies on mortar and concrete showed that DEF related expansion was not possible when the early temperatures were below 71°C. Based on the laboratory and field observations it was estimated that for DEF to occur in cast in-situ concrete, the initial curing temperature had to exceed 85°C. Hobbs also observed that the laboratory specimen showed a reduction in water/cement ratio, greatly prolonged the time to expansion, and resulted in a higher final expansion. Based on the study on the composition of cement, Hobbs concluded that no single product was responsible for the expansion, and that it was a combination of parameters like MgO, SO<sub>3</sub>, equivalent Na<sub>2</sub>O content, and the fineness of cement that contributed to the final expansion. Hobbs

established that not all cements having low contents of the above constituents were immune to DEF or vice-versa, and it was not possible to predict the susceptibility to expansion based on the cement composition alone.

Lawrence et al. (1999) presented case studies on concrete structures that showed signs of excessive cracking as early as one year after construction. Two types of noticeable cracks were noticed on the precast prestressed concrete box beams that were investigated. The first type was hairline map cracking as was observed in structures affected by ASR, while the second type of cracking, although it had a map type pattern, had cracks that were as wide as 6.35 mm and were predominantly confined to the end block region of the girder. Based on a review of fabrication and material documentation, chemical analysis, petrographic examination, and scanning electron microscopy, they concluded that the cracking was associated with DEF expansion while ASR was ruled out. During the investigation it was revealed that all other materials and storage conditions remaining the same, the box beams that were cast using ASTM Type III (high-alkali) cement showed signs of deterioration whereas those cast using ASTM Type III (low-alkali) cement did not show DEF deterioration and were declared to be sound beams.

Taylor et al. (2001) offers a good review of the developments that have been made in understanding the DEF phenomenon. The authors briefly review various topics pertaining to DEF such as temperature range, expansion, chemistry, microstructural changes, mechanism of expansion, physical chemistry of crystal growth, factors governing expansion, effect of concrete, or mortar micro structure expansion, among other relevant topics. From a review of previous work, the authors conclude that temperature was a critical factor for the formation of DEF, disputing the claim by some authors (Mielenz et al., 1995; Diamond 1996; Collepardi, 1999) that DEF can cause damage in concrete that had not experienced elevated temperatures. The authors also suggested exercising caution while extrapolating laboratory test results to field conditions. They also proposed that the traditional practice of studying expansion in mortar/concrete bars with different kinds of cement, by placing them in the same water

tank was unsound. The authors noted that although a lot of studies have been conducted on DEF, it was still not properly understood (in 2001) and that the effect of the various variables that affect DEF should be studied by varying one parameter at a time.

Collepari (2003) in his review of the state-of-the-art of DEF attack on concrete classifies ettringite formation in concrete as Early Ettringite Formation (EEF) and DEF. EEF, or primary ettringite, occurs homogeneously and immediately (within hours or days of a concrete pour). The related expansion does not cause localized and disruptive action as the concrete is still deformable. However, DEF occurs heterogeneously and at a later time (after months or years). The related expansion causes cracking and spalling of concrete as it occurs in rigid, stiff, and hardened concrete. The author further classifies DEF as External Sulphate Attack (ESA) where the environmental sulphate from water or soil penetrates the concrete structure, and Internal Sulphate Attack (ISA) where the sulphate attack occurs from the late sulphate release from gypsum-contaminated aggregates or thermal decomposition of ettringite. High permeability of concrete, sulphate-rich environment, and presence of water were identified as the necessary conditions for ESA related DEF. For ISA related DEF, micro-cracking in concrete, late sulphate release and exposure to water were considered three essential factors.

Barbarulo et al. (2005) conducted laboratory tests on mortar bars to study if a cementitious material could develop DEF under its own heat of hydration as was reported in various field observations (e.g., Hobbs, 1999; Lawrence et al., 1999). From the experimental work the researchers observed that the heat of hydration did indeed cause the formation of DEF. This was the first time that this was confirmed in a laboratory setting, although it was widely accepted from field observations. They also conducted studies to determine if concrete steam-cured long after its hydration process would present DEF symptoms in the long term. In this regard, one-year old mortar bars were subjected to one month of steam curing at 85°C. The test samples that did and did not expand from DEF previously, expanded further when subjected to reheating. This was the first time this observation was made, and the authors concluded that the DEF phenomenon was not solely related to the high temperature during the hydration process.

Ekolu et al. (2007) experimentally studied concrete mortar specimens with microcracks induced by ASR expansion and freeze-thaw cycles; the influence of the microcracks on DEF expansion was then investigated. The presence of the microcracks resulted in an early onset of DEF and also greater expansion strains in the mortar specimens. Maximum DEF related expansions were recorded for a critical range of ASR expansion, beyond which any further increase in microcracking reduced the extent of DEF expansion.

DEF due to high heat of hydration has been reported in structures with mass pour of concrete, like various parts of bridge structures (abutments, piers, wing walls and piles as reported in Wimpenny et al., 2007), concrete blockwork walls (Eriksen et al., 2006; Baldwin and Knights, 2010), and concrete armor units (Fozein Kwanke et al., 2009) in maritime works. DEF has also been increasingly detected in combination with ASR (Ingham, 2012), which has a similar expansion and cracking pattern.

Brunetaud et al. (2008) studied the effects of DEF related expansion on the dynamic modulus. The researchers concluded that for negligible swelling (expansion < 0.04 percent) the dynamic modulus slightly improved with time and reached a plateau within 1 to 2 years. For weak swelling that resulted in linear expansion (final expansion amplitude between 0.04–0.2 percent), the expansion rate was limited by the stiffness of the material by a linear relationship between the rate of expansion and the dynamic modulus. This behavior did not result in any notable modification of the concrete mechanical properties, at least until an expansion of 0.1 percent. Large swelling that resulted in sigmoidal expansion (final amplitude >0.4 percent), caused a decrease in the dynamic modulus. After the swelling reached its plateau, the dynamic modulus improved gradually due to filling of the previously open cracks by ettringite. The researchers observed that the compressive strength could decrease as much as 63 percent for an expansion of 1.2 percent. Pavoine et al. (2012) observed that the dynamic elastic modulus can drop (by 37 percent) in the course of inner sulphate attack. This, however, is compensated in the long term, where the formation of ettringite in the voids helps to a gradual increase in the dynamic elastic modulus.

Bouzabata et al. (2012) investigated the mechanical conditions acting on DEF expansion, including the analysis and quantification of the mechanical effects of restraint on DEF expansion. In this regard the following points on the mechanical behavior of concrete undergoing DEF expansion were analyzed: isotropy of stress-free expansion, anisotropy of expansion under restraint, and consequences of DEF expansion on compressive strength. From the experimental observation for a period of about 600 days the following conclusions were made: (a) under stress free conditions DEF expansion was isotropic; (b) compressive stresses decreased expansion due to DEF and caused cracks parallel to the restraint; (c) larger the restraint smaller was the DEF expansion observed; (d) DEF expansion in the stress-free direction of the restrained specimens remained unchanged to those of free expansion, which implied that the DEF expansion under restrained conditions was anisotropic; (e) the concrete compressive strength decreased significantly within 70 to 100 days (corresponding to significant expansion); (f) and a slight increase in compressive strength was observed after the expansion stabilized at about 180 days. The authors also noted that DEF is a more localized phenomena because once they crystalize, they cannot move easily in the cracks unlike ASR gel that can migrate in the porosity and cracks after their formation. Therefore the structural models have to take into account this localized effect to assess DEF damaged structures.

### **2.3.2 Review of Modeling DEF Induced Expansion Strains**

Limited literature is available on modeling the effects of DEF on reinforced concrete structures, a few of which are reviewed next.

Seignol et al. (2009) developed a new model to assess concrete structures subjected to the effects of DEF expansion. In their constitutive model, chemical degradation was represented by a prescribed expansive strain and a damage law. The variables representing the mechanical effects of DEF were explicitly dependent on the material moisture and the stress tensor. A model was also proposed to take into account the strong relationship between early-age temperature history and DEF development.

Using a finite element program, the authors illustrated the application of the model on a prototype structure affected by DEF.

Martin et al. (2010) conducted an experimental investigation on concrete cylinders to compare the effects of DEF-only expansion with combined effects of DEF and ASR expansion. Higher expansion strains were recorded in specimens that were subjected only to DEF when they were immersed in water, than when they were stored in 100 percent relative humidity (RH) atmosphere. The specimens subjected to DEF-only and DEF and ASR expansion showed similar maximum expansion strains when they were immersed in water. However, the specimens with combined DEF and ASR showed slightly early onset of expansion strains compared to the DEF-only specimens. When immersed in water, the ASR contribution to the overall expansion strain of the specimens was minimal, whereas when exposed to 100 percent RH atmosphere, ASR contributed to about one-third of the overall expansion strains. This was associated with the leaching of alkalis that could occur when the specimen was immersed in water. Martin et al. (2010) hypothesized that DEF mechanism occurred prior to ASR. Based on the expansion strains that were recorded from the concrete cylinders, they proposed a model for the expansion strains due to the combined effects of DEF and ASR. Their proposed model demonstrated the respective contributions of DEF and ASR. However, all parameters in the empirical model were inferred from a least-squares fit with the experimental results.

Martin et al. (2013) presented a chemo-mechanical model to reassess structures affected by ASR/DEF expansion. Their model took into account the coupling between the expansion and the moisture content by introducing coupling functions, thereby enabling the behavior of ASR to be simulated, as long as alkali leaching was not a factor. However, the model did not simulate the behavior of DEF affected structures. This was attributed to the inability of the model to account for the intense water uptake due to crack development in the structure.

Salgues et al. (2014) proposed a physio-chemical model to predict the kinetics and the amount of DEF in concrete subjected to curing at high temperatures. Several

phenomena like the thermodynamic equilibrium of hydrate crystallization, binding of ions to hydrated calcium silicates and the mass balance equation were considered. Their model was used to simulate the free expansion test of concrete cylinders subjected to DEF using a finite element program. The computed kinetics of ettringite formation were correlated with the measured expansion on the concrete cylinder specimens.

In the current research a minimalist, practical, and easy to implement approach to model the effects of DEF in reinforced concrete structures is proposed.

## **2.4 Structural Deterioration due to ASR/DEF**

Ingham and McKibbins (2013) give a brief review on the causes of cracking in structural concrete. Various factors like under-design, corrosion of reinforcement, thermal contraction of fresh concrete, and ASR and DEF are identified. The authors state that serviceability issues in concrete structures were in one way or the other related to concrete cracking. While concrete cracking may not result in failure of the structure, it is usually indicative of undesirable mechanisms taking place within the concrete structure. Few of the latest studies that were performed to study the effects of ASR/DEF induced deterioration on large-scale reinforced concrete structures are reviewed in the following subsections.

### **2.4.1 TxDOT Project #12-8XXIA006**

Deschenes et al. (2009) conducted experimental tests on near full-scale bent-cap specimen ( $b \times d \times l = 533 \times 1067 \times 8433$  mm) to study the effects of ASR/DEF deterioration on the structural capacity of these reinforced concrete members. Shear span-to-depth ( $a/d$ ) ratio of 1.85 (deep beam) and 3 (sectional) was accommodated at opposite ends of each specimen. This was one of the first studies to conduct such large scale structural testing to study the effects of ASR/DEF deterioration on reinforced concrete beams. The study included two non-reactive and four reactive bent-cap specimens. High-alkali Portland cement and reactive fine aggregates were used to promote ASR in the specimen. Hot mixing water and external heaters were used to promote the formation of DEF in the specimen. The completed concrete beams were



moved outdoors under conditions favorable for the development of realistic ASR and DEF damage. A sustained load was applied to replicate the impact of externally applied stresses on the propagation of ASR/DEF. The load conditioning on the specimens was maintained close to field representation. After a year of field exposure three (one non-reactive and two reactive) of the six specimens were tested in the laboratory. The results suggested that the ultimate shear strength was not diminished by ASR/DEF deterioration as long as the deteriorated concrete was actively confined by reinforcement. The longitudinal reinforcement minimized the expansion of the beam in the longitudinal direction. As a consequence, damage accumulated in the transverse direction and significant tensile strains generated in the transverse reinforcement. After yielding the confinement potential of the reinforcement was lost leading to accelerated expansion. The minimum shear reinforcement recommended by AASHTO (2007) failed to effectively restrain the long-term expansion due to ASR/DEF. Samples extracted out of the specimen core lacked any visible signs of deterioration. Within the structural core, the confining stresses introduced by the reinforcement prevented the development of severe cracking. Tests on deteriorated concrete cylinders indicated a reduction in elastic stiffness. However, the structural test of the specimen revealed that the load response of the deteriorated specimen was equivalent to the undamaged specimen, and the loss of elastic stiffness as indicated in the material testing was not representative of the deteriorated specimen. Deschenes et al. (2009) also observed that the deflection of the deteriorated specimen at any given service load was less than the undamaged beam. ASR/DEF deterioration did not have any effect on the failure mode of the sectional or deep beam shear spans. However, the authors note that the structural safety of structures subjected to long-term exposure and related deterioration need to be further investigated.

#### **2.4.2 TxDOT Project #0-6491**

A part of the study by Gianni et al. (2013) was to determine the effects of severe deterioration caused by ASR/DEF reaction. The test specimens were similar to those by Deschenes et al. (2009); however, the reinforcement details were altered to ensure flexure failure rather than shear failure. Of the total of three specimens, one was the non-

reactive specimen, and the *First* and *Second* reactive specimens, respectively, were subjected to deterioration due to ASR only and due to the combined effects of both ASR and DEF. The deterioration data also clearly suggested that the *Second* reactive specimen, which was subjected to combined ASR and DEF deterioration showed significantly higher expansion strains (1.25–1.95 percent at the end of 600 days) compared to the *First* reactive specimen, which was subjected to ASR-only deterioration (0.65–0.84 percent at about 700 days). However, the experimental testing of the specimen demonstrated that ASR/DEF deterioration effects did not have any adverse consequences on the ultimate flexural capacity of the specimen. In fact, both the deteriorated specimens showed higher ultimate load carrying capacity and ductility compared to the non-reactive specimen. However, the yielding of the tension reinforcement in the reactive specimen occurred prior to that on the non-reactive specimen. Gianni et al. (2013) concluded that although the effects of ASR and/or DEF did not negatively impact the load carrying capacity of the structure, the deterioration caused by this mechanism could be the cause of initiation of other deterioration mechanism (like steel corrosion/rebar fracture), which could affect the load carrying capacity of the structure.

#### **2.4.3 TxDOT Project #0-5722**

Bracci et al. (2012) conducted experimental studies on large-scale specimens ( $b \times d \times l = 1220 \times 610 \times 7620$  mm) to evaluate the experimental behavior of critical column lap splice regions under varying levels of premature concrete deterioration due to ASR/DEF. For this study, 16 large-scale column specimens with critical lap splice region were designed, constructed, subjected to deterioration (14 specimens were subjected to deterioration and 2 remained in a climate controlled laboratory and served as the control specimen), and later load tested in the laboratory. To simulate in-service gravity loading on the bridge column, unbonded post-tensioning strands were jacked to apply a total compression load of 2580 kN. The specimens were instrumented internally and external strain measurements were made to monitor the concrete and reinforcing strains especially during the deterioration and load testing phases. Reactive aggregates and

cement high in alkali content were used in the construction of the specimens to promote ASR in the specimen. Sodium Hydroxide (NaOH) was also used to increase the alkali content in the concrete mixture. The area of interest of the specimens was 1372 mm in length on either side of the centerline, which represented the splice region. The end regions were heavily reinforced with hoops to prevent failure in this region during load testing. Electrical heating wires were used to attain the 71°C threshold temperature to promote DEF in the specimens. The specimens were exposed to the environmental weather conditions, and supplemental water was sprinkled to accelerate ASR/DEF deterioration. Field deterioration data showed that direct sunlight had a large impact on the expansion due to ASR and minimal DEF related expansion. Due to the longitudinal restraint provided by the longitudinal reinforcement and the post-tensioning steel, the observed transverse surface strains were about 10 times larger than the longitudinal surface strains. The petrographic analysis showed that after a field exposure period of about two to three years, there was significant premature concrete deterioration due to ASR and minimal DEF was observed.

The specimens were structurally tested in two different test setups to evaluate the performance of the lap splice region. The four-point flexural load setup applied a constant moment demand and no shear demand across the entire splice region. The specimens were then subjected to a three-point flexural load test. The objective of the test was to evaluate the column splice performance by introducing large flexural moment demands that were not constant throughout the splice region, but were more critical at the middle section of the splice. Constant shear forces were also present in the splice region. The force-deformation results of the four-point flexure test showed that all the specimens had the same stiffness until first cracking. Between the first cracking and first yielding of the reinforcing steel, the deteriorated specimens were some 25–35 percent stiffer and had a slight increase in the yield strength when compared to the undamaged control specimen. Similarly, for the three-point flexural test the deteriorated specimen compared to the control specimen showed higher yield strengths and about 25–35 percent higher stiffness from post-cracking until first yield. The deterioration of the

specimen due to varying levels of ASR and minimal DEF did not have any overall detrimental effects on the structural response. The increase in stiffness and strength of deteriorated specimens was attributed to the volumetric expansion of concrete due to ASR/DEF that engaged the longitudinal and transverse reinforcement for a better confinement of the core concrete. The expansion also engaged the post-tensioning reinforcement and the longitudinal reinforcement to generate additional axial compression load. However, the detrimental effects of DEF could not be studied as very minor to no DEF had formed in the specimen.

#### **2.4.4 TxDOT Project #0-5997**

Mander et al. (2012) carried out experimental investigations to study the effects of deterioration caused by ASR/DEF on bridge bent-caps. Four large-scale specimens (one non-reactive and three reactive) were designed and constructed as part of this study. The specimens were designed as ‘C’ shaped beams such that one end of the specimen represented a straddle bent and the other end represented a cantilever bent. Few of the research tasks in this current research are a direct extension of the work conducted by Mander et al. (2012), therefore a few aspects of this research are reviewed in further detail in what follows.

#### **Specimen Design, Construction and Curing**

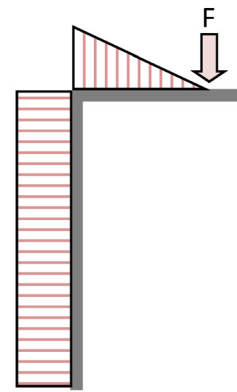
Figure 2-1 shows the two bridge bents that were selected as a basis for the design of the C-beam specimens that were tested by Mander et al. (2012). Figure 2-1a shows a cantilever bent that are typically constructed with minimum compression steel in the bent-cap. On the other hand, straddle bents (Figure 2-1b) are constructed with both tension and compression steel in the bent-cap. To represent the cantilever bent and the straddle bent, a singly reinforced and a doubly reinforced bent-cap specimen were considered in the design of the test specimen.

Figure 2-2 presents the experimental specimen details that were adopted by Mander et al. (2012). Four specimens with the same design were constructed as C-shaped sub-assemblages consisting of two D-regions. The C-shaped sub-assemblage

specimens had a constant cross-section, 610 mm wide by 914 mm deep throughout. The only difference between the two sides of the C-beam was the varying compression steel in the bent-caps near the D-regions. The scale factor for the specimens was approximately 50 to 75 percent of full-scale for the cantilever bent and straddle bent, respectively. The longitudinal reinforcement, scaled to replicate the cantilever and straddle bents described previously, consist of 10 #8 (25 mm) rebars running continuously on the tension side of the specimen and is hooked at the end of each bent. The singly reinforced bent-cap section (S) has two #8 bars on the compression face. These bars were provided for construction purposes in order to tie the transverse steel and form an enclosed cage. The doubly reinforced bent-cap section (D) has 10 #8 bars in both the tension and compression faces of the beam.

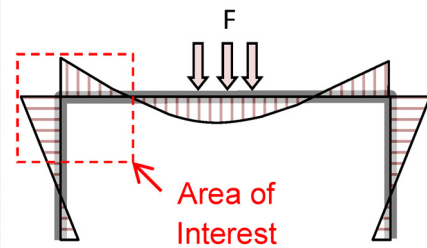
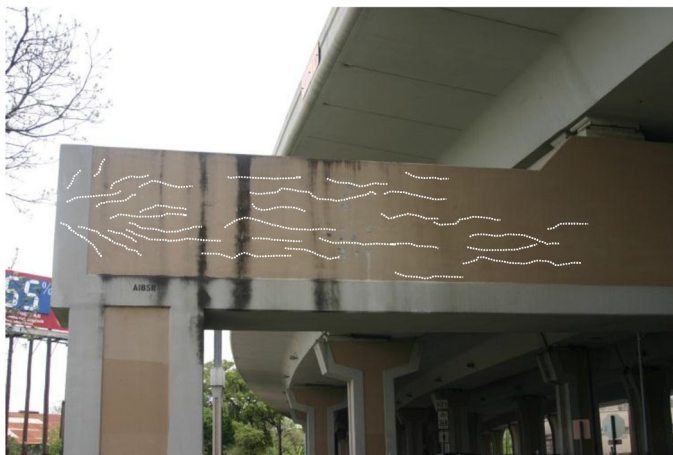
The longitudinal side face bent reinforcement (distributed along the bent-cap web) consists of three sets of equally spaced #4 (13 mm) rebars. Transverse bent-cap reinforcement consists of closed stirrups with a center-to-center spacing of 114 mm starting at the column face. The longitudinal column reinforcement consists of 10 #8 rebars used in the tension region along with five sets of equally spaced #8 rebars throughout the mid-region of the column section and five #8 rebars along the compression face. Transverse column reinforcement consists of #4 overlapping hoops spaced at 114 mm center-to-center. The beam-column joint was reinforced with four #4 U-bars at 203 mm spacing that continued from the transverse bent reinforcement. Prestress loads to simulate gravity loads were applied to the specimen at a height of 914 mm from the column face.

In order to promote ASR/DEF in the specimen, Type III cement with high alkali content was used in the mix along with reactive aggregates. NaOH solution was added in the concrete mix to accelerate premature concrete deterioration. Electrical resistive wiring was used to heat the specimen to 77°C, which is above the threshold temperature to promote DEF in the specimen. Three of the four specimens (Specimen 2, 3, and 4) were stored outdoors exposing them to Texas weather conditions. To accelerate the formation of ASR/DEF the specimens were watered using a sprinkler system. One of the



Schematic BMD

(a) *Cantilever Bent (San Antonio, TX)*



Schematic BMD

(b) *Straddle Bent (Houston, TX)*

Note: White dotted lines signify concrete cracking

**Figure 2-1: Prototype Reinforced Concrete Bridge Bents (Adopted from Mander et al., 2012).**

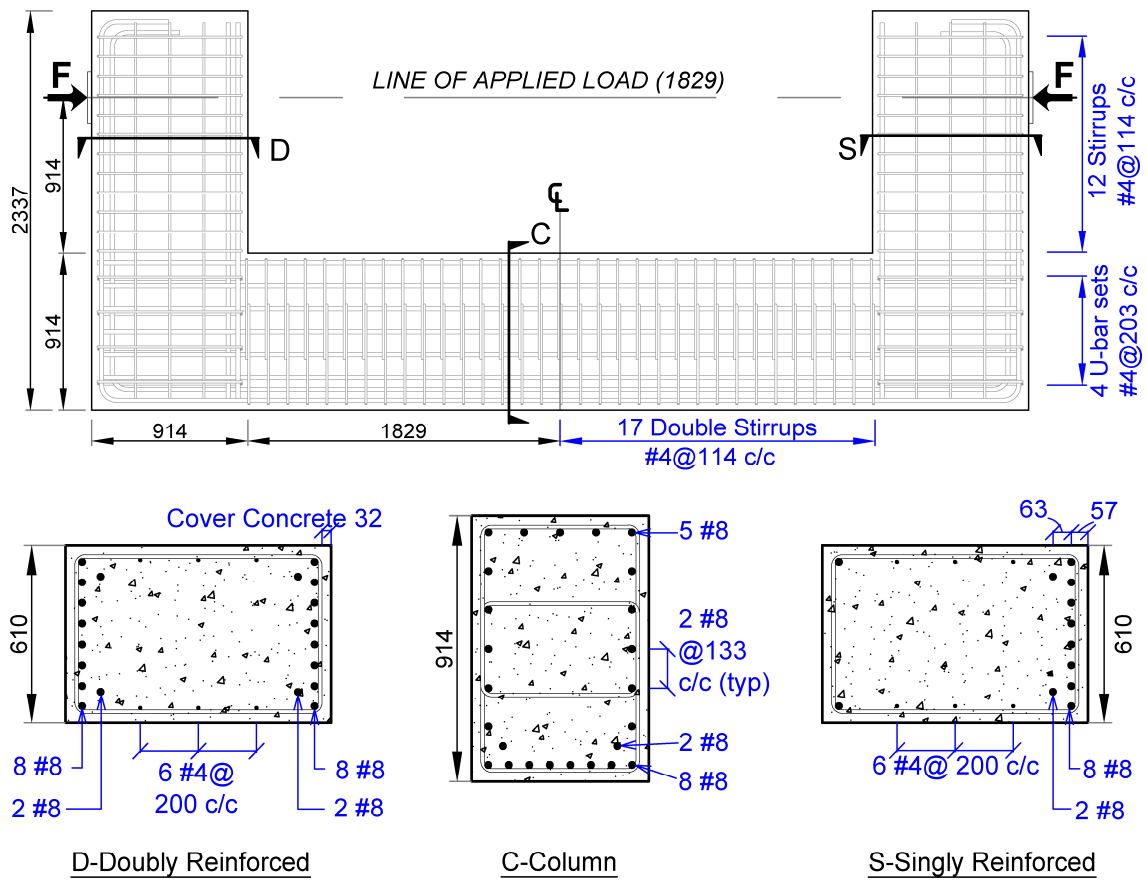


**Figure 2-2: Reinforcement Details of Experimental C-beam Specimen.**

specimens (Specimen 1) remained in a controlled environment within the laboratory and did not receive any supplemental water, and served as the control specimen.

### **Deterioration Data**

In order to know the progress of ASR/DEF deterioration in the specimens, data was collected at regular intervals from the three C-beam specimens in the field. The time-dependent progression of surface strains in the beam, the beam-column joint and the column were recorded between the DEMEC points. This included the surface concrete strains in the longitudinal and transverse direction and the surface strains transverse to the concrete arch in the beam and the beam-column joint. The behavior of core concrete was recorded using the concrete gages that were embedded in the specimen core. Similarly, the strains in the reinforcing steel were recorded using the strain gages that were attached to the reinforcing bars. The deterioration data was recorded and reported for a period of nine months for Specimen 2 and 24 months for Specimen 4.

### **Experimental Test Setup and Instrumentation**

The layout of the experimental test setup for Specimen 1 and 2 were different from Specimen 4. The setup for Specimen 4 was a simpler setup which used one actuator. Apart from the simplification, there were no apparent differences in the two test setups and they worked and performed in a similar manner. The experimental test setup that was used for testing Specimen 4 is shown in Figure 2-3. The experimental test setup was designed to be a self-reacting system. For ease of setup in the laboratory the column was placed on two hinge supports and the beams were oriented vertically. The plan and elevation of the test setup are shown in Figure 2-3. The setup consists of one 979 kN MTS actuator in displacement control. The actuator was placed on one side of the specimen and three high strength DYWIDAG threadbars were aligned vertically on the other side to create a leverage mechanism which gave a total capacity of 2643 kN.

Figure 2-4 shows the external instrumentation layout that was adopted for Specimen 4. The specimens were externally instrumented using linear variable differential transformers (LVDTs) and string-potentiometers (SP), and were internally

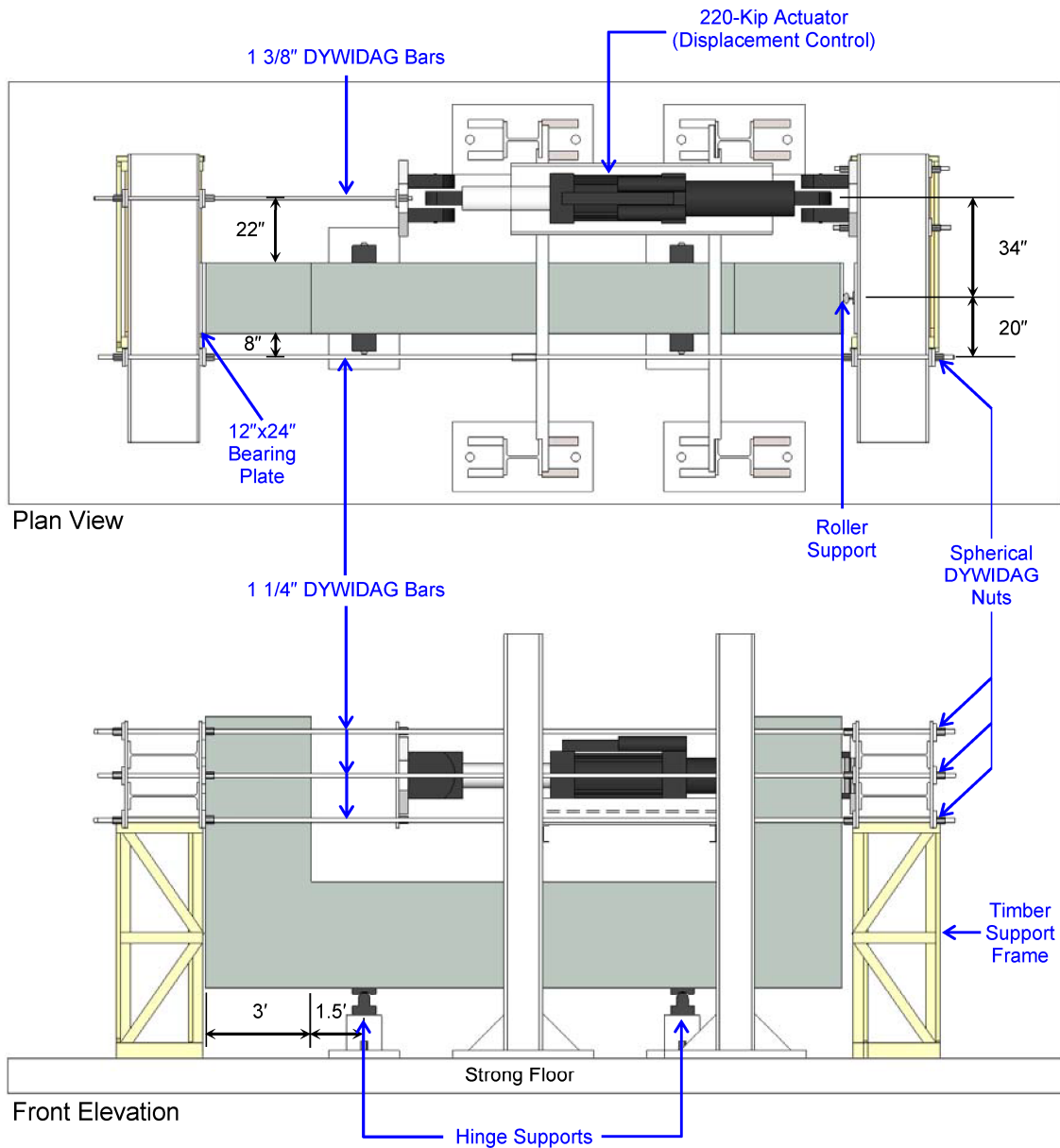


instrumented using strain gages (SG) attached to steel and embedded concrete gages (KM). String Potentiometers connected from a rigid external column to the specimen were used to measure the global displacements at the applied loading points. Experimental deformations associated with the SAT and truss modeling were measured using LVDTs mounted to aluminum truss members that were rigidly connected to the specimen between selected nodal points as shown in Figure 2-4b.

### **Experimental Observations**

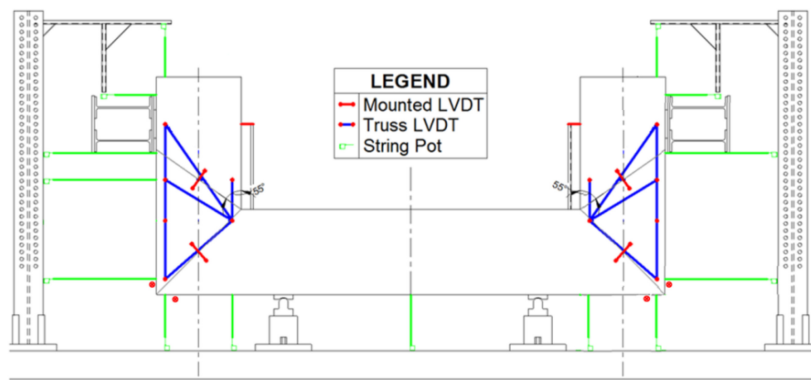
Two out of the three field conditioned specimens, Specimens 2 and 4, respectively, showing *slight* and *moderate* amounts of ASR/DEF deterioration were tested after a little under 1.5 years and 2.5 years from the time of casting. A test of the field conditioned concrete cylinder indicated that there was reduction in the compressive strength of concrete. The control specimen and the two ASR/DEF deteriorated specimen were load tested in the laboratory. The tests revealed that the load-deformation behavior of the ASR/DEF deteriorated specimens was quite similar to the control specimen, and in fact the deteriorated specimens showed slightly higher ultimate peak load. It was observed that the ASR/DEF deteriorated specimens showed a slightly higher initial and general overall stiffness when compared to the control specimen. This was attributed to the beneficial prestressing effects in the reinforcement arising from the confining effect they had on the expansion of the core concrete. It was noted that the final mode of failure in all the specimens was a brittle joint shear failure, irrespective of the extent of ASR/DEF induced damage.

As in the earlier experimental study by Deschenes et al. (2009) and Bracci et al. (2012), it was concluded from the findings that ASR/DEF did not affect the load carrying capacity of the reinforced concrete bent-cap. However, it remains to be seen how severe ASR/DEF deterioration can affect the structural capacity of reinforced concrete members.

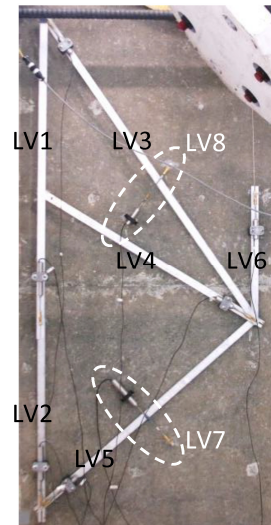


Note: 1 kip = 4.448 kN and 1 inch = 25.4 mm

**Figure 2-3: Experimental Test Setup for Specimen 4.  
(Adopted from Liu, 2012).**



(a) Layout of External Instrumentation



(b) LVDT Truss Setup

**Figure 2-4: External Instrumentation Layout for C-beam Specimen 4.  
(Adopted from Mander et al., 2012)**

## **2.5 Historic Developments in Strut-and-Tie Modeling**

Truss models have been used as computational tools for the analysis and design of reinforced concrete beams since the early 1900s. Ritter (1899) suggested that after cracking occurs in a reinforced concrete beam due to diagonal tensile stresses, the beam can be idealized as a parallel chord truss with compression diagonals inclined at  $45^\circ$  with respect to the longitudinal axis. Mörsch (1909) independently proposed a similar idea of converting reinforced concrete beams into an equivalent truss. Rausch (1929) extended the plane truss concept for beams for the treatment of members subjected to torsion. In this development, a series of component plane trusses capable of resisting shear action were connected to form a space truss that idealized the torsion member.

The truss modeling technique was later picked up by Nielson (1967) and Lampert and Thurlimann (1968). Based on the theory of plasticity the authors derived the fundamental equilibrium equations for shear. These theories were primarily based on the yielding of reinforcing steel, and so were called the plasticity truss model.

### **2.5.1 Compression Field Theory and Softened Truss Model (Collins vs. Hsu)**

The compression field theory by Collins (1978) and the softened truss model by Hsu et al. (1987) are two popular models that were developed in the late 1970s and early 1980s. The models have subsequently been advanced and used widely to analyze shear in reinforced concrete members. The compression field theory and the softened truss model in its original form are reviewed in this section.

It was widely accepted that the assumption of the angle of inclination  $\theta = 45^\circ$  of the diagonal concrete compressive stresses with the longitudinal axis gave conservative estimates of shear capacity. Mitchell and Collins (1974) proposed an expression to determine the inclination angle of diagonal compression by minimizing external displacement. The authors presented a theoretical model for structural concrete in pure torsion which was called the diagonal compression field theory. The model was capable of predicting the complete post-cracking torsional behavior of structural concrete members with a wide variety of symmetrically reinforced cross-sectional shapes.

Collins (1978) extended the diagonal compression field theory for its application to reinforced concrete members in shear. In his theory it was assumed that once cracking commences, the concrete cannot resist any tension and the shear will be carried by a diagonal compression field. It was considered that the average strains in different directions were related to one another by requirements of compatibility which were represented by Mohr's circle of strain. Assuming that the direction of the largest average compressive stress and strain coincided, the angle of principal compression was determined from the compatibility conditions. It was suggested that the ultimate shear capacity of the reinforced concrete member was reached either when the longitudinal steel yielded or when the average principal concrete compressive stress reached its limiting value. In this theory, in addition to satisfying the equilibrium and compatibility conditions, the material stress-strain characteristics were also considered.

Hsu et al. (1987) developed a theory of shear transfer in initially uncracked concrete. Shear stresses were introduced into the compression strut resulting in a biaxial failure condition which resulted in a better prediction of the shear strength of reinforced concrete members. The softened truss model was applied to the shear transfer problem and was able to predict the shear transfer strength and shear deformations of initially uncracked specimens. The theory also predicted that the ultimate failure was caused by the crushing of concrete in the compression struts that were formed after concrete cracking. It was also observed that the transverse reinforcement parallel to and in the vicinity of the shear plane had an effect on the shear strength.

Hsu (1988) summarized the softened truss model theory for shear and torsion. 11 shear and 17 torsion equations were derived from equilibrium, compatibility and material stress-strain relationships. The softened stress-strain relation was used for concrete in compression, and hence the name softened truss model. The system of equations was solved to predict test results of various reinforced concrete structures subjected to shear and torsion. Apart from predicting the shear and torsional strengths the theory also predicted the deformation, such as shear deflection, angle of twist, and steel and concrete strains throughout the structure's post-cracking loading history.

Mau and Hsu (1987) applied the softened truss model (Hsu, 1988) to predict the shear strength of deep beams with web reinforcement. In the case of simple deep beams with a concentrated load, the top load and the bottom support creates a compressive stress transverse to the horizontal axis of the beam. The authors note that for small shear span over depth  $a/d$  ratios, these transverse compression stresses should not be neglected as this could have significant effect on the shear strength of the web. To take this into account an effective transverse compression in the beam web was introduced into the softened truss model. The theory was able to predict the shear strength of deep beams with vertical web reinforcement with good accuracy. It was also identified that the shear span ratio and the transverse and longitudinal reinforcement index had a major effect on the maximum shear stress of deep beams. Additionally, the theory predicted that the transverse reinforcement was ineffective in increasing the shear strength of deep beams with  $a/d$  ratios below 0.5.

### **2.5.2 Other Developments Contemporary to Compression Field Theory**

Marti (1985) studied the application of consistent equilibrium and ultimate strength considerations for the design and detailing of reinforced concrete beams. The author used the truss model to investigate the equilibrium between applied loads, reactions and internal forces in the reinforcement and concrete. The stress fields consisted of struts and ties, nodes, fans and arches. The fans and arches were replaced by statically equivalent struts with finite dimensions to develop statically admissible stress fields. The proposed design methodology was adaptable to arbitrary geometries of the structure and various loading situations. These were the first attempts in the development of the SAT method as it is known today. However, application of SAT modeling was limited to a few types of structures.

Schlaich et al. (1987) noted the need for a unified design concept, which was consistent for all types of structures and that could be applied to all parts of the structure. The authors proposed a SAT methodology, which was a generalization of the truss analogy method for beams. With the SAT approach, the entire structure (which is a combination of B-regions and D-regions) could be modeled and analyzed, rather than

relying on past experiences or rules of thumb. The authors demonstrated how the SAT model can be constructed using a load path method and presented examples on how to utilize the SAT method to analyze structures with significant D-regions such as deep beams with openings, corbels and other complex structures. The use of SAT modeling technique for the design of D-regions was widely promoted by Collins and Mitchell (1991) and MacGregor (1992).

### **2.5.3 Modified Compression Field Theory and Fixed Angle Softened Truss Model**

To address the shortcomings with the compression field theory by Collins (1978) and the softened truss model by Hsu et al. (1987) and to enable the determination of contribution of concrete to the shear resistance mechanism of reinforced concrete members, improvements were suggested to these methods. This gave rise to the Modified Compression Field Theory (MCFT) by Vecchio and Collins (1986) and the fixed angle softened truss model by Pang and Hsu (1996). These theories are discussed in detail in this section.

Based on the compression field theory, Vecchio and Collins (1986) proposed the MCFT. The MCFT took into account the tensile stresses in concrete between the cracks. Additionally, from experimental test on panel elements, it was determined that in cracked concrete elements subjected to high tensile strains in a direction perpendicular to compression strains, the concrete compressive stress was a function of the concrete compressive strain  $\varepsilon_2$  and the co-existing principal tensile strain  $\varepsilon_1$ . This essentially made the concrete softer and the softening coefficient was found to be a function of the tensile strain  $\varepsilon_1$  and the strain  $\varepsilon'_c$  corresponding to maximum concrete compressive stress  $f'_c$ . Average stress-strain relation for cracked concrete in tension was also proposed. In lieu of following complex stress variations in cracked concrete, only the average stress states, and the stress state at the cracks were considered. It was also assumed that for equilibrium to exist across cracks there should be a local crack shear stress accompanied by a small local crack compressive stress across the crack. The crack pattern was idealized as a series of parallel cracks all occurring at the same angle to the

longitudinal axis. By considering equilibrium, compatibility and the material stress strain relations, the theory was capable of predicting the response of reinforced concrete elements subjected to in-plane shear and axial stresses. This method proved to be suitable for predicting the response of beams loaded in shear, flexure, and axial loads.

Collins et al. (1996) presented a simple and unified method for the shear design of both prestressed and non-prestressed concrete members. Simplifying assumptions were made to the MCFT to apply this model for the design of beams. The shear stresses were assumed to be uniform over the effective shear area. The highest longitudinal strain  $\varepsilon_x$  in the web was used to calculate the principal tensile strain  $\varepsilon_t$ . For design purposes,  $\varepsilon_x$  was approximated as the flexural reinforcement strain. The expression for nominal shear strength  $V_n = V_c + V_s + V_p$ , is a combination of concrete  $V_c$ , steel  $V_s$  and prestress or axial  $V_p$  contributions, and included the tensile stress factor  $\beta$  and the direction of the principal compressive stress  $\theta$ . For the purposes of design the authors presented suitable values of  $\beta$  and  $\theta$  as a function of the longitudinal strain  $\varepsilon_x$  and the shear stress level  $v/f_c'$  for members with shear reinforcement, and as a function of  $\varepsilon_x$  and  $s_x$  (crack spacing at  $\theta = 90^\circ$ ) for member without web reinforcement. With these proposed values for  $\beta$  and  $\theta$  the MCFT was simplified enough to perform hand calculations. The new procedure explicitly considered the influence of shear upon the longitudinal reinforcement and gave a physical significance to the parameters being calculated. This work was the basis of the sectional design model for shear that was included later in AASHTO LRFD Bridge Design Specifications (2004).

Bentz et al. (2006) tried to further simplify the MCFT in an attempt to enable performing 'back of the envelope' calculations for determining the shear strength of reinforced concrete elements. The authors present simple equations for the parameters  $\beta$  and  $\theta$  as they give a continuous range of values and are more convenient for spreadsheet calculations. These simple equations are used to predict the shear strength of reinforced concrete elements and they showed suitable agreement with a selection of experimental results.



Pang and Hsu (1995) tested 13 full-sized reinforced concrete panels to study the behavior of reinforced concrete elements subjected to membrane shear. The softened truss model developed by Hsu (1988) was used to predict the shear stress versus shear strain relationship of the test panels with good accuracy. Based on the study the authors recommended that the softened truss model based on rotating angle was applicable to membrane elements with a transverse to longitudinal reinforcement ratio of 0.4 to 2.5 or for a range of rotating angle  $\theta$  between  $33^\circ$  to  $57^\circ$ . A fixed angle softened truss model was recommended for membrane elements outside this range.

Pang and Hsu (1996) presented a more generalized softened truss model called the fixed angled softened truss model. In this model the direction of the cracks was assumed to incline at a fixed angle following the principal stresses of the applied loading. In the earlier softened truss model proposed by Hsu (1988), the angle of the cracks coincided with the rotating angle (hence called rotating angle softened truss model) following the post-cracking principal stresses of concrete. Because the model assumed that the concrete struts were oriented in the direction of the post-cracking principal stresses, it did not allow shear stresses to exist along the cracks. Thus this model was unable to capture the contribution of concrete to shear resistance. With the introduction of the fixed angle softened truss model this shortcoming was overcome. In addition to the three constitutive laws of concrete and steel that were used for the rotating angle softened truss model, the fixed angle softened truss model required an additional constitutive law for the stress-strain relation of cracked concrete in shear. This relation was determined from full-size panel tests (Pang and Hsu, 1995). By incorporating the additional constitutive law, the fixed angle softened truss was able to capture the contribution of concrete towards the shear resistance of reinforced concrete members which was widely observed in laboratory tests.

Hsu (1994, 1996) developed a unified theory for reinforced concrete structures subjected to bending, axial loads, shear, and torsion. In this development the author suggests that available models for reinforced concrete can be broadly classified into six models and classifies their applicability as follows:

- SAT model: Applicable to local regions with irregular angles of concrete struts. The model satisfies the stress equilibrium but not the strain compatibility.
- Bernoulli compatibility truss model: Applicable to bending and axial loads at service and ultimate load stages. It satisfies the parallel stress equilibrium, Bernoulli's linear strain compatibility and the uniaxial constitutive laws of concrete.
- Equilibrium (plasticity) truss model: Applicable to shear and torsion at ultimate load stage and is based on rotating angle. It satisfies the two-dimensional stress equilibrium and material plasticity conditions.
- Mohr compatibility truss model: Applicable to shear and torsion at service load stage and is based on rotating angle. It satisfies the two-dimensional stress equilibrium, Mohr's circular strain compatibility and the uniaxial constitutive laws of concrete.
- Softened truss model: Applicable to shear and torsion at service and ultimate load stage and is based on rotating angle. It satisfies the two-dimensional stress equilibrium, Mohr's circular strain compatibility and the softened biaxial constitutive laws of concrete.
- Fixed-angle softened truss model: Applicable to shear and torsion at service and ultimate load stage and is based on fixed angle. It satisfies the two-dimensional stress equilibrium, Mohr's circular strain compatibility and the softened biaxial constitutive laws of concrete. This model takes into account the concrete contribution to shear strength.

Hsu (1998) questioned the validity of the MCFT proposed by Vecchio and Collins (1986). According to MCFT the contribution of concrete to shear originated from the average tensile stress of concrete transmitted across the cracks. Two assumptions were made in MCFT in order to maintain static equivalency at local cracks. A crack shear stress was imposed on the concrete struts and the yield stress of bare steel bars was used for the average stress of steel embedded in concrete. Hsu considered the two assumptions made were flawed because of the following reasons. First, the angle of

inclination of the concrete strut is oriented along the post-cracking principle compressive stress. Imposing crack shear stress along this plane violated the basic principles of mechanics. Secondly, the average stress-strain relation of concrete in tension was used along with the local stress-strain relation of bare steel, rather than the average stress-strain relation of reinforcing steel embedded in concrete. As the bare steel yield stress is higher than the yield stress of the average stress-strain curve of steel embedded in concrete, the predicted yield stress of the shear element included an unwarranted concrete strengthening which cannot be used to justify the concrete contribution to shear strength of reinforced concrete members.

Mander (1998) solicited an opinion from Collins who was one of the original authors of MCFT. Collins (1998) presented an article to clarify the issues that led to erroneous conclusions by Hsu (1998). Collins presented a numerical example to clarify the specifics of the MCFT procedure. Collins notes that the average principal tensile stress in concrete and the average tensile stress in the reinforcement were used unlike what was claimed by Hsu. It is also stated that in the MCFT reasonable simplifications were made such that the average principal compression strain, average principal compressive concrete stress and the crack direction all occur at the same angle. Although, in terms of average stresses there is no concrete shear stress on the crack plane, in terms of local stresses, equilibrium requires shear stresses on the crack plane. A comparison with experimental shear stress-shear strain results of a panel element tested by Pang and Hsu (1996) with the MCFT and the rotating angle SAT showed that the behavior of the specimen was predicted quite well by the MCFT as by the rotating angle strut and tie method. In conclusion Collins states that the MCFT makes simplifying assumptions about the complex behavior of cracked reinforced concrete elements subjected to shear and that the softened truss model presented by Hsu is limited in scope, more complex and did not offer any significant improvement in the accuracy of results.

#### **2.5.4 Force Transfer Method**

Sritharan et al. (2000) and Sritharan and Ingham (2003) in their study of large-scale seismic tests on bridge joints and an accompanying analytical study, developed a so-called Force Transfer Method (FTM) for the seismic design and assessment of concrete bridge joints subjected to in-plane loading. In this method the reinforcement details were established based on a SAT model representing the joint D-region. The aim of this method was to obtain satisfactory joint performance while ensuring a constructable joint detail without congestion of reinforcing steel in the joint. The authors also presented several guidelines, joint mechanisms and design/assessment models to facilitate the model. Unlike traditional design approaches for the joint, where the joint shear is treated as an independent force, the FTM considered the joint shear to be a part of the complete force transfer mechanism across the beam-column joint. The FTM provided reduced and less conservatism in the joint reinforcement design which helped relieve congestion and thereby improve constructability.

Sritharan (2005) represented a set of bridge tee joints from an experimental program with detailed force transfer models based on SAT concepts. These detailed SAT models were able to explain the failure of reinforced concrete cap beam joints and identify the shortcomings with the External Force Transfer Model (EFTM) which was widely accepted as a design method for bridge joints in seismic regions. The detailed SAT models confirmed that modeling joint shear as a component of the total force transfer across the joint enabled utilization of the beam reinforcement for the joint force transfer, thereby resulting in reduced shear reinforcement and improved constructability of the joint. This study substantiated the earlier findings that the EFTM provided insufficient details for reinforced concrete bridge joints and also resulted in excessive amounts of joint reinforcement for prestressed joints. The models also revealed that the force transfer in bridge joints could be characterized by two parallel mechanisms-the clamping and the splice mechanism. The analytical model presented also revealed shortcomings with the EFTM. The magnitude and orientation of the external joint strut were incorrectly assumed in the EFTM and the participation of the splice mechanism

was not considered. The analysis showed that as prestressing force in the cap-beam increased there was insignificant contributions to the joint transfer by the external joint strut and the splice mechanism, both of which required additional reinforcement in the joint region. The EFTM also ignored the disturbance to the cap beam region adjacent to the column compression side. The development of the detailed SAT model also highlighted that tensile resistance of cracked concrete played a significant role in the force transfer across joints.

While all of the above theories can provide some insight about the shear strength of a reinforced concrete structure, little, if any, insight has been shed on the shear deformation of the structure. This is considered to be an important aspect to be established, especially in those cases where the ductility of the structure becomes an important factor. Historic developments in Compatibility based Strut-and-Tie modeling is discussed in what follows, where the equilibrium, compatibility and material constitutive laws are directly taken into account to determine the force and deformation of the structure.

## **2.6 Evolution of Compatibility Strut-and-Tie Modeling**

The major contribution to the field of C-STM has come from a limited number of authors. Therefore, this section of the literature review is grouped by author rather than in chronological order.

Kupfer (1964) related the crack angle to the shear and flexural stresses by minimizing the strain energy over an idealized single truss unit of a cracked thin webbed T-beam element. The study determined that Mörsch's (1909) truss model with a constant  $45^\circ$  angle overestimated the required shear reinforcement by 15–25 percent. Leonhardt (1965) used the truss analogy to explain the mechanism of failure of beams at ultimate shear load. It was observed that the inclination of shear cracks was not just  $45^\circ$ , but varied considerably. The estimation of the angle  $\theta$  by Kupfer (1964) and Baumann (1972) were based on the assumption of linear elastic behavior of cracked concrete and reinforcement.

Dilger (1966) formulated the cracked elastic shear stiffness approach by expanding Kupfer's (1964) study to include the effects of the inclination of shear steel. Using strain energy concepts of an analogous truss, the inclination of the compression truss was determined and the shear distortions calculated using Williot's principles. However, Kupfer and Dilger restricted their truss models to the B-region.

Paulay (1971) conducted laboratory tests on coupling beams to study their performance under cyclic loading. From this study it was evident that for cracked beams there was a complex interaction between the flexural reinforcement, stirrups and the concrete struts formed between cracks. Four major load transfer mechanisms and the associated distortions in cracked coupling beams were identified as: (a) shear transfer by truss action and consequent distortions; (b) arch action and compression across the main diagonal of the beam; (c) flexure and associated rotations; and (d) tying action of the flexural reinforcement and consequent elongation of the beam. Based on the above mechanisms the author was able to predict the stiffness after diagonal cracking with reasonable accuracy.

Hwang and Lee (1999) used a softened truss model based on the SAT concept which satisfied equilibrium, compatibility and material constitutive laws to determine the shear strength of exterior beam-column joints. The primary purpose of this study was to study the behavior and for the evaluation of external beam-column joints under seismic loading. The proposed model consisted of diagonal, horizontal and vertical shear transfer mechanisms. The statically indeterminate system comprised of a single diagonal compression strut constituting the diagonal mechanism; the horizontal mechanism consisted of a horizontal tie and two flat struts; and a vertical tie and two steep struts constituted the vertical mechanism. The joint shear strengths computed from the model compared well with experimental data. Hwang and Lee (2000) also studied the applicability of their proposed softened SAT model to predict the shear strength of interior beam-column joints under seismic loading, and were shown to provide satisfactory results. Hwang et al. (2000a) applied the proposed softened SAT model for the prediction of the shear strength of deep beams, and comparison with experimental

results showed reasonable accuracy. They also pointed out that the ACI 318-95 provisions were conservative. Hwang et al. (2000b,c) applied the softened SAT to corbels and squat walls and were able to predict the shear strength with reasonable accuracy. However, for any of the above cases, the softened SAT model did not determine the deformation capacity which is very important especially under seismic loading conditions.

Kim and Mander (1999; 2000a) developed a Cyclic Inelastic Strut-Tie modeling approach in order to study the structural behavior under lateral loading when the structural concrete members are subjected to a combination of shear and flexure. Both the constant angle truss and the variable angle truss were investigated and a numerical integration scheme was adopted to enable the proper selection of element models and their dimensioning. The modeling technique was validated against experimentally observed behavior of shear-critical reinforced concrete members subjected to reverse cyclic loading. The model was able to capture the combined response of shear and flexure quite well, but was unable to model the gradual loss of strength due to the effects of cyclic loading. Kim and Mander (2000b) presented a theoretical framework around the SAT modeling approach to predict the inelastic performance of beam-column joints. It was demonstrated that the post-elastic behavior of beam-column joints could be effectively modeled using the SAT technique with a fan-shaped crack pattern.

Kim and Mander (2005) studied the effect of discrete distribution of transverse reinforcement on shear strength of reinforced concrete beams and columns. Correction factors were proposed for rectangular and circular hoops and spiral reinforcement to eliminate the disconnect between the code formulations that were based on an implied smeared distribution of transverse steel and the discrete distribution of transverse reinforcement that were found in reality. It was observed that the correction factor for rectangular hoops were more significant than that for circular hoops and spirals.

Kim and Mander (2007) studied the influence of transverse reinforcement on the cracked elastic shear stiffness of concrete elements. Various truss models were studied to investigate the viability of using the more convenient continuum truss model instead of

the discrete truss model without losing accuracy. To study this, comparisons were made between the continuum and discrete truss models, constant and variable angle truss models and rectangular and circular hoops and spirals. From the study it was concluded that the shear deformation and strength behavior of a cracked reinforced concrete beam-column could be represented by any reasonable constant angle or variable angle truss model. The transverse steel volume and the crack angle were identified to be the important parameters. The authors also specified the spacing limits for rectangular hoops and circular hoops and spirals beyond which the discrete truss model must be used. The continuum model provided satisfactory results for tighter hoop spacing. It was also found that the strength and stiffness were affected by the discrete number of hoops or spirals that crossed the crack plane. Good agreement between the analytically predicted crack angles and the experimental results were also observed.

To et al. (2001) conducted studies to explore if the SAT models were capable of capturing the nonlinear force-displacement response of reinforced concrete bridge knee joint assemblages subjected to monotonic loading. All the constituent members of the SAT were located at the force centroid of the corresponding force-transfer mechanism. From their STM models the authors were successful in modeling the monotonic force-deformation behavior of the knee joint with sufficient accuracy. They were also able to predict the events that caused certain nonlinear behavior in the structure. However, there remain a few shortcomings to this model. Separate different models had to be used to model the loads causing joint opening and joint closing. Also, the models were not representative of the reinforcement layout of the actual structure. Various factors were used to model the compressive strength of the concrete compressive struts depending on the tensile strains, extent of cracking, strain hardening of adjacent rebars etc. It becomes difficult for practicing engineers to come up with an appropriate reduction factor for the compressive strength of concrete struts when the particular conditions as specified by the authors are not met. The authors also note that the greater complexity of the proposed STM technique would be a limiting factor for the application of this technique for design practice.



To et al. (2002) adopted the SAT model developed earlier (To et al., 2001) to model full-scale reinforced concrete bridge portal frames and circular columns, and obtain their force-displacement envelopes. The analysis included the tension stiffening effects of concrete; however a trial-and-error procedure was used to determine the concrete shear strength using MCFT. The force-deformation response from the SAT model proved to be superior in comparison to those obtained from conventional planar frame models. Again, this model had some of the shortcomings as noted earlier (To et al., 2001).

To et al. (2003) used a nonlinear cyclic SAT model to analyze the nonlinear cyclic force-deformation response of concrete cantilever beams and large-scale concrete bridge knee-joint systems. The force-deformation results from the model compared well with the experimental results. However, the models could not model the strength degradation exhibited by the knee joint as a result of cumulative concrete damage. There were also discrepancies with the loading and unloading branches of the force-displacement response and this was attributed to the inability to model the Bauschinger effect of the reinforcement steel.

To et al. (2009) presented a computer-based SAT model to capture the nonlinear cyclic response of an entire reinforced concrete structural system. The nonlinear force-deformation results from the SAT model proposed by the authors compared well with the experimental results and were also useful in identifying the failure event sequence. The authors also proposed a hybrid modeling solution that incorporates nonlinear SAT model into conventional planar frame modeling technique. The hybrid model captured the beneficial aspects of both the SAT and planar frame models and proved to be a time-effective modeling solution compared to the SAT. However, as in the earlier model by the authors, various arbitrary reduction factors have been applied to obtain the effective strength of the concrete struts and elastic stiffness.

Zhu et al. (2003) developed a Compatibility-Aided Strut-and-Tie (CASTM) model to predict the crack width of diagonal cracks occurring at the re-entrant corners of dapped ends of bridge girders and the ledges of inverted T bent-caps. For the

development and calibration of the CASTM, the authors tested seven full-scale T bent-caps with different reinforcement details. Two of these specimens were reinforced with diagonal reinforcing steel to study their effect on controlling the crack width. These were modeled as a system of two subtrusses in the CASTM. The first subtruss constituted the hanger and flexure steel, whereas the second subtruss included the diagonal bars. The two trusses were combined by displacement compatibility. The CASTM was able to predict the crack width with good accuracy, especially in the service load range.

Salem and Maekawa (2006) presented a computer-aided nonlinear SAT modeling approach, and validated this model by comparing analytical and experimental force-deformation results for reinforced concrete deep beams. The authors compared both the linear and nonlinear SAT models and determined that the linear SAT model was more conservative than the nonlinear SAT model in predicting the ultimate load. The load-deformation results from the analysis did not compare well with the experimental results beyond the elastic limit. The model was also not able to estimate the deformation capacity of the deep beams. One major disadvantage with this model was that a nonlinear finite element analysis had to be performed to determine the layout of the proposed nonlinear SAT model.

Scott et al. (2012a) formulated a Compatibility Strut-and-Tie Model (C-STM) for analyzing the nonlinear force-deformation behavior of structural concrete members with significant D-regions. In this formulation the deformation compatibility and the nonlinear constitutive material properties were considered in addition to the normal SAT force equilibrium conditions. The C-STM was presented as a minimalist computational analysis tool. Based on a convergence study, it was determined that the proposed single-point Gauss truss model was sufficient to capture the truss mechanism for a cantilever system. The C-STM was a combination of two mechanisms that contributed towards the shear resistance mechanism of the structure; the arch mechanism acting through the center of the cross section and the truss action acting along the outside stirrup legs. The truss and arch model geometries were determined based on the reinforcement layout and expressions were proposed to determine the elastic truss member axial rigidities. It was

also noted that post-analysis strength checks that were not implicitly modeled in the C-STM had to be performed to identify critical failure mechanisms.

Scott et al. (2012b) presented the implementation of the C-STM approach developed earlier (Scott et al., 2012a), to model the force-deformation response and the internal nonlinear strain behavior of structures with significant D-regions. The authors presented a step-by-step procedure on how the C-STM model could be implemented in SAP2000 v.14 (2009), which is a widely used commercially available structural analysis software. The C-STM was validated against three large-scale reinforced concrete bent-caps. The overall force-deformation behavior of the bent-caps modeled by the C-STM compared well with the experimental results. The C-STM was also able to model the internal strains of the structure with good accuracy and gave an insight into the progression of the nonlinear mechanisms within the structure. The authors however noted that the C-STM was unable to accommodate the second-order effects associated with the compression softening of concrete struts. This is a major shortcoming with this model, as the reduced compressive strength of the diagonal compression members can lead to sudden failure of the structure. Additionally, the analysis was conducted in force-control, thereby making it impossible to accommodate reverse cyclic loading effects.

Li and Tran (2012) proposed a rational semi-empirical approach to compute the angle of inclination of compression struts in the variable angle truss model for shear critical reinforced concrete beams subjected to flexure and shear. This method was developed by advancing the method originally proposed by Kim and Mander (1999). The concrete contribution to shear was addressed by utilizing the strain compatibility condition. The results from the model for inclination angle of the compression strut and shear strength of reinforced concrete beams were consistent with experimental results.

Pan and Li (2013) developed a truss-arch model to predict the shear strength of shear critical reinforced concrete columns subjected to cyclic loading. It is well known that the shear strength of reinforced concrete columns is transferred partly by the truss mechanism and partly by the arch mechanism. The proposed model took into account the contributions of concrete and transverse reinforcement to shear in the truss model,

and the concrete contribution to shear strength provided by the arch action. The deformation compatibility between the truss model and the arch model were incorporated into the model. The experimental results that were considered in this study indicated that the shear span-to-depth ratio and the axial-load ratio had significant effect on the shear strength of reinforced concrete columns. From the comparison of the measured and predicted shear strengths, a good correlation was found. This indicated that the proposed model represented the effects of the shear span-to-depth ratio and the axial-load ratio well.

The proposed research will attempt to overcome the shortcomings of the C-STM presented by Scott et al. (2012a,b). The main scope in this regard is to implement the softened concrete compression model directly into the analysis. An attempt is also made to implement the model in displacement-control, in order to enable the model to simulate reverse cyclic loading on the structure. Comparisons are made with experimental results to validate the advancements in the C-STM technique.

## **2.7 Research Questions Arising**

Based on the extensive literature review presented in this section, the following gaps are identified giving rise to the research questions listed below.

*Is there a straight forward way to determine the expansion caused by premature concrete deterioration mechanisms like ASR and/or DEF, and how can these be incorporated into a model to determine the load carrying capacity of deteriorated reinforced concrete structures?*

Extensive research has been done in the past to determine the expansion caused by concrete deterioration mechanisms like ASR and/or DEF in concrete. Most of the studies have been limited to studying their effects on plain concrete, while some studies pertain to reinforced concrete. However, the models developed to estimate the expansion caused by ASR/DEF in concrete are complex and difficult to adapt and implement for practicing engineers. Therefore there is a need for a simple model to estimate the degree of volumetric expansion caused by these deterioration mechanisms in reinforced concrete.

The expansion models related to ASR/DEF that have been developed in the past often require FEM analyses as part of the implementation to study potential adverse effects they may have on the performance of reinforced concrete structures. Such FEM can be a protracted task, moreover the interpretation of results from FEM models may be either cumbersome or ambiguous. There is a need for a simple method for the implementation of the concrete expansion models, in order to determine the structural effects that ASR/DEF deterioration mechanism may impart on the load carrying capacity of structural concrete members. There is also a need to understand the changes in the internal behavior of a structure caused by the deterioration mechanisms. The implementation of a simplified concrete deterioration model into the C-STM can be an effective way to determine the load carrying capacity and the internal behavior of structures affected by ASR and/or DEF. The current research will address these issues.

***Does concrete deterioration caused by internal reactions like ASR and/or DEF have any effect on the load carrying capacity of reinforced concrete structures?***

There is a general understanding that concrete deterioration mechanisms like ASR and DEF cause expansion of concrete leading to severe cracking and thus serviceability issues. However, there is a lack of knowledge in determining the effects that concrete deterioration caused by ASR and/or DEF could have on the load carrying capacity of reinforced concrete structures. Although studies have been conducted in the past, most of the studies are limited to plain concrete and there is limited studies on reinforced concrete. Few of the studies conducted in the past and reviewed in the literature review, suggest that mild to moderate amounts of ASR related deterioration in reinforced concrete has no detrimental effects on the stiffness or the load carrying capacity of the deteriorated structure. However, the authors also acknowledge that the effects of severe ASR and/or DEF effects on the structure needs to be established. The current study will address this issue through the field monitoring and experimental load testing of a C-beam specimen showing severe signs of deterioration due to ASR/DEF. The deterioration data of this specimen will be compared to the other specimens that showed *slight* and *moderate* amounts of deterioration due to ASR/DEF (Mander et al., 2012).

The experimental force-deformation results of the severely damaged specimen will also be compared to the force-deformation results of specimens with *slight* and *moderate* levels of ASR/DEF deterioration. This will permit conclusions to be drawn with respect to the effects that severe ASR/DEF deterioration may have on the load carrying capacity of reinforced concrete structures.

***Is there a mechanics based, straight forward-to-implement method available to determine the force-deformation and internal behavior of structures with significant D-regions?***

Extensive research has been conducted in the field of shear in reinforced concrete beams in the past. Many of the methods just give an idea of the ultimate load at failure of the shear critical members, and few of them have been found to be overly conservative. These methods also do not give any idea about the entire force-deformation behavior of the structure or the internal mechanisms that could eventually lead to the failure of the structure. This is an important aspect that needs to be addressed, especially when determining the behavior and capacity of existing structures.

Many of the modeling approaches that give the force-deformation behavior of a structure are FEM based approaches and may be difficult to implement for practicing engineers. These techniques could also prove to be cumbersome in “seeing” what goes on within the structure and understanding the structure’s internal behavior. This aspect is especially important for analyzing existing structures and checking new designs.

Therefore, there is still a lack of a widely accepted mechanics based, easy to implement method. The C-STM analysis technique developed by Scott et al. (2012a,b) is a significant contribution in this direction. This technique helps to understand the overall force-deformation and internal behavior of the structure. However, there are certain shortcomings that are associated with this analysis technique that needs to be overcome, specifically the implementation of the softened concrete model into the analysis and determining the displacement at failure, and the inability of the technique to model the loading and unloading cycles. These aspects of the C-STM technique will be addressed in this research.

### **3 DISPLACEMENT-BASED COMPATIBILITY STRUT-AND-TIE METHOD AND APPLICATION TO MONOTONIC AND CYCLIC LOADING**

#### **3.1 Summary**

The Compatibility Strut-and-Tie Method (C-STM) is an efficient minimalist nonlinear modeling approach for shear-critical reinforced concrete members. This section presents two key improvements to the C-STM to better model overall behavior through failure. First, modified softened diagonal concrete struts are incorporated directly into the analysis, thereby eliminating any need for post-processing analysis, to enable accurate modeling of the failure load. Second, modeling modifications are made so that the analysis may be conducted in displacement-control, thereby permitting cyclic loading and post-peak (failure) load-displacement behavior to be predicted. The modifications are implemented in SAP2000 and verified with experimental results for both monotonic and cyclic loading cases. It is observed that the C-STM predicts the overall force-deformation behavior of the structure quite well. Additionally, the C-STM also predicts the internal strain-dependent behavior of the structure and gives insights into the cause of failure of the structure. By implementing the proposed modifications to the C-STM, the analysis technique can be greatly improved.

### 3.2 Introduction

Truss models have been used for the analysis and design of reinforced concrete beams since the dawn of the 20<sup>th</sup> century (Ritter, 1899; and Morsch, 1909), where a cracked reinforced concrete beam was essentially treated as an equivalent plastic truss. In the earlier truss approaches, the diagonal crack angles were commonly assumed to form at 45°, and the truss model approach was used as a lower bound solution to determine the shear strength of reinforced concrete structures. Dilger (1966) determined the inclination of the compression truss and shear distortions using strain energy concepts on an analogous truss; however the shear distortions in the beam were often greatly underestimated. Based on experimental tests of coupling beams, Paulay (1971) showed that there was a complex interaction between the shear and flexural reinforcement, and the resulting cracked concrete. Experiments showed that after diagonal cracking occurred in beams with small shear-span to depth ratio, a considerable amount of the transverse shear force was resisted by arch action. In evaluating the post-cracked behavior of coupling beams, shear transfer by truss action, arch action, flexural rotations and beam elongations were considered to be the important components contributing to the stiffness.

Mander (1983) developed a column analysis model accounting for both flexure and shear. This was further developed by Chang and Mander (1994) to enhance the shear portion of the analysis and was known as the Cyclic Inelastic Strut-Tie model. Kim and Mander (1999; 2000a) advanced the Cyclic Inelastic Strut-Tie modeling approach in order to study the behavior of structural concrete members subjected to a combination of shear and flexure. The authors developed the Two-Point Gauss truss model to unify the flexure and shear analysis methods for concrete member including both Beam (B-) and Disturbed (D-) regions. Kim and Mander (2000b) presented a theoretical framework around the SAT modeling approach to predict the inelastic performance of beam-column joints. It was demonstrated that the post-elastic behavior of beam-column joints could be effectively modeled using the SAT technique with a fan-shaped crack pattern.



To et al. (2001, 2003) also conducted investigations to model the force-deformation response of various reinforced concrete elements using SAT models, and were able to model their monotonic and cyclic response. Li and Tran (2012) proposed a semi-empirical approach to compute the angle of inclination of compression struts in the variable angle truss model for shear-critical reinforced concrete beams subjected to flexure and shear. The concrete contribution to shear was addressed by utilizing the strain compatibility condition. Pan and Li (2013) developed a truss-arch model to predict the shear strength of shear-critical reinforced concrete columns subjected to cyclic loading. The proposed model took into account the contributions of concrete and transverse reinforcement to shear in the truss model, and the concrete contribution to shear strength provided by the arch action. The deformation compatibility between the truss and the arch models were incorporated into the model.

The need for a minimalistic computational approach to perform nonlinear analysis of shear-critical reinforced concrete structures was emphasized by Scott et al. (2012a,b). Consequently, a *Compatibility Strut-and-Tie Method* (C-STM) analysis was proposed as a minimalistic computational technique to model the force-deformation behavior of reinforced concrete bridge piers with significant D-regions. The combined truss and arch action that contribute to the shear resistance of reinforced concrete members were captured well in this technique by proposing an arch-breadth scalar ( $\eta$ ). Formulations were developed to define the axial rigidities of the constituent steel and concrete elements of the C-STM model and to model the diagonal concrete struts that were softened due to the presence of orthogonal tensile strains. One of the shortcomings that was identified by Scott et al. (2012b) in the implementation of the C-STM analysis technique was the inability to easily accommodate the compression softening effects on the diagonal concrete struts directly into the analysis procedure. Additionally, the C-STM analysis was carried out in force-control, whereby, the force was incrementally applied to the structure and the corresponding displacements obtained. In this manner the nonlinear monotonic force-deformation behavior of the structure was captured. However, because of the force-controlled nature of the computational modeling, a direct

prediction of the force and displacement corresponding to post-peak (softening) behavior was not possible. As the actual failure mode and displacement were elusive, significant post-analysis assessment was required to infer the point and mode of failure and this often lead to an overestimation of the failure load and displacement.

Truss models based on (differential) panel elements have been used now for some time in the analysis and design of certain concrete structures. The Modified Compression Field Theory (MCFT) proposed by Vecchio and Collins (1986) and the Softened Truss Model proposed by Hsu (1988) for shear and torsion, both account for equilibrium, compatibility and material stress-strain relations to model the force-deformation response of shear-critical structural members. Of particular significance of these approaches is their ability to model the softened effects of concrete. These models were developed based on experimental observations from panel elements subjected to shear. Both of these approaches were classified as the rotating angle models, as the direction of the concrete strut was inclined along the post-cracking principal stresses in concrete at every stage. As the concrete compressive struts were oriented along the principal compressive stress, it could not allow shear stresses to exist along the cracks, and therefore did not take into account the contribution of concrete to the shear resistance of reinforced concrete members. To take into account the contribution of concrete toward shear resistance, a fixed angle softened truss model was developed by Pang and Hsu (1996) where the cracks were inclined at a fixed angle following the principal stresses resulting from the applied loading.

In this study two key modifications are proposed and implemented to the force-controlled C-STM technique developed by Scott et al. (2012a) to be able to predict the point of failure of shear-critical reinforced concrete members with good accuracy. The first being the modifications made to the softened model of the diagonal concrete struts and implementing them directly into the analysis; and the second to conduct the C-STM analysis is displacement-control. Using displacement-control permits the modeling of reversed cyclic loading.

The veracity of the suggested modifications to the C-STM analysis is verified by comparing the results of the C-STM analysis with the results from the experimental study by Bracci et al. (2000) on bent-caps for monotonic loading and the study on coupling beams by Paulay (1969, 1971) for the case of cyclic loading.

### 3.3 Softened Concrete Model for Diagonal Concrete Struts

From the works of Vecchio and Collins (1986), Mau and Hsu (1987), and Hsu and Zhang (1997) it is known that the compression strength of diagonal concrete struts in reinforced concrete beams and panel elements is reduced as a result of the tensile strain acting orthogonal to the compression strain. This phenomenon is known as concrete softening.

Scott et al. (2012a) recast the softening coefficient proposed by Vecchio and Collins (1986) as:

$$\zeta = \frac{1}{1 + \left\langle \frac{C_\varepsilon \varepsilon_2 - 0.0012}{3\varepsilon_{co}} \right\rangle} \quad (3-1)$$

where  $\langle \bullet \rangle$  are Macaulay brackets;  $C_\varepsilon = |\varepsilon_1 / \varepsilon_2|$ ;  $\varepsilon_1$  = the principal tensile strain acting perpendicular to compression strut;  $\varepsilon_2$  = the compression strain (negative) in the diagonal member; the value 0.0012 may be thought of as a cracking strain such that only for values of  $\varepsilon_1 > 0.0012$  the concrete softens; and  $\varepsilon_{co}$  typically equals 0.002. Knowing the principal compressive axial strain  $\varepsilon_{2i}$  in the  $i^{\text{th}}$  concrete strut and the strain in the transverse tie  $\varepsilon_t$ , the tensile strain  $\varepsilon_1$  was determined using Mohr's circle; thus giving the ratio of principal tension to principal compression strains as:

$$C_\varepsilon = \left| \frac{\varepsilon_1}{\varepsilon_2} \right| = \left( \tan^2 \theta_i + \frac{|\varepsilon_t / \varepsilon_{2i}|}{\cos^2 \theta_i} \right) \quad (3-2)$$

in which  $\theta_i$  = diagonal strut angle relative to the longitudinal direction; and the ratio  $\varepsilon_1/\varepsilon_{2i}$  was determined from an elastic analysis of the structure without tension stiffening effects such that  $C_\varepsilon$  remained constant.

Figure 3-1a presents compression softening strain ratio  $\varepsilon_1/\varepsilon_2$  data obtained from over 200 panel tests as presented in Vecchio (2000), who proposed the following empirical equation for concrete softening:

$$\zeta = \frac{1}{1 + 0.35(-\varepsilon_1/\varepsilon_2 - 0.28)^{0.8}} \quad (3-3)$$

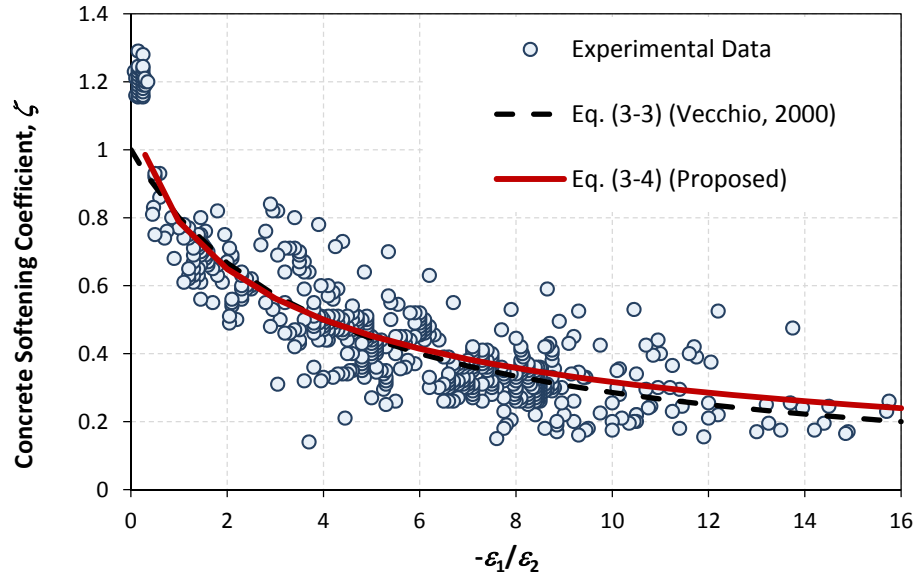
The panel test data presented by Vecchio et al. (2000) may be alternatively represented by:

$$\zeta = \frac{1}{1 - 0.25(\varepsilon_1/\varepsilon_2)} \quad (3-4)$$

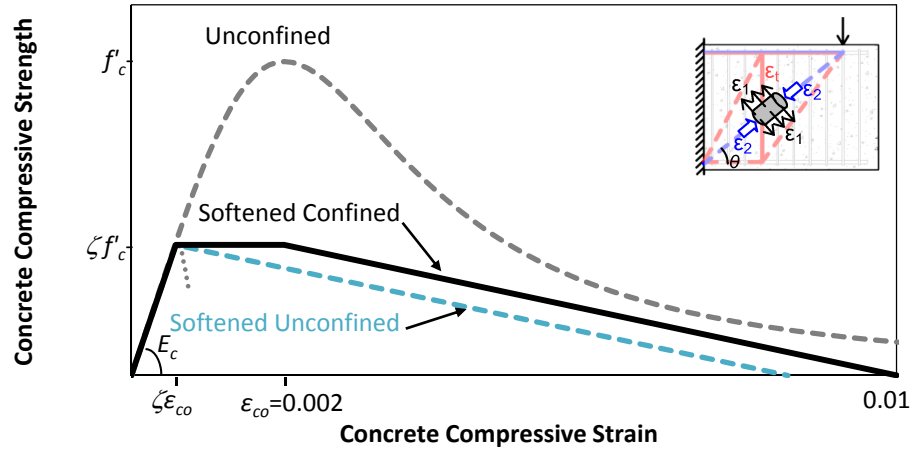
It can be observed from Figure 3-1a that the proposed equation represents the panel test results quite well.

Once the concrete softening coefficient  $\zeta$  is determined, the softened constitutive stress-strain relation for the diagonal concrete strut can be defined by modifying accordingly any viable combined confined and unconfined stress-strain model for concrete such as that proposed by Mander et al. (1988) or Karthik and Mander (2011).

Based on experimental force-deformation results of deteriorated reinforced concrete structures tested by Mander et al. (2014), it was evident that a simple model is necessary to discriminate between softened confined and softened unconfined concrete. Softened unconfined concrete occurs where there is an absence of completely enclosed or hooked hoops around a badly strain-damaged concrete section which results in large transverse strains. It is proposed to distinguish between confined and unconfined softened concrete by the two different softened concrete models shown in Figure 3-1b. The softened confined concrete model can be represented as a linear response in



(a) Compression Softening Data Obtained from Panel Tests (Vecchio, 2000)



(b) Softened Concrete Model

**Figure 3-1: Diagonal Concrete Web Elements.**

accordance with Model A of Vecchio and Collins (1993), whereas the softened unconfined model neglects the plateau at peak softened concrete strength as shown in Figure 3-1b.

In the C-STM analysis, the principal tension strain  $\varepsilon_1$ , may be assessed from indicator (dummy) strain members where  $AE = 1$ . When placed perpendicular to the diagonal concrete struts, the computed forces are equal to the transverse strain. The results are used in (3-4) to determine the reduced (softened) concrete stress-strain model. However, note that the softened model for concrete is somewhat sensitive to  $\varepsilon_1$  and the value of  $\varepsilon_1$  is dependent on where the transverse strain member is placed relative to the diagonal concrete element. In cases where the strain  $\varepsilon_1$  cannot be determined directly from the analysis, the procedure presented in Scott et al. (2012a) may be used.

### **3.4 Implementation of Analysis in Displacement-Control**

Experiments in the laboratory can be conducted either in load-control or displacement-control. In the case of load-controlled tests, the structure/specimen is subjected to an incremental force, and the corresponding displacement at equilibrium is measured. On the other hand, in the case of a displacement-controlled test, the structure is subjected to an incremental displacement via actuators and the corresponding response is the force which is captured via load cells or inferred from hydraulic pressure. Most laboratory tests are conducted in displacement-control. Thus, while trying to model and simulate the experimental results, it is essential to conduct the analysis to reflect such behavior.

In the C-STM analysis carried out by Scott et al. (2012b), the analysis was carried out in force-control. While satisfactory results were obtained, the analysis was not truly representative of the actual testing procedure especially when the analysis approach the peak load. A shortcoming of conducting the analysis in force-control is that it is unable to determine the force and corresponding displacement at failure of the structure directly from the analysis as demonstrated by Scott et al. (2012b). It is important to quantify the post-peak behavior of the structure to give an insight into the ductility of the structure, which is a critical information that needs to be captured,

especially in shear-critical structures that may fail in a very brittle manner. Scott et al. (2012b), who conducted their analysis in load-control by using incremental steps in force, required significant post-processing of their results to identify the force and the corresponding displacement at which a reinforced concrete member failed. In order to overcome this shortcoming, the current investigation uses a displacement-control strategy. This better represents the experimental test results. Using this analysis technique it is possible to capture the overall force and deformation behavior under cyclic loading and to model the post-peak behavior through failure.

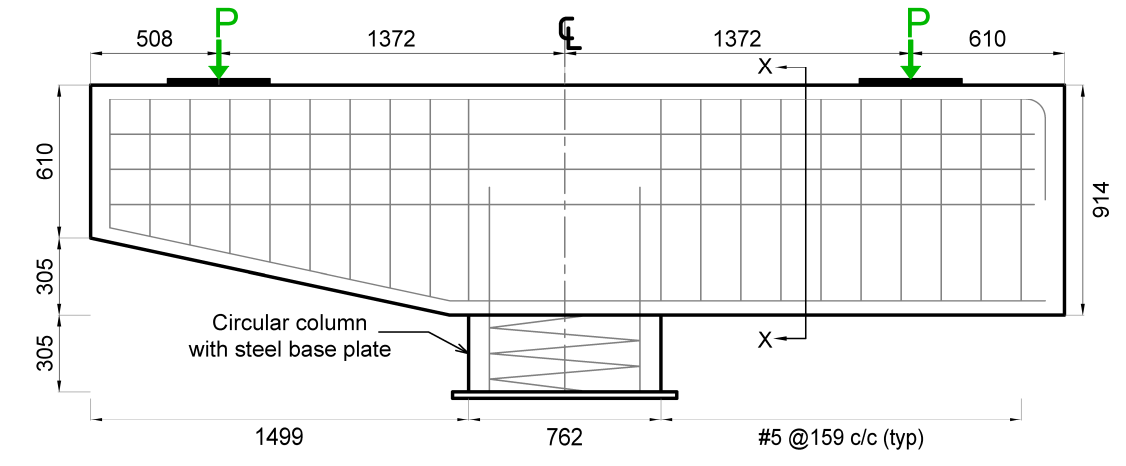
The effectiveness of the above two improvements to the C-STM analysis procedure is validated by implementing the C-STM analysis technique for monotonic and cyclic load cases in what follows.

### **3.5 Monotonic Loading Modeling Validation: Bridge Bent-Cap**

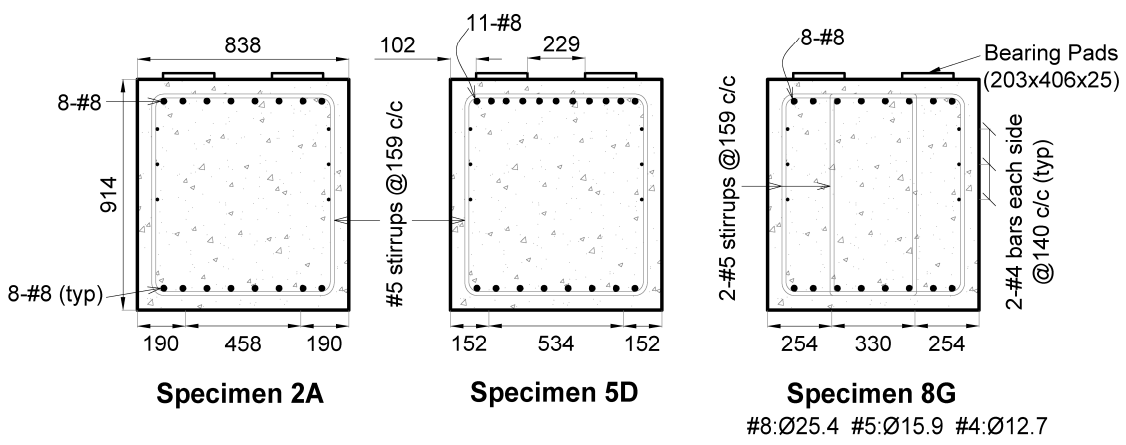
Bridge bent-caps used in Texas have shown signs of distress near the column-to-bent-cap negative moment connection. Full scale physical models were experimentally tested by Bracci et al. (2000) in order to determine their nonlinear performance through to failure and investigate the cause of the cracks. A FEM model of the specimens was analyzed by Powanusorn (2003) to simulate the force-deformation behavior of the bent-cap specimens. In this study three specimens were chosen to validate the displacement-based C-STM procedure.

Figure 3-2 present the reinforcement layout and cross-section of the three bent-cap specimens selected for the analysis. The reported material strength data are presented in Table 3-1. As no test day concrete strength results were available, the 28 day strength was assumed for the analysis of the specimen. The preliminary code-based computations for the bent-cap specimens are presented in detail in Appendix A2.

Figure 3-3 shows the C-STM model adopted which overlays the elevation of the specimen. Using the modeling procedure described in Scott et al. (2012a), the C-STM analysis with the proposed improvements was implemented for the experimental reinforced concrete bent-cap specimen in order to provide an informative analysis. Based on the guidelines laid out by Scott et al. (2012a), the C-STM geometry, member axial rigidities and material stress-strain relation (excluding diagonal concrete web elements) were established.



(a) Front Elevation



(b) Cross-Section (Section X-X)

**Figure 3-2: Elevation and Cross Section of Selected Bent-Cap Specimens.**



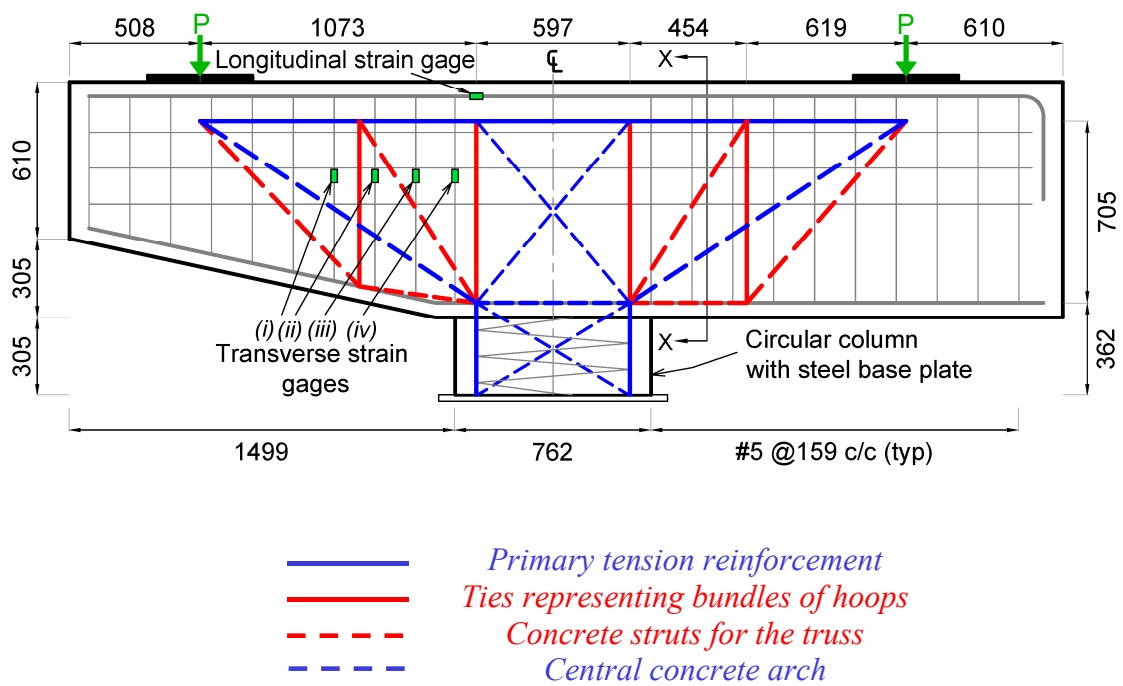
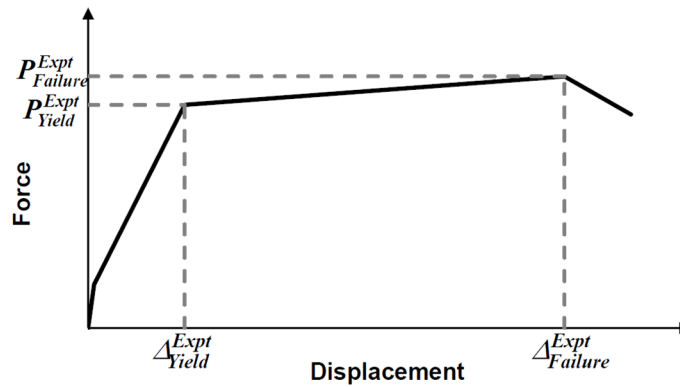


**Figure 3-3: C-STM Model for Bent-Cap Specimen.**

**Table 3-1: Material Properties, and Experimental Results for Bent-Cap Specimens.**

		Specimen 2A	Specimen 5D	Specimen 8G
<b>Material Properties</b>	$f'_c$ (MPa) <sup>#</sup>	42.7	37.9	36.5
	$f'_t$ (MPa)	2.21	2.07	2.00
	$E_c$ (MPa)	30960	29130	28615
<b>Experimental Results</b>	$P_{Yield}^{Expt}$ (kN)	1468	1890	1535
	$P_{Failure}^{Expt}$ (kN)	<b>1797</b>	<b>2068</b>	<b>1926</b>
	$\Delta_{Yield}^{Expt}$ (mm)	6.35	8.13	8.13
	$\Delta_{Failure}^{Expt}$ (mm)	19.56	12.70	32.00 <sup>†</sup>
	$\mu$	3.08	1.56	>3.94

<sup>#</sup> TxDOT Class C Concrete-Average compression strength of three 28-day cylinder tests (Section 15.3, ACI 318-99). <sup>\*</sup> Expected critical failure mode capacity. <sup>†</sup> Specimen was not loaded to ultimate failure. Superscript: *b*=beam; *f*=flexure; *s*=shear; SAT=strut-and-tie; Expt=Experiment. Notations for experimental results:



The softened stress-strain relationship for the diagonal concrete struts were based on the softened confined model shown in Figure 3-1b, as no significant structural damage was observed around the diagonal strut elements, and the hoops were fully lapped. The strains  $\varepsilon_1$  and  $\varepsilon_2$  were obtained by first performing a C-STM analysis with strain indicator-members perpendicular to the diagonal concrete elements. For Specimen 2A, the ratio  $\varepsilon_1/\varepsilon_2$  was found to be -7.17 at the peak softened compressive stress. Thus according to (3-4) the concrete softening coefficient is  $\xi = 0.36$ . The softened stress-strain relation was established and implemented as a tri-linear curve for confined softened concrete as shown in Figure 3-1b. In order to conduct the analysis in displacement control and preserve the correct boundary conditions, near-rigid loading frames and additional supports were introduced into the model. However, it was necessary to ensure that the introduction of additional elements in the model did not adversely affect the behavior of the structure. Figure 3-4 shows the nonlinear concrete material properties that were used for the concrete elements in the C-STM analysis of the three bent-cap specimens.

Figure 3-5 shows the experimentally obtained force-deformation response and the C-STM results along with the external load causing beam flexure and flexure yielding for all the three bent-cap specimens. As these are only a strength-based approach, no predictions of the structure's global deformation could be made; the forces are thus represented by horizontal lines in Figure 3-5. From these results, no definitive conclusions regarding either the load or the displacement capacity of the bent-cap specimen can be drawn.

### **3.6 C-STM Results and Discussion**

The C-STM approach was used to computationally model the force-deformation and internal strain behavior of the bent-cap specimens; the simulated results were also compared to Bracci et al. (2000) experimental observations. Figure 3-5 presents a comparison of the experimental results with the computational C-STM response implemented in version 17.0.0 of SAP2000 (2014) for the bent-cap specimens.

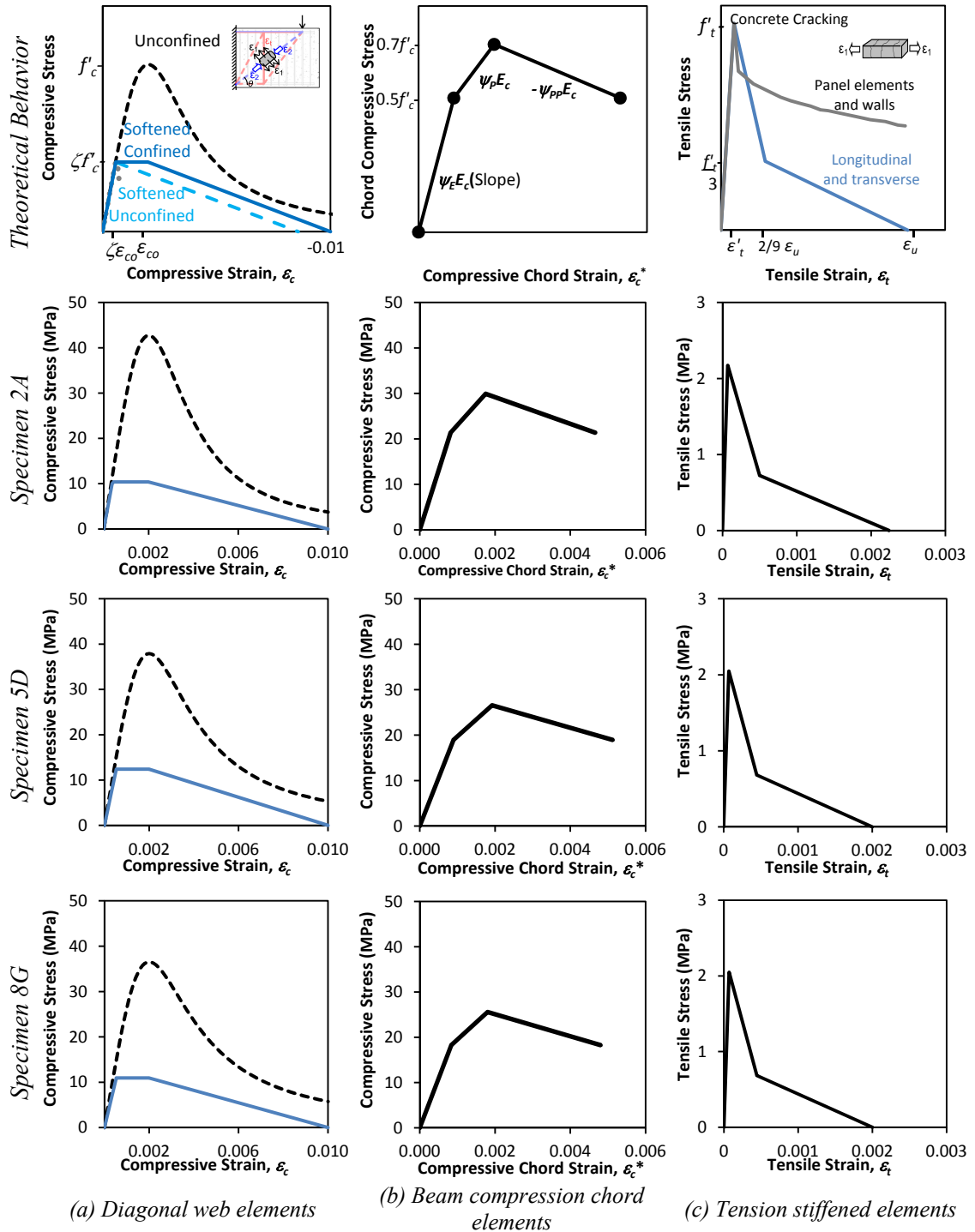
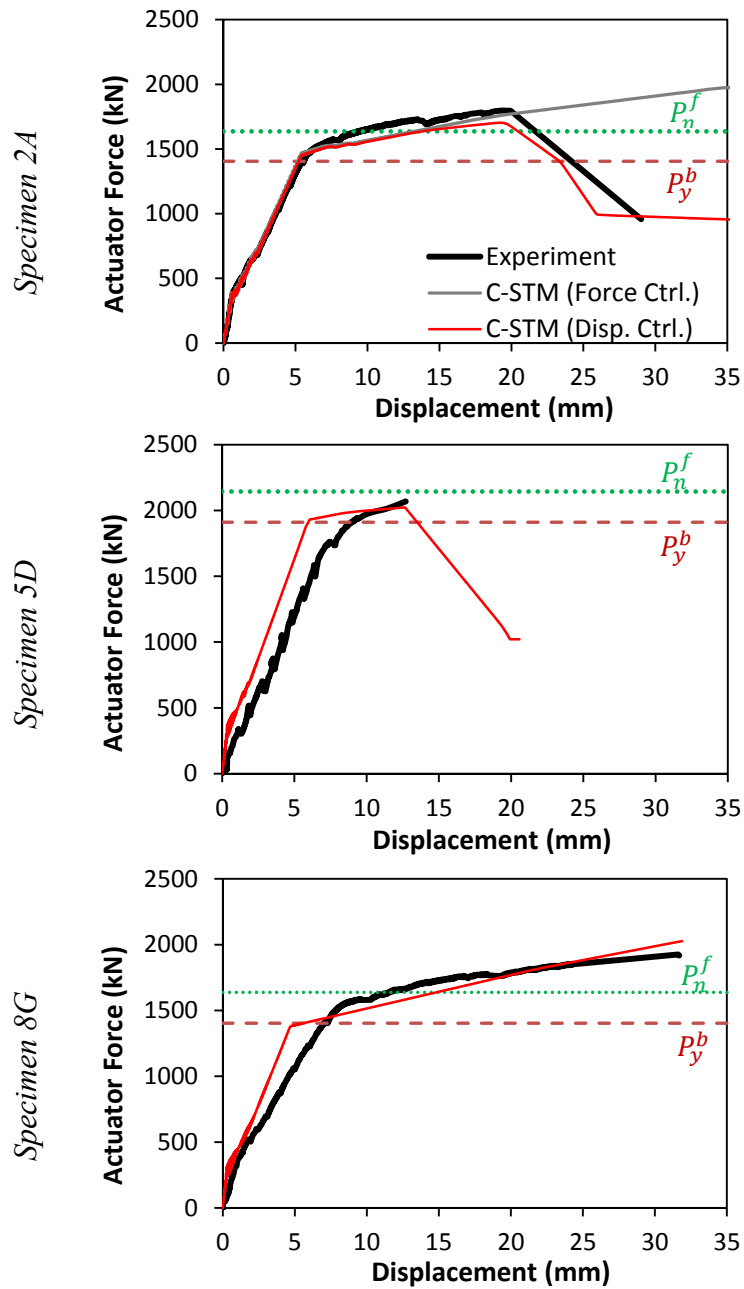


**Figure 3-4: Cracked Reinforced Concrete Material Properties.**

Specimen 2A in Figure 3-5 shows the C-STM force-deformation results obtained from both force-control and deformation-control implementation of the analysis. It is evident that the analysis in force-control fails to capture the post-peak behavior of the bent-cap specimen, especially the descending branch. Because of the improvements introduced to the C-STM technique, the computational modeling in displacement-control captures the post-peak behavior quite well; accurate predictions of the load and displacement of the specimen at failure were also possible. However, it was also observed that the point of failure was sensitive to the peak softened concrete strength which was dependent on the location along the diagonal strut where the transverse strains  $\varepsilon_t$  were measured.

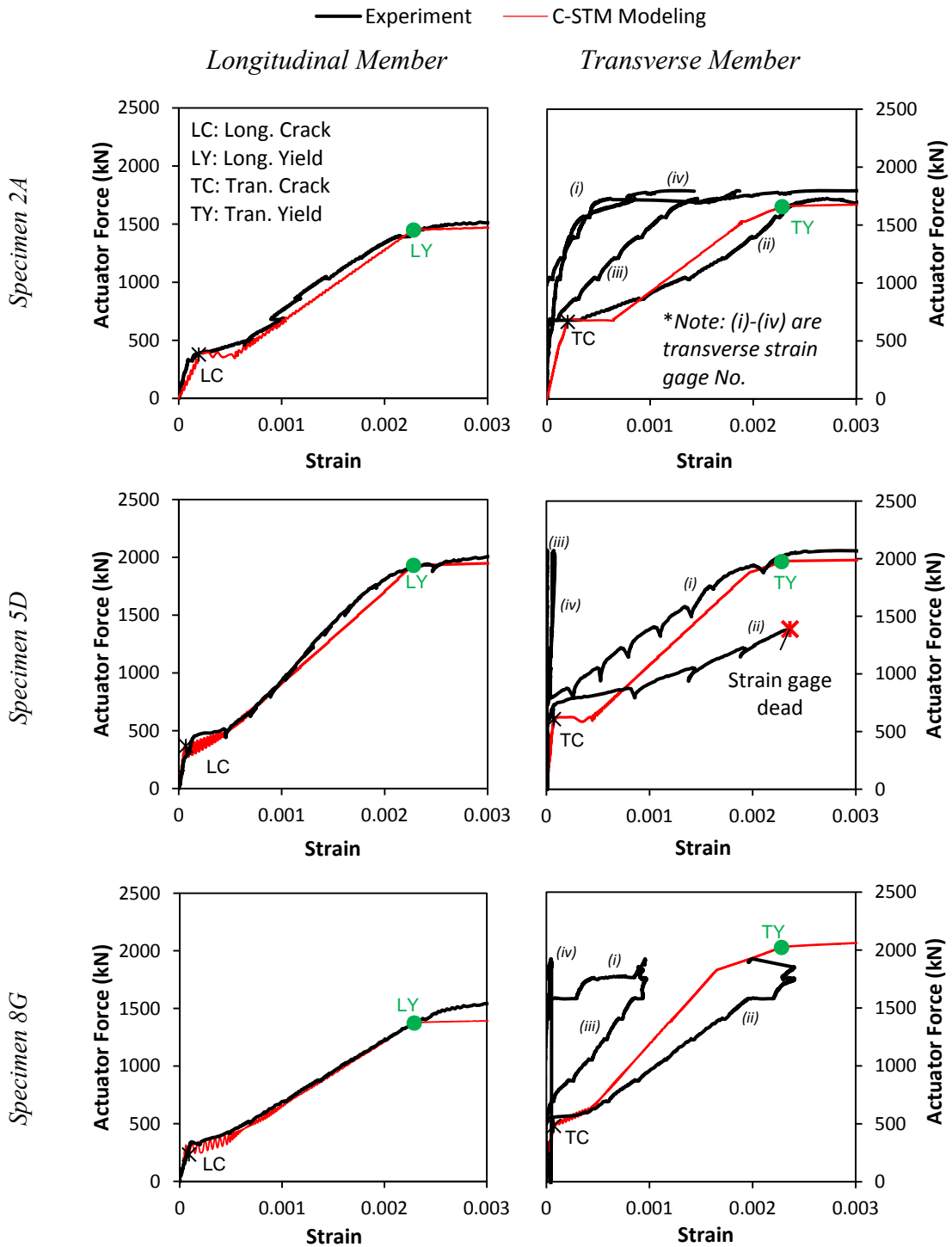
Figure 3-6 shows a comparison of strains obtained experimentally from strain gages with the corresponding member strains obtained from the C-STM analysis in both longitudinal and transverse members. It is evident that the C-STM also predicts the internal member strains quite well.

Figure 3-7a shows the order of nonlinear hinge formation observed in the C-STM analysis. These nonlinear events are indicated as points on the force-deformation curve (Figure 3-7b), and provide insight into the progression of the nonlinear hinges relative to the global force-deformation behavior of the structure. From Figure 3-7b it is evident that there is a drastic change in the slope of the overall force-deformation response when the longitudinal tensile reinforcement yields (Event 6). As the load increased, the steel yield propagated (Event 7) along the top longitudinal reinforcing bars. The next nonlinear mechanism was the yielding of the transverse steel elements (Events 8 and 9) which resulted in large shear deformations and indicated the widening of the diagonal shear cracks observed close to the ultimate load. Once the transverse steel yielded, the stiffness reduced slightly with additional load being carried by the corner-to-corner arch diagonal until the onset of concrete crushing (Event 10). As the displacements increased, the diagonal arch softened and the applied load reduced. In the C-STM analysis it was observed that after the arch diagonal on the right side of the specimen reached its peak softened stress, the strains in the arch diagonal on the left portion of the specimen

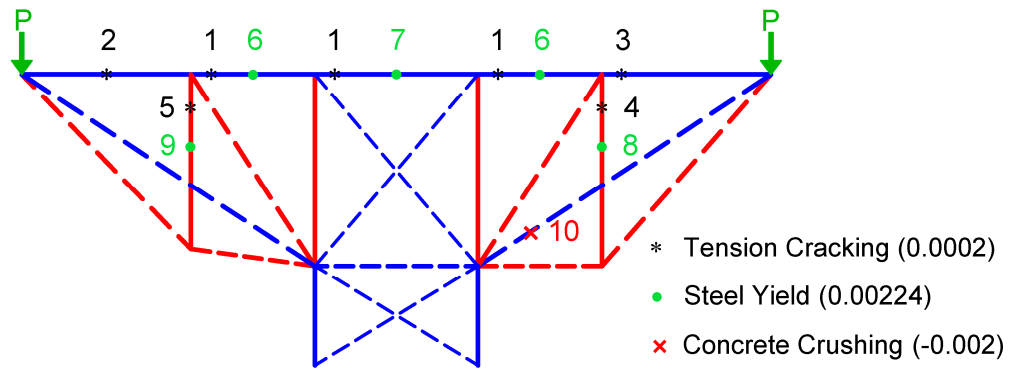


Note:  $P_n^f$  = Nominal strength and  $P_y^b$  = yield strength.

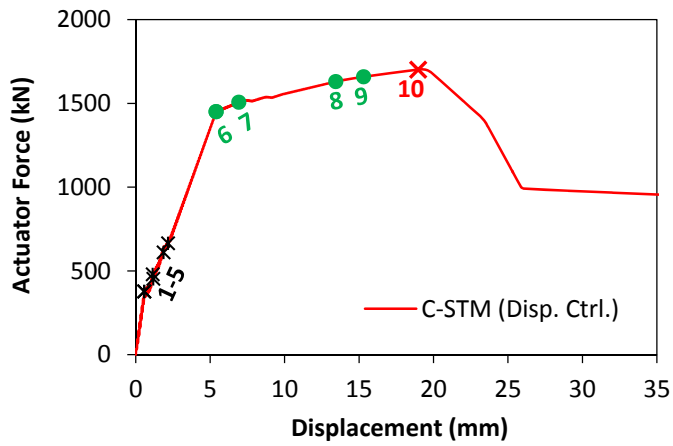
**Figure 3-5: Comparison of Experimental and C-STM Results.**



**Figure 3-6: Comparison of Internal Member Strains Obtained from C-STM Analysis with Experimental (Bracci et al., 2000) Results.**



(a) Sequence of Nonlinear Events Formation



(b) Progression of Nonlinear Events along the Force-Deformation Curve

**Figure 3-7: Failure Analysis of Specimen 2A**



continued to increase. The commencement of the descending portion of the load-deformation curve corresponds to the point when the stress in the arch diagonal on the left side of the specimen started to decrease.

### **3.7 Cyclic Loading Modeling Validation: Coupling Beam**

Paulay (1969, 1971) tested reinforced concrete coupling beams to investigate the flexure-shear interaction in these structural members and their overall behavior under cyclic loading. Coupling beam specimens with different span-to-depth ratios were investigated in his experimental study. The adjoining shear walls were simulated by means of heavily reinforced end blocks that enabled the loads to be transferred to the 152 mm thick coupling beam specimen. Test beam 312 was selected for this modeling study. C-STM was used to simulate the force-deformation characteristics and the internal strain behavior of the specimen and the modeled results were compared with Paulay's experimental observations. The dimensions and cross-section of the coupling beam, and two C-STM models based on different numerical integration schemes are presented in Figure 3-8.

Two integration schemes, namely the Boole's Rule and Two-Point Gauss (Kim and Mander, 1999) were used to represent two different C-STM models as presented in Figure 3-8a and b respectively. The two models differed from each other in the way transverse stirrups were lumped into the vertical ties and the diagonal concrete members. The top and bottom chords were placed along the centroid of the top and bottom reinforcing bars of the specimen. The vertical ties were located based on the numerical integration scheme adopted. The concrete members of the truss were sized based on the recommendations made in Kim and Mander (2000a) and the concrete arch for the Two-Point Gauss model was sized based on recommendations in Holden et al. (2003). The end blocks were modeled to be sufficiently strong and were not the subject of this study as was the case in the experimental program. Displacements were applied along the centerline of the coupling beam by means of a loading frame. The applied displacements were transferred to the coupling beam via the end blocks. The displacements were applied in three complete loading and unloading cycles to replicate the loading sequence during the actual test.

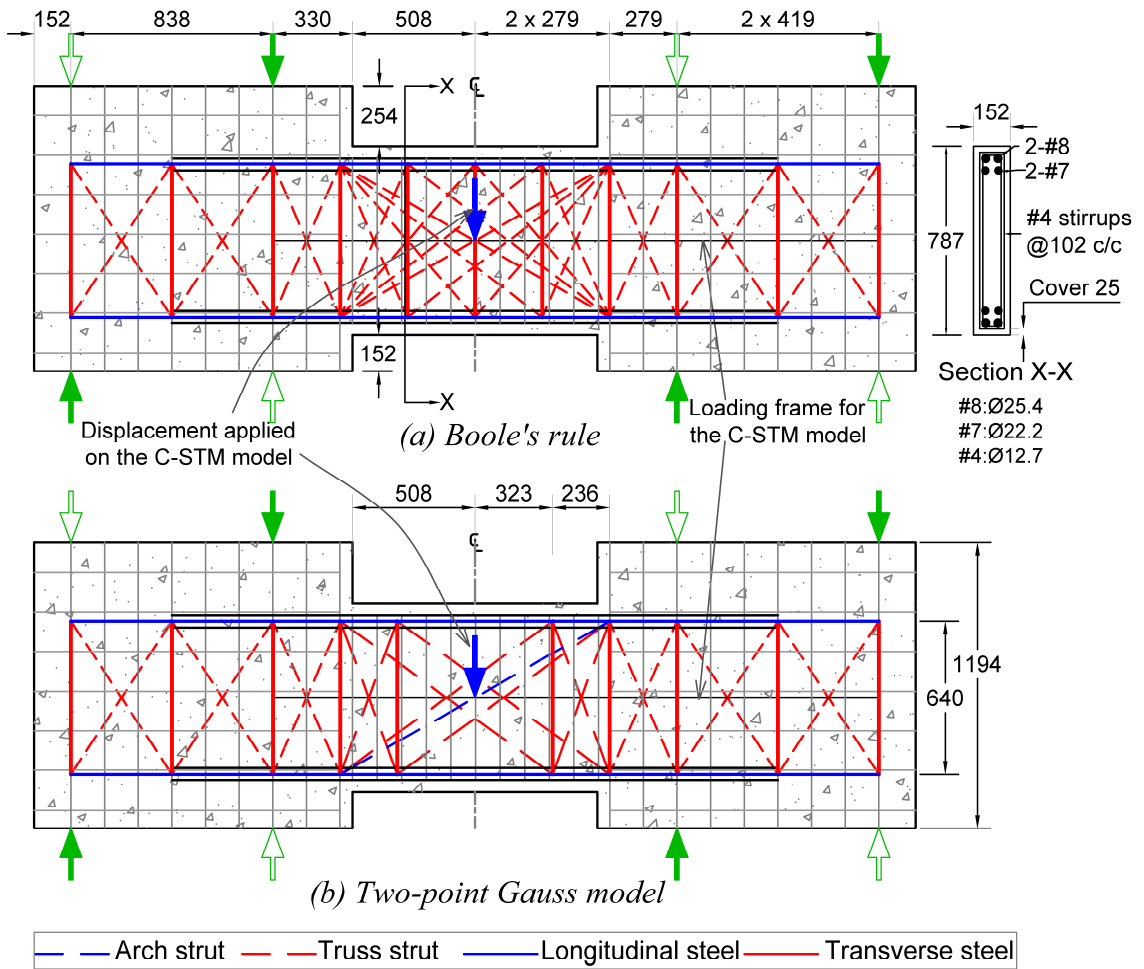


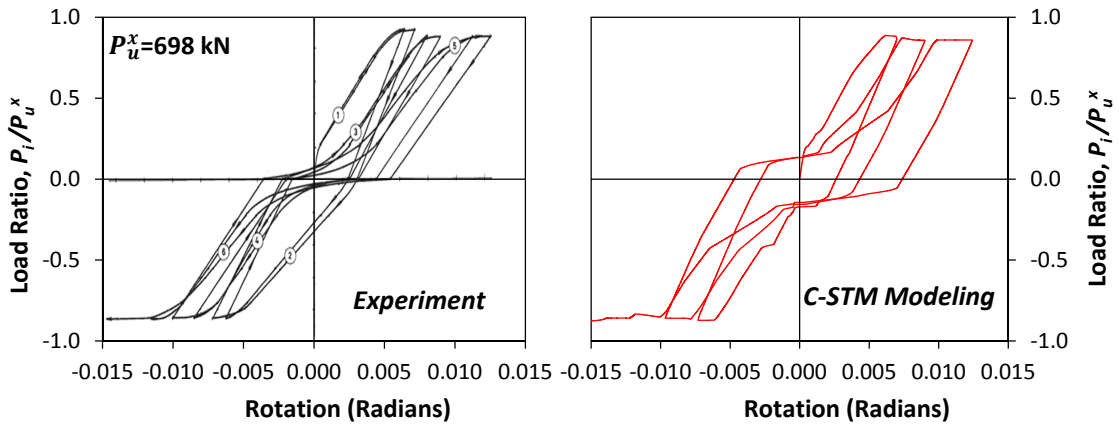
**Figure 3-8: Elevation, Cross-Section and C-STM of Coupling Beam 312.**

### 3.8 C-STM Results and Discussion

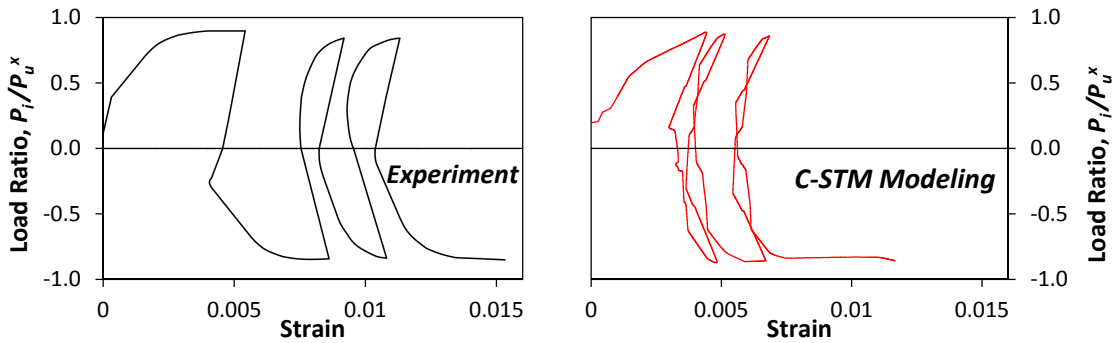
Figure 3-9a compares the overall load-rotation behavior of the coupling beam obtained from the C-STM analysis with the experimental results. Considering the complexity of the structure, the results obtained from the C-STM analysis are in good agreement with the experimental results. The main discrepancies between the analytical and experimental results are during the first load reversal cycle and the unloading stiffness. These differences are attributed to the limited flexibility of defining the concrete hysteresis behavior in the software package (SAP2000, 2014) that was used for the C-STM analysis. In this particular analysis the pivot hysteresis model provided better results when compared to the Kinematic or the Takeda concrete hysteresis model. It was observed that the overall force-rotation behavior obtained using either of the two C-STM models gave comparable results, therefore only C-STM results based on Boole's rule are presented herein.

Figure 3-9b shows a comparison of the strains in the stirrups at the centerline of the coupling beam. The experimental results presented are from one of the total five strain gages placed along the length of the stirrup at the centerline. The experimental results also showed that the strains in the stirrups varied widely along the length of the stirrup. However, the C-STM provides the average strain in the vertical tie member along the centerline of the coupling beam, as the strains at different locations along the vertical tie could not be determined through the analysis. Although the strains do not precisely agree, a favorably close trend is evident for the strain profile obtained by the C-STM analysis when compared to the experimental results. The difference in the strain values are likely due to creep strains during the experimental testing, that was conducted over a period of four days. Additionally, the distribution of strains in the stirrups along the centerline of the coupling beam could not be obtained from the Two-Point Gauss truss model due to its configuration.

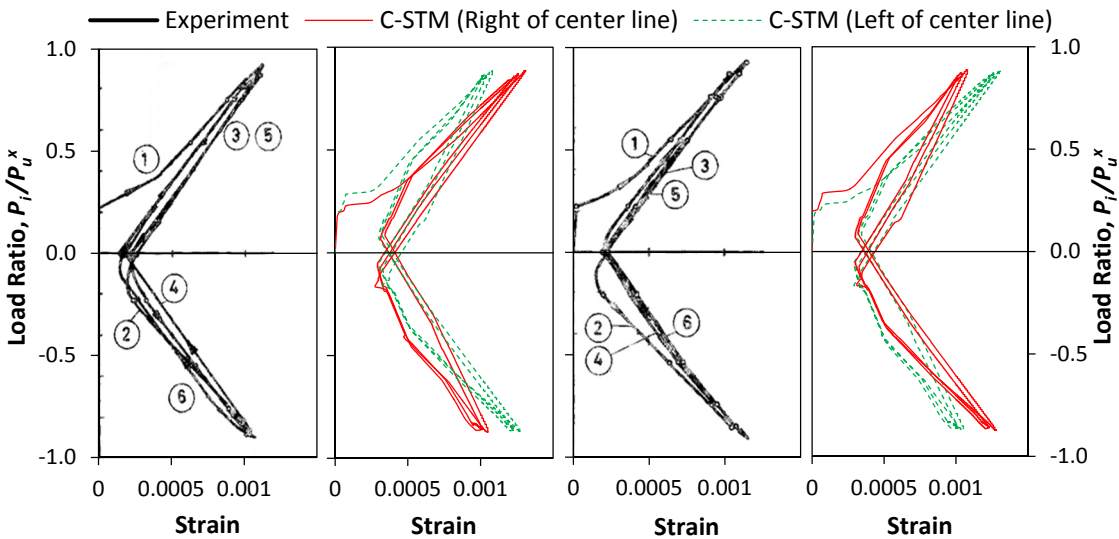
Figure 3-9c compares the strain history in the top and bottom flexural reinforcement. The experimental strain measurements were made at the centerline of the coupling beam. For the analytical C-STM results, the strains in the top and bottom chord



(a) Overall Force-Rotation Behavior of Coupling Beam 312



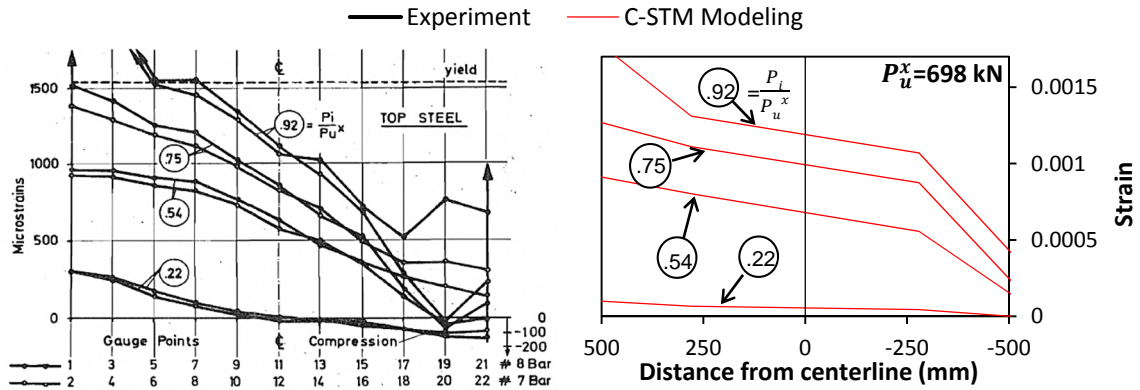
(b) Behavior of Transverse Reinforcement Along Centerline of Coupling Beam 312



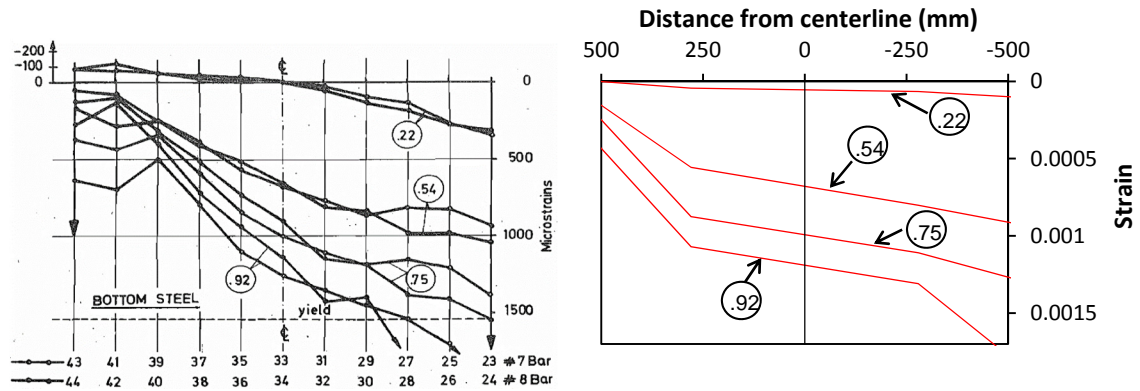
(c) Top Flexural Reinforcement History (d) Bottom Flexural Reinforcement History

Note:  $P_u^x = 698$  kN. Experimental results from Paulay (1969).

**Figure 3-9: Comparison of Experimental and C-STM Results for Coupling Beam 312.**



(a) Top Flexural Reinforcement Strains



(b) Bottom Flexural Reinforcement Strains

Note: Experimental results from Paulay (1969)

**Figure 3-10: Spatial Distribution of Strains along Coupling Beam Reinforcement.**

just to the left and right of the centerline are presented. Again, good agreement is evident throughout both the loading and unloading cycles.

Figure 3-10 presents a comparison of the spatial distribution of strains along the flexure reinforcement of the coupling beam. Figure 3-10a and b compares the top and bottom flexural reinforcement strains respectively, from the first load cycle that were obtained experimentally (from strain gages placed along the length of the reinforcement) with strains obtained from the C-STM analysis. Similar trends are evident between the experimental and C-STM results for different load ratios. Note that the internal strain behavior obtained from both the C-STM models were similar for the cases presented in Figures 3-9c and 3-10.

### **3.9 Closure and Key Findings**

The C-STM analysis technique is a minimalist analysis approach that can be used to provide a deeper insight into the nature of flexure-shear interaction in shear-critical structures. Previous shortcomings identified with the existing force-controlled implementation of the C-STM analysis (Scott et al., 2012a,b) were addressed. The two necessary improvements to the C-STM model were (i) the implementation of the softened concrete model for diagonal strut members directly into the analysis; and (ii) the displacement-controlled implementation of the analysis. The discrimination between compression softened models for confined and unconfined concrete was also established. By implementing the proposed changes to the C-STM analysis, satisfactory results were obtained for both monotonic and cyclic loading of shear-critical structures. It was demonstrated that the displacement-controlled C-STM analysis technique is a reliable computational technique that can quite accurately assess the behavior of shear-critical structures and predicts the overall force-deformation behavior of the structure. Moreover, the C-STM predicted the internal behavior of the structure quite well and provided further insight for longitudinal and transverse steel yield and diagonal arch crushing events as they occurred. The proposed improvements enable the post-peak falling branch of the force-deformation response to be captured and predict the failure load and displacement with good accuracy.

## 4 MODELING ASR/DEF EXPANSION IN REINFORCED CONCRETE STRUCTURES\*

### 4.1 Summary

Despite several attempts to develop a model for ASR/DEF related expansion in reinforced concrete, there is a dearth of simple practical approaches. A minimalist semi-empirical model is developed to simulate the expansion strains caused by ASR/DEF expansion in reinforced concrete. The model accounts for the reinforcement ratio and also takes into consideration the effects of externally applied compressive and tensile loads that, respectively, inhibit and promote ASR/DEF related expansion. The reaction kinetics are implicitly included in the proposed model via the ASR/DEF related model input parameters. The model takes into account the variation in temperature and moisture (degree of saturation) and thus expands the applicability of the proposed model to concrete structures exposed to field conditions. A rate form of the equation is also derived which can be easily implemented in a computer program to do an incremental expansion strain analysis taking into account the daily variations in temperature and moisture content. A comparison of the model with expansion data obtained from small-scale reinforced concrete specimens stored under constant temperature and fully saturated conditions shows good promise. The application of the proposed model to large-scale reinforced concrete spliced column specimens which exhibit damage resulting from ASR/DEF related expansion, also shows good comparison with field measured expansion strain data. The model captures well both the longitudinal and transverse expansion strains in the specimens. Considering the wide scatter of the field measured expansion data, the model does a good simulation of the expansion results,

---

\* Previously published work is available to the public through National Technical Information Service. Mander, J.B., Karthik, M.M., and Hurlebaus, S. (2015). "Structural Assessment of "D" Region Affected by Premature Concrete Deterioration: Technical Report." *Report No. FHWA/TX-15/0-5997-2*, Texas A&M Transportation Institute, College Station, Texas, USA.

with most of the results lying between the extremities of the experimental data observed. It is demonstrated that if appropriate values are assigned to the limited input parameters required for the model, the proposed minimalist semi-empirical model can be effectively used to model ASR/DEF induced expansion strains in reinforced concrete structures.

## **4.2 Introduction**

Alkali-Silica Reaction (ASR) can be described as a chemical reaction between the alkalis in the cement and the reactive silica in the aggregates, which react to form alkali-silica gel. This gel absorbs moisture and expands causing the concrete to crack. Delayed Ettringite Formation (DEF) is the formation of ettringite in hardened concrete when the concrete is subjected to high temperatures, generally greater than 70°C, during curing and is exposed to moisture later in its life. This, like ASR, causes the hardened concrete to expand and thereby induces tensile cracking.

The effects of ASR and DEF on long term concrete behavior have been studied extensively over the past few years. Studies have shown that several factors affect ASR expansion in concrete, such as alkali content of the cement, reactivity of aggregates, temperature, and humidity, among others. The majority of previous studies, however, have concentrated on the effects of ASR on plain concrete; only a few are related to reinforced concrete. It has been established that external restraint (compressive) stresses and passive restraint stresses induced by reinforcement (confinement) can significantly influence the expansion caused by ASR on reinforced concrete (Hobbs, 1988; Jones and Clark, 1996; Multon et al., 2006). The effect of DEF induced expansion on reinforced concrete also has gained significant attention in recent times. Again, there is sufficient evidence to show that externally applied stresses and/or internal restraint stresses induced by confining or longitudinal reinforcement can significantly reduce the expansion caused by DEF in reinforced concrete (Bouzabata et al., 2012).

Although extensive research has been conducted to model the expansion caused by ASR in concrete, a review of past investigations show that a majority of the work has been limited to plain concrete. The effects of compressive stresses on ASR expansion have not been solved by predictive models using the concepts of chemoelasticity



(Multon et al., 2006). Additionally, most of the research combines the finite element method with the chemical mechanism to come up with a model for expansion in concrete due to ASR (Ulm et al., 2000; Li and Coussy, 2002; Capra and Sellier, 2003; to name a few). These methods are complex and difficult to effectively implement in a regular design office engineering practice.

The present study presents a minimalist semi-empirical strain-based model for the analysis of swelling strains in reinforced concrete members due to ASR/DEF expansion. The proposed model is then validated against experimental observations made on small-scale specimens cast and cured in saturated conditions in a laboratory test setting. Later, modifications are proposed to the model to account for realistic field temperature and moisture content (partial saturation) variations. Finally, the proposed model is used to simulate the expansion strains observed in field-cured large-scale specimens showing signs of ASR and DEF. Considering the wide variability in the experimental data, one can observe that the proposed minimalist model is able to satisfactorily capture the expansion strains in reinforced concrete.

#### 4.3 Modeling ASR/DEF Expansion in Saturated Prisms

Based on an examination of experimental results, ASR/DEF induced expansion over time follows the general form presented in Figure 4-1 for plain and reinforced concrete. Therefore, a semi-empirical model to estimate the expansion strains caused by evolving ASR/DEF expansion in reinforced concrete is developed herein. A hyperbolic tangent function is proposed for the backbone equation which has the general form:

$$\varepsilon(t) = \varepsilon_{\rho}^{\max} \tanh\left\langle \frac{t-t_o}{t_r} \right\rangle \quad (4-1)$$

in which  $\varepsilon(t)$  = the expansion strain in reinforced concrete due to the combined effects of ASR and DEF expansion at time  $t$ ;  $\varepsilon_{\rho}^{\max}$  = the maximum expansion in reinforced concrete, which is a function of reinforcement ratio  $\rho$ ;  $t_o$  = the initiation time when expansion due to ASR/DEF commences;  $t_r$  = the “rise time” of the hyperbolic tangent

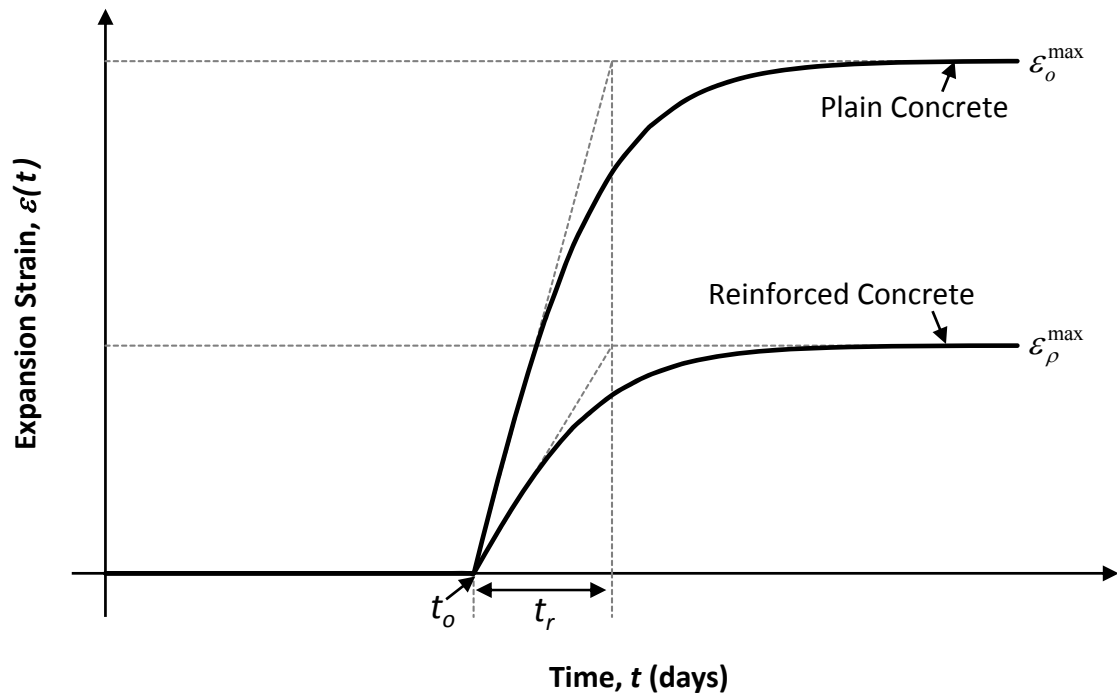


Figure 4-1: Expansion Model for ASR/DEF Induced Expansion in Concrete.

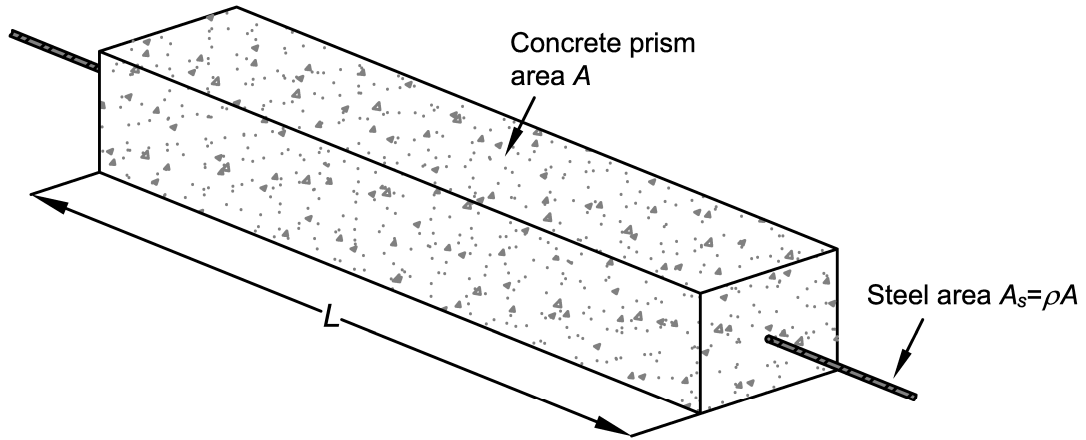
line, which is the time from the beginning of ASR/DEF induced expansion to when the maximum expansion is reached along the tangent line; and  $\langle \bullet \rangle$  are the Macaulay brackets, which represent a common engineering notation used to describe if  $t - t_o < 0$ , then  $\langle t - t_o \rangle = 0$ . The parameters  $t_o$  and  $t_r$  are empirically determined from the experimental expansion observations.

The other unknown parameter in (4-1), the maximum expansion in concrete  $\varepsilon_\rho^{\max}$ , is determined based on a strain energy approach. The strain energy density  $u$  of the concrete prism of area  $A$ , length  $L$  as shown in Figure 4-2a, and subjected to an axial stress,  $\sigma$ , is given by:

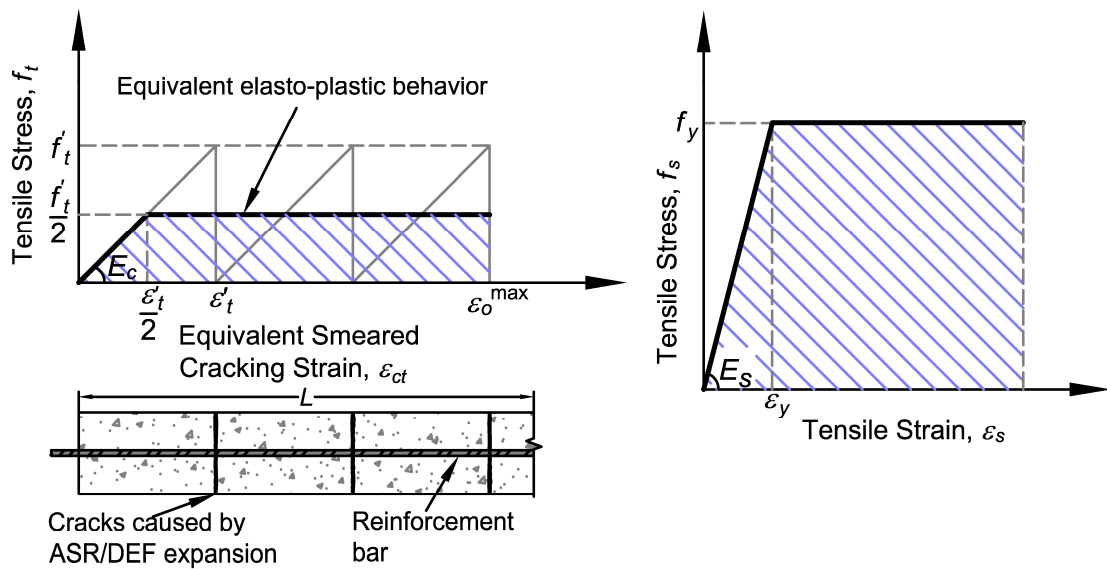
$$u = \int_0^\varepsilon \sigma d\varepsilon \quad (4-2)$$

where  $\varepsilon$  and  $\sigma$ , respectively, are the strain and stress. In the simple case, to compute the strain energy in reinforced concrete, the strain energy in concrete  $U_c$  and steel  $U_s$  needs to be calculated.

Figure 4-2b shows an equivalent elasto-plastic stress-strain relation of concrete in tension that is adopted for this study. This can be explained as follows. Consider the rectangular concrete specimen in Figure 4-2b with a single reinforcing bar running through the center of the specimen. The longitudinal free expansion of the concrete specimen is restrained by the reinforcing bar. As the ASR/DEF induced expansion within the concrete proceeds over time, the concrete reaches its maximum tensile strength and a crack forms about the mid-length of the specimen. This results in the concrete tensile strength at the crack to be zero. As further expansion occurs, the maximum concrete tensile strength is reached mid-way on either side of the cracked specimen, resulting in cracks at every quarter-point of the specimen; the next cracks form at the  $1/8^{\text{th}}$  points of the concrete specimen. This phenomenon may be considered as a *divide and conquer mechanism*; accordingly the process continues until the cracks are spaced about the maximum aggregate size. At its final cracked state, as shown in



(a) Idealized Reinforced Concrete Prism Subjected to the Expansion Effects of ASR/DEF



(b) Elasto-Plastic Model of Concrete in Tension

(c) Elasto-Plastic Model of Reinforcing Steel

Figure 4-2: Stress-Strain Models for Components of Reinforced Concrete.

Figure 4-2b, the tensile strength of concrete at the cracks will be zero, but the concrete will possess some tensile strength between the cracks. The effective saw tooth model of the tensile stress-strain relation averaged over the length of the prism of concrete can be represented by the equivalent elasto-plastic model shown in Figure 4-2b. The concrete strain energy density, which is the shaded area beneath the stress-strain curve shown in Figure 4-2b, is given as:

$$u_c = \frac{E_c}{2} \left[ \varepsilon_{ct}^2 - \left\langle \varepsilon_{ct} - \frac{\varepsilon'_t}{2} \right\rangle^2 \right] \quad (4-3)$$

in which  $E_c$  = Young's modulus of concrete;  $\varepsilon_{ct}$  = tensile strain in concrete;  $\varepsilon'_t$  = strain corresponding to tensile strength of concrete  $f'_t$ .

Figure 4-2c shows the elasto-plastic stress-strain relation of reinforcing steel. Depending on the reinforcement ratio of the reinforced concrete structure, two cases require consideration. First, when the expansion strains caused by the combined ASR/DEF expansion are greater than the yield strain of the reinforcing steel, and second when the strains are below the yield strain. The strain energy density of steel, which is the area under the curve in Figure 4-2c, is given by:

$$u_s = \frac{E_s}{2} \left[ \varepsilon_s^2 - \left\langle \varepsilon_s - \varepsilon_y \right\rangle^2 \right] \quad (4-4)$$

in which  $E_s$  = Young's modulus of steel;  $\varepsilon_s$  = tensile strain in steel; and  $\varepsilon_y$  = yield strain of reinforcing steel. When the strain is below the yield strain, the term  $\left\langle \varepsilon_s - \varepsilon_y \right\rangle = 0$ .

Multiplying (4-3) and (4-4) with their respective concrete and steel volume gives the total strain energy of concrete  $U_c$  and steel  $U_s$ , respectively. Using the principle of conservation of energy, the work done by ASR/DEF related expansion in plain concrete  $U_{PC}$  is equal to the work done by ASR/DEF related expansion in reinforced concrete  $U_{RC}$ , that is:

$$U_{PC} = U_{RC} = U_c + U_s \quad (4-5)$$

The maximum strain in plain concrete is represented by  $\varepsilon_o^{\max}$  as shown in Figure 4-2b. Assuming strain compatibility in reinforced concrete results in the same strain in concrete and steel, that is,  $\varepsilon_{ct} = \varepsilon_s$ . Making necessary substitutions in (4-5) and rearranging the terms gives the following conditional quadratic equation:

$$\frac{1}{2} \rho n \varepsilon_s^2 \left( 1 - \left\langle 1 - \frac{\varepsilon_y}{\varepsilon_s} \right\rangle^2 \right) + \frac{\varepsilon'_t}{2} \varepsilon_s - \frac{\varepsilon'_t}{2} \varepsilon_o^{\max} = 0 \quad (4-6)$$

Solving (4-6) for the two cases, Case I when the expansion strains are beyond the yield strain of the reinforcement and Case II where the expansion strains are less than the yield strain, respectively, gives rise to the following two equations:

For  $\varepsilon_s > \varepsilon_y$ :

$$\varepsilon_{\rho}^{\max} = \frac{\varepsilon_o^{\max} \left[ 1 + \left( \rho n \frac{\varepsilon_y}{\varepsilon'_t} \right) \left( \frac{\varepsilon_y}{\varepsilon_o^{\max}} \right) \right]}{1 + \left( 2 \rho n \frac{\varepsilon_y}{\varepsilon'_t} \right)} \quad (4-7a)$$

For  $\varepsilon_s < \varepsilon_y$ :

$$\varepsilon_{\rho}^{\max} = \frac{\varepsilon'_t}{2 \rho n} \left[ \sqrt{1 + 4 \rho n \frac{\varepsilon_o^{\max}}{\varepsilon'_t}} - 1 \right] \quad (4-7b)$$

in which  $\varepsilon_{\rho}^{\max}$  = the maximum expansion strain possible for a particular reinforcement ratio  $\rho$ . Substituting (4-7) into (4-1) gives the expression for ASR/DEF induced expansion strain with time. It is evident from the (4-1) and (4-7) that the proposed minimalist semi-empirical formulation requires only a few physical parameters, specifically  $\varepsilon_o^{\max}$ ,  $t_0$ , and  $t_r$ . The reinforcement ratio  $\rho$  can be determined from the cross-section properties while the remaining parameters  $\varepsilon_y$  and  $\varepsilon'_t$  can be determined knowing the reinforcing steel and concrete material properties.

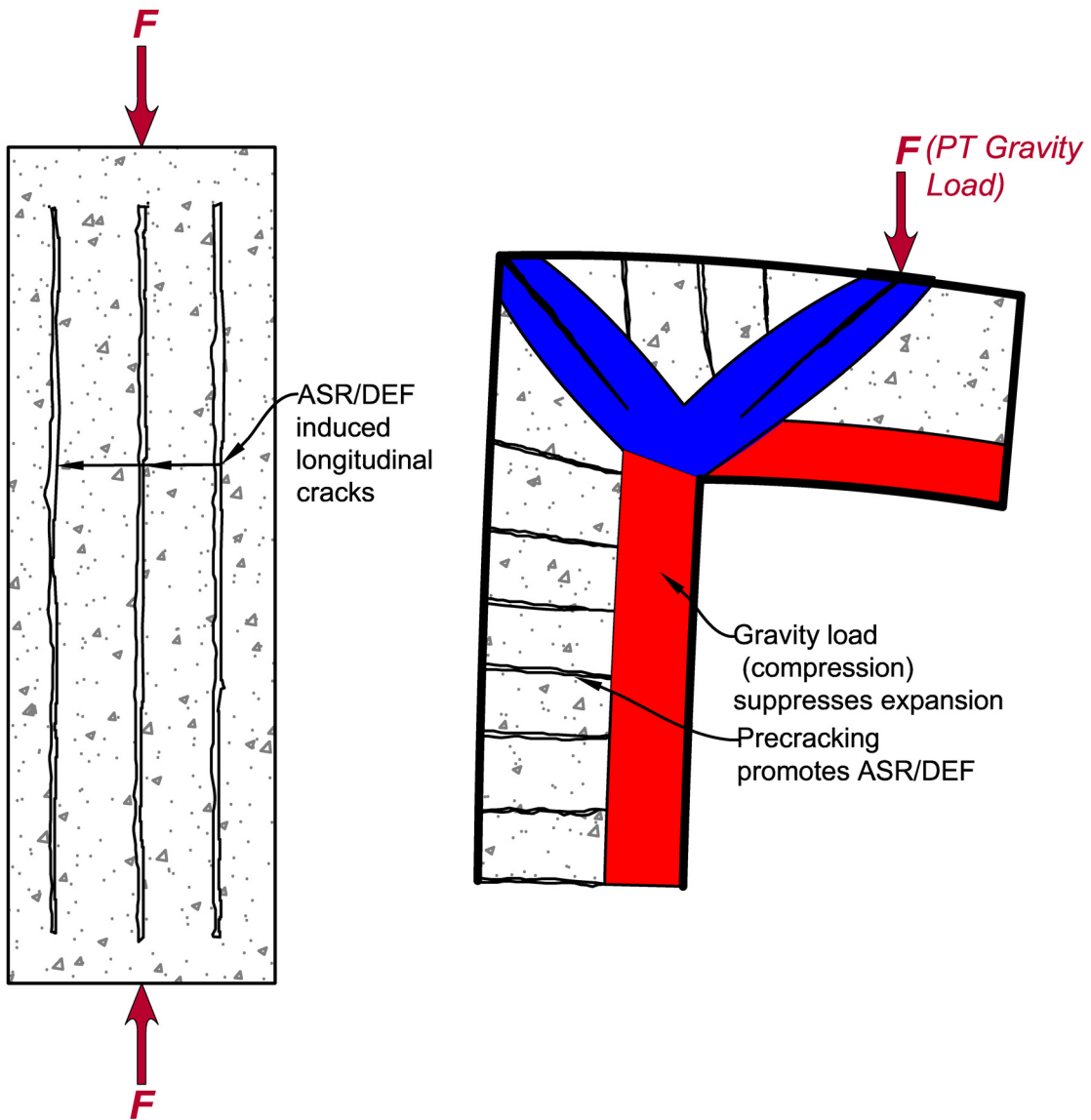
However, in the presence of post-tensioning (PT) compressive loads or cracks induced by tensile loads as shown in Figure 4-3, contributions from the compressive/tensile loads toward ASR/DEF induced expansion need to be accounted for. The derivation of the related equations is shown below.

Figure 4-4a shows an equivalent elasto-plastic stress-strain relation of concrete in tension as explained earlier. In the presence of a constant compressive force  $P$  applied across the section, by means of a constant axial load or post-tensioned prestress, the concrete experiences a compressive strain  $\varepsilon_{cpre}$  as shown in Figure 4-4a. This compressive effect essentially further increases resistance to the expansion caused by ASR/DEF in reinforced concrete. The concrete strain energy density, which is the shaded area beneath the stress-strain curve shown in Figure 4-4a, is given as:

$$u_c = \frac{E_c}{2} \left[ (\varepsilon_{cpre} + \varepsilon_{ct})^2 - \left\langle \varepsilon_{ct} - \frac{\varepsilon'_t}{2} \right\rangle^2 \right] \quad (4-8)$$

in which  $E_c$  = Young's modulus of concrete;  $\varepsilon_{ct}$  = tensile strain in concrete;  $\varepsilon'_t$  = strain corresponding to tensile strength of concrete  $f'_t$ ; and  $\varepsilon_{cpre}$  = compressive strain corresponding to the compressive stress in concrete  $f_{cpre} = P/A_c$  where  $A_c$  = cross-sectional area of concrete.

Figure 4-4b shows the elasto-plastic stress-strain relation of reinforcing steel. Here again, in the presence of applied compressive force, the reinforcement experiences a compressive strain  $\varepsilon_{spre}$ . Depending on the reinforcement ratio and the compressive load applied on the reinforced concrete structure, two cases have to be considered. First, when the expansion strains caused by ASR/DEF expansion are greater than the yield strain of the reinforcing steel, and second when the strains are below the yield strain. The strain energy density of steel, which is the shaded area in Figure 4-4b, is given by:

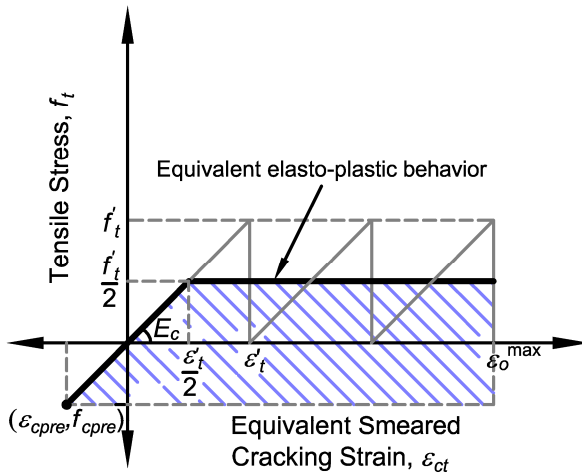


(a) Constant Axial Load due to PT Suppresses Expansion

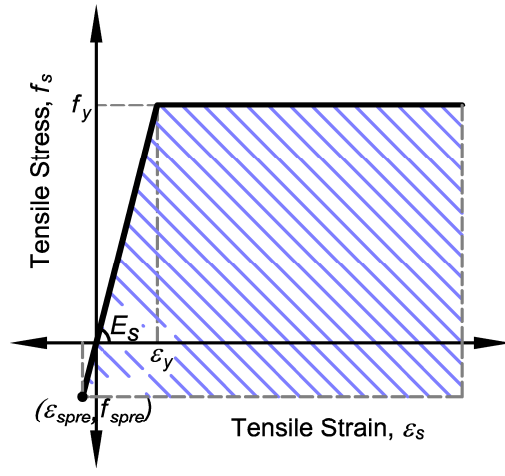
(b) PT Gravity Load Suppresses Expansion on the Compression Side and Precracks Promotes Expansion along the Tension Side

**Figure 4-3: Effects of Compressive and Tensile Loads on ASR/DEF Induced Expansion.**

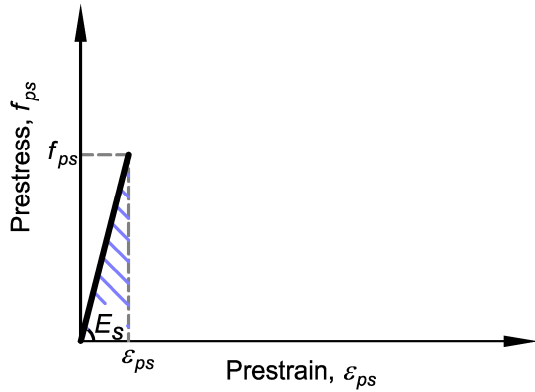




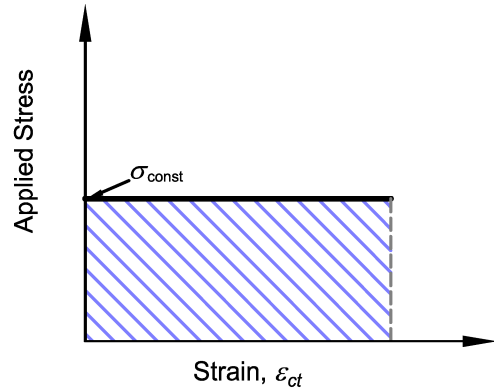
(a) Elasto-Plastic Model of Concrete in Tension Subjected to Compressive Forces



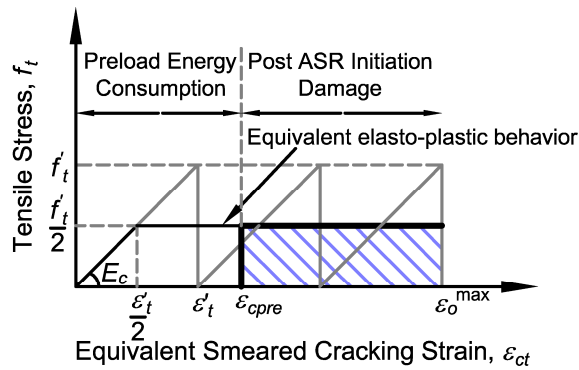
(b) Elasto-Plastic Model of Reinforcing Steel Subjected to Compressive Forces



(c) Elasto-Plastic Model of Prestressing Steel



(d) Constant Applied Stress



(e) Elasto-Plastic Model of Precracked Concrete in Tension

**Figure 4-4: Stress-Strain Models for Various Components.**

$$u_s = \frac{E_s}{2} \left[ (\varepsilon_{spre} + \varepsilon_s)^2 - \langle \varepsilon_s - \varepsilon_y \rangle^2 \right] \quad (4-9)$$

in which  $E_s$  = Young's modulus of steel;  $\varepsilon_s$  = tensile strain in steel;  $\varepsilon_y$  = yield strain of reinforcing steel; and  $\varepsilon_{spre}$  = compressive strain corresponding to the compressive stress in steel  $f_{spre} = P/A_s$  where  $A_s$  = total cross-sectional area of reinforcing steel.

In the presence of prestressing strands, their contribution to the strain energy density of the structure also needs to be accounted for. The strands are tensioned well below their yield strength, and the area of the shaded region under the stress-strain curve in Figure 4-4c is given as:

$$u_{ps} = \frac{E_s}{2} \varepsilon_{ps}^2 \quad (4-10)$$

in which  $\varepsilon_{ps} = P/(E_s A_{ps})$  = prestrain in the strands where  $A_{ps}$  = area of prestressing strands.

Finally, the constant applied compressive force results in a constant compressive stress  $\sigma_{const}$  across the concrete structure as shown in Figure 4-4d. The strain energy density due to the constant applied stress is given as:

$$u_{const} = \sigma_{const} \varepsilon_{ct} \quad (4-11)$$

Multiplying (4-8)–(4-11) with their respective concrete and steel volume gives the total strain energy of concrete  $U_c$ , reinforcing steel  $U_s$ , prestressing strands  $U_{ps}$ , and constant stress  $U_{const}$ . Using the principle of conservation of energy, the work done by ASR/DEF related expansion in plain concrete  $U_{PC}$  is equal to the work done by ASR/DEF related expansion in reinforced concrete  $U_{RC}$ , which may or may not be subjected to a constant applied load, that is:

$$U_{PC} = U_{RC} = U_c + U_s + U_{ps} + U_{const} \quad (4-12)$$

The maximum strain in plain concrete is represented by  $\varepsilon_o^{\max}$  as shown in Figure 4-4a. Assuming strain compatibility in reinforced concrete results in the same strain in concrete and steel, that is,  $\varepsilon_{ct} = \varepsilon_s$ . Making necessary substitutions in (4-12) and rearranging the terms gives the following conditional quadratic equation:

$$\frac{1}{2} \rho n \varepsilon_s^2 \left( 1 - \left\langle 1 - \frac{\varepsilon_y}{\varepsilon_s} \right\rangle^2 \right) + \varepsilon_s \left( \frac{\varepsilon'_t}{2} - \varepsilon_{cpre} - \rho n \varepsilon_{spre} - \frac{\sigma_{const}}{E_c} \right) - \frac{\varepsilon'_t \varepsilon_o^{\max}}{2} + \frac{\varepsilon_{cpre}^2}{2} + \frac{\rho n \varepsilon_{spre}^2}{2} + \frac{\rho_{ps} n \varepsilon_{ps}^2}{2} = 0 \quad (4-13)$$

in which  $\rho = A_s/A_c =$  reinforcement ratio;  $\rho_{ps} = A_{ps}/A_c =$  prestressing strand ratio; and  $n = E_s/E_c =$  modular ratio. Solving (4-13) for the two cases, Case I when the expansion strains are beyond the yield strain of the reinforcement and Case II where the expansion strains are less than the yield strain (then  $\varepsilon_y = \varepsilon_s$  in 4-13), respectively, gives rise to the following two equations:

For  $\varepsilon_s > \varepsilon_y$  :

$$\varepsilon_{\rho}^{\max} = \frac{\varepsilon_o^{\max} \varepsilon'_t + \rho n (\varepsilon_y^2 - \varepsilon_{spre}^2) - \varepsilon_{cpre}^2 - \rho_{ps} n \varepsilon_{ps}^2}{2 \left( \frac{\varepsilon'_t}{2} - \varepsilon_{cpre} + \rho n (\varepsilon_y - \varepsilon_{spre}) - \frac{\sigma_{const}}{E_c} \right)} \quad (4-14a)$$

For  $\varepsilon_s < \varepsilon_y$  :

$$\varepsilon_{\rho}^{\max} = \frac{\frac{\varepsilon'_t}{2} - \varepsilon_{cpre} - \rho n \varepsilon_{spre} - \frac{\sigma_{const}}{E_c}}{\rho n} \left( \pm \sqrt{1 - \frac{\rho n (\varepsilon_{cpre}^2 + \rho n \varepsilon_{spre}^2 + \rho_{ps} n \varepsilon_{ps}^2 - \varepsilon'_t \varepsilon_o^{\max})}{\left( \frac{\varepsilon'_t}{2} - \varepsilon_{cpre} - \rho n \varepsilon_{spre} - \frac{\sigma_{const}}{E_c} \right)^2}} - 1 \right) \quad (4-14b)$$

In (4-13) and (4-14)  $\varepsilon_{cpre}$ ,  $\varepsilon_{spre}$  and  $\sigma_{const}$  are positive for tensile strains induced by tensile loads and negative for compressive strains induced by compressive loads. In the case where no prestressing strands are present,  $\rho_{ps} = 0$ . The parameters

$\varepsilon_{cpre}$ ,  $\varepsilon_{spre}$ ,  $\varepsilon_{ps}$  and  $\sigma_{const}$  can be determined from the applied axial load  $P$ , and the corresponding cross-sectional areas. In the case of a reinforced concrete member without constant applied loads or prestress the terms  $\varepsilon_{cpre}$ ,  $\varepsilon_{spre}$ ,  $\varepsilon_{ps}$  and  $\sigma_{const}$  are zero.

The work done by ASR/DEF expansion on concrete is further reduced if the concrete is pre-cracked due to tensile prestrains, that is,  $\varepsilon_{pc} > \varepsilon'_t$ . In this case the concrete strain energy density, which is the shaded area beneath the stress-strain curve shown in Figure 4-4e, is given by:

$$u_c = \frac{E_c}{2} \left[ \varepsilon'_t (\varepsilon_{ct} - \varepsilon_{cpre}) \right] \quad (4-15)$$

Equating the work done by ASR/DEF related expansion in plain concrete and reinforced concrete as before, the maximum expansion can be computed using the following equations:

For  $\varepsilon_s > \varepsilon_y$ :

$$\varepsilon_\rho^{\max} = \frac{\varepsilon_o^{\max} \varepsilon'_t + \rho n (\varepsilon_y^2 - \varepsilon_{spre}^2) + \varepsilon'_t \varepsilon_{cpre} - \left( \frac{\varepsilon'_t}{2} \right)^2}{2 \left( \frac{\varepsilon'_t}{2} + \rho n (\varepsilon_y - \varepsilon_{spre}) - \frac{\sigma_{const}}{E_c} \right)} \quad (4-16a)$$

For  $\varepsilon_s < \varepsilon_y$ :

$$\varepsilon_\rho^{\max} = \frac{\frac{\varepsilon'_t}{2} - \rho n \varepsilon_{spre} - \frac{\sigma_{const}}{E_c}}{\rho n} \left( \pm \sqrt{1 - \frac{\rho n \left( \rho n \varepsilon_{spre}^2 + \rho_{ps} n \varepsilon_{ps}^2 - \varepsilon'_t \varepsilon_o^{\max} - \varepsilon'_t \varepsilon_{cpre} + \left( \frac{\varepsilon'_t}{2} \right)^2 \right)}{\left( \frac{\varepsilon'_t}{2} - \rho n \varepsilon_{spre} - \frac{\sigma_{const}}{E_c} \right)^2}} - 1 \right) \quad (4-16b)$$

In (4-14b) and (4-16b) it is important to consider only the positive value of  $\varepsilon_\rho^{\max}$  as it is an expansive strain and cannot be negative. Substituting the relevant expression for  $\varepsilon_\rho^{\max}$  into (4-1) gives the expression for ASR/DEF induced expansion strain with time.

The following section investigates the influence of variation in temperature, and also the degree of saturation on the expansion caused by the ASR/DEF mechanisms in reinforced concrete.

#### 4.4 Modifications to Account for Temperature and Moisture Variations

It is well known that the reactive material content and environmental factors such as temperature and humidity, stress conditions, boundary restraint, and moisture supply, all affect the extent of expansion rate caused by ASR/DEF in concrete. In the proposed expansion model, the reactive material content is implicitly taken into account when estimating the parameters  $\varepsilon_o^{\max}$ ,  $t_o$ , and  $t_r$ . The effects of the restraints are also taken into account in the expression proposed for maximum expansion  $\varepsilon_\rho^{\max}$ .

To account for the effects of the other two important factors, temperature and moisture content (degree of saturation), necessary modifications to the proposed expansion equation are considered here. Implicit in the earlier development of the proposed equations were: (i) constant temperature; and (ii) saturated conditions (water bath) were used for curing. However, the temperature and moisture content conditions of an actual structure subjected to ASR/DEF expansion may vary on a daily basis. To account for these real field temperature and moisture variations, modifications are proposed to (4-1) to include their effects.

Eq. (4-1) can be slightly modified to include the effects of temperature  $T$ :

$$\varepsilon_{t,T} = \varepsilon_\rho^{\max} \tanh \left\langle \frac{t - t_o}{t_{r,T}} \right\rangle \quad (4-17)$$

where the parameters are defined as before and  $\varepsilon_\rho^{\max}$  is given by (4-7), (4-14) or (4-16).

Ulm et al. (2000) defined the characteristic time  $\tau_c$  associated with ASR product formation as:

$$\tau_c(\theta) = \tau_c(\theta_o) \exp \left[ \frac{U_c}{\theta \theta_o} (\theta_o - \theta) \right] \quad (4-18)$$

in which  $\tau_c(\theta_o) =$  characteristic time at standard temperature of  $\theta_o = 311^\circ\text{K} = T_o = 38^\circ\text{C}$  (100°F) and  $U_c = 5400 \pm 500^\circ\text{K} =$  activation energy constant of the characteristic time  $\tau_c$ .  $(\theta_o - \theta)^\circ\text{K}$  can be re-written as  $(T_o - T) = -\Delta T^\circ\text{C}$  (say). By the definition of the two terms  $\tau_c$  and  $t_r$ ,  $t_r \approx 2\tau_c$ . Therefore, the rise time of the tangent line  $t_r$  is assumed to follow the same relation as (4-18) proposed by Ulm et al. and is given by:

$$t_r(\theta) = t_r(\theta_o) \exp\left[\frac{U_c}{\theta\theta_o}(\theta_o - \theta)\right] \quad (4-19)$$

Substituting for  $\theta = \theta_o + \Delta T$ ,  $U_c = 5400^\circ\text{K}$  and as  $\Delta T \ll \theta_o$  ( $=311^\circ\text{K}$ ) then  $\Delta T/\theta_o \rightarrow 0$ , thus (4-19) may be simplified to give:

$$t_{r,T} = t_{r,T_o} \exp\left(\frac{T_o - T}{18}\right) \quad (4-20)$$

where  $t_{r,T_o}$  = rise time of the tangent line to the hyperbolic expansion curve at standard temperature  $T_o = 38^\circ\text{C}$ . Finally substituting  $T_o = 38^\circ\text{C}$  in (4-20) leads to:

$$t_{r,T} = t_{r,T_o} \exp\left(\frac{38 - T}{18}\right) \quad (4-21)$$

which may now be substituted into (4-17) to give:

$$\varepsilon_{t,T} = \varepsilon_\rho^{\max} \tanh\left(\exp\left(\frac{T - 38}{18}\right) \left\langle \frac{t - t_o}{t_{r,T_o}} \right\rangle\right) \quad (4-22)$$

Eq. (4-22) gives the modified expression for the expansion caused by ASR/DEF in reinforced concrete taking into consideration the temperature variations.

To account for the variations in moisture content, necessary modifications to (4-22) need to be made. Figure 4-5 shows the variation of characteristic time  $\tau_c$  at  $311^\circ\text{K}$  with the degree of saturation  $S$ , where the data points are adapted from Ulm et al. (2000). The experimental data can be reasonably well represented by the exponential

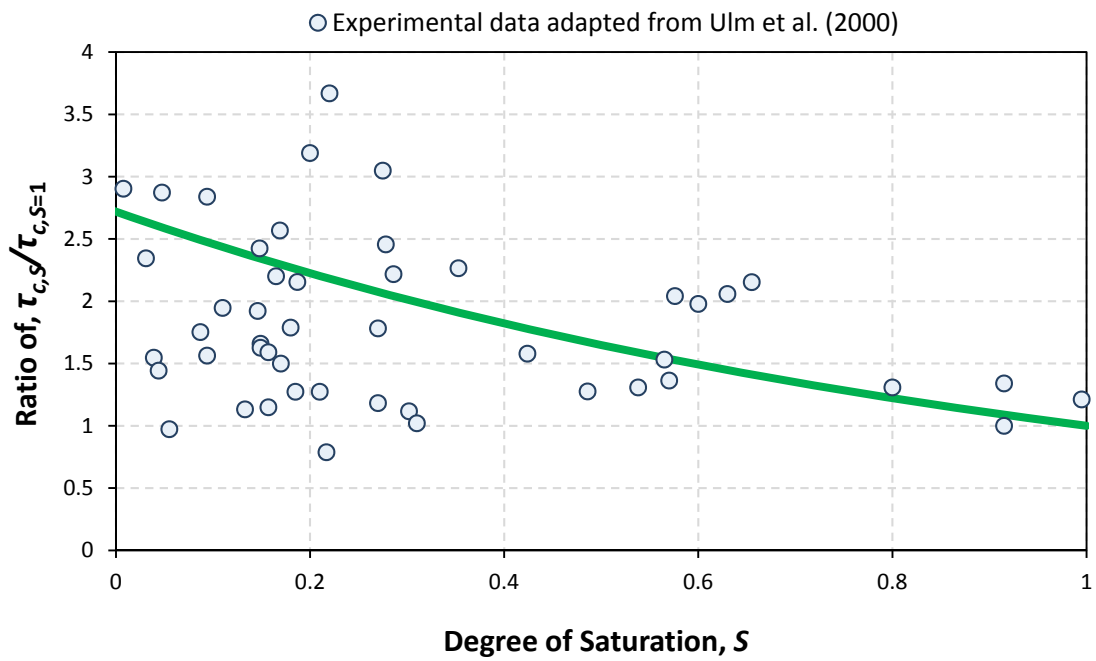


**Figure 4-5: Variation of Characteristic Time with Relative Weight Increase.**

function  $e^{1-S}$ . Incorporating this into the modified equation (4-22) leads to the following overall time-dependent expansion strain model:

$$\varepsilon_{t,T,S} = \varepsilon_{\rho}^{\max} \tanh \left( \exp \left( \frac{T}{18} + S - 3.11 \right) \left\langle \frac{t - t_o}{t_{r,T_o}} \right\rangle \right) \quad (4-23)$$

Eq. (4-23) represents the proposed model, modified for temperature and moisture content variations, for expansion strains in reinforced concrete caused by ASR/DEF expansion. Note that at standard temperature of 38°C (100°F) and degree of saturation of  $S = 1$ , (4-23) reverts back to (4-1).

Differentiating (4-23) with respect to time gives the expansion strain rate as follows:

$$\frac{d\varepsilon_{t,T,S}}{dt} = \dot{\varepsilon}_{t,T,S} = \frac{\varepsilon_{\rho}^{\max}}{t_{r,T_o}} \exp \left( \frac{T}{18} + S - 3.11 \right) \left[ 1 - \left( \frac{\varepsilon_{t,T,S}}{\varepsilon_{\rho}^{\max}} \right)^2 \right] \quad (4-24)$$

which is an ordinary differential equation with variable coefficients dependent on temperature and degree of saturation,  $T$  and  $S$ . Because in field conditions  $T$  and  $S$  vary constantly, (4-24) requires a numerical solution as follows:

$$\varepsilon_{i+1} = \varepsilon_i + \left( \dot{\varepsilon}_{t,T,S} \right)_i \Delta t \quad (4-25)$$

in which  $\Delta t$  = time increment and the parameters with subscript  $i$  denote their value at the  $i^{\text{th}}$  time interval; and  $\dot{\varepsilon}_{t,T,S}$  is the temperature and saturation dependent strain rate given by (4-24). Eq. (4-25) can be easily solved computationally in an incremental time-stepping fashion. Daily temperatures and degree of saturation (assessed from rainfall records) are used directly in (4-24).

#### 4.5 Validation of Proposed Model for ASR Related Expansion

The proposed expansion equation is validated against the experimental observations from Hobbs (1988) and Jones and Clark (1996), in which, expansion was caused by ASR in saturated reinforced concrete specimens. In the laboratory tests conducted by

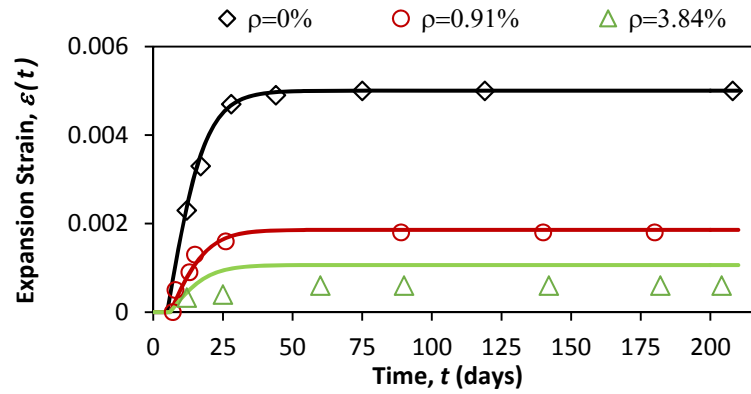


Hobbs, and Jones and Clark, the specimens were moist cured at a constant temperature of 20°C and 38°C, respectively. The literature does not provide all the information required as input for the proposed model. Therefore, typical values for the unknown parameters are assumed in the following. In Figure 4-6 the experimental data are plotted as data points, and the solid lines represent the results from the proposed model.

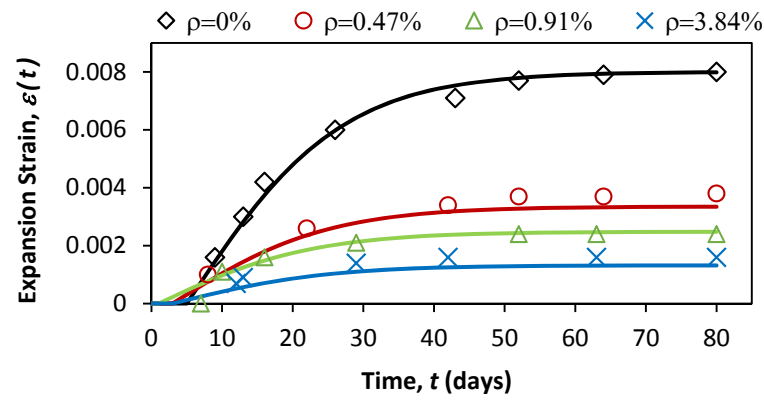
Figure 4-6a and b show a comparison of the experimental data with the results from the proposed semi-empirical model for Series I and II respectively, of Hobbs (1988). For Series I  $\varepsilon_o^{\max} = 0.005$  and  $t_r = 5$  days were adopted based on the experimental observations, and a modular ratio of  $n = 20$ , about three times the typical values of modular ratio, was assumed to account for creep effects in the reinforced concrete specimen. The value of reinforcement yield strain  $\varepsilon_y = 0.0022$ , and concrete tensile strain corresponding to  $f'_t$ ,  $\varepsilon'_t = 0.1\varepsilon_{co} = 0.0002$  (Karthik and Mander, 2011) were assumed. For Series II, values of  $\varepsilon_o^{\max} = 0.008$ ,  $t_r = 8$  days and the modular ratio  $n = 20$  (that includes creep effects) were adopted. Similar to Series I, values of  $\varepsilon_y = 0.0022$  and  $\varepsilon'_t = 0.0002$  were assumed.

Figure 4-6c shows a comparison of the experimental and analytical results that were obtained for the experimental tests conducted by Jones and Clark (1996). In this case  $\varepsilon_o^{\max} = 0.0059$ ,  $t_r = 39$  days and the modular ratio  $n = 20$  (that includes creep effects) were adopted. The value of yield strain  $\varepsilon_y = 0.0022$  is assumed, and the tensile fracture strain is estimated from  $\varepsilon'_t = f'_t(1 + c_f) / E_c = 0.0004$ , where  $f'_t = 0.625\sqrt{f'_c}$ ;  $E_c = 4700\sqrt{f'_c}$ ; and  $c_f = 2$  is the creep coefficient.

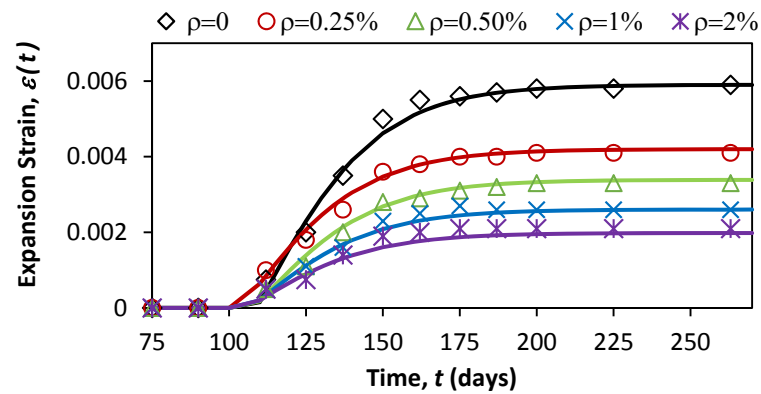
The results presented in Figure 4-6 suggest that if reasonable values are adopted for the few parameters that are required for the proposed model, an adequate prediction can be made for the expansion caused by ASR reaction in reinforced concrete.



(a) Hobbs (1988)-Series I



(b) Hobbs (1988)-Series II



(c) Jones and Clark (1996)

Note: Experimental data points are shown as symbols, and solid lines are derived using the proposed model.

**Figure 4-6: Model Validation for ASR Expansion with Experimental Data in Reinforced Concrete.**

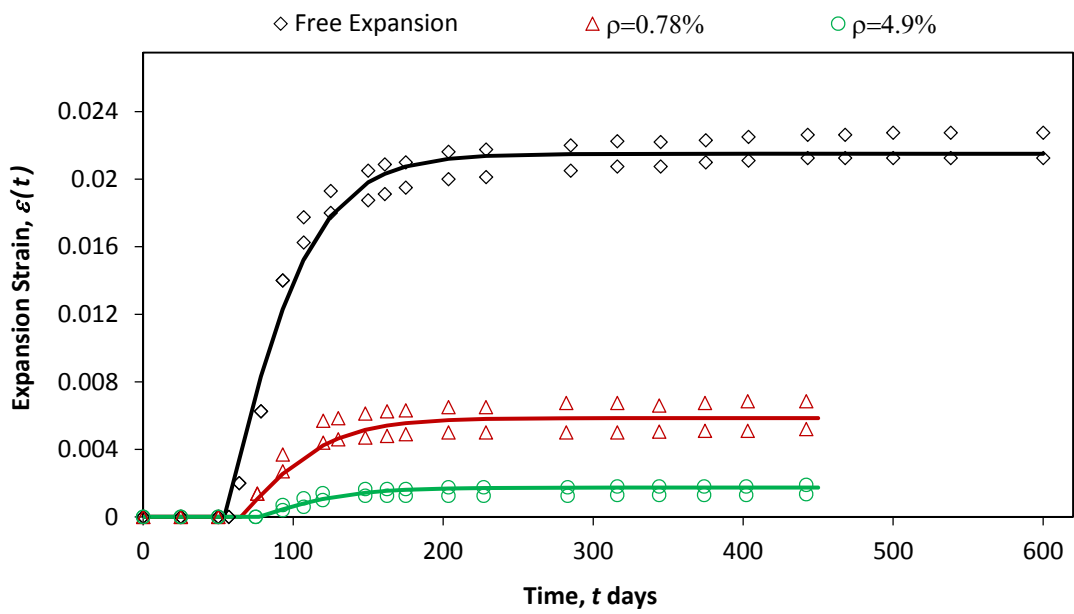
#### 4.6 Validation of Proposed Model for DEF Related Expansion

Limited relevant data are available for studying DEF related expansion in reinforced concrete. Bouzabata et al. (2012) studied the effects of restraints on DEF induced expansion in concrete. In their experimental study,  $40 \times 40 \times 160$  mm ( $b \times d \times l$ ) concrete prism specimens were subjected to expansion caused by DEF, and restrained by a setup that was composed of two stainless steel plates connected by four threaded stainless steel bars. To obtain different restraint levels, threaded bars consisting of either 2 or 5 mm diameter were used. Although the restraints in this study were provided externally, their effect in restraining the expansion caused by DEF in concrete can be considered similar to that of the reinforcement in concrete. The expansion strains obtained over time from this study, plotted as data points in Figure 4-7, show similar expansion characteristics as shown by ASR induced strains in reinforced concrete, so the same equation is used to model the expansion strains caused by DEF in concrete.

The following parameters were identified from the experimental observations to model the expansion strains:  $\varepsilon_o^{\max} = 0.0215$  and  $t_r = 60$  days. In this study concrete with compressive and tensile strength of  $f'_c = 46.5$  MPa and  $f'_t = 2.4$  MPa, respectively, and 304 stainless steel with yield strength of  $f_y = 280$  MPa were used (Multon, 2013). The properties required for the model were calculated to be  $\varepsilon_y = 0.00145$  based on  $E_s = 193$  GPa,  $n = 17$  (that includes creep effects), and  $\varepsilon'_t = 0.00013$ . Figure 4-7 shows a comparison of the experimental data with the proposed model results. It is evident that the proposed model simulates well the DEF induced expansion in concrete.

From Figures 4-6 and 4-7 it is clear that the proposed minimalist semi-empirical model can be used efficiently to simulate the expansion strains caused by ASR/DEF in reinforced concrete members. Additionally, the model requires limited input data.

In each of the above laboratory studies, the specimens were cured at a constant temperature and saturated conditions to accelerate the ASR and DEF reactions. The following section demonstrates how the developed theory can be used to obtain a reasonable prediction of the expansion strain in post-tensioned reinforced concrete



Note: Experimental data points are shown as symbols, and solid lines are derived using the proposed model.

**Figure 4-7: Model Validation for DEF Expansion with Experimental Data (Bouzabata et al., 2012) in Reinforced Concrete.**

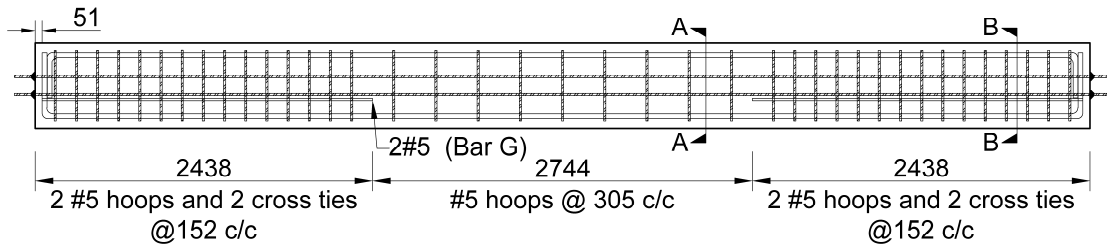
members, which are exposed to environmental conditions, and as a result subjected to the daily variations in temperature and moisture content.

#### **4.7 Application of Proposed Model to Post-Tensioned Reinforced Concrete Column Specimen**

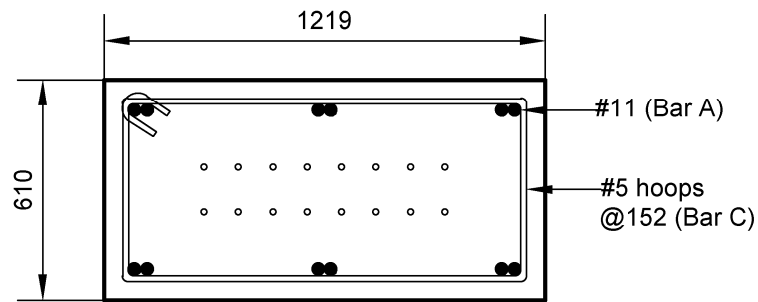
The proposed model for ASR/DEF related expansion in reinforced concrete members subjected to field conditions under varying temperature and moisture content is validated against the expansion results recorded by the experimental program conducted by Bracci et al. (2012). The purpose of that experimental study was to investigate the impact of ASR/DEF related expansion in columns within lap splice regions. As part of the study, large-scale column specimens were designed, constructed, subjected to ASR/DEF related deterioration, and tested to failure under a 4-point bending setup. High alkali content cement and aggregates with reactive silica along with Sodium Hydroxide in the mix water were used to incorporate the necessary ingredients to promote ASR expansion in a laboratory setting. To promote DEF related expansion in the specimen, each specimen was subjected to curing temperatures in excess of 71°C by means of an electrical resistive wiring setup. After curing, each specimen was conditioned in an outdoor environment subject to the daily variation of temperature and humidity for varying periods of up to 5 years. To further accelerate ASR/DEF related expansion in the specimen, all specimens were wetted for 15 minutes, four times per day by a sprinkler system that was installed.

The cross-section and the reinforcement details of the column specimens are shown in Figure 4-8. The column specimens were prestressed using unbonded post-tensioned strands to simulate in-service gravity load effects. The expansion data in the column specimen, primarily from the splice region, were collected on a regular basis from the strain and concrete gages embedded in the specimen and DEMEC points on the surface of the specimen. In the following, the expansion results obtained from the proposed model are compared to the measured expansion data.

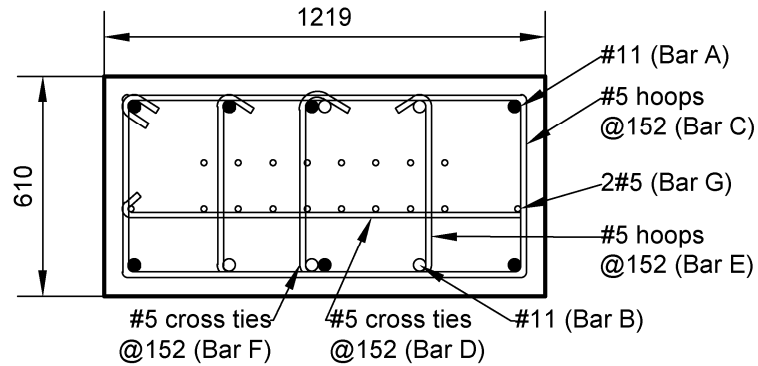
The data collected from the specimen DEMEC points were categorized into two sets as shown in Figure 4-9a. One set of data was collected in the longitudinal and transverse direction on the specimen large face (1220 mm wide), and the second set was



(a) Reinforcement Layout



(b) Section A—A: Splice Region



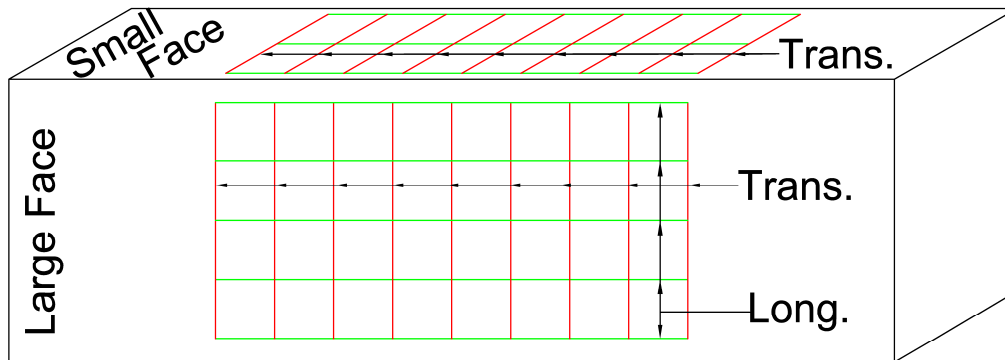
(c) Section B—B: End Region

**Figure 4-8: Reinforcement Details of Splice Column Specimen.**

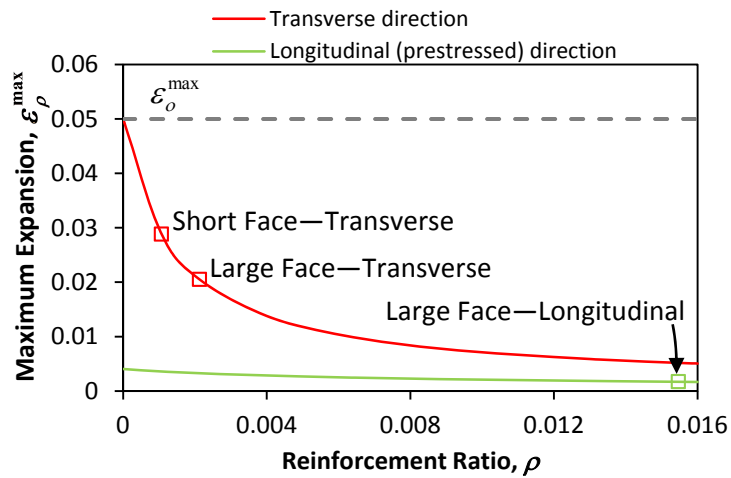
collected in the transverse direction on the specimen small face (610 mm wide). The reinforcement ratio in the small and large face are computed to model the expansion results. The variation of maximum expansion  $\varepsilon_{\rho}^{\max}$  with the reinforcement ratio  $\rho$  is shown in Figure 4-9b. It is clear from Figure 4-9b that the expansion strains decrease with an increase in the reinforcement ratio. It is also evident from Figure 4-9b that the presence of the compressive loads significantly reduces the maximum expansion. Figure 4-9c shows the variation of observed daily average temperature for the period the specimen was exposed to the field conditions.

All of the data required to model ASR/DEF related expansion results are not available from the literature. Therefore, certain assumptions are made based on the experimental observations that were made on the C-beam specimen from a study by Mander et al. (2012), where the same materials were used in the specimen construction. From the experimental results reported by Mander et al. (2012), the rise time of the tangent line at standard temperature  $t_{r,t_0}$  is assumed as 120 days. Since no data are available on the expansion caused in plain concrete  $\varepsilon_o^{\max}$ , this parameter is deduced from the largest crack observed on the C-beam specimen from an unreinforced part of the specimen. The largest crack that was observed at the knee-joint of the C-beam specimen was about 30 mm wide, where the top face of the column in the joint region was essentially unreinforced. A crack width of 30 mm across a section with a total width of 610 mm results in an expansion strain of approximately 0.05. Hence a value of  $\varepsilon_o^{\max} = 0.05$  is adopted in this study to model the ASR/DEF related expansion. Based on the experimental results reported by Bracci et al. (2012) the time  $t_o$  when expansion strains initiate is deduced to be 130 days.

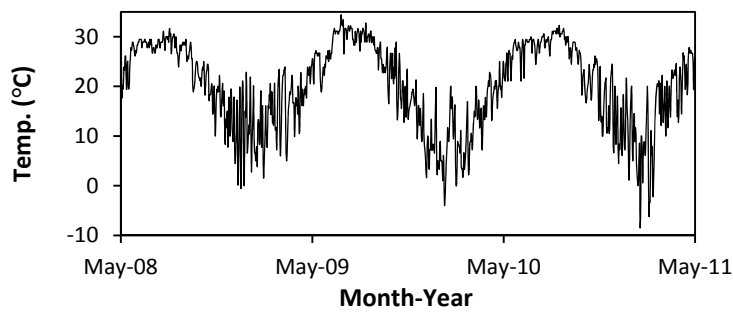
Figures 4-10 to 4-12 present a comparison of the model results with the experimental data obtained from the column specimen. Of the 14 total specimens that were exposed to the accelerated environmental deterioration program, three specimens (Specimens 4, 8, and 12) are used herein to compare the model expansion results with the experimental results as these specimens were exposed to the field conditions for



(a) DEMEC Layout on Splice Column Specimen



(b) Variation of Maximum Expansion with Reinforcement Ratio



(c) Observed Average Daily Temperature

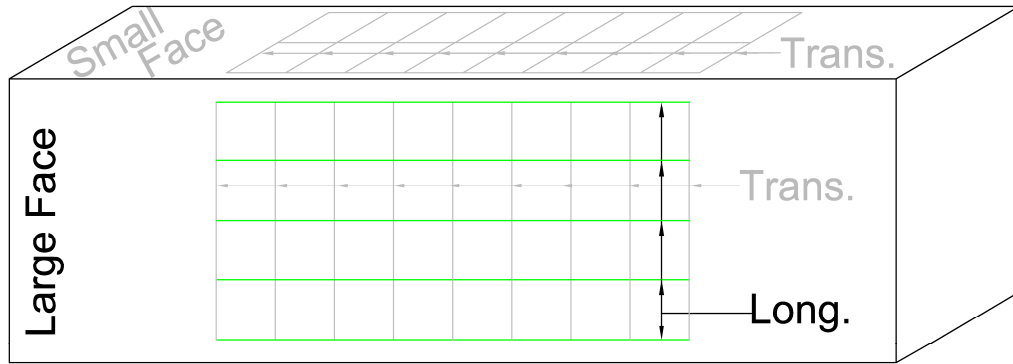
**Figure 4-9: Information Pertinent to Model Expansion Strains in Splice Column Specimens.**



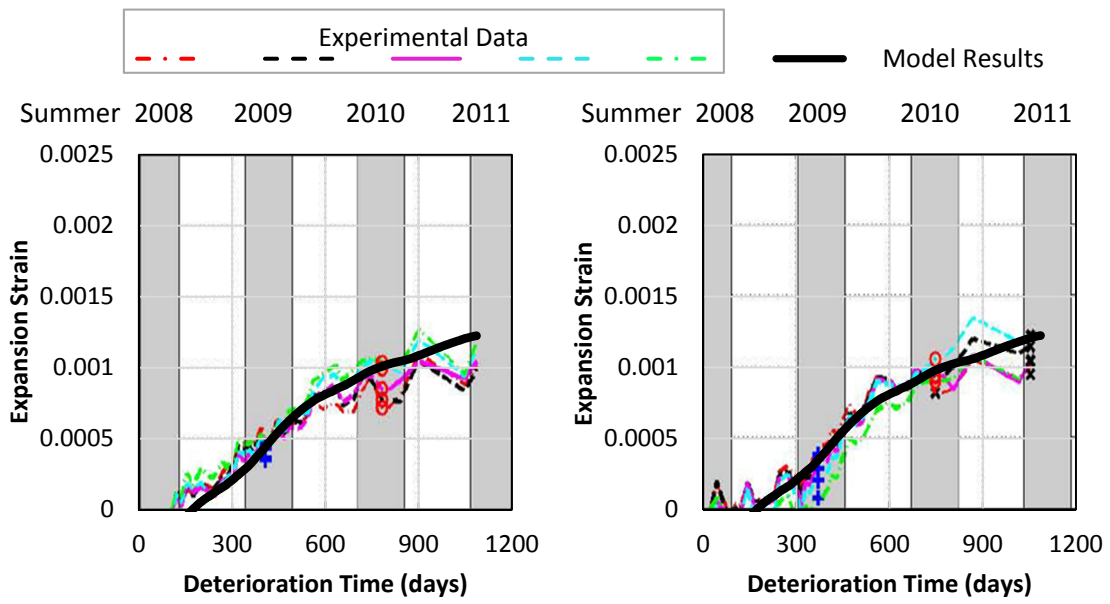
lengthy time periods. Of the three specimens, the concrete compressive strength at the time of testing of the specimen was reported only for Specimen 8, as the other two specimens were still being subjected to the deterioration program. An average compressive strength of  $f'_c = 36.5$  MPa that was reported for Specimen 8 is adopted for this study. Based on this the concrete parameters are computed as  $E_c^{actual} = 30.1$  GPa,  $f'_t = 3.8$  MPa, and  $\epsilon'_t = 0.000125$ . The reinforcing steel that was used in the study was reported to have a yield strength of 448 MPa, which results in a yield strain of  $\epsilon_y = 0.0022$ . Taking into account the creep effects of concrete,  $E_c = 10$  GPa, which results in a modular ratio of  $n = 19.9$  being adopted. The degree of saturation is assumed as  $S=0.2$ .

Figure 4-10 shows the growth of the expansion strain with time in the longitudinal direction of the specimen large face and a comparison of the model with the field observations. In the longitudinal direction of the specimen large face, the reinforcement ratio of reinforcing steel and the post-tensioning strands is computed as  $\rho = 0.0155$  and  $\rho_{ps} = 0.003$ , respectively. In addition to the material properties presented earlier, additional parameters are computed to determine the maximum expansion possible due to the application of the post-tensioning force in the longitudinal direction. The total post-tensioned prestress force applied to the beam was 2582.2 kN, which results in a constant stress of  $\sigma_{const} = 3.48$  MPa. The prestressing strands were stressed to  $0.7 f_{pu} = 1158.3$  MPa, which results in  $\epsilon_{ps} = 0.0058$ . Based on the axial load  $P$ , and the cross-section area of concrete and steel the compressive strains in concrete and steel, respectively, were determined as  $\epsilon_{cre} = 0.00012$  and  $\epsilon_{spre} = 0.00112$ . Because the applied PT force does not lead to yielding of the longitudinal reinforcing steel, (4-14b) is used to determine the maximum expansion, which is calculated to be  $\epsilon_{\rho}^{max} = 0.0017$ .

Figures 4-11 and 4-12 show the growth of the expansion strain with time in the transverse direction of the specimen large face and small face, respectively. A comparison of the model with the field observations is also shown. The reinforcement ratio in the transverse direction on the large face and short face, respectively, are



(a) DEMEC Layout on Splice Column Specimen

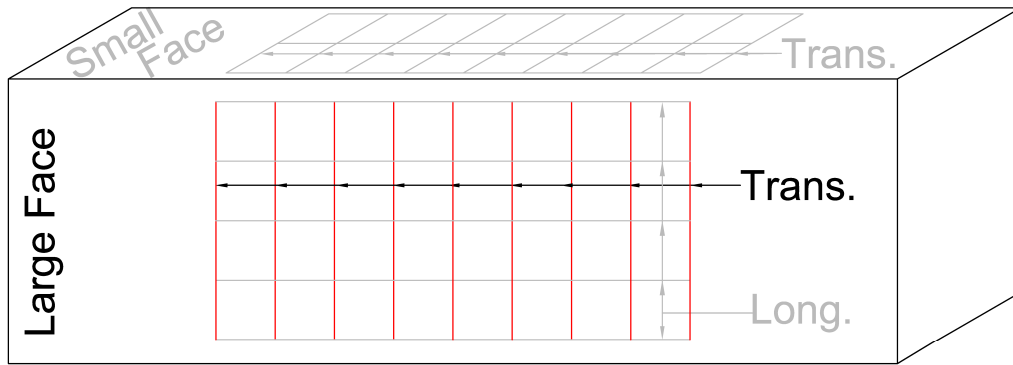


(b) Specimen 4

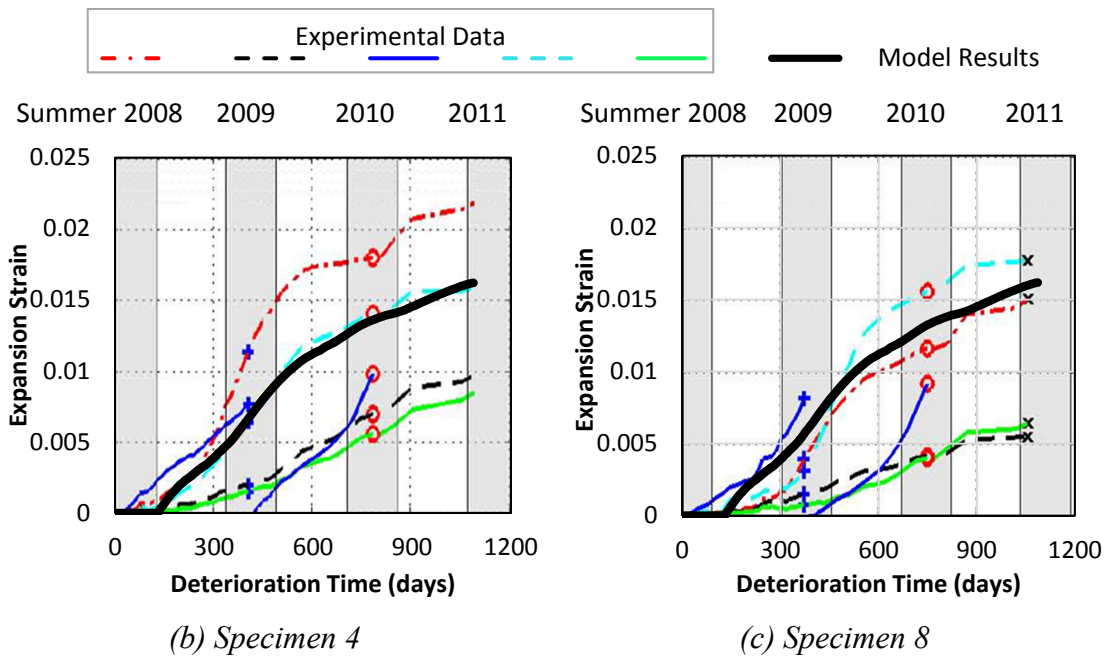
(c) Specimen 8

Note: Experimental data from Bracci et al. (2012)

**Figure 4-10: Comparison of Experimental and Model Strain Propagation Results on Specimen Large Face—Longitudinal Direction.**

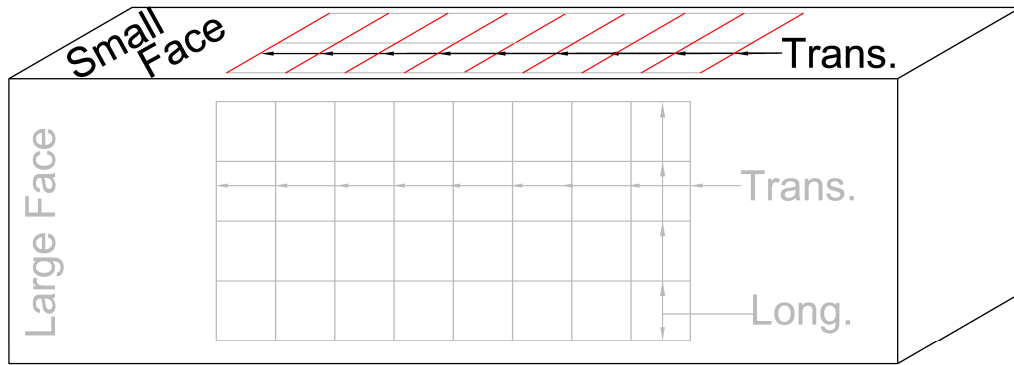


(a) DEMEC Layout on Splice Column Specimen

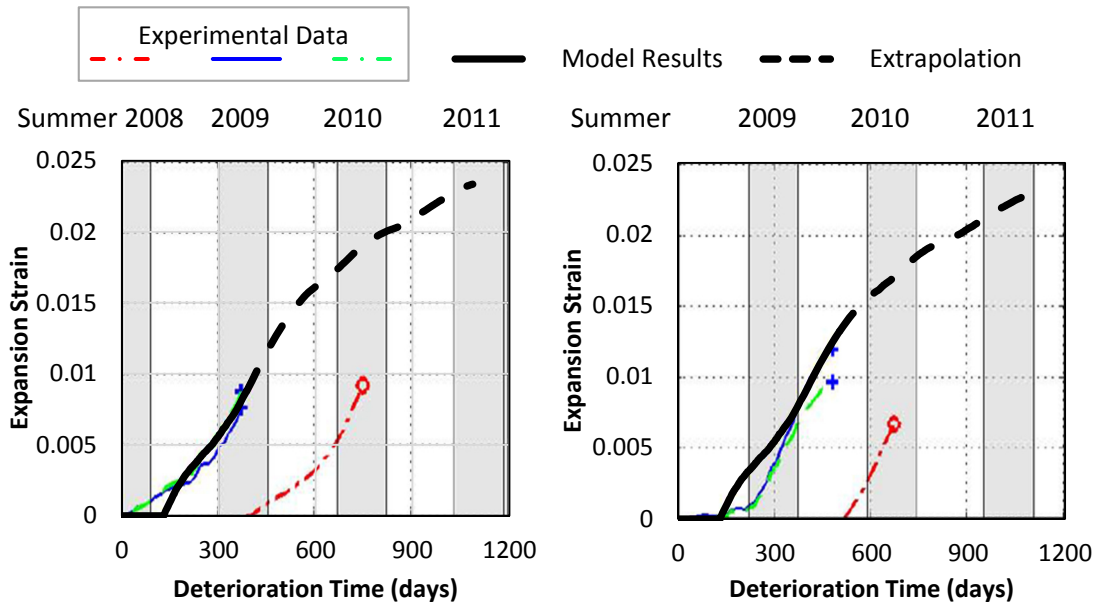


Note: Experimental data from Bracci et al. (2012)

**Figure 4-11: Comparison of Experimental and Model Strain Propagation Results on Specimen Large Face—Transverse Direction.**



(a) DEMEC Layout on Splice Column Specimen



Note: Experimental data from Bracci et al. (2012)

**Figure 4-12: Comparison of Experimental and Model Strain Propagation Results on Specimen Small Face—Transverse Direction.**

computed as  $\rho = 0.0021$  and  $0.0011$ . The parameters  $\varepsilon_{cpre} = \varepsilon_{spre} = \varepsilon_{ps} = \sigma_{const} = 0$  as the longitudinal post-tension force does not have any impact on the ASR/DEF related expansion in the transverse direction. Based on these properties, the maximum possible strain due to ASR/DEF related expansion (using 4-14a) is computed to be  $\varepsilon_{\rho}^{\max} = 0.0205$  and  $0.0288$ , respectively, for the large face and the short face.

#### 4.8 Discussion

Figures 4-10 to 4-12 present a comparison of the ASR/DEF related expansion strains simulated by the proposed model with the experimental data on post-tensioned reinforced concrete members. The simulation of expansion strains in the longitudinal direction was more complicated compared to the transverse strains, because of the PT force that further restrains ASR/DEF induced expansion in the longitudinal direction. The expansion strains have to overcome the prestrain in concrete to result in any expansion strains measured at the DEMEC points. Hence, the concrete prestrain  $\varepsilon_{cpre} = 0.00012$  was deducted from the final expansion strains obtained. This results in a slightly delayed start to the expansion strains as shown by the field data and the simulation results in Figure 4-10. It is also evident from Figure 4-10 that the expansion results from the model compare well with the field data collected from the column specimen.

The post-tensioning forces do not have any impact on the ASR/DEF induced expansion caused in the transverse direction, and hence the model computations are straight forward. Figure 4-11 shows the transverse expansion strains along the large face of the specimen. The proposed model simulates the expansion caused in the outer two sets of DEMEC points quite well. Figure 4-12 shows a comparison of the modeled expansion results with the field data for the expansion strains in the transverse direction of the specimen small face. In this case the field data were collected for just under 400 days. The field data for Specimen 8 indicate that expansion strains were observed from day 1 of the deterioration period. However, for the simulation results the expansion initiation time was maintained at  $t_o = 130$  days to be consistent. Again reasonable agreement is evident between the simulated results and the observed field data.

Considering the complex nature of ASR/DEF related expansion in reinforced concrete and the vagaries associated with the expansion data gathered from the field, Figures 4-10 to 4-12 show that the proposed model can be used to simulate the expansion strains in reinforced concrete without or with PT forces with reasonable accuracy.

#### **4.9 Closure and Key Findings**

The existing models for predicting the expansion caused by ASR/DEF are limited mainly to plain concrete. Additionally, they are complex and typically require a finite element model to implement their effects on structures. In this section a semi-empirical minimalist model was proposed that is capable of estimating ASR/DEF induced expansion strains in reinforced concrete structures. The model requires only a limited number of input parameters that are related to the expansion characteristics, and material properties. The key findings from this study are summarized below:

- The proposed model can simulate the expansion caused by ASR and/or DEF in laboratory specimens cured under standard laboratory conditions of constant temperature and complete saturation to accelerate ASR/DEF expansion.
- It is necessary to extend the basic laboratory based model to take into account the widely varying field temperature and moisture (degree of saturation) conditions.
- The effects of compressive and tensile prestrains are included in the model. This is an important aspect as compressive forces suppress the expansion caused by ASR/DEF mechanisms, whereas tensile forces and initial cracking further promote and accelerate ASR/DEF induced expansion.
- By taking into account the appropriate reinforcement ratios, the proposed model is able to simulate ASR/DEF induced expansion strains in both the longitudinal and transverse directions.
- Considering the spread of the observed ASR/DEF induced surface expansion strains, the model provides a very satisfactory estimate of the expansion strain in reinforced concrete specimens exposed to field conditions with varying temperature and degree of saturation.

## 5 DETERIORATION DATA OF LARGE-SCALE SPECIMEN WITH HEAVY ASR/DEF DETERIORATION\*

### 5.1 Summary

Limited field data are available from reinforced concrete specimens exposed to environmental conditions that are subjected to severe deterioration due to ASR/DEF induced expansion strains. The progression of surface strains, and internal reinforcement and concrete strains are measured, respectively, using DEMEC points installed on the surface of the specimen, and embedded steel and concrete gages. The progression of surface cracks with time and the final crack widths on the specimen are also recorded. From the strain gage measurements it is evident that both the transverse and longitudinal reinforcement yielded within six months to one year of field exposure. The recorded surface strains, which is closely related to the reinforcement layout in the region, compare well with the internal steel and concrete strain gages, thus giving a good indication of the internal strains. Owing to the lower reinforcement ratio in the transverse direction and hence less restraint to expansion, the measured expansion strains in the transverse direction, in general, are greater than the strains in the longitudinal direction. The ASR/DEF induced map cracking merged with the initial load induced cracks, and the crack width and density grew with time. By the end of the five year exposure period, the C-beam specimen showed severe cracking, with the largest surface crack being measured at 30 mm. The field observations and instrument data show that ASR/DEF deterioration can cause severe surface cracking and large expansion strains on field exposed reinforced concrete structures. However, the effect of such severe deterioration on the structure's load carrying capacity is unknown at this time.

---

\* Previously published work is available to the public through National Technical Information Service. Mander, J.B., Karthik, M.M., and Hurlbaas, S. (2015). "Structural Assessment of "D" Region Affected by Premature Concrete Deterioration: Technical Report." *Report No. FHWA/TX-15/0-5997-2*, Texas A&M Transportation Institute, College Station, Texas, USA.

## 5.2 Introduction

It is well known that concrete deterioration mechanisms like ASR and DEF cause concrete cracking, which may lead to serviceability issues. The expansion strains caused by ASR on small to medium-scale prism specimens have been extensively recorded (Hobbs, 1988; Swamy and Asali, 1989; Jones and Clark, 1996; Fan and Hanson, 1998; Ahmed et al., 1988; Monette et al., 2002; Mohammed et al., 2003 among others). Multon et al. (2005) investigated the effects of ASR on large-scale concrete specimens subject to moisture gradient. Recently, greater emphasis is on investigating the combined effects of ASR and DEF induced expansion strains in large-scale reinforced concrete specimens. Studies by Deschenes et al. (2009), Bracci et al. (2012), Mander et al. (2012) and Gianni et al. (2013) has shown that mild to moderate amounts of cracking are not uncommon. One common conclusion was that the effects of long-term expansions induced by ASR/DEF mechanisms were unknown. It was also concluded that greater levels of deterioration caused by ASR/DEF mechanisms may possibly lead to other deterioration mechanisms like steel corrosion and rebar fracture.

The present study is a direct extension of the earlier research by Mander et al. (2012). As part of this investigation, four C-beam specimens each based on the same design were constructed, of which one (Specimen 1) was the control specimen and three others (Specimens 2, 3, and 4) were conditioned outdoors in a natural (but accelerated moisture via a sprinkler system) Texas environment. Specimens 2 and 4 were conditioned outdoors for a period of nine months and two years, respectively. The level of deterioration observed in Specimens 2 and 4 were classified as *slight* and *moderate*. The field observations and measured strains from Specimens 2 and 4 have been reported in part by Mander et al. (2012) and Liu (2012). Specimen 3 was further subjected to outdoor conditioning for a total of five years. During that period data from Specimen 3 were routinely collected from the concrete gages (KM), strain gages (SG), and DEMEC points on the specimen surface. This section presents the deterioration data that were collected from Specimen 3 for a period of just over five years.



### 5.3 Visual Inspections and Observations over Time

The condition of Specimen 3 at the end of its five-year exposure period is shown in Figure 5-1. It is evident from the figure that the specimen is excessively cracked, and the damage by ASR/DEF deterioration can be categorized as being *heavy*. The width of the widest crack observed on the north face of the specimen was measured at 30 mm. A similar crack was observed on the south side of the specimen and was measured to be 11 mm wide. The difference in the extent of damage due to ASR/DEF on the north and south face is attributed to the variation in the amount of moisture that was available from the sprinkler system to promote ASR/DEF expansion.

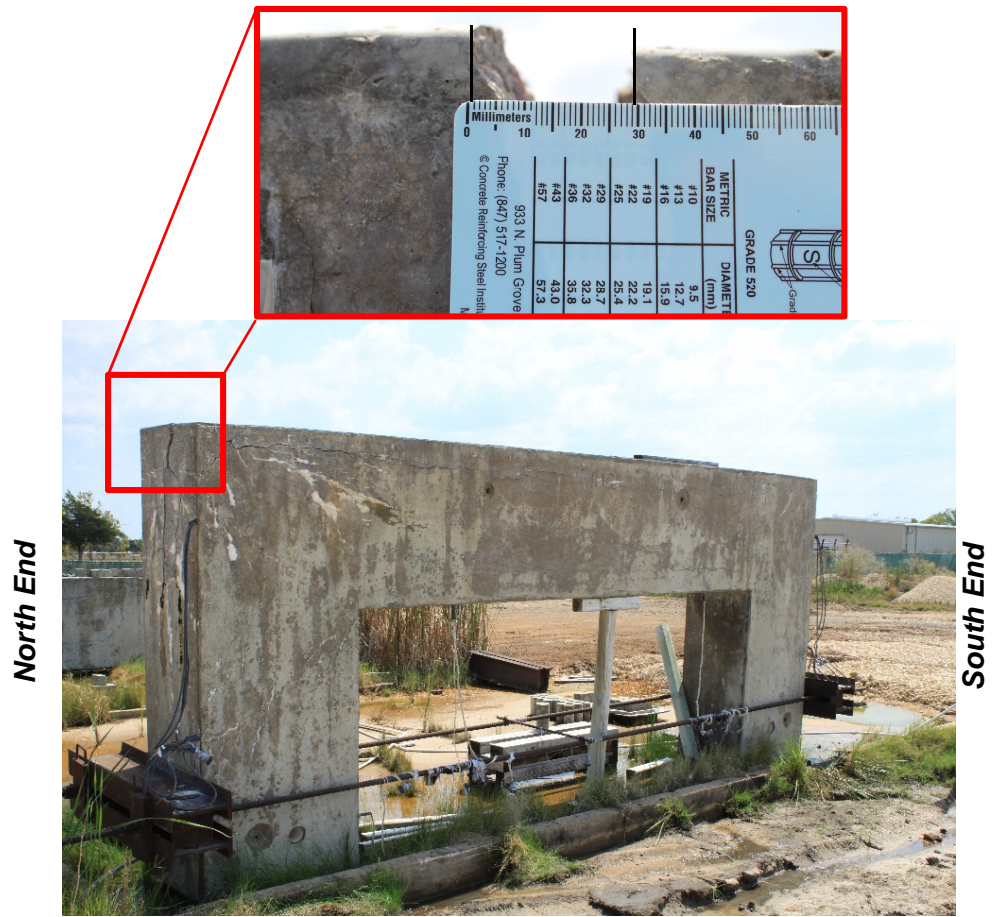
Figure 5-2 presents the crack pattern that was recorded for Specimen 3 at different time periods of its exposure. The cracks that were observed at Day 0 (first day of exposure) were imposed load-induced cracks caused by the tie-bar loads that were applied to simulate gravity loads. With field conditioning the map cracking that was induced by the ASR expansion in the specimen grew with time and eventually merged with the load-induced cracks. It is evident from Figure 5-2 that by 13 months (day 406) of exposure the specimen was excessively cracked on the north, south, and top faces of the specimen. As these faces of the specimen were excessively cracked, more emphasis was placed on mapping the cracks on the west face of the specimen at the time when the final mapping of cracks was performed at the end of the five-year conditioning period prior to the specimen being transported to the laboratory for testing. Over time, the formation of new cracks was also accompanied by the widening of existing cracks.

Figure 5-3 shows the crack widths that were measured on Specimen 3 at the end of its exposure period. Because of the large number of cracks on the specimen, the cracks are classified into different ranges of crack widths. It is evident from Figure 5-3 that the widest cracks are observed on the top edge of the north and south faces and on the edges of the specimen on the top face. This is attributed to the lack of transverse reinforcement across the column top face. It can also be seen in Figure 5-3 that the largest crack on the specimen west and top faces was aligned along the longitudinal column reinforcement and the skin reinforcement, respectively. It is also evident from

Figure 5-3 that the cracks follow the compression stress trajectories, and the widest cracks are observed where the restraint (reinforcement) is least, and natural tension cracking from load effects is greatest.

Figure 5-4 shows the progression of cracks in Specimen 3 at 48, 76, 129, 176, 406, and 1829 days of exposure. At 48 days of exposure (Figure 5-4a), very few new cracks developed in addition to the load induced cracks. However, by 76 days of exposure (Figure 5-4b) the existing load induced cracks grew in length and map cracking caused by ASR expansion were also observed. Commencement of longitudinal cracks that aligned with the reinforcement layout of the specimen was also observed. This indicates that the expansion due to ASR occurred between 48 and 76 days of exposure. These cracks further provided a path for moisture ingress into the specimen, which resulted in the accelerated formation of cracks caused by ASR expansion. This is evident from the state of the specimen observed at 129 (Figure 5-4c) and 176 (Figure 5-4d) days. At this stage many of the load-induced cracks had grown further and the map cracks caused by ASR/DEF merged with these cracks. By 406 days of exposure (Figure 5-4e), numerous cracks were observed on the specimen, especially the top and north face of the specimen, in addition to the longitudinal cracks that developed along the specimen reinforcement. The final state of the specimen at the end of its exposure period (1829 days = 5 years and 4 days) is shown in Figure 5-4f and it is evident that the specimen is in a state of severe cracking. While the existing cracks grew considerably, the addition of many new cracks was also observed.

Based on the visual observations presented in Figure 5-1 through 5-4, it is quite evident that Specimen 3 is subjected to excessive cracking due to ASR/DEF induced expansion. The damage caused by ASR/DEF induced deterioration to Specimen 3 can be classified to be *heavy*.



(a) West Face



(b) North Face

30 mm wide crack  
11 mm wide crack



(c) South Face

Figure 5-1: Deteriorated State of Specimen 3 at Texas A&M Riverside Campus.

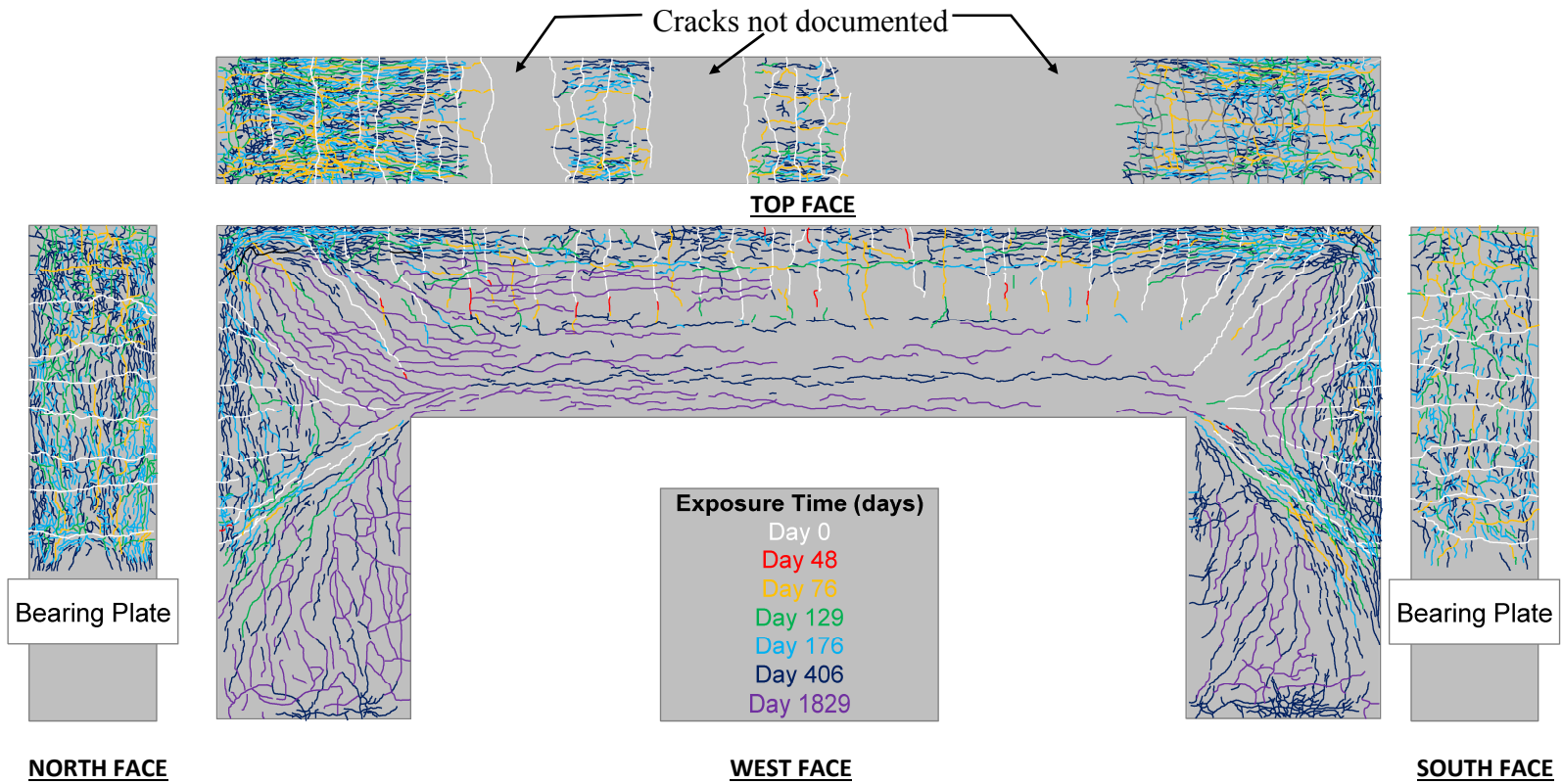


Figure 5-2: Crack Pattern over Time in Specimen 3.

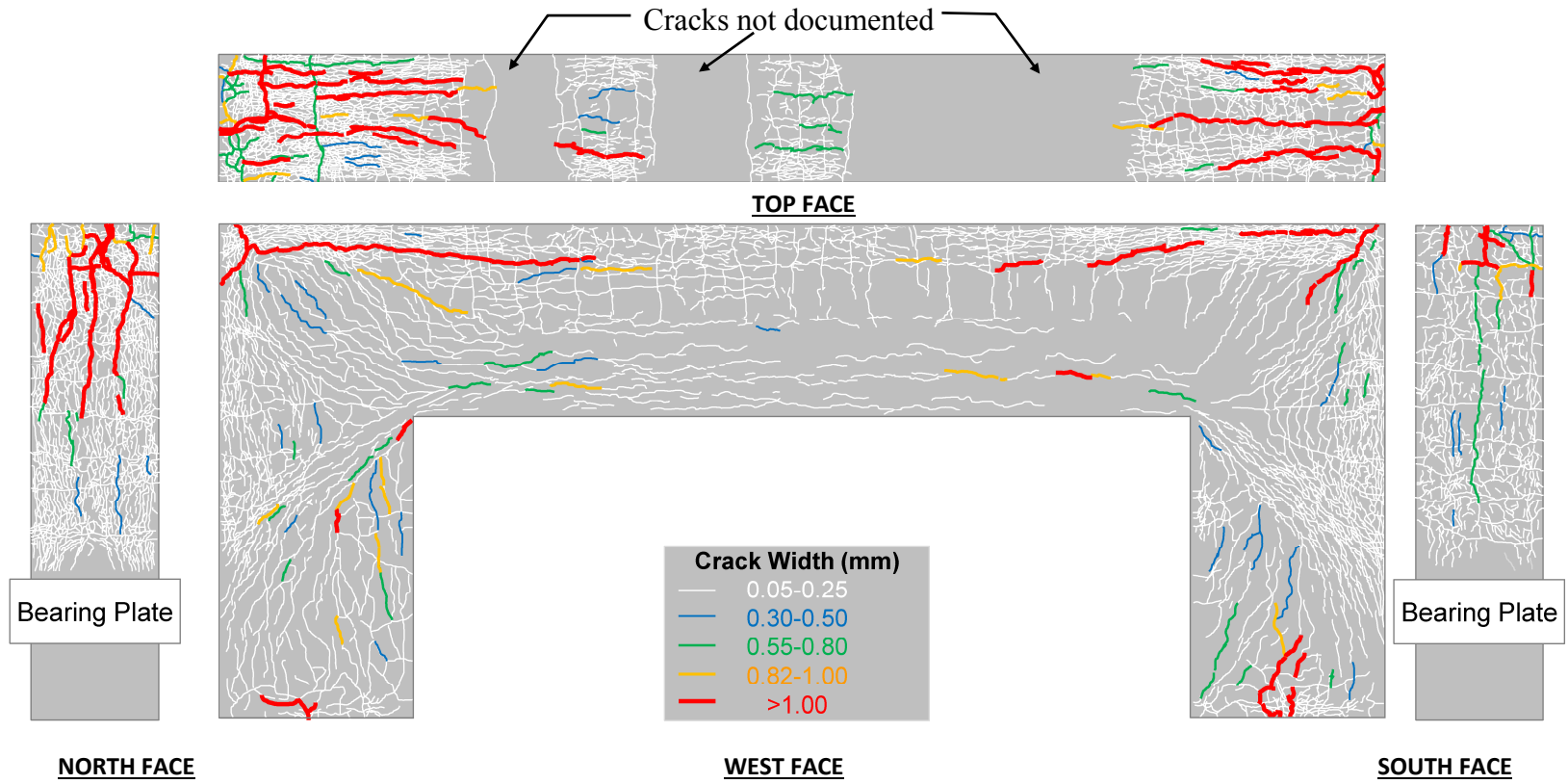
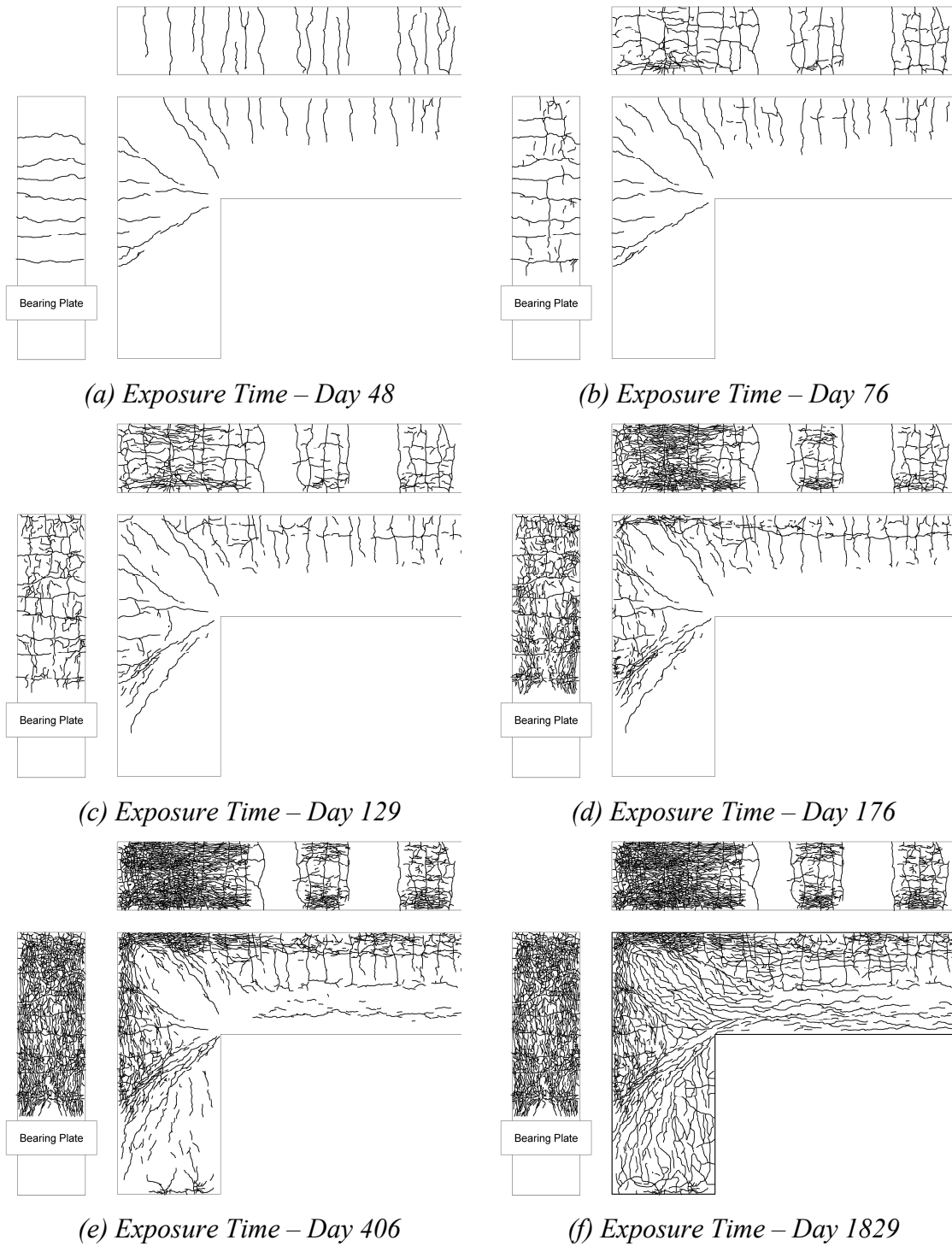


Figure 5-3: Final Crack Widths on Specimen 3.



**Figure 5-4: Progression of Cracks on Specimen 3 with Time.**



#### 5.4 Surface Concrete Strains

The progression of ASR/DEF induced expansion strains with time was recorded from a system of DEMEC points that were installed at the time of construction on the surface of the specimen. Longitudinal and transverse DEMEC measurements were made in the beam, column, and the beam-column joint. Additionally, the expansion strains transverse to the compressive diagonal strut in the beam and beam-column joint were also recorded. Typical DEMEC gage lengths were 267 mm. However, the gage lengths along the transverse direction of the beam and column short-widths were 249 mm.

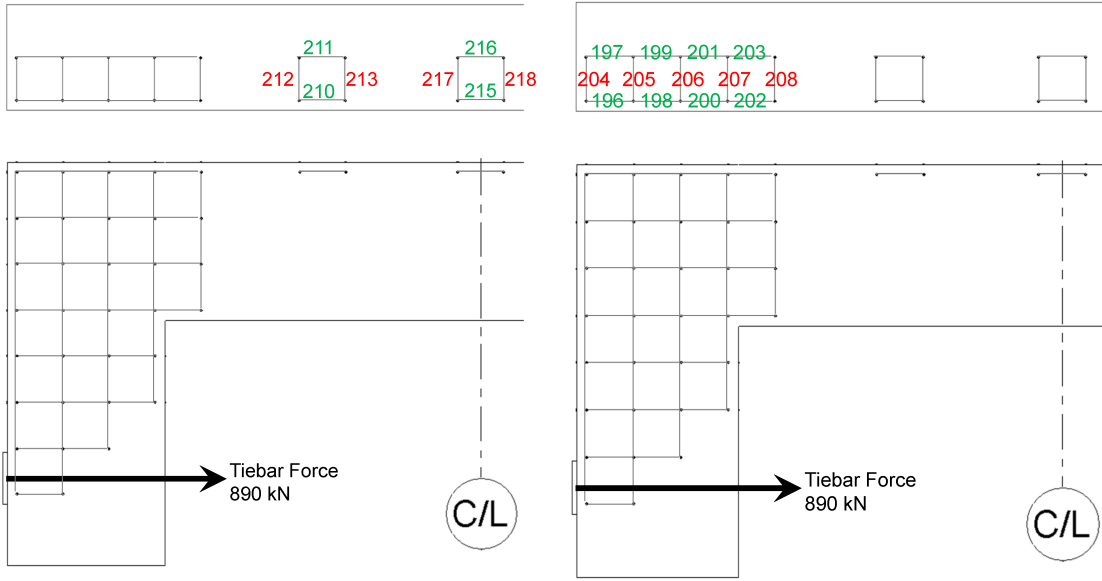
The surface expansion strains that were recorded from the DEMEC points on Specimen 3 are presented in Figures 5-5 to 5-8. In most cases it can be seen that measurable expansion strains are recorded at about 60 days of exposure. While the initial rate of expansion is high, the rate of strain reduced over a period of some two years. It appears that most of the ASR/DEF expansion was complete by the end of the 5-year field observation period. DEMEC data presented in each figure are grouped based on the region of the specimen and the direction in which the measurements are made.

Figure 5-5a and b present the layout of the DEMEC points on the top face of the C-beam specimen in the member and joint regions, respectively. The expansion strains in both the longitudinal and transverse directions are measured. Figure 5-5c shows the longitudinal and transverse expansion strains in the member region of the specimen top face. It is evident from the figure that the final expansion strains in the transverse direction are about three times the expansion strains in the longitudinal direction. This is primarily attributed to the fact that there is more longitudinal reinforcing steel restraining the expansion ( $\rho = 0.0308$ ) compared to the hoops in the transverse direction ( $\rho = 0.0019$ ). Figure 5-5d shows the expansion strains in both the longitudinal and transverse direction in the joint region of the specimen top face. As in the earlier case, the expansion strains in the transverse direction are much higher than the expansion strains in the longitudinal direction. Additionally, it should be noted that there are no transverse U-bars ( $\rho \approx 0$ ) on the top face of the C-beam specimen, leaving transverse

expansion of concrete essentially unconstrained. This explains why the transverse expansion strains in the joint region (Figure 5-5d) are on an average 1.5–2 times the transverse expansion strains in the member region (Figure 5-5c). The expansion strain recorded at DEMEC 204 is over 12 percent. This strain was measured over a gage length of 249 mm. However, the cracks on the knee-joint of the specimen were concentrated at about the middle of the specimen close to the center DEMEC stud. Therefore, a more realistic strain at DEMEC 204 would be about five percent considering the entire width of the specimen (610 mm), instead of the 249 mm gage length. Given that  $\rho \rightarrow 0$ , an unrestrained maximum expansion strain can thereby be assigned as  $\varepsilon_o^{\max} = 0.05$ . This result is subsequently used in the transient expansion modeling analysis in the next sections. The expansion strains recorded in Specimens 2 and 4 during their nine months (Liu, 2012) and two years (Mander et al., 2012) exposure period, respectively, are comparable to the strains recorded in Specimen 3 for the same time period.

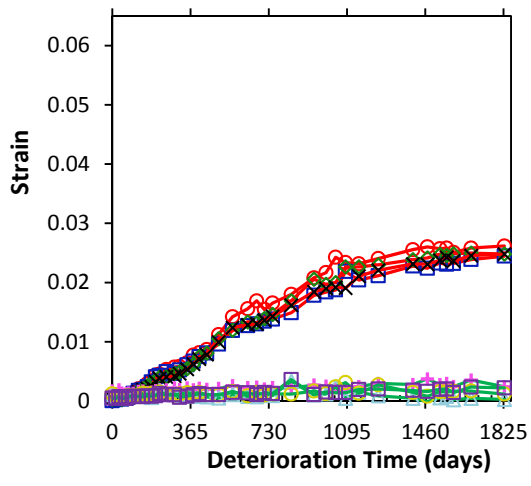
Figure 5-6a and b, respectively, show the layout of the vertical and horizontal DEMEC points in the joint region of the C-beam specimen. The vertical and horizontal longitudinal expansion strains are shown in Figure 5-6c and d, respectively. In both the cases the strains are broadly classified into two categories: expansion strains close to the edge of the specimen and expansion strains away from the edge of the specimen. It was previously shown (Mander et al., 2011) that the reinforcement did not reach its yield capacity within the development length zone. Therefore, the restraint provided by the longitudinal reinforcement against the expansion strains in the longitudinal direction varies with the distance from the specimen edge. Hence, the expansion strains recorded closer to the edge of the specimen are greater than the expansion strains that are recorded farther away from the edge where the bar strains are greater. This is evident from Figure 5-6c and d. In Figure 5-6c and d the strains measured away from the edge in the joint region are comparable whereas the expansion strains measured closer to the edge in the vertical direction (Figure 5-6c) are about 2 times the expansion strains measured close to the edge in the horizontal direction. This is likely because the longitudinal side reinforcement in the beam consisted of only 3 sets of #4 (13 mm) bars, whereas 5 sets of



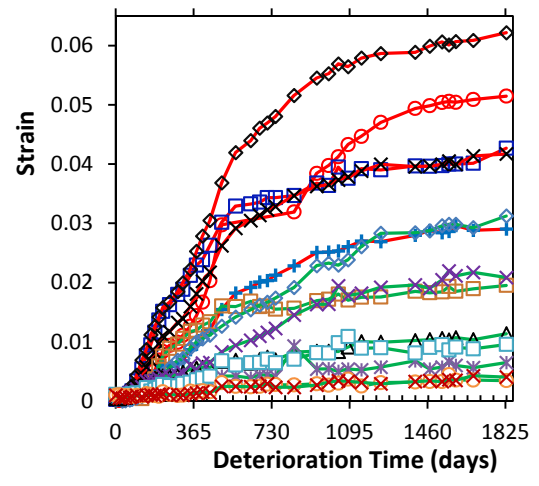


(a) DEMEC Layout on Member Top Face

(b) DEMEC Layout on Joint Top Face



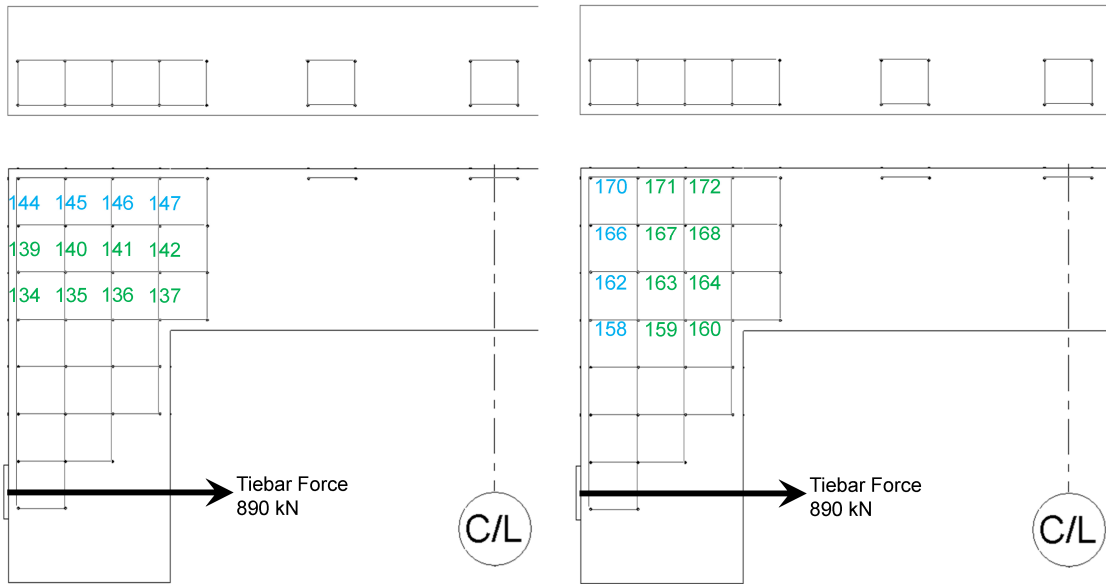
(c) DEMEC Strains in Member



(d) DEMEC Strains in Joint

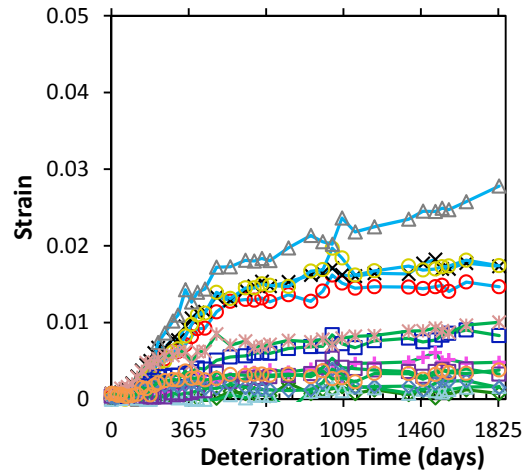
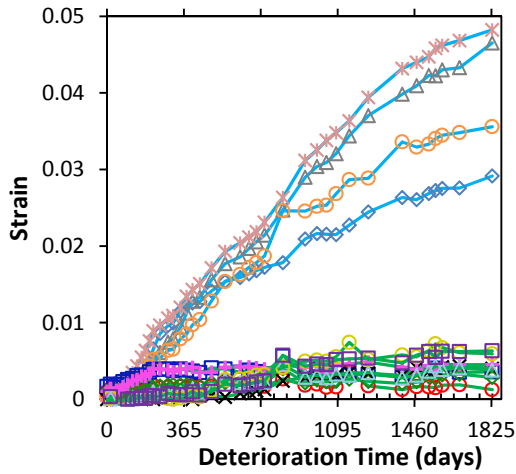
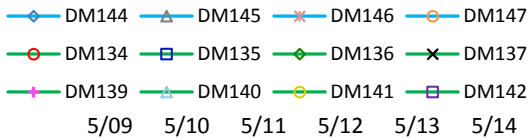
Note: ○ DM204 : Gage length = specimen width (610 mm) to account for concentrated crack

**Figure 5-5: Horizontal Surface Concrete Strains from DEMEC Points on C-beam Top Face–Specimen 3.**



(a) Vertical DEMEC Layout in Joint

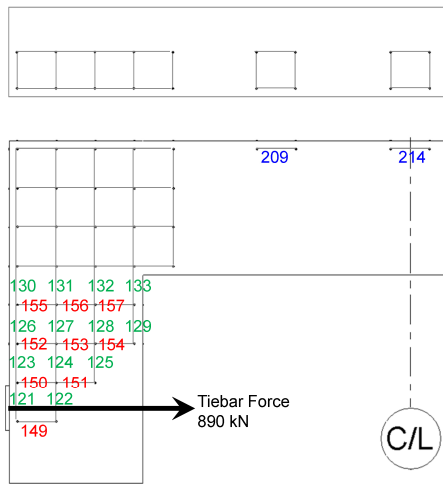
(b) Horizontal DEMEC Layout in Joint



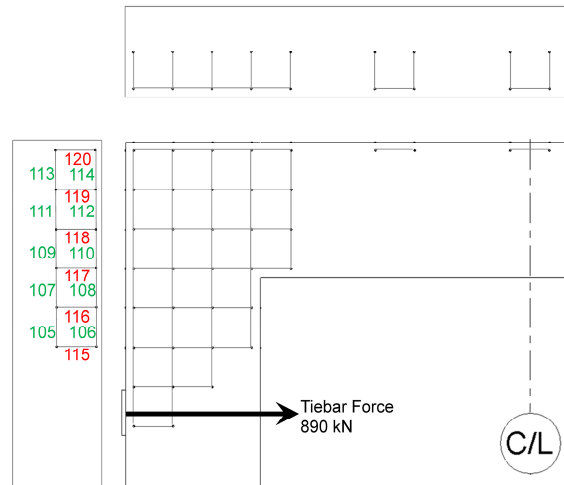
(c) Vertical DEMEC Strains in Joint

(d) Horizontal DEMEC Strains in Joint

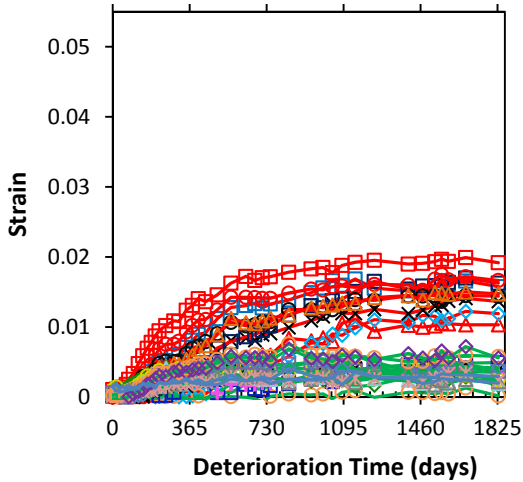
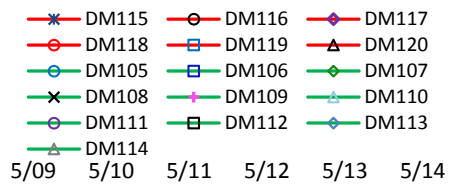
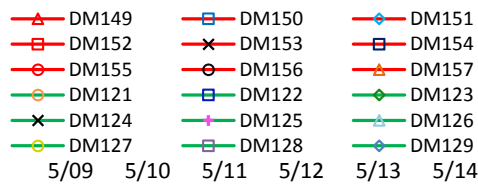
**Figure 5-6: Vertical Surface Concrete Strains from DEMEC Points in Joint Region—Specimen 3.**



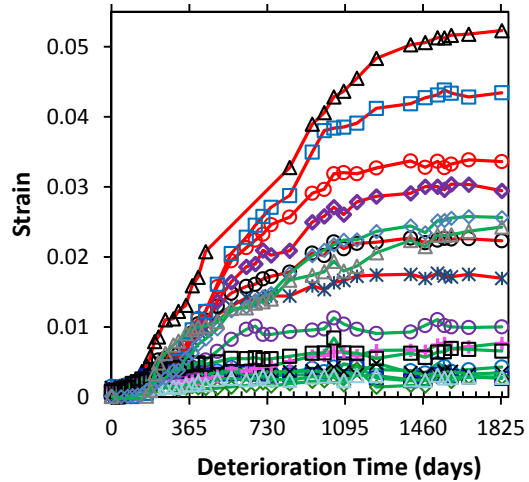
(a) In-Plane DEMEC Layout: Beam and Column



(b) DEMEC Layout: Beam Short-Width



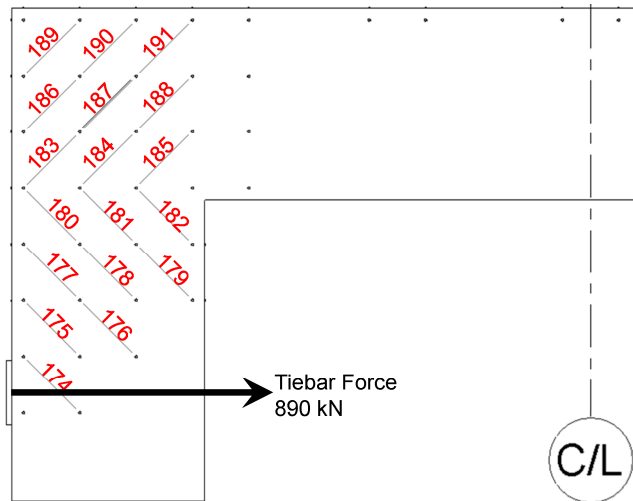
(c) In-Plane Strains in Beam and Column Region



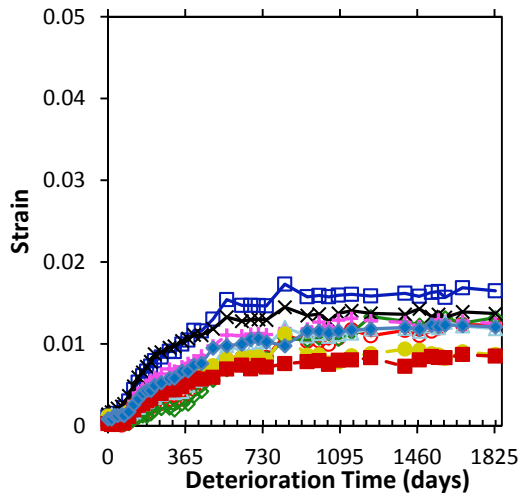
Note: —▲— DM120 : Gage length = specimen width (610 mm) to account for concentrated crack

(d) Strains along Beam Short-Width Region

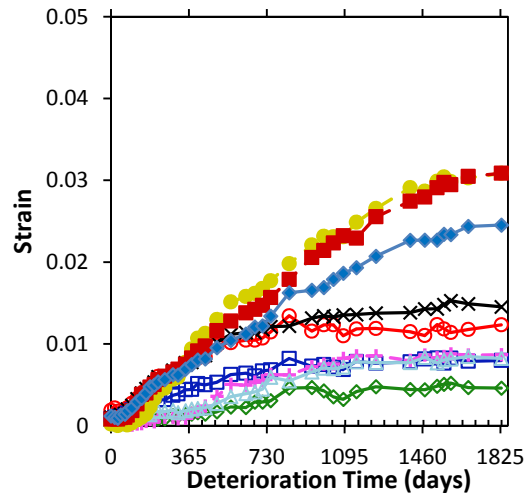
Figure 5-7: Vertical Surface Concrete Strains from DEMEC Points in Beam and Joint Region—Specimen 3.



(a) DEMEC Layout Transverse to Diagonal Strut in Beam and Joint Region



(b) Strains in Beam



(c) Strains in Joint

**Figure 5-8: Diagonal Surface Concrete Strains from DEMEC Points in Beam and Joint Region—Specimen 3.**

#8 (25 mm) bars were used as the longitudinal side reinforcement in the column. In other words, the beam was lightly reinforced in the longitudinal direction compared to the column, and hence provided less restraint to ASR/DEF induced expansion, which results in greater measured surface strains. These expansion strains are comparable to the strains recorded during the same time frame for Specimens 2 and 4 that were previously presented in Liu (2012) and Mander et al. (2014), respectively.

Figure 5-7a shows the DEMEC points in the in-plane longitudinal direction in the column, and longitudinal and transverse direction in the beam. Figure 5-7b shows the DEMEC points in the longitudinal and transverse direction along the short-width of the beam. Figure 5-7c shows the strains in the longitudinal and transverse direction in the in-plane direction. As in the earlier cases, it is evident that the expansion strains in the transverse direction were about twice the expansion strains in the longitudinal direction. This is due to the greater amount of longitudinal reinforcing steel ( $\rho = 0.0210$ ) compared to the transverse hoops ( $\rho = 0.0035$ ). Similar observations are made in Figure 5-7d, where the transverse expansion strains on an average are about three times the longitudinal expansion strains. Larger strains are observed close to the top edge of the knee-joint because of the influence of the very wide crack that is formed in this region. This crack also influenced the longitudinal strains observed at DEMEC points DM113 and DM114 close to the specimen top edge. The strains in Specimen 3 shows similar strains observed in Specimens 2 and 4 (presented in Liu, 2012 and Mander et al., 2012) during the same time period.

Figure 5-8a shows the diagonal DEMEC layout in the beam and beam-column joint region. These DEMEC measurements were made transverse to the main diagonal compressive strut in the beam and joint region. These transverse strains led to the compression softening of the diagonal concrete struts. Figure 5-8b and c show the strains that were measured in the beam and joint regions, respectively. Comparing Figure 5-8b and c it can be seen that the strains measured transverse to the main compressive diagonal strut in the joint region were greater compared to the beam region. This implies

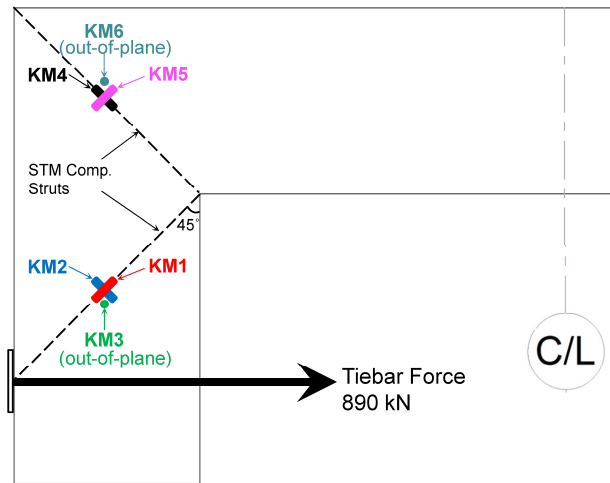
that the compressive diagonal strut in the joint region is likely to be subjected to greater compression softening compared to the compressive diagonal strut in the beam.

### **5.5 Internal Concrete Strains**

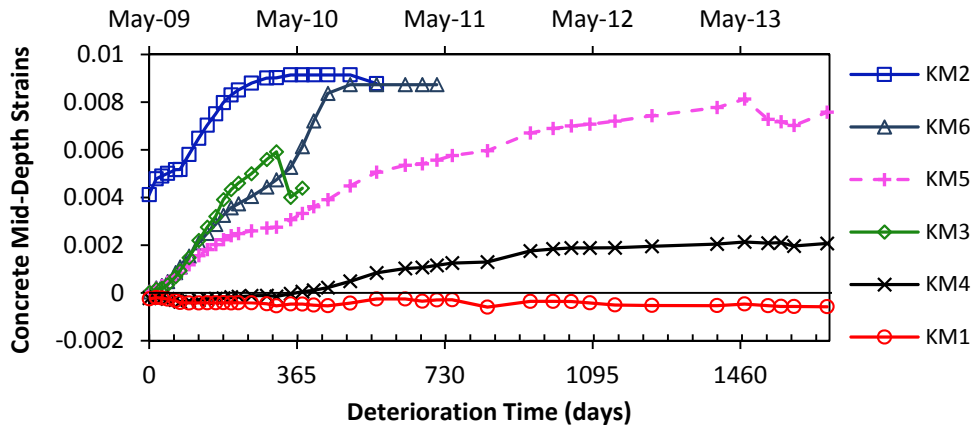
To monitor the strains in the core concrete, concrete gages (KM) were embedded in the C-beam specimen core concrete, providing a total of six KM gages embedded on each side of the C-beam specimen, in which, three gages each were placed within the beam region (KM1–KM3) and beam-column joint (KM4–KM6).

The concrete strain along the main diagonal compression strut formed between the point of loading and the inner knee-joint in the beam was measured using gage KM1, which was aligned along the compression strut. Similarly, KM4 measured the compressive strains along the diagonal compression strut joining the outer and inner knee-joints. Figure 5-9b shows that compressive strains were recorded in gage KM1 (Specimen 3). Although gage KM4 initially measured compressive strains, from about 300 days of exposure it recorded tensile strains. This could likely be because of localized strains caused due to a reactive site that could have existed close to KM4 location.

Gages KM2 and KM5 measured in-plane strains transverse to the diagonal compression strut. While KM2 in Specimen 3 stopped recording data just after 500 days, both KM2 and KM5 measure tensile strains. Tensile strains of 0.008 were measured in KM5 at the end of the exposure period of Specimen 3. Gages KM3 and KM6 measured transverse strains along the short-width (out-of-plane) perpendicular to the compression strut. Both the gages stopped functioning before two years of exposure, however, it is evident from Figure 5-9b that they too recorded significant tensile strains perpendicular to the diagonal compression struts. It is evident that the core concrete tended to expand across the short-width of the specimen because the transverse hoops, which were restricted to the perimeter of the cross-section provided minimal restraint against ASR/DEF expansion in that direction. The observations show similar trends for Specimens 2 and 4 which can be found in Liu (2012) and Mander et al. (2012), respectively.



(a) Concrete Gage Layout for C-beam Specimen



(b) Concrete Strain in Mid-Depth

**Figure 5-9: Mid-Depth Concrete Strains Measured from Concrete Gages—Specimen 3.**

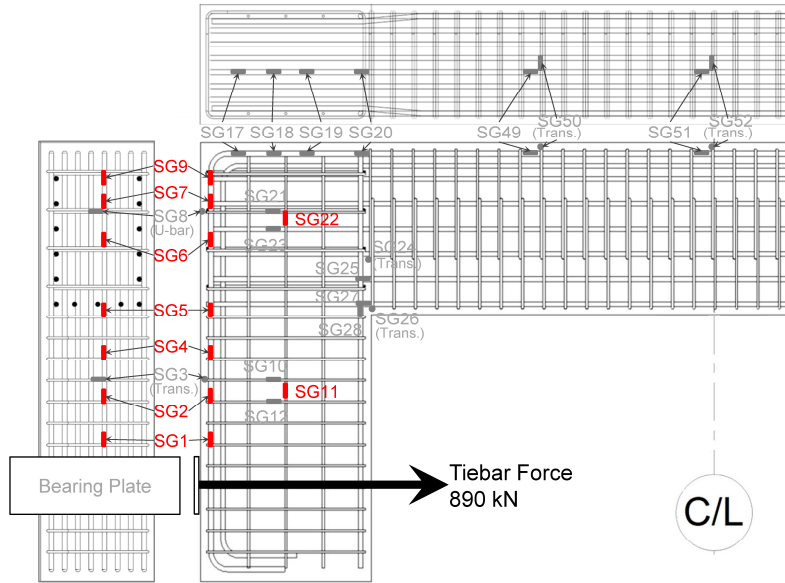
## 5.6 Reinforcing Steel Strains

Figures 5-10 to 5-13 present the reinforcing strains in the longitudinal and transverse steel at various regions for C-beam Specimen 3. The C-beam specimen was post-tensioned before it was conditioned in the field to simulate gravity loads. Therefore, prestrains were recorded in the strain gages. Under field exposure conditions, the strains in the steel quickly increased reaching close to or above the yield strain of the reinforcement.

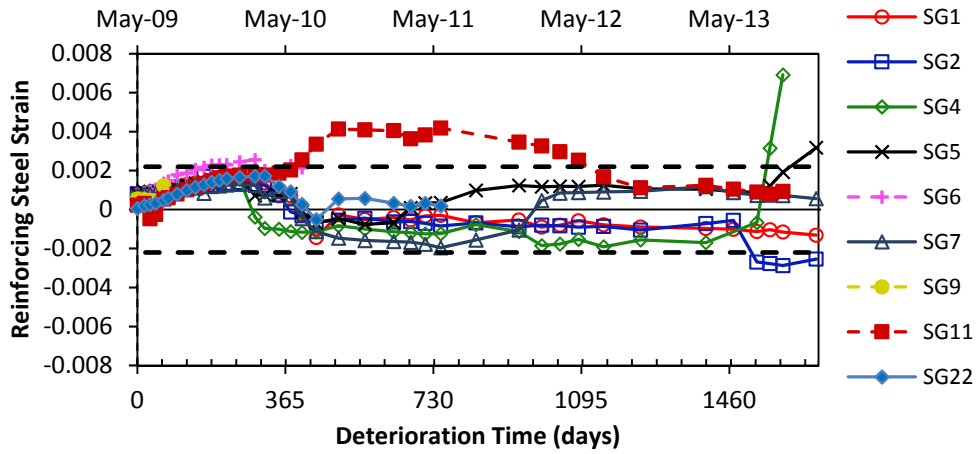
Figures 5-10 and 5-11 shows the tensile strains that were recorded in the longitudinal reinforcement steel in the beam and column, respectively. For Specimen 3 it can be seen that the tensile strains in the reinforcement reached yield strain (0.0022) at around 300 days of exposure. However, after about one-year of exposure, decreasing tensile strains and eventually compressive strains were recorded in many gages in both the beam and the column. It is to be noted that several longitudinal cracks were formed just over the longitudinal steel. This likely promoted greater ingress of moisture, which in turn promoted the expansion of ASR gel. Therefore, the strains recorded from the strain gage are more likely to be localized strains that are influenced by ASR/DEF reactive sites close to the strain gages and therefore does not give a good measure of the reinforcement strains beyond 360 days of exposure.

Figure 5-12 shows the strains that were recorded from the transverse reinforcement and the U-bars in the joint region. For Specimen 3 it can be seen that the tensile strains in the transverse reinforcement reached yield between 180–240 days, much earlier than the longitudinal reinforcement. This can be attributed to the reinforcement ratio in the transverse direction generally being less compared to the longitudinal direction in the various regions of the C-beam specimen. Hence, less restraint is offered to ASR/DEF induced expansion in the transverse direction, which in turn causes greater expansion strains and yields the transverse steel reinforcement earlier. Again, after a period of 300–360 days scattered strains are observed, which are



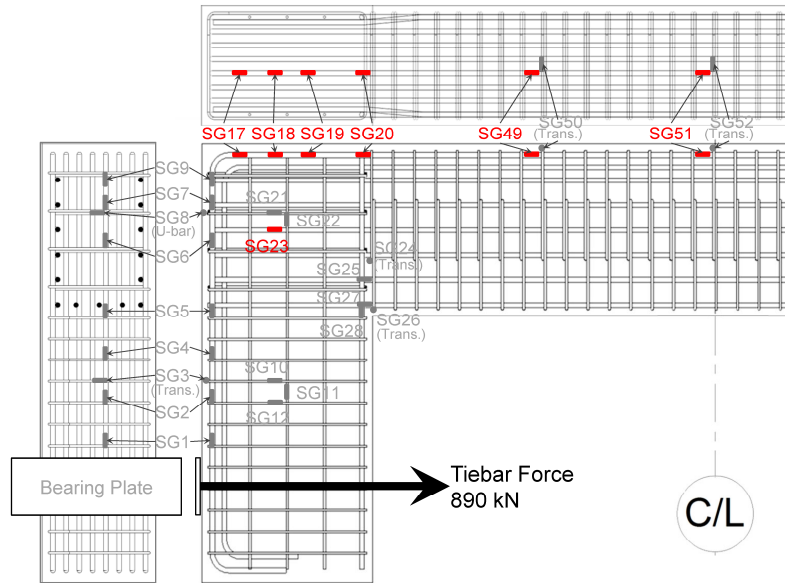


(a) Strain Gage Layout

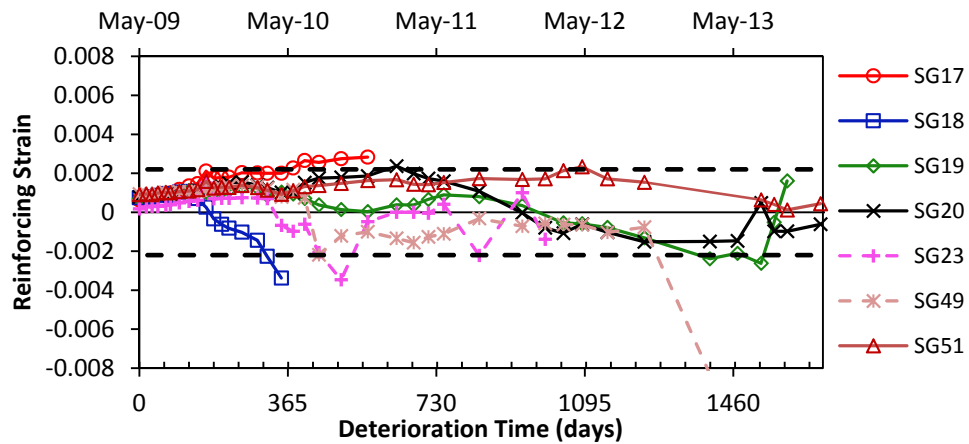


(b) Strain in Longitudinal Reinforcement

Figure 5-10: Longitudinal Reinforcing Steel Strains in Beam-Specimen 3.

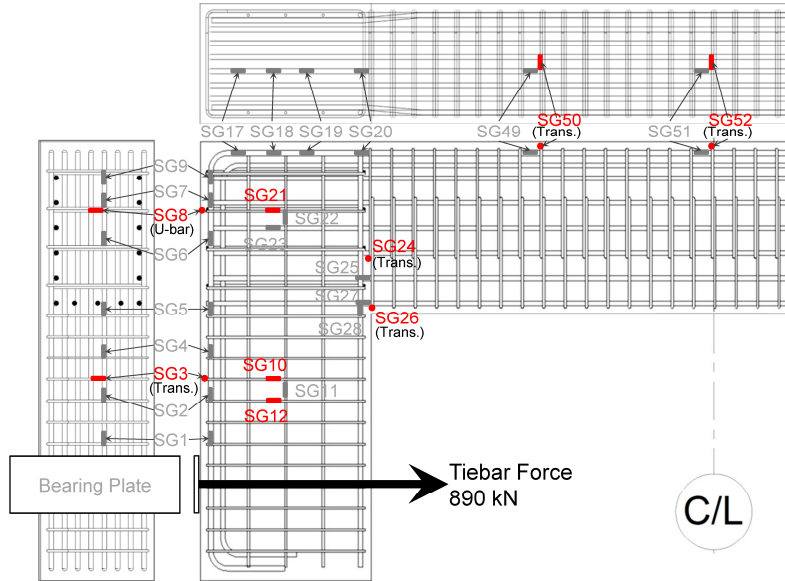


(a) Strain Gage Layout

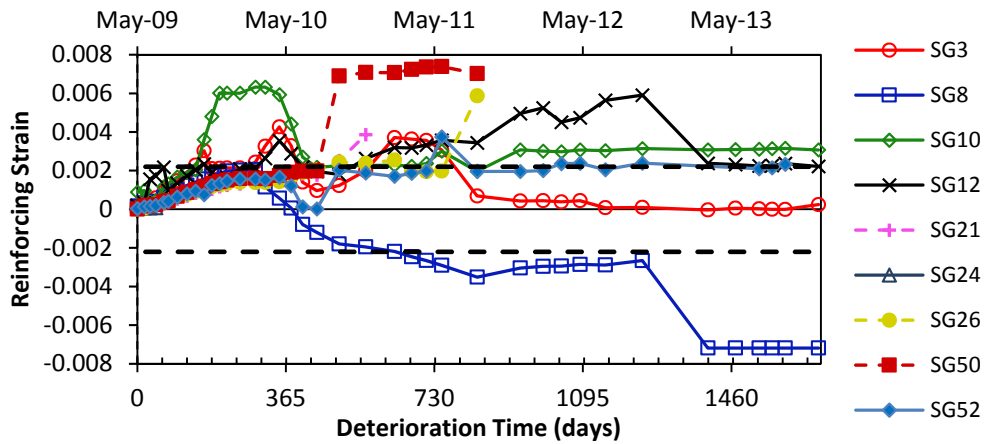


(b) Strain in Longitudinal Reinforcement

Figure 5-11: Longitudinal Reinforcing Steel Strains in Column–Specimen 3.

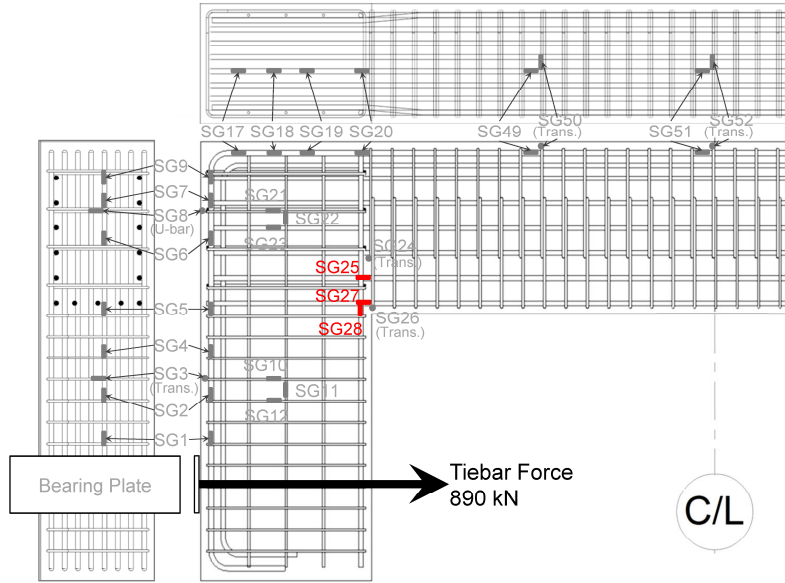


(a) Strain Gage Layout

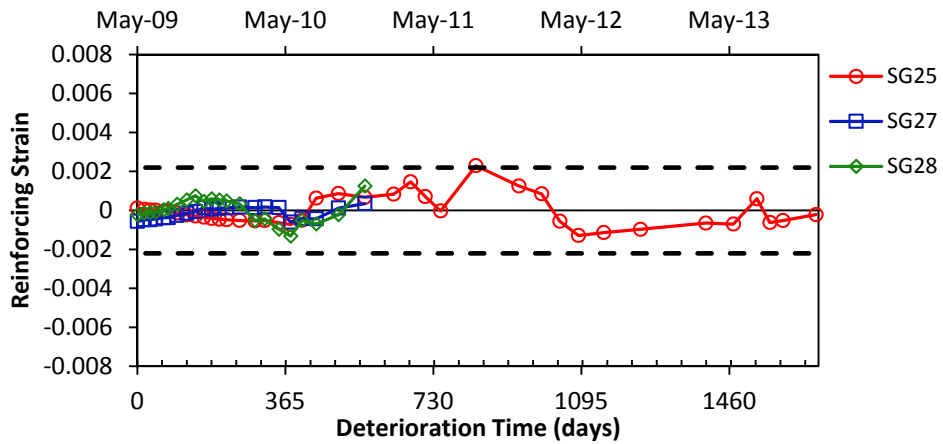


(b) Strain in Transverse Reinforcement

Figure 5-12: Transverse Reinforcing Steel and U-bar Strains.



(a) Strain Gage Layout



(b) Strain in Longitudinal Reinforcement

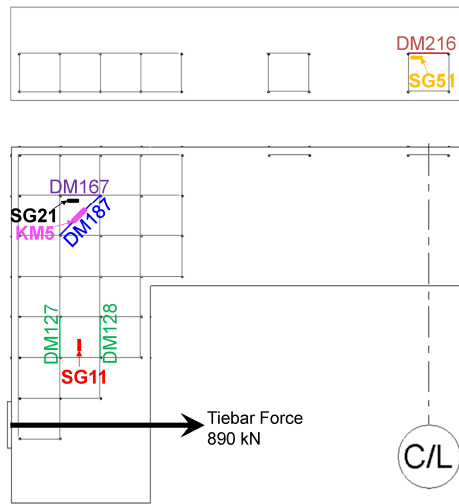
Figure 5-13: Reinforcing Steel Strains in Compression Zone.

likely localized strains and therefore unreliable. Figure 5-13b finally shows the reinforcement strains in the compression region. For Specimen 3 the recorded strains remain close to zero with minor variations for about 360 days of exposure. Beyond that period, the strain gage data become unreliable.

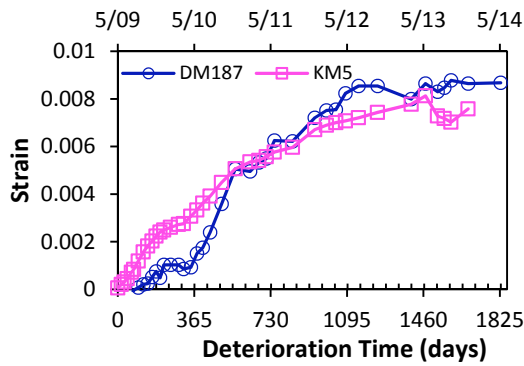
## **5.7 Discussion and Comparison**

From the field data for the C-beam specimen presented in this study, it is evident that over several years, ASR/DEF reactions continue to increase and cause significant expansion in reinforced concrete. The embedded concrete gages and strain gages attached to the reinforcement give the internal strains in the structure. It is evident from the strain gage measurements, that both the transverse and longitudinal reinforcement started to yield between six months to one year of exposure. Many of the embedded gages either stopped functioning or were influenced by localized effects of ASR/DEF expansion (especially after one year of conditioning) and therefore cannot be relied on completely to obtain general strains in concrete and the reinforcement steel.

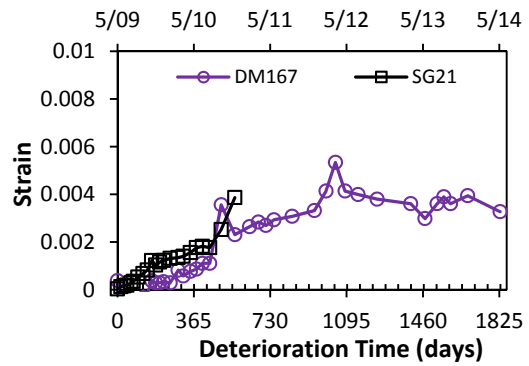
The surface concrete strain measurements obtained from the DEMEC points installed on the specimen surface gave valuable information on the expansion strains in the C-beam specimen. Figure 5-14 shows a comparison of the external surface strains obtained from the DEMEC points to the corresponding internal strains obtained from strain gages and concrete gages. Figure 5-14a shows the locations of the DEMEC points and the internal strain gage or concrete gage that were closest to the location and orientation of the DEMEC readings. Figure 5-14b shows a comparison of strain measurements from DM187 and KM5 that were made transverse to the concrete diagonal strut in the joint region. Although the strain values do not match exactly, the strain measurements from the DEMEC points and the concrete gages compare very well. Figure 5-14c compares the external surface strains from DM167 with the internal strains obtained from SG21 along the direction of the longitudinal column reinforcement in the C-beam joint region. The strain gage did not record readings beyond 1.5 years of exposure. However, up to that point, the strains compare well between the DEMEC



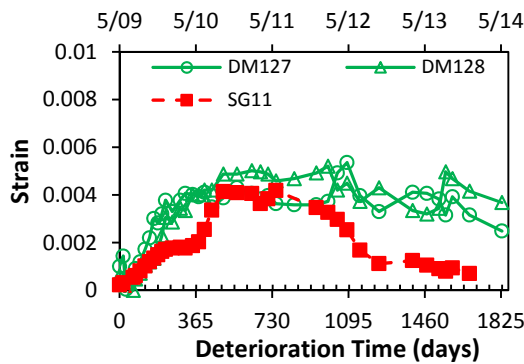
(a) Strain Measurement Locations on the C-beam Specimen



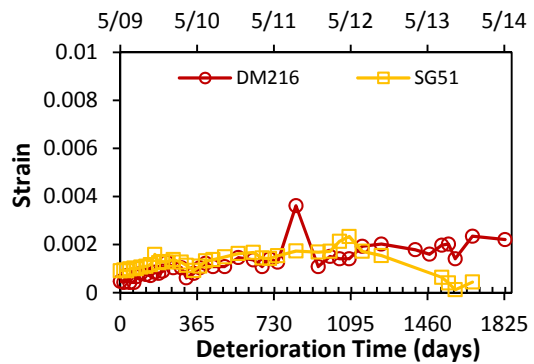
(b) DM187 vs. KM5



(c) DM167 vs. SG21



(d) DM127 and DM128 vs. SG11



(e) DM216 vs. SG51

**Figure 5-14: Comparison of Surface Strains from DEMEC (DM) Points to the Internal Strains from Strain Gages (SG) and Concrete Gages (KM) for C-beam Specimen 3.**

points and the strain gage. Figure 5-14d compares the longitudinal strains from DM127 and DM128 with SG11 on the beam longitudinal reinforcement. A good comparison between the strain measurements from the DEMEC points and the strain gage is observed until about 2.5 years. Beyond this, the strains recorded by the strain gage decrease. Figure 5-14e compares strains between DM216 and SG51 in the direction of column longitudinal reinforcement on the C-beam specimen top face. The DEMEC and strain gage expansion strain measurements compare very well with each other for about 3 years, beyond which the internal strains recorded by the strain gage starts falling. The possible reason for decreasing tensile strains recorded by strain gages beyond 2.5 to 3 years in Figure 5-14d and e could be because of the localized formation of ASR gel in the vicinity of the strain gage or due to faulty wiring and the formation of a corrosive layer between the strain gage and rebar. Another possibility could be debonding between the reinforcement bar and the cement paste that was reported in the petrographic analysis of C-beam Specimen 4 (Liu, 2012).

Overall, it is evident from Figure 5-14 that although the strains measured from the DEMEC points are just surface strains, they are very similar to the internal strains that are measured from the strain gages and concrete gages. However, beyond about 2.5 years, the external strains did not compare well with the internal strains. This is possibly due to the limitations on the range of strains that could be measured by the strain and concrete gages, and the influence of localized effects on internal strain measurements. The surface strains are also closely related to the reinforcement layout in the region that the expansion strain measurements were made. It is also clear from the data presented in the earlier section that, in general, the expansion strains in the transverse direction were always greater than the strains in the longitudinal direction because of the smaller reinforcement ratio in the transverse direction and hence less restraint to expansion.

Although the expansion data and the crack widths recorded in this study may seem unlikely in ordinary structures, these observations cannot be completely ruled out in actual structures. For instance, a bridge pier constructed with high alkali content cement and highly reactive aggregates in a coastal region, when continuously exposed to

high moisture and salt water, could likely see similar large expansion strains and crack widths.

## **5.8 Closure and Key Findings**

The premature concrete deterioration caused by ASR/DEF induced expansion were monitored by measuring the surface concrete strains through the DEMEC points, and from concrete gages embedded within concrete and strain gages attached to the steel reinforcement. The specimen was loaded with post-tensioned tie-bars to simulate gravity loads on the structure. This load application initially resulted in load-induced cracks that formed a pathway for moisture ingress into the specimen and evidently helped accelerate the formation of ASR gel in the specimen. The map cracking resulting from ASR/DEF merged with the initial load-induced cracks. Over time, new cracks ceased to form and the existing cracks grew in width. The largest crack width that was observed was 30 mm wide. Based on the condition of C-beam Specimen 3, the specimen may be categorized as displaying *heavy* deterioration from ASR/DEF expansion.

The transverse and longitudinal steel strains exceeded their yield strain between six months to one year of field conditioning. In general, the expansion strains recorded along the direction of the transverse reinforcement were greater than those along the direction of the longitudinal direction, because of the smaller reinforcement ratio in the transverse direction, and hence less restraint to expansion. A comparison of the external expansion strains measured from the DEMEC points with the internal strains from the strain gage and concrete gages showed that the external strains were quite similar to the internal strains recorded.

Although the physical condition of Specimen 3 is concerning, it is not known how the severe nature of ASR/DEF deterioration caused in the specimen affects its structural load carrying capacity. Section 7 presents the overall and internal results from the experimental load testing of Specimen 3.



## 6 APPLICATION OF PROPOSED EXPANSION MODEL TO ESTIMATE EXPANSION STRAINS IN C-BEAM SPECIMENS\*

### 6.1 Summary

A minimalist semi-empirical method to model the expansion strains caused by ASR/DEF related expansion in reinforced concrete was presented in Section 4. The implementation of the proposed method to simulate the expansion caused by ASR/DEF in large-scale reinforced concrete C-beam specimens that were exposed to the environmental conditions is presented in this section. To effectively account for expansion strains caused by ASR/DEF expansion in reinforced concrete, it is necessary to consider the orientation of the exposure face, the reinforcement details, and the location of the strain measurements. The effects of precracks caused by tensile prestrains are also taken into account in simulating the expansion strains of the C-beam specimen. The modified expansion model is able to capture the average longitudinal and transverse expansion strains in the different regions of the specimen quite well. The model is also able to simulate the variation in the expansion that was observed within and outside of the reinforcement development length zone, and closer to and away from the specimen edges within the development length zone. Considering the wide scatter of the observed expansion results that were measured from the C-beam specimens, the model provides a satisfactory simulation of the expansion results, with most of the results lying between the extremities of the experimental data observed. Providing appropriate values are assigned to the limited input parameters required in the analysis, it is shown that the

---

\* Previously published work is available to the public through National Technical Information Service. Mander, J.B., Karthik, M.M., and Hurlebaus, S. (2015). "Structural Assessment of "D" Region Affected by Premature Concrete Deterioration: Technical Report." *Report No. FHWA/TX-15/0-5997-2*, Texas A&M Transportation Institute, College Station, Texas, USA.

minimalist semi-empirical formulation can be effectively used to model ASR/DEF induced expansion in reinforced concrete members.

## **6.2 Introduction**

As part of a large scale experimental program described in Mander et al. (2012), reinforced concrete C-beam specimens representing cantilever and straddle bent bridge piers were cast and cured to promote ASR/DEF induced expansion in reinforced concrete. Figure 6-1 presents the reinforcement layout and the cross-section details of the C-beam specimens. To promote ASR in the specimen, high alkali content cement and aggregates with reactive silica along with Sodium Hydroxide mixed in water were used. The specimens were subjected to curing temperatures in excess of 77°C by means of an electrical resistive wiring setup to promote DEF related expansion in the specimen. The specimens were then transported outdoors and subjected to environmental conditions, as any actual bridge under service would be exposed to. To accelerate the expansion caused by ASR/DEF for purposes of the experimental study, a sprinkler system was installed and the specimens were sprinkled with water at regular intervals. Of the four specimens constructed, Specimen 1 was the control specimen and was stored indoors, while Specimens 2, 3, and 4 were conditioned outdoors and subjected to ASR/DEF deterioration for varying periods of time.

Of the three deteriorated C-beam specimens, Specimen 3 was conditioned in the field for five years with significant effects of ASR and DEF deterioration observed. The data from the strain and concrete gages embedded in the specimen and DEMEC points on the surface of the specimen were collected on a regular basis. The model proposed for ASR/DEF related expansion in reinforced concrete is applied to the C-beam specimens, and the results are compared to the field measured DEMEC data obtained for Specimen 3. Later the model is also applied to Specimens 2 and 4 to ensure the repeatability of the proposed expansion model.

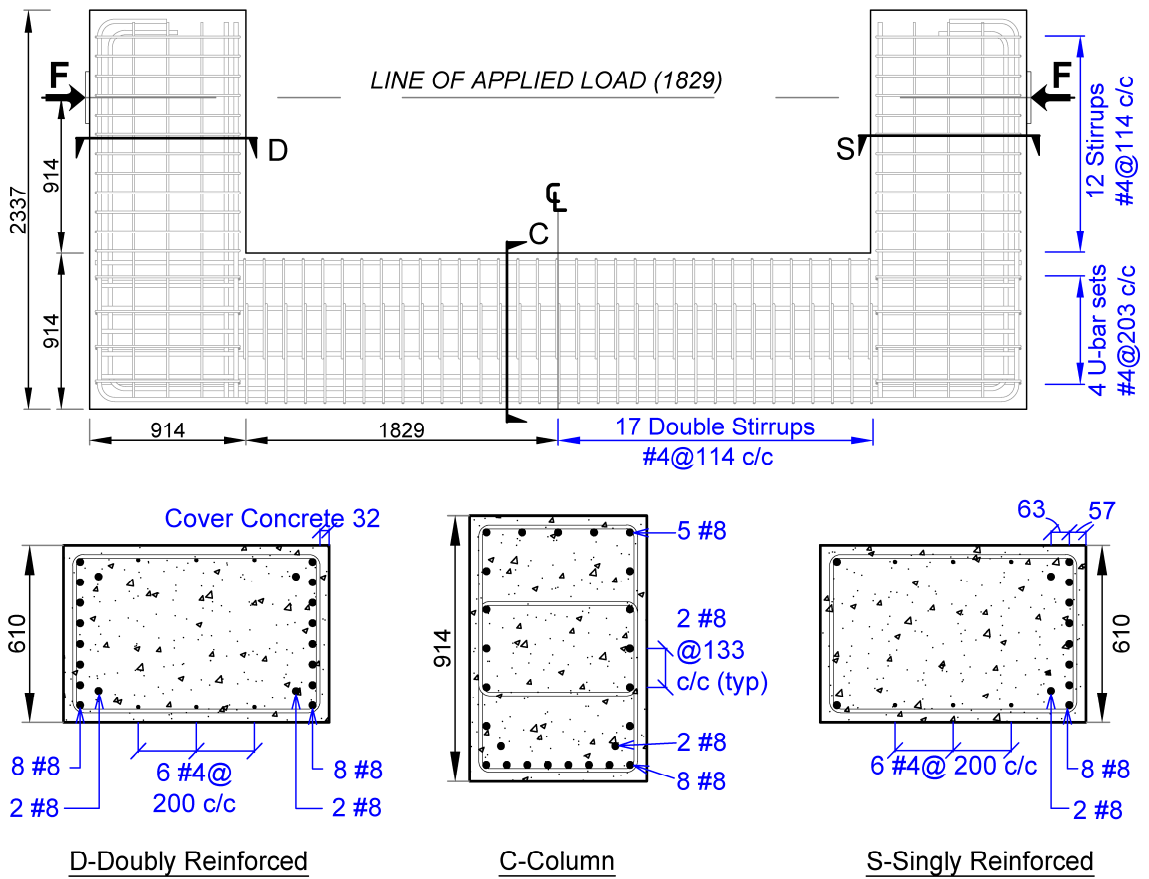


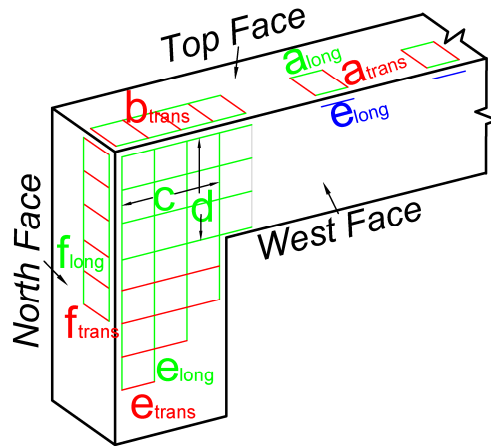
**Figure 6-1: Reinforcement Layout of C-beam Specimen.**

### 6.3 Parameters for Modeling Expansion in C-beam Specimen

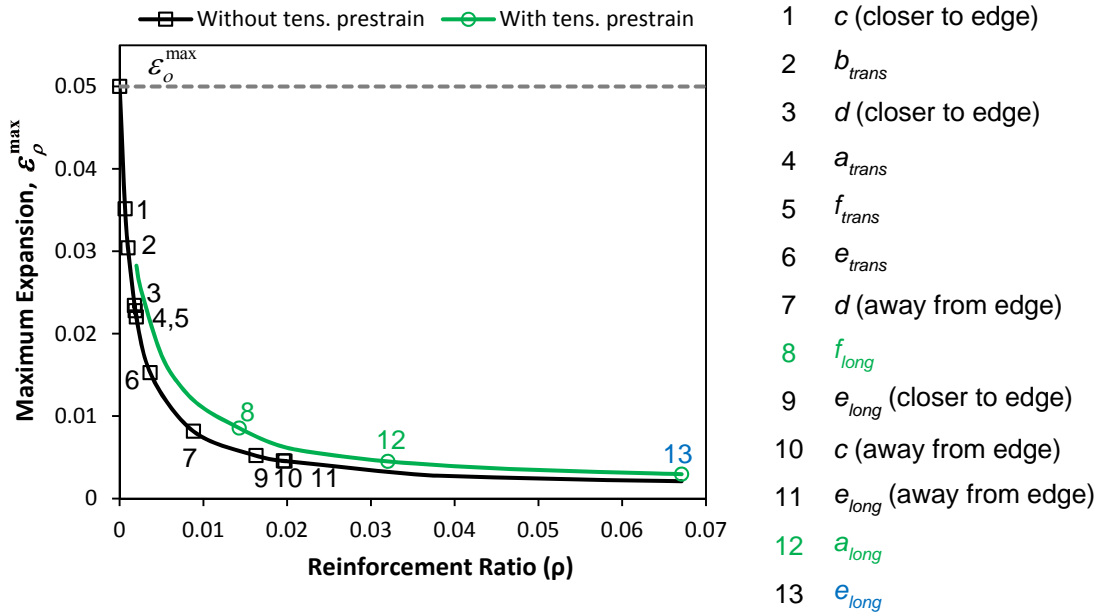
To represent the data collected from the DEMEC points in a meaningful and logical way, the C-beam specimen is divided into different regions and the DEMEC data categorized accordingly. Figure 6-2a identifies the various regions of the C-beam specimen used in this study to model expansion strains. The C-beam specimen is divided into the top face where the exposure face is horizontal, and the west and north side faces where the exposure face is vertical. Figure 6-2a also shows the location and orientation of DEMEC points on the surface of the C-beam specimen that are used for the purpose of comparison in this study. Longitudinal and transverse strain measurements were made in the different regions of the specimen.

The C-beam specimens were subjected to both ASR and DEF expansion. Since no clear evidence is available on when and how much each of the two expansion mechanisms contributes toward the total expansion strains in the specimen, the combined effects of the two expansion mechanisms are considered in modeling the overall expansion. From the experimental results, the time  $t_o$  when expansion strains initiate is taken as 60 days. The rise time of the tangent line  $t_{r,t_o}$  is deduced to be 120 days from the expansion data of Specimen 3. Since no data are available on the expansion caused by ASR/DEF expansion in plain concrete  $\varepsilon_o^{\max}$ , this parameter is inferred from the largest crack observed from an unreinforced part of the specimen. It should be noted that the top face of the column in the joint region was essentially unreinforced. A crack width of 30 mm across a total section width of 610 mm, results in an expansion strain of approximately 0.05. Therefore, for this study the value of  $\varepsilon_o^{\max} = 0.05$  is adopted.

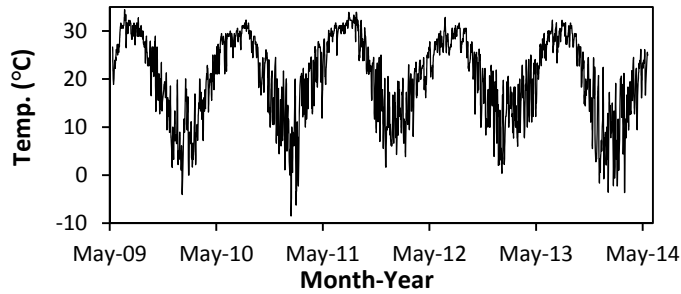
Figure 6-2b shows the relationship between the reinforcement ratio and the maximum expansion strain computed for the various regions of the C-beam specimen. As expected the maximum expansion strain in the C-beam specimen decreases with increasing reinforcement ratio. The C-beam specimen was subjected to tie-bar forces to simulate the effects of gravity loads on the structure. These induced tensile stresses



(a) DEMEC Layout of C-beam Specimen



(b) Variation of Maximum Expansion with Reinforcement Ratio



(c) Observed Average Daily Temperature

**Figure 6-2: Information Pertinent to Model Expansion Strains in C-beam Specimen.**

promote cracking. These effects are also taken into account while computing the maximum expansion strain,  $\varepsilon_{\rho}^{\max}$ . In Figure 6-2b two curves are presented, one where no tensile prestrain effects on the expansion strain are considered, and the other with the tensile prestrain effects considered. It is clear that for the same reinforcement ratio, the maximum expansion strain is greater when the tensile prestrain effects are considered. This is complimentary to the case where compressive strains cause lower expansion strains as shown in Figure 4-9b. The computation of the reinforcement ratio is discussed in detail in Appendix A3.

To account for the variation in expansion due to temperature and moisture content, the average daily temperature and rainfall amounts obtained from the closest weather station to the site where the specimens were conditioned. Additionally, to obtain a reasonable estimate of the actual amount of moisture that the specimens were subjected to due to supplemental water from the sprinkler system, a series of rain gages were installed at various locations on Specimen 3. For this study a degree of saturation of  $S = 0.1$  is assumed for the horizontal exposure surfaces, and for strains measured in the horizontal direction caused by cracks in the vertical direction. The vertical cracks allow better ingress of moisture into the specimen, and the related expansion causes horizontal strains. For strains measured in the vertical direction caused by horizontal cracks on the vertical exposure face, a degree of saturation of  $S = 0.05$  is adopted as the horizontal cracks do not allow for moisture ingress into the specimen as well as the vertical cracks. The temperature and moisture content data are used in the computation of expansion strains in the reinforced concrete C-beam specimens. Figure 6-2c shows the variation of the daily average temperature recorded at the closest weather station to the site for the period when Specimen 3 was exposed to field conditions.

Also taken into account in the computation of the maximum expansion strain are the tensile strains induced by the applied tie-bar force used to mimic gravity loads on the specimen. The C-STM model of the C-beam specimen that is developed in Section 8 is used to determine the initial strains. As shown in Figure 6-3, an 890 kN load corresponding to the tie-bar force is applied, and the corresponding tensile strains are

obtained from the model. The values of the tensile strains in concrete and steel are shown in Figure 6-3. The applied tie-bar force causes tensile stresses in the longitudinal direction along the outer edges of the specimen, which results in a tensile prestrain. However, there are no stresses applied in the out-of-plane direction of the specimen, hence there are no prestrains that contribute to the expansion in the out-of-plane direction. However, the presence of transverse reinforcement restrains the expansion in the out-of-plane direction.

Another important parameter that is required for the implementation of the proposed expansion model is the reinforcement ratio of the specimen. As the DEMEC points were located on the surface of the specimen, the influence of reinforcing steel are different at the various DEMEC locations. Hence, it is essential to carefully compute the reinforcement ratio for the different regions of the specimen. In this study, various reinforcement ratios are computed based on the location and direction of the DEMEC strain measurements, and is explained in detail in Appendix A3.

#### **6.4 Modeling ASR/DEF Expansion in C-beam Specimen**

Table 6-1 presents the properties of C-beam specimens that are used in calculating the reinforcement ratios, where  $kd_{col}$  and  $kd_{beam}$  are the depth of the neutral axis from the extreme compression fiber for the column and the beam, respectively, and  $l_d$  is the development length of the reinforcement. Table 6-2 presents the reinforcement ratio and the maximum expansion strains (computed using 4-16a) for the various regions of C-beam Specimen 3 (see Appendix A3 for details).

For the purpose of comparing the modeled expansion results with the field data, the averages of the DEMEC data from Specimen 3 are computed and presented as data points in Figure 6-4. The upper and lower extremities of the observed field data are also presented. The surface strains in both the longitudinal and transverse directions are considered for the different regions described in Figure 6-2a. Figure 6-4 also shows a comparison of the proposed model results represented by solid lines with the field data.

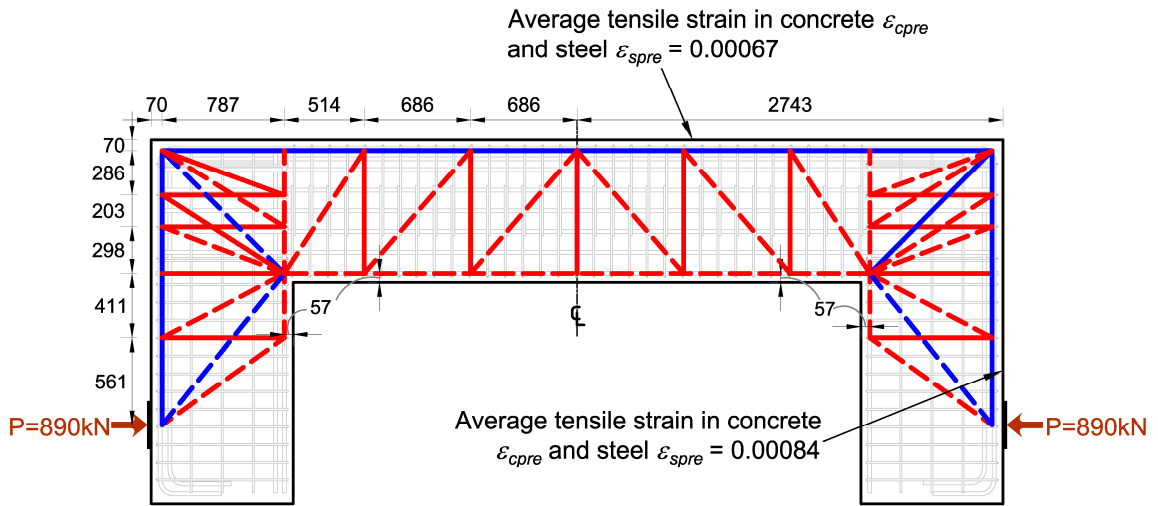


**Figure 6-3: Computation of Average Tensile Loads from C-STM in the C-beam Specimen due to Post-Tension Load.**

**Table 6-1: Properties for C-beam Specimen.**

	<b>Specimen 3</b>	<b>Specimen 2</b>	<b>Specimen 4</b>
$f'_c$ (MPa)	40.9	38.6*	27.6*
$kd_{col}$ (mm)	355	341	378
$kd_{beam}$ (mm)	287	270	307
$l_d$ (mm) for #8 bars	1072	1102	1306
$l_d$ (mm) for #4 bars	429	442	511

\*Results from Mander et al. (2012).



Figure 6-4a and b, respectively, consider the member region and the joint region of the C-beam specimen top face. In the top face member region, the expansion strains in the transverse and longitudinal directions are considered. The concrete and steel volume from the extreme tension fiber to the neutral axis are used in the computation of the reinforcement ratio. In the longitudinal direction, DEMEC measurements were made along two lines, one close to the edge of the column, and the other closer to the middle of the column cross-section as shown in the legend of Figure 6-4. As the DEMEC readings were limited to two lines, the measured strains could be more localized and the reinforcement ratios are computed accordingly as shown in Appendix A3. The tensile strains due to the tie-bar force computed from the C-STM analysis as shown in Figure 6-3 results in a tensile concrete and steel strain of 0.00067 and are appropriately incorporated into computing the maximum expansion strain  $\varepsilon_{\rho}^{\max}$ . Figure 6-4a shows the expansion results obtained in the transverse and longitudinal direction on the column top face member region of the C-beam specimen.

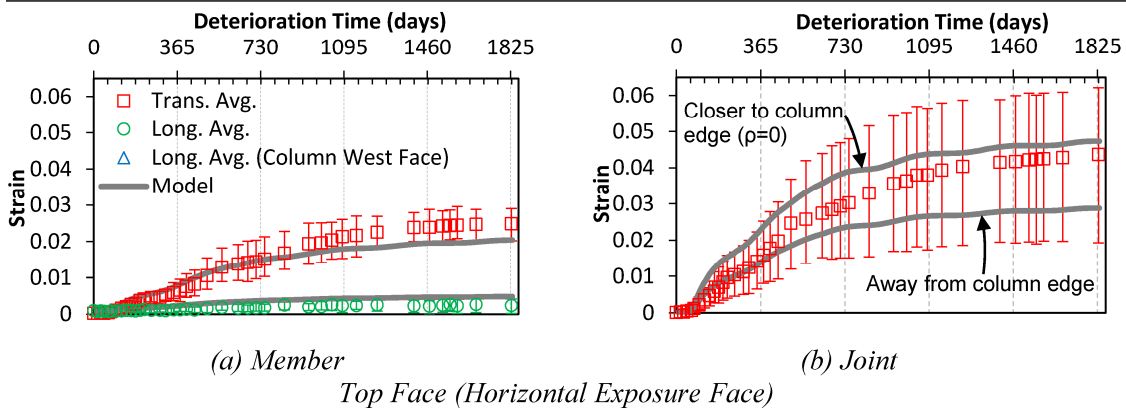
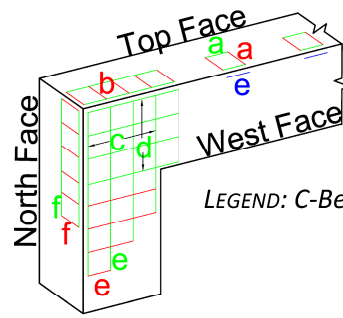
Figure 6-4b considers the transverse expansion strains in the joint region of the C-beam specimen top face. As there were no transverse U-bars in the joint region, that region was essentially unreinforced in the transverse direction. Therefore a reinforcement ratio of  $\rho = 0$  is assigned for this case. However, the transverse reinforcement in the column region would partially restrain the expansion strains caused in the joint region away from the edge of the joint. Therefore, a case with one-half the transverse reinforcement ratio in the column member region is also presented in Figure 6-4b.

Figure 6-4c and d, respectively, consider the expansion strain in the vertical and horizontal directions for the beam-column joint region of the C-beam specimen's west face. Concrete and steel volume in half the section-depth (305 mm) is considered for calculating the reinforcement ratio.

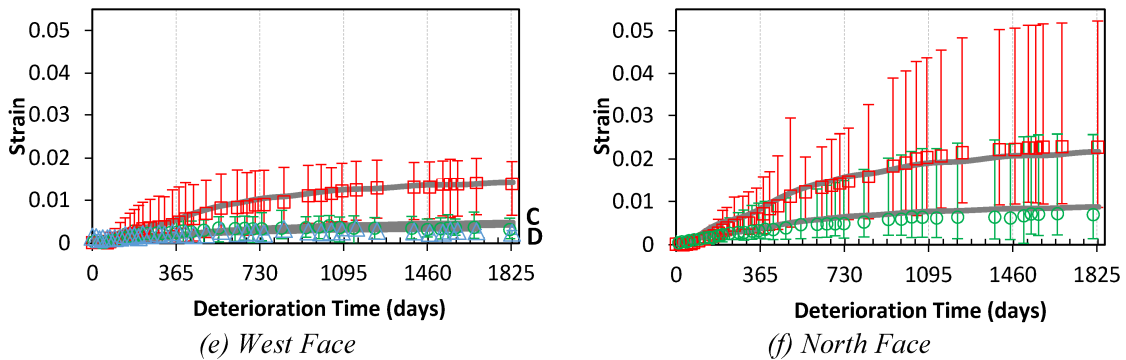
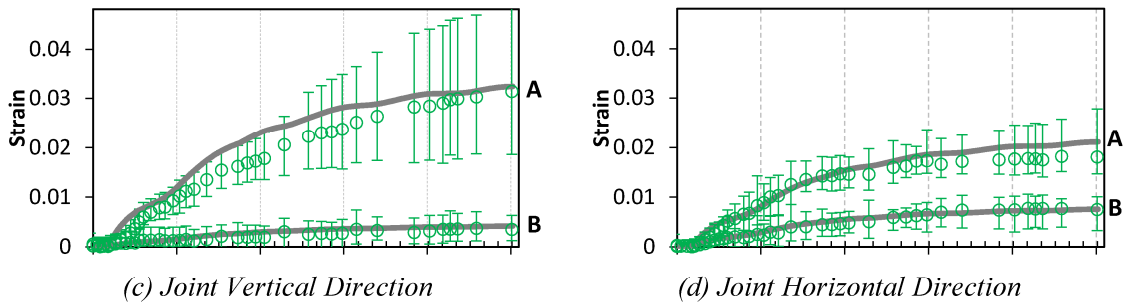
Depending on the location of the DEMEC points in the vertical direction of the beam-column joint, separate reinforcement ratios are computed as shown in Appendix A3. Additionally, Mander et al. (2011) showed that to develop the full yield

**Table 6-2: Computation of Reinforcement Ratio and Maximum Expansion Strain for C-beam Specimen 3.**

Region	Dir.	Section Depth (mm)	Concrete Width (mm)	Rebar Considered	$\rho$	Max. Exp. Strain	Comments
				No.-#Bar			
(a) Column Top-Member	Long	559	71	----	0.03202	0.0045	$f'_c = 40.9$ MPa; $kd_{col} = 355$ mm; $kd_{beam} = 287$ mm Avg. $\rho$ of edge (4 #8, $\rho = 0.05122$ ) and interior (1 #8, $\rho = 0.01281$ ) strips. $\epsilon_{cpre} = \epsilon_{spre} = 0.00067$ .
	Trans	559	---	#4	0.00198	0.02202	
(b) Column Top-Joint	Trans			----	0.00099	0.03040	$\rho = 0$ close to edge and $\rho =$ half of (a) Column Top-Member Trans. (0.00198) away from edge.
(c) West Face Joint Vertical	Long	305	157	5 #8	0.01974	0.004532	Considering edge and scaled for 2 <sup>nd</sup> level of DEMECs. $l_d = 1072$ mm, $x = 400$ mm, $\rho = 0.0529$ .
	Long	305	600	3 #4	0.00065	0.03514	Considering interior and scaled for 1 <sup>st</sup> level of DEMECs. $l_d = 429$ mm $x = 133$ mm, $\rho = 0.00208$ .
(d) West Face Joint Horizontal	Long	305	914	12 #8 4 #4	0.00881	0.00816	Scaled for 2 <sup>nd</sup> level of DEMECs. $l_d = 1072$ mm, $x = 400$ mm, $\rho = 0.0236$ .
	Long	305	914	5 #8 4 #4	0.00186	0.02278	Considering interior region and scaled for 1 <sup>st</sup> level of DEMECs. $l_d = 1072$ mm, $x = 133$ mm, $\rho = 0.01496$ .
(e) West Face-Beam	Long	305	914	10 #8 3 #4	0.01954	0.00456	Considering steel and concrete in 305 mm depth
					0.01628	0.00519	Scaled for 2 <sup>nd</sup> level of DEMECs. $l_d = 1072$ mm, $x = 893$ mm, $\rho = 0.01954$
	Trans	305	---	#4	0.00364	0.01526	
(e) West Face-Column	Long	305	124	5 #8	0.0671	0.00296	
(f) North Face-Beam	Long	627	71		0.01428	0.00855	Avg. $\rho$ of edge (1 #8 and 2 #4, $\rho = 0.01713$ ) and interior (1 #8, $\rho = 0.01142$ ) strips. $\epsilon_{cpre} = \epsilon_{spre} = 0.00084$ .
	Trans	627	---	#4	0.00177	0.02341	



Top Face (Horizontal Exposure Face)



Side Faces (Vertical Surface Exposed)

Note: A/B: Within dev. length zone closer/away from edge; C/D: Inside/outside dev. length zone

**Figure 6-4: Observed and Computed ASR/DEF Induced Expansion Strains—Specimen 3.**

strength of the reinforcement, the reinforcing bars transverse to the member edge should be longer than the bar development length  $l_d$ . Therefore, scaled reinforcement ratios are considered for DEMEC points within the development length zone. Figure 6-4c shows two curves for the expansion results from the model. Curve A corresponds to the case where the expansion strains are computed closer to the top edge of the specimen within the development length zone. Curve B represents expansion strains computed away from the top edge within the development length zone.

Figure 6-4d shows a comparison of the model with the field data for the horizontal expansion strains from DEMEC points in the direction of the column longitudinal reinforcement in the joint region. As in the earlier case, half section-depth of 305 mm is used for the computation of reinforcement ratio, and the reinforcement ratio is scaled down accordingly within the development length zone. In Figure 6-4d, Curves A and B, respectively, correspond to the case where the expansion strains are computed closer to the edge and away from the edge of the specimen, both still within the development length zone.

Figure 6-4e shows the longitudinal expansion strains in the column, and the longitudinal and transverse expansion strains in the beam of the C-beam specimen's west face. The reinforcement ratios are computed considering half-depth (305 mm) of the cross-section. The DEMEC points in the column of the specimen west face are located close to the specimen top edge, and the reinforcement ratio is computed accordingly to account for the localized nature of the DEMEC readings. The tensile concrete and steel strains due to the applied tie-bar force are computed to be 0.00067 from the C-STM model shown in Figure 6-3, and they are incorporated into computing the maximum expansion strains. For the longitudinal expansion strains in the beam of the C-beam specimen west face, scaled reinforcement ratios are considered for DEMEC points within the development length zone. Figure 6-4e shows the expansion results from the model, where Curves C and D, respectively, represent the expansion strains inside and outside the development length zone. In this case it is observed that there is

negligible difference between the two cases, as the DEMEC measurements were made somewhat away from the specimen edges.

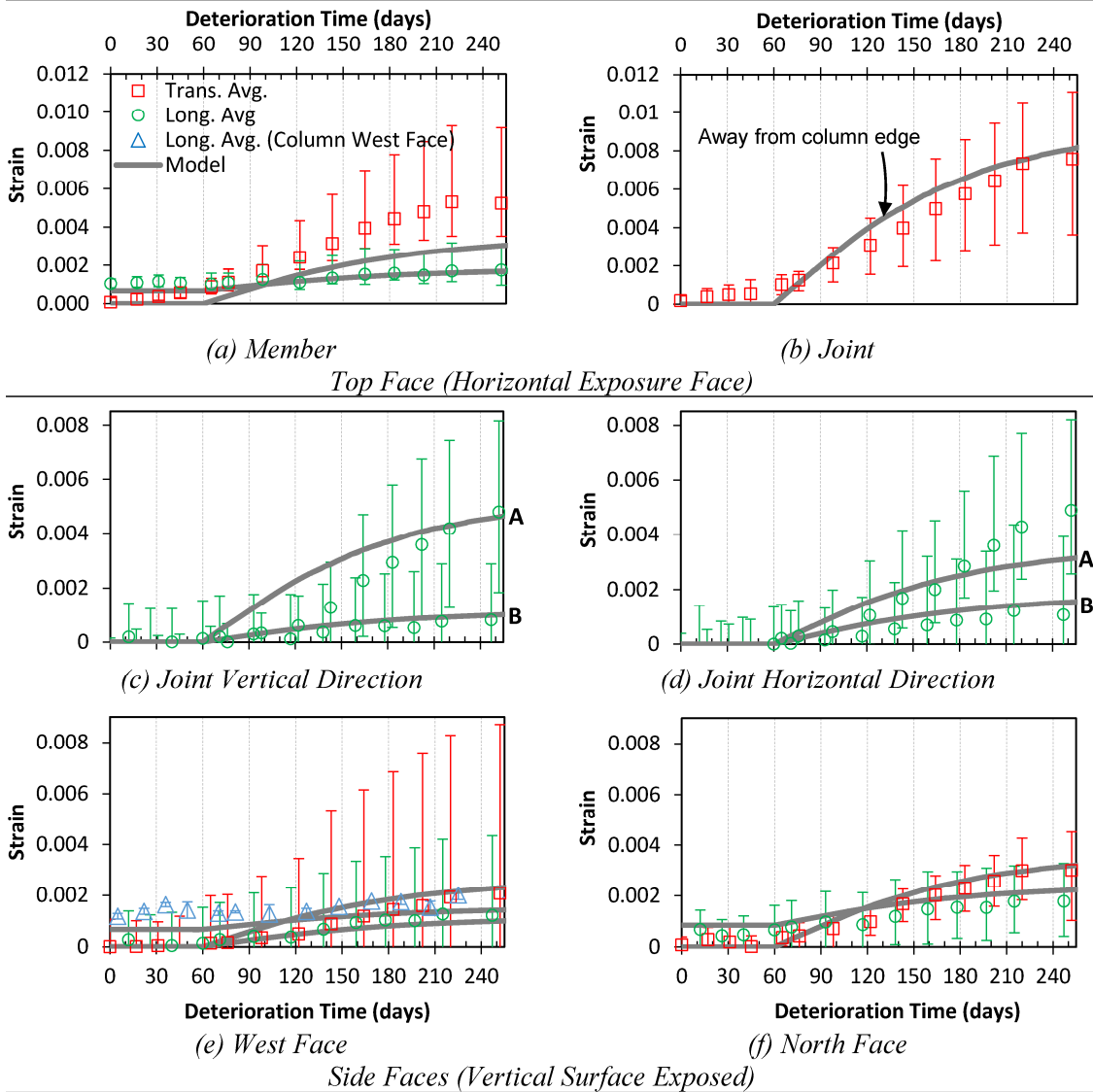
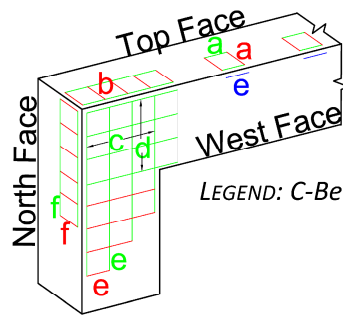
Figure 6-4f shows the expansion strains in the longitudinal and transverse direction of the C-beam specimen's north face. The depth of the beam cross-section from the extreme tension fiber to the neutral axis is considered for the computation of the reinforcement ratios. As in the case of the column top face, the longitudinal DEMEC measurements in the beam were made along two lines, one close to the edge of the beam, and the other closer to the middle of the beam cross-section, as shown in the legend of Figure 6-4. The strains measured could be more localized as the DEMEC readings were limited to two lines, and the reinforcement ratios are computed accordingly as shown in Appendix A3. The tensile strains due to the tie-bar force computed from the C-STM analysis as shown in Figure 6-3, results in a tensile concrete and steel strain of 0.00084 and are appropriately incorporated in computing the maximum expansion strain. Figure 6-4f shows the simulated transverse and longitudinal expansion strains on the C-beam specimen north face.

## **6.5 Expansion Modeling of Companion Tests**

To ensure the repeatability of the proposed expansion model, the model was also applied to two other deteriorated C-beam specimens (Specimens 2 and 4) that were part of the study by Mander et al. (2012). Specimens 2 and 4 were subjected to the outdoor deterioration program for nine months and two years, respectively, and were classified as *slightly* and *moderately* deteriorated specimens. In a manner similar to that of Specimen 3, the reinforcement ratios and the corresponding maximum expansion strain are calculated for Specimens 2 and 4. Table 6-1 shows the properties of Specimens 2 and 4 that are necessary for the computation of the reinforcement ratios for the different regions of the C-beam specimens. Tables 6-3 and 6-4, respectively, show the computation of reinforcement ratio and the maximum expansion strains for Specimens 2 and 4. Figure 6-5 shows a comparison of the expansion strains obtained from the model with the field data for the different regions of the C-beam Specimen 2. Similarly, Figure 6-6 compares the expansion from the model with the field data for Specimen 4.

**Table 6-3: Computation of Reinforcement Ratio and Maximum Expansion Strain for C-beam Specimen 2.**

Region	Dir.	Section Depth (mm)	Concrete Width (mm)	Rebar Considered	$\rho$	Max. Exp. Strain	Comments
				No.-#Bar			
(a) Column Top-Member	Long	573	71	----	0.03125	0.00378	$f'_c = 38.6$ MPa; $kd_{col} = 341$ mm; $kd_{beam} = 270$ mm Avg. $\rho$ of edge (4 #8, $\rho = 0.050$ ) and interior (1 #8, $\rho = 0.0125$ ) strips. $\epsilon_{cpre} = \epsilon_{spre} = 0.00067$ .
	Trans	573	---	4	0.00193	0.01135	
(b) Column Top-Joint	Trans				0.00097	0.03036	$\rho = 0$ close to edge; $\rho =$ half of (a) Column Top-Member Trans. (0.00193) away from edge.
(c) West Face Joint Vertical	Long	305	157	5 #8	0.01919	0.00394	Considering edge and scaled for 2 <sup>nd</sup> level of DEMECs. $l_d = 1102$ mm, $x = 400$ mm, $\rho = 0.0529$ .
	Long	305	600	3 #4	0.00063	0.0181	Considering interior and scaled for 1 <sup>st</sup> level DEMECs. $l_d = 442$ mm, $x = 133$ mm, $\rho = 0.00208$ .
(d) West Face Joint Horizontal	Long	305	914	12 #8 4 #4	0.00857	0.00577	Scaled for 2 <sup>nd</sup> level of DEMECs. $l_d = 1102$ mm, $x = 400$ mm, $\rho = 0.0236$ .
	Long	305	914	5 #8 4 #4	0.00181	0.01169	Considering interior region and scaled for 1 <sup>st</sup> level of DEMECs. $l_d = 1102$ mm, $x = 133$ mm, $\rho = 0.01496$ .
(e) West Face-Beam	Long	305	914	10 #8 3 #4	0.01954	0.0039	
					0.01583	0.00431	Scaled for 2 <sup>nd</sup> level of DEMECs. $l_d = 1102$ mm, $x = 893$ mm, $\rho = 0.01954$
	Trans	305	---	#4	0.00364	0.00857	
(e) West Face-Column	Long	305	124	5 #8	0.0671	0.00281	$\epsilon_{cpre} = \epsilon_{spre} = 0.00067$ .
(f) North Face-Beam	Long	645	71		0.01389	0.00543	Avg. $\rho$ of edge (1 #8 and 2 #4, $\rho = 0.01667$ ) and interior (1 #8, $\rho = 0.011114$ ) strips. $\epsilon_{cpre} = \epsilon_{spre} = 0.00084$ .
	Trans	645	---	#4	0.00172	0.01195	



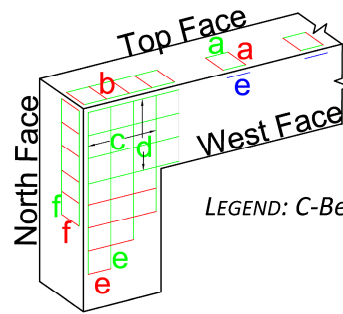
Note: A/B: Within development length zone closer/away from edge

**Figure 6-5: Observed and Computed ASR/DEF Induced Expansion Strains—Specimen 2.**

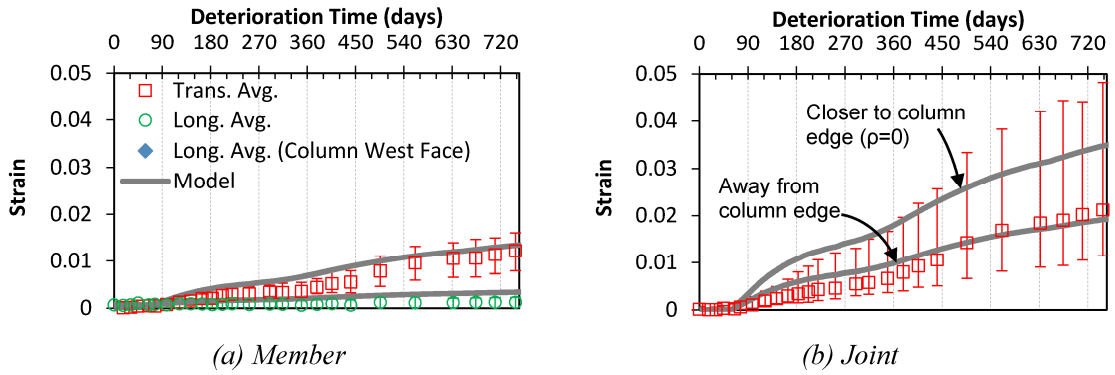
**Table 6-4: Computation of Reinforcement Ratio and Maximum Expansion Strain for C-beam Specimen 4.**

Region	Dir.	Section Depth (mm)	Concrete Width (mm)	Rebar Considered	$\rho$	Max. Exp. Strain	Comments
				No.-#Bar			
							$f'_c = 27.6$ MPa; $kd_{col} = 378$ mm; $kd_{beam} = 307$ mm
(a) Column Top-Member	Long	536	71	----	0.03339	0.00389	Avg. $\rho$ of edge (4 #8, $\rho = 0.05343$ ) and interior (1 #8, $\rho = 0.01334$ ) strips. $\epsilon_{cpre} = \epsilon_{spre} = 0.00067$ .
	Trans	536	---	4	0.00207	0.01921	
(b) Column Top-Joint	Trans			----	0.00104	0.02753	$\rho = 0$ close to edge and $\rho =$ half of (a) Column Top-Member Trans. (0.00207) away from edge.
(c) West Face Joint Vertical	Long	305	157	5 #8	0.01621	0.00394	Considering edge and scaled for 2 <sup>nd</sup> level of DEMECs. $l_d = 1306$ mm, $x = 400$ mm, $\rho = 0.0529$ .
	Long	305	600	3 #4	0.00054	0.01794	Considering interior and scaled for 1 <sup>st</sup> level of DEMECs. $l_d = 511$ mm, $x = 133$ mm, $\rho = 0.00208$ .
(d) West Face Joint Horizontal	Long	305	914	12 #8 4 #4	0.00723	0.00577	Scaled for 2 <sup>nd</sup> level of DEMECs. $l_d = 1306$ mm, $x = 400$ mm, $\rho = 0.0236$ .
	Long	305	914	5 #8 4 #4	0.00153	0.01168	Considering interior region and scaled for 1 <sup>st</sup> level of DEMECs. $l_d = 1306$ mm, $x = 133$ mm, $\rho = 0.01496$ .
(e) West Face-Beam	Long	305	914	10 #8 3 #4	0.01954	0.00398	
					0.01336	0.0052	Scaled for 2 <sup>nd</sup> level of DEMECs. $l_d = 1306$ mm, $x = 893$ mm, $\rho = 0.01954$ .
	Trans	305	---	#4	0.00364	0.01336	
(e) West Face-Column	Long	305	124	5 #8	0.06714	0.00269	$\epsilon_{cpre} = \epsilon_{spre} = 0.00067$ .
(f) North Face-Beam	Long	607	71	----	0.01474	0.00496	Average $\rho$ of edge (1 #8 and 2 #4, $\rho = 0.01769$ ) and interior (1 #8, $\rho = 0.01180$ ) strips. $\epsilon_{cpre} = \epsilon_{spre} = 0.00084$ .
	Trans	607	---	#4	0.00182	0.01083	





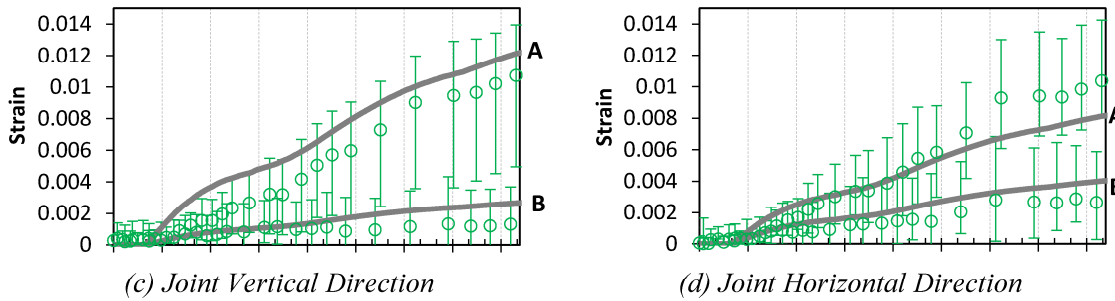
LEGEND: C-Beam Specimen DEMEC Locations



(a) Member

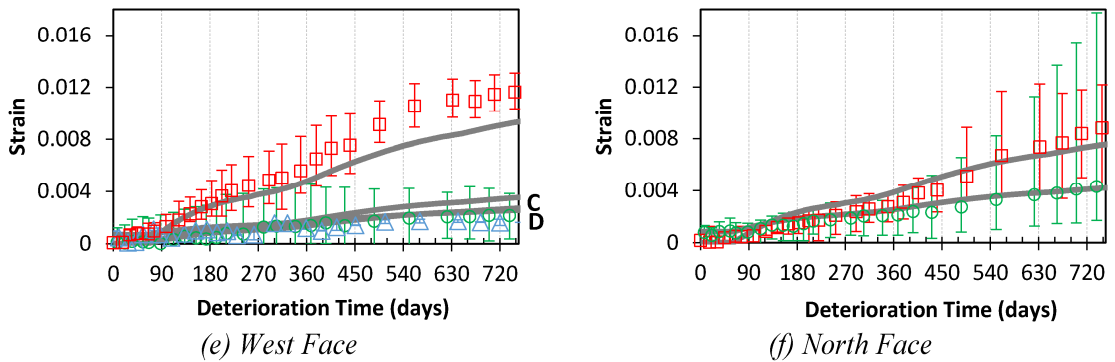
(b) Joint

Top Face (Horizontal Exposure Face)



(c) Joint Vertical Direction

(d) Joint Horizontal Direction



(e) West Face

(f) North Face

Side Faces (Vertical Surface Exposed)

Note: A/B: Within dev. length zone closer/away from edge; C/D: inside/outside dev. length zone

**Figure 6-6: Observed and Computed ASR/DEF Induced Expansion Strains—Specimen 4.**

## 6.6 Discussion

Considering the complex nature of ASR/DEF related expansion in reinforced concrete and the vagaries associated with the expansion data gathered from the field, a comparison of the simulated expansion strain results and the field observations show that the proposed model can be used to simulate the expansion strains in reinforced concrete reasonably well. In most cases the simulated results are within the range of measured field expansion data for the specimens.

The effects of tensile strains caused by gravity loads on ASR/DEF expansion are also taken into account in the model to simulate the expansion results with good accuracy. The tie-bar force that was applied to simulate gravity loads in the C-beam specimens result in tensile stresses along the tension side of the specimens. These tensile stresses cause pre-cracking that promoted ASR/DEF expansion. The tensile prestrains along the direction of the longitudinal reinforcement are considered in the model. However, the tie-bar force did not produce out-of-plane stress in the transverse direction of the specimen and hence the tensile prestrains are not considered in modeling the strains along the direction of the transverse reinforcement.

The computed expansion strains from the model are compared to the strains from the DEMEC points, which measured surface strains. In Section 5 it was demonstrated that similar strains are recorded between the DEMEC points that measure external expansion strains, and the internal strain gages that measure the internal strains. However, when very large surface strains were measured on the specimens, the DEMEC readings did not compare well with the internal strains because of the limitations on the range of strains that could be measured by the internal gages, and the influence of localized effects on the internal strain measurements. Additionally, it is possible to install DEMEC points on existing structures and monitor them over time, to get an estimate of the parameters that are required to drive the model. As demonstrated in the section, it is extremely important to compute the relevant reinforcement ratio, as this affects the extent of expansion that can be caused by ASR/DEF.

Due to the orientation of the specimen during its field conditioning, different parts of the specimen were subjected to various amounts of moisture and hence different degrees of saturation. To account for this, the degree of saturation for the horizontal exposure faces and for strains caused by vertical cracks on the vertical exposure faces are assumed to be greater than the degree of saturation for the strains caused by horizontal cracks in the vertical exposure face. This assumption is also backed by the field expansion data. In an actual structure, many of these parameters cannot be determined realistically, and therefore it is important to assume relevant values based on sound reasoning.

The results of this investigation show that if appropriate values are assigned to the limited input parameters required for the model, the proposed minimalist semi-empirical model can be effectively used to model the ASR/DEF induced expansion strains in reinforced concrete members that are exposed to field conditions.

## **6.7 Closure and Key Findings**

By taking into account the appropriate input parameters for the proposed expansion model, the expansion strains caused by ASR/DEF in reinforced concrete specimen can be estimated within reasonable bounds as demonstrated in this section. Considering the wide scatter in the field measured strains, the model predicts the general expansion behavior reasonably well. The key observations and findings from this section are summarized below:

- Considering the complex nature of the C-beam specimen, and the side scatter of measured ASR/DEF induced expansion strains, the proposed model captures the expansion strains quite well.
- The proposed model takes into account the tensile prestrains caused by the tie-bar force (which simulates gravity loads) in the direction of the longitudinal reinforcement.
- Depending on the region of the specimen that is being considered, the moisture content and hence the degree of saturation can be different. Especially, on the

horizontal exposure faces, water tends to pool/stand for longer when compared to the vertical exposure face, where the water runs off almost immediately.

- The orientation of the cracks can also lead to differences in the expansion strain behavior. On vertical exposure faces, vertical cracks that cause horizontal expansion strains allow for more rapid water ingress into the specimen through the cracks, when compared to horizontal cracks, which results in vertical strains.
- The expansion data obtained from the field vary widely. Much of the scatter can be explained based on the influence of the neighboring reinforcement, the location of strain (DEMEC) measurements, and the orientation of the exposure face.

## 7 EXPERIMENTAL FORCE-DEFORMATION BEHAVIOR OF LARGE REINFORCED CONCRETE SPECIMENS WITH HEAVY ASR/DEF DETERIORATION\*

### 7.1 Summary

Earlier research has shown that *slight* and *moderate* amounts of deterioration caused by ASR/DEF induced expansion in reinforced concrete specimens does not markedly or detrimentally affect its structural load carrying capacity. However, effects of severe (late-stage) ASR/DEF deterioration on the load carrying capacity of structures is not known. A large-scale reinforced concrete C-beam specimen that is exposed to field conditions for a period of five years, and shows *heavy* ASR/DEF deterioration, is load tested in the laboratory. The specimen is externally instrumented using linear variable differential transformers (LVDTs) and string-potentiometers (SP), and is internally instrumented using strain gages attached to the reinforcement and embedded concrete gages. Experimental deformations associated with truss modeling are measured using LVDTs mounted to aluminum truss members that are connected to the specimen between selected nodal points. Comparison of force-deformation results of the severely deteriorated specimen with the undamaged control specimen, and slightly and moderately ASR/DEF deteriorated specimens show that there is no reduction in the load-carrying capacity. The mode of failure of the specimen is a brittle joint-shear failure, similar to the other specimens. However, a reduction in the ductility of the *heavily* deteriorated specimen is observed. Post-failure examination shows a significant degree of corrosion in the longitudinal and transverse reinforcement. Significant bulging and complete de-bonding of the lapped transverse U-bars in the specimen knee-joint caused considerable loss in confinement of the softened concrete, resulting in an embrittled performance and sudden early loss of load in the

---

\* Previously published work is available to the public through National Technical Information Service. Mander, J.B., Karthik, M.M., and Hurlebaus, S. (2015). "Structural Assessment of "D" Region Affected by Premature Concrete Deterioration: Technical Report." *Report No. FHWA/TX-15/0-5997-2*, Texas A&M Transportation Institute, College Station, Texas, USA.

*heavily* damaged specimen. There is evidence of hidden corrosion in the specimen, and it is not known how further corrosion in conjunction with severe ASR/DEF deterioration could affect the future behavior of the structure.

## 7.2 Introduction

To study the effects of ASR/DEF deterioration on reinforced concrete bridge bents, a total of four specimens were designed, constructed, subjected to outdoor weather conditioning, and finally tested in the laboratory to identify the ultimate load carrying capacity. Of the four specimens, Specimen 1 was the control specimen and was stored indoors under climate controlled conditions, without exposure to moisture. Specimens 2, 3, and 4 were placed outdoors and weathered for varying durations up to five years. To accelerate the possibility of deterioration from the effects of ASR/DEF a supplemental water sprinkler system was used to increase the number of wetting and drying cycles experienced. Specimens 2 and 4, respectively, were conditioned for a period of nine months and two years and were classified to have *slight* and *moderate* deterioration due to ASR/DEF effects. The control Specimen 1 and the deteriorated Specimens 2 and 4 were tested in the laboratory and their results presented in Mander et al. (2012). From the results reported in Mander et al., it was evident that Specimens 2 and 4 with *slight* and *moderate* amounts of ASR/DEF deterioration had greater stiffness and strength, and slightly greater ductility when compared to the *undamaged* control Specimen 1. The mode of failure in all the three specimens was observed to be the same, which was a brittle joint shear failure within the beam-column joint. It was concluded that the slightly higher strength was due to the beneficial effect of the prestress induced by the ASR and/or DEF induced swelling strains in the concrete.

Specimen 3, which is the specific subject of this experimental investigation, was subjected to the deterioration program for a total exposure period of five years. From the field observations, Specimen 3 can be classified as having *heavy* deterioration due to ASR/DEF effects. It is considered important to compare the performance of Specimen 3 with the *undamaged* control Specimen 1, and the deteriorated Specimens 2 and 4 to evaluate the significance of *heavy* deterioration due to ASR/DEF effects.

This section presents the experimental procedures along with the overall force-deformation behavior of Specimen 3. The experimental test results are compared with the three C-beam specimens previously tested. Conclusions are drawn on how heavy ASR/DEF deterioration affects the structural performance of reinforced concrete bridge piers.

### **7.3 Experimental Investigation**

#### **7.3.1 Concrete Compressive Strength**

During construction of the specimen, standard 100 mm by 200 mm concrete cylinders were cast according to ASTM Standard C31 (ASTM-C31, 2008), so that concrete compression strength data from cylinder tests in accordance with ASTM C39 (ASTM-C39, 2008) could be determined by accepted practices. One-half of these cylinders were stored in a curing/fog room at 100 percent humidity and 23°C, while the other half were stored at the same location and conditions as the specimen. Figure 7-1a and b, respectively, show the physical state of the concrete cylinders that were conditioned in the fog room under 100 percent humidity and in the field adjacent to Specimen 3. Compared to the fog room cured cylinders, it is evident that the concrete cylinders that were conditioned outdoors and subjected to alternate wetting and drying cycles are more heavily damaged from the adverse swelling strain effects of ASR/DEF.

Table 7-1 presents the measured compressive strength of standard 100 mm by 200 mm concrete cylinders at the time of testing for Specimens 3. Owing to the severely cracked nature of the field-cured cylinders, they consistently show much lower compressive strength compared to the fog room cured specimen.

#### **7.3.2 Experimental Test Setup**

The experimental setup that was used by Mander et al. (2012) to test Specimen 4 is adapted for testing Specimen 3. Figure 7-2a and b, respectively, show the three-dimensional view and the actual experimental test setup. Figure 7-3 shows the plan and front elevation view of the experimental test setup. One 979 kN MTS (model 244.51S) actuator in displacement control was used in this setup. As in the earlier tests of C-beam



(a) Wet-Room Cured Cylinder

(b) Field-Cured Cylinder

**Figure 7-1: Comparison of Cured and Field Cylinders (at 1977 days).**

**Table 7-1: Concrete Material Properties of C-beam Specimen 3.**

Concrete Properties	28 days		Time of Testing 1977 days	
	Wet-Room Cured	Field-Cured	Wet-Room Cured	Field-Cured
$f'_c$ (MPa)	35 36.6; 34.3	36 36.2; 35.4	41 37.6; 42.1; 42.1; 41.8	13 10.9; 12.7; 11.7; 15.8
$E_c$ (MPa) = $4700\sqrt{f'_c}$ (MPa)	27800	28200	30100	16950

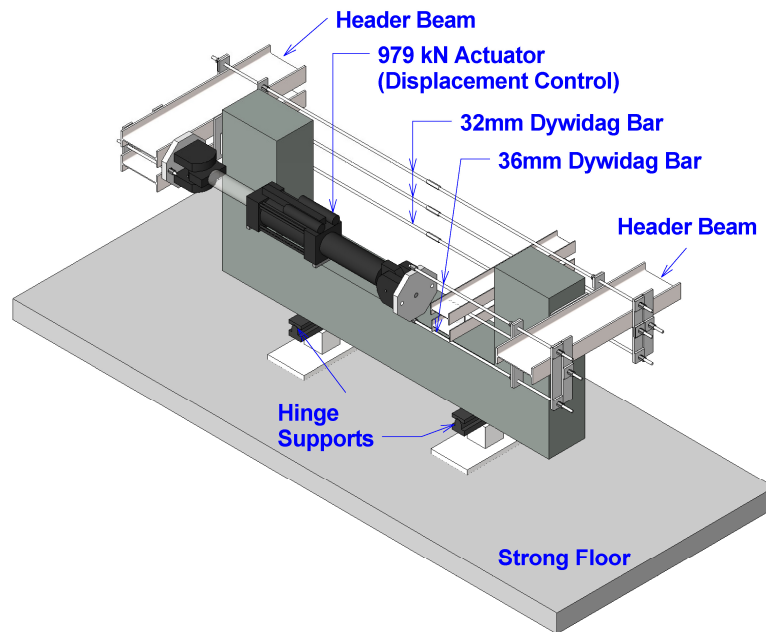


specimens by Mander et al. (2012), the specimen was oriented such that the column was placed on two hinge supports, and the beams were oriented vertically. The actuator was placed on one side of the specimen at a distance of 560 mm from the surface of the specimen to the centerline of the actuator. On the other side of the specimen three 32 mm diameter high strength DYWIDAG threadbars were aligned vertically at a distance of 203 mm from the surface of the specimen to the center of the bars. A leverage mechanism was created between the actuator and the DYWIDAG threadbars using a roller support on one side of the specimen. With this setup a 2.7:1 mechanical lever arm was created using a single actuator to create a total loading capacity of 2643 kN. As it was unclear how ASR/DEF deterioration affected Specimen 3, a single test was performed to determine the ultimate strength capacity and the behavior of Specimen 3, without any prejudice toward the singly or the doubly reinforced beams.

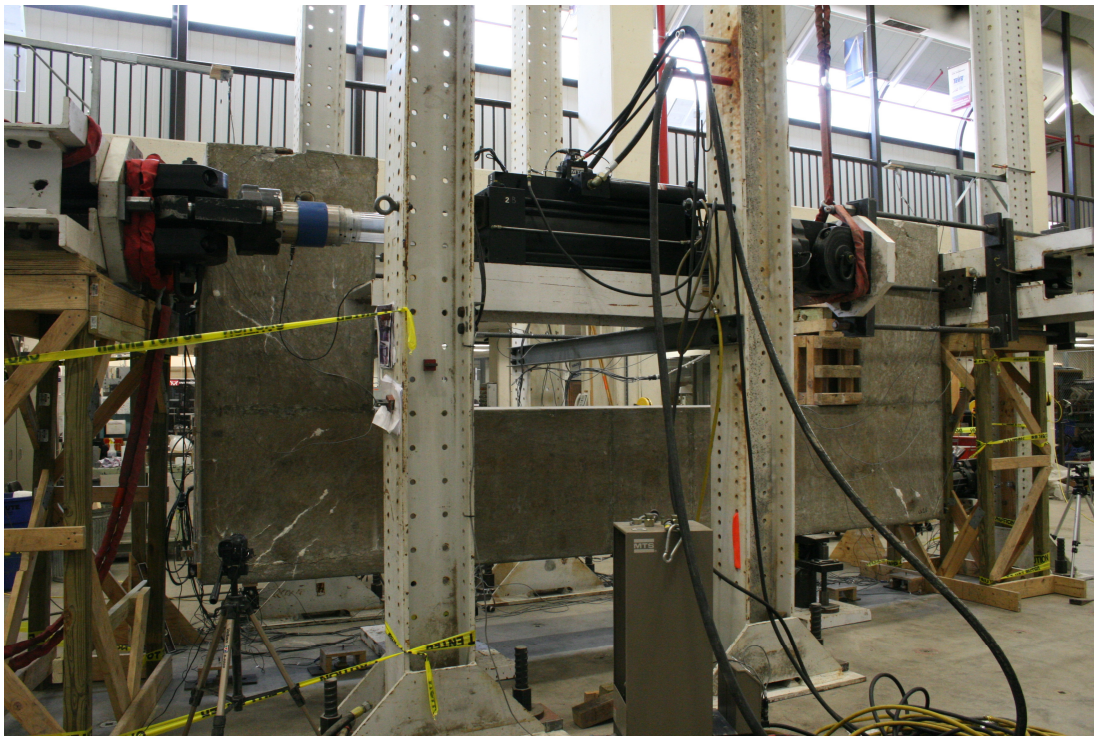
### **7.3.3 Instrumentation**

Figure 7-4 shows the external and internal instrumentation layout used to obtain experimental results to determine the overall force-deformation results, and to understand the internal behavior and failure mechanism of the specimen. Experimental data obtained from the instrumentation are also used to compare the analytical modeling results that are presented in the Section 8. The specimen was externally instrumented using linear variable differential transformers (LVDTs) and string-potentiometers (SP), and was internally instrumented using strain gages attached to steel and embedded concrete gages. The global displacements at the applied loading points on the specimen are obtained by taking an average of the measured displacements above and below the header beam. The drift of the beam relative to the column is measured using two LVDTs mounted to a rigid structure that was fixed to the column surface of the specimen. The overall deflected shape of the specimen is obtained from the externally mounted string pots secured to the external structure or mounted on the strong floor of the laboratory.

As shown in Figure 7-4b the experimental deformations associated with the SAT and truss modeling are measured using LVDTs mounted to aluminum truss members that were connected to the specimen between selected nodal points. Each node point had



(a) 3-D View of the Experimental Setup



(b) Experimental Setup at High-Bay Laboratory, Texas A&M University, College Station

**Figure 7-2: Experimental Test Setup for C-beam Specimen 3.**

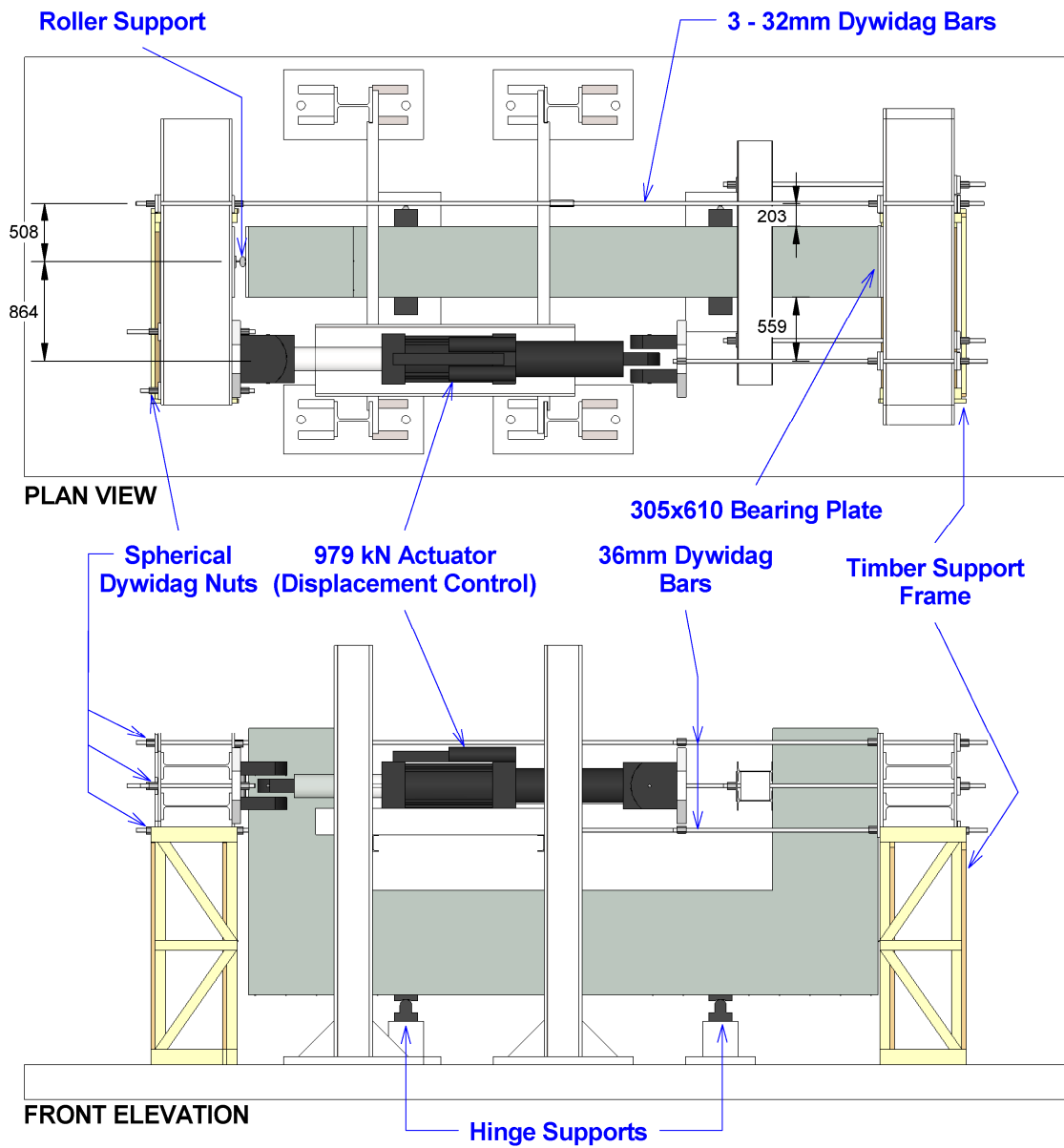
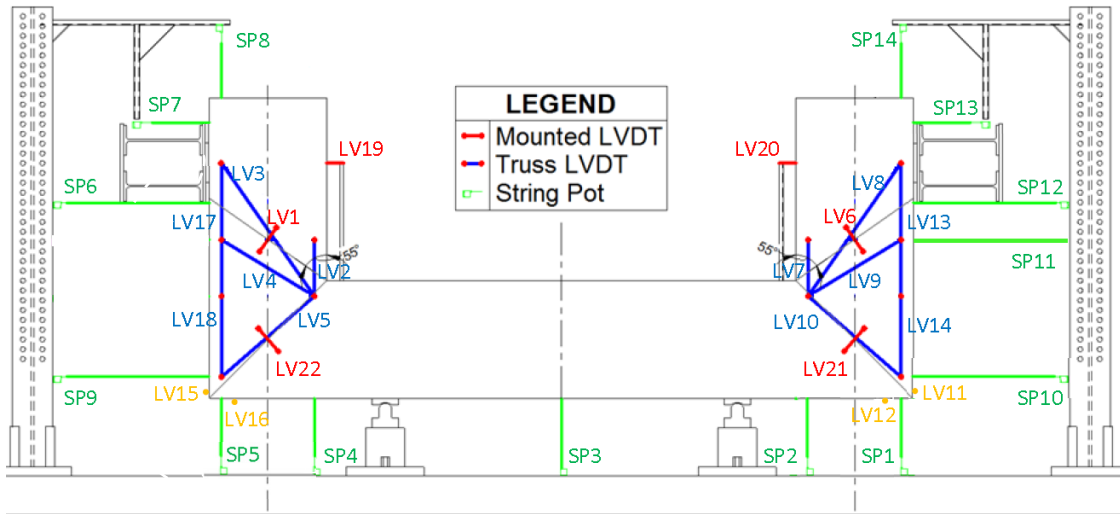


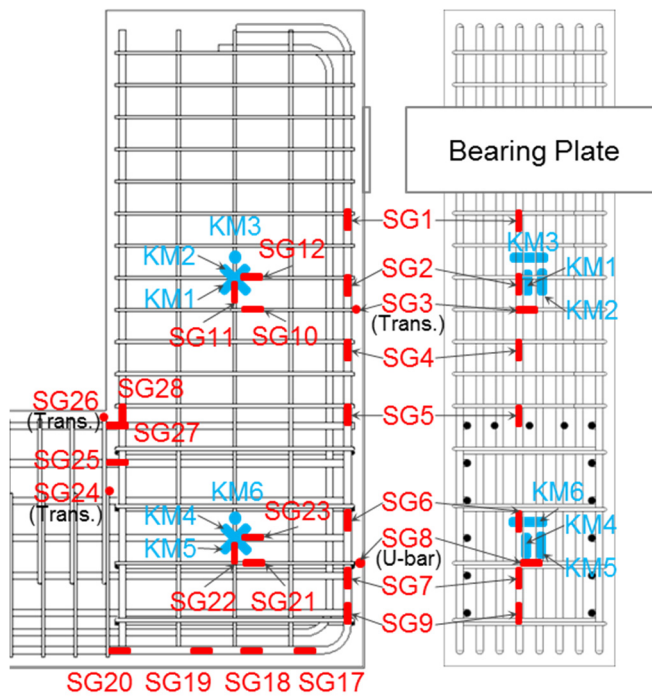
**Figure 7-3: Experimental Setup for Specimen 3: Plan and Front Elevation View.**



(a) External Instrumentation Layout



(b) LVDT Truss Setup



(c) Internal Instrumentation Layout

**Figure 7-4: External and Internal Instrumentation Layout.**

an embedded DEMEC connector securely attached into the specimen. Aluminum members with pin-slotted end connections were attached to two DEMEC connectors of interest, and the LVDTs were attached to measure the relative deformations between the node points. Each of the two beams of the specimen had six members with six node points (Figure 7-4b). Crack widths or inferred principal tensile strains perpendicular to the corner-to-corner arch struts in the beams, and joints were measured with four LVDTs mounted perpendicular to the anticipated crack angles ( $55^\circ$  and  $45^\circ$  in the beam and joint, respectively).

In order to provide insight into the internal deformation strains, an assortment of strain gages were affixed to the reinforcing steel at locations shown in Figure 7-4c. To measure the strain in the corner-to-corner concrete struts of the beam and joint regions, embedded concrete gages were secured to the center of the cross-section and oriented in the three principal directions relative to the arch strut as shown in Figure 7-4c. The concrete strains in the direction of the diagonal struts were denoted as gages KM1 and KM4; the concrete strains perpendicular to these struts were denoted as gages KM2 and KM5; and the concrete strains in the out-of-plane transverse direction were denoted as gages KM3 and KM6 (Figure 7-4c).

#### **7.3.4 Experimental Testing Procedure and Loading History**

At the end of the deterioration phase, Specimen 3 was transported back to the laboratory for experimental testing. The tie-bar force on the specimen was released before setting up the C-beam specimen for the load test. Strain gages were attached to each of the two DYWIDAG bars during the removal of the tie-bars to measure the residual tie-bar force. From the data, the average residual strain in the tie-bars was recorded as 0.00173, which corresponds to a total residual tie-bar force of 705 kN (cross-section area of 36 mm DYWIDAG bars =  $1019 \text{ mm}^2$ ), amounting to 21 percent in time-dependent prestress loss over the five-year conditioning period. The release of the tie-bar forces mimicking the gravity loads had minimal effect, if any, on the cracks that were caused by ASR/DEF expansion indicating the permanent damage that was caused on the specimen.

The effects of ASR/DEF on the structural performance of Specimen 3 were not known before the structural testing. Therefore, to obtain unbiased results from the structural testing, a single test was performed without protecting either of the two beams as was done with the control specimen (Mander et al., 2012).

Initially the specimen was loaded to 890 kN as a trial run to ensure that the experimental setup and the mounted instrumentation were performing as expected and then the specimen was fully unloaded. Later the specimen was loaded continuously until failure without any pauses. The specimen reached its ultimate load capacity of 2215 kN before failing in a sudden brittle manner.

### **7.3.5 Experimental Performance**

Figure 7-5 shows the physical condition of the singly reinforced side of C-beam Specimen 3 at various loads during the test. It is evident that there are no visible changes in the physical appearance of the specimen at the knee-joint when the load is increased from 0 kN (Figure 7-5a) to 890 kN (Figure 7-5b). Similarly, there are no visually identifiable new cracks or difference in the crack width when the load is increased from 890 kN (Figure 7-5b) to 2215 kN (Figure 7-5c) just before the failure of the specimen. However, Figure 7-5d shows that just after failure a large portion of the cover concrete in the beam-column region spalled off.

Similarly, Figure 7-6 shows the physical condition of the doubly reinforced side of C-beam Specimen 3 before the load testing began and just after the failure of the specimen. As evident in Figure 7-6, no visible changes in the crack size were observed at the knee-joint of the doubly reinforced side of Specimen 3.

### **7.3.6 Force-Displacement Behavior**

Figure 7-7 presents the observed experimental force-displacement behavior of C-beam Specimen 3. The tip displacement is plotted as the average displacements measured by the string pots that were placed just above and below the header beams, while the total tip displacement is the sum of the tip displacements of the singly and doubly reinforced beams.

Figure 7-7a and b, respectively, show the force-deformation response of the doubly reinforced and the singly reinforced beam. The response of the doubly reinforced beam is found to be stiffer than the singly reinforced beam. The tip displacement observed on the doubly reinforced beam is about half of what is observed in the singly reinforced beam.

Figure 7-7c shows the force versus total tip-displacement of the C-beam specimen. The ultimate load capacity of Specimen 3 was 2215 kN. It is evident from Figure 7-7c that as soon as the ultimate load carrying capacity was achieved, the specimen suddenly failed in a brittle fashion.

### **7.3.7 Failure Assessment**

As in the case with the control Specimen 1, and *slightly* and *moderately* deteriorated Specimens 2 and 4 reported in Mander et al. (2012), the failure model of the *heavily* deteriorated Specimen 3 was a brittle joint shear within the beam-column joint region. The failure was triggered by concrete softening of the joint corner-to-corner diagonal strut. Figure 7-8b shows the strains that were recorded in the internal concrete gages KM4–KM6 located in the beam-column joint as shown in Figure 7-8a. The initial offset that is observed in the concrete gages is due to the expansion strains that were recorded during the deterioration phase of Specimen 3. As noted in the earlier section, the tensile strains measured in KM4 along the corner-to-corner diagonal strut is likely due to the localized formation of ASR gel around the concrete gage. However, it is to be noted that high tensile strains are recorded in concrete gages KM5 and KM6 that were perpendicular to the compressive diagonal strut. Although much variation in the strains is not observed during the experimental loading phase of Specimen 3, it is evident from Figure 7-8b that the tensile strains transverse to the diagonal strut caused significant softening of the corner-to-corner arch strut of the C-beam specimen. The transverse reinforcement in the joint region did not have sufficient capacity to take the force redistributed immediately following the initial failure mode. The insufficient anchorage





*(a) At 0 kN*



*(b) At 890 kN*



*(c) At 2215 kN (Just before Failure)*



*(d) Just after Failure*

**Figure 7-5: Condition of Specimen 3 at Various Loads: Singly Reinforced Beam**



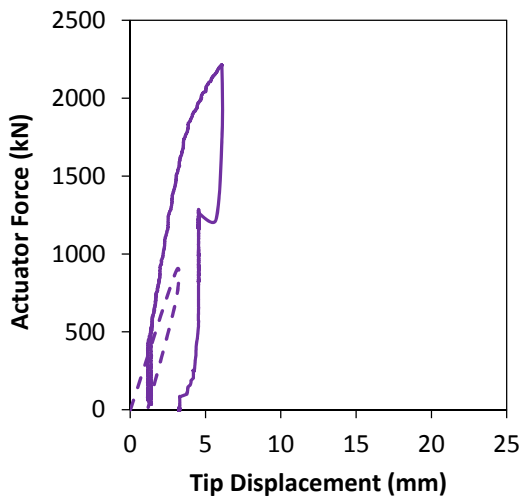
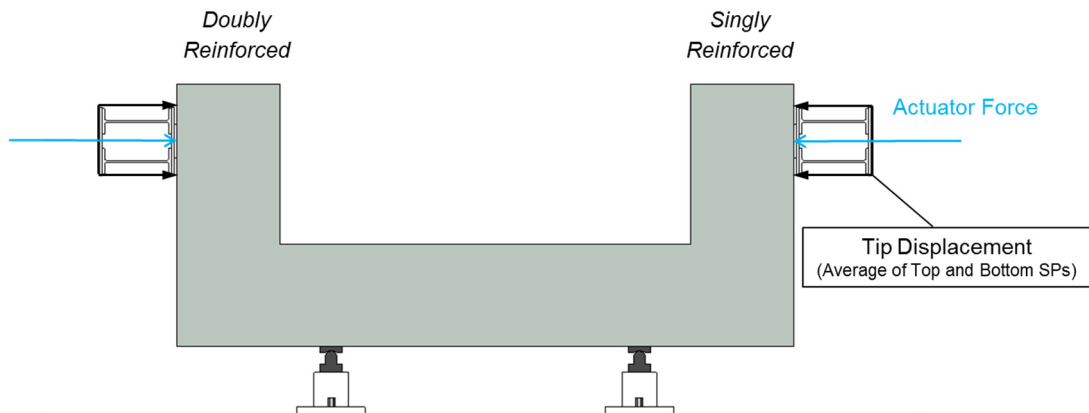


*(a) At 0 kN*

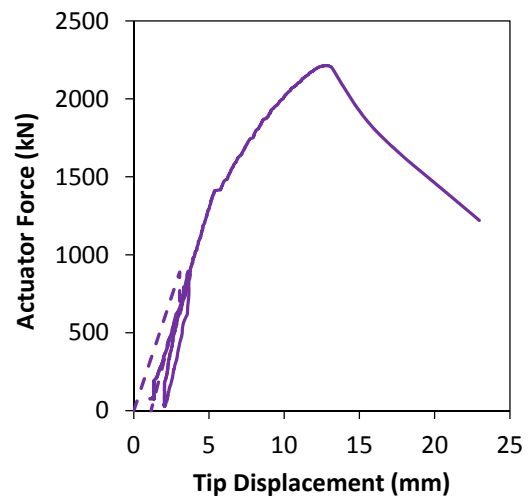


*(b) At 2215 kN*

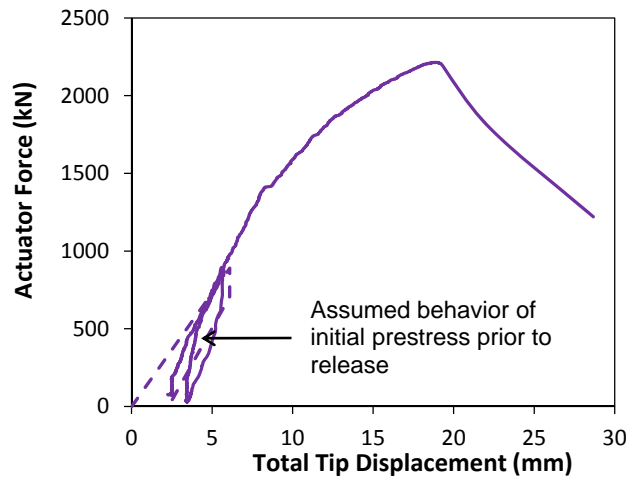
**Figure 7-6: Condition of Specimen 3 at Various Loads: Doubly Reinforced Beam.**



(a) *Doubly Reinforced Beam*

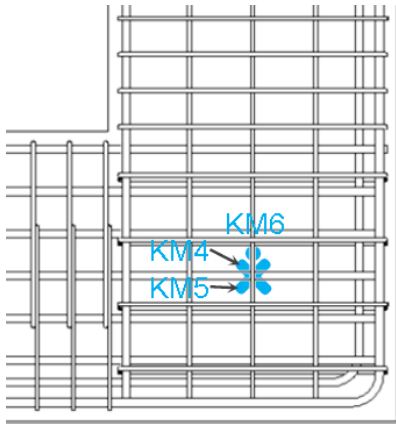


(b) *Singly Reinforced Beam*

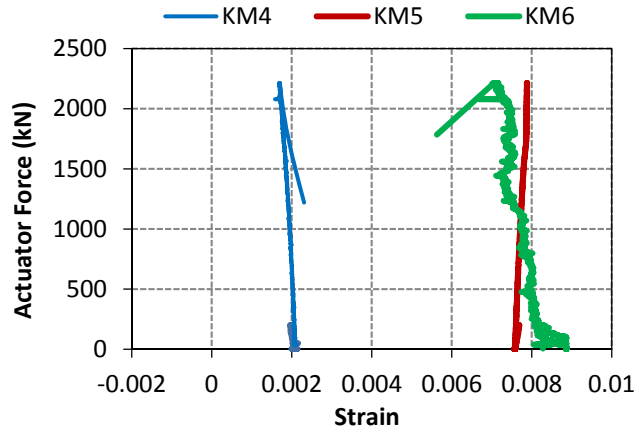


(c) *Total Tip Displacement*

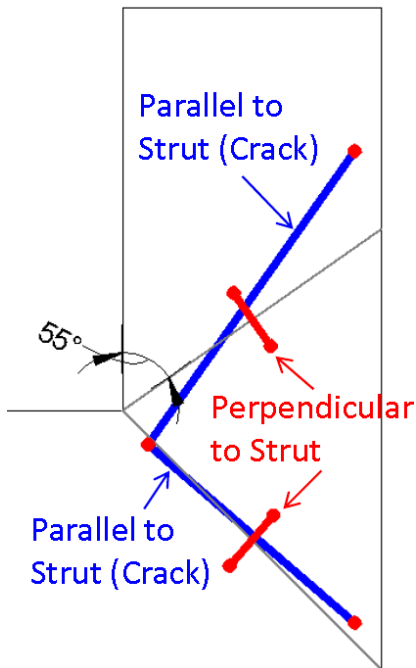
**Figure 7-7: Force-Displacement Behavior of C-beam Specimen 3.**



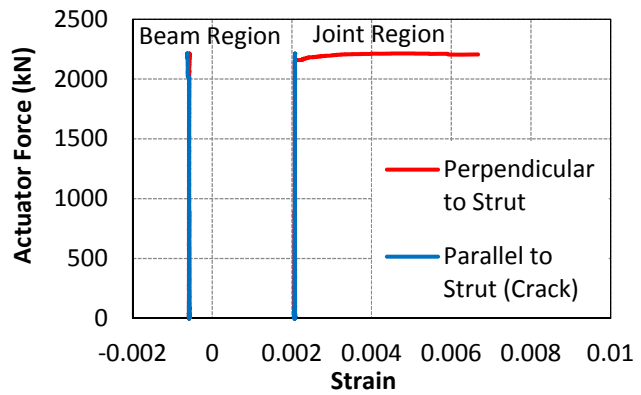
(a) Location of KM Gages at the Failure Joint



(b) Internal Concrete Strain Recorded in the KM Gages (Initial Offset due to Strains Recorded during Deterioration Phase)



(c) Truss LVDTs Located Parallel and Perpendicular to Diagonal Struts



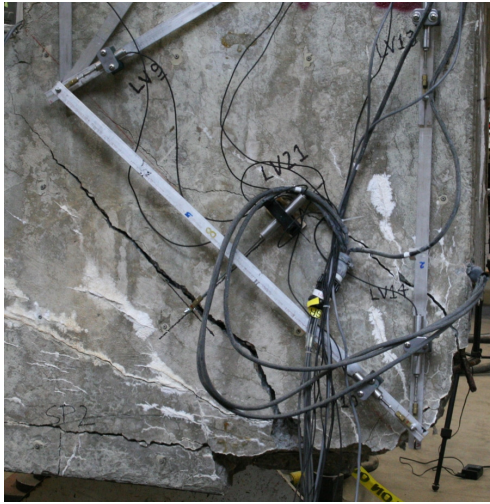
(d) Inferred LVDT Strains in the Specimen

**Figure 7-8: Internal and External Strains at Critical Regions of C-beam Specimen 3.**

of the transverse U-bars in the joint region and the lack of transverse reinforcement along the back face of the column resulted in a brittle failure of the C-beam specimen. This in turn resulted in the sudden bursting of cover concrete in the knee-joint of the specimen.

The displacements that were measured by the truss LVDTs shown in Figure 7-8c are used to infer the strains parallel and perpendicular to the diagonal struts. Figure 7-8d shows the strains parallel and perpendicular to the diagonal strut in the beam and the joint of the singly reinforced side of C-beam Specimen 3. The initial offset shown in Figure 7-8d are the expansion strains that were recorded during the deterioration phase. Strains both parallel and perpendicular to the struts did not alter much until the specimen reached close to its ultimate load capacity. As shown in Figure 7-8d, the strain perpendicular to the corner-to-corner diagonal strut in the beam-column region increased rapidly just before the specimen reached its ultimate load capacity. It is evident that the strain perpendicular to the diagonal strut caused rapid softening of the diagonal compression member leading to the sudden ductile failure of the C-beam specimen. The failure mechanism of Specimen 3 is similar to that of the other C-beam specimens presented Mander et al. (2012). However, it is noted that the growth of strains perpendicular to the struts in the Specimens 1, 2, and 4 were more gradual, leading to a more overall ductile force-deformation behavior of the C-beam specimens.

Figure 7-9 shows the physical state of the failed end of C-beam Specimen 3. Figure 7-9a clearly shows a significant crack along the diagonal compression strut in the beam-column joint of the C-beam specimen. As shown in Figure 7-8d, the tensile strain transverse to the diagonal strut causes the formation of the crack along the diagonal strut. Figure 7-9a also shows spalling of the cover concrete in the exterior knee-joint of the specimen. Figure 7-9b and c show the opposite faces of the exterior knee-joint after all the loose concrete was removed. It is evident that diagonal cracks are observed on both faces of the specimen. Also, seen in Figure 7-9c is the crushing of cover concrete in the interior corner, which initiated before the specimen reached its ultimate load carrying



(a) Failure of Diagonal Strut and Bursting of Concrete at Exterior Corner



(b) Exterior Corner after Removal of Spalled Concrete (Opposite Face in c)



(c) Interior and Exterior Corner after Removal of Spalled Concrete (Opposite Face Shown in b)



(d) Anchorage Debonding of U-bars, and Lateral Displacement of Longitudinal Steel, in the External Beam-Column Joint



(e) Under Side of Exterior Corner Joint after Removal of Spalled Concrete



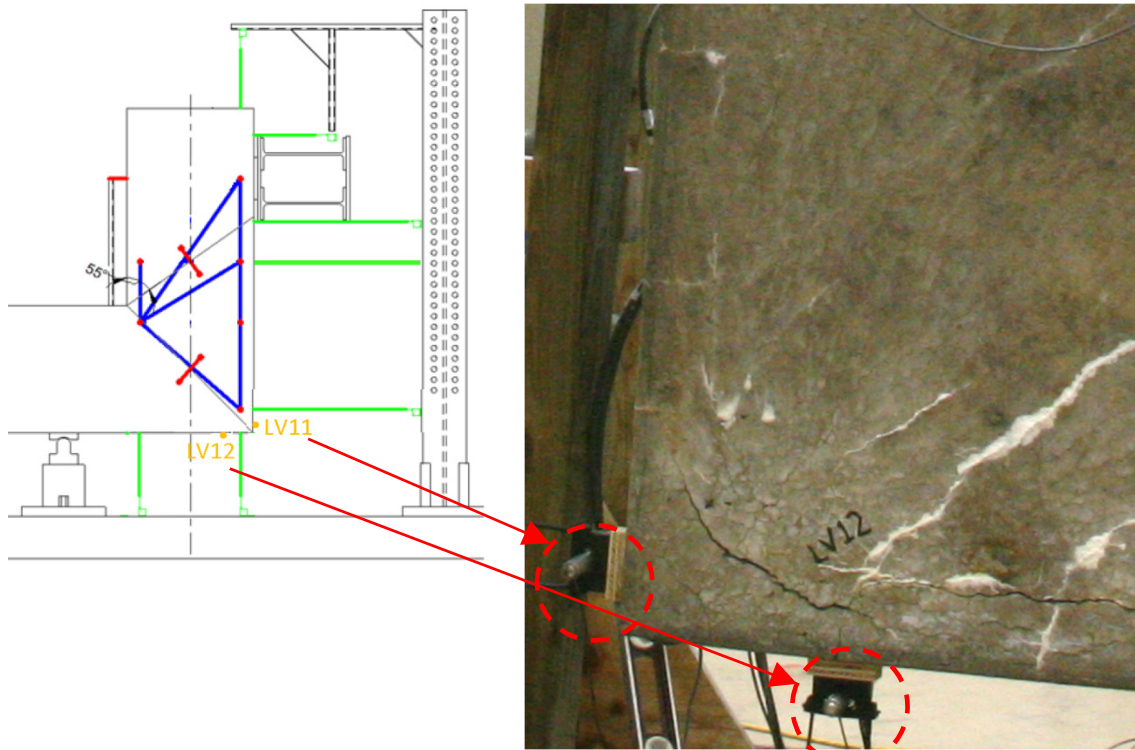
(f) Corrosion of Longitudinal Steel at the Exterior Knee-Joint

**Figure 7-9: Physical State of the Failed End after Load Testing of Specimen 3.**



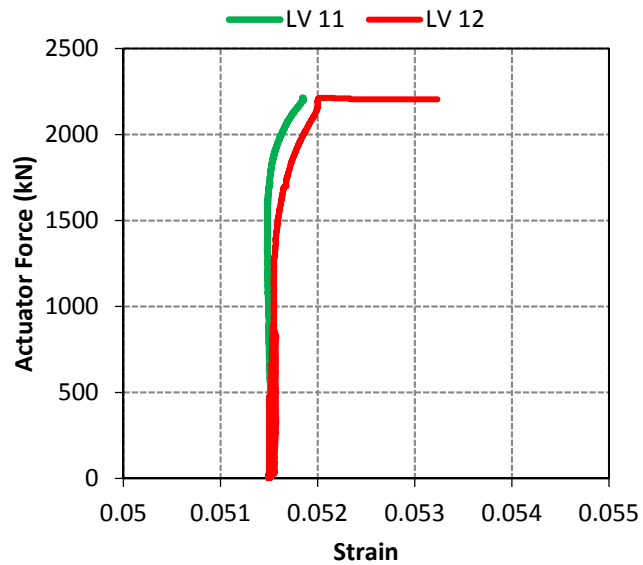
capacity. Figure 7-9d shows the physical condition of the specimen at the exterior joint along the cap-face of the specimen beam-column joint after all the loose concrete was removed. It is evident from Figure 7-9d that there is debonding and pullout of the U-bars, which results in the transverse U-bars bulging out of the specimen. Also evident in Figure 7-9d is the bulging of the external longitudinal reinforcement. Figure 7-9e shows the bottom side (column face) of the beam-column joint where the specimen failed. As shown in the photograph, a large portion of cover concrete spalled from this region. Evidently, the absence of transverse reinforcement in the column face of the beam-column joint resulted in the bulging of the specimen in the lateral direction, resulting in the spalling of cover concrete. Figure 7-9f shows a close-up view of the corrosion observed in the longitudinal reinforcement. Corrosion of longitudinal and transverse reinforcement is also evident in Figure 7-9b–f.

The out-of-plane behavior at the column and cap-face of the beam-column joint is shown in Figure 7-10. As shown in Figure 7-10a and b, the strains in the out-of-plane direction in the beam column-joint were monitored using LVDT 11 and 12, which were, respectively, mounted on the cap and column face of the joint. The strains are deduced from displacements recorded by the LVDTs over their gage length. As shown in Figure 7-10c, the out-of-plane strains in the column face were slightly greater than the strains recorded in the beam-face. It is seen that the out-of-plane strains in the column face of the specimen suddenly increased immediately after the specimen reached its ultimate load, supporting the sudden bursting behavior of the specimen. This is evidently due to the lack of transverse reinforcement in the column face of the beam-column joint.



(a) Layout of LVDTs to Compute Out-of-Plane Strains

(b) LVDTs Attached to the Specimen to Measure Out-of-Plane Strains



(c) Strains in the Out-of-Plane Direction in the Cap and Column Face

**Figure 7-10: Observed Out-of-Plane Strains in the Beam-Column Joint of C-beam Specimen 3.**

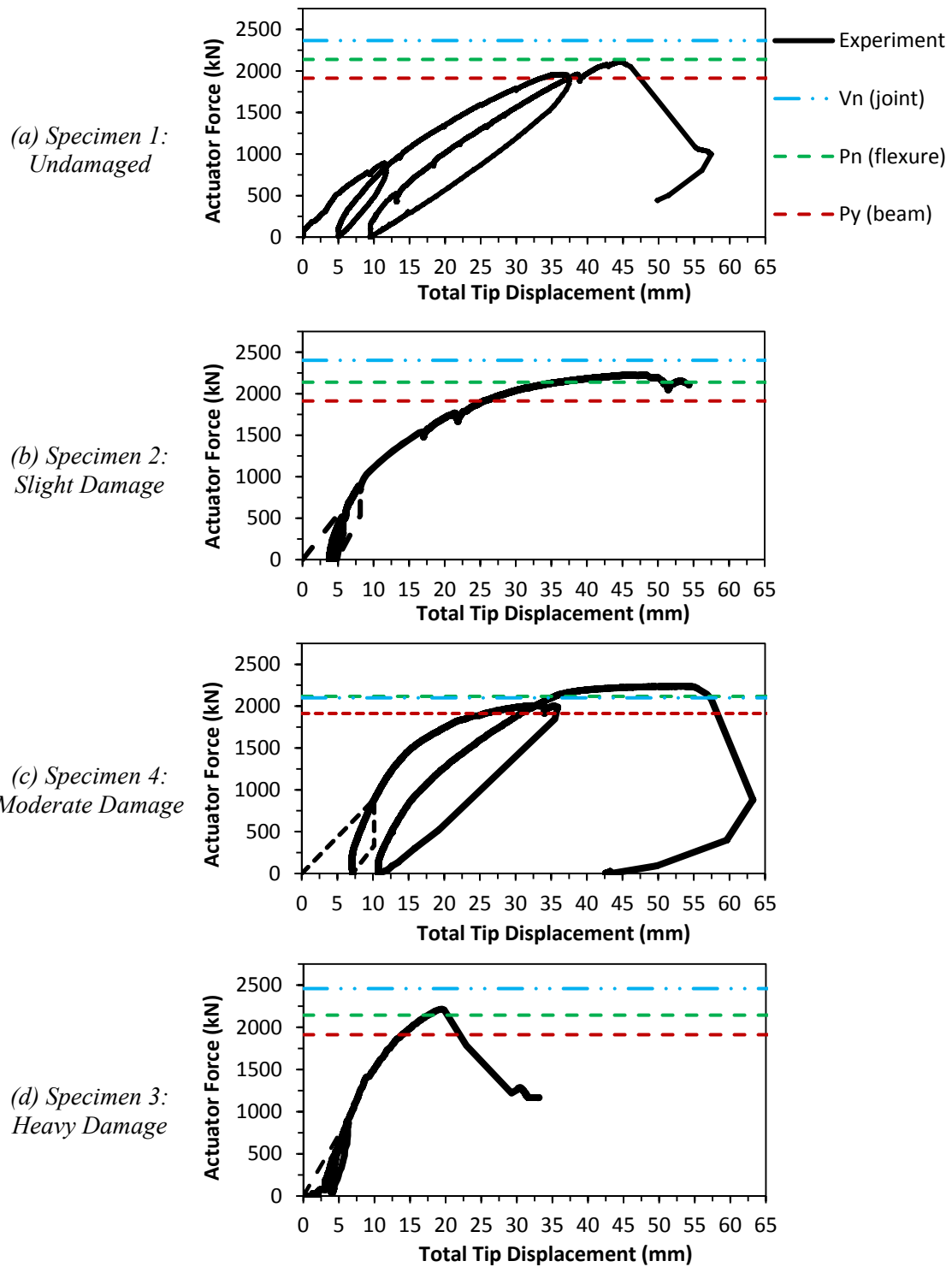
#### 7.4 Discussion and Comparison with Previous Tests

Figure 7-11 presents a comparison of the force-deformation behavior of all four C-beam specimens. It is to be noted here that Specimen 1 was the *undamaged* control specimen and was not subjected to ASR/DEF deterioration. Specimens 2 and 4 showed *slight* and *moderate* amounts of deterioration due to ASR/DEF expansion, and Specimen 3 was subjected to *heavy* damage due to ASR/DEF related expansion. Also presented in Figure 7-11 are the joint shear capacity, the nominal load capacity, and the yield load of the C-beam specimens, which were computed in accordance with the procedure detailed in Appendix A1.

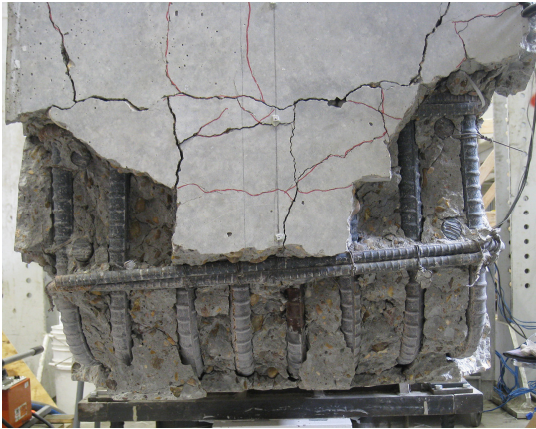
In contrast with the control (*undamaged* by ASR/DEF) Specimen 1, which had a load capacity of 2108 kN, the ultimate load capacity of Specimen 3 was 2215 kN. This result for Specimen 3 is close to the ultimate load capacity of Specimens 2 and 4, which were recorded at 2224 kN and 2237 kN, respectively. The increasing levels of stiffness observed from the control Specimen 1, to the deteriorated Specimens 2, 4, and 3 in that order, is attributed to the beneficial prestressing effects on concrete from the longitudinal and transverse reinforcement arising from the ASR/DEF induced concrete expansion. Although higher ductility was observed in Specimens 2 and 4 compared to the control Specimen 1, Specimen 3 with *heavy* ASR/DEF deterioration showed somewhat less ductility. However, the extent of damage caused by ASR/DEF deterioration in Specimen 3 did not result in a reduced load carrying capacity.

Figure 7-12 shows a comparison of the post-failure condition of each knee-joint for the four C-beam specimens. It is evident from Figure 7-12a and b that Specimens 1 and 2 which were *undamaged* and *slightly* damaged, respectively, showed no signs of corrosion in the longitudinal or transverse reinforcement. In addition, the lapped U-bars in Specimens 1 and 2 remain tied together and are intact. Figure 7-12c (*i* and *ii*) shows the post peak-load condition of the *moderately* damaged Specimen 4. The onset of corrosion in the longitudinal and transverse reinforcement is evident in the photographs. Also note bulging of the lapped U-bars close to the bottom edge of the knee-joint, indicating the onset of loss of confinement restraint in the softened concrete.





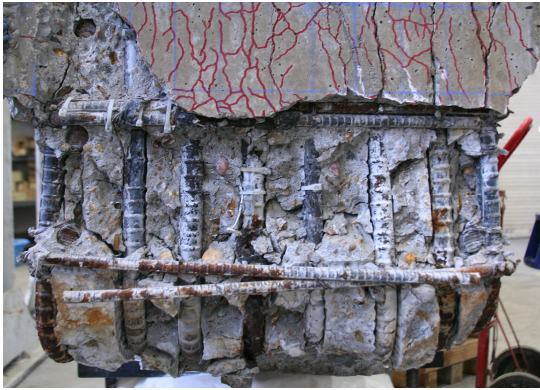
**Figure 7-11: Comparison of Force-Deformation Behavior of C-beam Specimens Subjected to ASR/DEF Deterioration.**



*(a) Specimen 1: Undamaged by ASR/DEF*



*(b) Specimen 2: Slight ASR/DEF Damage*



*(i) Front View*



*(ii) View from Bottom*

*(c) Specimen 4: Moderate ASR/DEF Damage*



*(i) Front View*



*(ii) View from Bottom*

*(d) Specimen 3: Heavy ASR/DEF Damage*

**Figure 7-12: Corrosion and Post-Peak Load Damage at Failure: A Comparison of the Four C-beam Specimens at the Knee-Joint.**

Figure 7-12d (*i* and *ii*) shows the post-failure physical condition of *heavily* damaged Specimen 3, where a significant degree of corrosion may be observed in the longitudinal and transverse reinforcement. From Figure 7-12d it is evident that there is significant bulging and complete de-bonding of the lapped U-bars close to the bottom edge of the Specimen 3 knee-joint. The lapped U-bars further away from the edge of the knee-joint also show signs of significant bulging. It is evident that the loss of anchorage and bulging of the U-bars in Specimen 3 caused considerable loss in confinement of the softened concrete, resulting in an embrittled performance and sudden early loss of load in the *heavily* damaged C-beam Specimen 3.

### **7.5 Key Findings from the Experimental Testing Program**

C-beam Specimen 3, which was the subject of this experimental study, was located in the field and allowed to deteriorate over a period of five years. Based on measured strains and visual observations, Specimen 3 was categorized to have sustained *heavy* deterioration due to ASR/DEF expansion. Based on the experimental load testing of Specimen 3 to failure, the following key findings are summarized:

- In spite of the large number of cracks and heavy damage observed on the C-beam specimen during the deterioration phase, the experimental program showed that the load carrying capacity of the *heavily* deteriorated specimen was similar to the *slightly* and *moderately* damaged C-beam specimens. All the deteriorated specimens had higher load carrying capacity compared to the undeteriorated control specimen.
- The force-deformation response of the *heavily* damaged C-beam specimen was observed to be much stiffer than all the other C-beam specimens owing to the higher prestress effects due to ASR/DEF expansion. However, the overall ductility of the specimen was much less compared to the other specimens.
- The failure mechanism of Specimen 3 was observed to be the same as the other three C-beam specimens, in spite of its *heavily* deteriorated state. As in the earlier cases the failure mechanism was classified to be brittle joint shear failure in the beam-column joint. This mechanism resulted mainly because of insufficient

anchorage of the transverse U-bars in the joint region and also due to the lack of out-of-plane reinforcement along the column face in the joint region.

- A significant amount of corrosion was observed in the longitudinal and transverse reinforcement in the beam-column joint. However, the corrosion of reinforcement did not seem to affect the load carrying capacity of the C-beam specimen. It is not clear if more severe exposure conditions like higher humidity or exposure to salt water could lead to more rapid and severe corrosion, and how that would affect the load carrying capacity of the C-beam specimen.

## 8 FORCE DEFORMATION MODELING OF EXPERIMENTAL RESULTS\*

### 8.1 Summary

To extend the value of experimental tests it is essential to be able to model the structural behavior of complex reinforced concrete structures with rigorous mathematical or computational structural models. Current code based approaches are lower-bound force-based approaches that do not give any estimate on the load-deformation behavior of existing reinforced concrete structures. The Compatibility Strut-and-Tie Model (C-STM) approach is used to model the force-deformation behavior of experimentally tested C-beam specimens, without and with ASR/DEF deterioration. Modified cover and core concrete material properties are recommended to account for the effects of ASR/DEF deterioration in the C-STM approach. The ASR/DEF expansion model presented in Section 4 is used to assess the prestressing forces to be applied on the longitudinal and transverse reinforcement to account for the restraining effects offered by the reinforcement to ASR/DEF induced core concrete swelling. The overall force-deformation behavior and the internal strains obtained from the C-STM analysis compare well with the experimental results, both in the case of the structure without and with ASR/DEF induced expansion. A failure analysis from the C-STM technique shows that the final event which results in the collapse of the C-beam specimens without and with ASR/DEF damage is the compression softening of the corner-to-corner (arch) strut in the beam-column joint. The progression of nonlinear events obtained from the C-STM analysis also compare well with the visual observations that were made during the experimental test. From the results presented, the C-STM analysis is able to successfully

---

\* Previously published work is available to the public through National Technical Information Service. Mander, J.B., Karthik, M.M., and Hurlebaus, S. (2015). "Structural Assessment of "D" Region Affected by Premature Concrete Deterioration: Technical Report." *Report No. FHWA/TX-15/0-5997-2*, Texas A&M Transportation Institute, College Station, Texas, USA.

model the behavior of the C-beam specimens with good accuracy. Additionally, by properly accounting for the effects of ASR/DEF deterioration in reinforced concrete, various levels of deterioration can be successfully modeled in the C-STM approach.

## **8.2 Introduction**

Over the past decade, premature concrete deterioration has compromised the structural longevity of a large number of reinforced concrete bridge bent-caps. A thorough understanding of the structural behavior in disturbed regions is required in order to assess the integrity of bridges that show premature concrete deterioration. The force-based approaches of the current code design methods (AASHTO, 2010; ACI 318-08) result in conservative lower-bound solutions. Hence, these methods are not appropriate for modeling the complex behavior of D-regions as a means to evaluate the degradation in strength. Additionally, the different analysis methodologies within a code have different levels of inherent conservatism. Although this may be justifiable from a design point of view, when design provisions are applied in an inverse form to analyze a structure, the methods may lead to deceptive results. Therefore, it is desirable to have an advanced analysis technique that can be adopted by practicing engineers and implemented as a method of assessing the nonlinear behavior of reinforced concrete structures with significant D-regions.

The experimental investigation described in earlier sections herein was specifically designed to replicate typical bridge bents that currently exist in Texas. A key aim of the experiments was to investigate the structural performance of large-scale reinforced concrete specimens without and with ASR/DEF induced damage. To extend the value of these experimental tests it is essential that the results can be captured and replicated with rigorous mathematical or computational structural models. To that end, this section uses the displacement based C-STM, as advanced in Section 3. The aim is to analyze each specimen through the same displacement path and compare the modeled force-deformation response with the experimental observations. The C-STM incorporates deformation compatibility into the analysis and considers the contribution of the truss and the arch mechanism toward shear and flexure resistance. C-STM

provides a holistic view of the structural behavior and a complete force-deformation pathway to failure.

Another key objective is the ability to model the effect of premature concrete deterioration in bridge bents into the C-STM analysis. Based on field observations and understanding of how ASR/DEF related expansion affects the structure, certain modifications to the material property are proposed and incorporated into the C-STM modeling technique. These recommendations include assessing the deteriorated concrete cover and core properties, and the prestressing stresses caused by ASR/DEF related expansion in the longitudinal and transverse reinforcement. The prestressing stresses to be applied on the C-STM model can be obtained from the proposed model for ASR/DEF expansion strains presented in Section 4 and applied to the C-beam specimens in Section 6.

This section first presents the modified material properties to be taken into account to model ASR/DEF related expansion in reinforced concrete. Next, the C-beams are analyzed using the beam theory and SAT model, from which it is demonstrated that it is not possible to capture the overall performance of the structure. The structure is then modeled using the C-STM technique without and with the effects of ASR/DEF, and the results are compared with the experimental results.

### **8.3 Modified Material Properties to Account for ASR/DEF**

The effects of ASR/DEF on the structure can be taken into account in the C-STM analysis technique by modifying the material properties. Based on visual inspection and discretion of the field engineer, the extent of damage on the structure can be categorized into three classes: *slight*, *moderate*, and *heavy* damage. The following sub-sections show how to assess the modified material properties for the various extents of deterioration caused by ASR/DEF expansion in reinforced concrete.

### 8.3.1 Assessment of Deteriorated Cover Concrete Properties

The assigned concrete strength within each concrete truss member needs to be appropriately factored to account for the damage caused by ASR/DEF expansion in cover concrete. The modified concrete strength is defined as:

$$f'_{cASR} = \lambda f'_c \quad (8-1)$$

where  $\lambda$  = the strength reduction factor that is based on the extent of damage observed. The right column of Figure 8-1 shows the average of the modeled transverse tensile expansion strains  $\varepsilon_1$  in the beam and column of the deteriorated C-beam specimens. The horizontal bands indicate the range of transverse strains for *undamaged* ( $0 < \varepsilon_1 < 0.0012$ ), *slight* ( $0.0012 < \varepsilon_1 < 0.006$ ), *moderate* ( $0.006 < \varepsilon_1 < 0.016$ ), and *heavy* ( $\varepsilon_1 > 0.016$ ) damage. Substituting the range of  $\varepsilon_1$  values into (3-1) results in the following range of strength reduction factors; default values of  $\lambda$  are also recommended if precise values of  $\varepsilon_1$  are unknown but the visually observed degree of damage is as indicated in Figure 8-1:

- *Undamaged* concrete             $\lambda = 1$                     Default  $\lambda = 1$ .
- *Slight* damage                     $0.55 < \lambda < 1$                 Default  $\lambda = 0.75$ .
- *Moderate* damage                 $0.30 < \lambda < 0.55$             Default  $\lambda = 0.40$ .
- *Heavy* damage                     $\lambda < 0.30$                     Default  $\lambda = 0.30$ .

The out-of-plane photographs and the crack pattern observations presented in Figure 8-1 show the physical state of the C-beam specimens that fall into the category of *undamaged*, *slight*, *moderate*, and *heavy* damage. Note that the crack pattern on *moderately* damaged Specimen 4 looks similar to the crack pattern on the *heavily* damaged Specimen 3. However, the cracks in the out-of-plane direction of Specimen 3 were wider compared to Specimen 4 as shown in the photographs in Figure 8-1. Additionally, the crack width strains (sum of crack widths/overall width) in the beam and column out-of-plane region were about one-half that of the surface strains that were measured from the DEMEC points from the same region. Thus, it is possible to relate the



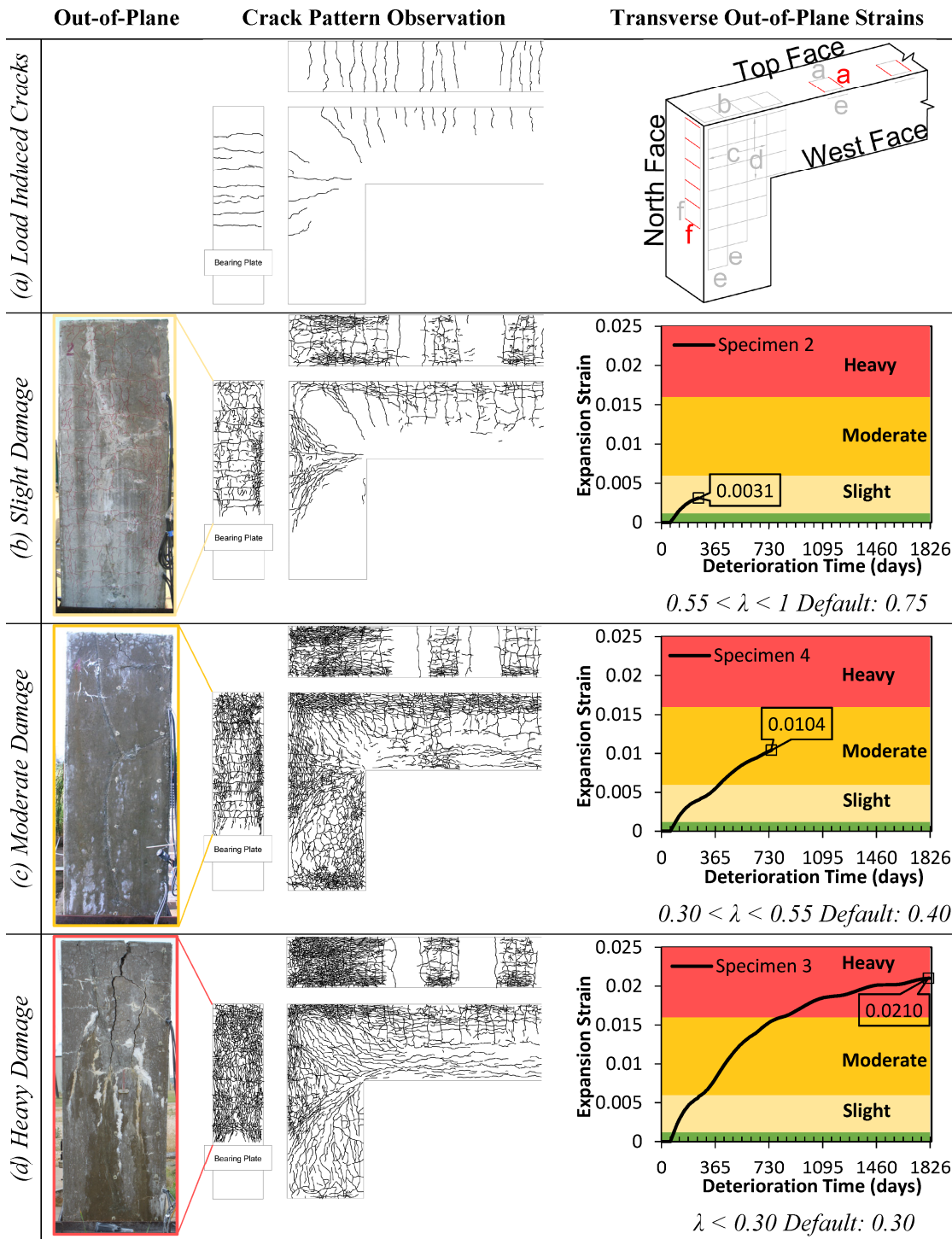


**Figure 8-1: Deteriorated Specimen Appearance, and the Modeled Transverse Strains in the C-beam Out-of-Plane Direction.**

crack width strains with the actual expansion strains and thereby determine the extent of damage caused by ASR/DEF expansion on the structure from Figure 8-1.

### 8.3.2 Assess Concrete Core Confinement and Modify Concrete Properties

ASR/DEF effect causes the concrete to swell. The swelling of core concrete is constrained by longitudinal and transverse reinforcement, which effectively confines the core concrete. To account for this effect, the confinement ratio ( $K_{cc} = f'_{cc} / f'_{co}$  where  $f'_{co}$  = in situ concrete strength) has to be determined to obtain the confined concrete stress  $f'_{cc}$ . The procedure to evaluate the confinement ratio (Mander et al., 1988) is described in Appendix A1.

### 8.3.3 Prestressing Effect in Reinforcement Caused by Concrete Swelling

The constraint offered by longitudinal reinforcement and transverse hoops to the swelling of core concrete puts tensile strains on the reinforcing steel, which in turn puts the concrete into a state of prestress. The prestressing forces can be evaluated based on the expansion strains in the specimen, at the end of its exposure period. For this, the expansion model that was presented earlier in Section 4 and later applied to the C-beam specimens in Section 6 can be used to determine the expansion strains and hence compute the corresponding prestressing force. In lieu of the above exhaustive expansion strain analysis, the following recommended values may be used.

Depending on the extent of damage (*slight, moderate, or heavy*) due to ASR/DEF effects, the following recommendations are made for prestressing stresses  $f_{ps}$  in the longitudinal reinforcement:

- Undamaged concrete  $f_{ps} = 0$ .
- Slight damage  $f_{ps} = 0.3f_y$ .
- Moderate damage  $f_{ps} = 0.5f_y$ .
- Heavy damage  $f_{ps} = 1.1f_y$ .

in which  $f_y$  = yield stress of longitudinal reinforcement. Similarly the recommendations for prestressing stresses in hoops are:

- Undamaged concrete  $f_{ps} = 0$ .
- Slight damage  $f_{ps} = 0.5f_{yh}$ .
- Moderate damage  $f_{ps} = 1.0f_{yh}$ .
- Heavy damage  $f_{ps} = 1.25f_{yh}$ .

in which  $f_{yh}$  = yield stress of transverse hoops.

Appropriate modifications to the stress-strain behavior of the reinforcing steel have to be made to account for the prestressing effects. The modified stress-strain relation of steel is shown in Figure 8-2 in which  $\epsilon_{ps}$  = prestrain corresponding to prestressing stress  $f_{ps}$ .

#### 8.4 C-beam Structure

The experimental specimen was designed as a “C” shape sub-assembly such that two large-scale bridge bent components were placed back-to-back, so that they could be tested as a self-reacting system. Figure 8-3 a and b represents the prototype structures based on which the C-beam specimens were modeled. The C-beam specimen had a constant cross-section of 914 mm deep and 610 mm wide that was symmetrical with the exception of the beam compression steel. The physical model scale factor of the specimen ends representing the singly reinforced cantilever bent and the doubly reinforced straddle bent were approximately 0.5 and 0.75, respectively.

Figure 8-3c presents the reinforcing layout and cross-section of the C-beam specimen. The longitudinal reinforcement consisted of 10 #8 (25 mm) bars running continuously around the outside and hooked at the end of each beam. For construction purposes the singly reinforced beam had two straight #8 compression bars. The doubly reinforced beam had symmetrical compression and tension reinforcement.

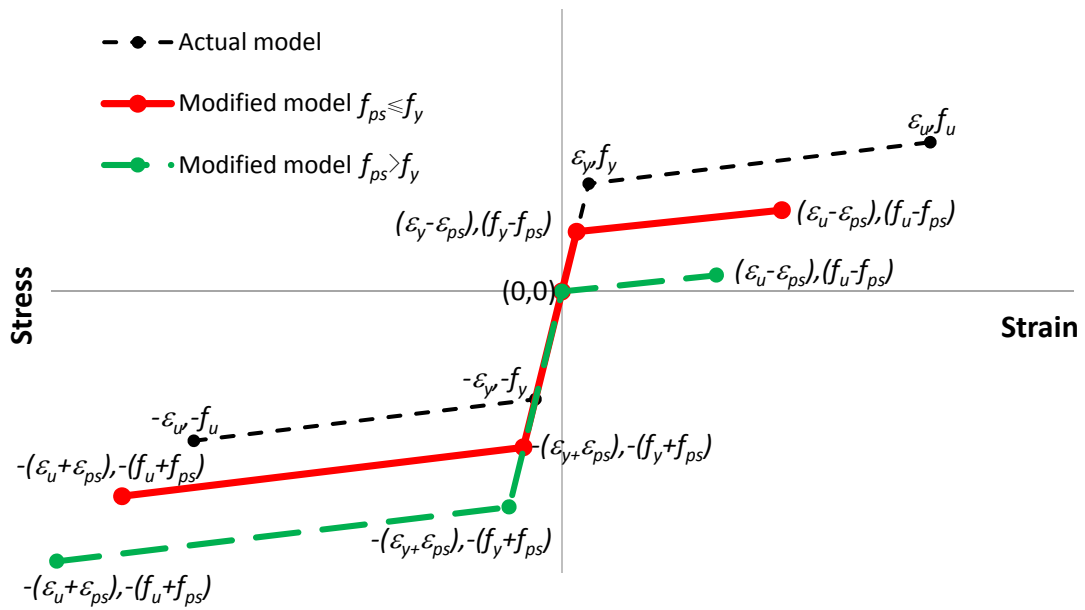
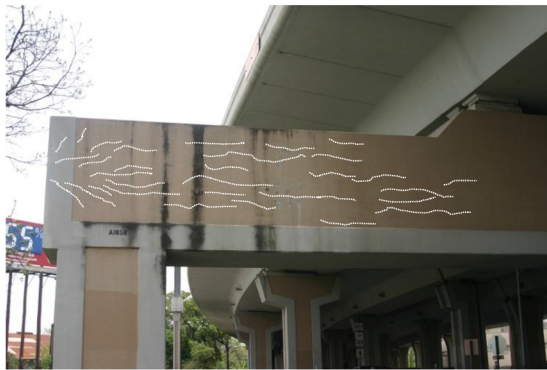
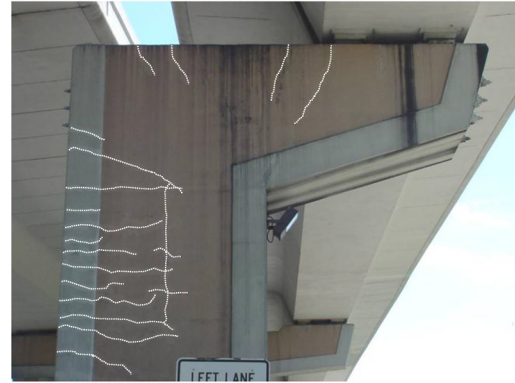


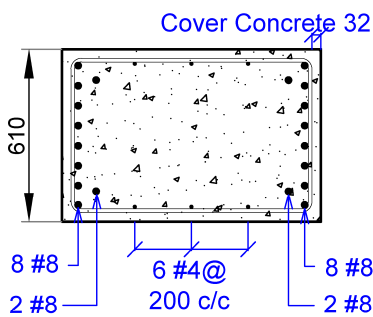
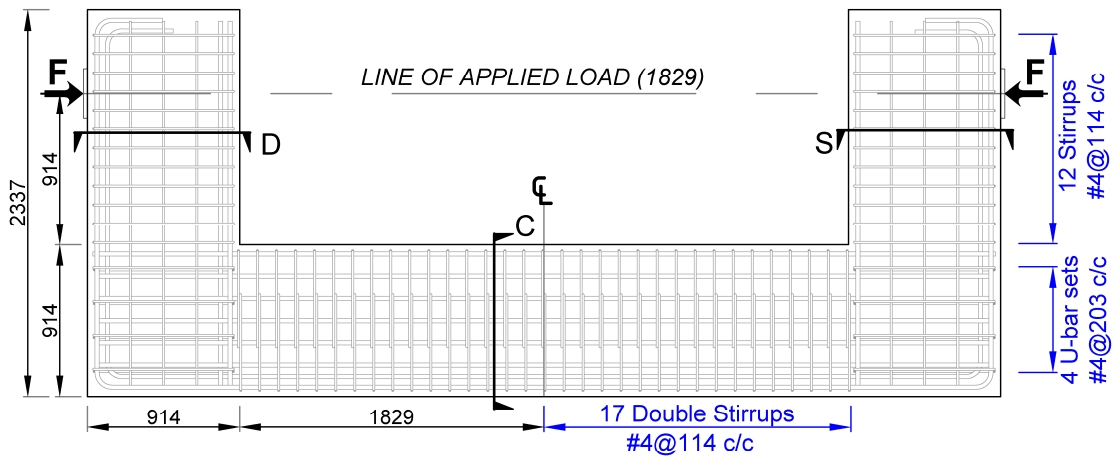
**Figure 8-2: Modified Stress-Strain Model for Steel to Account for Prestressing Effects due to ASR/DEF.**



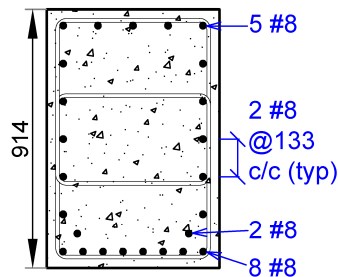
(a) Straddle Bent



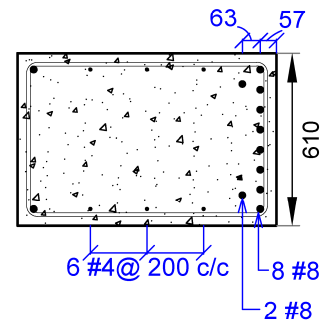
(b) Cantilever Bent



D-Doubly Reinforced



C-Column



S-Singly Reinforced

(c) Reinforcement Details

**Figure 8-3: Representative Structures, and Elevation and Cross-Section of the C-beam Specimens.**

The longitudinal distribution steel in the beam (distributed along the beam web) consisted of three sets of equally spaced #4 (13 mm) bars. Transverse beam reinforcement consisted of closed stirrups with a center-to-center spacing of 114 mm starting at the column face. The longitudinal column distribution steel consisted of five sets of equally spaced #8 bars. Overlapping #4 stirrups spaced at 114 mm centers were used for the transverse column reinforcement. The beam-column joint was reinforced with four #4 U-bars at 203 mm centers continuing from the transverse beam reinforcement.

Table 8–1 presents the reported material strength data on the test day and experimental test results. Specimen 1 was the control specimen. This specimen was not conditioned under alternate wetting and drying cycles outdoors; therefore, it did not have any ASR/DEF induced damage. Specimens 2, 4 and 3, which were respectively conditioned outdoors for nine months, two years, and five years showed *slight*, *moderate* and *heavy* amounts of damage due to ASR/DEF related expansion.

## 8.5 Preliminary Analysis

The code-based design approaches that use the AASHTO *LRFD Bridge Design Specifications* (2010) (that are described in detail in Appendix A1) are used to predict the response of C-beam Specimens 1, 2, 4 and 3. A summary of the analysis results are presented in Table 8–1. Detailed computations can be found in Appendix A4.

Figure 8-4 shows the experimental force-deformation curves of the four C-beam specimens. Also plotted on these graphs are the strength capacities obtained from the code-based analyses. For Specimens 2, 4 and 3, the prestress applied to mimic gravity effects while the specimens were conditioned in the field was not accurately captured. Hence the experimental results are shown with an initial offset. The dashed lines show the computed (assumed) behavior of this initial prestress effect prior to release of the prestress. As can be seen from Figure 8-4, the analysis results do not give any indication of the overall behavior of the structure, and hence the strength-only predictions are represented as horizontal lines.

From the results of the preliminary analyses presented in Table 8–1 and shown in Figure 8-4, the externally applied load causing yielding based on beam flexure  $P_y^b$  and the SAT  $P_y^{\text{SAT}}$  methods agree well with the experimental observations. However, the sectional shear approach  $V_n^s$  had the largest discrepancy and did not accurately represent the specimen capacity. These predictions are unduly harsh because the shear capacity is calculated in a D-region where the sectional theory breaks down. It is for this reason a SAT analysis needs to be conducted. The SAT analysis would imply that the beam-column joint would fail even before the beam yielded, thus suggesting that the structure fails in a very brittle manner. However, this is not the case as can be seen from the experimental results (Figure 8-4) and hence the SAT analysis predicts a somewhat faulty picture about the expected structural behavior. Moreover, it is not clear how the observed effects of ASR/DEF damage can be included in these simple methods.

It can be concluded from these results that it is inconclusive as to what will be the failure mode of the specimen, as it is observed that the joint capacity is (theoretically) undependable. Additionally, the SAT analysis does not take into account the effects of ASR/DEF damage. To better understand the behavior of the structure and its final mode of failure, the C-STM analysis is applied in what follows.

## **8.6 Strength and Deformation Capacity Using C-STM**

### **8.6.1 C-STM Model**

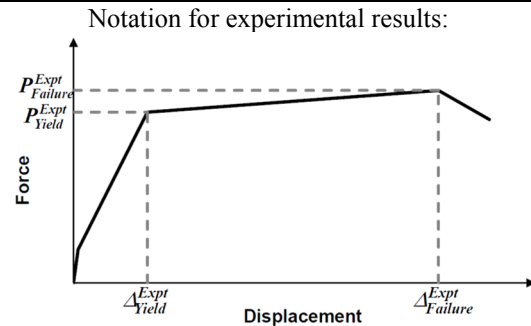
Even though the C-STM is a minimalist model, the C-STM analysis is able to provide a good insight into the overall force-deformation behavior and to understand the nonlinear mechanics within the C-beam specimens that lead to different modes of behavior and eventual failure. The development of the displacement-controlled C-STM has been extensively discussed in Section 3, and its force-controlled predecessor in Scott et al. (2012a,b).

Figure 8-5 shows the C-STM topologies for the C-beam specimens (*a*) without and (*b*) with ASR/DEF induced damage. The cantilever beams are modeled using a single-point Gauss quadrature model (Scott et al., 2012a), and the joints are modeled

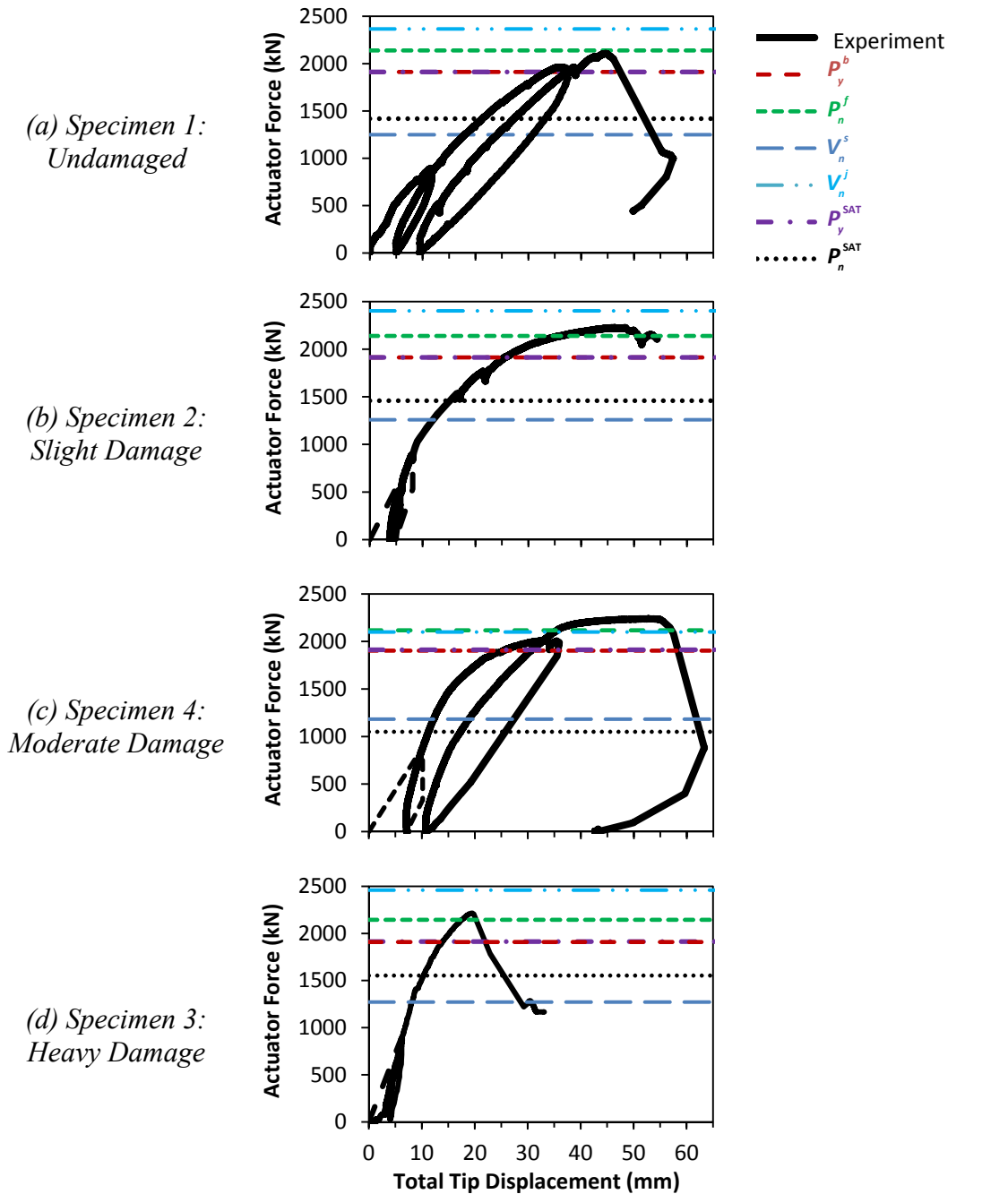
**Table 8–1: Material Properties, Stage 1 and 2 Analyses, and Experimental Results.**

Material Properties	Specimen 1		Specimen 2		Specimen 4		Specimen 3		
	$f'_c$ (MPa)	37.2		38.6		27.6		40.9	
$f'_t$ (MPa)	2.07		1.60		---		---		
$E_c$ (GPa)	28.9		29.4		24.9		30.3		
Age at testing (months)	13		16		29		65		
Stage 1 Analyses (Sectional)	Beam reinforcement	Double	Single	Double	Single	Double	Single	Double	Single
	$M_y^b$ (kN.m)	1749	1730	1749	1731	1742	1721	1750	1734
	$P_y^b$ (kN)	<b>1913</b>	<b>1890</b>	<b>1913</b>	<b>1895</b>	<b>1904</b>	<b>1882</b>	<b>1913</b>	<b>1895</b>
	$M_n^f$ (kN.m)	1955	1920	1956	1925	1936	1875	1959	1932
	$P_n^f$ (kN)	<b>2140</b>	<b>2100</b>	<b>2140</b>	<b>2104</b>	<b>2117</b>	<b>2051</b>	<b>2144</b>	<b>2113</b>
	$\phi_j P_n^f$ (kN)	1926	1890	1926	1894	1905	1846	1930	1902
	$V_n^s$ (kN)	<b>1250</b>	<b>1268</b>	<b>1259</b>	<b>1277</b>	<b>1183</b>	<b>1201</b>	<b>1272</b>	<b>1294</b>
$V_n^j$ (kN)	<b>2366</b>	<b>2398</b>	<b>2402</b>	<b>2433</b>	<b>2100</b>	<b>2126</b>	<b>2460</b>	<b>2491</b>	
Stage 2 Analyses (SAT)	$P_y^{SAT}$ (kN)	1908		1908		1908		1908	
	$\phi_y P_y^{SAT}$ (kN)	1336		1336		1336		1336	
	$P_n^{SAT}$ (kN)	<b>1415*</b>		<b>1468*</b>		<b>1050*</b>		<b>1552*</b>	
	$\phi_j P_n^{SAT}$ (kN)	991		1028		735		1086	
Experimental Results	$P_{Yield}^{Expt}$ (kN)	1957		1957		1957		--	
	$P_{Failure}^{Expt}$ (kN)	<b>2108</b>		<b>2224</b>		<b>2237</b>		<b>2215</b>	
	$\Delta_{Yield}^{Expt}$ (mm)	37.8		23.4		27.9		--	
	$\Delta_{Failure}^{Expt}$ (mm)	42.9		49.3		55.1		19.6	
	$\mu$	1.13		2.11		1.97		--	
	$P_n^{SAT} / P_{Failure}^{Expt}$	0.67		0.66		0.47		0.70	

\*Expected critical failure mode capacity.  
 Superscript:  $b$ =beam;  $f$ =flexure;  $s$ =shear;  $j$ =joint;  
 SAT=strut-and-tie; Expt=Experiment.







$P_y^b$  = External load causing flexural yield;  $P_n^f$  = External load causing beam flexure;  $V_n^s = V_s + V_c$  = Nominal beam shear;  $V_n^j = V_{\text{truss}} + V_{\text{arch}}$  = Joint shear;  $P_y^{\text{SAT}}$  = External load based on longitudinal steel yield from SAT;  $P_n^{\text{SAT}}$  = External load based on node capacity from SAT

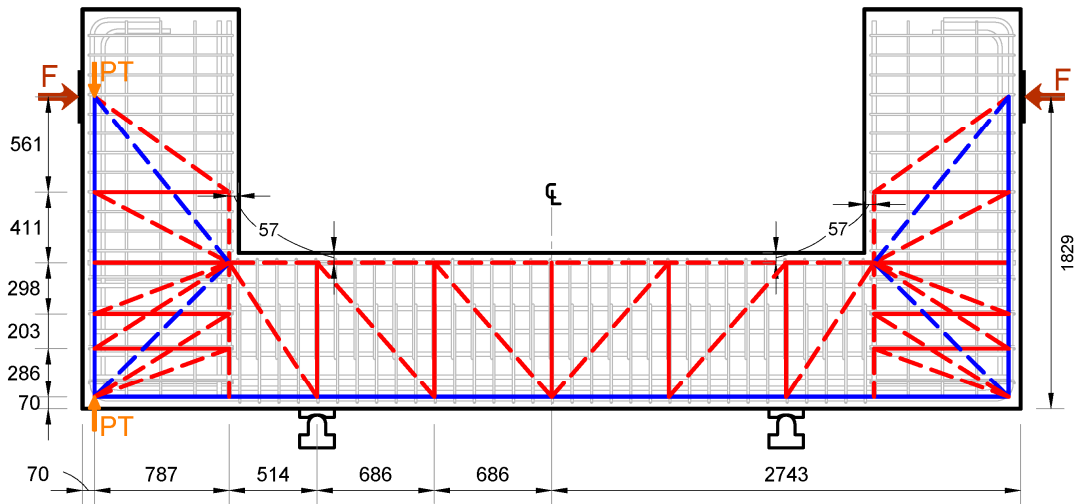
Note: Experimental results of Specimens 1, 2, and 4 are from Mander et al. (2012).

**Figure 8-4: Experimental, Code Based Predictions and C-STM Results.**

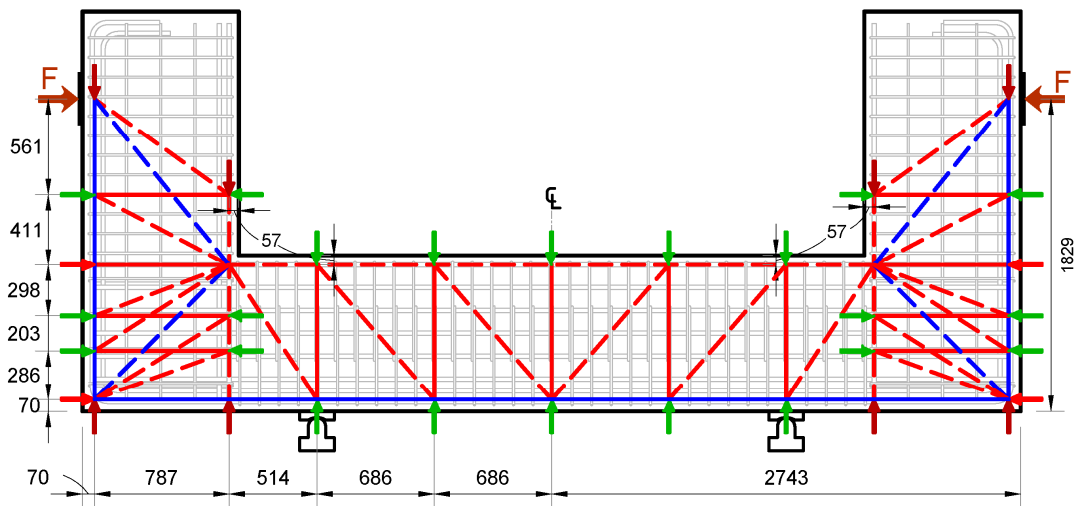
using a two-point Gauss model (Kim and Mander, 1999). To provide a better representation of the actual reinforcement layout, the transverse ties in the joint are aligned with the U-bar reinforcement. The sum of longitudinal tension steel and three sets of web distribution steel are considered for computing the representative areas of the tension chord. The compression chord is defined as the compression longitudinal steel.

Figure 8-5a shows the C-STM model that is developed for Specimen 1, which was the control specimen and had no ASR/DEF induced damage. Initial post-tension loads (shown as PT in Figure 8-5a) were applied to the tension chord of the protected beam in order to replicate post-tensioning effects in accordance with Phase I and Phase II of testing (Mander et al., 2012). This model essentially represents the C-STM analysis *without* any ASR/DEF effects. Row 2 of Figure 8-6 shows the nonlinear concrete stress-strain relations that were derived for the constituent elements of the C-STM model of Specimen 1.

Specimens 2, 4, and 3 showed *slight, moderate, and heavy* damage due to the effects of ASR/DEF. Figure 8-5b shows the C-STM model for C-beam Specimens 2, 3, and 4. Prestressing forces are applied on the longitudinal and transverse members in the beam and column in order to replicate the prestress effects that arise as a consequence of the swelling within the core concrete due to ASR/DEF effects. Depending on the extent of ASR/DEF deterioration, the strength reduction factor for cover concrete recommended in Section 8.3 is adopted. The confinement ratio (Mander et al., 1988) is calculated to be  $K_{cc} = f'_{cc} / f'_{co} = 1.20$  for the beam and  $K_{cc} = 1.28$  for the column for Specimen 2. For Specimen 4, the confinement ratio is calculated to be  $K_{cc} = 1.28$  for the beam and  $K_{cc} = 1.35$  for the column. Similarly for Specimen 3 the confinement ratio is calculated as  $K_{cc} = 1.21$  for the beam and  $K_{cc} = 1.31$  for the column. As both the cover and core concrete areas contribute to the area of the strut in the C-STM model, a weighted average value of concrete compressive strength is used in the C-STM model. The computation of the effective concrete compressive strength for Specimen 3 is presented in detail in Appendix A5.



(a) Specimen 1: Without ASR/DEF Damage



(b) Specimen 2,3, and 4: With ASR/DEF Damage

- Primary tension reinforcement
- Ties representing bundles of hoops
- - - Concrete struts for the truss
- - - Central concrete arch
- Initial confinement effect in hoops and longitudinal steel due to concrete swelling, modeled as a set of externally applied nodal forces
- Additional forces representing the prestress effect actively induced in the reinforcing steel caused by ASR/DEF induced concrete swelling

Note: The additional forces in (b) represent the prestress effect actively induced in the reinforcing steel caused by ASR/DEF induced concrete swelling.

**Figure 8-5: Modeling the C-beam Specimens without and with ASR/DEF Damage.**

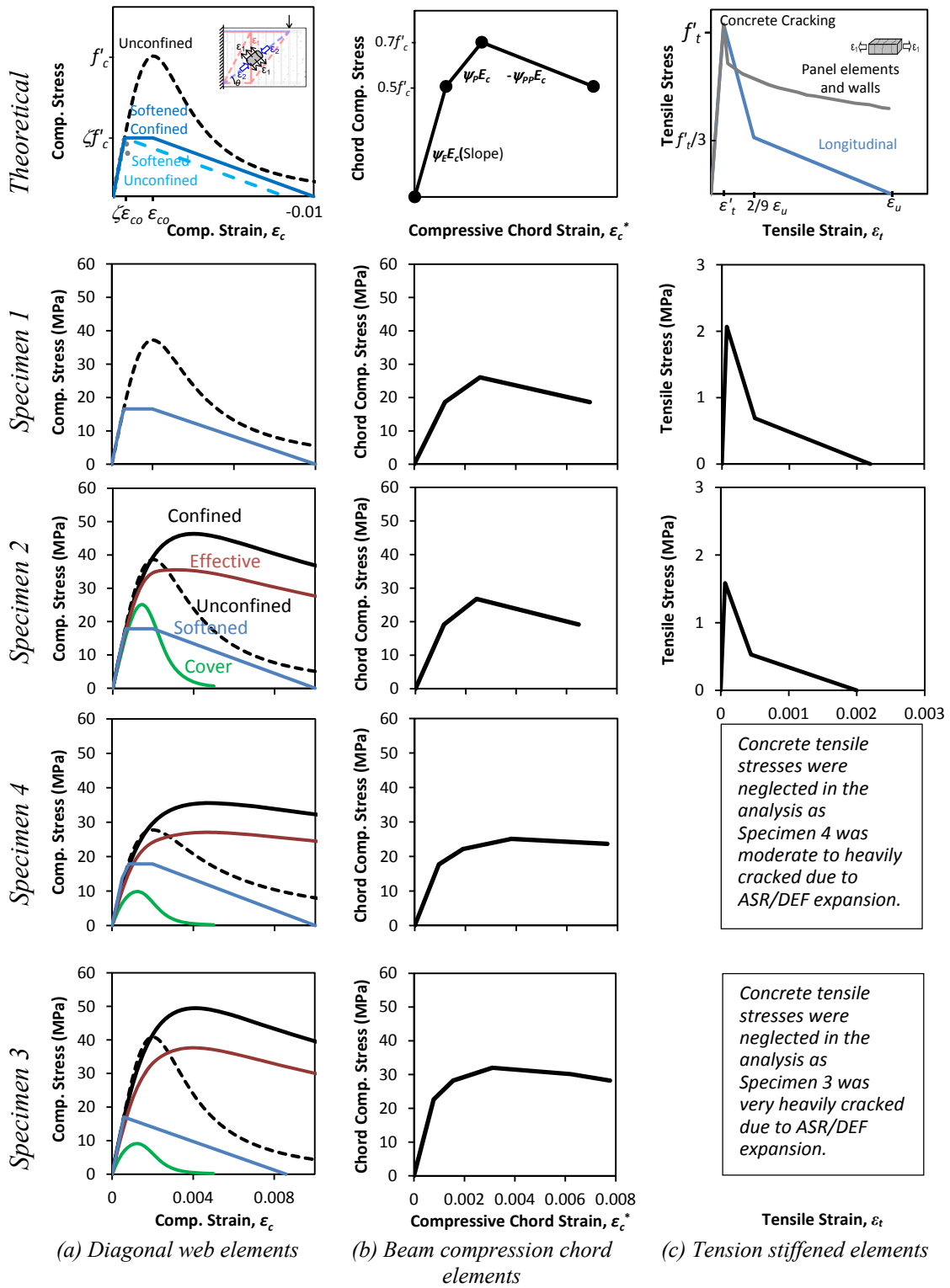


**Figure 8-6: Cracked Reinforced Concrete Material Properties.**

The prestress in the longitudinal and transverse reinforcement is deduced from the ASR/DEF expansion model presented in Section 4. Table 8-2 presents the prestrains for the different longitudinal and transverse members of the C-STM for Specimens 2, 4, and 3. Detailed computations for the prestrains are presented in Appendix A5. Based on the prestrains and the area of the steel member, the prestress force on the C-STM members is back calculated. The stress-strain relation of the reinforcement are also modified accordingly as presented in Figure 8-2.

Rows 3, 4 and 5 of Figure 8-6, respectively, show the different nonlinear concrete stress-strain relationships that were derived for Specimens 2, 4 and 3.

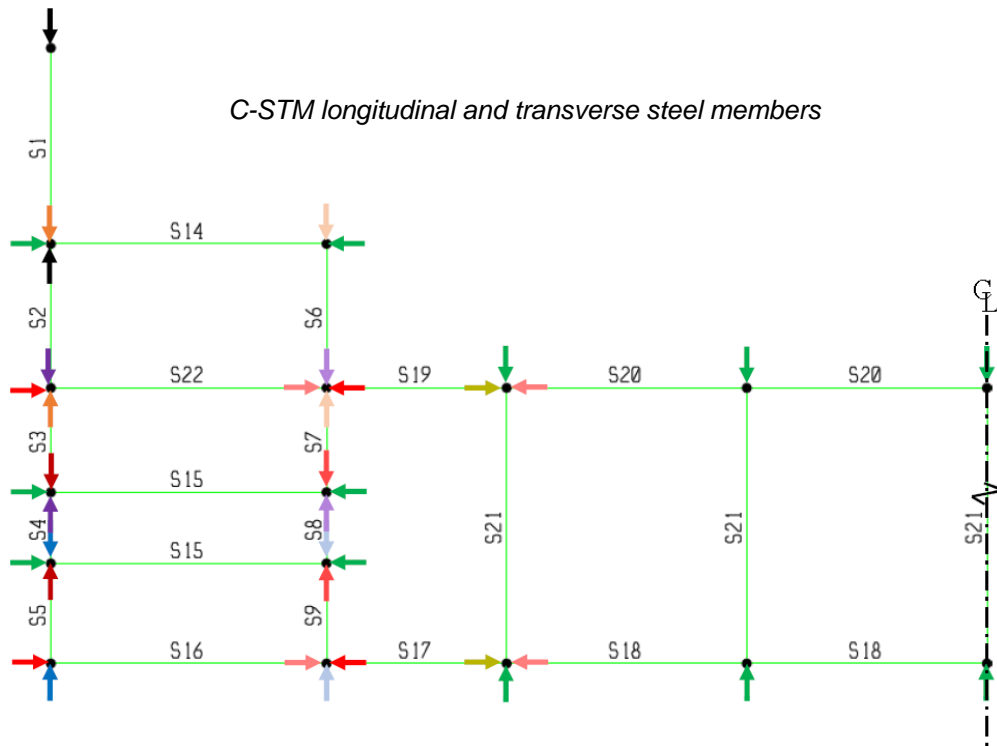
### **8.6.2 Results of C-STM Analysis**

Figure 8-7 presents the overall force-deformation results obtained from the C-STM analysis for the four C-beam specimens, along with a comparison of the results with the experimental behavior. Specimen 1 was the control specimen and had no damage arising from adverse ASR/DEF effects, whereas Specimens 2, 4, and 3, respectively, showed *slight, moderate, and heavy* damages due to ASR/DEF expansion. The C-STM simulates the overall behavior of each specimen quite well. In the case of Specimen 1, the initial tension-stiffening effect is captured well by the C-STM. In the case of the deteriorated specimens, ASR/DEF expansion strains caused by the swelling of concrete put the reinforcing steel into a state of tension, which in turn prestressed the concrete. When this prestress effect is modeled accordingly by applying external loads and modifying the steel stress-strain relations (Figure 8-2), the behavior of the C-beam specimens affected by ASR/DEF expansion is accurately captured. It is to be noted that the confined softened concrete model presented in Section 3.3 was used in modeling the softened concrete behavior of the diagonal concrete struts. While this results in good simulation results for Specimens 1, 2, and 4, it is evident from Figure 8-7d that using confined softened model led to an over-estimation of the ductility of the structure. However, the unconfined softened model results in good agreement between the experimental observations and the C-STM modeled results. Due to the presence of large tensile strains

**Table 8-2: Prestrains in C-STM Members for C-beam Specimens.**

Member	Specimen 2	Specimen 4	Specimen 3
S1	0.0018	0.0044	0.0079
S2	0.0016	0.0036	0.0065
S3	0.0017	0.0038	0.0076
S4	0.0020	0.0046	0.0104
S5	0.0028	0.0068	0.0181
S6	0.0010	0.0027	0.0042
S7	0.0008	0.0021	0.0031
S8	0.0010	0.0027	0.0043
S9	0.0016	0.0043	0.0088
S14/S15	0.0032	0.0075	0.0217
S16/S22	0.0018	0.0044	0.0057
S17/S19	0.0014	0.0028	0.0034
S18/S20	0.0014	0.0025	0.0034
S21	0.0030	0.0133	0.0204

*Note: Detailed computation of prestrains for Specimen 3 presented in Appendix A5.*



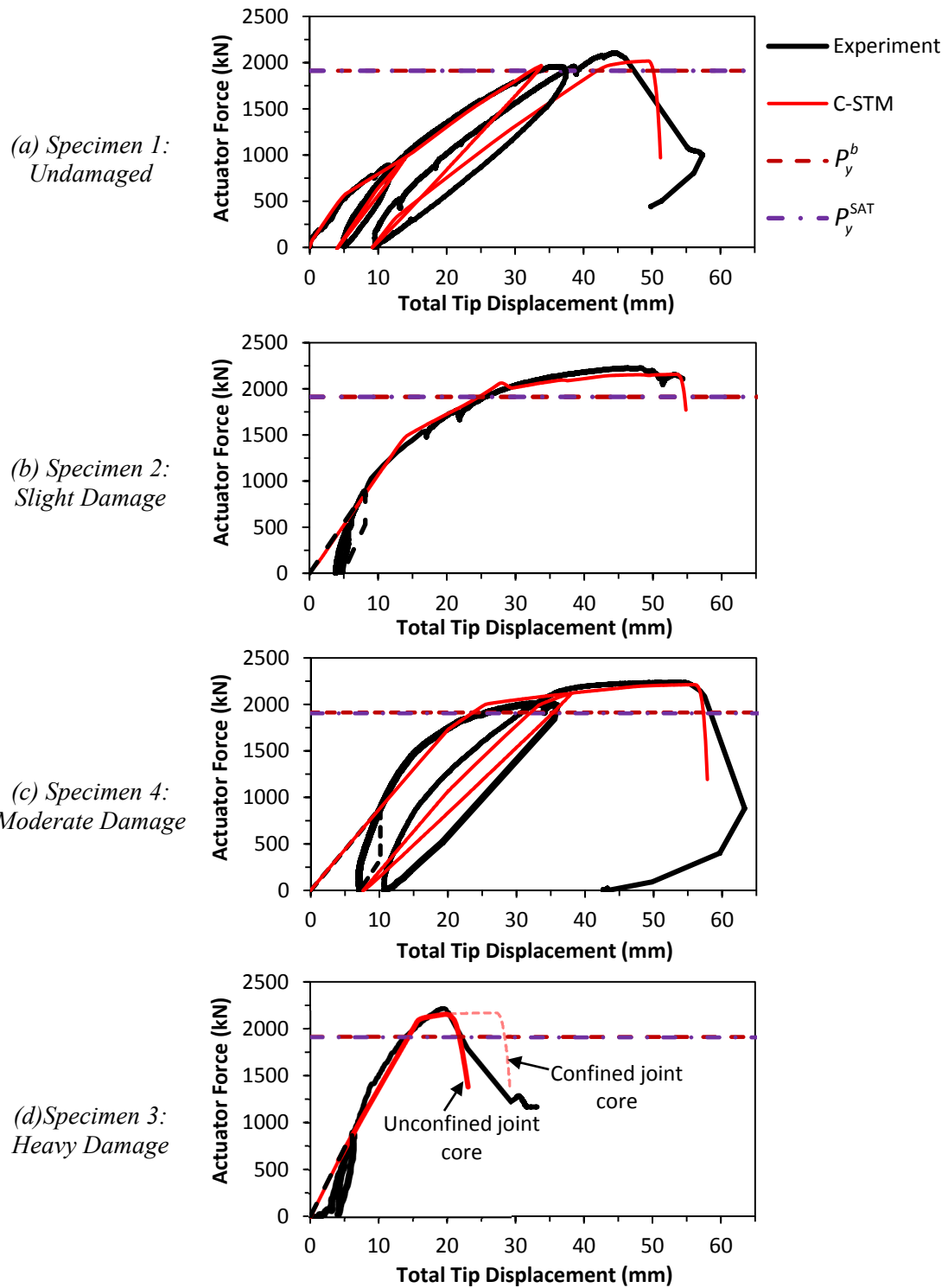


**Figure 8-7: Comparison of Experimental and C-STM Results for C-beam Specimens Subjected to ASR/DEF Deterioration.**

in the badly damaged joint region that had poor reinforcement detailing, the use of the unconfined softened model is justified for Specimen 3.

The difference observed between the modeled and the observed behavior during the unloading and reloading is attributed to the partial opening/closing of cracks in the presence of shear deformations. This leads to a greater hysteresis in the experimental results than obtained through the C-STM modeled results, where concrete opening/closing is crisp and tight.

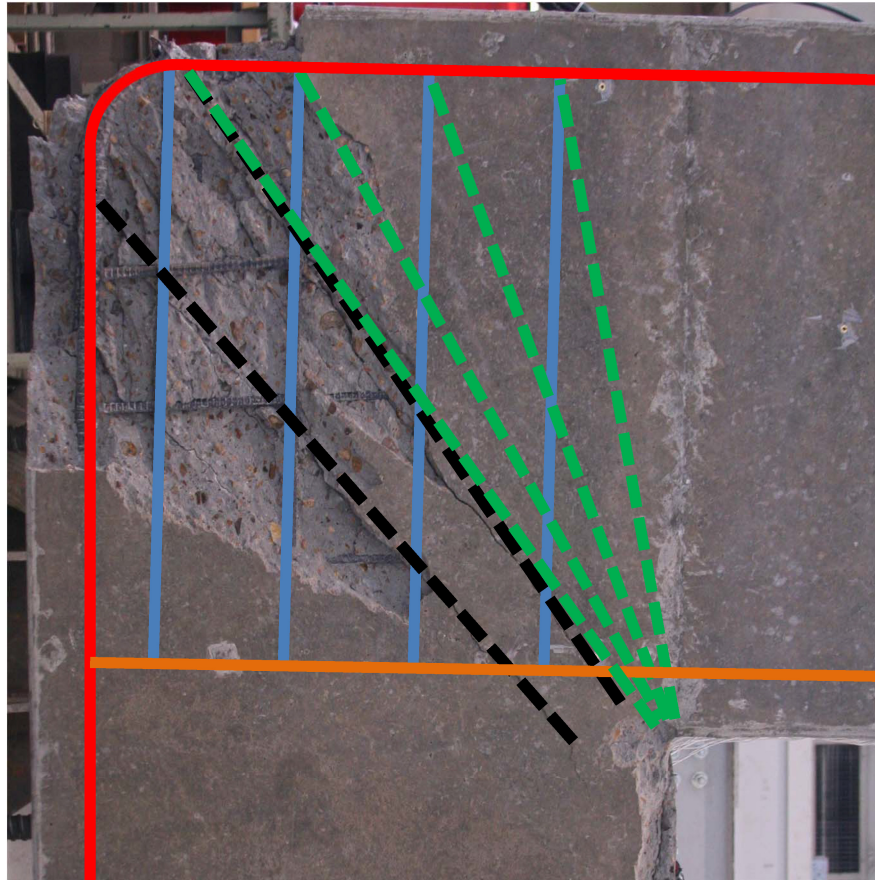
The experimental results confirm that for all tests, as shown in Figure 8-8, the beam-column joint was most critical, and the CTT node is the most critical node. The joint is overlaid with the truss and the arch members as was observed from the crack pattern.

### **8.6.3 Interrogation of Internal Strains from C-STM and Comparison with Experimental Results**

To further substantiate the veracity of the C-STM approach, it is of interest to compare the strains in the individual C-STM members to the strain data obtained from the internal strain gages and KM gages, and the externally mounted LVDTs in the experimental setup. This permits confirmation of the C-STM modeling strategy, and in particular replicates the micro-level behavior of the structure as well as possible.

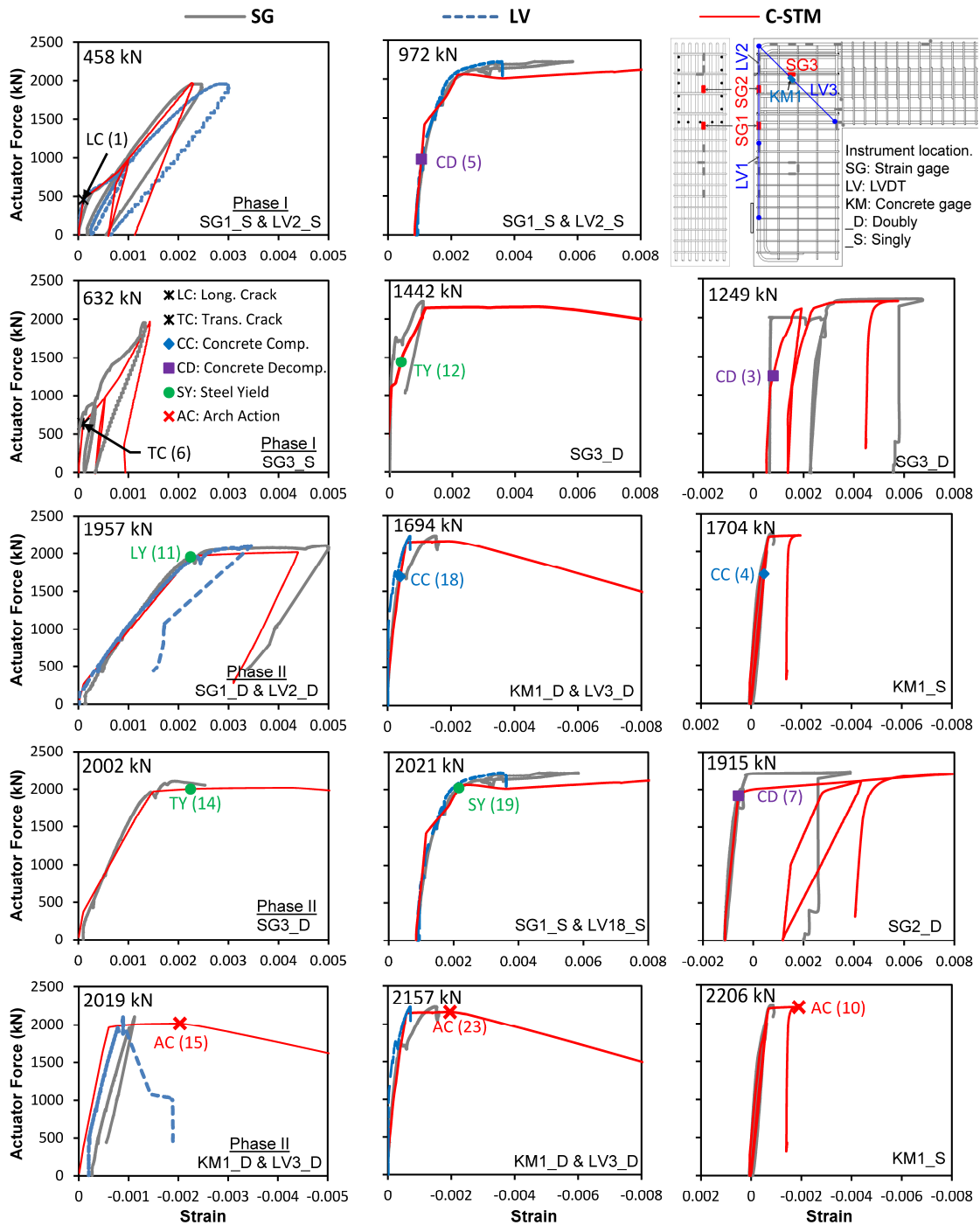
Figures 8-9 and 8-10, respectively, show a comparison of the modeled internal strain behavior with the experimentally observed instrument results for Specimens 1, 2 and 4, and Specimen 3. The development of nonlinear behavior in the C-STM with increasing levels of force is also shown. The event numbers in the parenthesis refers to the order of formation of nonlinear mechanisms in the specimen which are discussed in detail in Section 8.6.4. The instrument data that are used for comparison are noted in the bottom of each plot, and the location of these instruments is shown in the top right hand corner of Figure 8-9. Good agreement between the C-STM results and the experimental results is evident in Figure 8-9.





- Tension ties
- Beam chord
- Transverse ties
- - - Truss action
- - - Arch action

**Figure 8-8: Failure Pattern Observed at the Beam-Column Joint of C-beam Specimen 1.**



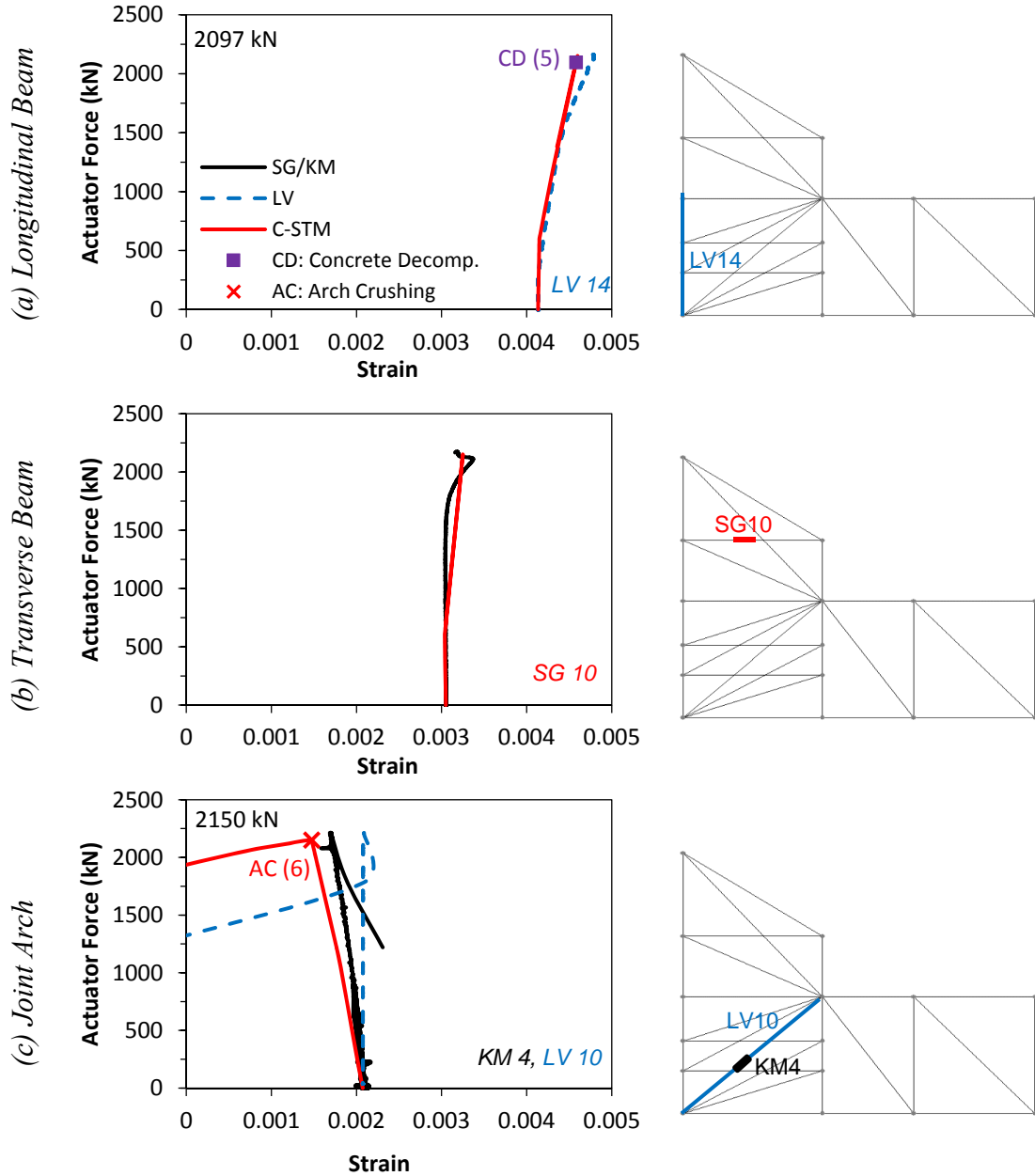
*Specimen 1*

*Specimen 2*

*Specimen 4*

*Note: Tensile strains are positive. Refer Figure 8-11 for progression of nonlinear events presented as numbers in paranthesis in each plot.*

**Figure 8-9: Experimental (Mander et al., 2012) vs. C-STM Comparison of Internal Nonlinear Concrete and Steel Response for C-beam Specimens.**



Note: Tensile strains are positive. Refer Figure 8-11 for progression of nonlinear events presented as numbers in paranthesis in each plot.

**Figure 8-10: Experimental vs. C-STM Comparison of Nonlinear Concrete and Steel Response: Specimen 3.**

In Figure 8-9 the events longitudinal cracking (LC) and transverse cracking (TC) refer to concrete cracking of the longitudinal and transverse members. Concrete compression (CC) refers to when the elastic limit of concrete is exceeded and concrete decompression (CD) refers to the stage when the effects of the applied prestress are overcome by the applied loading and the concrete strains become tensile (positive). Steel yield (SY) occurs when the steel reaches its yield strain and arch crushing (AC) refers to the concrete crushing of the corner-to-corner arch diagonal in the beam column joint.

Due to the severe nature of deterioration in Specimen 3, most of the internal sensors had failed (assumed to be due to rebar corrosion and localized ASR/DEF effects). Therefore only limited internal strain data were gathered during the test. Figure 8-10 shows a comparison of internal strains obtained from C-STM with the experimental strains obtained from the limited number of embedded strain and concrete gages, and the surface mounted LVDTs from Specimen 3. The initial offset in the strain data is due to the strains caused by expansion of concrete during the deterioration phase. It is evident that the increase in strain with the applied load was almost linear until the ultimate load was achieved. This was owing to the high amounts of prestress that the structure was subjected to due to the expansion caused by ASR/DEF. Even though the strains obtained from the C-STM do not precisely agree with experimental data, the trends shown by the model are quite similar to the experimental data.

In the case of Specimens 2, 4 and 3, the transverse steel yields ahead of the longitudinal flexure yielding of reinforcing steel. This is in agreement with the experimental results, where it was observed from field strain gage measurements that the hoop bars were subjected to significant strains due to the effects of ASR/DEF, which leads to the early yielding of hoops. As in the case of Specimen 1, the final event that eventually leads to the failure of the specimens is the crushing of the joint arch member. Beyond this point, when the deformations on the specimens increased, the arch was unable to sustain the load, and as a consequence “softening” occurred. This leads to physical instability during the experiment and a sudden failure. In a similar manner,

during computational modeling, the post-peak behavior of the arch led to numerical instability and thus sudden failure.

For all the C-beam specimens, the internal strains from C-STM shows similar trends with the experimentally obtained strain data. Although the strains do not precisely match with the experimental data, the trends are nevertheless indicative. Differences can be ascribed to the fact that strain gages were located across cracks, and hence the data obtained from the strain gages may not necessarily be truly indicative of the average strains between the nodes in the structure. This provides evidence that the C-STM not only models the macro-behavior well, but also represents quite well the behavior at the micro-level.

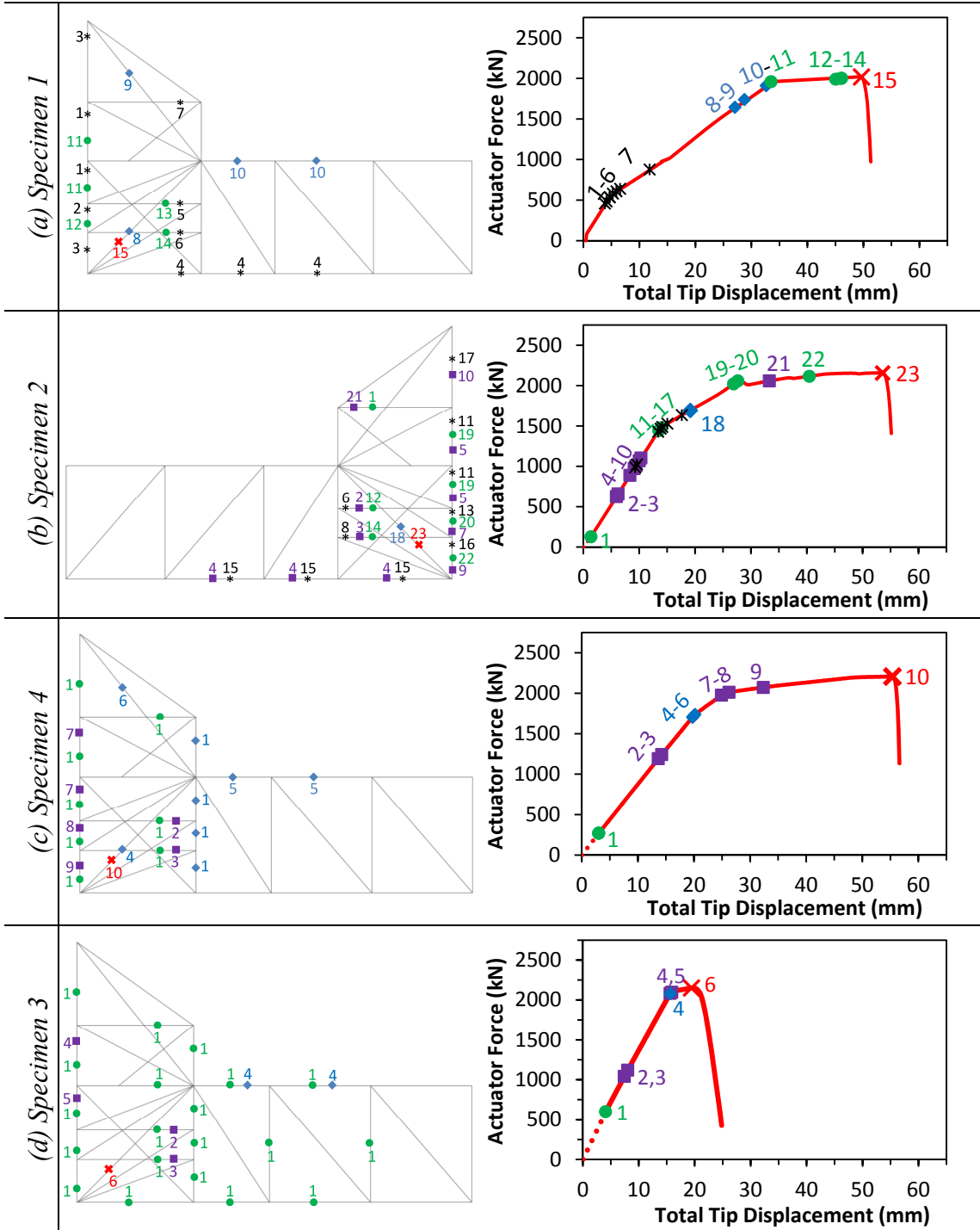
#### **8.6.4 Failure Analysis**

All the nonlinear mechanisms that developed progressively in the various constituent members of the C-STM are presented in this sub-section. Figure 8-11a–d show the development of nonlinear hinges formed during the C-STM analysis (left column of Figure 8-11) of the four specimens. When this information is combined with the overall force-deformation behavior of the specimens (the graphs in Figure 8-11), some insight into the progression of nonlinear hinge formation with respect to the global force-deformation behavior of the structure is obtained. These modeled outcomes shown in Figure 8-11 agree well with the visual observations made during each experiment.

It should be noted that Specimens 3 and 4 were heavily cracked due to the effects of ASR/DEF related expansion. Therefore, for Specimens 3 and 4 the concrete tensile strength is neglected in the C-STM analysis. As noted earlier, prestress forces are applied to the C-STM model to simulate the effects of expansion caused by ASR/DEF on the structure. Concrete decompression in Figure 8-11 refers to the stage when the effects of the applied prestress are overcome by the applied loading and the concrete strains become tensile (positive).

Based on field observed strain gage data in Specimens 2, 3, and 4, it is evident that the reinforcement yielded prior to testing. Similar observations are made in the C-STM analysis. For Specimens 1 and 2, a major change in stiffness in the force-

✱ Concrete Cracking ◆ Concrete Compression ■ Concrete Decompression ● Steel Yield ✕ Concrete Crushing



Note: Specimens 1, 2, 4, and 3 respectively, had no, slight, moderate, and heavy ASR/DEF damage.

**Figure 8-11: Computed Sequence of Nonlinear Behavior Events.**

deformation behavior occurs when the longitudinal steel in the beam-column region yielded (Event 11 in Figure 8-11a, and Events 19–20 in Figure 8-11b, respectively). However, in Specimen 4 the major change in stiffness of the force-deformation behavior happens when decompression occurs in the longitudinal concrete member in the beam and the beam-column region of the specimen (Events 7–8 in Figure 8-11c). Similar observations are also made for Specimen 3 where the major change in stiffness occurs during the decompression of longitudinal concrete members in the beam and beam-column region (Events 4–5 in Figure 8-11d) just before the failure of the specimen.

From Figure 8-11 it is evident that by overlaying the commencement of formation of nonlinear hinges in the different members of the C-STM on the overall force-deformation behavior of the specimen, a deep insight into the internal mechanism of the specimen behavior can be obtained.

It is also of interest to investigate the actual cause of failure in order to avoid any misconceptions about the failure mode. Due to the extent of relatively serious damage at the CTT node of the knee joint, it is tempting to surmise this led to the failure of the structure. However, an in-depth forensic analysis into the strains parallel and perpendicular to the arch strut in the beam-column joint is instructive in shedding some light into the actual cause of failure of the structure. Figure 8-12 shows the strains measured parallel to the strut (and crack) along with the strains measured perpendicular to the crack from the experiment and the C-STM analysis. Given the vagaries of strain measurements in highly cracked concrete elements, satisfactory agreement between the experimental observations and the computed response is evident. This agreement provides some further vindication of the adopted C-STM minimalist model.

It is evident from Figure 8-12 that the strains measured perpendicular to the cracks are significantly higher in the beam-column joint when compared to the beam region. The tensile strain acting orthogonal to the compression member results in the concrete softening phenomenon, which causes a reduction in the compressive strength of the concrete arch. This fully explains why the failure occurred in the beam-column joint

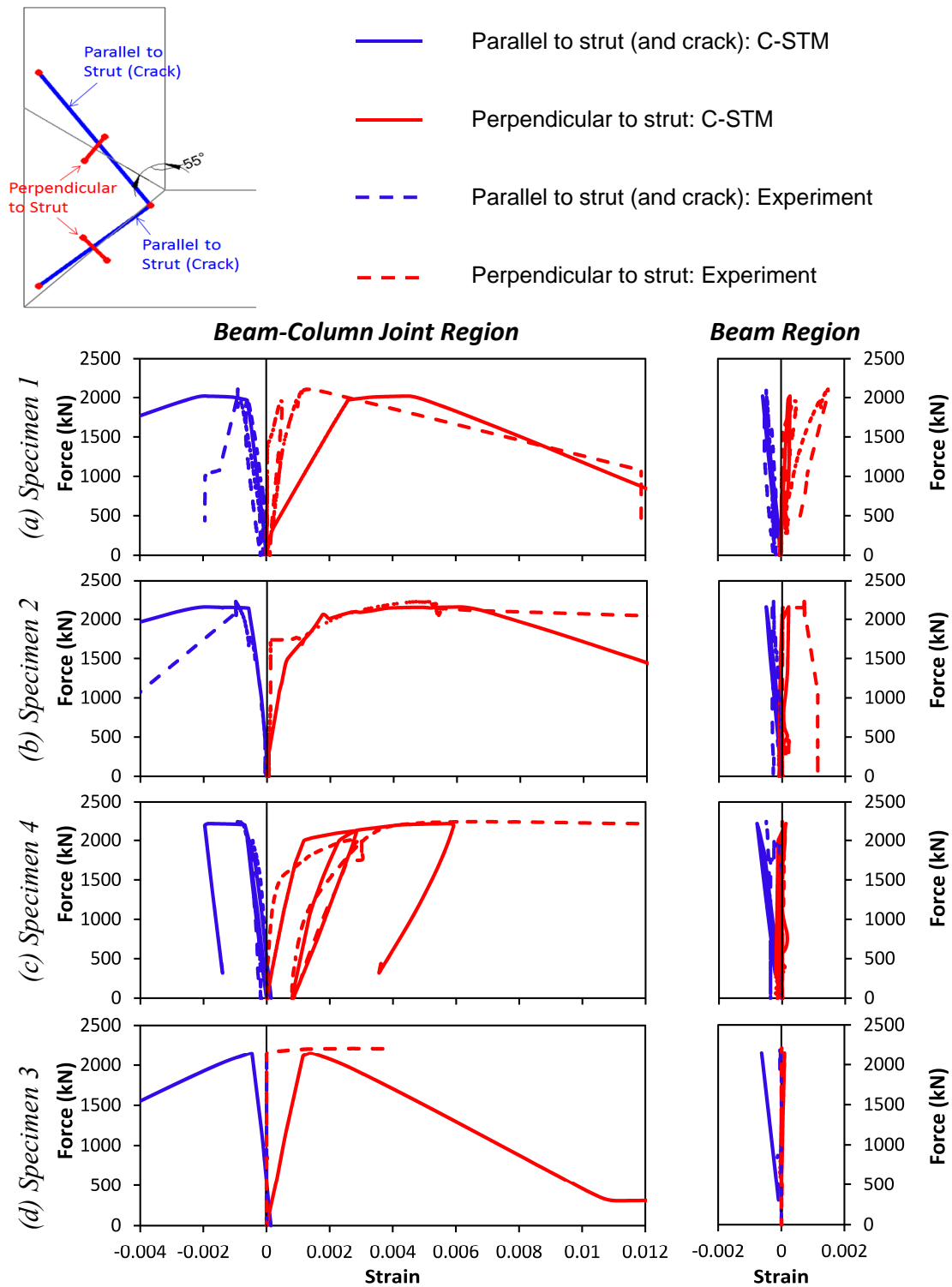


**Figure 8-12: Comparison of Strains Parallel and Perpendicular to Crack in the Joint and Beam Region.**



and not in the beam region of the structure. Based on the experimental and computational evidence, the final sequence of events is postulated as follows:

- Concrete softening phenomenon causes concrete arch to fail in the beam-column joint.
- Significant out-of-plane concrete dilation concurrently results.
- Hoops in the beam-column joint attempt to restrain this dilation.
- As the hoops are lapped and not adequately hooked between the two outer faces of steel, the lack of transverse confining action causes large dilation to develop with consequent failure of the core concrete near the CTT node region.
- Cover concrete (unconfined) outside the CTT node region crushes and spalls off.

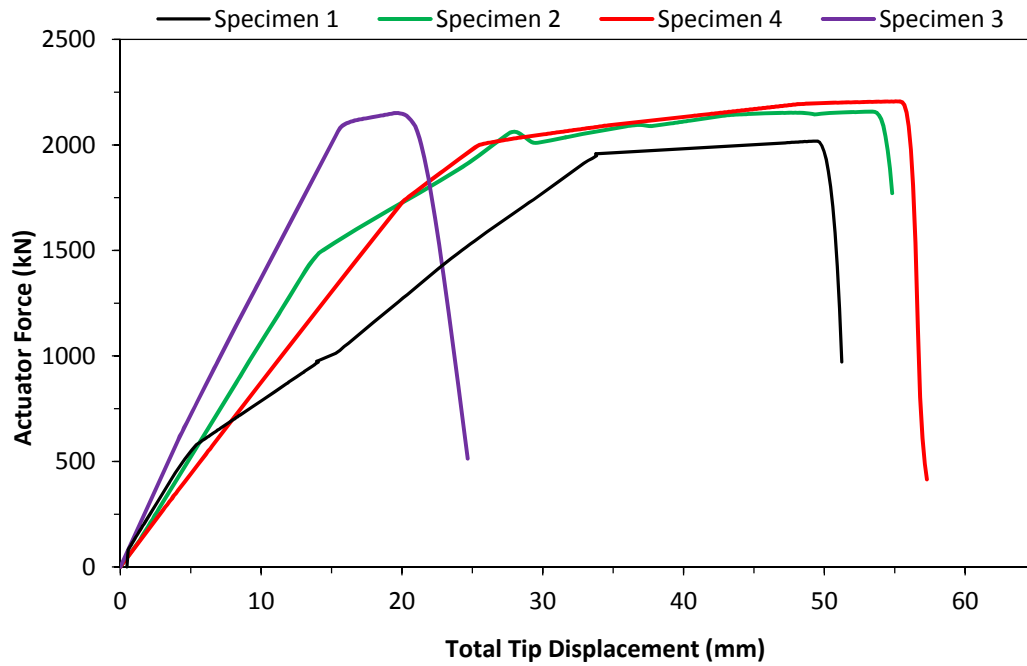
In summary, it is clearly evident from the above that the final event which results in the collapse of the C-beam specimens without and with ASR/DEF damage is the compression softening of the corner-to-corner (arch) strut in the beam-column joint and the CTT node failure is an outcome of that failure mechanism.

## **8.7 Discussion**

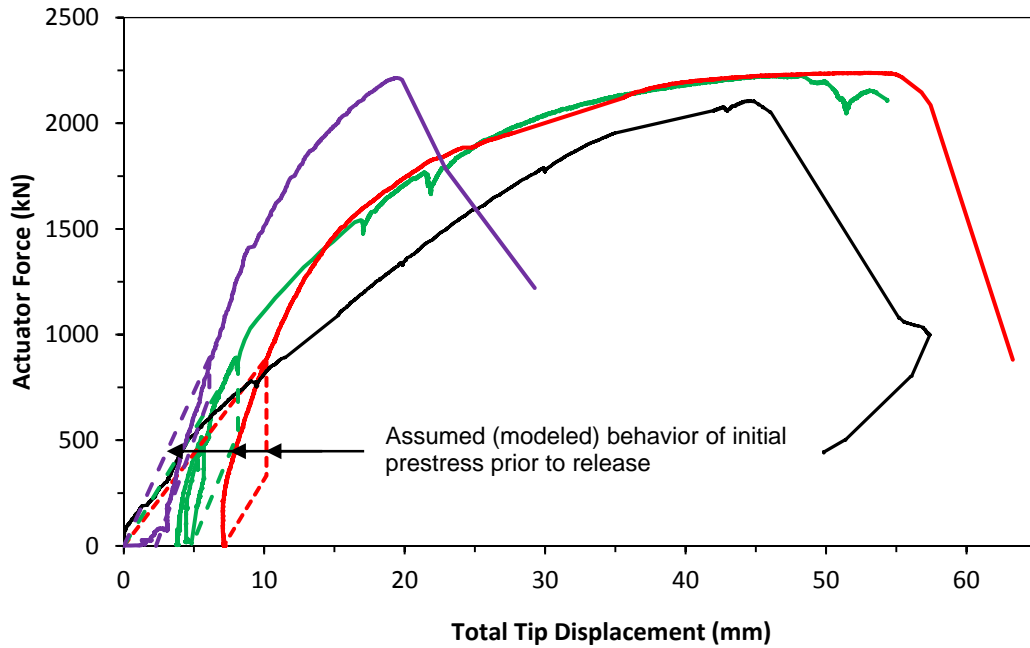
Figure 8-13a shows overall force-deformation behavior of all the four C-beam specimens obtained from the C-STM model. The stiffness change in the control Specimen 1 at about 578 kN was due to the first cracking of concrete. For Specimens 2, 4, and 3, the major stiffness changes were at 1490 kN, 2002 kN, and 2068 kN, respectively. This change in stiffness happened when the decompression of the prestress effect occurred at the critical cross-sections.

Figure 8-13b presents the experimental performance of the C-beam specimens. The behavior of the specimens during the initial prestress process was not captured accurately. Therefore, the initial displacement of the experimental results is offset based on the C-STM observations.

It is evident from Figure 8-13 that the computationally modeled C-STM results are in good agreement with the experimental observations from the C-beam specimens.



(a) C-STM Results



(b) Experimental Performance

Figure 8-13: Force-Deformation Results for C-beam Specimens.

A comparison between the C-STM and experimental ultimate load capacity for the four C-beam specimens is presented in Table 8-3. As shown by the ratio C-STM/Expt. in Table 8-3, the ultimate load computed from the C-STM is slightly conservative with a difference of not more than four percent.

The various levels of deterioration caused by ASR/DEF expansion on the concrete structure were also successfully modeled into the C-STM, and the results are in good agreement with the experimental observations. The C-STM also overcomes the difficulties associated with identifying the cause of failure and the failure mechanism associated with the C-beams. Additionally, they also provide an insight into the sequence of behavior modes that led to the failure of the structure and if the structural response was ductile or brittle.

**Table 8-3: Ultimate Load Capacity of C-beam Specimens.**

	<b>C-STM (kN)</b>	<b>Experiment (kN)</b>	<b>C-STM/Expt.</b>
Specimen 1 ( <i>Undamaged Control Specimen</i> )	2019	2108	0.96
Specimen 2 ( <i>Slight ASR/DEF deterioration</i> )	2157	2224	0.97
Specimen 4 ( <i>Moderate ASR/DEF deterioration</i> )	2206	2237	0.99
Specimen 3 ( <i>Heavy ASR/DEF deterioration</i> )	2154	2215	0.97

### **8.8 Key Findings from C-STM Modeling**

As discussed and shown in this section, although the beam methods and the SAT method give some indication of the strength of the structure, they are unable to predict the overall behavior of the structure. It is also not known how to model the damage caused

by the effects of ASR/DEF on the structure into these methods. The C-STM technique has definite advantages and is summarized below:

- The C-STM is capable of modeling the overall performance and the internal behavior of the structure, and the results compare well with the experimental observations.
- The additional strength and stiffness of deteriorated specimens as observed from the experimental and C-STM results is attributed to the concrete swelling due to ASR/DEF effects, which in turn puts the reinforcement steel into a state of active prestress. These effects, when appropriately modeled in the C-STM, capture well the overall behavior of the structure.
- By taking into account the appropriate material properties and the prestressing effects caused by ASR/DEF expansion, *slight*, *moderate*, and *heavy* levels of deterioration caused by ASR/DEF expansion can be directly modeled in the C-STM analysis.
- From a failure analysis based on the results obtained from the C-STM, the trigger mechanism and the final cause of failure of the structure can be accurately captured, which at times is elusive during experimental investigations.
- The C-STM approach gives the engineer/analyst insight into the complexities of the internal behavior throughout the structure and the D-regions in particular, and finally identifies the actual cause of failure.

## 9 C-STM APPLICATION TO TEXAS BRIDGE PIERS\*

### 9.1 Summary

It is important to analyze the overall load-deformation behavior of large concrete bridge piers that may be subject to premature concrete deterioration caused by ASR/DEF expansion. The ASR/DEF expansion model that was presented in Section 4 is used to estimate the maximum possible expansion strain in the various regions of the deteriorated bridge piers. An estimate of the parameters required for the expansion model is also made based on free expansion tests on core samples extracted from the structure. Estimates are made on the maximum possible total crack widths that may be observed. The prestressing forces to be applied on the longitudinal and transverse members of the C-STM to account for the effects of ASR/DEF are also estimated based on the expansion model. Modified concrete cover and core properties are determined and the C-STM analysis is performed for the bridge piers without and with the effects of ASR/DEF induced deterioration. The C-STM analysis results show that the load carrying capacity of the structure is beyond its design load capacity. In addition, the force-deformation response of the bridge pier with ASR/DEF deterioration is stiffer with lower ductility, and the load carrying capacity is not significantly negatively impacted. However, the estimated crack widths are beyond acceptable in-service standards, and these cracks may act as pathways for moisture into the bridge pier that may cause aggressive reinforcement corrosion. The ASR/DEF expansion model and the C-STM analysis technique can be used in conjunction to estimate the force-deformation behavior, internal behavior, and failure sequence of reinforced concrete structures with ASR/DEF deterioration. Although, there is no significant negative impact on the load carrying capacity of the bridge pier, the excessive amounts of cracking caused by

---

\* Previously published work is available to the public through National Technical Information Service. Mander, J.B., Bracci, J.M., Hurlbaas, S., Grasley, Z., Karthik, M.M., Liu, S-H., and Scott, R.M. (2012). "Structural Assessment of "D" Region Affected by Premature Concrete Deterioration: Technical Report." Report No. FHWA/TX-12/0-5997-1, Texas A&M Transportation Institute, College Station, Texas, USA.

ASR/DEF expansion could be a cause of concern and may lead to hidden reinforcement corrosion.

## **9.2 Introduction**

A significant number of large concrete structures in Texas exhibit premature concrete deterioration, a large portion of which is attributed to the effects of ASR/DEF induced expansion in concrete. Previous experimental observations show that severe concrete cracking is possible in structures affected by these deterioration mechanisms. The appearance of these structures provide an impression that they may be unsafe, and is a cause of major concern for inspecting engineers and the members of the public alike. It is essential to investigate the serviceability and structural longevity of these deteriorating concrete structures, to establish if they can perform in a safe manner for the remainder of their service life.

As demonstrated in earlier sections, existing code-based analysis and design techniques are based on the performance of sound concrete and have limitations in assessing the performance of structures that show signs of potential premature deterioration. The tools that were developed in the earlier sections to assess the expansion strains caused by ASR/DEF are used to estimate the progression of strains with time, and the total crack widths. In addition, to evaluate the overall force-deformation behavior of the structures, the C-STM analysis technique is employed.

In this investigation, two bridge piers that are part of the San Antonio “Downtown Y” located along I-10 and I-35 in Bexar County, are analyzed. An eight mile stretch of I-10 and I-35 west of downtown San-Antonio were double-decked to increase the traffic lane capacity. The project was constructed in multiple phases from 1984 to 1991. Two large bridge piers, H19C and I5C, which are part of the Downtown Y have since shown signs of premature concrete deterioration caused by ASR/DEF related expansion. The problem commenced within a few years after construction and remains a cause of concern. While the pier-cap of H19C was post-tensioned, pier I5C is a reinforced concrete structure. The aim of this investigation is to estimate the possible amount of ASR/DEF related expansion strains in the structure, and assess whether these

large bridge piers are or could become in jeopardy of losing a measure of their strength capacity due to ASR/DEF effects, and whether the general safety of the bridge is now or will in the future be impaired.

### **9.3 Analysis Methods**

#### **9.3.1 ASR/DEF Expansion**

The minimalist semi-empirical model that was developed in Section 4 to simulate the evolution of expansion strains with time in reinforced concrete structures is used to model the expansion strains that piers H19C and I5C may be subjected to. The major challenge in modeling expected cracking in concrete structures with ASR and/or DEF expansion potential, is determining appropriate values of the maximum free expansion strain  $\varepsilon_o^{\max}$ , the associated rise time  $t_r$ , and the expansion initiation time  $t_o$ . For ASR, it may be possible to infer appropriate parameter values if the source of the aggregate, supplier, and mix design are known. The heat of hydration, which is the primary cause of DEF potential, may be assessed if the weather and curing conditions at the time of concrete casting are known. Better still, it would be ideal to have standard concrete specimens subject to free-expansion tests during the inception of construction, to establish the maximum free expansion strain and the rise time of the constituent concrete. It might also be feasible to evaluate these parameter based on free expansion tests performed on cores extracted from the structure. However, there are various limiting factors, and all of this aforementioned information is seldom available.

In the absence of any information available at the time of casting of a structure, a solution based on the maximum expansion strain  $\varepsilon_o^{\max}$  and rise time  $t_r$  observed in the experimental C-beam specimens tested herein may be used. This may be considered as an upper-bound solution owing to the reason that the experimental C-beam specimens were intentionally subjected to severe material and environmental conditions to promote accelerated ASR and DEF expansion.

To simplify the analysis, a satisfactory solution may be obtained if time steps of one month are used. Figure 9-1 shows the average monthly maximum and minimum

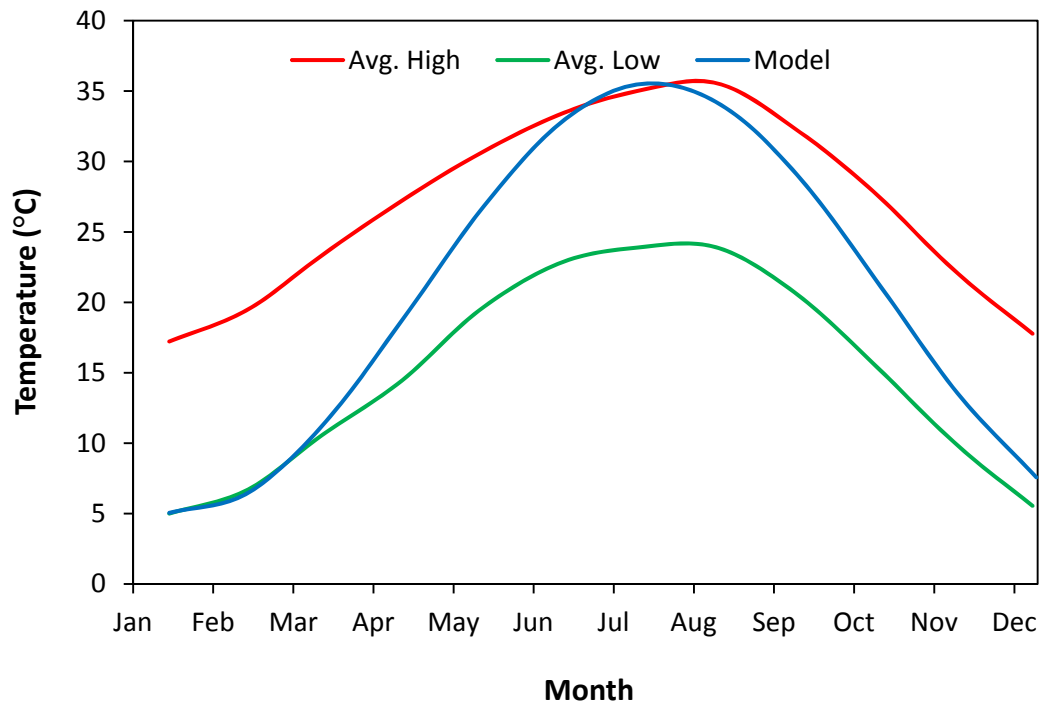


**Figure 9-1: Model Representing the Maximum and Minimum Temperature Variations in a Year in San Antonio, TX.**



temperatures recorded in San Antonio, TX. Also shown in Figure 9-1 is the model used to simulate the variation of this monthly average temperatures. In the winter months at low temperatures the ASR/DEF induced expansion slows down compared to the hot summer months. A sine curve, presented in (9-1), is used to capture the maximum and the minimum temperatures  $T$  in the summer and winter months respectively.

$$T = \left( \frac{T_{\max} + T_{\min}}{2} \right) + \left( \frac{T_{\max} - T_{\min}}{2} \right) \sin \left( \frac{2\pi(t - t_a)}{365} \right) \quad (9-1)$$

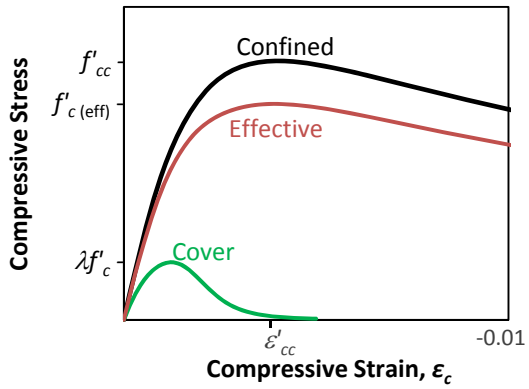
where  $T_{\max}$  and  $T_{\min}$  are respectively the recorded maximum average summer and minimum average winter temperature;  $t_a = 140$  days (assumed to represent San Antonio temperature data); and  $t =$  time in days.

### 9.3.2 C-STM Analysis

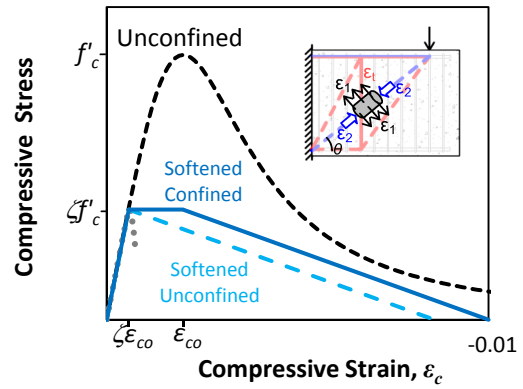
The force-based C-STM analysis technique that was developed by Scott et al. (2012a, b) and later converted to a more universally applicable displacement-based analysis in Section 3 is used herein to analyze bridge piers H19C and I5C. The effects of ASR/DEF on these concrete structures is taken into account by modifying the associated material properties; specifically the deteriorated cover concrete, the confined core concrete strength, and the softened concrete properties. As both the cover and core concrete areas contribute to the area of the strut in the C-STM model, as shown in Figure 9-2a, a weighted average of concrete compressive strength is used for the “effective” arch and strut members in the C-STM model. The effects of tensile strains transverse to diagonal compression members are taken into account through the concrete softening coefficient  $\zeta$  given by:

$$\zeta = \frac{1}{1 - 0.25(\varepsilon_1/\varepsilon_2)} \quad (9-2)$$

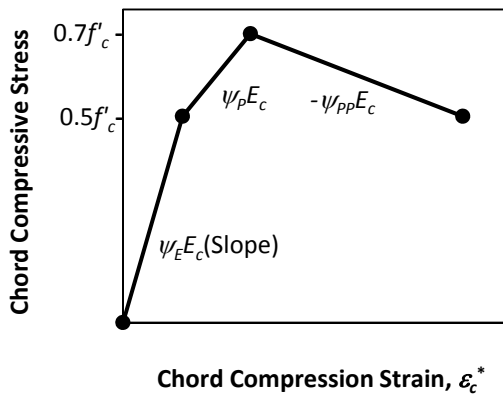
where  $\varepsilon_2 =$  the compressive strain parallel to the diagonal strut or arch members; and  $\varepsilon_1 =$  the tensile strain transverse to the strut, and is inferred using dummy tie elements in the C-STM.



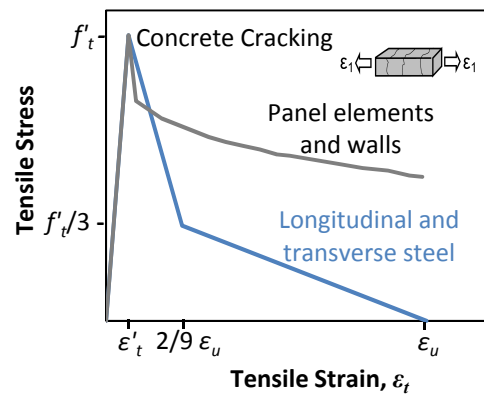
(a) Effective Concrete Strength



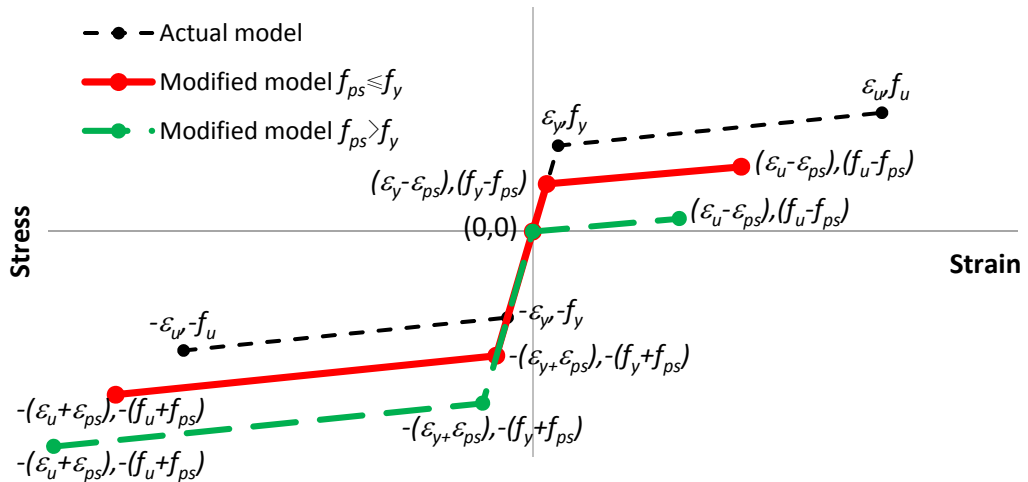
(b) Softened Concrete Model for Diagonal Web Elements



(c) Compression Chord Members



(d) Tension Stiffened Members



(e) Modified Steel Behavior to Account for Prestressing Effects due to ASR/DEF

Figure 9-2: Cracked Reinforced Concrete Material Properties.

Figure 9-2b shows the softened confined and softened unconfined concrete models. Softened unconfined concrete occurs where there is an absence of completely enclosed or hooked hoops around a badly strain-damaged concrete section which results in large transverse strains. Figure 9-2c shows the stress-strain relation for concrete chord members in compression where  $\psi$  = the compatibility correction factor (Scott et al., 2012a) that transforms the centroid of the concrete stress block to the centroid of the compression reinforcement. Figure 9-2d shows the stress-strain relation for concrete tension stiffened members.

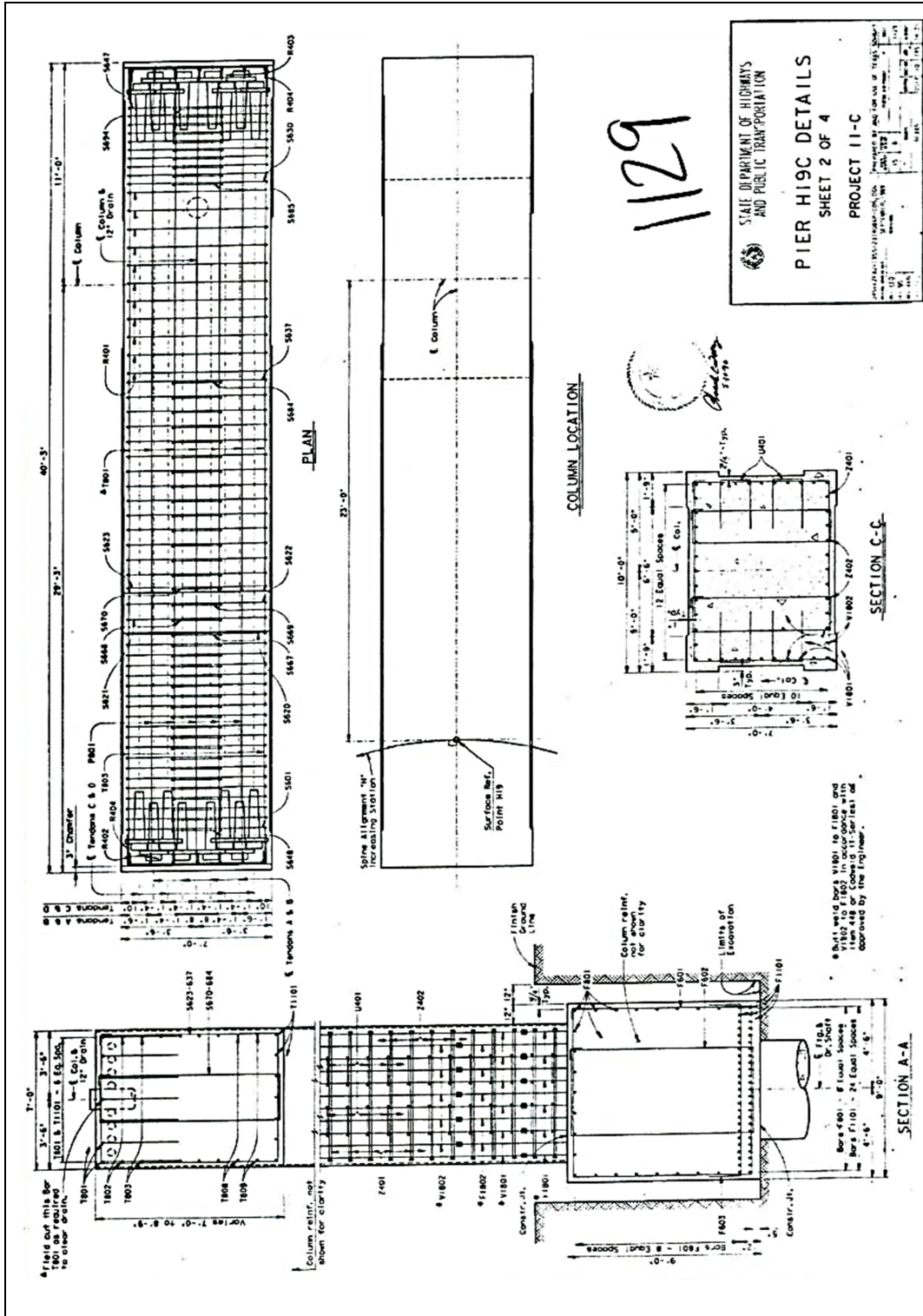
The constraint imposed by longitudinal reinforcement and transverse hoops to the swelling of core concrete in turn puts the reinforcing steel into a state of tensile strain, which in turn puts the concrete into a state of prestress. The prestressing forces are evaluated based on the ASR/DEF induced expansion strains in the specimen, at the end of its exposure period. Appropriate modifications, as shown in Figure 9-2e, are made to the stress-strain relation of reinforcing steel to account for the prestress effects.

## **9.4 Analysis of Pier H19C**

### **9.4.1 The Structure**

Figures 9-3 and 9-4 present the construction drawings for the reinforcing layout and cross-section of pier H19C. The overall height of the pier from the column footing is 8.23 m. Included in this height is the cap beam whose overall length is 12.27 m. The free cantilever portion that extends from the face of the column is 7.39 m long. The longitudinal reinforcement for the column consists of a total of 44 #18 (57 mm) rebars with eleven bars along each of the short and long faces. The cantilever portion consists of two different rectangular cross-sections with overall depths varying between 2.67–2.13 m and 2.13–1.83 m. The top (tensile) and bottom (compressive) reinforcement consist of seven #8 (25 mm) and #11 (35 mm) bars, respectively, with additional #8 bars distributed along the side faces of the beam to provide torsional strength. Transverse reinforcement in the column is provided by #4 (13 mm) closed stirrups with a center-to-center spacing of 305 mm. For the bent-cap beam, #6 (19 mm) closed double stirrups





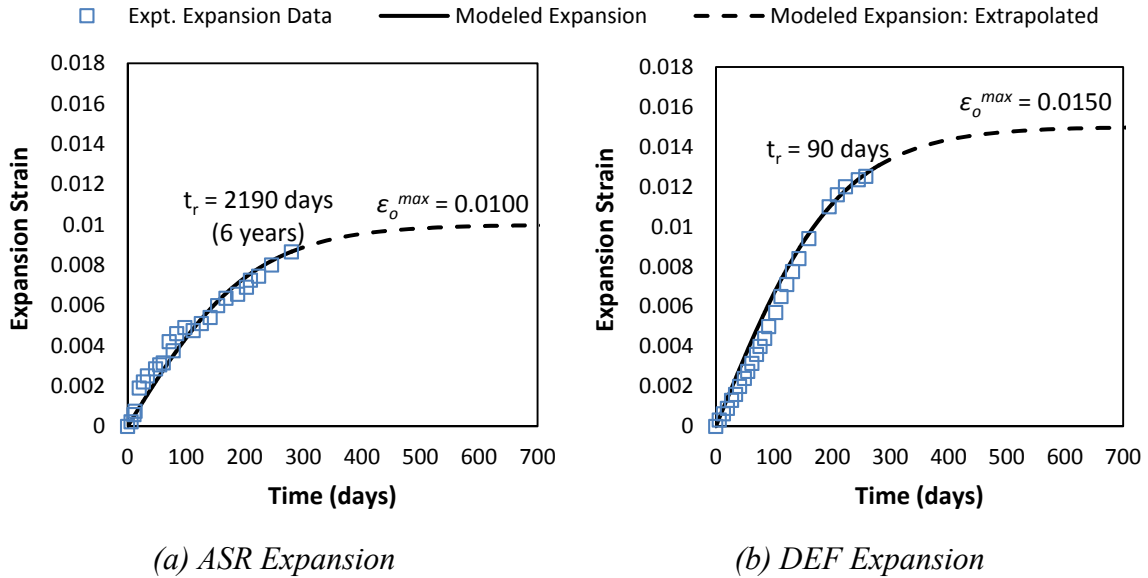
with varying spacing are used. Grade 60 steel with yield strength  $f_y = 414$  MPa is used throughout for longitudinal and transverse reinforcement. The compressive strength of concrete specified during construction was  $f'_c = 34.5$  MPa. Since, existing in-situ strength of steel and concrete is not available; the specified design strengths have been adopted for the analyses.

The bent-cap is post-tensioned (PT) using eight tendons, each consisting of 19 15.2 mm diameter strands with an ultimate tensile strength of 1862 MPa. The strands were post-tensioned to a total of 24600 kN. The PT tendons are straight in the free cantilever portion, but have a draped profile over the beam-column joint region. At the crown point the draped tendon is 229 mm below the upper face of the concrete pier.

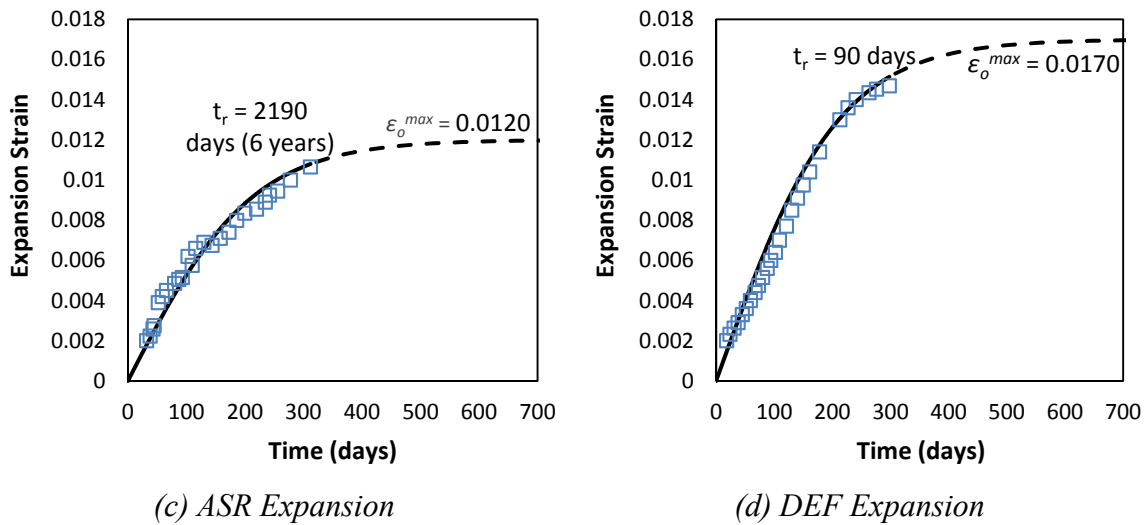
#### **9.4.2 Modeling Potential Free Expansion Strain due to ASR and/or DEF**

To perform a realistic assessment of ASR/DEF induced expansion strains within pier H19C, it is essential to identify the input parameters required for the proposed expansion model based on field evidence. Specifically, the expansion initiation time  $t_o$ , the maximum expansion strain  $\varepsilon_o^{\max}$ , and the expansion rise time  $t_r$  have to be determined. The San Antonio “Y”, of which pier H19C is a part of, was built in the mid-1980s to the early part of 1990s. It is reported by Boenig et al. (2000), that in late 1995 the department of transportation became aware of premature concrete deterioration in a large number of bridge piers belonging to the San Antonio “Y” system. Therefore, for this study it is assumed that the initiation time of the expansion strains was in the early 1995, which results in  $t_o \approx 5$  years.

To study the expansion potential of pier H19C, Williams (2005) and Folliard et al. (2006) conducted free expansion tests on concrete cores extracted from the pier. The ASR susceptibility was determined by a modified ASTM C1260 test where the cores were immersed in a one normal Sodium Hydroxide (NaOH) solution at 80°C. Similarly, the DEF potential was studied from core samples stored in water at 22.8°C. Data points in Figure 9-5 shows the experimentally recorded ASR and DEF induced expansion potential from core samples. The modeled expansion potential based on the recorded



*Free Expansion Strains Assuming the Cores were taken from a 'Quiet Zone'.*



*Free Expansion Strains Assuming Expansion Strains Equal to Reinforcement Yield Strain Existed Prior to when Cores were Extracted.*

**Figure 9-5: Modeling Free Expansion Results for Parameter Identification.**

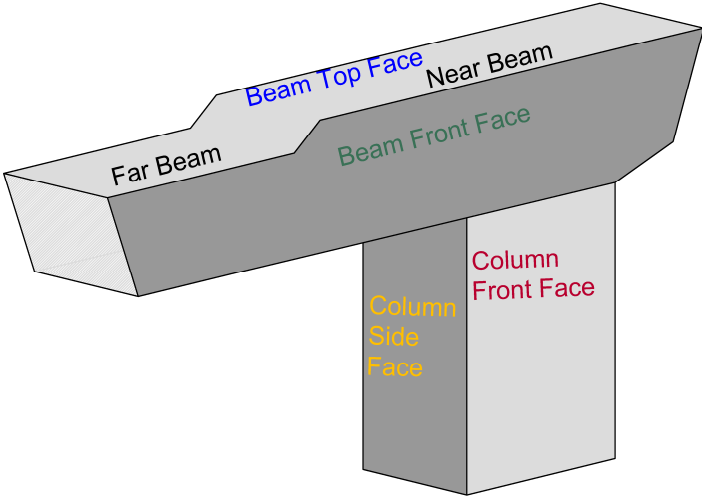
data, and the model parameters  $t_r$  and  $\varepsilon_o^{\max}$  are also shown in Figure 9-5. The cores were extracted from a region in the specimen where relatively less damage due to ASR/DEF expansion were observed, and it is hypothesized that the cores were extracted from a ‘quiet zone’. A ‘quiet zone’ is defined herein as that zone that is roughly midway between major cracks and is mostly undamaged. Thus results plotted in Figure 9-5a, b assume that there was no prior ASR/DEF expansion that took place in the region where the cores were extracted from. Therefore, this may be viewed as the lower bound, or the least expansion that can be expected in the constituent concrete. However, because of the uncertainty associated with this assumption and lack of more conclusive evidence, Figure 9-5c, d show the modeled free expansion strains assuming that expansion strains corresponding to the reinforcement yield strain existed before the cores were extracted from the pier. This may be considered as the likely case for free expansion, whereas the parameters adopted from the C-beam specimens in Section 5 may be considered as the upper bound. Since the ASR and DEF expansion tests were performed at different temperature and test conditions, it is not appropriate to combine the measured ASR and DEF free expansion strains. Therefore, in the following section, the expansion strains due to ASR and DEF are modeled separately, and then their results combined to assess the overall range of possible expansion strains.

#### **9.4.3 Expansion Strain Modeling based on Experimental Evidence from C-beam Specimens**

In the absence of information available from core samples, it is essential that these parameters be estimated from previously observed experimental evidence. In the present study, the maximum possible upper-bound expansion solution is established based on the parameters  $\varepsilon_o^{\max} = 0.05$  and  $t_r = 120$  days observed in the experimental C-beam specimens. The degree of saturation is assumed as  $S = 0.01$ . The parameter  $S$  does not affect the maximum expansion strain  $\varepsilon_\rho^{\max}$ , but only affects the rate at which this strain is achieved.



Sheet 9-1a shows the various regions of pier H19C identified to model the ASR/DEF expansion strains. To simulate the expansion strains in the various regions of pier H19C, it is important to carefully determine the reinforcement ratio. As the full yield strength of the reinforcement is not developed within the bar development length (Mander et al., 2011), the reinforcement ratios for the C-STM members within the development length zone are scaled down accordingly. The C-STM model for pier H19C (presented later) is used to determine the tensile and compressive prestrains in the members due to the dead weight of the pier and the girders, and the post-tension load. The computation of the reinforcement ratio and the maximum expansion strains for the various regions of pier H19C is presented in engineering computation Sheets 9-1a to k.

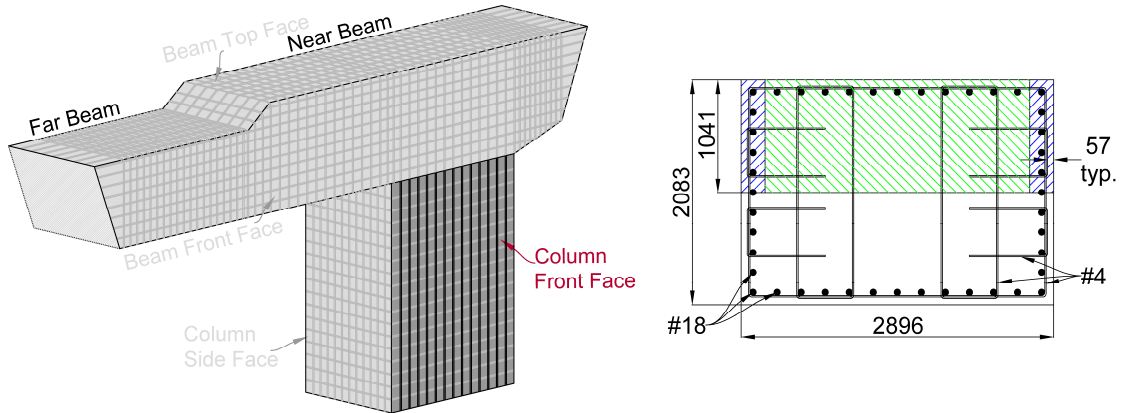
Sheet 9-1 a	COMPUTATION OF REINFORCEMENT RATIO $\rho$ AND MAXIMUM EXPANSION STRAIN $\epsilon_{\rho}^{\max}$ FOR PIER H19C	1 11
GENERAL NOTES		
<p><u>Computation of Reinforcement Ratio</u></p> <p>In all the cases presented below for computing the longitudinal reinforcement ratio, the following points are to be noted. Outside the development length zone, all the reinforcement steel and concrete, in the entire depth of the cross-section considered, contribute to the reinforcement ratio. However, within the development length zone, the effects of localized reinforcement were considered. The total area of reinforcement along the longitudinal member edges (shaded blue in the cross-section) are much greater when compared to the region away from the member edge (shaded green in the cross-section). Therefore, the region away from the longitudinal member edges will see greater expansion. Hence, for regions within the development length zone the reinforcement ratio corresponding to the region away from the longitudinal edges are scaled accordingly based on their distance.</p>		
		

Sheet 9-1 b	COMPUTATION OF REINFORCEMENT RATIO $\rho$ AND MAXIMUM EXPANSION STRAIN $\epsilon_p^{\max}$ FOR PIER H19C	2 11	
GENERAL NOTES (CONT.)			
<u>General Parameters Used</u>			
$f'_c = 34.5 \text{ MPa}$	$\epsilon'_t = 0.000125$	$\epsilon_y = 0.00207$	$\epsilon_o^{\max} = 0.05$
$E_c^{\text{actual}} = 29255 \text{ MPa}$	$f_y = 414 \text{ MPa}$	$n = \frac{E_s}{E_c/3} = 20.51$	$t_r(\theta_o) = 250 \text{ days}$
$f'_t = 3.65 \text{ MPa}$	$E_s = 200 \text{ GPa}$		$t_o = 1000 \text{ days}$
<u>Maximum Expansion Strain</u>			
<p>The structure was subjected to a combination of PT loads and gravity loads, which may result in few sections of the structure being precracked and certain others in compression. Due to the complex nature of the structure and the combined loading conditions, the tensile and compressive prestrains were obtained from the C-STM analysis of the structure. The structure is subjected to the gravity loads from the pier and the girder and the PT loads, to determine the prestrains. Eq. 4-14a (which is repeated below for convenience) was used in the computation of the expansion strains <math>\epsilon_p^{\max}</math>. Few other parameters that are required to compute <math>\epsilon_p^{\max}</math> are:</p>			
$P = 19719 \text{ kN}$	Far Beam	Near Beam	
$A_{ps} = 21290 \text{ mm}^2$	$A_c = 4227088 \text{ mm}^2$	$A_c = 5121280 \text{ mm}^2$	
$f_{ps} = 926.7 \text{ MPa}$	$\rho_{ps} = 0.00503$	$\rho_{ps} = 0.00416$	
$\epsilon_{ps} = 0.0046$	$\sigma_{\text{const}} = 4.67 \text{ MPa}$	$\sigma_{\text{const}} = 3.85 \text{ MPa}$	
$\epsilon_p^{\max} = \frac{\epsilon_o^{\max} \epsilon'_t + \rho n (\epsilon_y^2 - \epsilon_{\text{spre}}^2) - \epsilon_{\text{cpre}}^2 - \rho_{ps} n \epsilon_{ps}^2}{2 \left( \frac{\epsilon'_t}{2} - \epsilon_{\text{cpre}} + \rho n (\epsilon_y - \epsilon_{\text{spre}}) - \frac{\sigma_{\text{const}}}{E_c} \right)}$			4-14a
<u>Development Length (ACI 318-08)</u>			
Mander et al. (2011) established that to develop the full yield strength of the reinforcement, the reinforcing bars transverse to the member edge should be longer than the bar development length $l_d$ .			
#18 bars: $(l_d) = \left( \frac{f_y \psi_t \psi_e}{20 \lambda \sqrt{f'_c}} \right) d_b = \left( \frac{60000(1)(1)}{20(1)\sqrt{5000}} \right) \left( \frac{18}{8} \right) = 95.5" \times 25.4 = 2426 \text{ mm}$			
#8 bars: $(l_d) = \left( \frac{f_y \psi_t \psi_e}{20 \lambda \sqrt{f'_c}} \right) d_b = \left( \frac{60000(1)(1)}{20(1)\sqrt{5000}} \right) \left( \frac{8}{8} \right) = 42.4" \times 25.4 = 1077 \text{ mm}$			

Sheet 9-1 c	COMPUTATION OF REINFORCEMENT RATIO $\rho$ AND MAXIMUM EXPANSION STRAIN $\epsilon_p^{\max}$ FOR PIER H19C	3 11
----------------	---	---------

**COLUMN FRONT FACE**

Concrete and steel volume in half the section-depth  $d = 1041$  mm is considered for calculating the reinforcement ratio.



Separate reinforcement ratios are computed considering the blue and the green shaded regions separately and also for the entire shaded region (shaded blue + green). In this case the effects of tensile/compressive prestrains are neglected in the computation of  $\epsilon_p^{\max}$  as the column front face has a combination of both tensile and compressive strains.

$$\epsilon_{opre} = \epsilon_{spre} = 0$$

	Close to member edges (shaded blue)	For interior regions (shaded green)	Considering entire half-depth
Area of steel, $A_s$	12826 mm <sup>2</sup> (5-#18 bars)	28217 mm <sup>2</sup> (11-#18 bars)	53869 mm <sup>2</sup> (21-#18)
Area of concrete, $A_c$	(1041)(222.5) = 231622 mm <sup>2</sup>	(1041)(2450.6) = 2551075 mm <sup>2</sup>	(2896)(1041) = 3014736 mm <sup>2</sup>
$\rho$	0.05535	0.01106	0.01786
$\epsilon_p^{\max}$			0.0048

For members 1 and 5 that are within the specimen development length zone the reinforcement ratio in the interior regions (shaded green) is scaled down.

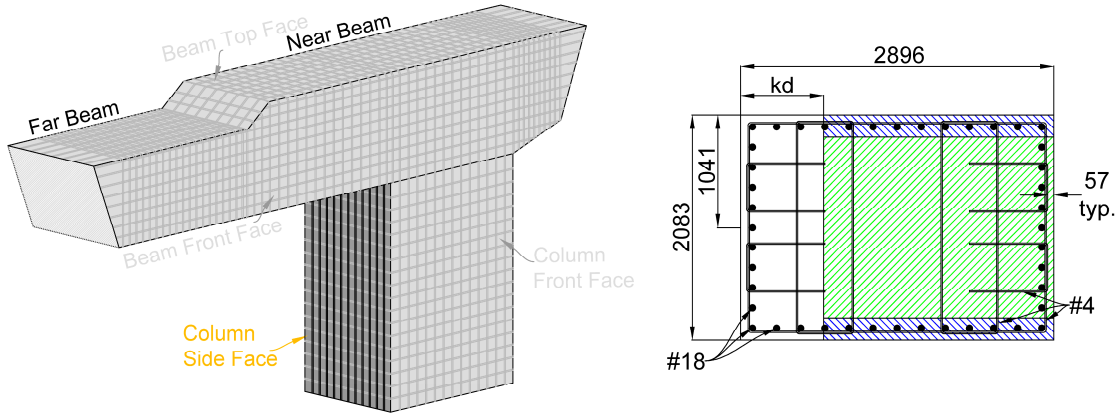
Scaled reinforcement ratio for Member 1/5

$l$	1418.8 mm
$\rho_{reduced} = \rho(l/l_d)$	0.01106(1418.8/2426) = 0.00647
$\epsilon_p^{\max}$	0.0101

Sheet 9-1 d	COMPUTATION OF REINFORCEMENT RATIO $\rho$ AND MAXIMUM EXPANSION STRAIN $\epsilon_p^{\max}$ FOR PIER H19C	4 11
----------------	---	---------

COLUMN SIDE FACE

Section depth  $d$  = overall depth  $D$  - depth to neutral axis  $kd_{col} = 2896 - 767.1 = 2129$  mm.



Separate reinforcement ratios are computed considering the blue and the green shaded regions separately and also for the entire shaded region (shaded blue + green).

The tensile prestrains computed from the C-STM model are  $\epsilon_{cpre} = \epsilon_{spre} = 0.000048$

	Close to member edges (shaded blue)	For interior regions (shaded green)	Considering entire half-depth
Area of steel, $A_s$	25652 mm <sup>2</sup> (10-#18 bars)	23087 mm <sup>2</sup> (9-#18 bars)	74391 mm <sup>2</sup> (29-#18)
Area of concrete, $A_c$	(2129)(204.2) = 434742 mm <sup>2</sup>	(2129)(1674.4) = 3565011 mm <sup>2</sup>	(2129)(2082.8) = 4434281 mm <sup>2</sup>
$\rho$	0.05904	0.00648	0.01678
$\epsilon_p^{\max}$			0.0051

For members 1 and 5 that are within the specimen development length zone the reinforcement ratio in the interior regions (shaded green) is scaled down.

Scaled reinforcement ratio for Member 1/5

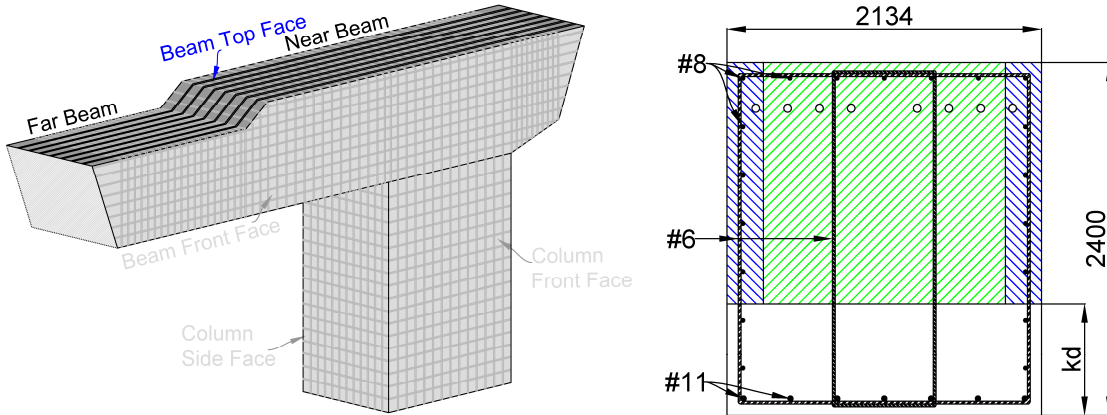
$l$	1418.8 mm
$\rho_{reduced} = \rho(l/L_d)$	0.00648(1418.8/2426) = 0.00379
$\epsilon_p^{\max} =$	0.0150

Sheet 9-1 e	COMPUTATION OF REINFORCEMENT RATIO $\rho$ AND MAXIMUM EXPANSION STRAIN $\epsilon_p^{\max}$ FOR PIER H19C		5 11
<b>BEAM TOP FACE-FAR BEAM</b>			
Section depth $d$ = overall depth $D$ - depth to neutral axis $kd_{col} = 1981 - 597 = 1384$ mm.			
Separate reinforcement ratios are computed considering the blue and the green shaded regions separately and also for the entire shaded region (shaded blue + green).			
The tensile prestrains computed from the C-STM model are $\epsilon_{cpre} = \epsilon_{spre} = -0.0001$			
	Close to member edges (shaded blue)	For interior regions (shaded green)	Considering entire half-depth
Area of steel, $A_s$	3040 mm <sup>2</sup> (6-#8 bars)	2534 mm <sup>2</sup> (5-#8 bars)	8614 mm <sup>2</sup> (17-#8)
Area of concrete, $A_c$	(1384)(246.6) = 341294 mm <sup>2</sup>	(1384)(1640.4) = 2270175 mm <sup>2</sup>	(1384)(2133.6) = 2952902 mm <sup>2</sup>
$\rho$	0.00890	0.00112	0.00292
$\epsilon_p^{\max}$			0.0047
For members 53 and 57 that are within the specimen development length zone the reinforcement ratio in the interior regions (shaded green) is scaled down.			
Scaled reinforcement ratio for Member 53/57			
$l$	965.2 mm		
$\rho_{reduced} = \rho(l/l_d)$	0.00112(965.2/1077) = 0.0010		
$\epsilon_p^{\max} =$	0.0055		

Sheet 9-1 f	COMPUTATION OF REINFORCEMENT RATIO $\rho$ AND MAXIMUM EXPANSION STRAIN $\epsilon_p^{\max}$ FOR PIER H19C	6 11
----------------	---	---------

**BEAM TOP FACE-NEAR BEAM**

Section depth  $d$  = overall depth  $D$  - depth to neutral axis  $kd_{col} = 2400 - 759.5 = 1640.5$  mm.



Separate reinforcement ratios are computed considering the blue and the green shaded regions separately and also for the entire shaded region (shaded blue + green).

The tensile prestrains computed from the C-STM model are  $\epsilon_{cpre} = \epsilon_{spre} = -0.000096$

	Close to member edges (shaded blue)	For interior regions (shaded green)	Considering entire half-depth
Area of steel, $A_s$	2534 mm <sup>2</sup> (5-#8 bars)	2534 mm <sup>2</sup> (5-#8 bars)	7601 mm <sup>2</sup> (15-#8)
Area of concrete, $A_c$	$(1640.5)(246.6) = 404547$ mm <sup>2</sup>	$(1640.5)(1640.4) = 2690912$ mm <sup>2</sup>	$(1640.5)(2133.6) = 3500171$ mm <sup>2</sup>
$\rho$	0.00626	0.00094	0.00217
$\epsilon_p^{\max}$			0.0060

For members 21 and 23 that are within the specimen development length zone the reinforcement ratio in the interior regions (shaded green) is scaled down.

Scaled reinforcement ratio for Member 21/23

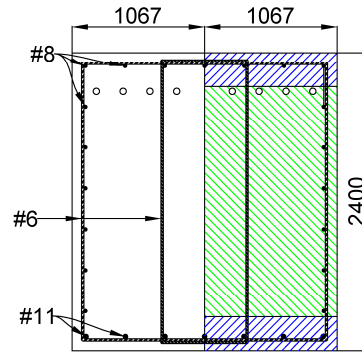
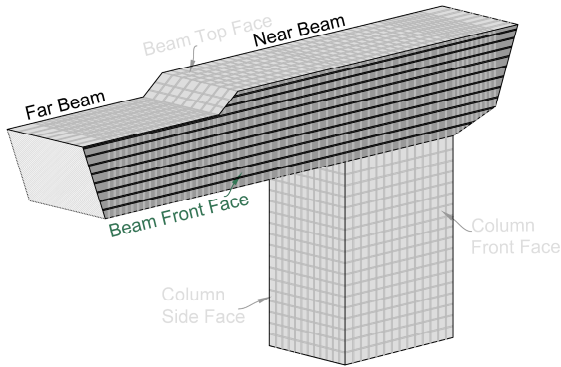
$l$	608.1 mm
$\rho_{reduced} = \rho(l/l_d)$	$0.00094(608.1/1077) = 0.00053$
$\epsilon_p^{\max} =$	0.0071

Sheet 9-1 9	COMPUTATION OF REINFORCEMENT RATIO $\rho$ AND MAXIMUM EXPANSION STRAIN $\epsilon_p^{\max}$ FOR PIER H19C		7 11
<b>BEAM FRONT FACE-FAR BEAM</b>			
Concrete and steel volume in half the section-depth $d = 1067$ mm is considered for calculating the reinforcement ratio.			
<p>Separate reinforcement ratios are computed considering the blue and the green shaded regions separately and also for the entire shaded region (shaded blue + green). In this case the effects of tensile/compressive prestrains are neglected in the computation of <math>\epsilon_p^{\max}</math> as the beam front face has a combination of both tensile and compressive strains.</p>			
$\epsilon_{spre} = \epsilon_{spre} = 0$			
	Close to member edges (shaded blue)	For interior regions (shaded green)	Considering entire half-depth
Area of steel, $A_s$	1520 mm <sup>2</sup> (3-#8 bars)	3040 mm <sup>2</sup> (6-#8 bars)	7434 mm <sup>2</sup> (9-#8 and 3-#11)
Area of concrete, $A_c$	$(1067)(351) = 374517$ mm <sup>2</sup>	$(1067)(1279) = 1364800$ mm <sup>2</sup>	$(1067)(1981) = 2113727$ mm <sup>2</sup>
$\rho$	0.00406	0.00223	0.00352
$\epsilon_p^{\max}$			0.0155
<p>For members 53 and 57 that are within the specimen development length zone the reinforcement ratio in the interior regions (shaded green) is scaled down.</p>			
Scaled reinforcement ratio for Member 53/57			
$l$	965.2 mm		
$\rho_{reduced} = \rho(l/l_d)$	$0.00223(965.2/1077) = 0.0020$		
$\epsilon_p^{\max}$	0.0218		

Sheet 9-1 h	COMPUTATION OF REINFORCEMENT RATIO $\rho$ AND MAXIMUM EXPANSION STRAIN $\epsilon_p^{\max}$ FOR PIER H19C	8 11
----------------	---	---------

**BEAM FRONT FACE-NEAR BEAM**

Concrete and steel volume in half the section-depth  $d = 1067$  mm is considered for calculating the reinforcement ratio.



Separate reinforcement ratios are computed considering the blue and the green shaded regions separately and also for the entire shaded region (shaded blue + green). In this case the effects of tensile/compressive prestrains are neglected in the computation of  $\epsilon_p^{\max}$  as the beam front face has a combination of both tensile and compressive strains.

$$\epsilon_{opre} = \epsilon_{spre} = 0$$

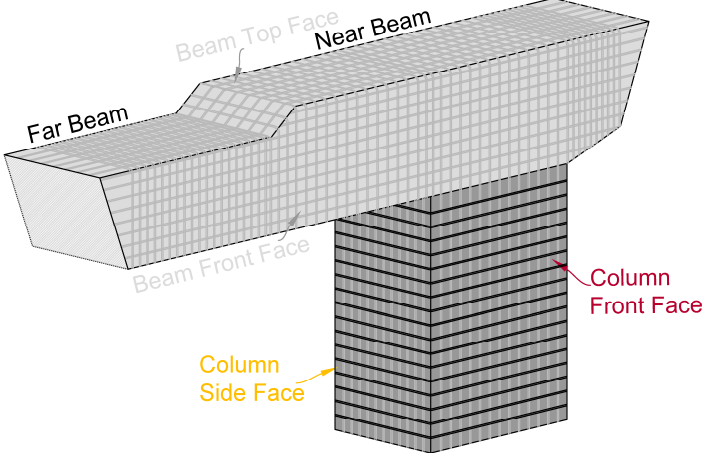
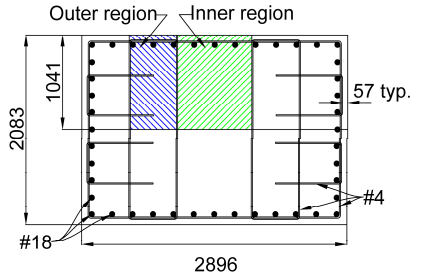
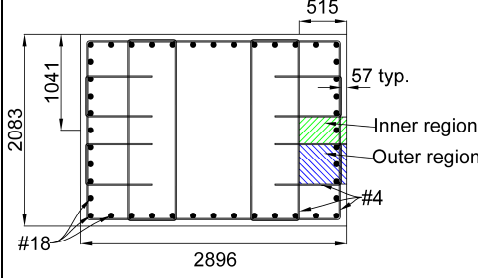
	Close to member edges (shaded blue)	For interior regions (shaded green)	Considering entire half-depth
Area of steel, $A_s$	1520 mm <sup>2</sup> (3-#8 bars)	3040 mm <sup>2</sup> (6-#8 bars)	7434 mm <sup>2</sup> (9-#8 and 3-#11)
Area of concrete, $A_c$	$(1067)(259.8) =$ 277207 mm <sup>2</sup>	$(1067)(1880.4) =$ 2006387 mm <sup>2</sup>	$(1067)(2400) =$ 2560800 mm <sup>2</sup>
$\rho$	0.00549	0.00151	0.00290
$\epsilon_p^{\max}$			0.0175

For members 21 and 23 that are within the specimen development length zone the reinforcement ratio in the interior regions (shaded green) is scaled down.

Scaled reinforcement ratio for Member 21/23

$l$	608.1 mm
$\rho_{reduced} = \rho(l/l_d)$	$0.00151(608.1/1067) = 0.00085$
$\epsilon_p^{\max}$	0.0320



Sheet 9-1 i	COMPUTATION OF REINFORCEMENT RATIO $\rho$ AND MAXIMUM EXPANSION STRAIN $\epsilon_p^{\max}$ FOR PIER H19C		9 11	
COLUMN TRANSVERSE				
Due to the complex nature of the hoop layout, and corresponding localized expansion strains, the reinforcement ratios are computed accordingly.				
				
				
<b>Column Front Face</b>		<b>Column Side Face</b>		
	Inner Region (Shaded Green)	Outer Region (Shaded Blue)	Inner Region (Shaded Green)	Outer Region (Shaded Blue)
$A_s$ (mm <sup>2</sup> )	126.65 (1 leg of #4 bar)	253.35 (2 legs of #4 bar)	126.65 (1 leg of #4 bar)	253.35 (2 legs of #4 bar)
$d_s$ (mm <sup>2</sup> )	(1041)(305) = 317505		(515)(305) = 157075	
$\rho$	0.0004	0.0008	0.00081	0.00161
Average $\rho$	0.0006		0.00121	
$\epsilon_p^{\max}$	0.03583		0.02790	

Sheet 9-1 j	COMPUTATION OF REINFORCEMENT RATIO $\rho$ AND MAXIMUM EXPANSION STRAIN $\epsilon_p^{\max}$ FOR PIER H19C		10 11
FAR BEAM TRANSVERSE			
	<p>Section depth <math>d</math> = overall depth <math>D</math>  - depth to neutral axis <math>kd_{col} = 1981 - 597 = 1384</math> mm.</p>		
	<b>Far Beam Front Face</b>	<b>Far Beam Top Face</b>	
	(Shaded Blue)	Inner Region (Shaded Green)	Outer Region (Shaded Blue)
$A_s$ (mm <sup>2</sup> )	570.1 (2 legs of #6 bar)	570.1 (2 legs of #6 bar)	253.35 (1 leg of #6 bar)
$ds$ (mm <sup>2</sup> )	(1067)(3175/19) = 178301	(1384)(3175/19) = 231274	
$\rho$	0.0032	0.00246	0.00123
Average $\rho$	--		
$\epsilon_p^{\max}$	0.01647	0.02274	

Sheet 9-1 k	COMPUTATION OF REINFORCEMENT RATIO $\rho$ AND MAXIMUM EXPANSION STRAIN $\epsilon_p^{\max}$ FOR PIER H19C		11 11
CLOSE BEAM TRANSVERSE			
	Section depth $d$ = overall depth $D$ - depth to neutral axis $kd_{col}$ = $2400 - 759.5 = 1640.5$ mm.		
	Close Beam Front Face	Close Beam Top Face	
	(Shaded Blue)	Inner Region (Shaded Green)	Outer Region (Shaded Blue)
$A_s$ (mm <sup>2</sup> )	570.1 (2 legs of #6 bar)	570.1 (2 legs of #6 bar)	253.35 (1 leg of #6 bar)
$ds$ (mm <sup>2</sup> )	(1067)(3048/14) = 232301	(1640.5)(3048/14) = 357160	
$\rho$	0.00245	0.00159	0.0008
Average $\rho$	--		
$\epsilon_p^{\max}$	0.01942	0.02806	

Figure 9-6 shows the variation of ASR/DEF induced expansion strains in the longitudinal and transverse directions of the various regions of pier H19C. This may be considered as the upper bound to expansion strains that the structure may experience, as they are based on input parameters identified from the experimental C-beam specimens that were subject to severe deterioration conditions.

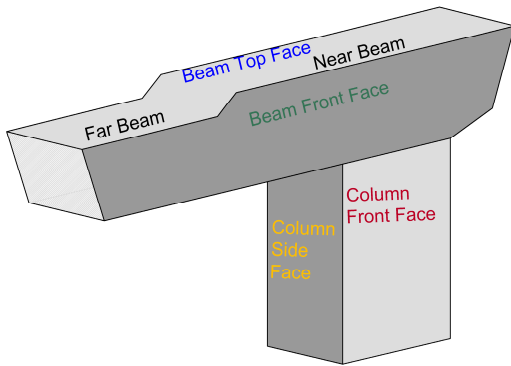
In Section 8.3.1 it was shown that the transverse out-of-plane surface expansion strains are about twice the crack width strains (sum of crack widths/overall width). As shown in Table 9-1, knowing the member width, an approximate estimate of the sum of all the crack widths that may be observed across the width of the cross-section may be made. These may be considered as the upper-bound of the total crack widths that may be observed in the structure.

**Table 9-1: Maximum Potential Crack Width in Pier H19C based on Modeled Transverse Expansion Strains.**

<b>Pier Region</b>	<b>Width (mm)</b>	<b>Modeled maximum expansion strain</b>	<b>Crack width strains</b>	<b>Estimated total crack width across the width (mm)</b>
Column front face	1981*	0.0370 ((Figure 9-6a)	0.0185	37
Column side face	1219*	0.0288 (Figure 9-6b)	0.0144	18
Beam front face	2191 <sup>+</sup>	0.0185 (average of far beam Figure 9-6c and near beam Figure 9-6e top face)	0.0093	20
Beam top face	2134	0.0262 (average of far beam Figure 9-6d and near beam Figure 9-6f top face)	0.0131	28

\*The width of the member within the architecture detail of the column is considered.

<sup>+</sup>Average depth of the pier cap with varying cross section.



LEGEND: Different Regions of Pier H19C

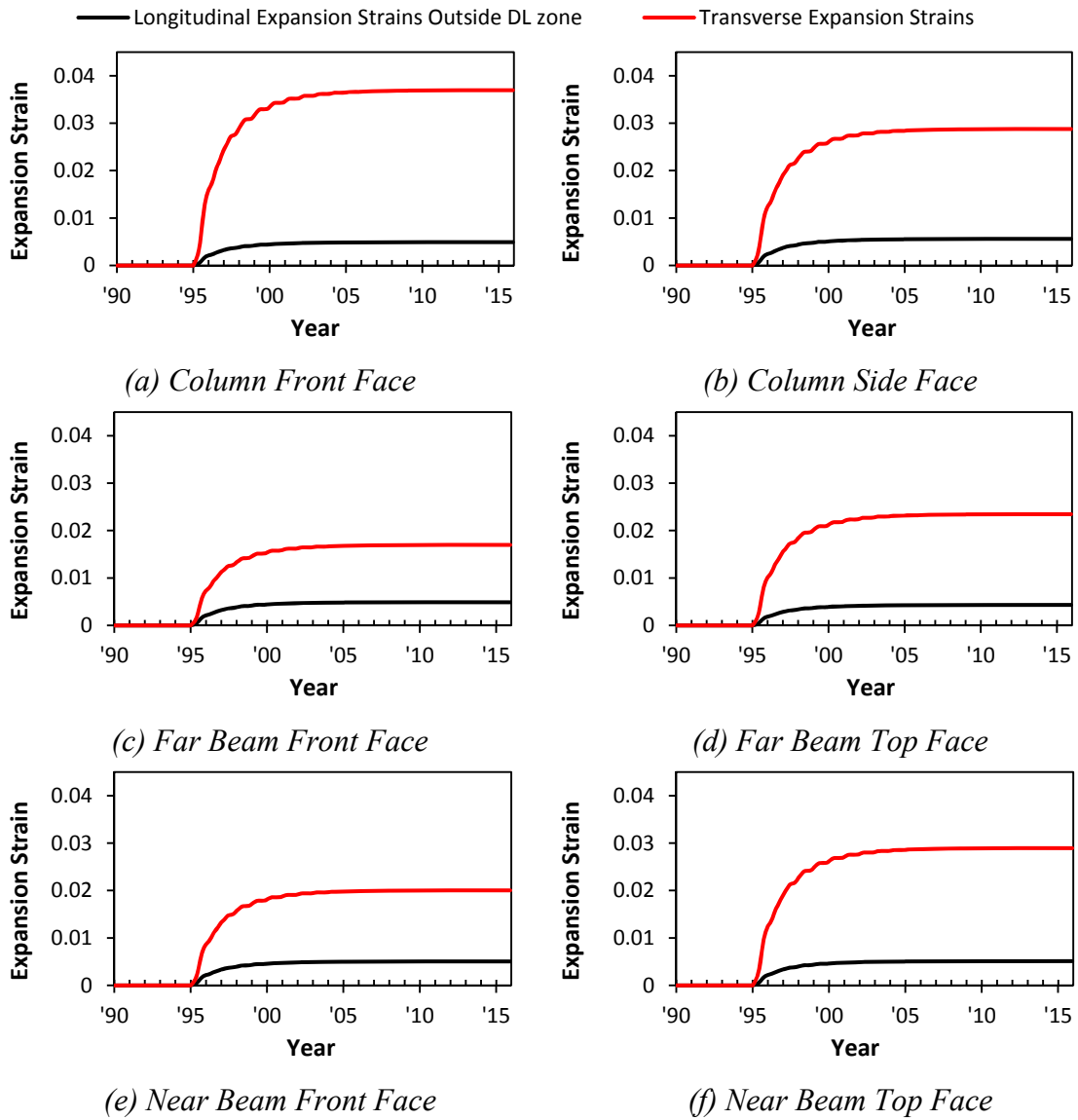


Figure 9-6: Modeled ASR/DEF Induced Expansion Strains in Pier H19C based on Observations from Experimental C-beam Specimens.

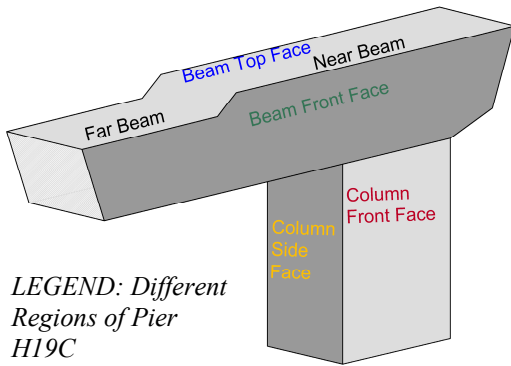
#### 9.4.4 Expansion Strain Modeling based on Free Expansion Tests

Based on the parameters that were identified in the earlier subsection, the expansion strains in the various regions of the pier H19C are modeled. Figure 9-7 presents the modeled expansion strains in the column and the beam region of the pier. Note that the expansion strains are presented as a range of values, with upper and lower-bounds based on the two sets of input parameters presented in Figure 9-5.

It was reported in Williams (2005) and Folliard et al. (2006) that forensic analysis results showed evidence of ASR and DEF in the cores extracted from pier H19C. However, it was concluded that there was insignificant amounts of ASR gel to cause any deterioration, and DEF was concluded to be the predominant cause of deterioration in pier H19C. Figure 9-7 presents the expansion strains resulting from DEF only, along with the possible expansion strains that may be expected if ASR and DEF were to take place simultaneously.

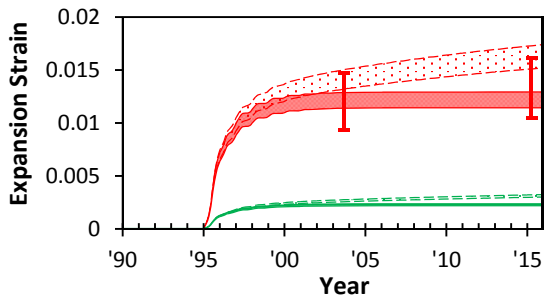
To validate the modeled expansion strains presented in Figure 9-7, the expansion strains are back inferred from the crack widths that were measured on the pier. Williams (2005) made crack width measurements in August of 2003, however only the large crack widths were mapped. As part of the current study, crack width on the structure were recorded in March of 2015. Figure 9-8 shows the crack mapping and the crack widths measured across the north, west and east faces of the pier column. The cracks were recorded only in the region within the architecture detail of the column.

The top row of Figure 9-8 shows the longitudinal cracks that were mapped on the column faces. The large crack widths on the column are mapped through the entire height of the column, whereas the smaller cracks were mapped along different horizontal lines, such that the largest number of crack widths were captured. The crack width of the mapped cracks are shown in the second row of Figure 9-8. It is evident from Figure 9-8 that the largest crack widths were recorded at the mid-width of the column, and they progressively decreased towards the column edges. This is attributed to the reinforcement detail of the column (shown in the third row of Figure 9-8), where the largest cracks are recorded in the region between the hoops where the restraint to

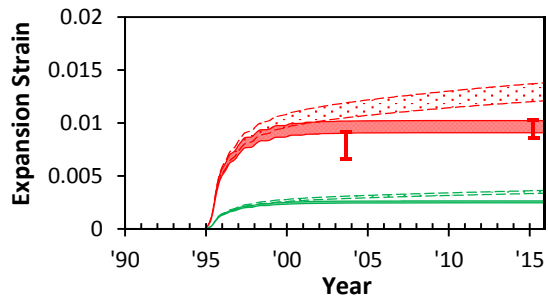


LEGEND: Different Regions of Pier H19C

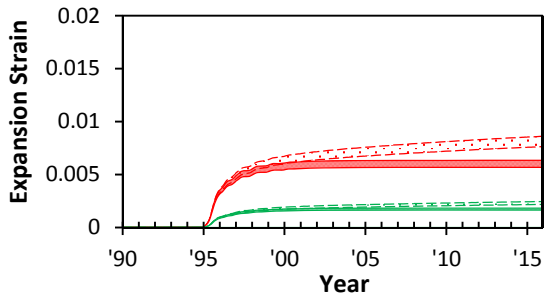
- Transverse Strains: ASR+DEF
- Transverse Strains: DEF
- Longitudinal Strains: ASR+DEF
- Longitudinal Strains: DEF
- Range of Inferred Transverse Expansion Strains from Measured Crack Widths



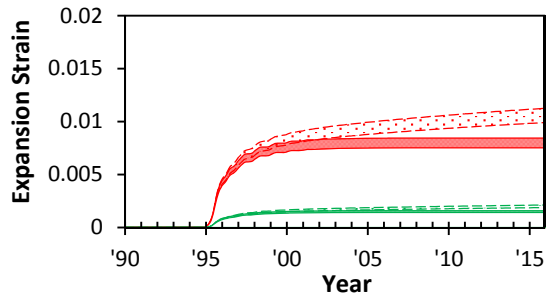
(a) Column Front Face



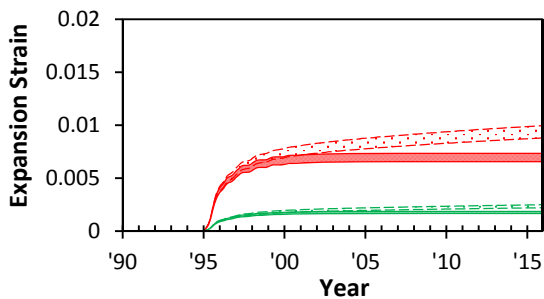
(b) Column Side Face



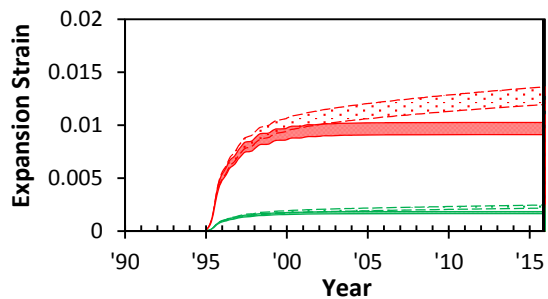
(c) Far Beam Front Face



(d) Far Beam Top Face



(e) Near Beam Front Face



(f) Near Beam Top Face

Figure 9-7: Modeled ASR/DEF Induced Expansion Strains in Pier H19C based on Free Expansion Tests on Cores from H19C.

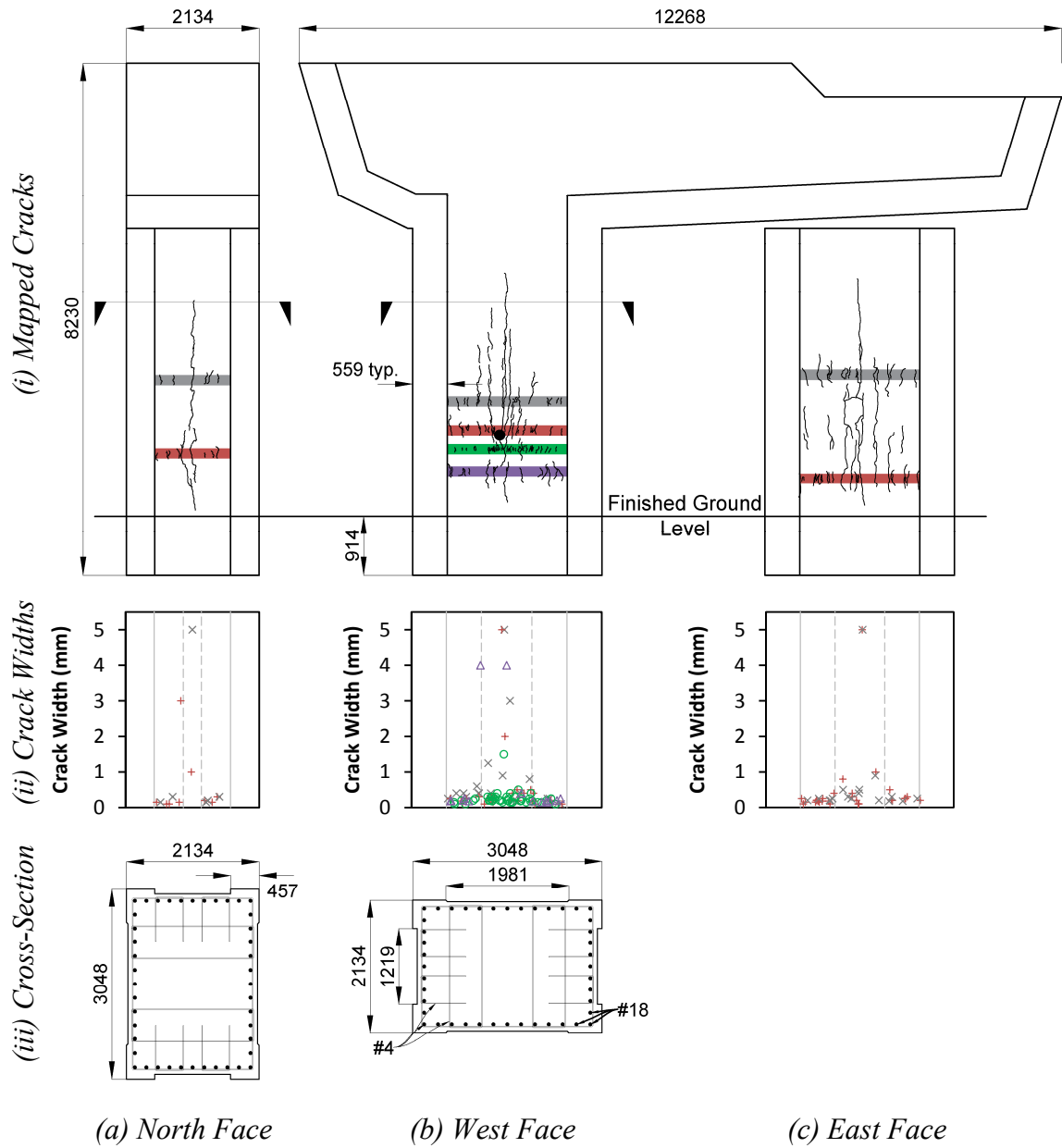


**Figure 9-8: Distribution of Crack Widths Across Column Face.**



expansion is least when compared to the rest of the cross-section. It is also observed that there is negligible change in crack widths over a 12 year period from 2003 to 2015.

Based on earlier experimental evidence, the crack width strains (sum of crack widths/section width) are approximately one-half the expansion strains. The range of expansion strains inferred from the crack widths measured in 2003 and 2015 are plotted in Figure 9-7. It is evident from Figure 9-7a, b that the modeled expansion strains caused by DEF in the column faces agree well with the expansion strains inferred from the crack widths. Considering the complex nature of the expansion phenomena, and the wide variability of crack distribution, the expansion model appears to predict the DEF induced expansion strains quite well.

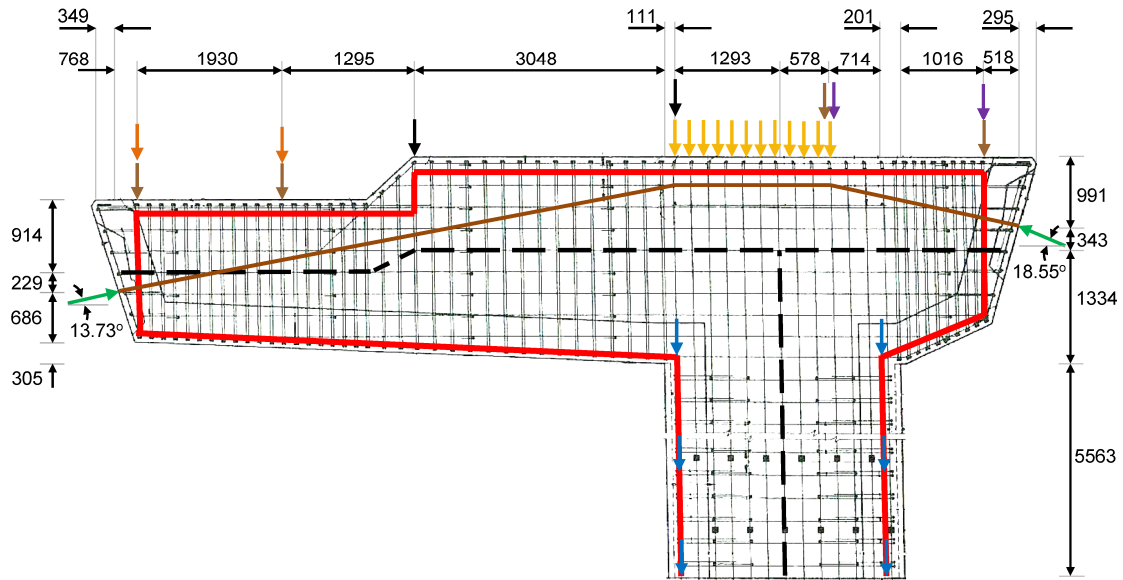
#### **9.4.5 Loading**

The structure is subjected to three categories of loads:

- Externally applied loads.
- Internal forces from post-tensioning.
- Prestressing forces due to ASR/DEF effects.

The externally applied loads are the live loads due to traffic on the bridge deck. Pier H19C supports two girders, one on each side of the bent-cap. Each girder supports two lanes of traffic. Two AASHTO design trucks spaced 15.24 m apart are used for the moving load case to calculate the maximum shear in the interior support. Using an impact factor of 33 percent, the axial load on each point of support of the girder is determined to be 725 kN. Two cases of the externally applied live loads are considered as shown in Figure 9-9.

The self-weight of the pier is applied as point loads distributed across the different node points, and the self-weight from the girders are applied as point loads on the bent-cap at the bearing pads where the girders are supported. The post-tensioned tendons are straight in the beam overhangs, but have a curvature over the beam-column joint. The bearing forces between the post-tensioning tendons and the concrete must be accounted for, and this is achieved by a system of equivalent transverse distributed loads over the beam-column joint. The system of post-tensioning forces must be such that the



	1583 kN ( $D_{\text{girder}}+D_{\text{pier}}$ ) 222 kN ( $D_{\text{pier}}$ ) 142 kN ( $D_{\text{pier}}$ )	Dead loads (D)
	19719 kN	Post-tension force after losses
	5.9 kN/mm	Downward post-tension reaction force over column region
	725 kN	Live load-Case 1
	725 kN	Live load-Case 2

**Figure 9-9: Loads on Pier H19C.**

system is in internal-equilibrium. The internal forces from post-tensioning is determined to be 19720 kN after long-term losses. The bent-cap with the externally applied loads and internal forces is shown in Figure 9-9.

There are additional loads on the structure due to compatibility requirements arising from the ASR/DEF expansion effects. These loads are induced due to the prestressing effects that are caused by the swelling of core concrete due to ASR/DEF. These prestressing forces are applied on the longitudinal and transverse rebars in the beam and column to account for the effects caused by the swelling of core concrete.

Owing to the complex nature of the structure and the loading, some preliminary analysis is performed on the structure. Considering a center-line model for the structure and based on the dead loads, post-tensioning forces, and live loads, the bending-moment diagram for the normal service regime of the structure is determined. Figure 9-10 shows the resulting bending moment diagram for:

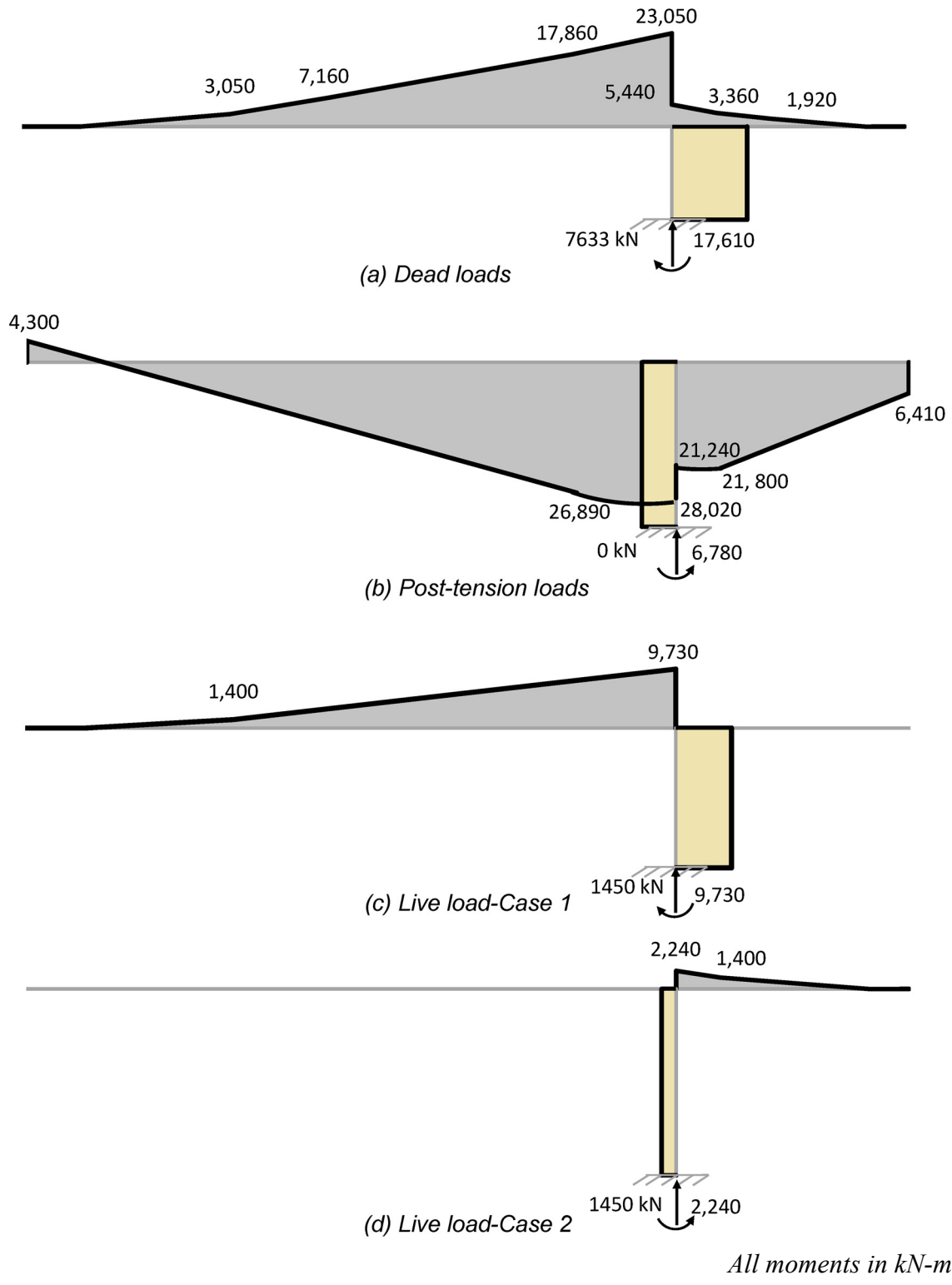
- Dead loads only.
- Post-tension forces only.
- Live loads only – Case 1.
- Live loads only – Case 2.

For the different load cases in the normal service range, the axial load and moment at the base of the column can be determined. These loads are then factored to obtain a combination of the different factored load cases as presented in Table 9-2.

**Table 9-2: Column Axial Load and Moment for Various Load Combinations.**

<b>Load case</b>	<b>Axial load (kN)</b>	<b>Moment (kN-m)</b>
D + P	7633	10830
1.25D + P	9541	15230
D + P + (L+I) Case 1	9083	20560
1.25D + P + 1.75(L + I) Case 1	12079	32260

D = Dead loads; P = post-tensioning forces; L = Live load and I=Impact load



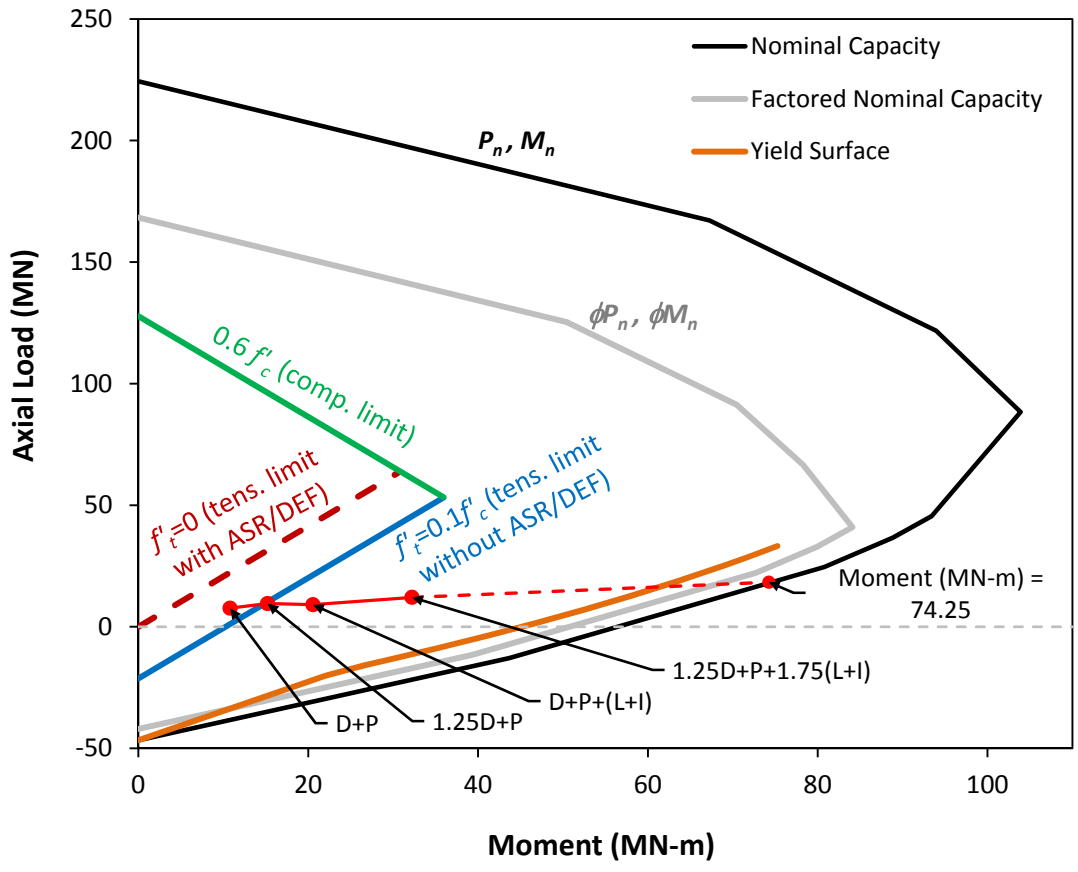
**Figure 9-10: Bending Moment Diagram for Normal Service Regime of Pier H19C.**

Figure 9-11 shows the column interaction diagram, both the nominal capacity and the factored nominal capacity are presented in this figure. Also presented are the yield surface, and the tension (cracking surface) and compression limits assuming tensile and compressive concrete strengths as  $0.1 f'_c$  and  $0.6 f'_c$ , respectively. In addition, a cracking surface with a concrete tensile strength of  $f'_t = 0$  is shown in Figure 9-11 that corresponds to a cracked structure due to ASR/DEF induced expansion strains.

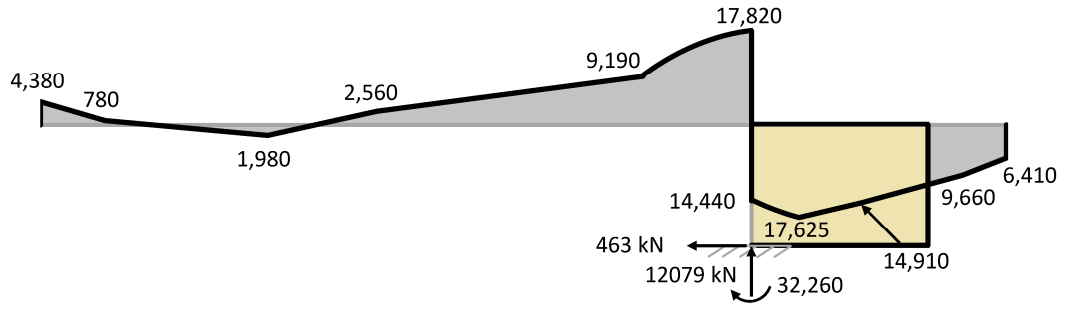
The axial load and moment for the different load cases shown in Table 9-2 are plotted as points on the column interaction diagram as shown in Figure 9-11. It is evident from the figure that in the case of a sound structure without ASR/DEF deterioration, the structure remains largely uncracked up to load case 1.25D + P. In contrast, for a structure deteriorated by ASR/DEF expansion strains, the tensile capacity may be assumed to be lost. Thus, the red dashed failure surface for  $f'_t = 0$  in Figure 9-11 applies—all loads are outside this limit once ASR/DEF deterioration and cracking progresses.

By extending the line representing the different load cases in Figure 9-11, the moment at the point of intersection on the column interaction diagram may be obtained. From the interaction diagram for the column, the overstrength factor is determined to be  $\Omega = \phi M_n / M_u = (0.9)(74250) / (32260) = 2.07$ . This shows that the column has sufficient moment capacity and is expected to form a flexural mechanism due to yielding of tensile column steel; the overhang is less likely to fail mainly due to the load balancing effect of the large post-tensioning force. Figure 9-12 shows the bending moment diagram for the factored load cases.

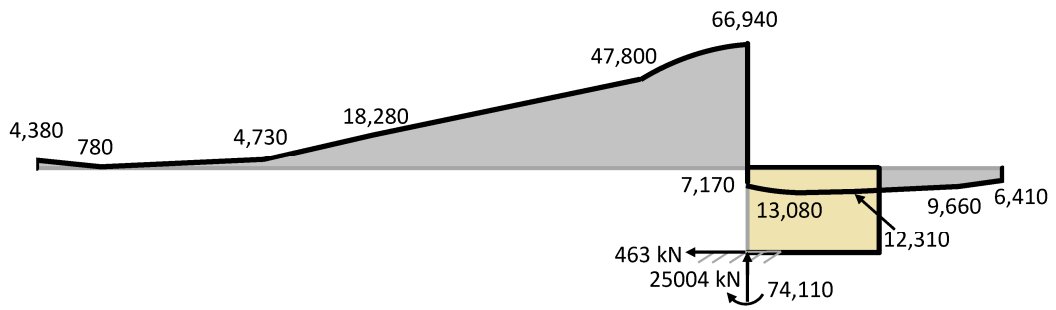
For Case 2 of (L+ I) load, the loads are applied externally to a region near the beam-column joint; a highly disturbed region. Hence, it is best to analyze this load case using the C-STM analysis method as presented next.



**Figure 9-11: Column Interaction Diagram with Different Load Cases.**



(a)  $1.25D + P + 1.75(L+I)$



(b)  $2.07[1.25D + 1.75(L+I)] + P$

*All moments in kN-m*

**Figure 9-12: Bending Moment Diagrams for (a) the Design Ultimate Strength and (b) for Overload at Incipient Mechanism Formation.**

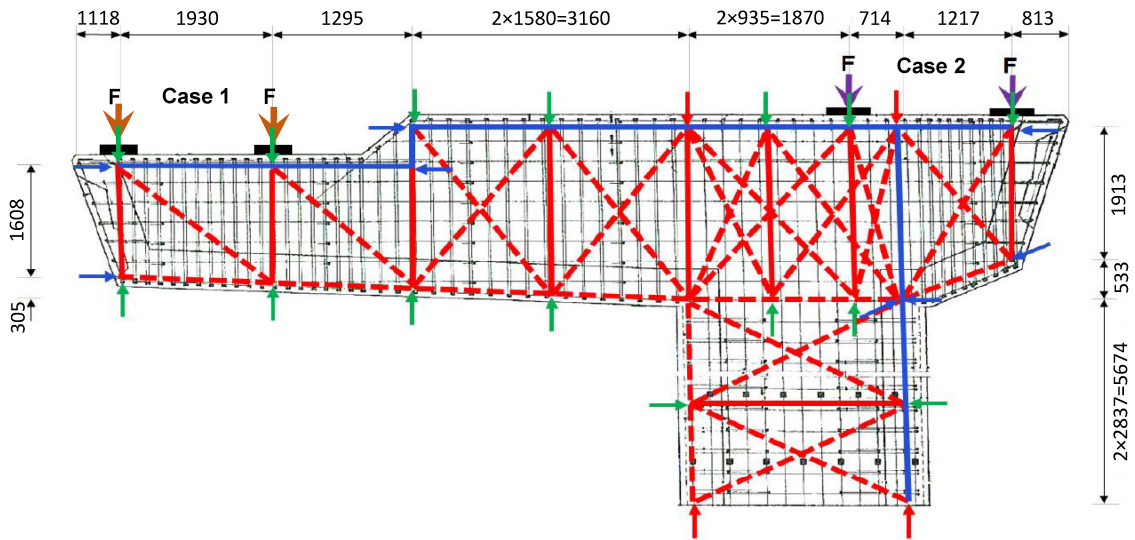
#### 9.4.6 The C-STM Model

Figure 9-13a and b, respectively, show the truss and arch action of the C-STM model that is developed for pier H19C. (The truss and the arch mechanism function together, but are shown separate for clarity.) As shown in Figure 9-13a the C-STM technique is used to analyze Case 1 and Case 2 of (L+I) where live loads are applied via the two bearing pads resting on the left and right side of the pier, respectively.

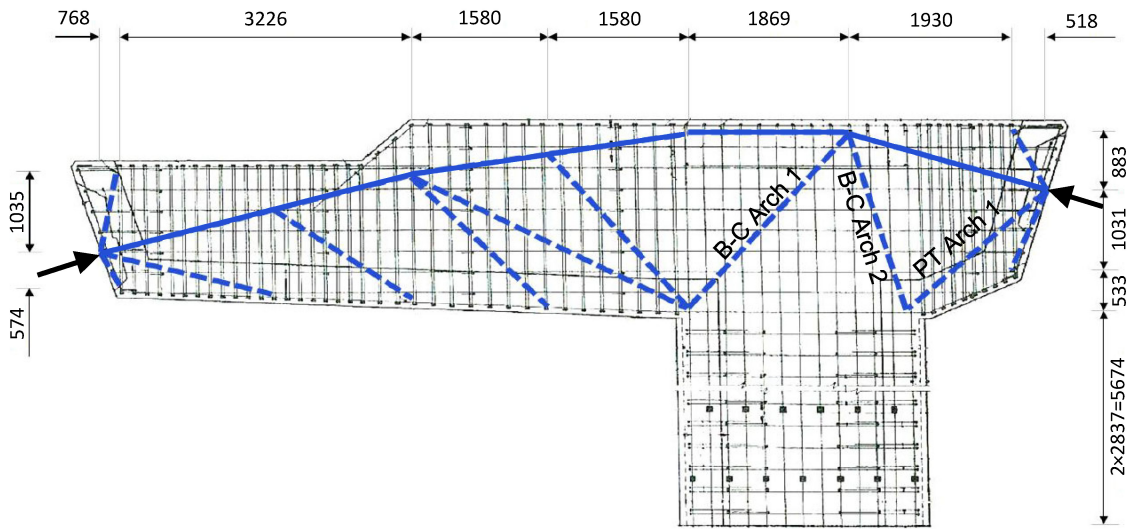
The beam-column joint of the pier is modeled using the *Three-Point Gauss* truss model. The arch mechanisms formed due to the compressive force in the post-tensioned tendons are positioned along the centroid of the tendons for simplicity. The rest of the truss and arch action were modeled based on the probable stress flow paths in the structure. As there was no local failure observed at the anchorage zone, the C-STM was modeled to replicate this observation at the end zones.

The pier is analyzed without and with damage due to ASR/DEF expansion. Prestressing forces are applied on the longitudinal and transverse reinforcements in the beam and the column in order to replicate the prestress effects that arise as a consequence of the swelling within the core concrete due to ASR/DEF expansion. The prestress in the longitudinal and transverse reinforcement is deduced from the modeled ASR/DEF expansion strains presented in Figure 9-6 and Figure 9-7. Detailed computations for the prestrains based on modeled expansion strains from Figure 9-6 are presented in engineering computation Sheets 9-2a to d.





(a) C-STM Truss action

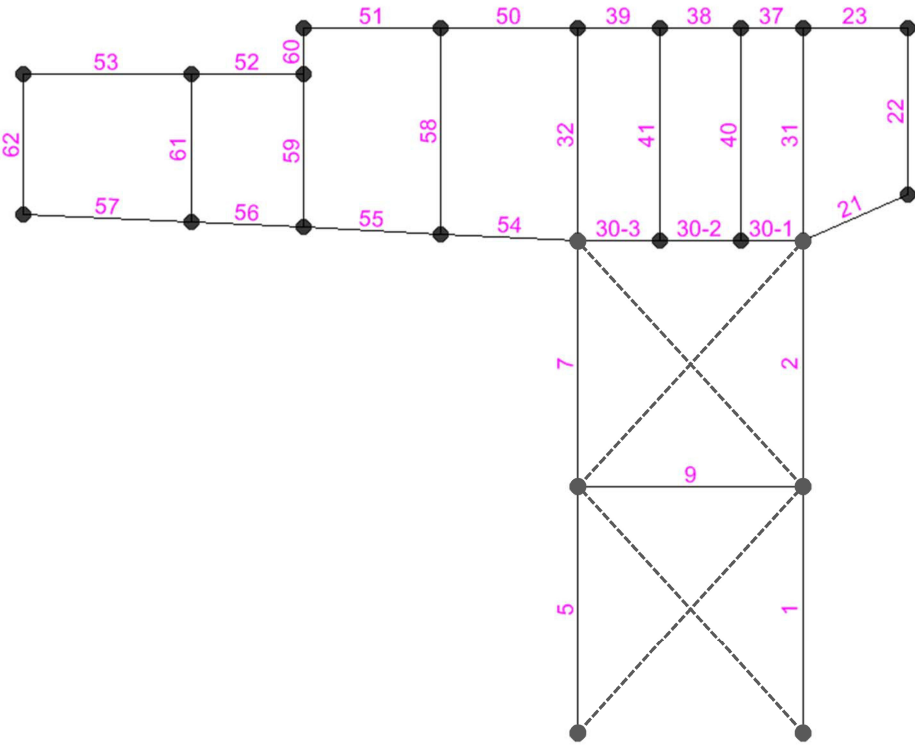


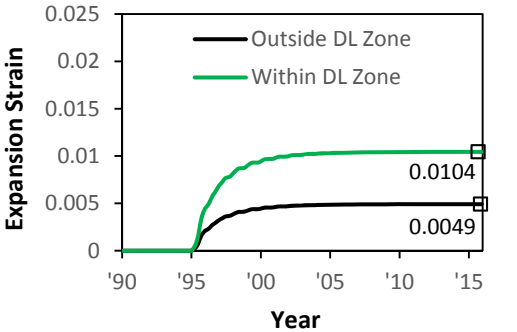
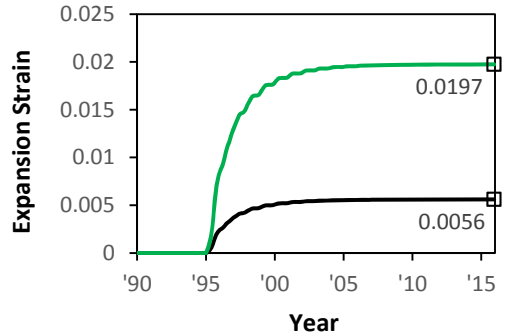
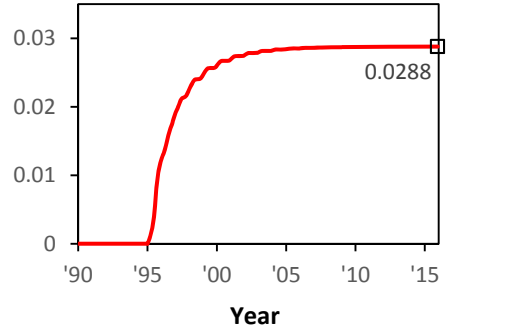
(b) C-STM Arch action

- Primary tension reinforcement and PT tendon
- Ties representing bundles of hoops
- - - Concrete struts for the truss
- - - Central concrete arch
- Initial confinement effect in hoops and longitudinal steel due to concrete swelling, modeled as a set of externally applied nodal forces
- 
- 

Note: The additional nodal forces represent the prestress effect actively induced in the reinforcing steel caused by ASR/DEF induced concrete swelling.

**Figure 9-13: C-STM Model for Pier H19C.**

Sheet 9-2 a	EXPANSION MODEL AND COMPUTATION OF PRESTRAINS IN THE VARIOUS MEMBERS OF THE C-STM MODEL FOR PIER H19C	1 4
GENERAL NOTES		
Development length of #8 bars = 1077 mm Development length of #18 bars = 2426 mm		
Distance to center of C-STM members $l$ from edges of the structure that are within the development length		
Member	$l$ (mm)	
1/5	1418.8	
21/23	608.1	
53/57	965.2	
		

Sheet 9-2 b	EXPANSION MODEL AND COMPUTATION OF PRESTRAINS FOR THE VARIOUS MEMBERS OF THE C-STM MODEL FOR PIER H19C	2 4
COLUMN MEMBERS		
LONGITUDINAL MEMBERS		
 <p>Expansion model for column front face</p>	 <p>Expansion model for column side face</p>	
<p>Tension Members: Prestraints are computed considering the average of the expansion strains in the column front face and the column side face.</p>		
Member 1 (within DL Zone)	$(0.0104 + 0.0197) / 2 = 0.0151$	
Member 2 (Outside DL Zone)	$(0.0049 + 0.0056) / 2 = 0.0053$	
<p>Compression Members: Prestraints are computed from the expansion strains in the column front face.</p>		
Member 5 (within DL Zone)	0.0104	
Member 7 (Outside DL Zone)	0.0049	
TRANSVERSE MEMBERS		
<p>The prestrain in the transverse members of the column is: 0.0288</p>	 <p>Expansion model for transverse column members</p>	

Sheet 9-2 c	EXPANSION MODEL AND COMPUTATION OF PRESTRAINS FOR THE VARIOUS MEMBERS OF THE C-STM MODEL FOR PIER H19C	3 4
<b>FAR BEAM MEMBERS</b>		
LONGITUDINAL MEMBERS		
Expansion model for far beam top face	Expansion model for far beam front face	
Tension Members: Prestraints are computed considering the average of the expansion strains in the far beam front face and the far beam top face.		
Member 53 (within DL Zone)	$(0.0047 + 0.0053) / 2 = 0.005$	
Member 52 (Outside DL Zone)	$(0.0043 + 0.0049) / 2 = 0.0046$	
Compression Members: Prestraints are computed from the expansion strains in the far beam front face.		
Member 57 (within DL Zone)	0.0053	
Member 56 (Outside DL Zone)	0.0049	
TRANSVERSE MEMBERS		
The prestrain in the transverse members of the far beam is: 0.0235		
	Expansion model for far beam transverse members	

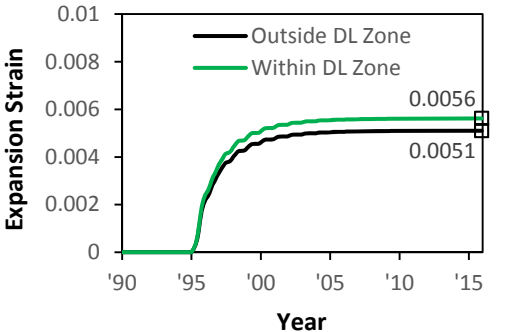
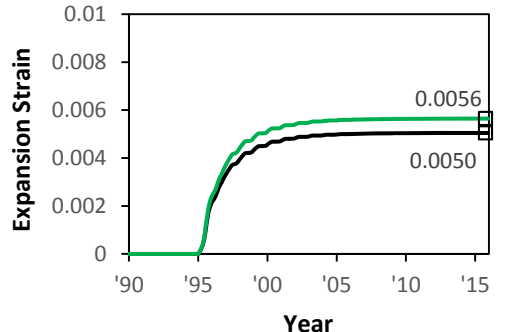
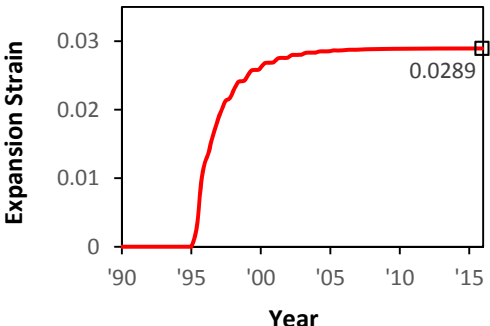
Sheet 9-2 d	EXPANSION MODEL AND COMPUTATION OF PRESTRAINS FOR THE VARIOUS MEMBERS OF THE C-STM MODEL FOR PIER H19C	4 4
NEAR BEAM MEMBERS		
LONGITUDINAL MEMBERS		
		
Expansion model for close beam top face	Expansion model for close beam front face	
Tension Members: Prestraints are computed considering the average of the expansion strains in the near beam front face and the near beam top face.		
Member 23 (within DL Zone)	$(0.0056 + 0.0056) / 2 = 0.0056$	
Member 37-39, 50-51 (Outside DL Zone)	$(0.0051 + 0.0050) / 2 = 0.00505$	
Compression Members: Prestraints are computed from the expansion strains in the near beam front face.		
Member 21 (within DL Zone)	0.0056	
Member 30, 54-55 (Outside DL Zone)	0.0050	
TRANSVERSE MEMBERS		
The prestrain in the transverse members of the near beam is: 0.0289		
Expansion model for near beam transverse members		

Table 9-3 presents the prestrains for the different longitudinal and transverse members of the C-STM for pier H19C. Based on the prestrains and the area of the steel member, the prestressing forces on the C-STM members are calculated. The stress-strain relation of the reinforcement are also modified as shown in Figure 9-2e.

To replicate a logical sequence of loading, the C-STM model is first loaded with the dead loads from the pier followed by the post-tensioning forces. Next in the sequence are the dead loads from the girder and the live plus impact loads. This completes the analysis due to normal service loads. In the case of the analysis which includes the effects of ASR/DEF expansion, the prestress forces caused by concrete core expansion are applied next followed by factored loads, and finally the structure is loaded to failure.

The confinement ratio is calculated to be  $K_{cc} = 1.20$  for the beam and  $K_{cc} = 1.04$  for the column core concrete. Figure 9-14 shows the different nonlinear concrete stress-strain relationships that are derived for pier H19C without and with ASR/DEF effects. As both the cover and core concrete areas contribute to the area of the strut in the C-STM model, a weighted average of concrete compressive strength is used in the C-STM model with ASR/DEF effects.

The tensile strains transverse to the diagonal arch members are evaluated to determine the softened concrete stress-strain relation for these members. Owing to hoop reinforcement being completely enclosed the softened confined model is assumed for the softened diagonal concrete members. Due to the heavy damage assumed for pier H19C, the concrete tensile strength is neglected in the C-STM analysis with ASR/DEF effects.

#### **9.4.7 C-STM Results and Discussion**

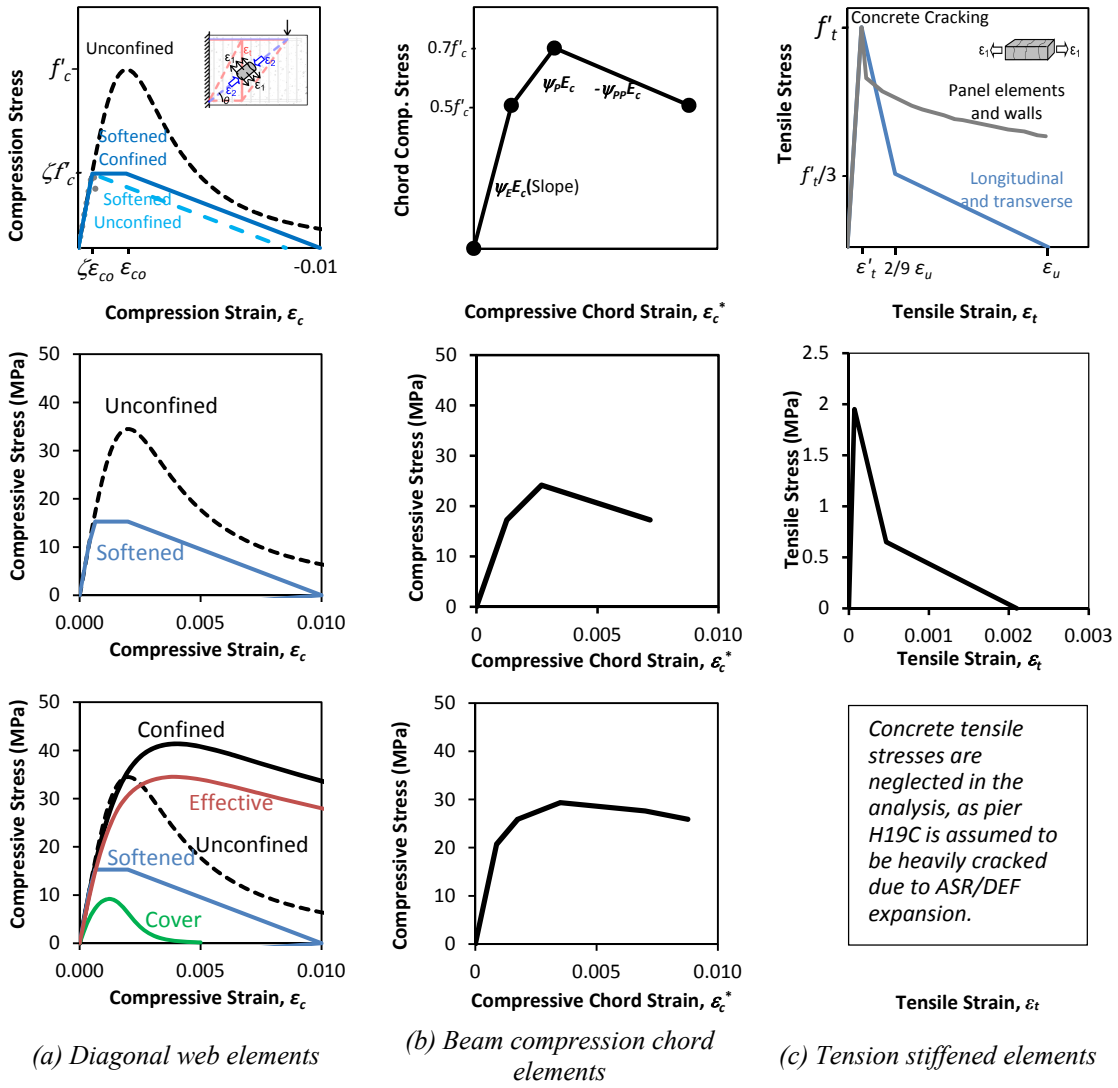
The C-STM model is used to analyze both Case 1 and Case 2 live load cases. The prestrains obtained from modeled expansion strains presented in Figure 9-6 and Figure 9-7 are evaluated for the C-STM analysis including the effects of ASR/DEF. Figure 9-15 shows the force-deformation plot from the C-STM analysis. The tip deformations  $\delta_1$  and  $\delta_2$  are measured positive downward and are as shown in the inset

**Table 9-3: Prestrains in the C-STM Members of Pier H19C.**

Column Members			
<i>Member</i>		<i>Prestrain</i>	
1		0.0151	
Tension Members Outside DL		0.0053	
5		0.0104	
Compression Members outside DL		0.0049	
Transverse Members		0.0288	
Beam Members			
<i>Far Beam</i>		<i>Near Beam</i>	
53	0.0050	23	0.0056
Tension Members Outside DL	0.0046	Tension Members Outside DL	0.0051
57	0.0053	21	0.0056
Compression Members Outside DL	0.0049	Compression Members Outside DL	0.0050
Transverse Members	0.0235	Transverse Members	0.0289

*C-STM Members*



Row 1: Theoretical nonlinear behavior.  
 Row 2: Modeled behavior, without ASR/DEF effects.  
 Row 3: Modeled behavior, with ASR/DEF effects.

**Figure 9-14: Cracked Reinforced Concrete Material Properties for Pier H19C.**



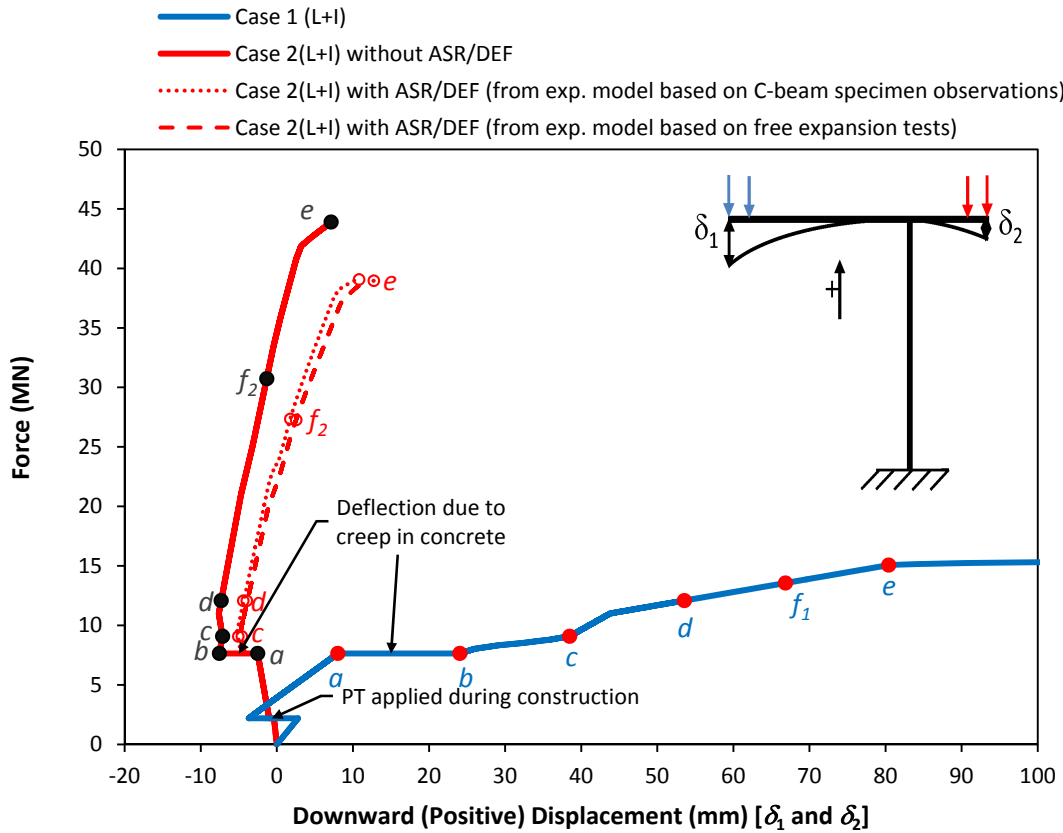
in Figure 9-15. The column axial loads computed for the different load combinations (Table 9-2) are presented as points along the force-deformation curve.

The as-built overstrength factor provided can be defined as:

$$\Omega = \frac{\text{Factored capacity}}{\text{Factored (code) load demand}} = \frac{\phi M_n}{M_u} \quad (9-3)$$

The following findings are made from the C-STM analysis.

- Case 1 of (L + I) loads, flexural yielding of the column tensile steel was determined to be the cause of structural failure.
- The maximum nominal capacity of the pier without ASR/DEF deterioration  $P_{n1} = 15.1$  MN. It is observed that the factored capacity  $\phi P_{n1} = 0.9 \times 15.1 = 13.6$  MN is well over the factored axial load demand of  $P_u = 1.25D + P + 1.75(L + I) = 12.1$  MN. Thus, the overstrength factor provided is obtained as  $\Omega = \phi P_{n1} / P_u = 1.12$ .
- The prestressing effects due to ASR/DEF did not have a profound effect on Case 1 of (L + I) as the structure is predominantly governed by flexure in the column, and the results are not presented.
- For Case 2 of (L + I), the measured tip displacements  $\delta_2$  are much smaller. The final mode of failure was the crushing of the softened joint arch (B-C Arch 2) underneath the Case 2 (L + I) load in the beam-column joint, and the failure is classified as shear-brittle.
- For the structure without ASR/DEF deterioration the maximum nominal capacity  $P_{n2} = 43.9$  MN and the factored capacity  $\phi P_{n2} = 0.70 \times 43890 = 30.7$  MN, that results in an overstrength factor of  $\Omega = \phi P_{n2} / P_u = 2.54$ .
- For Case 2 of (L + I) analysis with ASR/DEF damage on the structure, additional prestressing forces are applied on the longitudinal and transverse steel in the beam and the column following the normal service regime. This results in a stiffer structural response with a decrease in the maximum nominal capacity.



- (a)  $D + P$  = Self-weight + Post-tension (after losses).
- (b)  $(D+P) + \text{Creep}$  = Self-weight + Post-tension (after losses) + Creep deflections.
- (c)  $D + P + (L+I)$  = Maximum service load.
- (d)  $1.25 D + 1.75 (L+I)$  = Ultimate load demand.
- (e)  $P_n$  = Nominal maximum capacity.
- $(f_1) \phi P_{n1}$  = Factored capacity (where  $\phi = 0.9$  for flexure).
- $(f_2) \phi P_{n2}$  = Dependable capacity (where  $\phi = 0.7$  as for SAT modeling requirements).

**Figure 9-15: Force-Deformation for Case 1 and Case 2 Live Load.**

- It is evident from Figure 9-15 that irrespective of the two different modeled expansion strains (Figure 9-6 and Figure 9-7) that were used to compute the prestrains, there is negligible difference in the overall force deformation behavior of the structure.
- The ultimate load at failure, which is due to the crushing of the joint-arch as in the earlier case without ASR/DEF deterioration, is found to be  $P_{n2}^{ASR/DEF} = 39$  MN and the factored capacity  $\phi P_{n2}^{ASR/DEF} = 0.7 \times 39 = 27.3$  MN, that results in an overstrength factor of  $\Omega = \phi P_{n2}^{ASR/DEF} / P_u = 2.26$ .

Although, there is a slight decrease in the ultimate load for the structure affected by ASR/DEF (Case 2 live load), because of its high reserve strength (overstrength) capacity the structure can be deemed to remain safe with regard to its load carrying capacity. In addition, the cracking caused by ASR/DEF expansion can act as a pathway for moisture ingress which in turn can lead to the corrosion of the reinforcing steel, and thus could have some adverse effects on the structure.

## 9.5 Analysis of Pier I5C

### 9.5.1 The Structure

Figure 9-16 presents the reinforcing layout and cross-section of pier I5C. The overall height of the pier from the column footing is 10.67 m. The hammerhead portion of the pier has an overall length of 6.93 m with a free cantilever portion extending 3.73 m from the column face. The longitudinal reinforcement for the column consists of a total of 50 #11 (35 mm) bars with 11 bars along each of the two short faces and 14 bars along each long face. The hammerhead pier-cap beam consists of two layers of #11 bars as the top (tensile) reinforcement and one layer of 13 #5 (16 mm) bars for the bottom (compressive) reinforcement, with #8 (25 mm) bars distributed along the side faces of the beam to provide torsional strength. Transverse reinforcement in the column is provided by #4 (13 mm) closed stirrups with a center-to-center spacing of 305 mm. For the cap beam, #6 (19 mm) closed double stirrups with a center-to-center spacing of 152 mm is used.

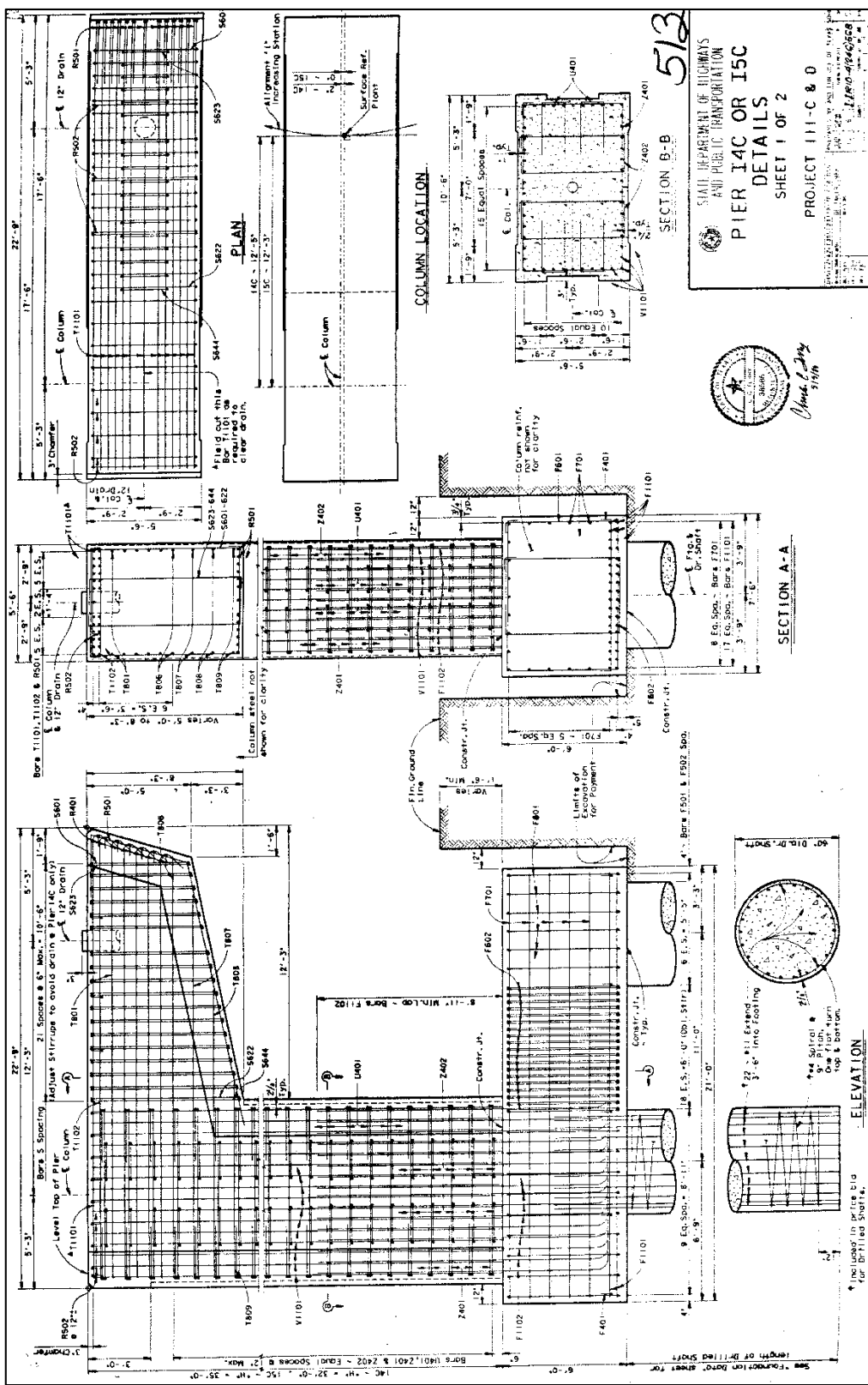


Figure 9-16: Layout and Reinforcement Detail of Pier I5C (Adopted from Mander et al., 2012).

Grade 60 reinforcing steel with yield strength  $f_y = 414$  MPa and Class C concrete with  $f'_c = 25$  MPa were specified for constructing pier I5C. In the absence of more precise information on the existing in-situ strength of steel and concrete, the specified design strengths have been adopted for the analyses.

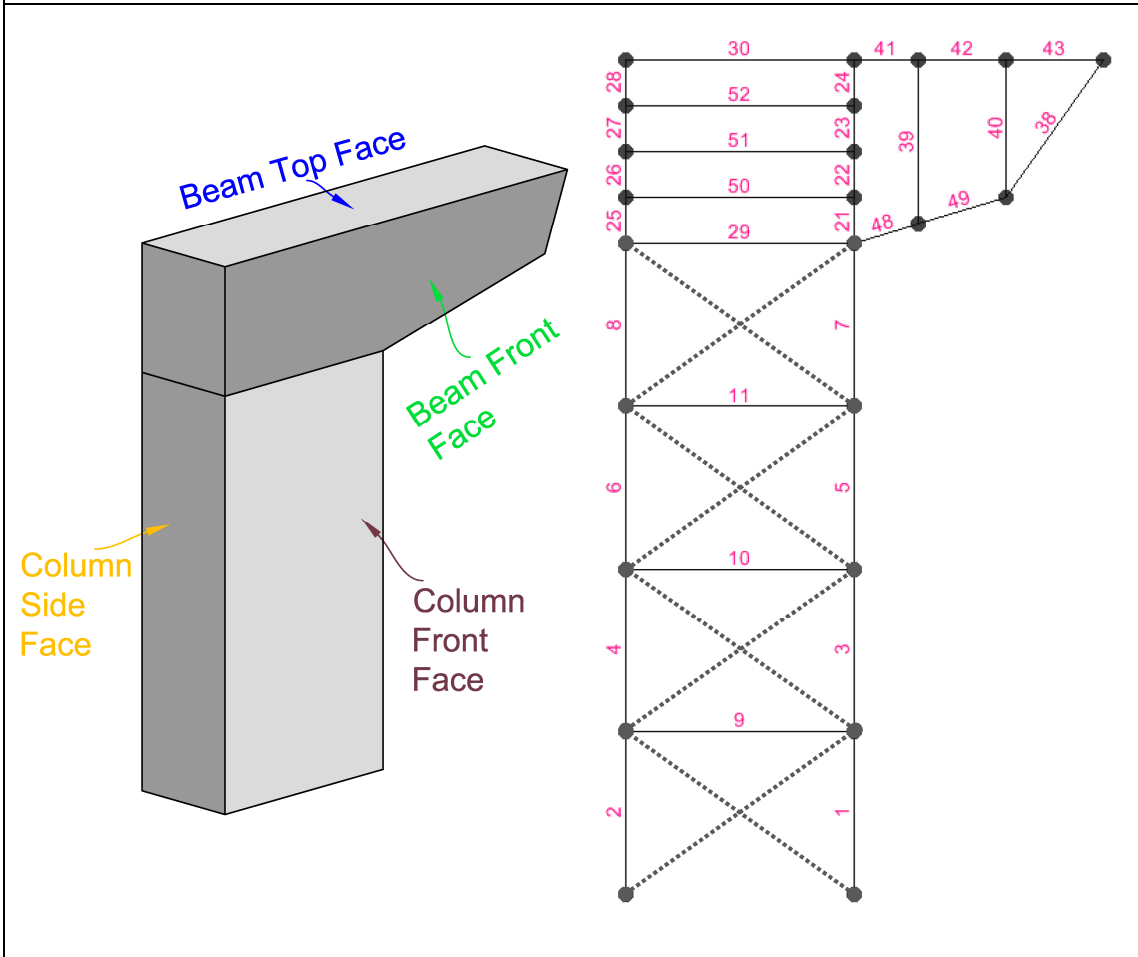
### 9.5.2 Expansion Strain Modeling due to ASR/DEF

Unlike in the case of pier H19C, there are no free expansion strain test results from core samples available for pier I5C. However, both piers I5C and H19C belong to the San Antonio Downtown Y highway system. Therefore, in light of the lack of any specific information, it is assumed that the constituent materials of the two piers are similar, and thus may be subject to the same ASR/DEF expansion potential. The parameters  $\varepsilon_o^{\max}$  and  $t_r$  presented in Figure 9-5 are used to model the potential expansion strains in pier I5C. An upper-bound solution for the expansion strains is also established based on the parameter values for  $\varepsilon_o^{\max} = 0.05$  and  $t_r = 120$  days observed in the experimental C-beam specimens. It is also worth to note that pier I5C was retrofitted and the cracks sealed to prevent further deterioration. Hence, the modeled expansion strains presented herein may be considered as the potential expansion if the structure was not retrofitted.

Sheet 9-3 shows the various regions of pier I5C identified to model the ASR/DEF expansion strains. To simulate the expansion strains in the various regions of pier I5C, it is important to carefully determine the reinforcement ratio in each of these regions. For the C-STM members within the development length zone, the reinforcement ratios are scaled down accordingly, as the full yield strength of the reinforcement is not developed within the bar development length (Mander et al., 2011). The C-STM model of pier I5C (presented later) is used to determine the tensile prestrains in the members due to the dead weight of the pier and the girders. The computation of the reinforcement ratio and the maximum expansion strain for the various regions of pier I5C is presented in engineering computation Sheets 9-3a to h.

Sheet 9-3 a	COMPUTATION OF REINFORCEMENT RATIO $\rho$ AND MAXIMUM EXPANSION STRAIN $\epsilon_{\rho}^{max}$ FOR PIER 15C	1 8
----------------	---	--------

GENERAL NOTES



*Different Regions of Pier 15C*

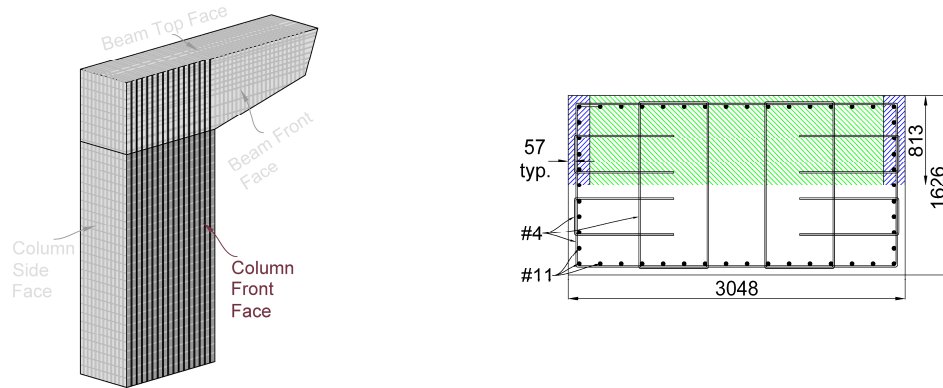
*C-STM Members of pier 15C*

Sheet 9-3 b	COMPUTATION OF REINFORCEMENT RATIO $\rho$ AND MAXIMUM EXPANSION STRAIN $\epsilon_p^{max}$ FOR PIER 15C	2 8	
GENERAL NOTES (CONT.)			
<u>General Parameters Used</u>			
$f'_c = 24.8$ MPa	$\epsilon'_t = 0.000125$	$\epsilon_y = 0.00207$	$\epsilon_o^{max} = 0.05$
$E_c^{actual} = 24822$ MPa	$f_y = 414$ MPa	$n = \frac{E_s}{E_c/3} = 24.17$	$t_r(\theta_o) = 250$ days
$f'_t = 3.1$ MPa	$E_s = 200$ GPa		$t_o = 1000$ days
<u>Maximum Expansion Strain</u>			
The tensile prestrains in the structure are computed from the C-STM model, and are used accordingly in Eq. 4-16a (repeated here) to compute the expansion strains ( $\epsilon_p^{max}$ ).			
$\epsilon_p^{max} = \frac{\epsilon_o^{max} \epsilon'_t + \rho n (\epsilon_y^2 - \epsilon_{spre}^2) + \epsilon'_t \epsilon_{spre} - (\epsilon'_t/2)^2}{2(\epsilon'_t/2 + \rho n (\epsilon_y - \epsilon_{spre}) - \sigma_{const}/E_c)}$			4-16a
<u>Development Length (ACI 318-08)</u>			
Mander et al. (2011) established that to develop the full yield strength of the reinforcement, the reinforcing bars transverse to the member edge should be longer than the bar development length $l_d$ .			
$\#11 \text{ bars: } (l_d) = \left( \frac{f_y \psi_t \psi_c}{20 \lambda \sqrt{f'_c}} \right) d_b = \left( \frac{60000(1)(1)}{20(1)\sqrt{3600}} \right) \left( \frac{11}{8} \right) = 68.75" \times 25.4 = 1746 \text{ mm}$			
$\#8 \text{ bars: } (l_d) = \left( \frac{f_y \psi_t \psi_c}{20 \lambda \sqrt{f'_c}} \right) d_b = \left( \frac{60000(1)(1)}{20(1)\sqrt{3600}} \right) \left( \frac{8}{8} \right) = 50.0" \times 25.4 = 1270 \text{ mm}$			
<u>Computation of Reinforcement Ratio</u>			
In all the cases presented below the following points are to be noted for computing the longitudinal reinforcement ratio.			
Outside the development length zone, all the reinforcement steel and concrete, in the entire depth of the cross-section considered, contribute to the reinforcement ratio. However, within the development length zone, the effects of localized reinforcement were considered. The total area of reinforcement along the longitudinal member edges (shaded blue in the cross-section) are much greater when compared to the region away from the member edge (shaded green in the cross-section). Therefore, the region away from the longitudinal member edges will see greater expansion. Hence, for regions within the development length zone the reinforcement ratio corresponding to the region away from the longitudinal edges was scaled accordingly based on their distance.			

Sheet 9-3 c	COMPUTATION OF REINFORCEMENT RATIO $\rho$ AND MAXIMUM EXPANSION STRAIN $\epsilon_p^{max}$ FOR PIER 15C	3 8
----------------	--	--------

**COLUMN FRONT FACE**

Concrete and steel volume in half the section-depth  $d = 813$  mm is considered for calculating the reinforcement ratio.



Separate reinforcement ratios are computed considering the blue and the green shaded regions separately and also for the entire shaded region (shaded blue + green). In this case the effects of tensile/compressive prestrains are neglected in the computation of  $\epsilon_p^{max}$  as the column front face has a combination of both tensile and compressive strains.

$$\epsilon_{opre} = \epsilon_{spre} = 0$$

	Close to member edges (shaded blue)	For interior regions (shaded green)	Considering entire half-depth
Area of steel, $A_s$	4790 mm <sup>2</sup> (5-#11 bars)	13412 mm <sup>2</sup> (14-#11 bars)	22992 mm <sup>2</sup> (24-#11)
Area of concrete, $A_c$	(813)(195) = 158490 mm <sup>2</sup>	(813)(2848) = 2315507 mm <sup>2</sup>	(813)(3048) = 2478024 mm <sup>2</sup>
$\rho$	0.03023	0.00579	0.00928
$\epsilon_p^{max}$			0.0067

For members 24/28, 23/27, 22/26, 1/2 that are within the specimen development length zone the reinforcement ratio in the interior regions (shaded green) is scaled down.

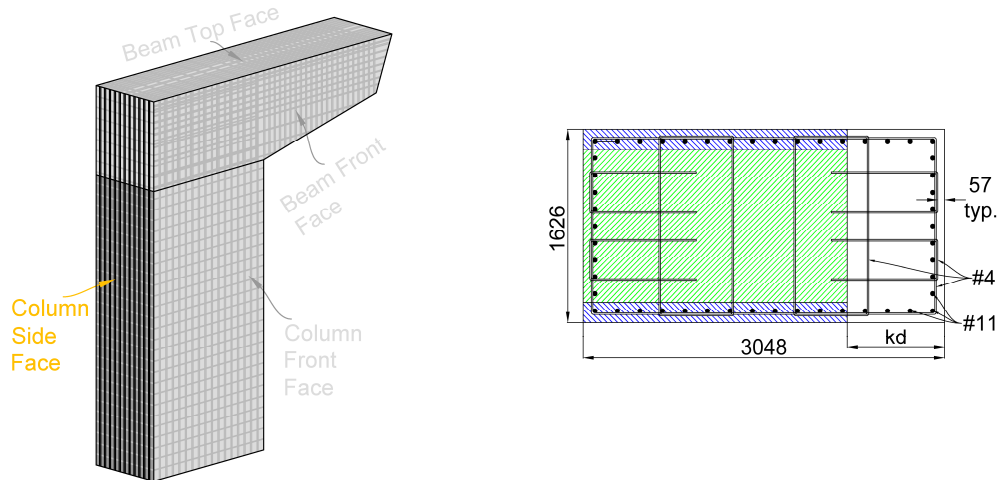
Member	l (mm)	$\rho_{reduced} = \rho(l/l_d)$ [ $\rho = 0.00579$ ]	$\epsilon_p^{max}$
24/28	287.5	0.00095	0.0288
23/27	862.3	0.00286	0.0159
22/26	1437.1	0.00477	0.0112
1/2	1019.3	0.00338	0.0143



Sheet 9-3 d	COMPUTATION OF REINFORCEMENT RATIO $\rho$ AND MAXIMUM EXPANSION STRAIN $\epsilon_p^{\max}$ FOR PIER 15C	4 8
----------------	--	--------

COLUMN SIDE FACE

Section depth  $d$  = overall depth  $D$  - depth to neutral axis  $kd_{col} = 3048 - 820.4 = 2227.6$  mm.



Separate reinforcement ratios are computed considering the blue and the green shaded regions separately and also for the entire shaded region (shaded blue + green).

The tensile prestrains computed from the C-STM model are  $\epsilon_{opre} = \epsilon_{spre} = 0.00008$

	Close to member edges (shaded blue)	For interior regions (shaded green)	Considering entire half-depth
Area of steel, $A_s$	11496 mm <sup>2</sup> (12-#11 bars)	8622 mm <sup>2</sup> (9-#11 bars)	31614 mm <sup>2</sup> (33-#11)
Area of concrete, $A_c$	(2227.6)(171.3) = 381588 mm <sup>2</sup>	(2227.6)(1283) = 2858011 mm <sup>2</sup>	(2227.6)(1626) = 3622078 mm <sup>2</sup>
$\rho$	0.03014	0.00302	0.00873
$\epsilon_p^{\max}$			0.0074

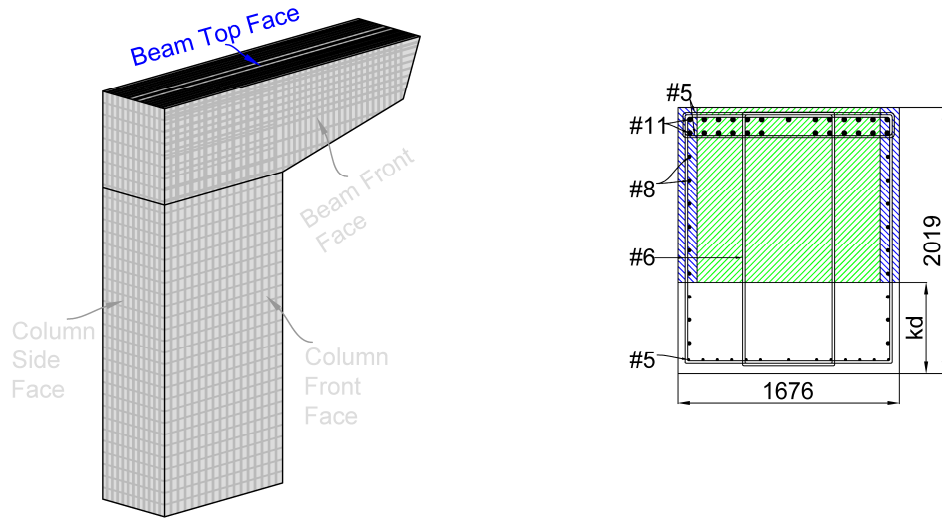
For members 24/28, 23/27, 22/26, 2/1 that are within the specimen development length zone the reinforcement ratio in the interior regions (shaded green) is scaled down.

Member	$l$ (mm)	$\rho_{reduced} = \rho \left( \frac{l}{l_d} \right) [\rho = 0.00302]$	$\epsilon_p^{\max}$
24/28	287.5	0.00049	0.0365
23/27	862.3	0.00149	0.0239
22/26	1437.1	0.00248	0.0179
1/2	1019.3	0.00176	0.0219

Sheet 9-3 e	COMPUTATION OF REINFORCEMENT RATIO $\rho$ AND MAXIMUM EXPANSION STRAIN $\epsilon_{\rho}^{\max}$ FOR PIER 15C	5 8
----------------	---	--------

**BEAM TOP FACE**

Section depth  $d$  = overall depth  $D$  - depth to neutral axis  $kd_{col} = 2019 - 696 = 1323$  mm.



Separate reinforcement ratios are computed considering the blue and the green shaded regions separately and also for the entire shaded region (shaded blue + green).

The tensile prestrains computed from the C-STM model are  $\epsilon_{spre} = \epsilon_{spre} = 0.00059$

	Close to member edges (shaded blue)	For interior regions (shaded green)	Considering entire half-depth
Area of steel, $A_s$	4956 mm <sup>2</sup> (6-#8+2-#11 bars)	20118 mm <sup>2</sup> (21-#11 bars)	30030 mm <sup>2</sup> (12-#8+25-#11)
Area of concrete, $A_c$	(1323)(145) = 191835 mm <sup>2</sup>	(1323)(1386.6) = 1834472 mm <sup>2</sup>	(1323)(1676.4) = 2217877 mm <sup>2</sup>
$\rho$	0.02583	0.01096	0.01353
$\epsilon_{\rho}^{\max}$			0.0070

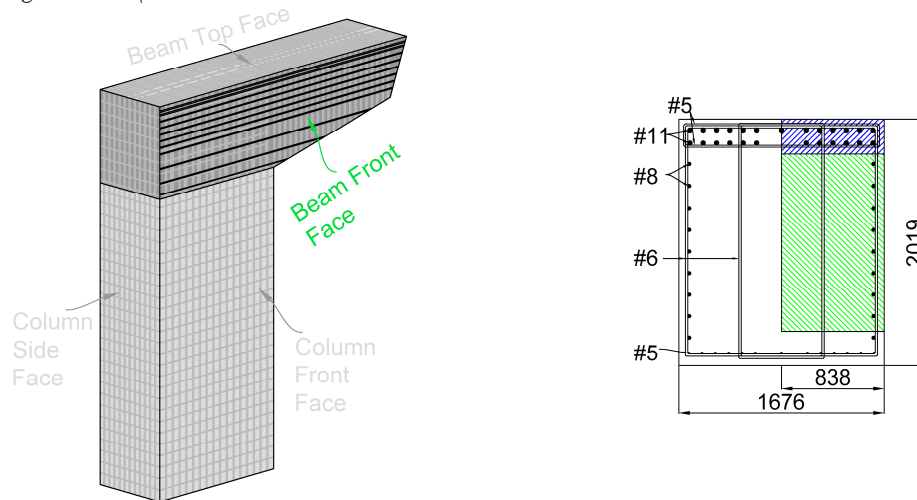
For members 30/29 and 43/49 that are within the specimen development length zone the reinforcement ratio in the interior regions (shaded green) is scaled down.

Member	l (mm)	$\rho_{reduced} = \rho(l/l_d)$ [ $\rho = 0.01096$ ]	$\epsilon_{\rho}^{\max}$
30/29	1424	0.00894	0.0094
43/49	609.6	0.00383	0.0168

Sheet 9-3 f	COMPUTATION OF REINFORCEMENT RATIO $\rho$ AND MAXIMUM EXPANSION STRAIN $\epsilon_p^{\max}$ FOR PIER 15C	6 8
----------------	--	--------

**BEAM FRONT FACE**

Concrete and steel volume in half the section-depth  $d = 838$  mm is considered for calculating the reinforcement ratio.



Separate reinforcement ratios are computed considering the blue and the green shaded regions separately and also for the entire shaded region (shaded blue + green). In this case the effects of tensile/compressive prestrains are neglected in the computation of  $\epsilon_p^{\max}$  as the beam front face has a combination of both tensile and compressive strains.

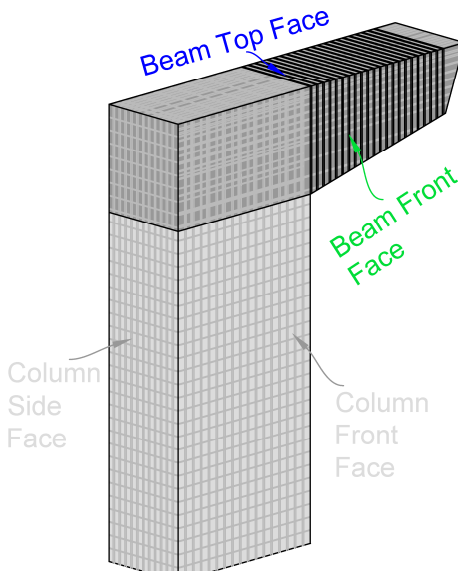
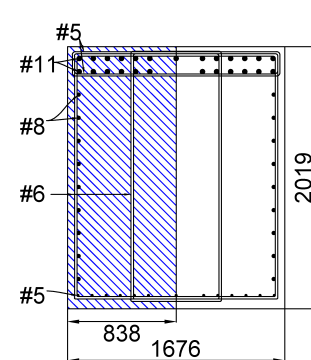
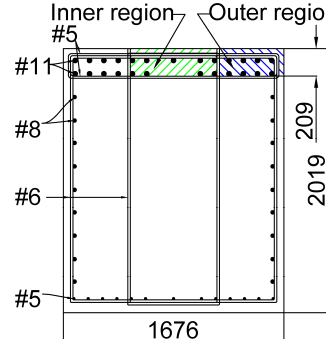
$$\epsilon_{spre} = \epsilon_{spre} = 0$$

	Close to member edges (shaded blue)	For interior regions (shaded green)	Considering entire half-depth
Area of steel, $A_s$	11496 mm <sup>2</sup> (12-#11 bars)	4054 mm <sup>2</sup> (8-#8 bars)	17244 mm <sup>2</sup> (12-#11 + 9-#8 + 6-#5)
Area of concrete, $A_c$	(838)(300) = 251400 mm <sup>2</sup>	(838)(1419.1) = 1189206 mm <sup>2</sup>	(838)(2019) = 1691922 mm <sup>2</sup>
$\rho$	0.04571	0.00341	0.01019
$\epsilon_p^{\max}$			0.0064

For member 43/49 that are within the specimen development length zone the reinforcement ratio in the interior regions (shaded green) is scaled down.

Member	l (mm)	$\rho_{reduced} = \rho(l/l_d)$ [ $\rho = 0.00341$ ]	$\epsilon_p^{\max}$
43/49	609.6	0.00164	0.0222

Sheet 9-3 g	COMPUTATION OF REINFORCEMENT RATIO $\rho$ AND MAXIMUM EXPANSION STRAIN $\epsilon_{\rho}^{max}$ FOR PIER 15C		7 8	
<b>COLUMN TRANSVERSE</b>				
Due to the complex nature of the hoop layout, and corresponding localized expansion strains, the reinforcement ratios are computed accordingly.				
<b>Column Front Face</b>		<b>Column Side Face</b>		
	Inner Region (Shaded Green)	Outer Region (Shaded Blue)	Inner Region (Shaded Green)	Outer Region (Shaded Blue)
$A_s$ (mm <sup>2</sup> )	126.65 (1 leg of #4 bar)	253.35 (2 legs of #4 bar)	126.65 (1 leg of #4 bar)	253.35 (2 legs of #4 bar)
$ds$ (mm <sup>2</sup> )	(813)(305) = 247965		(639)(305) = 194895	
$\rho$	0.00051	0.00102	0.00065	0.0013
Average $\rho$	0.00077		0.000975	
$\epsilon_{\rho}^{max}$	0.03258		0.02968	

Sheet 9-3 h	COMPUTATION OF REINFORCEMENT RATIO $\rho$ AND MAXIMUM EXPANSION STRAIN $\epsilon_{\rho}^{\max}$ FOR PIER 15C	8 8	
BEAM TRANSVERSE			
			
			
	Close Beam Front Face	Close Beam Top Face	
	(Shaded Blue)	Inner Region (Shaded Green)	Outer Region (Shaded Blue)
$A_s$ (mm <sup>2</sup> )	570.1 (2 legs of #6 bar)	768 (2-#6 and 1-#5 bar)	483 (1-#6 and 1-#5 bar)
$ds$ (mm <sup>2</sup> )	(838)(152) = 127376	(209)(152) = 31768	
$\rho$	0.00448	0.02418	0.01520
Average $\rho$	--	0.01970	
$\epsilon_{\rho}^{\max}$	0.01222	0.00412	

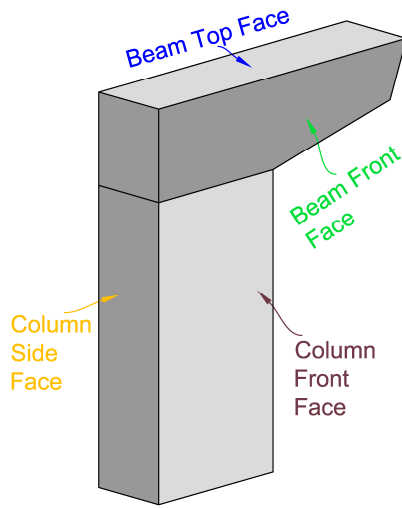
Figures 9-17 and 9-18 respectively show the variation of ASR/DEF induced expansion strains in the longitudinal and transverse directions of the various regions of pier I5C, based on input parameters deduced from the C-beam and the free-expansion test observations. Based on the maximum possible expansion strains presented in Figure 9-17, an estimate is made on the maximum possible crack width in the various regions of the pier. Table 9-4 shows the estimated maximum possible total crack widths that may be expected across the width of the column and the beam of pier I5C.

**Table 9-4: Maximum Potential Crack Width in Pier I5C based on Modeled Transverse Expansion Strains.**

<b>Pier Region</b>	<b>Width (mm)</b>	<b>Modeled maximum expansion strain</b>	<b>Crack width strains</b>	<b>Estimated total crack width across the width (mm)</b>
Column front face	2134*	0.0326 (Figure 9-17a)	0.0163	35
Column side face	762*	0.0297 (Figure 9-17b)	0.0149	11
Beam front face	2019 <sup>+</sup>	0.0122 (Figure 9-17c)	0.0061	12
Beam top face	1676	0.0041 (Figure 9-17d)	0.0021	3

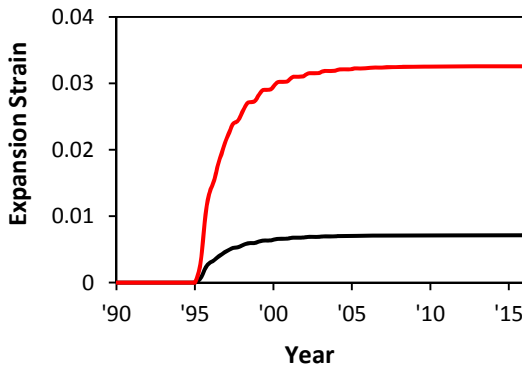
\*The width of the member within the architecture detail of the column is considered.

<sup>+</sup>Average depth of the pier cap with varying cross section.

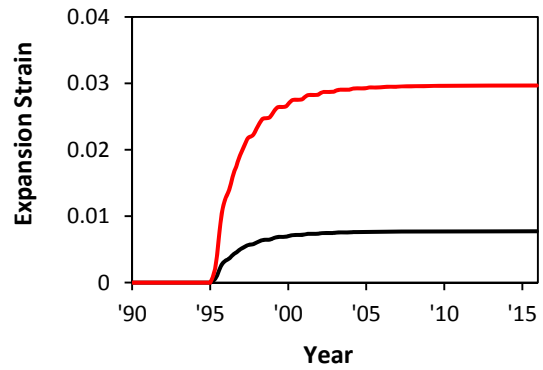


LEGEND: Different Regions of Pier 15C

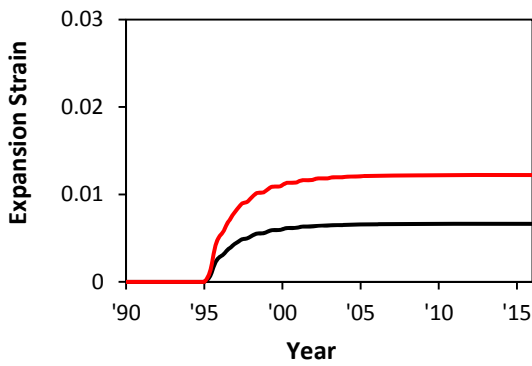
— Longitudinal Expansion Strains Outside DL Zone      — Transverse Expansion Strains



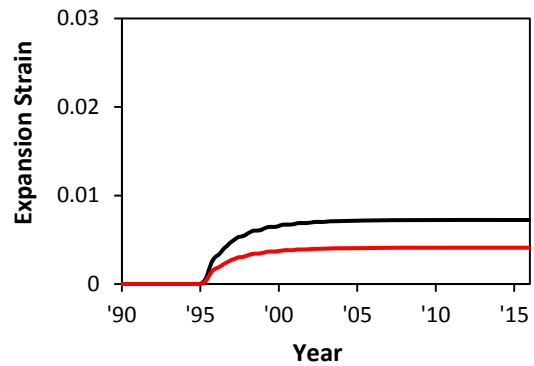
(a) Column Front Face



(b) Column Side Face

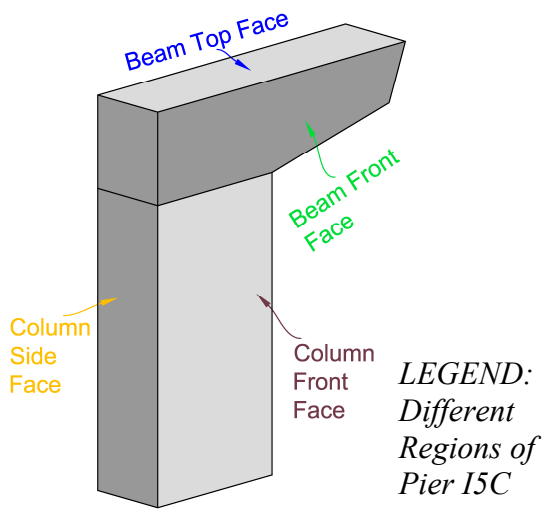


(c) Beam Front Face

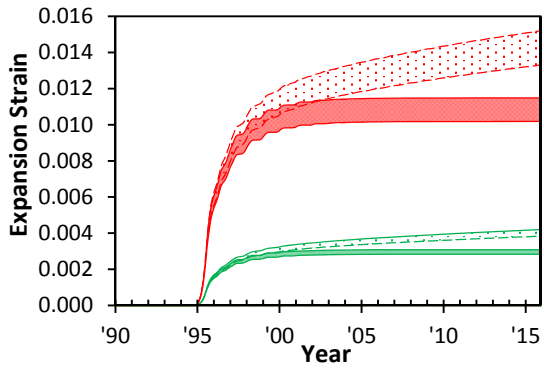


(d) Beam Top Face

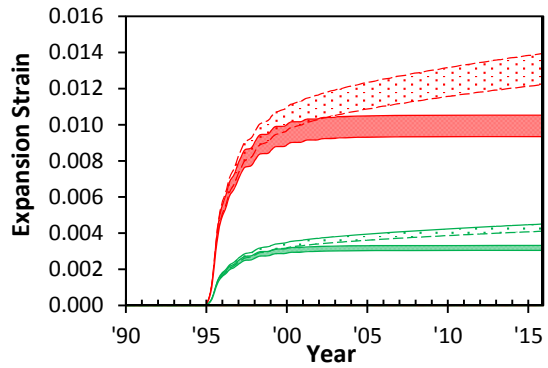
Figure 9-17: Modeled ASR/DEF Induced Expansion Strains in Pier 15C based on Observations from Experimental C-beam Specimens.



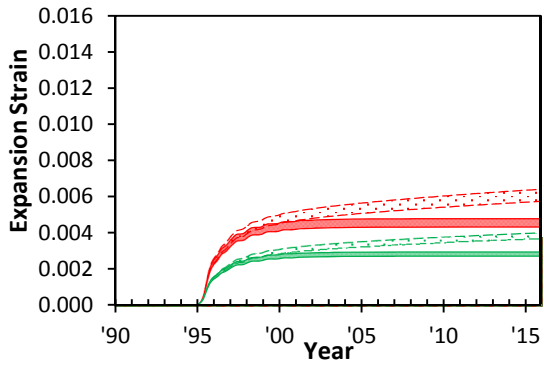
- ▨ Transverse Strains: ASR+DEF
- Transverse Strains: DEF
- ▨ Longitudinal Strains: ASR+DEF
- Longitudinal Strains: DEF



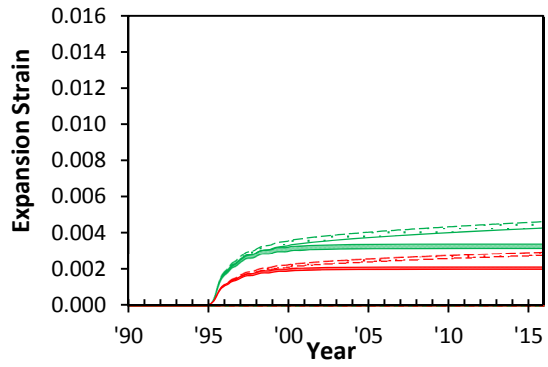
(a) Column Front Face



(b) Column Side Face



(c) Beam Front Face



(d) Beam Top Face

**Figure 9-18: Modeled ASR/DEF Induced Expansion Strains in Pier I5C based on Free Expansion Tests on Cores from H19C.**



### 9.5.3 The C-STM Model

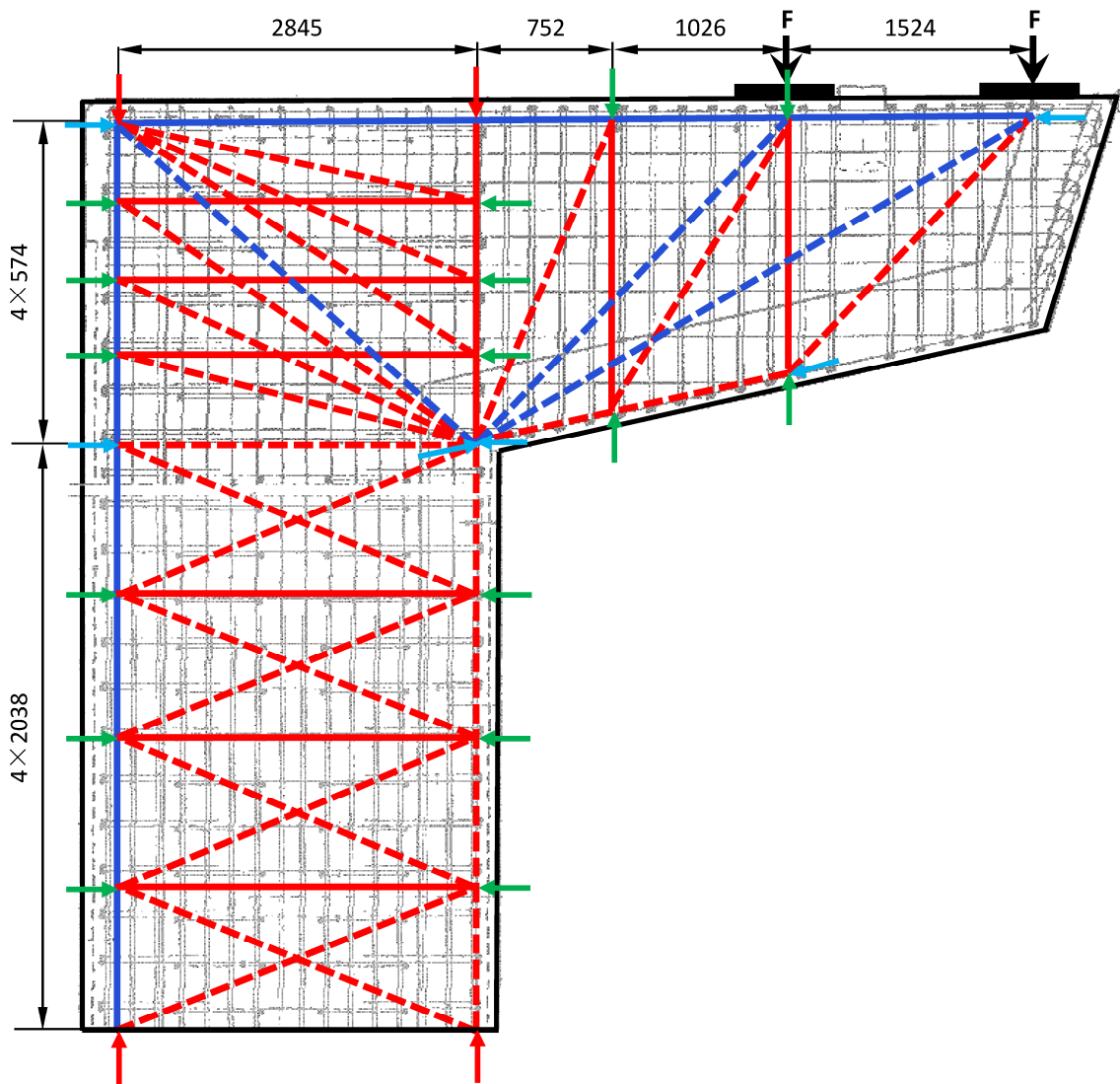
Figure 9-19 shows the C-STM model developed for pier I5C. The span that this pier supports is seated on two bearing pads near the outer part of the cantilever. These two pad locations are used to analyze the load capacity of the pier.

The cantilever portion of the pier is modeled using the single point Gauss truss model up to the bearing pad close to the column face, while the rest of the model is completed with a corner-to-corner diagonal arch from the outermost point of application of loads to the column face. The beam-column joint of the pier is modeled using a truss based on Boole's rule, where the ties clustered are at quarter points. This model was chosen to better represent the flow of stresses within the beam-column joint. The column was modeled using a simple truss model as shown in Figure 9-19.

The pier is analyzed without and with damage due to ASR/DEF effects. Prestressing forces are applied on the longitudinal and transverse reinforcements in the beam and the column in order to replicate the prestress effects that arise as a consequence of the swelling within the core concrete due to ASR/DEF effects. The prestressing forces are evaluated from the modeled expansion strains presented in Figure 9-17 and Figure 9-18. A detailed computation of the prestrains (based on Figure 9-17) in the various members of the C-STM are presented in engineering computation Sheets 9-4a to c.

Table 9-5 presents a summary of prestrains for the different longitudinal and transverse members of the C-STM model for pier I5C. Based on the prestrains and the area of the steel member, the prestress forces on the C-STM members are calculated. The stress-strain relation of the reinforcement are also modified accordingly as shown in Figure 9-2e.

To replicate a logical sequence of loading, the C-STM was first loaded with the dead loads from the pier followed by the dead loads from the girder. This was followed by the prestress forces due to ASR/DEF expansion and then finally the structure is loaded to failure.



- Primary tension reinforcement
- Ties representing bundles of hoops
- - - Concrete struts for the truss
- - - Central concrete arch
- Initial confinement effect in hoops and longitudinal steel due to concrete swelling, modeled as a set of externally applied nodal forces
- 
- 

Note: The additional nodal forces represent the prestress effect actively induced in the reinforcing steel caused by ASR/DEF induced concrete swelling.

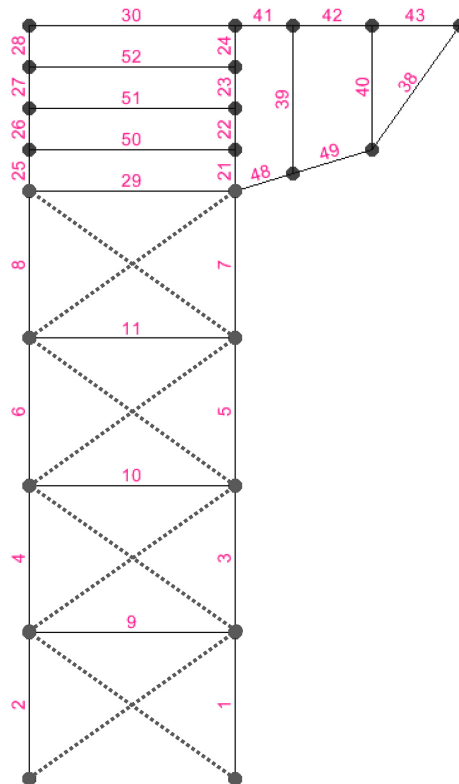
**Figure 9-19: C-STM Model of Pier 15C.**

GENERAL NOTES

Development length of #11 bars = 1746 mm  
 Development length of #8 bars = 1270 mm

Distance to center of C-STM members l from edges of the  
 structure that are within the development length

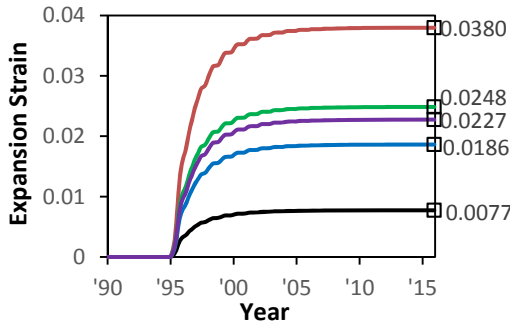
Member	l (mm)
24/28	287.5
23/27	862.3
22/26	1437.1
1/2	1019.3
30	1424
43	609.6



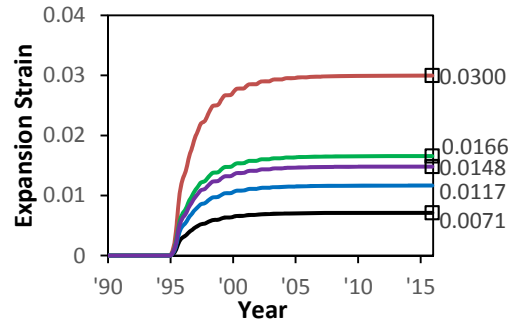
COLUMN MEMBERS

LONGITUDINAL MEMBERS

— Outside DL — Member 1/2 — Member 22/26 — Member 23/27 — Member 24/28



Expansion model for column side face



Expansion model for column front face

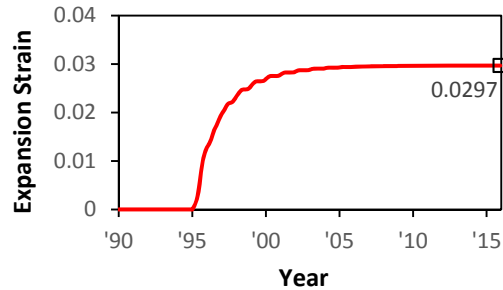
Tension Members: Prestraints are computed considering the average of the expansion strains in the column front face and the column side face.

Compression Members: Prestraints are computed from the expansion strains in the column front face.

Member	Prestrain	Member	Prestrain
Outside DL	$(0.0077 + 0.0071) / 2 = 0.0074$	Outside DL	0.0071
2	$(0.0227 + 0.0148) / 2 = 0.0188$	1	0.0148
26	$(0.0186 + 0.0117) / 2 = 0.0151$	22	0.0117
27	$(0.0248 + 0.0166) / 2 = 0.0207$	23	0.0166
28	$(0.0380 + 0.0300) / 2 = 0.0340$	24	0.0300

TRANSVERSE MEMBERS

The prestrain in the transverse members of the column is: 0.0297



Expansion model for transverse column members

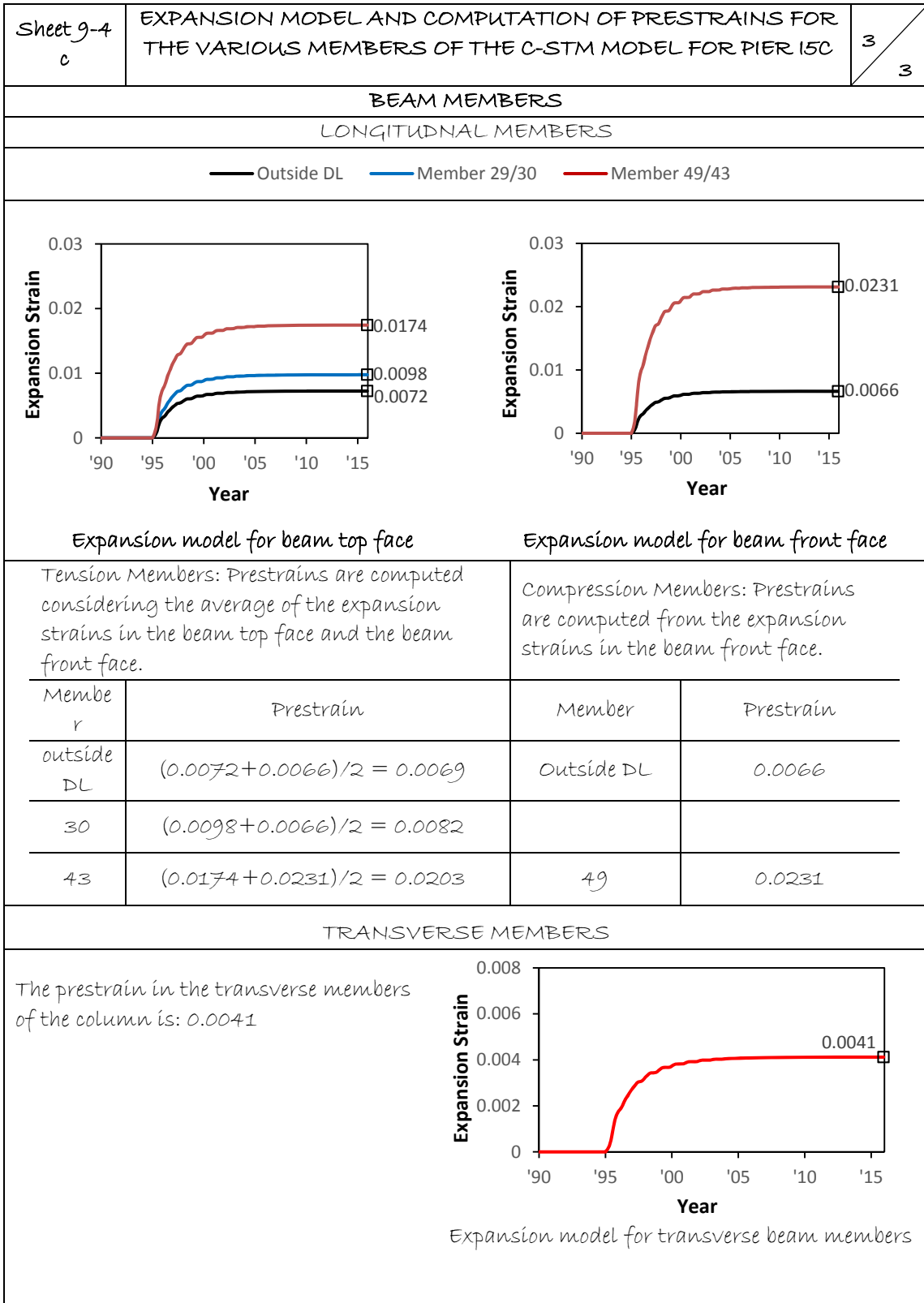
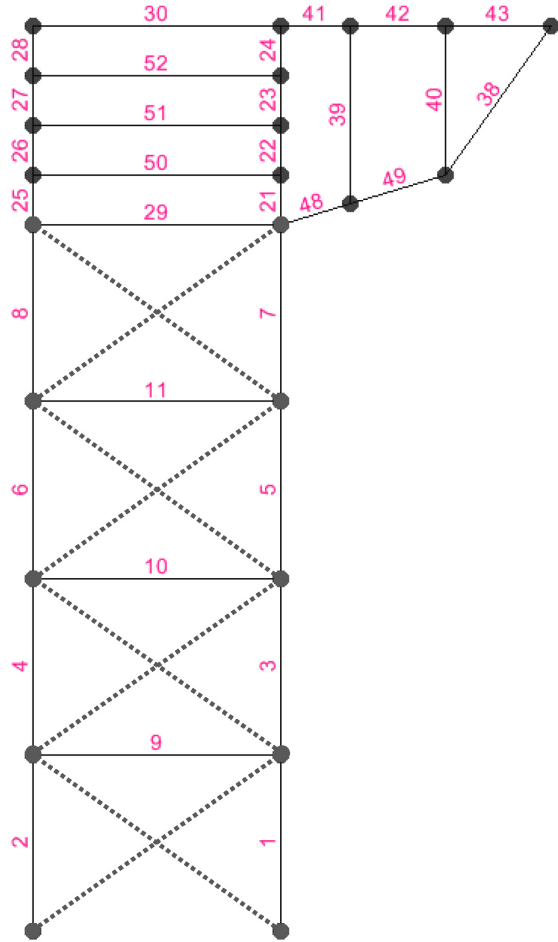


**Table 9-5: Prestrains in the C-STM Members of Pier I5C.**

<b>Column Members</b>	
<i>Member</i>	<i>Prestrain</i>
1	0.0148
22	0.0117
23	0.0166
24	0.0300
Compression Members outside DL	0.0071
2	0.0188
26	0.0151
27	0.0207
28	0.0340
Tension Members outside DL	0.0074
Transverse Members	0.0297
<b>Beam Members</b>	
49	0.0231
Compression Members outside DL	0.0066
30	0.0082
43	0.0203
Tension Members outside DL	0.0069
Transverse Members	0.0041



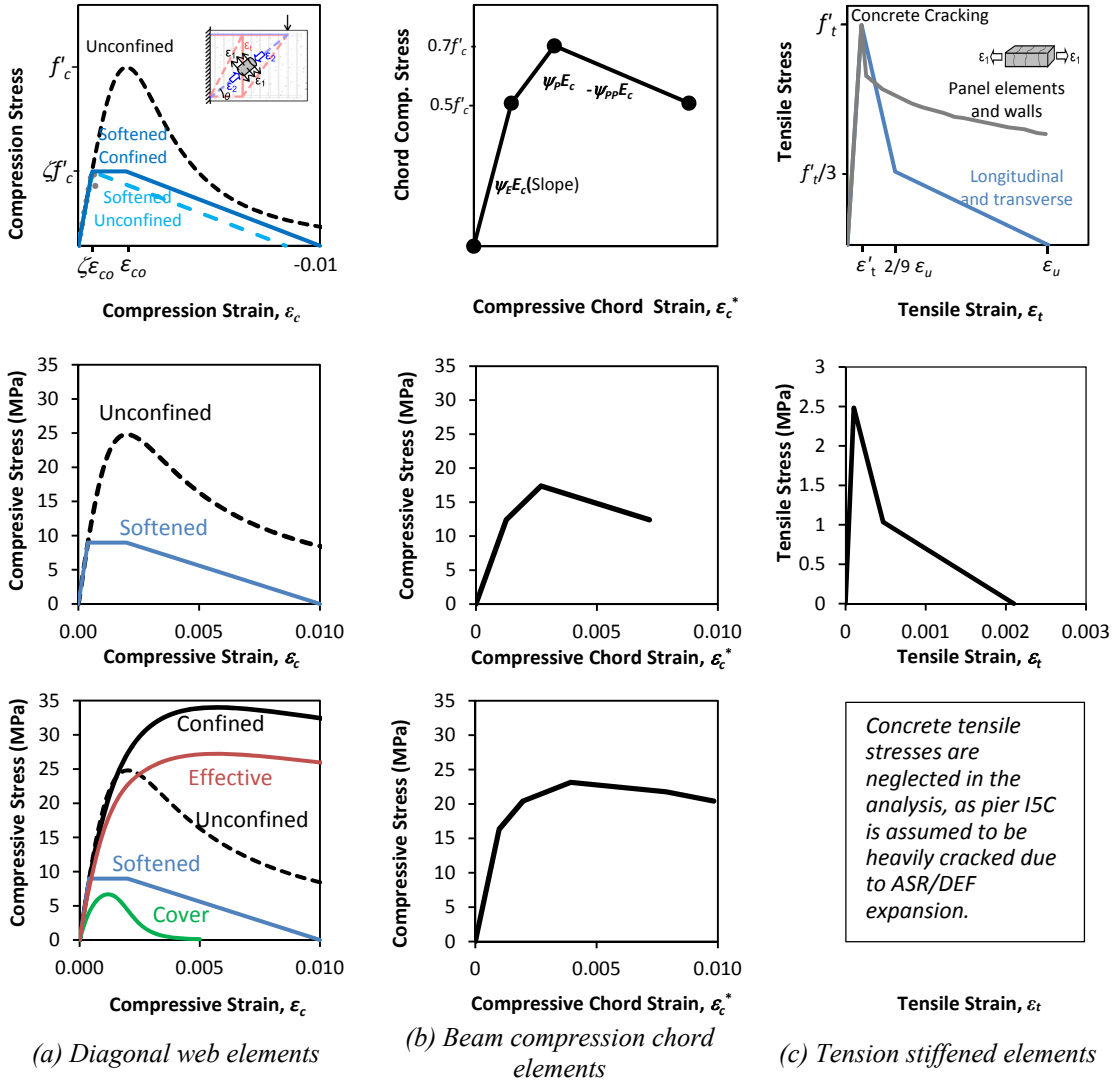
*C-STM Members*

The confinement ratio for the specimen is calculated to be  $K_{cc} = 1.37$  for the beam and  $K_{cc} = 1.06$  for the column core concrete. Figure 9-20 shows the different nonlinear concrete stress-strain relationships that are derived for pier I5C without and with ASR/DEF effects. As both the cover and core concrete areas contribute to the area of the strut in the C-STM model, a weighted average of concrete compressive strength is used in the C-STM model considering the effects of ASR/DEF deterioration. Owing to the hoop reinforcement being completely enclosed, the softened confined model is assumed for the softened diagonal concrete members. The concrete tensile strength is neglected in the C-STM analysis considering the present effects of ASR/DEF.

#### **9.5.4 C-STM Results and Discussion**

Figure 9-21 shows the force-deformation results obtained from C-STM analysis without and with ASR/DEF effects. The prestrains obtained from modeled expansion strains presented in Figure 9-17 and Figure 9-18 are evaluated for the C-STM analysis including the effects of ASR/DEF. The critical events that result in a major change in stiffness of the force-deformation behavior of the structure are marked as points along the force-deformation curve. The model captures the initial tension stiffening effects of the structure quite well. The cracking of concrete in the beam-column joint at around 5680 kN leads to the first major change in slope of the force-deformation curve. The next major nonlinear event that has a significant effect on the behavior of the structure occurs at 11200 kN and is caused by flexural yielding of the longitudinal beam reinforcement. This is followed by the yielding of the hoop reinforcement in the beam-column joint. The final event that leads to the failure of the pier is the crushing of the softened diagonal arch in the beam-column joint.

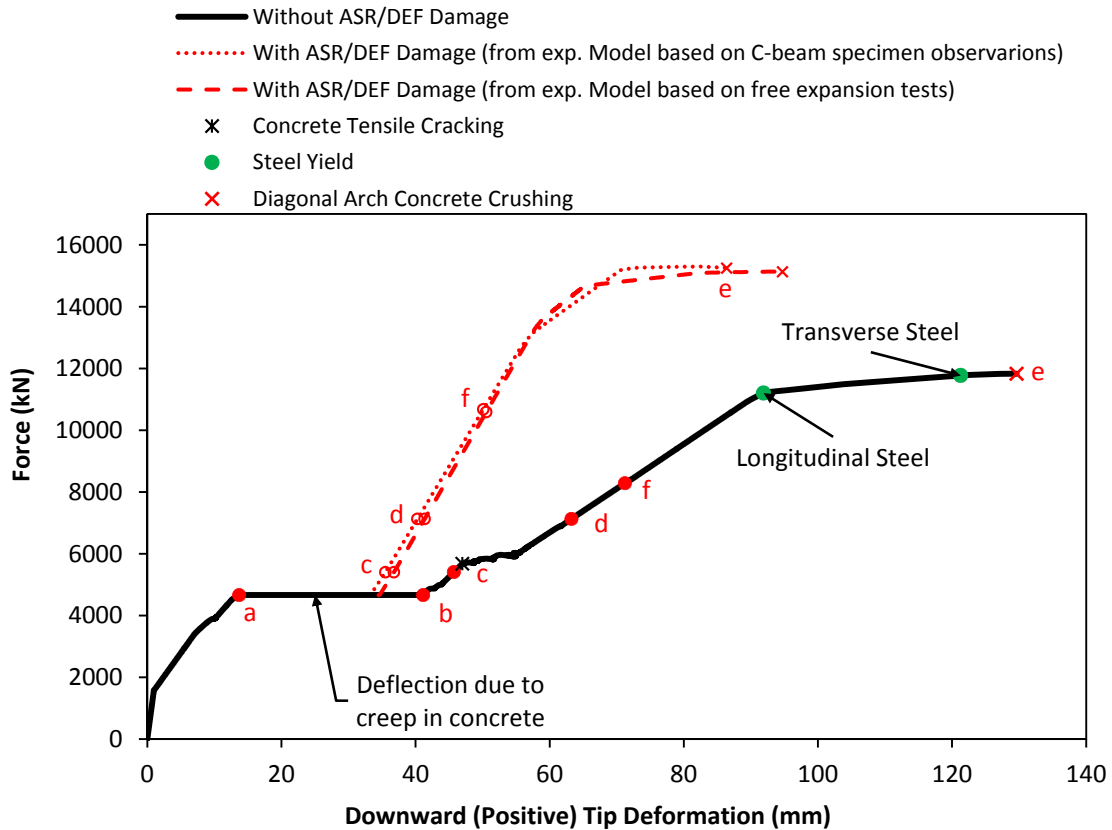
The structure affected by ASR/DEF deterioration has a stiffer force-deformation response due to the prestressing effects from ASR/DEF related expansion. The change in slope of the force-deformation curve at approximately 15000 kN corresponding to the onset of diagonal arch concrete softening. As in the case of the structure without ASR/DEF deterioration, the final event that causes the failure of the deteriorated pier is



Row 1: Theoretical nonlinear behavior.  
 Row 2: Modeled behavior, without ASR/DEF effects.  
 Row 3: Modeled behavior, with ASR/DEF effects.

**Figure 9-20: Cracked Reinforced Concrete Material Properties for Pier I5C.**





- (a) D = Self-weight.
- (b) D + Creep = Self-weight + Creep deflections.
- (c) D + (L+I) = Maximum service load.
- (d) 1.25 D + 1.75 (L+I) = Ultimate load demand.
- (e)  $P_n$  = Nominal maximum capacity.
- (f)  $\phi P_n$  = Factored capacity (where  $\phi = 0.7$  for shear).

**Figure 9-21: Force-Deformation of Pier I5C without and with ASR/DEF Damage.**

the crushing of the softened arch in the beam-column joint. It is also evident from Figure 9-21 that there is negligible difference in the overall force deformation behavior of the structure, irrespective of the modeled expansion strain presented in Figure 9-17 or Figure 9-18 that was used to compute the prestrains.

The nominal maximum capacity  $P_n$  of the bridge pier without ASR/DEF damage is found to be 11800 kN. However, the structure can be deemed unsuitable for use after the yielding of the longitudinal reinforcement at 11200 kN. However for the case with ASR/DEF damage, due to confining effects, the nominal maximum capacity  $P_n^{\text{ASR/DEF}}$  is approximately 15200 kN, which is about 36 percent higher than the nominal capacity of the structure without ASR/DEF deterioration, that is,  $P_n^{\text{ASR/DEF}} = 1.36P_n$ .

Although counterintuitive, the analysis shows that there has likely been significant stiffening and strengthening of the pier already, due to ASR/DEF damage arising from the effects of the swelling of the core concrete. It is to be noted, however, that there is a decrease in the ductility of the structure affected by ASR/DEF deterioration, and a more brittle failure could be expected. These findings are in agreement with the experimental observations made in Section 7.

- The factored ultimate load demand on the structure due to dead loads, and live plus impact loads  $P_u = 7130$  kN.
- The factored capacity of the structure without ASR/DEF deterioration  $\phi P_n = 0.7 \times 11200 = 7840$  kN. From this the overstrength factor is determined to be  $\Omega = 1.10$ .
- The factored capacity of the structure with ASR/DEF deterioration  $\phi P_n^{\text{ASR/DEF}} = 0.7 \times 15200 = 10640$  kN. From this the overstrength factor is determined to be  $\Omega = 1.49$ .

Based on the above findings, the ASR/DEF deteriorated structure can be deemed safe with regard to its load carrying capacity. However, there is a significant reduction in the ductility of the structure. In addition, the cracking caused by ASR/DEF expansion

can act as a pathway for moisture ingress which may in turn lead to early corrosion of the reinforcing steel; such early corrosion could have some unseen adverse effects on the structure.

## **9.6 Key Findings**

The key observations from the analysis of the two large bridge piers are as follows:

- Parameters required to model the expansion strains, specifically the maximum free expansion strain and the rise time, can be estimated by appropriately modeling the free expansion tests performed on core samples extracted from the structure. This information compiled with observed crack-width readings can be used to justify the initial conditions of the required analyses.
- The ASR/DEF expansion model shows that significant expansion strains and large crack widths are possible in reinforced concrete bridge piers that are subjected to the deterioration effects of ASR/DEF induced expansion.
- While ASR/DEF induced concrete expansion strains can cause severe cracking and adversely affect the appearance of a concrete bridge pier, analysis results show that the ultimate strength is not significantly negatively impaired. However, there may be a slight reduction in the ductility of the structure.
- For pier H19C it was observed that the factored capacity due to Case 1 loading that caused flexural yielding of the column was less than the factored capacity due to Case 2 loading, which caused shear failure at the beam-column joint. Both load cases had large overstrength factors.
- Pier I5C also exhibited sufficient overstrength factor, and was found to be critical at the beam-column joint. The final mode of failure was the crushing of corner-to-corner arch in the beam-column joint.
- The cracks caused by ASR/DEF expansion process can act as a pathway for moisture ingress into the structure, which may lead to accelerated corrosion of the reinforcing steel. It is not known how a combination of ASR/DEF expansion and corrosion can affect the strength, stiffness and ductility of the structure.

- Even though the load carrying capacity of the structure is not adversely affected by ASR/DEF expansion, owners cannot be complacent. The previously conducted tests (Section 7) have shown that significant cracking arising from ASR/DEF damage mechanisms act as a pathway to new and perhaps even more precarious damage—rebar corrosion. Thus it would behoove owners to continue to investigate this possibility in ongoing biannual federally mandated inspections.

## 10 SUMMARY, CONCLUSIONS, AND RECOMMENDATIONS\*

### 10.1 Summary

It has been observed that a significant number of large concrete bridge piers exhibit premature concrete deterioration. The deterioration has been attributed to the detrimental effects of ASR and DEF induced expansions. The excessive cracking on these reinforced concrete piers due to ASR/DEF effects has been a major concern for the state DOT engineers, and creates uncertainty about the strength and hence safety and longevity of the bridges affected. It is of utmost importance to assess the effects that *heavy* ASR/DEF deterioration of concrete can have on the structural performance of the reinforced concrete bridge piers.

In this research the effects of *heavy* ASR/DEF on structures were investigated by means of a dual experimental and analytical modeling program. The following were the main tasks identified in this research to study the behavior and assess the performance of reinforced concrete bridge piers subjected to the detrimental effects of ASR/DEF:

- Propose modifications to the force-based C-STM analysis technique to take into account the softened concrete model and conduct the analysis in displacement-control, and validate the proposed changes for monotonic and cyclic loading conditions.
- Monitor the ASR/DEF induced expansion strains in the *heavily* deteriorated C-beam Specimen 3, which was field conditioned for a total period of five years, through visual observations and mechanical measurements.
- Perform the destructive testing of *heavily* ASR/DEF deteriorated C-beam Specimen 3 and compare its performance with previously tested *undamaged* control, and *slight* and *moderately* deteriorated C-beam specimens.

---

\* Previously published work is available to the public through National Technical Information Service. Mander, J.B., Karthik, M.M., and Hurlebaus, S. (2015). "Structural Assessment of "D" Region Affected by Premature Concrete Deterioration: Technical Report." *Report No. FHWA/TX-15/0-5997-2*, Texas A&M Transportation Institute, College Station, Texas, USA.

- Determine the cause of failure of the C-beam specimen based on visual observations and the measurements made during the destructive testing of C-beam Specimen 3.
- Establish any effect ASR/DEF deterioration may have on the load carrying capacity of the bridge bents and investigate their causes.
- Develop and validate a minimalist semi-empirical analytical model to simulate the expansion strains induced by ASR and DEF in reinforced concrete structures.
- Apply the expansion model to the C-beam specimens to simulate the ASR/DEF induced expansion strains observed over time.
- Devise a method to incorporate the effects of ASR/DEF induced expansion strains into the C-STM analysis technique by inferring strains results from the ASR/DEF expansion model, and making necessary modifications to the concrete and steel material properties.
- Apply the modified displacement-based C-STM technique to model the force-deformation and internal behavior, and to assess the failure mode of the experimentally tested C-beam specimens without and with ASR/DEF deterioration.

A brief summary of the experimental and analytical program follows:

#### **10.1.1 Deterioration Program**

- Specimen 3 was constructed as part of the total four C-beam specimens that were designed and constructed to be representative of two typical bridge bents in Texas: *(i)* the cantilever bent and *(ii)* straddle bent.
- C-beam Specimen 3 was field conditioned for a total of five years, and based on the visual observations and strain measurements, Specimen 3 was classified as showing *heavy* deterioration due to ASR/DEF effects.

### 10.1.2 Destructive Load Testing

- At the end of the deterioration phase, C-beam Specimen 3 was transported back to the laboratory to determine the effects of *heavy* ASR/DEF deterioration on the load carrying capacity and structural performance of the C-beam specimen.
- Similar to the previously tested deteriorated C-beam specimens (Mander et al., 2012), the singly reinforced side of C-beam Specimen 3 failed. The failure mechanism, which was a brittle joint shear failure along the diagonal corner-to-corner concrete arch in the beam-column joint, was observed to be the same in all the four C-beam specimens. However, Specimen 3 showed a considerably stiffer response and reduced ductility when compared to the other C-beam specimens.
- It was concluded that the more brittle nature of failure was due to the lack of reinforcement in one side of the joint region, while the other side possessed lapped hoops, which evidently became ineffective at high levels of ASR/DEF induced expansion.
- In spite of the *heavy* damaged nature of cracking arising from concrete swelling caused by ASR/DEF deterioration, Specimen 3 had similar ultimate load capacity as the *slight* and *moderately* deteriorated specimens and all the three deteriorated specimens had higher load capacity than the *undamaged* control Specimen 1.
- After five years of outdoor conditioning, Specimen 3 exhibited a considerable degree of *hidden* corrosion damage in the reinforcing steel. However, the extent of corrosion observed in Specimen 3 did not have any adverse effect on its load carrying capacity. Nevertheless, due to corrosion, the lapped hoops in the beam-column joint zone were ineffectual in confining the joint core concrete. Consequently, due to the ill-confined concrete, any ductility capability the C-beam specimens previously exhibited (in Specimens 1, 2, and 4) was lost and the failure mode of Specimen 3 was sudden and brittle.

### 10.1.3 Analytical Modeling: ASR/DEF Expansion

- A minimalist semi-empirical model was developed and validated to simulate the expansion strains observed in reinforced concrete specimens subjected to ASR/DEF expansion. This model has few input parameters and is capable of taking into account the daily variations in temperature and degree of moisture saturation of concrete structures that are exposed to the environment.
- It was demonstrated that if the correct reinforcement ratios were computed, the model could simulate the expansion strains over time quite well. The developed model was used to simulate the expansion strains that were observed in the C-beam specimens, and generally good agreement between the model and observed data was observed.

### 10.1.4 Analytical Modeling: C-STM

- The robustness of the C-STM analysis technique as a suitable minimalist method to model the force-deformation behavior of reinforced concrete bridge piers with significant D-regions was demonstrated by Scott et al. (2012a, b). Certain deficiencies were identified in this technique, and modifications were proposed to the force-based C-STM.
- The C-STM takes into account the combined shear resistance provided by the truss and arch action. The model was implemented into widely used commercial structural analysis software (SAP2000, 2014) and validated against results from previously conducted large scale experiments for both monotonic and cyclic loading.
- To capture the more serious level of *heavy* damage caused by ASR/DEF expansion, a discrimination was made between softened confined and softened unconfined concrete. This was introduced into the C-STM analysis by slightly reducing the post-peak softened strain of the diagonal concrete compression strut.
- The effects of ASR/DEF on the structure were modeled into C-STM by applying prestress forces at the nodes to mimic the prestressing effects caused by the



restraint offered by reinforcement to the swelling of core concrete. Modifications were also made to the concrete properties to account for the cracking of cover concrete and swelling of core concrete.

- Based on ASR/DEF volume expansion modeling, a direct method is now available to compute the amount of prestress to be applied on the C-STM model to mimic the prestressing effects caused by swelling of concrete.
- It was observed that the C-STM modeled the overall and the internal behavior of the structure without and with ASR/DEF deterioration quite well. The C-STM also shed light into the progression of nonlinear failure mechanisms and the final mode of failure of the C-beam specimens.

## **10.2 Conclusions**

The key conclusions that can be drawn from the experimental testing and analytical modeling follows:

### **10.2.1 Concrete Deterioration due to ASR/DEF**

- ASR/DEF expansion in concrete can cause severe cracking in reinforced concrete structures. The largest crack that was observed on the *heavily* deteriorated C-beam Specimen 3 that was exposed to the environmental conditions and supplemental water supply for five years was found to be approximately 30 mm wide.
- The strains in the longitudinal and transverse reinforcement exceeded the yield strain over the course of the deterioration phase of C-beam Specimen 3 at one year and six months of exposure, respectively.
- The cracks act as a pathway for moisture ingress into the core of the specimen. In turn this moisture promotes a considerable amount of corrosion of the exposed reinforcing bars.
- Corrosion of reinforcement within the specimen was not self-evident during field inspections. There was none of the common rust stains that one would expect to observe when significant corrosion is present. Thus the true condition of

Specimen 3, while badly cracked from ongoing ASR/DEF damage, was quite *deceptive*.

### 10.2.2 Observations from Destructive Testing

- The cause of failure of Specimen 3 during its destructive load testing was observed to be a brittle joint shear failure through the corner-to-corner arch in the beam-column joint. This failure mode was the same as that observed in the previously tested C-beam specimens without and with varying levels of ASR/DEF induced deterioration.
- The trigger of the failure mechanism was the decompression of concrete that was prestressed due to the restraint offered by reinforcement to ASR/DEF induced concrete expansion. Once concrete decompression occurred, a redistribution of joint forces through the transverse reinforcement in the joint was necessary.
- Since the joint transverse reinforcement had limited capacity and as that reinforcement had already yielded during the deterioration/expansion phase, there was a sudden drop in resistance and the failure was quite sudden and brittle. As in the case of the other three C-beam specimens tested earlier, the lack of proper detailing in the beam-column joint led to this failure mechanism.
- However, the ultimate load capacity of the *heavily* deteriorated Specimen 3 was found on par with the *slightly* and *moderately* deteriorated specimens, and remained above the ultimate load capacity of the *undamaged* control Specimen 1.
- The stiffness of Specimen 3 was notably higher than the other three C-beam specimens. This was attributed to the higher level of concrete swelling observed in Specimen 3, which in turn put the concrete into a greater level of prestress and thereby more effectively confined the core concrete.
- Although no sign of corrosion was observed during the deterioration phase, (through spalling of cover concrete or rust stains on the concrete specimen) considerable amounts of corrosion in the reinforcement was observed after removal of the cover concrete after the experimental test. The deterioration period of five years was evidently not sufficient for the adverse effects of

corrosion to reduce rebar area to affect the overall results. Nevertheless, this outcome cannot be assumed to apply to longer term field exposure.

### **10.2.3 Observations from Analytical Modeling of ASR/DEF Expansion**

- The proposed minimalist semi-empirical model needs limited input parameters, which can be deduced from expansion observations and material properties.
- The model can simulate the expansion caused by ASR and/or DEF in reinforced concrete laboratory specimens cured under constant temperature and saturated conditions to accelerate ASR/DEF expansion.
- In addition to the effects of varying temperature and saturation on ASR/DEF induced expansion strains, the effects of compressive and tensile stresses were also included in the formulation.
- By taking into account the appropriate reinforcement ratios, the model was able to simulate the expansion strains in the longitudinal and transverse directions. Considering the complex nature of ASR/DEF expansion mechanism, and the wide scatter of field recorded data, the model was able to simulate the expansion strains quite well.

### **10.2.4 Inferences from Code-Based Analysis**

- An analysis procedure was used to evaluate the C-beam specimens based on the current code based methods, i.e., the flexural beam theory and the SAT method. It was observed that the beam theory and the SAT technique were able to predict the yield loads of the C-beam specimens with satisfactory accuracy.
- The factored externally applied load obtained from the nominal moment for the C-beam specimens was 0.83 to 0.91 times the ultimate load at failure from the experimental tests.
- The factored shear capacity was found to be close to 50 percent of the ultimate load obtained from the experiments for all the C-beam specimens.

- A similar observation was made from the SAT analysis, where the ratio of the factored externally applied load leading to node failure to the experimental results were between 0.33 to 0.49.
- It was concluded that the code-based analysis techniques could not give a satisfactory estimate of the failure load for any of the C-beam specimens.

#### **10.2.5 Observations from the C-STM Analysis**

- The displacement-based C-STM analysis was developed and validated against previously conducted large-scale experiments for both monotonic and cyclic loading. The displacement-based C-STM method shows much promise in the analysis of reinforced concrete structures possessing substantial D-regions.
- By inferring expansion strains from the ASR/DEF expansion model, and modifying the concrete and steel material properties, the effects of ASR/DEF on the C-beam specimens could be easily accounted for in the C-STM analysis.
- The C-STM technique was employed to model the experimental C-beam specimens and was able to simulate quite well the overall force-deformation behavior and the internal behavior of the *undamaged* control specimen (without any ASR/DEF deterioration) and the specimens with *slight*, *moderate* and *heavy* ASR/DEF deterioration.
- It was demonstrated that by carefully considering the effects of ASR/DEF on the structure, necessary modifications could be made to the C-STM to model structures affected by ASR/DEF expansion.
- The C-STM was able to model the internal behavior of the C-beam specimens quite well and also provided an insight into the complexities of the internal behavior throughout the structure and the D-regions in particular.
- The C-STM was also able to identify the progression of nonlinear mechanisms and the final mode of failure of the C-beam specimens, and was consistent with the experimental test observations.

### 10.3 Recommendations and Future Work

From the experimental and analytical results and observations it is clear that the joint detailing of the C-beam specimens, representing cantilever and straddle bridge bents, was insufficient to prevent failure of the beam-column joint. It is recommended that a greater amount of transverse reinforcement be provided in the beam-column joint to enable better shear transfer mechanism. It is also recommended that, where practicable, 135° hooks at the ends of all hoops and ties within the joint region be used to prevent any pull-out of the transverse reinforcement.

From the tests it was observed that the C-beam specimen with *heavy* ASR/DEF damage revealed *hidden* corrosion. Additional corrosion could become quite a serious threat over time. The effects of corrosion coupled with ASR/DEF effects on the overall performance of the structure are unknown. While some *slight* to *moderate* amount of ASR/DEF deterioration may appear to provide a beneficial strength gain (Mander et al., 2012), it is postulated that as time progresses there would be corresponding loss in capacity due to the corrosion of rebars. This deserves further investigation, particularly if ASR/DEF is associated with a marine environment or if deicing salts are used during the winter months.

#### 10.3.1 Present Practice

The swelling model that was developed in this study can be used to predict the expansion strains that are caused by ASR/DEF related expansion in reinforced concrete structures. With this model it is possible to obtain the progression of ASR/DEF induced expansion strains over time, and the maximum expansion strains and total crack widths that can be expected in the various regions of a structure. Based on the ASR/DEF expansion strains obtained, it is possible to compute the prestressing forces to be applied to the C-STM analysis to efficiently model the effects of ASR/DEF within the structure. Using the C-STM analysis it is possible to estimate the behavior, in terms of stiffness, strength and the post-peak failure mode of the structure under varying levels of ASR/DEF deterioration.

### **10.3.2 Future Work**

The minimalist semi-empirical modeling technique that was developed and validated in this study shows much promise as an efficient way to model ASR/DEF related expansion in reinforced concrete structures. However, due to the lack of sufficient information, the values of the moisture content for the vertical and horizontal exposure faces, which is an input parameter, had to be estimated based on rational arguments, observations, and judgment. The actual measured moisture content in the specimen can aid in further refining the expansion model.

Although the specimens in this study were subjected to accelerated deterioration conditions to promote ASR and DEF in a short time, it is not unlikely that a structure under service will show such damage. Structures close to the coastline that are constantly sprayed with salt water could become a very aggressive environment for ASR/DEF induced deterioration. It would be of interest to investigate how such severe exposure conditions could accelerate the expansion caused by ASR/DEF mechanisms, especially if there was a possibility of concurrent corrosion accelerated deterioration.

Although corrosion of steel had commenced during the deterioration phase in the present study, it did not adversely affect the overall load carrying capacity of the specimen. When structures prone to ASR/DEF expansion are exposed to more aggressive environments, such as coastal bridges, corrosion of steel will inevitably be accelerated. It would be of interest to investigate how rebar steel corrosion in conjunction with ASR/DEF deterioration affects the long-term behavior of the structure.

## REFERENCES

- AASHTO LRFD. (2004). "Bridge Design Specifications and Commentary." 3<sup>rd</sup> Edition, American Association of State Highway Transportation Officials, Washington, D.C., USA.
- AASHTO LRFD. (2007). "Bridge Design Specifications and Commentary." 4<sup>th</sup> Edition, American Association of State Highway Transportation Officials, Washington, D.C., USA.
- AASHTO LRFD. (2010). "Bridge Design Specifications and Commentary." 5<sup>th</sup> Edition, American Association of State Highway Transportation Officials, Washington, D.C., USA.
- ACI Committee 318. (1995). "Building Code Requirements for Structural Concrete (ACI 318-95) and Commentary (318R-95)." American Concrete Institute, Farmington Hills, Michigan, USA.
- ACI Committee 318. (1999). "Building Code Requirements for Structural Concrete (ACI 318-99) and Commentary (318R-99)." American Concrete Institute, Farmington Hills, Michigan, USA.
- ACI Committee 318. (2008). "Building Code Requirements for Structural Concrete (ACI 318-08) and Commentary." American Concrete Institute, Farmington Hills, Michigan, USA.
- Ahmed, T., Burley, E., and Rigden, S. (1998). "The Static and Fatigue Strength of Reinforced Concrete Beams Affected by Alkali-Silica Reaction." *ACI Materials Journal*, 95(4), 376–388.
- ASTM-C31. (2008). "Standard Practice for Making and Curing Concrete Test Specimens in the Field." American Society for Testing and Materials, West Conshohocken, Pennsylvania, USA.
- ASTM-C39. (2008). "Standard Test Method for Compressive Strength of Cylindrical Concrete Specimens." American Society for Testing and Materials, West Conshohocken, Pennsylvania, USA.
- ASTM-C1260 (2005). "Standard Test Method for Potential Alkali Reactivity of Aggregates (Mortar-Bar Method)." American Society for Testing and Materials, West Conshohocken, Pennsylvania, USA.

- Baldwin, N.J.R., and Knights, J. (2010). "Thermal Analysis of Pre-cast Concrete Blocks Exhibiting Delayed Ettringite Formation (DEF)." Proceedings of Structural Faults & Repair Conference, Edinburgh, UK.
- Barbarulo, R., Peycelon, H., Prené, S., and Marchand, J. (2005). "Delayed Ettringite Formation Symptoms on Mortars Induced by High Temperature due to Cement Heat of Hydration or Late Thermal Cycle." *Cement and Concrete Research*, 35(1), 125-131.
- Baumann, T. (1972). "Zur Frage der Netzbewehrung von Flächentragwerken (On the Problem of Net Reinforcement of Surface Structures)." *Bauingenieur*, 47(10), 367-377.
- Bažant, Z.P., and Steffens, A. (2000). "Mathematical Model for Kinetics of Alkali-Silica Reaction in Concrete." *Cement and Concrete Research*, 30(3), 419-428.
- Bentz, E.C., Vecchio, F.J., and Collins, M.P. (2006). "Simplified Modified Compression Field Theory for Calculating Shear Strength of Reinforced Concrete Elements." *ACI Structural Journal*, 103(4), 614-624.
- Bouzabata, H., Multon, S. Sellier, A., and Houari, H. (2012). "Effects of Restraint on Expansion due to Delayed Ettringite Formation." *Cement and Concrete Research*, 42(7), 1024-1031.
- Boenig, A., Fúnez, L., Klingner, R.E., and Fowler, T.J. (2000). "Bridges with Premature Concrete Deterioration: Field Observations and Large-Scale Testing." Report No. FHWA/TX-02/1857-1, Center for Transportation Research, The University of Texas at Austin, Austin, Texas, USA.
- Bracci, J.M., Keating, P.B., and Hueste, M.B.D. (2000). "Cracking in RC Bent Caps." Report No. FHWA/TX-01/1851-1, Texas Transportation Institute, The Texas A&M University System, College Station, Texas, USA.
- Bracci, J.M., Gardoni, P., Eck, M.K., and Trejo, D. (2012). "Performance of Lap Splices in Large-Scale Column Specimens Affected by ASR and/or DEF." Report No. FHWA/TX-12/0-5722-1, Texas Transportation Institute, The Texas A&M University System, College Station, Texas, USA.
- Brunetaud, X., Divet, L., and Damidot, D. (2008). "Impact of Unrestrained Delayed Ettringite Formation-Induced Expansion on Concrete Mechanical Properties." *Cement and Concrete Research*, 38(11), 1343-1348.



- Capra B, and Sellier A. (2003). "Orthotropic Modelling of Alkali-Aggregate Reaction in Concrete Structures: Numerical Simulations." *Mechanics of Materials*, 35(8), 817–830.
- Chang, G.A., and Mander, J.B. (1994). "Seismic Energy Based Fatigue Damage Analysis of Bridge Columns, Part I: Evaluation of Seismic Capacity." Report No. NCEER-94-0006, National Center for Earthquake Engineering Research, State University of New York at Buffalo, New York, USA.
- Charlwood, R.G., Solymar, S.V., Steele, R.R., and Curtis, D.D. (1992). "A Review of Alkali Aggregate Reactions in Hydroelectric Plants and Dams." *Proceedings of International Conference of Alkali-Aggregate Reactions in Hydroelectric Plants and Dams*, Fredericton, Canada.
- Clark, L.A. (1991). "Modeling the Structural Effects of Alkali-Aggregate Reactions on Reinforced Concrete." *ACI Materials Journal*, 88(3), 271–277.
- Collepari, M. (1999). "Damaged by Delayed Ettringite Formation." *Concrete International*, 21(1), 69–74.
- Collepari, M. (2003). "A State-of-the-Art Review on Delayed Ettringite Attack on Concrete." *Cement and Concrete Composites*, 25(4-5), 401–407.
- Collins, M.P. (1978). "Towards a Rational Theory for RC Members in Shear." *ASCE Journal of Structural Division*, 104(4), 649–666.
- Collins, M.P., and Mitchell, D. (1991). *Prestress Concrete Structures*. Prentice Hall, Englewood Cliffs, New Jersey, USA.
- Collins, M.P., Mitchell, D., Adebar, P., and Vecchio, F.J. (1996). "A General Shear Design Method." *ACI Structural Journal*, 93(1), 36–45.
- Collins, M.P. (1998). "Procedure for Calculating the Shear Response of Reinforced Concrete Elements: A Discussion." *ASCE Journal of Structural Engineering*, 124(12), 1485–1488.
- Deschenes, D.J., Bayrak, O., and Folliard, K.J. (2009). "ASR/DEF Damaged Bent Caps: Shear Tests and Field Implications." Report No. 12-8XXIA006, Texas Department of Transportation, Texas, , USA.
- Diamond, S. (1996). "Delayed Ettringite Formation-Process and Problems." *Cement and Concrete Composites*, 18(3), 205–215.

- Dilger, W. (1966). "Veränderlichkeit der Biege- und Schubsteifigkeit bei Stahlbetontragwerken und ihr Einfluß auf Schnittkraftverteilung und Traglast bei statisch unbestimmter Lagerung." Deutscher Ausschuss für Stahlbeton, Heft 179, Berlin, Germany.
- Ekolu, S.O., Thomas, M.D.A., and Hooton, R.D. (2007). "Implications of Pre-Formed Microcracking in Relation to the Theories of DEF Mechanism." *Cement and Concrete Research*, 37(2), 161–165.
- Eriksen, K., Edvardsen, C. and Jakobsen, U.H. (2006). "Delayed Ettringite Formation and Expansive Cracking in Unreinforced Concrete." *Proceedings of 8<sup>th</sup> International Concrete Conference and Exhibition, Concrete in Hot and Aggressive Environments*, Al Manamah, Bahrain.
- Fan S., and Hanson, J.M. (1998). "Effect of Alkali Silica Reaction Expansion and Cracking on Structural Behavior of Reinforced Concrete Beams." *ACI Structural Journal*, 95(5), 498–505.
- Farage, M., Alves, J.L.D., Fairbairn, E.M.R. (2004). "Macroscopic Model of Concrete Subjected to Alkali–Aggregate Reaction." *Cement and Concrete Research*, 34(3), 495–505.
- Fairbairn, E.M.R., Ribeiro, F.L.B., Lopes, L.E., Toledo-Filho, R.D., and Silvano, M.M. (2005). "Modelling the Structural Behavior of a Dam Affected by Alkali-Silica Reaction." *Communications in Numerical Methods in Engineering*, 22(1), 1–12.
- Folliard, K.J., Barborak, R., Drimalas, T., Du, L., Garber, S., Ideker, J., Ley, T., Williams, T., Juenger, M., Fournier, B., and Thomas, M.D.A. (2006). "Preventing ASR/DEF in New Concrete: Final Report." Report No. FHWA/TX-06/0-4085-5, Center for Transportation Research, The University of Texas at Austin, Austin, Texas, USA.
- Fozein Kwanke, N.J.C., Koenders, E.A.B., Bouwmeester, W.J., and Walraven, J.C. (2009). "Concrete Armor Units for Breakwaters." *Concrete International*, 31(10), 34–40.
- Fu, Y. (1996). "Delayed Ettringite Formation in Portland Cement Products." Ph.D. Thesis, University of Ottawa, Ontario.
- Furusawa, Y., Ohga, H., and Uomoto, T. (1994). "An Analytical Study Concerning Prediction of Concrete Expansion due to Alkali-Silica Reaction." *3<sup>rd</sup> International Conference on Durability of Concrete*, Nice, France, 757–780.

- Gianni, E., Folliard, K., Zhu, J., Bayrak, O., Kreitman, K., Webb, Z., and Hanson, B. (2013). "Non-Destructive Evaluation of In-Service Concrete Structures Affected by Alkali-Silica Reaction (ASR) or Delayed Ettringite Formation (DEF)–Part 1." Report No. FHWA/TX-13/0-6491-1, Center of Transportation Research, The University of Texas at Austin, Austin, Texas, USA.
- Glasser, D., and Kataoka, N. (1981). "The Chemistry of Alkali-Aggregate Reaction." *Cement and Concrete Research*, 11(1), 1–9.
- Gravel, C., Ballivy, G., Khayat, K., Quirion, M., and Lachemi, M. (2000). "Expansion of AAR Concrete Under Triaxial Stresses: Simulation with Instrumented Concrete Block." *Proceedings of 11<sup>th</sup> International Conference on AAR*, Center de Recherche Interuniversitaire sur le Béton, Québec, Canada, 949–958.
- Groves, G.W, and Zhang, X. (1990). "A Dilation Model for the Expansion of Silica Glass/OPC Mortars." *Cement and Concrete Research*, 20(3), 453–460.
- Heinz, D., and Ludwig, U. (1987). "Mechanism of Secondary Ettringite Formation in Mortars and Concretes Subjected to Heat Treatment." *ACI Special Publication (Concrete Durability)*, 100, 2059–2071.
- Hobbs, D.W. (1981). "The Alkali Silica Reaction–A Model for Predicting Expansion in Mortar." *Magazine of Concrete Research*, 33(17), 208–220.
- Hobbs, D.W. (1988). *Alkali-Silica Reaction in Concrete*. Thomas Telford, London, UK.
- Hobbs, D.W. (1999). "Expansion and Cracking in Concrete Associated with Delayed Ettringite Formation." *ACI Special Publication*, 177, 159–181.
- Holden, T., Restrepo, J., and Mander, J.B. (2003). "Seismic Performance of Precast Reinforced and Prestressed Concrete Walls." *Journal of Structural Engineering*, 129(3), 286–296.
- Hsu, T.T.C., Mau, S.T., and Chen, B. (1987). "Theory of Transfer Strength of Reinforced Concrete." *ACI Structural Journal*, 84(2), 149–160.
- Hsu, T.T.C. (1988). "Softened Truss Model Theory for Shear and Torsion." *ACI Structural Journal*, 85(6), 624–635.
- Hsu, T.T.C. (1994). "Unified Theory of Reinforced Concrete - A Summary." *Structural Engineering and Mechanics*, 2(1), 1–16.
- Hsu, T.T.C. (1996). "Toward a Unified Nomenclature for Reinforced Concrete Theory." *Journal of Structural Engineering*, 122(3), 275–283.

- Hsu, T.T.C., and Zhang, L.X. (1997). "Nonlinear Analysis of Membrane Elements by Fixed-Angle Softened-Truss Model." *ACI Structural Journal*, 94(5), 483–492.
- Hsu, T.T.C. (1998). "Stresses and Crack Angles in Concrete Membrane Elements." *ASCE Journal of Structural Engineering*, 124(12), 1476–1484.
- Huang, M., and Pietruszczak, S. (1996). "Numerical Analysis of Concrete Structures Subjected to Alkali-Aggregate Reaction." *Mechanics of Cohesive-Frictional Materials*, 1(4), 305–319.
- Huang, M., and Pietruszczak, S. (1999). "Modeling of Thermomechanical Effects of Alkali Silica Reaction." *Journal of Engineering Mechanics*, 125(4), 476–485.
- Hwang, S.J., and Lee, H.J. (1999). "Analytical Model for Predicting Shear Strengths of Exterior Reinforced Concrete Beam-Column Joints for Seismic Resistance." *ACI Structural Journal*, 97(1), 35–44.
- Hwang, S.J., and Lee, H.J. (2000). "Analytical Model for Predicting Shear Strengths of Interior Reinforced Concrete Beam-Column Joints for Seismic Resistance." *ACI Structural Journal*, 96(5), 846–858.
- Hwang, S.J., Lu, W.Y., and Lee, H.J. (2000a). "Shear Strength Prediction of Deep Beams." *ACI Structural Journal*, 97(3), 367–376.
- Hwang, S.J., Lu, W.Y., and Lee, H.J. (2000b). "Shear Strength Prediction for Reinforced Concrete Corbels." *ACI Structural Journal*, 97(4), 543–552.
- Hwang, S.J., Fang, W.H., Lee, H.J., and Yu, H.W. (2000c). "Analytical Model for Predicting Shear Strength of Squat Walls." *Journal of Structural Engineering*, 127(1), 43–50.
- Ingham, J., and McKibbins, L. (2013). "Briefing: Concrete Structures Affected by Cracking." *Proceedings of ICE-Forensic Engineering*, 166, 3–8.
- Jones, T.N., and Poole, A.B. (1986). "Alkali Silica Reactions in Several UK Concretes: The Effect of Temperature and Humidity on Expansion and the Significance of Ettringite Development." *Proceedings of 7<sup>th</sup> International Conference on Alkali Aggregate Reactions*. Noyes Publications, Park Ridge, New Jersey, USA, 446–450.
- Jones, A.E.K., and Clark, L.A. (1996). "The Effects of Restraint on ASR Expansion of Reinforced Concrete." *Magazine of Concrete Research*, 48(174), 1–13.

- Ingham, J. (2012). "Briefing: Delayed Ettringite Formation in Concrete Structures." *Proceedings of Institution of Civil Engineers Forensic Engineering*, 2, 59–62.
- Karthik, M.M, and Mander, J.B. (2011). "Stress-Block Parameters for Unconfined and Confined Concrete Based on a Unified Stress-Strain Model." *Journal of Structural Engineering*, 137(2), 270–273.
- Kelham, S. (1996). "The Effect of Cement Composition and Fineness on Expansion Associated with Delayed Ettringite Formation." *Cement and Concrete Composites*, 18(3), 171–179.
- Kim, J.H., and Mander, J.B. (1999). "Truss Modeling of Reinforced Concrete Shear-Flexure Behavior". Report No. MCEER-99-0005, State University of New York at Buffalo, New York, USA.
- Kim, J.H., and Mander, J.B. (2000a). "Cyclic Inelastic Strut-Tie Modeling of Shear-Critical Reinforced Concrete Members." *ACI Special Publication*, 193, 707–728.
- Kim, J.H., and Mander, J.B. (2000b). "Seismic Detailing of Reinforced Concrete Beam-Column Connections." *Structural Engineering and Mechanics*, 10(6), 589–601.
- Kim, J.H., and Mander, J.B. (2005). "Theoretical Shear Strength of Concrete Columns due to Transverse Steel." *Journal of Structural Engineering*, 131(1), 197–199.
- Kim, J.H., and Mander, J.B. (2007). "Influence of Transverse Reinforcement on Elastic Shear Stiffness of Cracked Concrete Elements." *Engineering Structures*, 29(8), 1798–1807.
- Kupfer, H. (1964). "Erweiterung der Mörsch schen Fachwerkanalogie mit Hilfe des Prinzips vom Minimum der Formänderungsarbeit (Generalization of Mörsch's Truss Analogy Using the Principle of Minimum Strain Energy)." *Comite Euro-International du Beton, Bulletin d'Information No. 40, CEB, Paris, France*, 44–57.
- Kurtis, K.E. (2003). "Chemical Additives to Control Expansion of Alkali-Silica Reaction Gel: Proposed Mechanisms of Control." *Journal of Material Science*, 38(9), 2027–2036.
- Lampert, P. and Thurlimann, B. (1968). *Torsionsversuche an Stahlbetonbalken (Torsion Tests of Reinforced Concrete Beams)*. Bericht 6506-2, Institute für Baustatik, ETH, Zürich, Switzerland.

- Larive, C., and Louarn, N. (1992). "Diagnosis of Alkali Aggregate Reaction and Sulphate Reaction in French Structures." Proceedings of 9<sup>th</sup> International Conference on Alkali Aggregate Reactions, London, UK, 587–598.
- Larive, C., Laplaud, A., and Joly, M. (1996). "Behavior of AAR-Affected Concrete: Experimental Data." Proceedings of 10<sup>th</sup> International Conference on AAR, Melbourne, Australia, 670–677.
- Larive, C. (1998). "Apports combinés de l'expérimentation et de la modélisation à la compréhension de l'alcali-réaction et de ses effets mécaniques." Report No. OA-28, ERLPC Collection, Laboratoire Central des Ponts et Chaussées, Paris, France.
- Larive, C., Joly, M., and Coussy, O. (2000). "Heterogeneity and Anisotropy in ASR-Affected Concrete: Consequences for Structural Assessment." Proceedings of 11<sup>th</sup> International Conference on AAR, Centre de Recherche Interuniversitaire sur le Béton, Québec, Canada, 969–978.
- Lawrence, B.L., Myers, J.J., and Carrasquillo, R.L. (1999). "Premature Concrete Deterioration in Texas Department of Transportation Precast Elements." ACI Special Publication, 177, 141–158.
- Léger P, Côté P, and Tinawi R. (1996). "Finite Element Analysis of Concrete Swelling due to Alkali-Aggregate Reactions in Dams." Computers and Structures, 60(4), 601–611.
- Leonhardt, F. (1965). "Reducing the Shear Reinforcement in Reinforced Concrete Beams and Slabs." Magazine of Concrete Research, 17(53), 187–198.
- Li, B., and Tran, C.T.N. (2012). "Determination of Inclination of Strut and Shear Strength Using Variable Angle Truss Model for Shear-Critical RC Beams." Structural Engineering and Mechanics, 41(4), 459–477.
- Li, K., and Coussy, O. (2002). "Concrete ASR Degradation: from Material Modeling to Structure Assessment." Concrete Science and Engineering, 4(13), 35–46.
- Liu, S.H. (2012). "Structural Assessment of D-regions Affected by Alkali Silica Reaction/Delayed Ettringite Formation." Ph.D. Thesis, Texas A&M University, College Station, Texas, USA.
- Mander, J.B. (1983). "Seismic Design of Bridge Piers." Ph.D Thesis, University of Canterbury, Christchurch, New Zealand.

- Mander, J.B., Priestley, M.J.N., and Park, R. (1988). "Theoretical Stress-Strain Model for Confined Concrete." *Journal of Structural Engineering*, 114(8), 1804–1826.
- Mander, J.B. (1998). "Shear Controversy." *ASCE Journal of Structural Engineering*, 124(12), 1374–1374.
- Mander, T.J., Mander, J.B., and Head, H. (2011). "Modified Yield Line Theory for Full-Depth Precast Concrete Bridge Deck Overhang Panels." *Journal of Bridge Engineering*, 16(1), 12–20.
- Mander, J.B., Bracci, J.M., Hurlebaus, S., Grasley, Z., Karthik, M.M., Liu, S-H., and Scott, R.M. (2012). "Structural Assessment of "D" Region Affected by Premature Concrete Deterioration: Technical Report." Report No. FHWA/TX-12/0-5997-1, Texas A&M Transportation Institute, College Station, Texas, USA.
- Mander, J.B., Karthik, M.M., and Hurlebaus, S. (2015). "Structural Assessment of "D" Region Affected by Premature Concrete Deterioration: Technical Report." Report No. FHWA/TX-15/0-5997-2, Texas A&M Transportation Institute, College Station, Texas, USA.
- Marti, P. (1985). "Basic Tools of Reinforced Concrete Beam Design." *Journal of the American Concrete Institute*, 82(1), 46–56.
- Martin, R.P., Renaud, J.C., and Toutlemonde, F. (2010) "Experimental Investigations Concerning Combined DEF and AAR." *Proceedings of 6<sup>th</sup> International Conference on Concrete under Severe Conditions*, Merida, Mexico, 287–295.
- Martin, R.P., Metalssi, O.O., and Toutlemonde, F. (2013) "Importance of Considering the Coupling Between Transfer Properties, Alkali Leaching and Expansion in the Modeling of Concrete Beams Affected by Internal Swelling Reactions." *Construction and Building Materials*, 49, 23–30.
- Mau, S.T., and Hsu, T.T.C. (1987). "Shear Strength Prediction for Deep Beams with Web Reinforcement." *ACI Structural Journal*, 84(6), 513–523.
- MacGregor, J.G. (1992). *Reinforced Concrete Mechanics and Design*. 2<sup>nd</sup> Edition, Prentice-Hall, Englewood Cliffs, New Jersey, USA.
- Mielenz, R.C., Marusin, S.L., Hime, W.G., and Jugovic, Z.T. (1995). "Investigation of Prestressed Concrete Railway Tie Distress." *Concrete International*, 17(12), 62–68.

- Mitchell, D., and Collins, M.P. (1974). "Diagonal Compression Field Theory-A Rational Model for Structural Concrete in Pure Torsion." *ACI Structural Journal*, 71(8), 396–408.
- Mohammed, T.U., Hamada, H., and Yamaji, T. (2003). "Alkali-Silica Reaction-Induced Strains over Concrete Surface and Steel Bars in Concrete." *ACI Materials Journal*, 100(2), 133–142.
- Monette, L.J, Gardner, N.J, and Grattan-Bellew, P.E. (2002). "Residual Strength of Reinforced Concrete Beams Damaged by Alkali-Silica Reaction-Examination of Damage Rating Index Method." *ACI Materials Journal*, 99(1), 42–50.
- Mörsch, E. (1909). *Concrete-Steel Construction*. McGraw-Hill, New York, USA, 368.
- Multon, S. (2004). "Evaluation Expérimentale et Théorique des Effets de l'alcali-réaction sur des Structures Modèles." Report No. OA 46, ERLPC Collection, Laboratoire Central des Ponts et Chaussées, Paris, France.
- Multon, S., Leclainche, G., Bourdarot, E., and Toutlemonde, F. (2004). "Alkali-Silica Reaction in Specimens Under Multi-Axial Mechanical Stresses." *Proceedings of CONSEC'04*, Seoul National University, Seoul, South Korea, 2004–2011.
- Multon, S., Seignol, J.F., and Toutlemonde, F. (2005). "Structural Behavior of Concrete Beams Affected by Alkali-Silica Reaction." *ACI Materials Journal*, 102(2), 67–76.
- Multon, S., Seignol, J.F., and Toutlemonde, F. (2006). "Chemomechanical Assessment of Beams Damaged by Alkali-Silica Reaction." *Journal of Materials in Civil Engineering*, 18(4), 500–509.
- Multon, S. (2013). Personal e-mail communication received September 20.
- Nielsen, M.P. (1967), "Am Forskydningsarmering I Jernbetonbjaelker (On Shear Reinforcement in Reinforced Concrete Beams)." *Bygningsstatistiske Meddelelser*, 38(2), 33–58.
- Olafsson, H. (1986). "The Effect of Relative Humidity and Temperature on Alkali Expansion of Mortar Bars." *Proceedings of 7<sup>th</sup> International Conference on AAR*, Noyes, Park Ridge. New Jersey, USA, 461–465.
- Odler, I. (1980). "Interaction Between Gypsum and C-S-H Phase Formed in C<sub>3</sub>S Hydration." *7<sup>th</sup> International Congress on the Chemistry of Cement*, Paris, France, 493–495.



- Pan., Z, and Li. B. (2013). "Truss-Arch Model for Shear Strength of Shear-Critical Reinforced Concrete Columns." *ASCE Journal of Structural Engineering*, 139(4), 548–560.
- Pang, X.B.D., and Hsu, T.T.C. (1995). "Behavior of Reinforced Concrete Membrane Elements in Shear." *ACI Structural Journal*, 92(6), 665–679.
- Pang, X.B.D., and Hsu, T.T.C. (1996). "Fixed-Angle Softened-Truss Model for Reinforced Concrete." *ACI Structural Journal*, 93(2), 197–207.
- Paulay, T. (1969). "The Coupling of Shear Walls." Ph.D. Thesis, University of Canterbury, Christchurch, New Zealand.
- Paulay, T. (1971). "Coupling Beams of Reinforced Concrete Shear Walls." *ASCE Journal of the Structural Division*, 97(ST3), 843–862.
- Pavoine, A., Brunetaud, X., and Divet, L. (2012). "The Impact of Cement Parameters on Delayed Ettringite Formation." *Cement and Concrete Composites*, 34(4), 521–528.
- Pesavento, F., Gawin, D., Wyrzykowski, M., Schrefler, B.A., and Simoni, L. (2012). "Modeling Alkali–Silica Reaction in Non-Isothermal, Partially Saturated Cement Based Materials." *Computational Methods in Applied Mechanics and Engineering*, 225(228), 95–115.
- Pettifer, K., and Nixon, P.J. (1980). "Alkali Metal Sulfate – A Factor Common to both Alkali Aggregate Reaction and Sulfate Attack on Concrete." *Cement and Concrete Research*, 10(2), 173–181.
- Pietruszczak, S. (1996). "On the Mechanical Behavior of Concrete Subjected to Alkali-Aggregate Reaction." *Computer and Structures*, 58(6), 1093–1097.
- Pietruszczak, S., and Winnicki, A. (2003). "Constitutive Model for Concrete with Embedded Sets of Reinforcement." *Journal of Engineering Mechanics*, 129(7), 725–738.
- Poole, A.B. (1992). "Alkali-Silica Reactivity Mechanisms of Gel Formation and Expansion." *Proceedings of 9<sup>th</sup> International Conference on Alkali-Aggregate Reaction*, London, 104, 782–789.
- Powanusorn, S. (2003). "Effect of Confinement on Shear Dominated Reinforced Concrete Elements." Ph.D. Thesis, Texas A&M University, College Station, Texas, USA.

- Rausch, E. (1929). “Berechnung des Eisenbetons gegen Verdrehung (Design of Reinforced Concrete in Torsion)”. Technische Hochschule, Berlin, Germany.
- Ritter, W. (1899). “Die Bauweise Hennebique (The Hennebique System).” Schweizerische Bauzeitung, Zürich, Switzerland.
- Salem, H.M., and Maekawa, K. (2006). “Computer-Aided Analysis of Reinforced Concrete Using a Refined Nonlinear Strut-and-Tie Model Approach.” *Journal of Advanced Concrete Technology*, 4(2), 325–336.
- Salgues, M., Sellier, A., Multon, S., Bourdarot, E., and Grimal, E. (2014). “DEF Modelling Based on Thermodynamic Equilibria and Ionic Transfers for Structural Analysis.” *European Journal of Environmental and Civil Engineering*, 18(4), 377–402.
- SAP2000 v14. (2009). “SAP2000, Advanced 14.0.0,” Computers and Structures, Inc., Berkeley, California, USA.
- SAP2000 v17. (2014). “SAP2000, Advanced 17.0.0,” Computers and Structures, Inc., Berkeley, California, USA.
- Saouma, V., and Perotti, L. (2006). “Constitutive Model for Alkali-Aggregate Reactions.” *ACI Materials Journal*, 103(3), 194–202.
- Schlaich, J., Schaefer, K., and Jennewein, M. (1987). “Toward a Consistent Design of Structural Concrete.” *PCI Journal*, 32(3), 74–150.
- Scott, R.M., Mander, J.B., and Bracci, J.M. (2012a). “Compatibility Strut-and-Tie Modeling: Part I—Formulation.” *ACI Structural Journal*, 109(5), 635–644.
- Scott, R.M., Mander, J.B., and Bracci, J.M. (2012b). “Compatibility Strut-and-Tie Modeling: Part II —Implementation.” *ACI Structural Journal*, 109(5), 645–653.
- Scrivener, K.L., and Taylor, H.F.W. (1993). “Delayed Ettringite Formation: A Microstructural and Microanalytical Study.” *Advances in Cement Research*, 5(20), 139–146.
- Scrivener, K.L., Damidot, D., and Famy, C. (1999). “Possible Mechanisms of Expansion of Concrete Exposed to Elevated Temperatures During Curing (Also Known as DEF) and Implications for Avoidance of Field Problems.” *American Society for Testing and Materials*, 21(1), 93–101.

- Seignol, J.F., Baghdadi, N., and Toutlemonde, F. (2009). "A Macroscopic Chemo-Mechanical Model Aimed at Re-Assessment of DEF Affected Concrete Structures." Proceedings of 1<sup>st</sup> International Conference on Computational Technologies in Concrete Structures, Jeju, South Korea, 422–440.
- Sritharan, S., Ingham, J.M., and Priestley, M.J.N. (2000). "Strut-and-Tie Model Concepts for Seismic Design and Assessment of Concrete Bridge Joints," Proceedings of 12<sup>th</sup> World Conference on Earthquake Engineering, Auckland, New Zealand.
- Sritharan, S., and Ingham, J.M. (2003). "Application of Strut-and-Tie Concepts to Concrete Bridge Joints in Seismic Regions." PCI Journal, 48(4), 66–90.
- Sritharan, S. (2005). "Strut-and-Tie Analysis of Bridge Tee Joints Subjected to Seismic Actions." Journal of Structural Engineering, 131(9), 1321–1333.
- Stanton, T.E. (1940). "Expansion of Concrete through Reaction between Cement and Aggregate." Proceeding American Society of Civil Engineers, 66, 1781–1811.
- Swamy, R.N., and Al-Asali, M.M. (1988). "Engineering Properties of Concrete Affected by Alkali-Silica Reaction." ACI Materials Journal, 85(5), 367–374.
- Swamy, R.N., and Al-Asali, M.M. (1989). "Effect of Alkali-Silica Reaction on the Structural Behavior of Reinforced Concrete Beams." ACI Materials Journal, 86(4), 451–459.
- Taylor, H.F.W., Famy, C., and Scrivener, K.L. (2001). "Delayed Ettringite Formation." Cement and Concrete Research, 31, 683–693.
- To, N.H.T., Ingham, J.M., and Sritharan, S. (2001). "Monotonic Nonlinear Strut-and-Tie Computer Models." Bulletin of the New Zealand Society for Earthquake Engineering, 34(3), 169–190.
- To, N.H.T., Ingham, J.M., and Sritharan, S. (2002). "Strut-and-Tie Computer Modelling of Reinforced Concrete Bridge Portal Frames." Bulletin of the New Zealand Society for Earthquake Engineering, 35(3), 165–189.
- To, N.H.T., Ingham, J.M., and Davidson, B.J. (2003). "Cyclic Strut-and-Tie Modeling of Reinforced Concrete Structures." 2003 Pacific Conference on Earthquake Engineering, 102–110.
- To, N.H.T., Sritharan, S., and Ingham, J.M. (2009). "Strut-and-Tie Nonlinear Cyclic Analysis of Concrete Frames." Journal of Structural Engineering, 135(10), 1259–1268.

- Ulm, F.J., Coussy, O., Kefei, L., and Larive, C. (2000). "Thermo-Chemo-Mechanics of ASR Expansion in Concrete Structures." *Journal of Engineering Mechanics*, 126(3), 233–242
- Vecchio, F.J., and Collins, M.P. (1986). "The Modified Compression-Field Theory for Reinforced Concrete Elements Subjected to Shear." *Journal of the American Concrete Institute*, 83(2), 219–231.
- Vecchio, F.J., and Collins, M.P. (1993). "Compression Response of Cracked Reinforced Concrete." *Journal of Structural Engineering*, 119(12), 3590–3610.
- Vecchio, F.J. (2000). "Analysis of Shear-Critical Reinforced Concrete Beams." *ACI Structural Journal*, 97(1), 102–110.
- Williams, S.A. (2005). "Structures Affected by Premature Concrete Deterioration: Diagnosis and Assessment of Deterioration Mechanisms." M.S. Thesis, The University of Texas at Austin, Austin, Texas, USA.
- Wimpenny, D.E., White, P.S. and Eden, M.A. (2007). "Two Case Studies of the Management of Bridges Diagnosed with Delayed Ettringite Formation." *Proceedings of 5<sup>th</sup> Institution of Civil Engineers International Bridge Design, Construction and Maintenance Conference*, Beijing, China, 448–457.
- Winnicki, A., and Pietruszczak, S. (2008). "On Mechanical Degradation of Reinforced Concrete Affected by Alkali-Silica Reaction." *Journal of Engineering Mechanics*, 134(8), 611–627.
- Zhu, R.R.H., Wanichakorn, W., Hsu, T.T.C., and Vogel, J. (2003). "Crack Width Prediction using Compatibility-Aided Strut-and-Tie Model." *ACI Structural Journal*, 100(4), 413–421.

## APPENDICES\*

Appendix A1: Analysis Schema

Appendix A2: Preliminary (Code-Based) Computations for Bent-Cap Specimens

Appendix A3: Computation of Reinforcement Ratio and Maximum Expansion Strain for  
C-beam Specimen 3

Appendix A4: Preliminary (Code-Based) Computations for C-beam Specimens

Appendix A5: Computations for Stage 3 C-STM Analysis for C-beam Specimens

---

\* Previously published work is available to the public through National Technical Information Service. Mander, J.B., Bracci, J.M., Hurlebaus, S., Grasley, Z., Karthik, M.M., Liu, S-H., and Scott, R.M. (2012). "Structural Assessment of "D" Region Affected by Premature Concrete Deterioration: Technical Report." *Report No. FHWA/TX-12/0-5997-1*, Texas A&M Transportation Institute, College Station, Texas, USA. Mander, J.B., Karthik, M.M., and Hurlebaus, S. (2015). "Structural Assessment of "D" Region Affected by Premature Concrete Deterioration: Technical Report" *Report No. FHWA/TX-15/0-5997-2*, Texas A&M Transportation Institute, College Station, Texas, USA.

## **A1 ANALYSIS SCHEMA**

This appendix presents a methodology for determining the structural capacity of cracked concrete bridge piers. The method is considered to be particularly useful for those portions of the bridge piers where disturbed regions may govern the behavior. The method is not really intended to be a substitute for existing design procedures, but rather a check on the capacity of new designs or existing sub-structures that may be showing signs of distress.

## A1.1 Introduction

The flowchart given in Figure A1-1 depicts the procedure and the branching decision points that either terminate the analysis or trigger additional analyses to provide additional insights into expected behavior of bridge piers. A summary of the notations used in the following sections along with what they represent are presented in Table A1-1.

**Table A1-1: Summary of Notations Used.**

<b>Notation</b>	<b>Comments</b>
$P_y^b = M_y^b / L_b$	Externally applied load causing first yield
$P_n^f = M_n^f / L_b$	Externally applied load causing flexural moment in the critical beam-column face
$V_n^s = V_c + V_s + V_p$	Nominal shear capacity provided by the section
$\phi_v V_n^s$	Factored shear capacity
$V_n^j = V_{\text{arch}} + V_{\text{truss}}$	Joint shear capacity
$V_{jv}$	Vertical shear in beam-column joint caused by $P_n^f$
$V_{jh}$	Horizontal shear in beam-column joint caused by $P_n^f$
$P_y^{\text{SAT}}$	Externally applied load causing first yield from SAT analysis
$P_n^{\text{SAT}}$	Externally applied load causing flexural shear demand from SAT analysis

As a prelude to the analysis, material properties are determined from the records, plans, in situ testing, or through non-destructive evaluations, which form an input for the various stages of analysis. After, a preliminary structural analysis, the first yield flexure capacity  $M_y^b$ , the nominal flexural moment  $M_n^f$ , the externally applied load causing

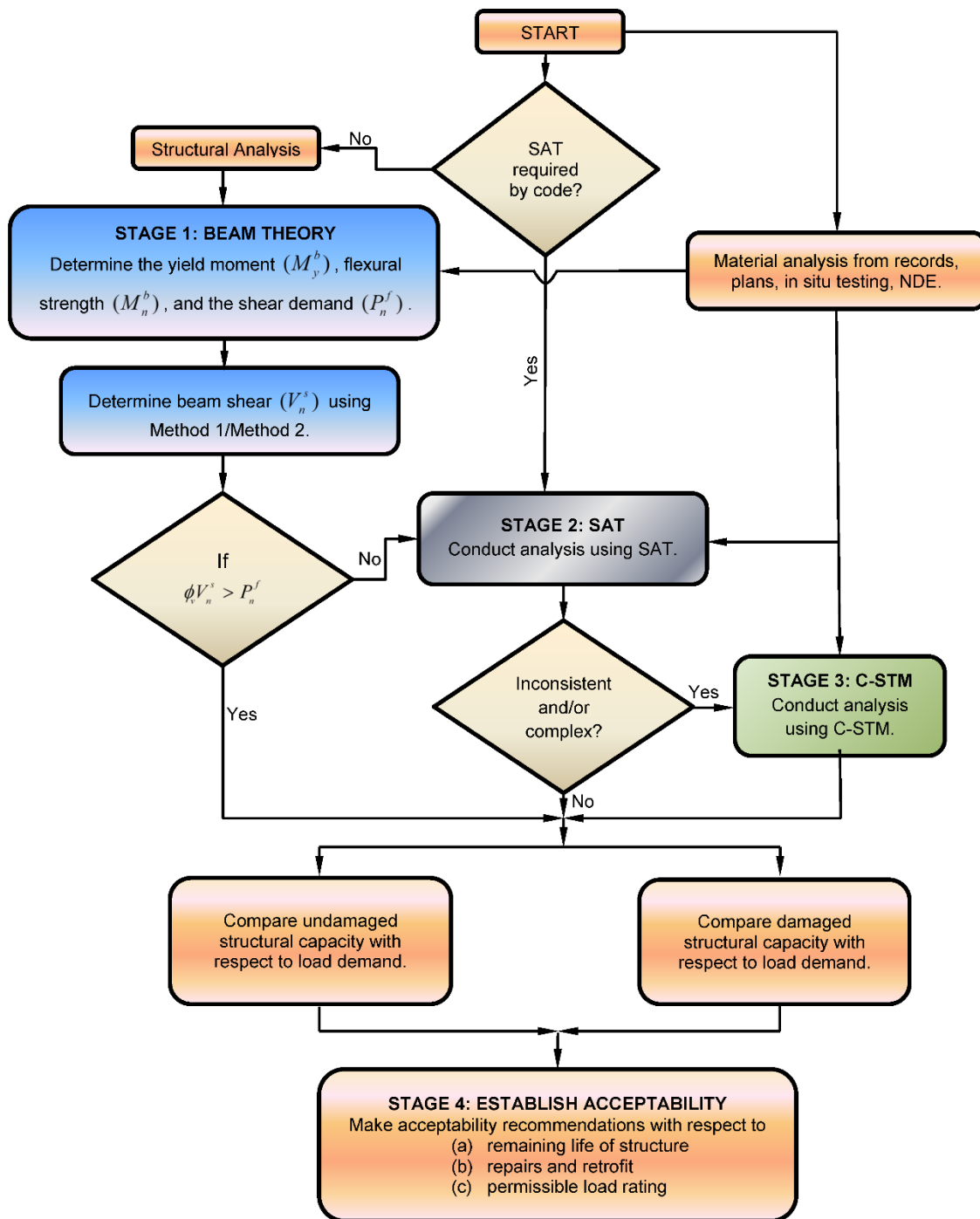


Figure A1-1: Flowchart for Analysis Procedure of Bridge Piers.



first yield and beam flexure ( $P_y^b = M_y^b / L_b$  and  $P_n^f = M_n^f / L_b$ , respectively, where  $L_b$  = length to the nearest inflexion point), and the beam shear  $V_n^s$  are determined as part of Stage 1 of the analysis. From Stage 1, if the factored shear capacity ( $\phi V_n^s$ , where  $\phi = 0.90$ ) is greater than the nominal external load causing beam flexure  $P_n^f$ , then there is a measure of reserve shear capacity; therefore the beam should fail in flexure. However, if the factored shear capacity is insufficient, or when the code mandates, additional analysis of the structure may be required. In the first instance this can be done using the strut-and-tie method, which forms Stage 2 of the analysis schema. If Stage 2 leads to conclusive results, further analysis may be unnecessary. However, in the event of inconsistent and/or complex results from Stage 2 analysis, Stage 3 analysis comprising a C-STM analysis may be required. Based on these analysis results, the acceptability of the structure can be established, which forms Stage 4 of the analysis. A detailed analysis procedure follows.

### **A1.2 Stage 1: Analysis Using Beam Theory**

As a first step in the analysis of a bridge pier as shown in Figure A1-2, it is assumed flexural plastic hinge forms first, and the analysis is conducted based on flexural bending theory. The following steps summarize this analysis technique:

#### ***Step 1: Determine first yield flexural capacity, $M_y^b$***

Calculate the beam yield moment  $M_y^b$  at first yield of longitudinal steel given by:

$$M_y^b = C_s(d - d') + C_c(d - kd / 3) \quad (\text{A1-1})$$

in which  $d$  = depth to the centroid of tensile reinforcement from the extreme compression fiber;  $d'$  = depth to the centroid of compression steel from the extreme compression fiber;  $C_s = A'_s f_s$  when  $f_s \leq f_y$  and  $C_c = 0.85 f'_c ab$  where  $A'_s$  = the area of

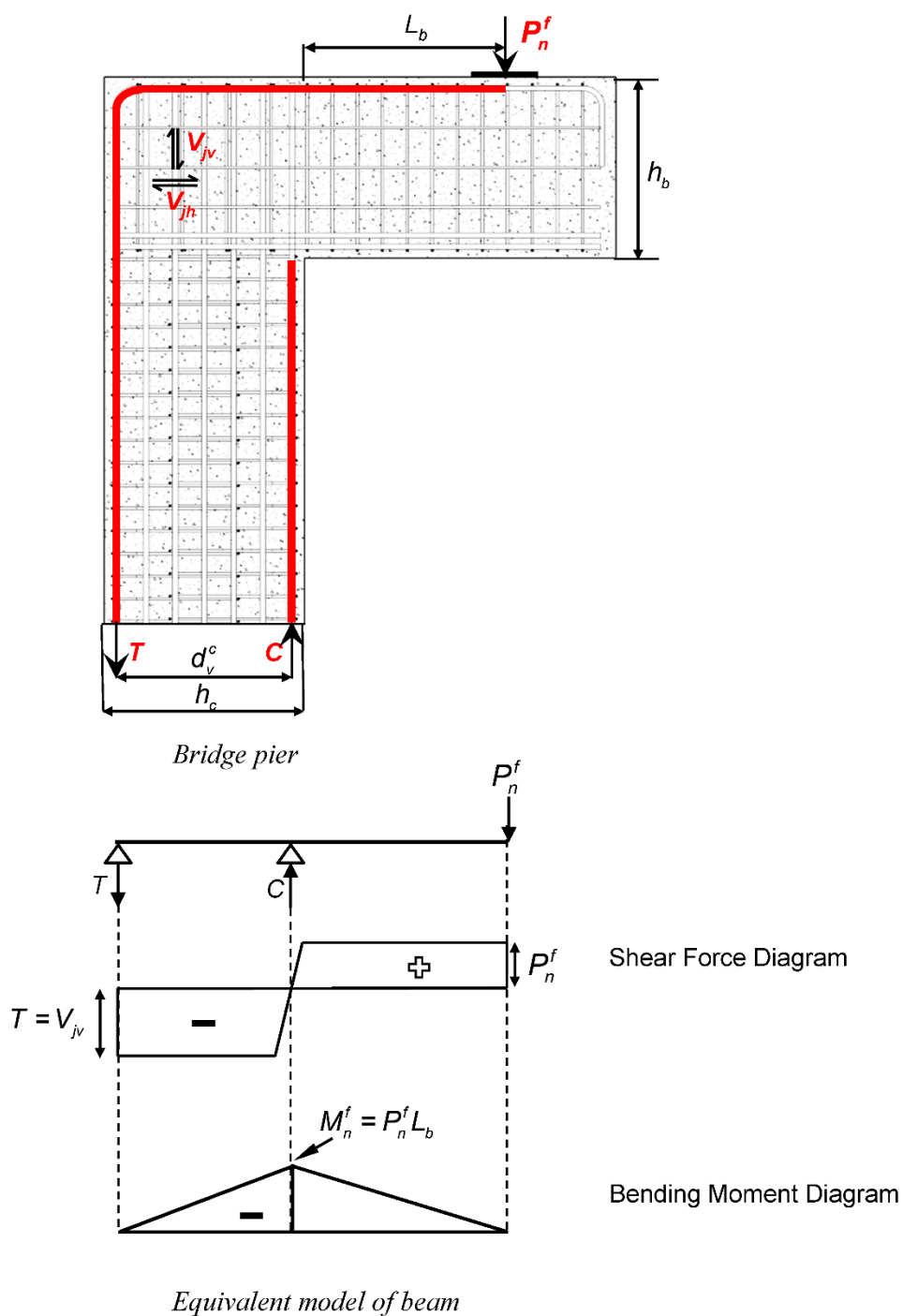


**Figure A1-2: Bridge Pier and Equivalent Beam Model for Flexure Analysis.**

compression reinforcement;  $f_s$  = stress in steel corresponding to strain  $\varepsilon_s$ ;  $f_y$  = yield stress of reinforcing steel;  $f'_c$  = concrete compressive strength;  $b$  = width of the section; and  $k$  is the elastic compression zone coefficient as given by Park and Paulay (1975):

$$k = \sqrt{(\rho_L + \rho'_L)^2 n^2 + 2(\rho_L + \rho'_L d'/d)n} - (\rho_L + \rho'_L)n \quad (\text{A1-2})$$

in which  $\rho_L$  = the ratio of tension reinforcement;  $\rho'_L$  = the ratio of compression reinforcement; and  $n$  = the modular ratio of steel to concrete.

The externally applied load causing first yield is given by:

$$P_y^b = M_y^b / L_b \quad (\text{A1-3})$$

where  $L_b$  = distance from the point of application of the load to the face of the column.

***Step 2: Determine nominal flexural moment,  $M_n^f$***

The flexural moment  $M_n^f$  of the beam is calculated as:

$$M_n^f = C_s(d - d') + C_c(d - a/2) \quad (\text{A1-4})$$

in which  $a = \beta_1 c$  is the depth of the equivalent rectangular stress-block for which  $c$  is the neutral axis depth and  $\beta_1$  = the equivalent rectangular stress-block parameter given as:

$$0.65 \leq \beta_1 = 0.85 - 0.05(f'_c(\text{MPa}) - 7) \leq 0.85 \quad (\text{A1-5})$$

***Step 3: Determine externally applied load based on flexure,  $P_n^f$***

Based on the flexural capacity  $M_n^f$ , the external load causing beam flexure  $P_n^f$  is determined:

$$P_n^f = M_n^f / L_b \quad (\text{A1-6})$$

***Step 4: Determine beam shear capacity,  $V_n^s$***

The shear capacity  $V_n^s$  of the beam is computed as:

$$V_n^s = V_c + V_s + V_p \quad (\text{A1-7})$$

in which  $V_p$  = component of shear carried by prestressing tendons, if any;  $V_s$  = shear carried by steel; and  $V_c$  = shear carried by concrete given by:

$$V_c = 0.083 \beta \sqrt{f'_c(\text{MPa})} b_v d_v \quad (\text{A1-8})$$

where  $f'_c$  = concrete strength;  $b_v$  = section web width across shear plane;  $d_v$  = effective shear depth taken as  $d_v = jd$  or not less than the greater of  $0.9d$  (where  $d$  = effective depth), or  $0.72h$  (where  $h$  = overall depth).

For sections with steel transverse to the longitudinal axis of the member ( $\alpha = 90^\circ$ ), the shear carried by the hoops and /or cross ties is given by:

$$V_s = A_v f_y \frac{d_v}{s} \cot \theta \quad (\text{A1-9})$$

where  $A_v$  = cross-sectional area of hoopset;  $s$  = hoopset spacing; and  $\theta$  = shear crack angle inclined from the longitudinal axis.

AASHTO LRFD (2010) specifications permit  $\beta$  and  $\theta$  in (A1-8) and (A1-9) to be calculated by one of the following two methods:

***Method 1: Simplified Procedure***

For reinforced (non-prestressed) concrete members, values of  $\beta = 2.0$  and  $\theta = 45^\circ$  can be used. Thus, the shear carried by concrete is the same as the well-known historic ACI-318 (2011) method.

***Method 2: General Sectional Procedure***

This method is based on the simplified version of the MCFT (Bentz et al., 2006). In this method the parameters  $\beta$  and  $\theta$  can be determined as described below.

For sections containing the minimum amount of transverse reinforcement as specified in AASHTO LRFD (2010),  $\beta$  is determined as:

$$\beta = \frac{4.8}{1 + 750\varepsilon_s} \quad (\text{A1-10})$$

where  $\varepsilon_s$  = net longitudinal tensile strain in the section at the centroid of the tensile reinforcement determined as explained later.

For sections that do not contain the minimum amount of shear reinforcement as specified in AASHTO LRFD (2010),  $\beta$  is determined as:

$$\beta = \frac{4.8}{(1 + 750\varepsilon_s)} \frac{51}{(39 + s_{xe})} \quad (\text{A1-11})$$

where  $s_{xe}$  = the crack spacing parameter is given by:

$$s_{xe} = s_x \frac{35}{a_g + 16} \leq 2000\text{mm} \quad (\text{A1-12})$$

where  $a_g$  = maximum aggregate size in mm;  $s_x$  = the smaller of either  $d_v$  (effective shear depth) or the maximum distance between layers of longitudinal crack control reinforcement, where the area of the reinforcement in each layer is not less than  $0.003b_v s_x$ .

The crack angle  $\theta$  for any of the above cases is given by:

$$\theta = 29 + 3500\varepsilon_s \quad (\text{A1-13})$$

In (A1-10), (A1-11), and (A1-13),  $\varepsilon_s$  can be determined from the following expression:

$$\varepsilon_s = \frac{\left( \frac{|M_u|}{d_v} + 0.5N_u + |V_u - V_p| - A_{ps}f_{po} \right)}{E_s A_s + E_p A_{ps}} \quad (\text{A1-14})$$

where  $|M_u|$  = factored moment, not to be taken less than  $|V_u - V_p| d_v$ ;  $V_u$  = factored shear force;  $V_p$  = component of shear carried by prestressing tendon;  $N_u$  = factored axial force taken as positive if tensile and negative if compressive;  $A_s$  = area of non-prestressing tensile steel;  $A_{ps}$  = area of prestressing steel on the flexural tension side of

the member;  $f_{po}$  (pretensioned members) = stress in strands when concrete is cast around them, and  $f_{po}$  (post-tensioned members) = average stress in the tendons when the post-tensioning is completed, or for usual levels of prestressing  $f_{po} = 0.7f_{pu}$  for both pre- and post-tensioning;  $f_{pu}$  = ultimate stress in the prestressing tendon;  $E_s$  and  $E_p$  = modulus of elasticity of reinforcing steel and prestressing steel, respectively; and  $A_s$  = area of reinforcing steel.

***Step 5: Check strength hierarchy.***

Once the externally applied load causing beam flexure  $P_n^f$  and the shear capacity  $V_n^s$  are calculated, the strength hierarchy can be determined based on:

IF  $\phi_v V_n^s > P_n^f$   
 THEN shear has a measure of reserve capacity and the beam should fail in flexure.

IF  $\phi_v V_n^s < \phi_f P_n^f$   
 THEN the factored shear capacity may be insufficient leading to a shear failure of the bridge pier.

In the above,  $\phi_v = 0.90$  and  $\phi_f = 0.90$  are the strength reduction factors for shear and flexure, respectively, as per AASHTO LRFD *Bridge Design Specifications* (2010).

***Step 6: Determine the shear capacity of the beam-column joint regions.***

In the beam-column joint zones, the code is silent on the amount of reinforcement needed. However, the seismic provisions (clause 5.10.11.4 AASHTO LRFD *Bridge Design Specifications*, 2010) note that the transverse reinforcement from the column should be continued into the cap and the shear resistance from normal weight concrete be limited to the following check:

$$V_h < 1.0bd\sqrt{f'_c(\text{MPa})} \quad (\text{A1-15})$$

The commentary notes: “The (shear) strength of the column connections in a column cap is relatively insensitive to the amount of transverse reinforcement, provided that there is a minimum amount and that the shear resistance is limited to the values specified.”

However, for the beam-column joint regions in bent caps, the joint shear capacity needs to be determined in the direction in which the shear steel (hoopsets) are oriented. Thus, the vertical shear in the joint  $V_{jv}$  determined from the shear force diagram (Figure A1-2) of the bridge bent cap, can be transformed as follows to obtain the horizontal shear in the joint:

$$V_{jh} = \frac{h_c}{h_b} V_{jv} \quad (\text{A1-16})$$

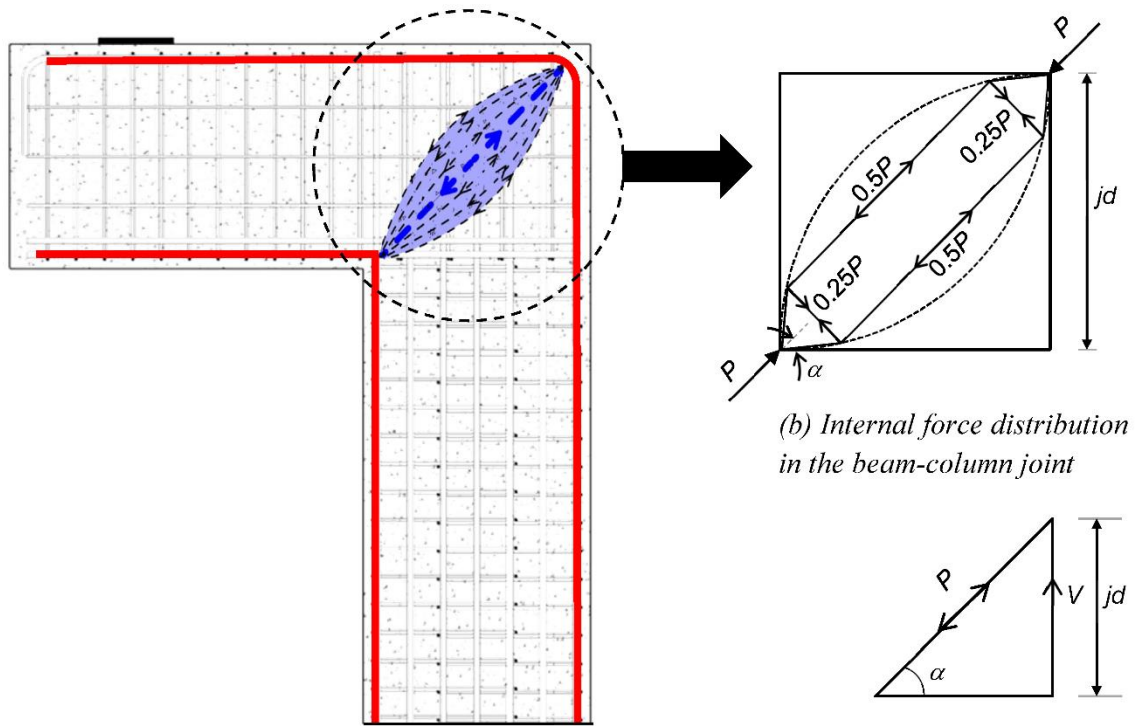
in which  $h_b$  and  $h_c$  are the overall depth of the beam and column, respectively.

The joint capacity can be assessed as:

$$V_n^j = V_{\text{arch}} + V_{\text{truss}} \quad (\text{A1-17})$$

where  $V_{\text{arch}}$  = shear carried by the corner-to-corner diagonal concrete arch (defined later); and  $V_{\text{truss}} = \Sigma A_{sv} f_y$  = the shear carried by the hoops and/or cross ties, in which  $\Sigma A_{sv}$  = the total area of steel given by all hoops/ties within the joint region.

There is a parabolic distribution of stress in the corner-to-corner arch in the beam-column zone which can further be simplified as shown in Figure A1-3a and b. From Figure A1-3c,  $V = P \sin \alpha$ . The total tensile force across the arch equals  $P/2 = (jd / \sin \alpha) b_w f_t'$ , which implies the shear contribution from the corner-to-corner joint arch is given by:



(a) Corner-to-corner arch in the beam-column joint

(b) Internal force distribution in the beam-column joint

(c)

**Figure A1-3: Joint Arch Mechanism in Beam-Column Joint.**



$$V_{\text{arch}} = 0.664\sqrt{f'_c(\text{MPa})}b_vjd \quad (\text{A1-18})$$

taking  $f'_t = 0.33\sqrt{f'_c(\text{MPa})}$

For the beam-column joint to be safe in shear, the following should be satisfied:

$$\phi V_n^j > V_{jv} \quad (\text{A1-19})$$

From the above analysis, if it is determined that the beam has a measure of reserve capacity, then the analysis can essentially be stopped at this point. However, if either the beam or the beam-column joint is a shear critical section, then further investigation is warranted. In such a case or when as required by the code, the SAT technique of analysis can be used for further analysis, which is discussed in the next section.

### **A1.3 Stage 2: Strut-And-Tie Analysis**

The SAT modeling technique is a lower-bound plastic truss model that is particularly useful for design. It can also be adopted for strength analysis and may be particularly useful for structures that possess stocky members and a significant number of D-regions. Using an SAT approach, a structure with D-regions is modeled as a truss, which consists of three types of elements: struts, ties, and nodes. Struts represent concrete that carries compressive loads, while tensile loads are carried by ties representing steel reinforcements. Struts and ties intersect at nodes. Nodes are labeled by the element forces intersecting at the nodes; “C” represents compression, while “T” stands for tension. Based on the type of member forces at the node, the nodes can be classified as CCC, CCT, CTT, and so on.

The truss geometry of the SAT model is based on the direction of stress flow in the D-region. The ties are aligned along the reinforcement layout, whereas the struts are oriented based on the compressive stress flow trajectories. It is also reasonable to determine the truss geometry based on the cracks that can be seen on a structural member as illustrated in Figure A1-4b.

Once the truss geometry is determined, the nodal geometries must be established in order to calculate the stresses on each of the nodal faces. These calculated stresses

must not exceed the allowable stresses for each nodal face. The nodes can be proportioned either as a hydrostatic node or as a non-hydrostatic node. In a hydrostatic node, the principal stresses are equal on all sides of the node; hence, the ratio of each nodal face is directly proportional to the force being applied to the nodal face. However, often the nodal dimensions are inconsistent with the beam details such as the location of the reinforcement and depth of the flexural compression zone. In the case of non-hydrostatic nodes, the stresses applied to each nodal face are different as the node is sized based on the beam details. As a result of this, the nodal geometry is synchronized with the beam details. Additionally, higher values of shear span-to-depth ratio can also lead to unrealistically large struts in the case of hydrostatic nodes.

Based on the above concepts, a SAT model for a cantilever bent and a straddle bent are shown in Figure A1-4. The forces in the truss elements can be determined by a simple truss analysis. The stresses in each of the truss elements and nodes are then checked against the allowable stresses.

The allowable concrete compressive stresses on the nodal face depend on the type of node. The allowable stresses in the nodal regions are defined as follows:

For	CCC nodes	$f_{cu} = 0.85f'_c$	
	CCT nodes	$f_{cu} = 0.75f'_c$	(A1-20)
	CTT nodes	$f_{cu} = 0.65f'_c$	

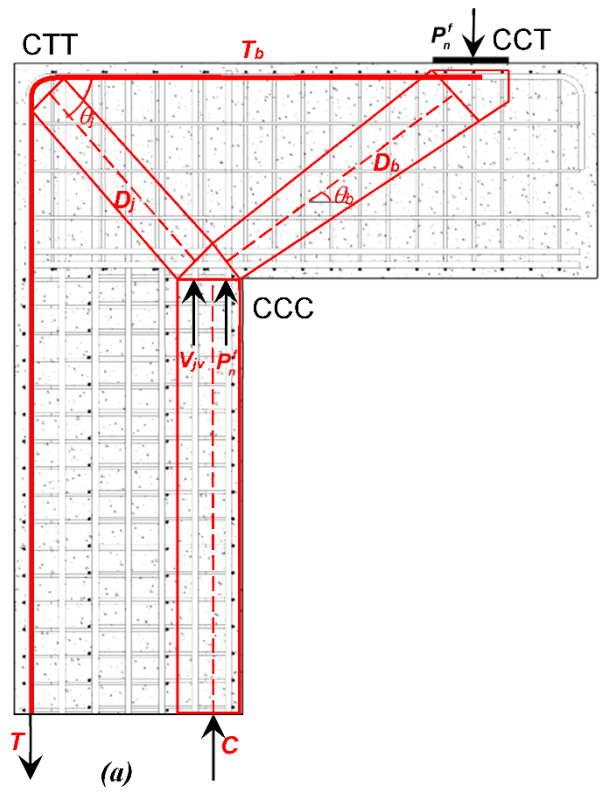
The limiting compressive stress within a strut  $f_{cu}$  is given by:

$$f_{cu} = \frac{f'_c}{0.8 + 170\varepsilon_1} \leq 0.85f'_c \quad (\text{A1-21})$$

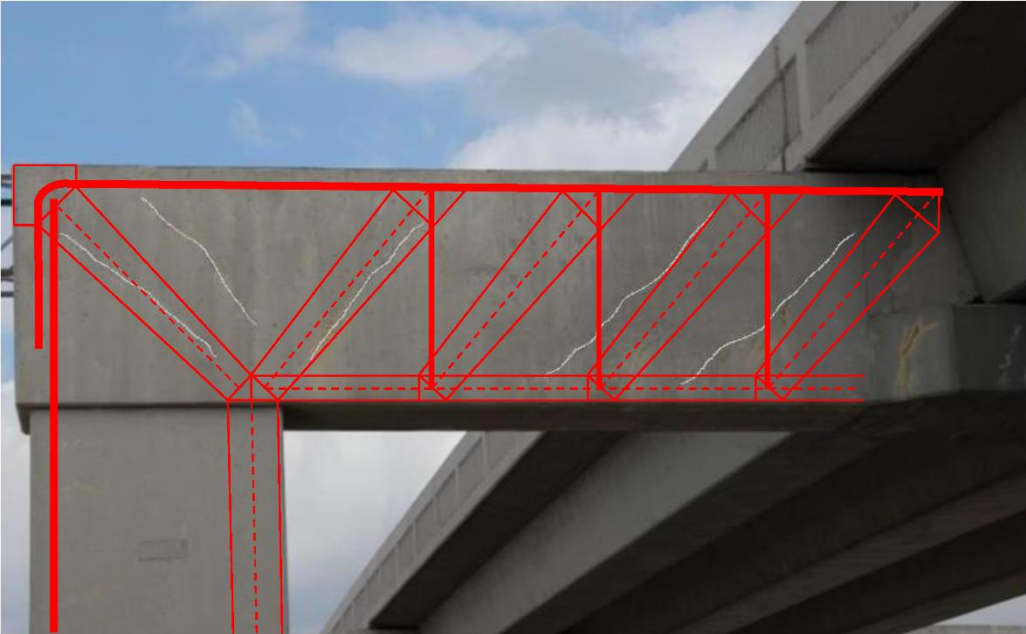
in which  $\varepsilon_1$  = principal tension strain given by:

$$\varepsilon_1 = \varepsilon_s + (\varepsilon_s + 0.002) \cot^2 \alpha_s \quad (\text{A1-22})$$

where  $\varepsilon_s$  = tensile strain in the direction of the tension tie; and  $\alpha_s$  = the smallest angle between the compressive strut and adjoining tension tie.



(a) Cantilever bent



(b) Straddle bent

**Figure A1-4: Strut-and-Tie Model of Bridge Bents.**

The nominal resistance of a strut/node is given as:

$$P_n = f_{cu} A_{cs} \quad (A1-23)$$

where  $A_{cs}$  = effective cross-sectional area of the strut/node.

The nominal resistance of a tension tie is given by:

$$P_n = f_y A_{st} + A_{ps} [f_{pe} + f_y] \quad (A1-24)$$

where  $f_y$  = yield strength of reinforcing steel;  $A_{st}$  = area of reinforcing steel in the tension tie;  $A_{ps}$  = area of prestressing steel;  $f_{pe}$  = stress in prestressing steel after losses.

A generalized stepwise procedure on how to determine the capacity of a bridge pier using a SAT model follows, and is also illustrated in Figure A1-4.

***Step 1: Determine the truss and node geometry***

The first step in conducting a SAT analysis is to determine the geometry of the truss and the nodes. The width of the compression chords in the column and the beam can be determined based on the depth of the triangular stress-block or the equivalent rectangular stress-block. The base of the CCC node can be proportioned based on the externally applied load that causes beam flexure  $P_n^f$  and the vertical component of shear in the beam-column joint  $V_{jv}$ . The width of the CCT node is taken to be equal to the width of the bearing pad, and the CTT node is dimensioned based on the bending radius of longitudinal reinforcement. The struts can be drawn based on the dimension of the nodes. This will also provide the inclination angle of the diagonal struts.

***Step 2: Solve the determinate truss***

It is assumed that the tensile reinforcement of the beam yields, that is,  $T_b = A_s f_y$ . Considering equilibrium of forces at the nodes, the forces in all the members of the truss can be determined.

### ***Step 3: Determine minimum applied load causing node failure***

Based on the nodal dimensions and the allowable stress (A1-20), the nodal capacity of each node can be determined. The minimum applied load causing node failure can then be back calculated.

### ***Step 4: Determine shear demand***

The shear demand on the bridge pier can be determined based on the most critical strut/tie or nodal zone.

While the SAT method is a relatively simple approach it suffers from two major drawbacks. First and foremost, the SAT approach is a lower bound plastic truss that gives no sense of what the related deformations are under a given set of applied loads. Second and related to this, is the fact that SAT does not give a unique solution. This feature was brought out strongly in research by Ley et al. (2007) who designed and tested several specimens with different reinforcing layouts, all designed by SAT methods. Ley et al. (2007) concluded that the ultimate failure load and mode cannot be predicted by the SAT method.

This calls for a more advanced analysis technique that adopts the concepts of the SAT method and gives an idea about the overall behavior of the structure. One such technique, the C-STM, was developed by Scott et al. (2012 a,b).

## **A1.4 Stage 3: Analysis Using Compatibility Strut-And-Tie Methods**

As mentioned above, SAT analysis methods are strictly lower bound solutions. Such solutions adhere to the principles of equilibrium, but are both silent on and unable to predict deformations of the structure.

### **A1.4.1 Stage 3.1: C-STM Based on Undamaged Material Properties**

To obtain a more holistic view of structural behavior that provides a complete force vs. deformation pathway to failure, compatibility of member deformations must be incorporated into the analysis. This approach is referred to as the C-STM.

A complete background and theoretical formulation of the C-STM is presented in Mander et al. (2012). As keeping track of this class of nonlinear analysis can be time consuming, it is suggested that nonlinear structural analysis software (e.g., SAP2000, 2014) be used for the analysis. In this stage of analysis, the undamaged material properties are used in evaluating the behavior of the structure.

#### **A1.4.2 Stage 3.2: C-STM Allowing for ASR/DEF Damage and Its Effects**

It is well-known that ASR/DEF may cause the concrete to deteriorate. The effects of ASR/DEF on the structure can be explained as follows:

- ASR/DEF effects cause the concrete to swell.
- This in turn may cause the cover concrete to badly crack and in some cases cause spalling.
- Meanwhile, swelling of the core concrete occurs, but this is constrained in part by the presence of longitudinal and transverse reinforcement.
- Tensile strains that are induced in the reinforcing steel put the concrete into a state of prestress.
- In turn, this prestress effect, which is similar to adding an axial force, increases the stiffness and can slightly enhance the strength of the members most affected by ASR/DEF.

The effects of ASR/DEF on the structure can be modeled in C-STM by introducing the effects of concrete deterioration and swelling. The latter causes confinement of the core concrete and prestressing of the reinforcing steel. Therefore, the stress-strain relation for concrete and steel need to be modified accordingly.

Based on an assessment of the extent of damage due to ASR/DEF effects observed in the structure, the damage can be categorized into three classes: *slight*, *moderate*, and *heavy* damage. Based on the damage class, the deteriorated concrete properties, and the prestressing forces in the longitudinal and transverse reinforcing steel are determined. A C-STM analysis with the modified properties gives the behavior of the structure with ASR/DEF damage.

### ***Procedure to Assess Concrete Core Confinement Ratio***

The effective confining stress in the  $x$  and  $y$  direction  $f'_{lx}$  and  $f'_{ly}$  are given as:

$$\begin{aligned}f'_{lx} &= k_e \rho_x f_y \\f'_{ly} &= k_e \rho_y f_y\end{aligned}\tag{A1-25}$$

where  $k_e$  = confinement effectiveness coefficient (defined below);  $f_y$  = yield stress of reinforcing steel; and  $\rho_x$  and  $\rho_y$  are the volumetric ratio of lateral confining steel parallel to the  $x$  and  $y$  axis, respectively, given as:

$$\begin{aligned}\rho_x &= \frac{A_{sx}}{sd_c} \\ \rho_y &= \frac{A_{sy}}{sb_c}\end{aligned}\tag{A1-26}$$

in which  $A_{sx}$  and  $A_{sy}$  = total area of lateral reinforcement parallel to the  $x$  and  $y$  axes, respectively;  $s$  = spacing of hoop sets;  $d_c$  = core dimension in  $y$  direction; and  $b_c$  = core dimension in the  $x$  direction. The confinement effectiveness coefficient  $k_e$  is the ratio of area of effectively confined core concrete  $A_e$  to the concrete core area of the section  $A_{cc}$ .

$$k_e = \frac{A_e}{A_{cc}}\tag{A1-27}$$

In rectangular sections the transverse steel bows outward between the longitudinal bars; hence, arching action will occur between the longitudinal bars that are fully supported in position by an angle bend in the transverse steel as shown in Figure A1-5. The arching action is assumed to take the form of a second-degree parabola with an initial tangent slope of  $45^\circ$ . The area of one such parabola is given by  $(w'_i)^2 / 6$ , where  $w'_i$  is the  $i^{th}$  clear transverse spacing between longitudinal bars in which arching action of concrete develops. In the case of a lightly confined rectangular section, the parameter  $w'$  along the  $y$  axis is taken as the depth of the neutral axis  $kd$  minus the distance from the extreme compression fiber to the longitudinal bar. The net area of

ineffectively confined concrete for the  $n$  longitudinal bars supported in the corners of the bent transverse hoops is given by:

$$\sum_{i=1}^n (w'_i)^2 / 6 \quad (\text{A1-28})$$

The total effectively confined core concrete area is defined as:

$$A_e = \left[ b_c d_c - \sum_{i=1}^n (w'_i)^2 / 6 \right] \left( 1 - 0.5 \frac{s'}{b_c} \right) \left( 1 - 0.5 \frac{s'}{d_c} \right) \quad (\text{A1-29})$$

in which  $s'$  = clear longitudinal spacing between hoop bars in which arching action of concrete develops.

The concrete core area of the rectangular section is given by:

$$A_{cc} = b_c d_c (1 - \rho_{cc}) \quad (\text{A1-30})$$

where  $\rho_{cc}$  = volumetric ratio of longitudinal steel in the confined core. Note that the term  $(1 - \rho_{cc})$  in the above equation effectively removes the presence of longitudinal bars from the confined concrete area. From these, the confinement effectiveness coefficient  $k_e$  can be determined from (A1-27).

The ratios  $f'_{lx} / f'_{co}$  and  $f'_{ly} / f'_{co}$  are determined, the smaller of these ratios is taken as  $f'_{l1} / f'_{co}$ , and the larger is taken as  $f'_{l2} / f'_{co}$ . The confinement ratio  $K_{cc} = f'_{cc} / f'_{co}$  is determined from the chart shown in Figure A1-6. Thus, the confined concrete stress is then determined as  $f'_{cc} = K_{cc} f'_{co}$ , where  $f'_{co}$  = in situ concrete strength.

The strain  $\varepsilon_{cc}$  corresponding to the maximum confined concrete stress  $f'_{cc}$  is defined as:

$$\varepsilon_{cc} = \varepsilon_{co} (1 + 5(K_{cc} - 1)) \quad (\text{A1-31})$$

in which  $\varepsilon_{co}$  = the strain corresponding to the unconfined concrete strength (typically  $\varepsilon_{co} = 0.002$ ).



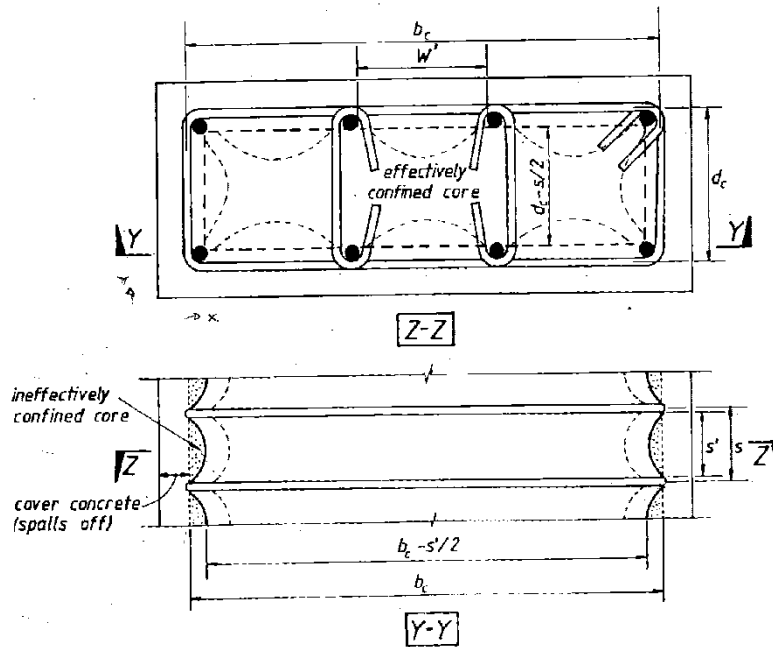


Figure A1-5: Assumed Arching Mechanism between Hoops for Rectangular Sections (Mander, 1983).

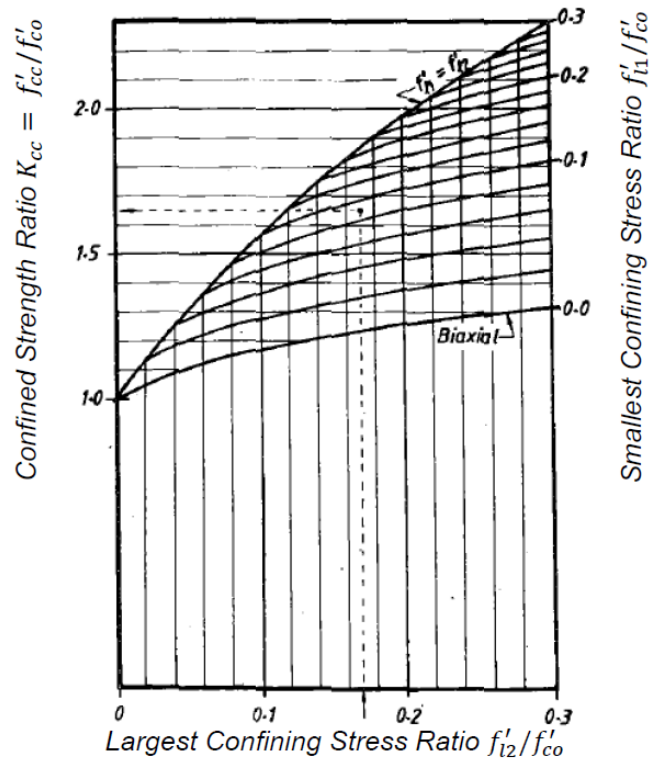


Figure A1-6: Confined Strength Determination from Lateral Confining Stresses for Rectangular Sections (Mander, 1983).

Based on the results from the three stages of analysis presented above, the structural capacity of the damaged/undamaged structure can be compared to the load demand on the structure. Based on these comparisons, acceptability criterion can be set for a structure; this constitutes Stage 4 of the analysis schema.

#### **A1.5 Stage 4: Establish Acceptability Of Structure**

Based on the analysis conducted on the structure in the above three stages, a structural engineer must be able to make recommendations and establish the acceptability of an existing structure that may or may not be subjected to any form of deterioration/damage. The engineer must be able to make acceptability recommendations with respect to:

- The remaining life of the structure: This would essentially give ample time for the state DOTs to plan ahead on how to deal with the existing structure and/or plan alternate strategies.
- Repairs or retrofit: Such remediation can be done in order to strengthen the existing structure and give it added service life to enable it to perform as designed.
- Permissible load rating: By limiting the permissible loads on the structure, the service life of the structure can be extended.

The first two stages of analysis, using beam theory and SAT analysis, would give the structural engineer just an idea about the maximum load that the structure can withstand before it starts to show signs of distress or even fails. However, Stage 3 of the analysis (where the C-STM technique is adopted) gives the overall force-deformation of the structure, which helps to better predict/model its behavior and make a more definitive engineering judgment on the structure's acceptability condition. The C-STM analysis technique will aid the structural engineer to make a more accurate educated prediction about the behavior of the structure.

### **A1.6 Key Steps in the Strength Assessment of Concrete Structures Deteriorated with ASR/DEF Effects**

The following key observations can be drawn from the analysis schema developed in this appendix:

- Stage 1 analysis that employs the well-known beam theory can be used to determine the capacity of structures assuming a plastic hinge forms first. In fact, it may not be required to do a SAT/C-STM analysis if it is deemed that the structure is critical in flexure. However, this theory breaks down if D-regions are critical and thus becomes invalid. Nevertheless, the approach is still an important step in an overall assessment of the structure. For example, the shear-force diagram can be used to inform the analyst in Stage 2 on how nodal geometry should be apportioned.
- Stage 2 (SAT) can be used for analysis of structures with D-regions and as a further analysis technique if Stage 1 of the analysis leads to inconclusive results. However, SAT methods are strictly lower bound solutions and are both silent on and unable to predict deformations of the structure.
- The effects of ASR/DEF cannot be dealt with using Stage 1 and 2 of the analysis as these are based on the performance of sound concrete. ASR/DEF causes concrete swelling to occur; therefore a compatibility method is required.
- C-STM is a minimalist analysis procedure. It can be used to obtain a holistic behavior of the structure and to incorporate the effects of ASR/DEF in predicting the structural performance.

### **Additional References for Appendix A1**

Ley, M.T., Riding, K.A., Widiyanto, Bae S., and Breen, J. (2007). "Experimental Verification of the Strut and Tie Model Design Method." *ACI Structural Journal*, Vol. 104, No. 6, 749–755.

Park, R., and Paulay, T. (1975). *Reinforced Concrete Structures*. Wiley, NY.

## **A2 PRELIMINARY (CODE-BASED) COMPUTATIONS FOR BENT-CAP SPECIMENS**

This appendix presents the application of the code-based design approaches that use the AASHTO *LRFD Bridge Design Specifications* (2010) that are described in detail in Appendix A1 and are used to predict the response of the three bent-cap specimens. This appendix supports material in Section 3.

## A2.1 Introduction

The code-based design approaches that use the AASHTO *LRFD Bridge Design Specifications* (2010) that were described in detail in Appendix A1 are used to predict the response of the three bent-cap specimens.

## A2.2 Stage 1 Analysis

Stage 1 of the analysis considered only normal beam theory. The yield moment  $M_y^b$  and the externally applied load at first yield  $P_y^b$  are calculated using (A1-1) and (A1-3), respectively. The nominal flexural moment  $M_n^f$  was calculated by normal practice as per the AASHTO *LRFD Bridge Design Specifications* (2010) and (A1-4). Based on the nominal flexural moment  $M_n^f$ , and knowing that the shear span to the face of the column  $L_b = 991$  mm, the external load  $P_n^f$  causing flexure on the bent-cap was computed using (A1-6). The shear capacity  $V_n^s$  is calculated from (A1-7). Since there are no prestressing tendons, the component of shear carried by tendons is  $V_p = 0$ . The parameters  $\beta$  and  $\theta$  are calculated based on Method 1 of the AASHTO *LRFD Bridge Design Specifications* (2010).

The next step of the analysis is to determine the strength hierarchy. The strength reduction factors for shear and flexure are  $\phi_s = 0.90$  and  $\phi_f = 0.90$ , respectively. It is observed that  $\phi_s V_n^s$  is less than  $\phi_f P_n^f$  for Specimen 2A and 5D. That is, the factored shear capacity is insufficient, which could lead to a shear failure of the bridge pier.

The computation for Stage 1 flexure and shear analysis are presented in Table A2-1 and Table A2-2 respectively.

It is important to investigate the shear in the beam-column joint, as this can be a critical section. From the shear force diagram of the equivalent beam model of the bent cap shown in Figure A2-1, it is observed that there is no shear in the beam-column joint. Hence, the beam-column joint is determined not to be critical.

**Table A2-1: Results for Stage 1 Flexure Analysis for Bent-Cap Specimens.**

	<b>Specimen 2A</b>	<b>Specimen 5D</b>	<b>Specimen 8G</b>	
$L_b$ (mm)	991	991	991	
$b_w$ (mm)	838	838	838	
$d'$ (mm)	82.6	82.6	82.6	
$\rho'_L$	0.00581	0.00581	0.00581	
$d$ (mm)	832	832	832	
$\rho_L$	0.00581	0.00799	0.00581	
$n$	6.46	6.86	7.31	
$k$	0.222	0.261	0.232	<i>Eq. (A1-2)</i>
$C_c$ (kN)	-1530	-2100	-1503	
$C_s$ (kN)	-285	-396	-316	
$T$ (kN)	1815	2500	1815	
$M_y^b$ (kN-m)	1393	1893	1388	<i>Eq. (A1-1)</i>
$P_y^b$ (kN)	<b>1406</b>	<b>1913</b>	<b>1401</b>	<i>Eq. (A1-3)</i>
$\beta_1$	0.74	0.78	0.79	<i>Eq. (A1-5)</i>
$M_n^f$ (kN-m)	1623	2124	1623	<i>Eq. (A1-4)</i>
$P_n^f$ (kN)	<b>1637</b>	<b>2144</b>	<b>1637</b>	<i>Eq. (A1-6)</i>

**Table A2-2: Results for Stage 1 Shear Analysis for Bent-Cap Specimens.**

	<b>Specimen 2A</b>	<b>Specimen 5D</b>	<b>Specimen 8G</b>	
$d_v$ (mm)	745.7	745.7	745.7	
$A_{sh}$ (mm <sup>2</sup> )	396	393	792	
$f'_c$ (MPa)	42.7	37.9	36.5	
$f_y$ (MPa)	448	448	448	
$V_c$ (kN)	676	641	627	<i>Eq. (A1-8)</i>
$V_s$ (kN)	832	832	1664	<i>Eq. (A1-9)</i>
$V_n^s$ (kN)	<b>1508</b>	<b>1472</b>	<b>2291</b>	<i>Eq. (A1-7)</i>

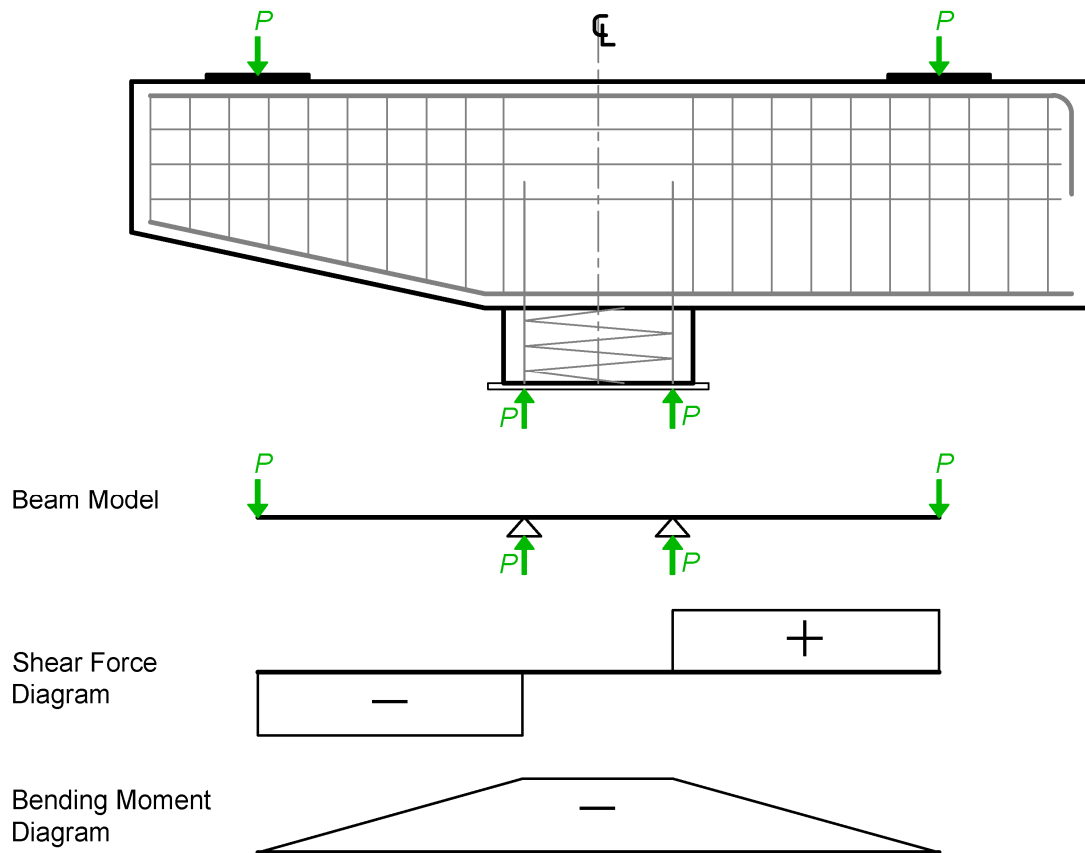


**Figure A2-1: Shear Force and Bending Moment Diagram of Equivalent Beam Model of Bent-Cap Specimens.**



From the above computations it is observed that the factored shear capacity of the bent cap is insufficient. This warrants further investigation, and the strut-and-tie technique is used for further analysis.

### A2.3 Stage 2 Analysis

Stage 2 of the analysis considers a SAT model developed for the bent cap as shown in Figure A2-2. The strut-and-tie model predictions are based on the procedure detailed in Appendix A1. No reduction factors are used in order to predict the actual response. Both the single panel and two panel SAT models are shown. The steps involved in the construct and analysis of the single panel SAT method is described below.

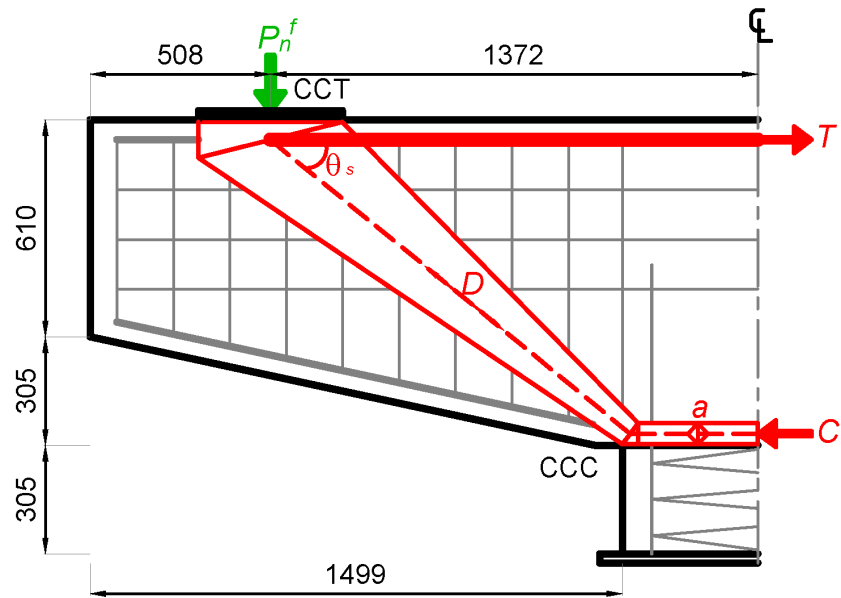
As an important first step in the strut-and-tie analysis to construct the SAT model it is required to determine the truss and node geometry. By equating the horizontal forces  $C$  and  $T$  in Figure A2-2a, the height  $a$  of the CCC node is:

$$a = \frac{T}{0.85f'_c b_w} = \frac{A_s f_y}{0.85f'_c b_w} \quad (\text{A2-1})$$

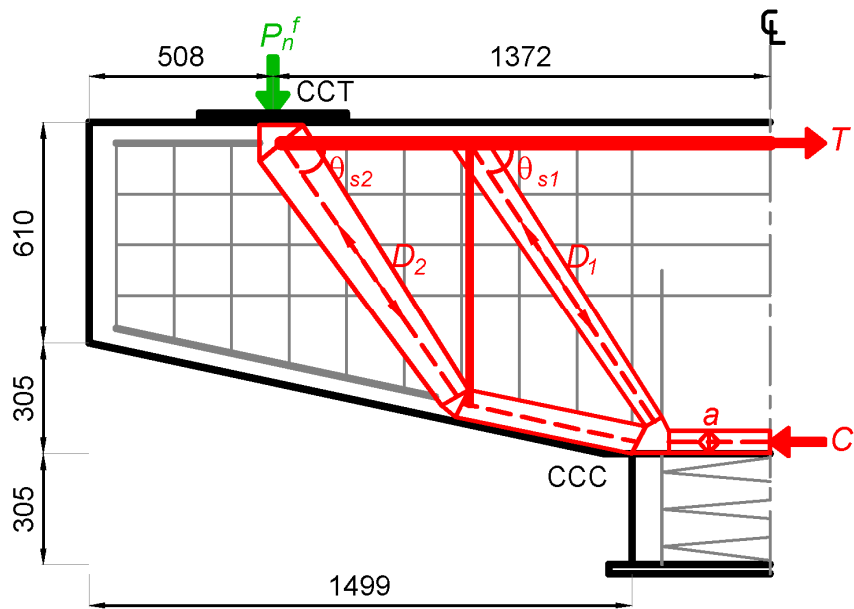
where the variables are as described earlier. The width of the CCT node equals the width of the bearing pad, which is 406 mm. The depth of the back face of the CCT node is taken as twice the distance from near face of the beam to the centroid of the tension reinforcement = 171.5 mm. The angle of inclination of the compression strut

$$\theta_s = \tan^{-1} \left( \frac{jd}{\text{shear span}} \right) = 36.8^\circ .$$

Taking moment equilibrium about the CCC node, the external load on the beam  $P_n^f = T(\tan \theta_s)$  can be determined. Thus,  $P_y^{\text{SAT}}$  based on longitudinal steel yield for each of the specimen is evaluated. Based on equilibrium of vertical forces at the CCT node, the strut force  $D$  can be determined. The bottom face of the CCC node is proportioned based on the vertical component of the strut force  $D$  and compressive force  $C$ .



(a) One panel model



(b) Two panel model

**Figure A2-2: SAT Model of Reinforced Concrete Bent-Cap Specimen 2A.**

An example on how to size the CCC node for Specimen 2A follows, with reference to Figure A2-2a:  $a = A_s f_y / 0.85 f'_c b_w = 59.7$  mm,  $\theta_s = \tan^{-1}(jd / L_b) = 36.8^\circ$ . Taking moments about  $C$  gives  $P_n^f = T \times jd / L_b = 1361$  kN. The diagonal force  $D = P_n^f / \sin \theta_s = 2269$  kN. By proportion the width of the bottom face of the CCC node is  $D \sin \theta_s (a / C) = 44.7$  mm. Thus knowing the two vertical faces of the node, the slant face can be determined. The values for the other two specimens can be found in Table A2-3.

**Table A2-3: Results for Stage 2 SAT Analysis for Bent-Cap Specimens.**

	<b>Specimen 2A</b>	<b>Specimen 5D</b>	<b>Specimen 8G</b>	<b>Comments</b>
$a$ (mm)	59.7	91.4	69.9	
$\theta_s$ (degrees)	36.8	36.8	36.8	
$T$ (kN)	1815	2495	1815	
$D$ (kN)	2269	3118	2269	
$P_y^{\text{SAT}}$ (kN)	1361	1873	1361	Based on longitudinal steel yield.
$\phi_v P_y^{\text{SAT}}$ (kN)	953	1311	953	
$P_n^{\text{SAT}}$ (kN)	1637	2144	1637	Based on node capacity.
$\phi_v P_n^{\text{SAT}}$ (kN)	1146	1501	1146	
$\phi_f P_n^f$ (kN)	1473	1930	1473	

Based on the geometry of the nodes, it is evident that the CCC node is the most critical node. As per AASHTO LRFD Design Specifications (2010) the strength of the critical CCC node is found from  $0.85 f'_c A_{\text{node}}$ , where  $A_{\text{node}}$  = the cross-sectional area of the inclined face of the CCC node.

Incidentally it is found that the strut force  $D$  is equal to the node strength of the CCC node. Therefore, the externally applied load based on node capacity  $P_n^{\text{SAT}} = P_n^f$ . However, the factored capacity  $\phi_v P_n^{\text{SAT}} < \phi_f P_n^f$ . The results obtained from the SAT analysis are presented in Table A2-3.

#### **A2.4 Summary**

A summary of Stage 1 and 2 analysis results, along with the material properties and experimental results of the three bent-cap specimens is presented in Table A2-4.

Figure A2-3 shows the experimentally obtained force-deformation response along with each of the code-based predictions. As each of the code-based techniques is only a strength-based approach, no predictions of the structure's global deformation can be made; hence, the predicted forces are represented by horizontal lines.

From the SAT analysis, it can be concluded that the joint capacity is undependable, even though  $P_n^{\text{SAT}} = P_n^f$ . The results are inconclusive, and this warrants a more advanced analysis be conducted using C-STM. Clearly it is desirable to have a more insightful analysis that can overcome these shortcomings.

Finally, a summary of results from all the three stages of analysis along with the experimental results are presented in Table A2-5.

**Table A2-4: Material Properties, Stage 1 and 2 Analyses, and Experimental Results.**

		<b>Specimen 2A</b>	<b>Specimen 5D</b>	<b>Specimen 8G</b>	<b>Comments</b>
<b>Material Properties</b>	$f'_c$ (MPa) <sup>#</sup>	42.7	37.9	36.5	
	$f'_t$ (MPa)	2.21	2.07	2.00	
	$E_c$ (MPa)	30959	29131	28614	
<b>Stage 1 Analyses (Sectional)</b>	$M_y^b$ (kN-m)	1393	1893	1388	<i>Eq.(A1-1)</i>
	$P_y^b$ (kN)	<b>1406</b>	<b>1913</b>	<b>1401</b>	<i>Eq.(A1-3)</i>
	$M_n^f$ (kN-m)	1623	2124	1623	<i>Eq.(A1-4)</i>
	$P_n^f$ (kN)	<b>1637</b>	<b>2144</b>	<b>1637</b>	<i>Eq.(A1-6)</i>
	$\phi_f P_n^f$ (kN)	1473	1930	1473	$\phi_f = 0.9$
	$V_n^s$ (kN)	<b>1508</b>	<b>1472</b>	<b>2291</b>	<i>Eq.(A1-7)</i>
<b>Stage 2 Analyses (SAT)</b>	$P_y^{SAT}$ (kN)	<b>1361*</b>	<b>1873*</b>	<b>1361*</b>	Based on longitudinal steel yield.
	$\phi_f P_y^{SAT}$ (kN)	953	1311	953	
	$P_n^{SAT}$ (kN)	1637	2144	1637	Based on node capacity.
	$\phi_f P_n^{SAT}$ (kN)	1146	1501	1146	
<b>Experimental Results</b>	$P_{Yield}^{Expt}$ (kN)	1468	1890	1535	
	$P_{Failure}^{Expt}$ (kN)	<b>1797</b>	<b>2068</b>	<b>1926</b>	
	$\Delta_{Yield}^{Expt}$ (mm)	6.35	8.13	8.13	
	$\Delta_{Failure}^{Expt}$ (mm)	19.56	12.70	32.00 <sup>†</sup>	
	$\mu$	3.08	1.56	>3.94	
	$P_n^{SAT} / P_{Failure}^{Expt}$	0.91	1.04	0.85	

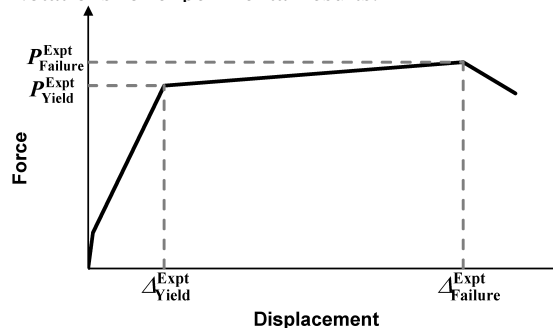
<sup>#</sup> TxDOT Class C Concrete-Average compression strength of three 28-day cylinder tests (Section 15.3, ACI 318-99).

\* Expected critical failure mode capacity.

<sup>†</sup> Specimen was not loaded to ultimate failure.

Superscript: *b*=beam; *f*=flexure; *s*=shear; SAT=strut-and-tie; Expt=Experiment.

Notations for experimental results:



- $p_y^b$  = External load causing flexural yield
- - -  $p_n^f$  = External load causing beam flexural
- - -  $V_n^s$  = Nominal beam shear
- · -  $p_y^{SAT}$  = SAT based external load for long. steel yield
- $p_n^{SAT}$  = SAT based external load for node capacity

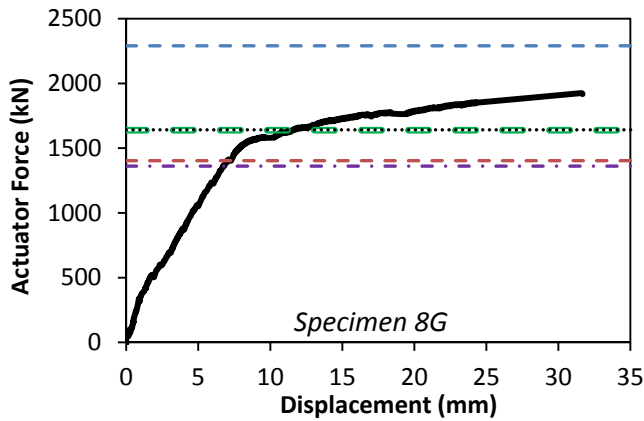
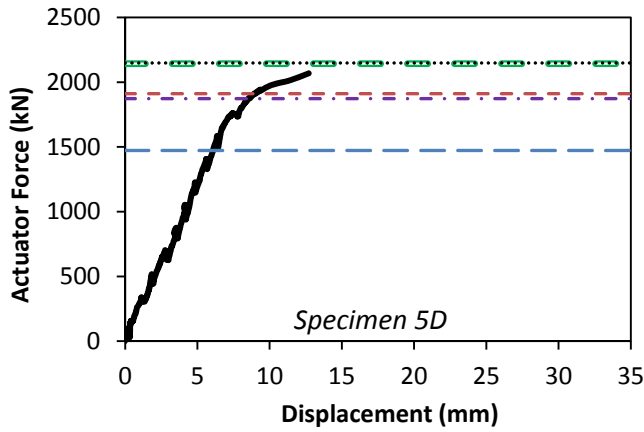
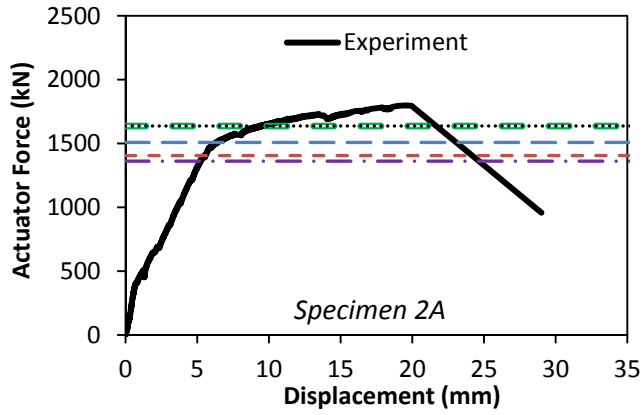


**Figure A2-3: Experimental, Stage 1, and Stage 2 Results.**

**Table A2-5: Summary of Results for Bent-Cap Specimens.**

Stage		Specimen 2A		Specimen 5D		Specimen 8G		Comments
		Capacity (kN)	Factored Capacity (kN)	Capacity (kN)	Factored Capacity (kN)	Capacity (kN)	Factored Capacity (kN)	
Stage 1: Beam Theory	$P_y^b$	1406	---	1913	---	1401	---	External load based on yield flexural resistance of the beam. External load based on nominal flexural capacity of the beam.
	$P_n^f$	1637	1473	2144	1930	1637	1473	
	$V_n^s$	1508	1282	1472	1251	2291	1947	Beam shear capacity.
Stage 2: SAT	$P_y^{SAT}$	1361	953	1873	1311	1361	953	External load based on yield of longitudinal steel in beam. External load based on critical CCC node.
	$P_n^{SAT}$	1637	N/A	2144	N/A	1637	N/A	
Stage 3: C-STM	$P_{C-STM}$	<b>1704</b>	1193	<b>2024</b>	1417	---	---	External load based on C-STM analysis.
Experiment	$P_{Failure}$	1797	---	2068	---	---	---	Maximum load at incipient failure.

### **A3 COMPUTATION OF REINFORCEMENT RATIO AND MAXIMUM EXPANSION STRAIN FOR C-BEAM SPECIMEN 3**

The computation of reinforcement ratio and the maximum expansion strain to simulate the ASR/DEF induced expansion in C-beam Specimen 3 is presented in this appendix. This appendix supports material in Section 6.



COMPUTATION OF REINFORCEMENT RATIO  $\rho$  AND MAXIMUM  
EXPANSION STRAIN  $\epsilon_{\rho}^{\max}$  FOR C-BEAM SPECIMEN 3

1  
8

GENERAL NOTES

General Parameters Used

$$\begin{array}{llll}
 f'_c = 41.0 \text{ MPa} & E_c^{\text{actual}} = 30270 \text{ MPa} & f'_t = 4.0 \text{ MPa} & \epsilon'_t = 0.000132 \\
 f_y = 448 \text{ MPa} & E_s = 200 \text{ GPa} & \epsilon_y = 0.00224 & \\
 t_r(\theta_o) = 120 \text{ days} & \epsilon_o^{\max} = 0.05 & n = \frac{E_s}{E_c/3} = 19.82 & 
 \end{array}$$

Maximum Expansion Strain

The C-beam specimens were subjected to tie-bar force to simulate gravity loads on the structure. This resulted in the specimen being precracked, which further accelerated the expansion process as these cracks provided a pathway for moisture ingress. To take into account the precracked nature of the specimen, Eq. 4-16a (which is repeated below for convenience) was used in the computation of the expansion strains  $\epsilon_{\rho}^{\max}$ .

$$\epsilon_{\rho}^{\max} = \frac{\epsilon_o^{\max} \epsilon'_t + \rho n (\epsilon_y^2 - \epsilon_{\text{spre}}^2) + \epsilon'_t \epsilon_{\text{spre}} - \left(\frac{\epsilon'_t}{2}\right)^2}{2 \left( \frac{\epsilon'_t}{2} + \rho n (\epsilon_y - \epsilon_{\text{spre}}) - \frac{\sigma_{\text{const}}}{E_c} \right)} \quad 4-16a$$

Development Length (ACI Equations)

Mander et al. (2011) established that to develop the full yield strength of the reinforcement, the reinforcing bars transverse to the member edge should be longer than the bar development length  $l_d$ .

$$\#8 \text{ bars: } l_d = \left( \frac{f_y \psi_t \psi_e}{20 \lambda \sqrt{f'_c}} \right) d_b = \left( \frac{65000(1)(1)}{20(1)\sqrt{f'_c}} \right) d_b = 3250 \frac{d_b}{\sqrt{f'_c}} = 42.20'' \times 25.4 = 1072 \text{ mm}$$

$$\#4 \text{ bars: } l_d = \left( \frac{f_y \psi_t \psi_e}{25 \lambda \sqrt{f'_c}} \right) d_b = \left( \frac{65000(1)(1)}{25(1)\sqrt{f'_c}} \right) d_b = 2600 \frac{d_b}{\sqrt{f'_c}} = 16.88'' \times 25.4 = 429 \text{ mm}$$

CASE 1	COMPUTATION OF REINFORCEMENT RATIO $\rho$ AND MAXIMUM EXPANSION STRAIN $\epsilon_{\rho}^{\max}$ FOR C-BEAM SPECIMEN 3	2 8
-----------	---	--------

COLUMN TOP FACE MEMBER REGION

Section depth  $d$  = overall depth  $D$  - depth to neutral axis  $kd_{col} = 914 - 355 = 559$  mm

**Direction: Transverse (a)**

Reinforcement type: #4 bars with c/s area  $A_s = 127$  mm<sup>2</sup> @ 114 mm c/c spacing

Reinforcement ratio  $\rho = A_s / (sd) = 0.00198$

Additionally, as there are no tensile prestrains in the transverse direction,  $\epsilon_{spre} = \epsilon_{spre} = 0$ .

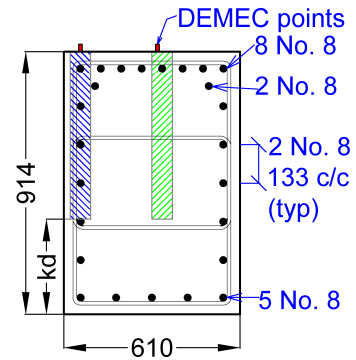
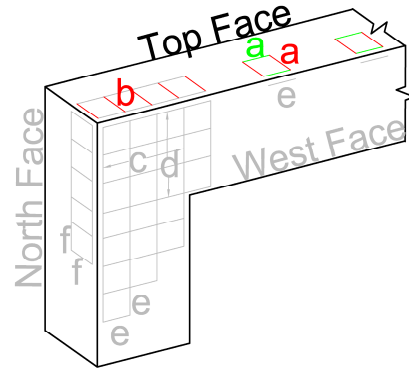
Maximum expansion strain  $\epsilon_{\rho}^{\max} = 0.02202$

**Direction: Longitudinal (a)**

DEMEC measurements are made along two lines, one close to the edge of the column, and the other closer to the middle of the column cross-section. As the DEMEC readings are limited to the two lines, the strains measured could be more localized. Therefore narrow strips under the DEMEC points are considered to compute the reinforcement ratio. Because of their localized effects the average reinforcement ratio is considered.

Width of strip,  $b = 70.7$  mm (shaded blue and green)

c/s area of concrete  $A_c = (559)(70.7) = 39521$  mm<sup>2</sup>



DEMEC points location	Close to column edge (shaded blue)	Close to column center (shaded green)
$A_s$ (mm <sup>2</sup> )	2027 (4-#8 bars)	507 (1-#8 bar)
$\rho = A_s / (bd)$	0.05122	0.01281
Average $\rho$	0.03202	

$\epsilon_{spre} = \epsilon_{spre} = 0.00067$  obtained from C-STM model.

$\epsilon_{\rho}^{\max} = 0.0045$

Figure G-4a shows the expansion results obtained in the transverse and longitudinal direction on the member region of the column top face of the C-beam specimen.

CASE II	COMPUTATION OF REINFORCEMENT RATIO $\rho$ AND MAXIMUM EXPANSION STRAIN $\epsilon_{\rho}^{\max}$ FOR C-BEAM SPECIMEN 3	3 8
------------	--	--------

COLUMN TOP FACE JOINT REGION

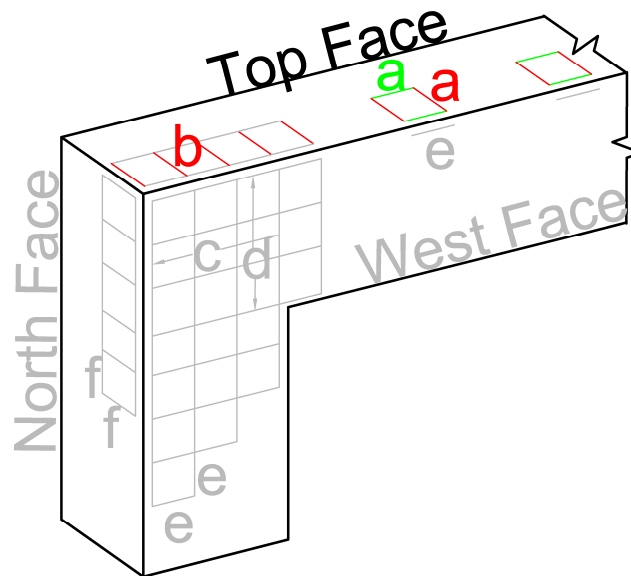
Direction: Transverse (b)

There are no transverse hoops on the column top face in the joint region. Therefore,  $\rho = 0$  is considered for the region close to the edge. However, in the region away from the edge and close to the column member region, the influence of transverse reinforcement in the column member region is considered. A  $\rho = 0.00198/2 = 0.00099$  is assumed.

Since there are no tensile prestrains in the transverse direction,  $\epsilon_{opre} = \epsilon_{spre} = 0$ .

$$\epsilon_{\rho}^{\max} = 0.0304$$

Figure 6-4b shows the transverse expansion strains in the joint region of the C-beam specimen top face.



CASE III	COMPUTATION OF REINFORCEMENT RATIO $\rho$ AND MAXIMUM EXPANSION STRAIN $\epsilon_p^{\max}$ FOR C-BEAM SPECIMEN 3	4 8
-------------	--	--------

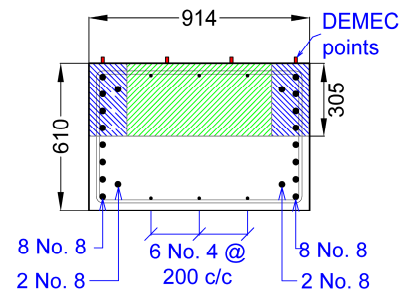
**BEAM COLUMN JOINT REGION**

Concrete and steel volume in half the section-depth  $d = 305$  mm is considered for calculating the reinforcement ratio.

**Direction: Vertical DEMEC Points along Beam Longitudinal Steel**

Depending on the location of the DEMEC points on the face of the beam cross-section, two separate reinforcement ratios are computed.

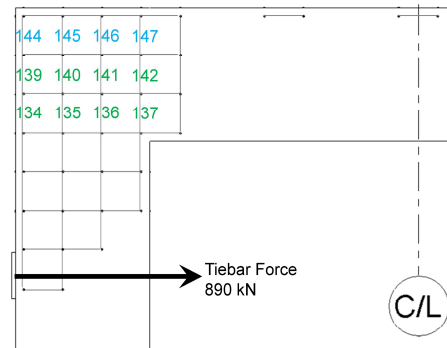
DEMEC location	Close to member edges (shaded blue)	For interior DEMEC points (shaded green)
Area of steel, $A_s$	2534 mm <sup>2</sup> (5-#8 bars)	380 mm <sup>2</sup> (3-#4 bars)
Area of concrete, $A_c$	(305) (157.2) = 47946 mm <sup>2</sup>	(305) (600.1) = 183031 mm <sup>2</sup>
$\rho$	0.0529	0.00208



The reinforcement ratio is scaled down for the DEMEC points close to the C-beam specimen edges.

Scaled reinforcement ratio for:	DEMEC 145 and 146 close to specimen top edge	DEMEC 139-142, still within the development length
$l$ (mm)	133.4	400.1
$\rho_{\text{reduced}} = \rho(l/l_d)$	$0.00208(133.4/429) = 0.000647$	$0.0529(400.1/1072) = 0.01974$
With $(\epsilon_{\text{cpre}} = \epsilon_{\text{spre}} = 0)$ , $\epsilon_p^{\max} =$	0.03514	0.00453

Figure 6-4c shows two curves for the expansion results from the model. Curve A corresponds to the case where the expansion strains are computed closer to the top edge of the specimen (within development length zone close to top edge) and Curve B for expansion strains computed away from the top edge (within development length zone away from top edge).



CASE IV	COMPUTATION OF REINFORCEMENT RATIO $\rho$ AND MAXIMUM EXPANSION STRAIN $\epsilon_p^{\max}$ FOR C-BEAM SPECIMEN 3	5 8
------------	--	--------

**BEAM COLUMN JOINT REGION**

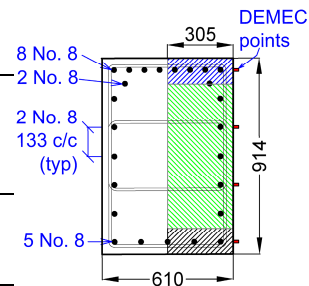
Concrete and steel volume in half the section-depth  $d = 305$  mm is considered for calculating the reinforcement ratio.

**Direction: Horizontal DEMEC Points along Column Longitudinal Steel**

Depending on the location of the DEMEC points on the face of the beam cross-section, two separate reinforcement ratios are computed.

For DEMEC within the development length zone and close to the specimen edges (first layer of DEMEC points 158, 162, 166, and 170) the portion shaded in green is used to compute the reinforcement ratio as the influence of the reinforcement at the extremes (shaded blue) is unlikely to influence the expansion close to the specimen edge.

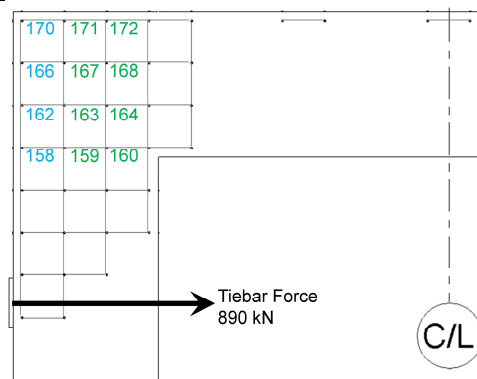
DEMEC location	Close to member edges (entire shaded region)	For interior DEMEC points (shaded green)
Area of steel, $A_s$	6587 mm <sup>2</sup> (12-#8 and 4-#4 u-bars, not shown)	3040 mm <sup>2</sup> (5-#8 and 4-#4 u-bars, not shown)
Area of concrete, $A_c$	(305)(914) = 278770 mm <sup>2</sup>	(305)(666.75) = 203359 mm <sup>2</sup>
$\rho$	0.0236	0.01496



The reinforcement ratio is scaled down for DEMEC points close to C-beam specimen edges.

Scaled reinforcement ratio for:	DEMEC 159, 163, 167, and 171 still within the development length	DEMEC 158, 162, 166, and 170 close to specimen edge
$l$ (mm)	400.1	133.4
$\rho_{reduced} = \rho(l/l_d)$	0.0236(400.1/1072) = 0.00881	0.01496(133.4/1072) = 0.001861
$(\epsilon_{cpre} = \epsilon_{spre} = 0), \epsilon_p^{\max} =$	0.00816	0.02278

Figure 6-4d shows the expansion strains, close and away from the specimen edge, obtained from the model.



CASE V	COMPUTATION OF REINFORCEMENT RATIO $\rho$ AND MAXIMUM EXPANSION STRAIN $\epsilon_p^{\max}$ FOR C-BEAM SPECIMEN 3	6 8
-----------	---	--------

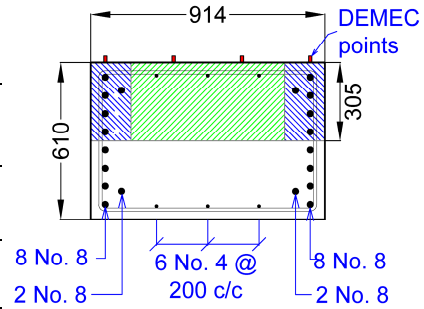
**BEAM WEST FACE**

Concrete and steel volume in half the section-depth  $d = 305$  mm is considered for calculating the reinforcement ratio.

**Direction: Longitudinal**

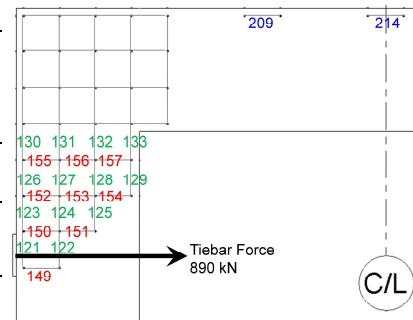
As the DEMEC points are considerably away from the specimen edge, the reinforcement in the entire half-depth of the cross-section  $d = 305$  mm is considered as localized effects near the edges are eliminated.

Area of steel, $A_s$	5447 mm <sup>2</sup> (10-#8 and 3-#4 bars)
Area of concrete, $A_c$	(305)(914) = 278770 mm <sup>2</sup>
$\rho$	0.01954
$(\epsilon_{cpre} = \epsilon_{spre} = 0), \epsilon_p^{\max} =$	0.00456



The reinforcement ratio is scaled down for the DEMEC points within the development length zone.

Scaled reinforcement ratio for:	DEMEC 123-125 within the development length zone
$l$ (mm)	806.5
$\rho_{reduced} = \rho(l/l_d)$	0.01954 (806.5/1072) = 0.01470
With $(\epsilon_{cpre} = \epsilon_{spre} = 0), \epsilon_p^{\max} =$	0.00559



**Direction: Transverse**

Reinforcement type: #4 bars with c/s area  $A_s = 127$  mm<sup>2</sup> @ 114 mm c/c spacing.

Reinforcement ratio  $\rho = A_s / (sd) = 0.00364$ .

As there are no tensile prestrains in the transverse direction,  $\epsilon_{cpre} = \epsilon_{spre} = 0$ .

Maximum expansion strain  $\epsilon_p^{\max} = 0.01526$ .

Figure 6-4e shows the expansion strain  $s$  in the longitudinal and transverse direction on the beam west face.

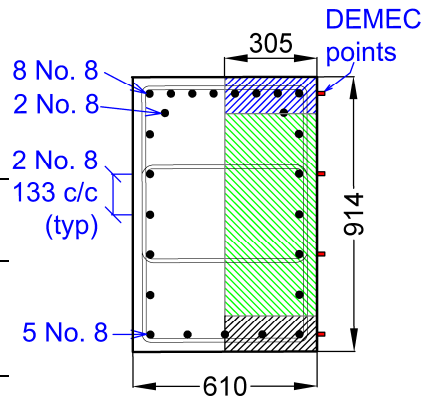
CASE VI	COMPUTATION OF REINFORCEMENT RATIO $\rho$ AND MAXIMUM EXPANSION STRAIN $\epsilon_p^{\max}$ FOR C-BEAM SPECIMEN 3	7 8
------------	--	--------

COLUMN WEST FACE

Direction: Longitudinal

The DEMEC points in the column of the specimen west face were located close to the specimen top edge; therefore the reinforcement ratio is calculated considering the area shaded in blue.

Area of steel, $A_s$	$2534 \text{ mm}^2$ (5-#8 bars)
Area of concrete, $A_c$	$(305)(123.8) = 37759 \text{ mm}^2$
$\rho$	$0.0671$



$$\epsilon_{cpre} = \epsilon_{spre} = 0.00067$$

obtained from C-STM model.

$$\epsilon_p^{\max} = 0.00296$$

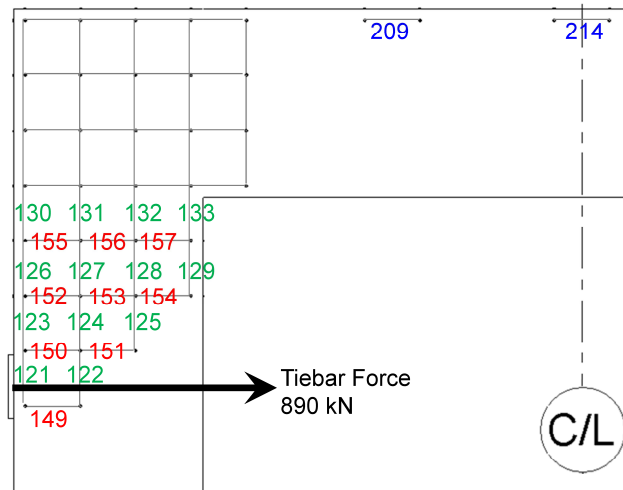


Figure 6-4e shows the expansion strains in the longitudinal direction on the column west face.

CASE VII	COMPUTATION OF REINFORCEMENT RATIO $\rho$ AND MAXIMUM EXPANSION STRAIN $\epsilon_p^{max}$ FOR C-BEAM SPECIMEN 3	8 8
-------------	--	--------

**BEAM NORTH FACE**

Section depth  $d$  = overall depth;  $D$  = depth to neutral axis;  $kd_{beam} = 914 - 287.3 = 626.7$  mm

**Direction: Transverse ( $f$ )**

Reinforcement type: #4 bars with c/s area  $A_s = 127$  mm<sup>2</sup> @ 114 mm c/c spacing

Reinforcement ratio  $\rho = A_s / (sd) = 0.00177$

As there are no tensile prestains in the transverse direction,  $\epsilon_{opre} = \epsilon_{spre} = 0$ .

Maximum expansion strain  $\epsilon_p^{max} = 0.0234$

**Direction: Longitudinal ( $f$ )**

DEMEC measurements are made along two lines, one close to the edge of the beam, and the other closer to the middle of the beam cross-section. As the DEMEC readings are limited to the two lines, the strains measured could be more localized. Therefore narrow strips under the DEMEC points are considered to compute the reinforcement ratio. Because of their localized effects the average reinforcement ratio is considered.

Width of strip,  $b = 70.7$  mm (shaded blue and green)

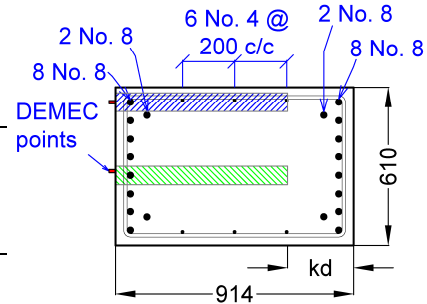
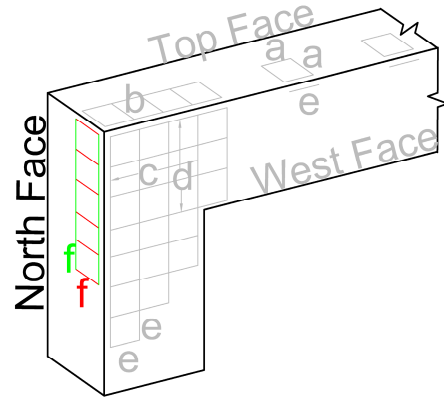
c/s area of concrete  $A_c = (626.7)(70.7) = 44308$  mm<sup>2</sup>

DEMEC points location	Close to beam edge (shaded blue)	Close to beam center (shaded green)
$A_s$ (in <sup>2</sup> )	760 mm <sup>2</sup> (1-#8 and 2-#4 bars)	507 mm <sup>2</sup> (1-#8 bar)
$\rho = A_s / (bd)$	0.01713	0.01142
Average $\rho$	0.01428	

$\epsilon_{opre} = \epsilon_{spre} = 0.00084$  obtained from C-STM model.

Maximum expansion strain  $\epsilon_p^{max} = 0.00855$

Figure 6-4f shows the expansion strain results on the north face of the C-beam specimen.





## **A4 PRELIMINARY (CODE-BASED) COMPUTATIONS FOR C-BEAM SPECIMENS**

This appendix presents the application of the code-based design approaches that use the AASHTO *LRFD Bridge Design Specifications* (2010) that are described in detail in Appendix A1 and are used to predict the response of the C-beam specimens. This appendix supports material in Section 8.

#### A4.1 Introduction

The code-based design approaches that use the AASHTO LRFD Bridge Design Specifications (2010) are used to predict the response of C-beam Specimens 1, 2, 4 and 3. This appendix presents the analysis procedure followed for the C-beam specimens. The computations for Stage 1 (beam theory), Stage 2 (SAT analysis) are presented herein. The material properties of the four C-beam specimens are presented in Table A4-1.

**Table A4-1: Material Properties for C-beam Specimens.**

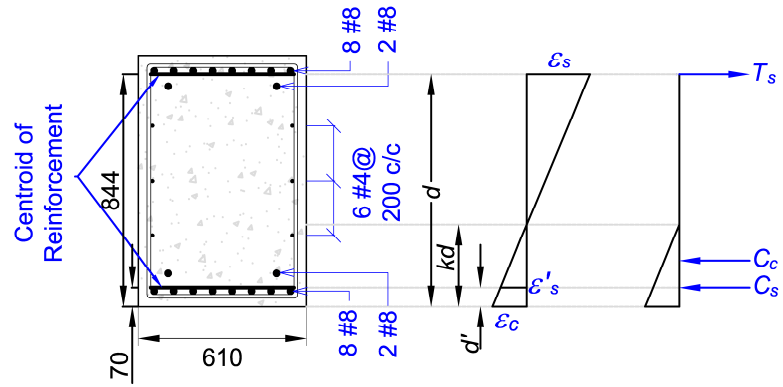
	<b>Specimen 1</b>	<b>Specimen 2</b>	<b>Specimen 4</b>	<b>Specimen 3</b>
$f'_c$ (MPa) (at time of testing)	37.2	38.6	27.6	40.9
$f'_t$ (MPa)	2.1	1.6	---	---
$E_c$ (MPa)	28890	29407	24856	30269
$f_y$ (MPa)	448	448	448	448
$E_s$ (GPa)	200	200	200	200

#### A4.2 Stage 1: Analysis Using Beam Theory

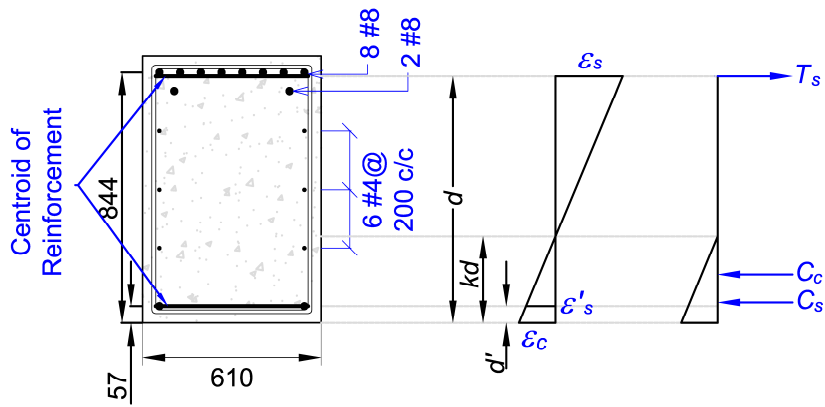
Stage 1 analysis as outlined in Appendix A1 is carried out for the C-beam specimens.

***Step 1: Determine first yield flexural capacity,  $M_y^b$***

The yield moment  $M_y^b$  and the externally applied load causing first yield  $P_y^b$  are calculated using (A1-1) and (A1-3), respectively. Figure A4-1 shows the stress and strain distribution for the double and singly reinforced beams of the C-beam specimens. The computation of the yield moment is presented in Table A4-2.



(a) Doubly reinforced beam



(b) Singly reinforced beam

**Figure A4-1: Strain and Stress Distribution for Computation of Yield Moment.**

**Table A4-2: First Yield Flexural Capacity and Corresponding Axial Load.**

	Specimen 1		Specimen 2		Specimen 4		Specimen 3	
	<i>Doubly</i>	<i>Singly</i>	<i>Doubly</i>	<i>Singly</i>	<i>Doubly</i>	<i>Singly</i>	<i>Doubly</i>	<i>Singly</i>
$A_s$ (mm <sup>2</sup> )	3980	3980	3980	3980	3980	3980	3980	3980
$A'_s$ (mm <sup>2</sup> )	3980	796	3980	796	3980	796	3980	796
$b$ (mm)	610	610	610	610	610	610	610	610
$d$ (mm)	844	844	844	844	844	844	844	844
$d'$ (mm)	70	57	70	57	70	57	70	57
$jd = d - d'$ (mm)	775	787	775	787	775	787	775	787
$\rho_L = A_s / (bd)$	0.00984	0.00984	0.00984	0.00984	0.00984	0.00984	0.00984	0.00984
$\rho'_L = A'_s / (bd)$	0.00984	0.00197	0.00984	0.00197	0.00984	0.00197	0.00984	0.00197
$n = E_s / E_c$	6.92		6.80		8.04		6.61	
$k = \sqrt{(\rho_L + \rho'_L)^2 n^2 + 2(\rho_L + \rho'_L d'/d)n - (\rho_L + \rho'_L)n}$								
$k$	0.271	0.299	0.270	0.297	0.285	0.317	0.267	0.293
$kd$ (mm)	228.9	252.5	228.1	251.0	240.8	267.7	225.6	247.7
$\varepsilon_c = \frac{\varepsilon_y(kd)}{d - kd}$	0.00083	0.00096	0.00083	0.00095	0.00089	0.00104	0.00082	0.00093
$\varepsilon'_s = \frac{\varepsilon_y(kd - d')}{d - kd}$	0.00058	0.00074	0.00058	0.00073	0.00063	0.00082	0.00056	0.00072
$C_c$ (kN) = $0.5\varepsilon_c E_c (kd)b$	-1677	-2135	-1695	-2135	-1628	-2108	-1699	-2126
$C_s$ (kN) = $A'_s \varepsilon'_s E_s$	-587	-151	-583	-147	-641	-165	-569	-147
$T_s$ (kN) = $A_s f_y$	2273	2273	2273	2273	2273	2273	2273	2273
$M_y^b = T_s (d - kd / 3) + C_s (kd / 3 - d')$								
$M_y^b$ (kN - m)	1749	1730	1749	1731	1742	1721	1750	1734
$P_y^b = M_y^b / L_b$ where $L_b = 914$ mm.								
$P_y^b$ (kN)	1913	1890	1913	1895	1904	1882	1913	1895

***Steps 2 and 3: Determine nominal flexural moment,  $M_n^f$  and axial load demand based on flexure,  $P_n^f$***

The nominal flexural moment  $M_n^f$  may be calculated by normal practice as per the AASHTO LRFD *Bridge Design Specifications* (2010) and (A1-4). However, in this study, for an accurate estimate of the nominal moment, calculations were performed in a spreadsheet considering the contribution of each layer of steel. The spreadsheets are presented in Tables A4-3 through A4-10 for both doubly and singly reinforced beam for all the four C-beam specimens. Based on the nominal flexural moment  $M_n^f$ , and knowing that the shear span to the face of the column  $L_b = 914$  mm, the externally applied load causing flexure on the bent cap is computed.

**Table A4-3: Computation of Flexural Moment and Corresponding Axial Load Demand for Doubly Reinforced Beam: Specimen 1.**

Input Parameters						Calculated Variables	
<i>Section Properties</i>		<i>Reinforcement Details</i>		<i>Reinforcement Properties</i>		$\alpha$	0.85
Breadth (mm)	610	Reinf.	Diameter (mm)	$E_s$ (GPa)	200	$\beta$	0.78
$a$ (shear span, mm)	914	Long.	25.4	$f_y$ (MPa)	448	Assume NA depth for equilibrium $c$ (mm)	105.3
<i>Concrete Properties</i>		Distribution	12.7				
$f'_c$ (MPa)	37.2	Stirrups	12.7				
Analysis							
<i>Layer</i>	<i>No: of bars</i>	<i>Area (mm<sup>2</sup>)</i>	<i>Dist. to layers from bottom (mm)</i>	<i>Strain</i>	<i>Stress in Steel (MPa)</i>	<i>Force in Concrete/ Steel (kN)</i>	<i>Moment (kN-m)</i>
Concrete	-----	-----	41.1	-0.003	-----	-1584.3	-65.1
(Bottom) 1	8	4054	57.2	-0.0014	-274.2	-1111.6	-63.5
Steel 2	2	1013	120.7	0.0004	87.6	88.7	10.7
Steel 3	2	253	257.2	0.0043	447.9	113.5	29.2
Steel 4	2	253	457.2	0.01	447.9	113.5	51.9
Steel 5	2	253	657.2	0.0157	447.9	113.5	74.6
Steel 6	2	1013	793.8	0.0196	447.9	453.9	360.3
Steel 7	8	4054	857.3	0.0214	447.9	1815.6	1556.4
					$M_n^f$ (kN-m)		<b>1954.6</b>
					$P_n^f$ (kN)		<b>2140.0</b>

**Table A4-4: Computation of Flexural Moment and Corresponding Axial Load Demand for Singly Reinforced Beam: Specimen 1.**

Input Parameters						Calculated Variables	
Section Properties		Reinforcement Details		Reinforcement Properties		$\alpha$	0.85
Breadth (mm)	610	Reinf.	Diameter (mm)	$E_s$ (GPa)	200	$\beta$	0.78
$a$ (shear span, mm)	914	Long.	25.4	$f_y$ (MPa)	448	Assume NA depth for equilibrium $c$ (mm)	148.5
Concrete Properties		Distribution	12.7				
$f'_c$ (MPa)	37.2	Stirrups	12.7				
Analysis							
Layer	No: of bars	Area (mm <sup>2</sup> )	Dist. to layers from bottom (mm)	Strain	Stress in Steel (MPa)	Force in Concrete/ Steel (kN)	Moment (kN-m)
Concrete	-----	-----	57.9	-0.003	-----	-2234.0	-129.4
(Bottom) 1	2	1013	57.2	-0.0018	-368.6	-373.5	-21.3
Steel 2	0	0	120.7	-0.0006	-112.4	0.0	0.0
Steel 3	2	253	257.2	0.0022	428.0	108.4	27.9
Steel 4	2	253	457.2	0.0062	447.9	113.5	51.9
Steel 5	2	253	657.2	0.0103	447.9	113.5	74.6
Steel 6	2	1013	793.8	0.013	447.9	453.9	360.3
Steel 7	8	4054	857.3	0.0143	447.9	1815.6	1556.4
					$M_n^f$ (kN-m)		<b>1920.4</b>
					$P_n^f$ (kN)		<b>2100.0</b>

**Table A4-5: Computation of Flexural Moment and Corresponding Axial Load Demand for Doubly Reinforced Beam: Specimen 2.**

Input Parameters						Calculated Variables	
<b>Section Properties</b>		<b>Reinforcement Details</b>		<b>Reinforcement Properties</b>		$\alpha$	0.85
Breadth (mm)	610	Reinf.	Diameter (mm)	$E_s$ (GPa)	200	$\beta$	0.77
$a$ (shear span, mm)	914	Long.	25.4	$f_y$ (MPa)	448	Assume NA depth for equilibrium $c$ (mm)	104.3
<b>Concrete Properties</b>		Distribution	12.7				
$f'_c$ (MPa)	38.6	Stirrups	12.7				
Analysis							
<i>Layer</i>	<i>No: of bars</i>	<i>Area (mm<sup>2</sup>)</i>	<i>Dist. to layers from bottom (mm)</i>	<i>Strain</i>	<i>Stress in Steel (MPa)</i>	<i>Force in Concrete/ Steel (kN)</i>	<i>Moment (kN-m)</i>
Concrete	-----	-----	40.1	-0.003	-----	-1606.2	-64.5
(Bottom) 1	8	4054	57.2	-0.0014	-271.0	-1098.8	-62.8
Steel 2	2	1013	120.7	0.0005	94.3	95.5	11.5
Steel 3	2	253	257.2	0.0044	447.9	113.5	29.2
Steel 4	2	253	457.2	0.0102	447.9	113.5	51.9
Steel 5	2	253	657.2	0.0159	447.9	113.5	74.6
Steel 6	2	1013	793.8	0.0198	447.9	453.9	360.3
Steel 7	8	4054	857.3	0.0217	447.9	1815.6	1556.4
					$M_n^f$ (kN-m)		<b>1956.4</b>
					$P_n^f$ (kN)		<b>2139.6</b>



**Table A4-6: Computation of Flexural Moment and Corresponding Axial Load Demand for Singly Reinforced Beam: Specimen 2.**

Input Parameters						Calculated Variables	
<b>Section Properties</b>		<b>Reinforcement Details</b>		<b>Reinforcement Properties</b>		$\alpha$	0.85
Breadth (mm)	610	Reinf.	Diameter (mm)	$E_s$ (GPa)	200	$\beta$	0.77
$a$ (shear span, mm)	914	Long.	25.4	$f_y$ (MPa)	448	Assume NA depth for equilibrium $c$ (mm)	145.3
<b>Concrete Properties</b>		Distribution	12.7				
$f'_c$ (MPa)	38.6	Stirrups	12.7				
Analysis							
<i>Layer</i>	<i>No: of bars</i>	<i>Area (mm<sup>2</sup>)</i>	<i>Dist. to layers from bottom (mm)</i>	<i>Strain</i>	<i>Stress in Steel (MPa)</i>	<i>Force in Concrete/ Steel (kN)</i>	<i>Moment (kN-m)</i>
Concrete	-----	-----	56.0	-0.003	-----	-2238.6	-125.2
(Bottom) 1	2	1013	57.2	-0.0018	-363.6	-368.5	-21.1
Steel 2	0	0	120.7	-0.0005	-101.8	0.0	0.0
Steel 3	2	253	257.2	0.0023	438.3	111.0	28.6
Steel 4	2	253	457.2	0.0064	447.9	113.5	51.9
Steel 5	2	253	657.2	0.0106	447.9	113.5	74.6
Steel 6	2	1013	793.8	0.0134	447.9	453.9	360.3
Steel 7	8	4054	857.3	0.0147	447.9	1815.6	1556.4
					$M_n^f$ (kN-m)		<b>1925.4</b>
					$P_n^f$ (kN)		<b>2104.4</b>

**Table A4-7: Computation of Flexural Moment and Corresponding Axial Load Demand for Doubly Reinforced Beam: Specimen 4.**

Input Parameters						Calculated Variables	
<b>Section Properties</b>		<b>Reinforcement Details</b>		<b>Reinforcement Properties</b>		$\alpha$	0.85
Breadth (mm)	610	Reinf.	Diameter (mm)	$E_s$ (GPa)	200	$\beta$	0.85
$a$ (shear span, mm)	914	Long.	25.4	$f_y$ (MPa)	448	Assume NA depth for equilibrium $c$ (mm)	115.7
<b>Concrete Properties</b>		Distribution	12.7				
$f'_c$ (MPa)	27.6	Stirrups	12.7				
<b>Analysis</b>							
<i>Layer</i>	<i>No: of bars</i>	<i>Area (mm<sup>2</sup>)</i>	<i>Dist. to layers from bottom (mm)</i>	<i>Strain</i>	<i>Stress in Steel (MPa)</i>	<i>Force in Concrete/ Steel (kN)</i>	<i>Moment (kN-m)</i>
Concrete	-----	-----	49.2	-0.003	-----	-1405.3	-69.1
(Bottom) 1	8	4054	57.2	-0.0015	-303.5	-1230.4	-70.3
Steel 2	2	1013	120.7	0.0001	25.6	26.0	3.1
Steel 3	2	253	257.2	0.0037	447.9	113.5	29.2
Steel 4	2	253	457.2	0.0089	447.9	113.5	51.9
Steel 5	2	253	657.2	0.0140	447.9	113.5	74.6
Steel 6	2	1013	793.8	0.0176	447.9	453.9	360.3
Steel 7	8	4054	857.3	0.0192	447.9	1815.6	1556.4
					$M_n^f$ (kN-m)		<b>1935.9</b>
					$P_n^f$ (kN)		<b>2117.3</b>

**Table A4-8: Computation of Flexural Moment and Corresponding Axial Load Demand for Singly Reinforced Beam: Specimen 4.**

Input Parameters						Calculated Variables	
Section Properties		Reinforcement Details		Reinforcement Properties		$\alpha$	0.85
Breadth (mm)	610	Reinf.	Diameter (mm)	$E_s$ (GPa)	200	$\beta$	0.85
$a$ (shear span, mm)	914	Long.	25.4	$f_y$ (MPa)	448	Assume NA depth for equilibrium $m c$ (mm)	177.4
Concrete Properties		Distribution	12.7				
$f'_c$ (MPa)	27.6	Stirrups	12.7				
Analysis							
Layer	No: of bars	Area (mm <sup>2</sup> )	Dist. to layers from bottom (mm)	Strain	Stress in Steel (MPa)	Force in Concrete/ Steel (kN)	Moment (kN-m)
Concrete	-----	-----	75.4	-0.003	-----	-2155.1	-162.5
(Bottom) 1	2	1013	57.2	-0.002	-403.9	-409.3	-23.4
Steel 2	0	0	120.7	-0.001	-192.0	0.0	0.0
Steel 3	2	253	257.2	0.0013	269.7	68.3	17.6
Steel 4	2	253	457.2	0.0047	447.9	113.5	51.9
Steel 5	2	253	657.2	0.0081	447.9	113.5	74.6
Steel 6	2	1013	793.8	0.0104	447.9	453.9	360.3
Steel 7	8	4054	857.3	0.0115	447.9	1815.6	1556.4
					$M_n^f$ (kN-m)		1874.8
					$P_n^f$ (kN)		2050.6

**Table A4-9: Computation of Flexural Moment and Corresponding Axial Load Demand for Doubly Reinforced Beam: Specimen 3.**

Input Parameters						Calculated Variables	
<b>Section Properties</b>		<b>Reinforcement Details</b>		<b>Reinforcement Properties</b>		$\alpha$	0.85
Breadth (mm)	610	Reinf.	Diameter (mm)	$E_s$ (GPa)	200	$\beta$	0.7535
$a$ (shear span, mm)	914	Long.	25.4	$f_y$ (MPa)	448	Assume NA depth for equilibrium $c$ (mm)	102.6
<b>Concrete Properties</b>		Distribution	12.7				
$f'_c$ (MPa)	40.9	Stirrups	12.7				
Analysis							
<i>Layer</i>	<i>No: of bars</i>	<i>Area (mm<sup>2</sup>)</i>	<i>Dist. to layers from bottom (mm)</i>	<i>Strain</i>	<i>Stress in Steel (MPa)</i>	<i>Force in Concrete/ Steel (kN)</i>	<i>Moment (kN-m)</i>
Concrete (Bottom)	-----	-----	38.7	-0.003	-----	-1638.5	-63.4
1	8	4054	57.2	-0.0013	-265.9	-1077.7	-61.6
Steel 2	2	1013	120.7	0.0005	105.2	106.7	12.9
Steel 3	2	253	257.2	0.0045	447.9	113.5	29.2
Steel 4	2	253	457.2	0.0104	447.9	113.5	51.9
Steel 5	2	253	657.2	0.0162	447.9	113.5	74.6
Steel 6	2	1013	793.8	0.0202	447.9	453.9	360.3
Steel 7	8	4054	857.3	0.0221	447.9	1815.6	1556.4
					$M_n^f$ (kN-m)		<b>1959.4</b>
					$P_n^f$ (kN)		<b>2143.7</b>

**Table A4-10: Computation of Flexural Moment and Corresponding Axial Load Demand for Singly Reinforced Beam: Specimen 3.**

Input Parameters						Calculated Variables	
Section Properties		Reinforcement Details		Reinforcement Properties		$\alpha$	0.85
Breadth (mm)	610	Reinf.	Diameter (mm)	$E_s$ (GPa)	200	$\beta$	0.7535
$a$ (shear span, mm)	914	Long.	25.4	$f_y$ (MPa)	448	Assume NA depth for equilibrium $m c$ (mm)	140.8
Concrete Properties		Distribution	12.7				
$f'_c$ (MPa)	40.9	Stirrups	12.7				
Analysis							
Layer	No: of bars	Area (mm <sup>2</sup> )	Dist. to layers from bottom (mm)	Strain	Stress in Steel (MPa)	Force in Concrete/ Steel (kN)	Moment (kN-m)
Concrete (Bottom)	-----	-----	53.1	-0.003	-----	-2248.3	-119.3
1	2	1013	57.2	-0.0018	-356.3	-361.0	-20.6
Steel 2	0	0	120.7	-0.0004	-86.0	0.0	0.0
Steel 3	2	253	257.2	0.0025	445.1	112.8	29.0
Steel 4	2	253	457.2	0.0067	447.9	113.5	51.9
Steel 5	2	253	657.2	0.0110	447.9	113.5	74.6
Steel 6	2	1013	793.8	0.0139	447.9	453.9	360.3
Steel 7	8	4054	857.3	0.0153	447.9	1815.6	1556.4
					$M_n^f$ (kN-m)		1932.3
					$P_n^f$ (kN)		2113.3

**Step 4: Determine beam shear capacity,  $V_n^s$**

The shear capacity  $V_n^s$  is calculated using (A1-7). Since there are no prestressing tendons, the component of shear carried by tendons  $V_p = 0$ . The parameters  $\beta$  and  $\theta$  are calculated based on Method 1 specified in the AASHTO LRFD *Bridge Design Specifications* (2010) presented in Appendix A1.

**Table A4-11: Computation of Beam Shear Capacity.**

	Specimen 1		Specimen 2		Specimen 4		Specimen 3	
$f'_c$ (MPa) (at time of testing)	37.2		38.6		27.6		40.9	
$f_y$ (MPa)	448		448		448		448	
$b_v$ (mm)	610		610		610		610	
$A_v$ (mm <sup>2</sup> )	254		254		254		254	
$s$ (mm)	114		114		114		114	
$\beta$ (per AASHTO Method 1)	2		2		2		2	
$\theta$ (degrees) (per AASHTO Method 1)	45		45		45		45	
	<i>Doubly</i>	<i>Singly</i>	<i>Doubly</i>	<i>Singly</i>	<i>Doubly</i>	<i>Singly</i>	<i>Doubly</i>	<i>Singly</i>
$d_v = jd$ (mm)	774.7	787.4	774.7	787.4	774.7	787.4	774.7	787.4
$V_c$ (kN) = $0.0316 \beta \sqrt{f'_c} b_v d_v$	480.4	484.9	489.3	493.8	413.7	418.1	502.6	511.5
$V_s$ (kN) = $A_v f_y \frac{d_v}{s} \cot \theta$	769.5	782.9	769.5	782.9	769.5	782.9	769.5	782.9
$V_n^s$ (kN) = $V_c + V_s$	1250	1268	1259	1277	1183	1201	1272	1294

**Step 5: Check strength hierarchy**

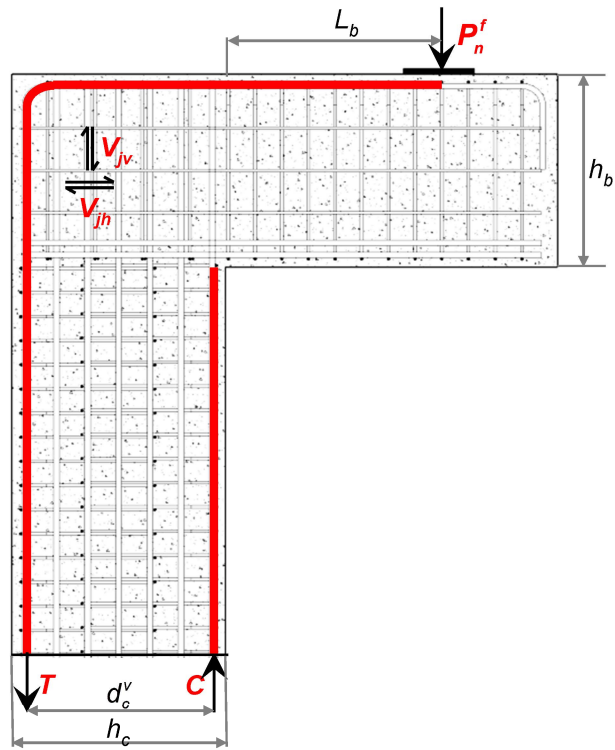
**Table A4-12: Checking Strength Hierarchy.**

	Specimen 1		Specimen 2		Specimen 4		Specimen 3	
	<i>Doubly</i>	<i>Singly</i>	<i>Doubly</i>	<i>Singly</i>	<i>Doubly</i>	<i>Singly</i>	<i>Doubly</i>	<i>Singly</i>
$\phi_v$	0.90 (AASHTO 5.5.4.2)							
$V_n^s$ (kN)	1249.9	1267.7	1258.8	1276.6	1183.2	1201.0	1272.2	1294.4
$\phi_f$	0.90 (AASHTO 5.5.4.2)							
$P_n^f$ (kN)	2140	2100	2140	2104	2117	2051	2144	2113
$\phi_v V_n^s$ (kN)	1125.4	1138.7	1134.3	1147.6	1063.1	1080.9	1143.2	1165.4
$\phi_f P_n^f$ (kN)	1926	1890	1926	1894	1905	1846	1930	1902

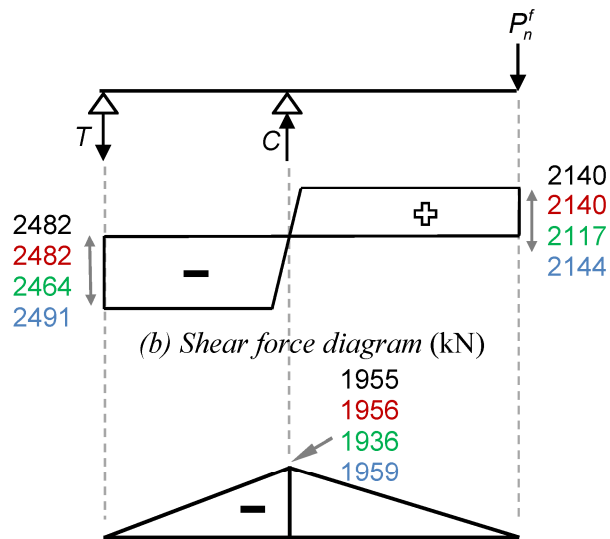
In all of the above cases  $\phi_v V_n^s < \phi_f P_n^f$ , that is the dependable shear capacity may be insufficient leading to a shear failure of the bridge pier.

**Step 6: Determine the shear capacity of the beam-column joint region**

It is important to investigate the shear in the beam-column joint, as this can be a critical section. Shear in the beam-column joint can be found from the shear force diagram of the equivalent beam model of the C-beam specimen shown in Figure A4-2. The horizontal shear  $V_{jh}$  can be computed from  $V_{jv}$  using (A1-16).



(b) Bridge pier physical model



(b) Shear force diagram (kN)

(c) Bending moment diagram of cap beam (kN-m)

Figure A4-2: Approach to determine shear in the beam-column joint for Specimen 1, Specimen 2, Specimen 4 and Specimen 3.



**Table A4-13: Computing the Vertical and Horizontal Shear in the Beam-Column Joint Caused by Flexural Axial Load Demand.**

	Specimen 1		Specimen 2		Specimen 4		Specimen 3	
	<i>Doubly</i>	<i>Singly</i>	<i>Doubly</i>	<i>Singly</i>	<i>Doubly</i>	<i>Singly</i>	<i>Doubly</i>	<i>Singly</i>
$P_n^f$ (kN)	2140	2100	2140	2104	2117	2051	2144	2113
$V_{jv}$ (kN)	2482	2438	2482	2447	2464	2380	2491	2455
$h_c = h_b$ (mm)	914		914		914		914	
$V_{jh} = \frac{h_c}{h_b} V_{jv}$ (kN)	2482	2438	2482	2447	2464	2380	2491	2455

The joint shear capacity of the joint is calculated based on (A1-17) considering the contribution of the hoops/ties within the joint  $V_{truss}$  and the corner-to-corner joint arch  $V_{arch}$  as described in Appendix A1. The computation for assessing the joint shear capacity is presented in Table A4-14.

**Table A4-14: Assessing the Joint Shear Capacity.**

	Specimen 1		Specimen 2		Specimen 4		Specimen 3	
$\Sigma A_{sv}$ (mm <sup>2</sup> ) (total area of hoops/ties in the joint region)	1014		1014		1014		1014	
$f_y$ (MPa)	448		448		448		448	
$f'_c$ (MPa)	37.2		38.6		27.6		40.9	
$b_v$ (mm)	610		610		610		610	
	<i>Doubly</i>	<i>Singly</i>	<i>Doubly</i>	<i>Singly</i>	<i>Doubly</i>	<i>Singly</i>	<i>Doubly</i>	<i>Singly</i>
$jd$ (mm)	774.7	787.4	774.7	787.4	774.7	787.4	774.7	787.4
$V_{truss}$ (kN)	454	454	454	454	454	454	454	454
$V_{arch}$ (kN)	1913	1944	1948	1979	1646	1673	2006	2037
$V_n^j$ (kN) = $V_{arch} + V_{truss}$	2366	2398	2402	2433	2100	2126	2460	2491
$\phi_v$	0.90							
$\phi_v V_n^j$ (kN)	2131	2157	2162	2189	1890	1913	2215	2242
$\phi_f$	0.90							
$\phi_f V_{jv}$ (kN)	2233	2193	2233	2202	2215	2140	2242	2211

In all of the above cases  $\phi_v V_n^j < \phi_f V_{jv}$ , that is the joint capacity is less than the demand, and hence there could be a shear joint failure.

From Stage 1 analysis it can be concluded that the factored shear capacity for both the beam and the joint are insufficient. Given that beam-column joints are strictly D-regions where beam theory is insufficient to explain the performance, this warrants further investigation and a SAT analysis is performed. Additionally, it is also required by the code to perform a SAT as the  $a/d$  ratio for the specimen is 1.08.

### A4.3 Stage 2: Strut-And-Tie Analysis

#### *Step 1: Determine the node geometry*

The crack angle in the beam-column joint is assumed to be  $45^\circ$ . The computation of the node dimensions and geometry for each of the C-beam specimen follows.

*CCT node:*

- The width of the CCT node is taken equal to the width of the bearing pad = 305 mm.
- The depth of the back face of the CCT node =  $2 \times$  distance from the extreme tension face to the centroid of the tension reinforcement =  $2 \times 69.85 = 139.7$  mm.

*CTT Node:*

- Width of the CTT node =  $\sqrt{2 \times (R + d_b / 2)^2}$  where  $R$  = bar bending radius = 101.6 mm and  $d_b$  = diameter of the column longitudinal rebar = 25.4 mm.

*CCC Node:*

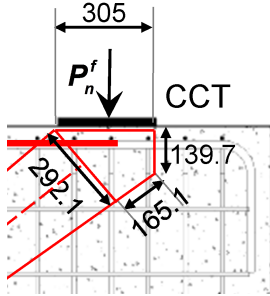
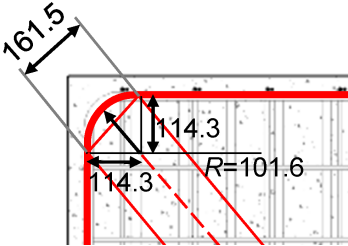
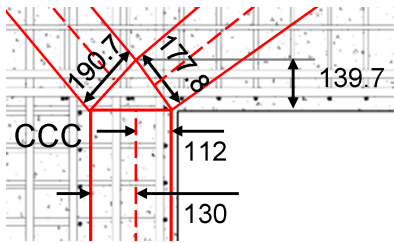
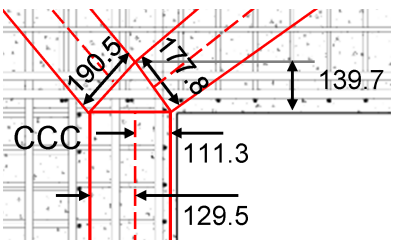
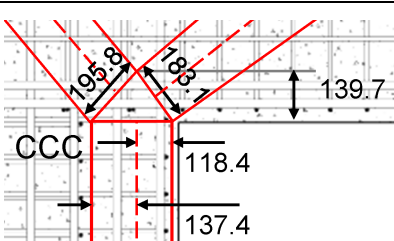
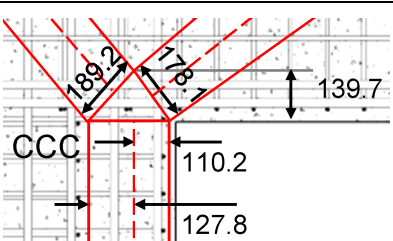
- The width of the bottom face of the CCC node is equal to the depth of compression zone of the column  $kd$  which is determined based on the equation for the elastic compression zone coefficient  $k$  as given in (A1-2).
- The bottom face is proportioned based on the ratio of  $a/b = V_{jv} / P_n^f$  (Figure in Table A4-15) obtained from Stage 1 of the analysis.
- Since the horizontal force in the CCC node is equal to the horizontal force in the CCT node, the height of the CCC node is assumed to be equal to the depth of the back face of the CCT node =  $2 \times 69.85 = 139.7$  mm.
- Knowing the above, the other sides of the CCC node can be determined as presented in Table A4-16.

After the node geometries are determined, all the SAT model dimensions and inclination angle can be obtained.

**Table A4-15: Computations for Sizing the CCC Node.**

<i>(a) Column cross section</i>		<i>(b) CCC node configuration</i>			
$A_s$ (mm <sup>2</sup> )	5067				
$A'_s$ (mm <sup>2</sup> )	2534				
$b$ (mm)	610				
$d$ (mm)	844				
$d'$ (mm)	57				
$\rho_L = \frac{A_s}{bd}$	0.00984				
$\rho'_L = \frac{A'_s}{bd}$	0.00492				
	<b>Specimen 1</b>	<b>Specimen 2</b>	<b>Specimen 4</b>	<b>Specimen 3</b>	
$n = E_s / E_c$	6.92	6.80	8.04	6.61	
	$k = \sqrt{(\rho_L + \rho'_L)^2 n^2 + 2(\rho_L + \rho'_L d'/d)n} - (\rho_L + \rho'_L)n$				
$k$	0.287	0.285	0.303	0.282	
$kd$ (mm)	241.3	241.3	256.5	238.3	
$V_{jv}$ (kN)	2482.1	2482.1	2464.3	2491.0	
$P_n^f$ (kN)	2140	2140	2117	2144	
$V_{jv} / P_n^f$	1.16	1.16	1.16	1.16	
$a$ (mm)	130.0	129.5	137.4	127.8	
$b$ (mm)	112.0	111.3	118.4	110.2	

**Table A4-16: Geometry and Dimensions of Nodes.**

<p style="writing-mode: vertical-rl; transform: rotate(180deg);"><b>CCT Node</b></p>		
<p style="writing-mode: vertical-rl; transform: rotate(180deg);"><b>CTT Node</b></p>		
<p style="writing-mode: vertical-rl; transform: rotate(180deg);"><b>CCC Node</b></p>	<p style="text-align: center;"><b>Specimen 1</b></p>	<p style="text-align: center;"><b>Specimen 2</b></p>
		
	<p style="text-align: center;"><b>Specimen 4</b></p>	<p style="text-align: center;"><b>Specimen 3</b></p>
		

**Step 2: Solve the determinate truss and determine strut and tie forces**

Assuming that the tension tie has yielded, that is  $T = A_s f_y$ , all the member forces can be determined based on joint equilibrium. Based on steel yield, the externally applied load required to cause yielding is determined and is presented in Table A4-17.

However, this is most unlikely to be the critical load, and the critical node needs to be identified.

**Table A4-17: Forces in the Struts and Ties of the SAT Model.**

	<b>Node forces based on steel yield</b>		
<b>CCT Node</b>	$A_s$ (mm <sup>2</sup> )	5067	
	$f_y$ (MPa)	448	
	$\theta_b$ (degrees)	40	
	$\theta_j$ (degrees)	45	
	$T = A_s f_y$ (kN)	2273.0	
	$D_b = T / \cos(\theta_b)$ (kN)	2966.9	
	$P^{SAT} = D_b \sin(\theta_b)$ (kN) = $P_y^{SAT}$	1908.3	
<b>CCC Node</b>	$C' = D_b \cos(\theta_b)$ (kN)	2273.0	
	$D_j = C' / \cos(\theta_j)$ (kN)	3216.0	
	$P_v^j = D_j \sin(\theta_j)$ (kN)	2273.0	

**Step 3 and 4: Determine minimum applied load causing node failure and determine shear demand**

Allowable stresses in the nodes based on AASHTO (2010) are presented in Table A4-18. From the allowable node stresses, the CTT node is found to be the critical node, and from (A1-20) the allowable stress at the node face is  $f_{cu} = 0.65 f'_c$ . The axial load required to cause the failure of the CTT node can be back calculated based on the allowable nodal stress and the area of the node. The results are presented in Table A4-18.

**Table A4-18: Allowable Node Stresses and Axial Load Required to Cause CTT Node Failure.**

Specimen	1	2	4	3
$f'_c$ (MPa)	37.2	38.6	27.6	40.9
<b>Allowable Stresses</b>				
CCC Node $f_{cu} = 0.85 f'_c$ (MPa)	31.7	32.8	23.4	34.8
CCT Node $f_{cu} = 0.75 f'_c$ (MPa)	27.9	29.0	20.7	30.7
CTT Node $f_{cu} = 0.65 f'_c$ (MPa)	24.2	25.1	17.9	26.5
Node capacity $D_{j(\text{node})}$ (kN) = $F_{cu}$	2384.2	2473.2	1765.9	2615.5
Axial load that causes nodal failure, $P_n^{\text{SAT}}$ (kN) = $P_y^{\text{SAT}} D_{j(\text{node})} / D_j$	1414.5	1467.9	1049.8	1552.4

**A4.4 Summary and Discussion**

A summary of results from Stage 1 and 2 analysis of all four C-beam specimens are presented in Table A4-19. For all four specimens it is evident that  $P_n^{\text{SAT}}$  computed from the SAT analysis is less than  $P_n^f$  calculated from the beam flexure theory. Also,  $\phi_y P_n^{\text{SAT}} < \phi_f P_n^f$  for all the specimens. Therefore, the joint capacity is technically undependable for all four specimens.

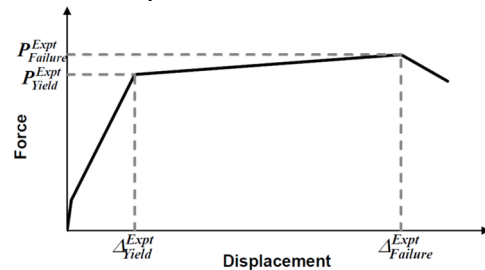
**Table A4-19: Material Properties, Stage 1 and 2 Analyses, and Experimental Results.**

		Specimen 1		Specimen 2		Specimen 4		Specimen 3	
Material Properties	$f'_c$ (MPa)	37.2		38.6		27.6		40.9	
	$f'_t$ (MPa)	2.07		1.60		--		--	
	$E_c$ (MPa)	28890		29407		24856		30269	
	Age at testing (months)	13		16		29		64	
Stage 1 Analyses (Sectional)	Beam reinforcement	Double	Single	Double	Single	Double	Single	Double	Single
	$M_y^b$ (kN-m)	1749	1730	1749	1731	1742	1721	1750	1734
	$P_y^b$ (kN)	<b>1913</b>	<b>1890</b>	<b>1913</b>	<b>1895</b>	<b>1904</b>	<b>1882</b>	<b>1913</b>	<b>1895</b>
	$M_n^f$ (kN-m)	1955	1920	1956	1925	1936	1875	1959	1932
	$P_n^f$ (kN)	<b>2140</b>	<b>2100</b>	<b>2140</b>	<b>2104</b>	<b>2117</b>	<b>2051</b>	<b>2144</b>	<b>2113</b>
	$\phi_f P_n^f$ (kN)	1926	1890	1926	1894	1905	1846	1930	1902
	$V_n^s$ (kN)	<b>1250</b>	<b>1268</b>	<b>1259</b>	<b>1277</b>	<b>1183</b>	<b>1201</b>	<b>1272</b>	<b>1294</b>
$V_n^j$ (kN)	<b>2366</b>	<b>2398</b>	<b>2402</b>	<b>2433</b>	<b>2100</b>	<b>2126</b>	<b>2460</b>	<b>2491</b>	
Stage 2 Analyses (SAT)	$P_y^{SAT}$ (kN)	<b>1908</b>		<b>1908</b>		<b>1908</b>		<b>1908</b>	
	$\phi_y P_y^{SAT}$ (kN)	1336		1336		1336		1336	
	$P_n^{SAT}$ (kN)	<b>1415*</b>		<b>1468*</b>		<b>1050*</b>		<b>1552*</b>	
	$\phi_y P_n^{SAT}$ (kN)	991		1028		735		1086	
Experimental Results	$P_{Yield}^{Expt}$ (kN)	1957		1957		1957		--	
	$P_{Failure}^{Expt}$ (kN)	<b>2108</b>		<b>2224</b>		<b>2237</b>		<b>2215</b>	
	$\Delta_{Yield}^{Expt}$ (mm)	37.8		23.4		27.9		--	
	$\Delta_{Failure}^{Expt}$ (mm)	42.9		49.3		55.1		19.6	
	$\mu$	1.13		2.11		1.97		--	
	$P_n^{SAT} / P_{Failure}^{Expt}$	0.67		0.66		0.47		0.70	

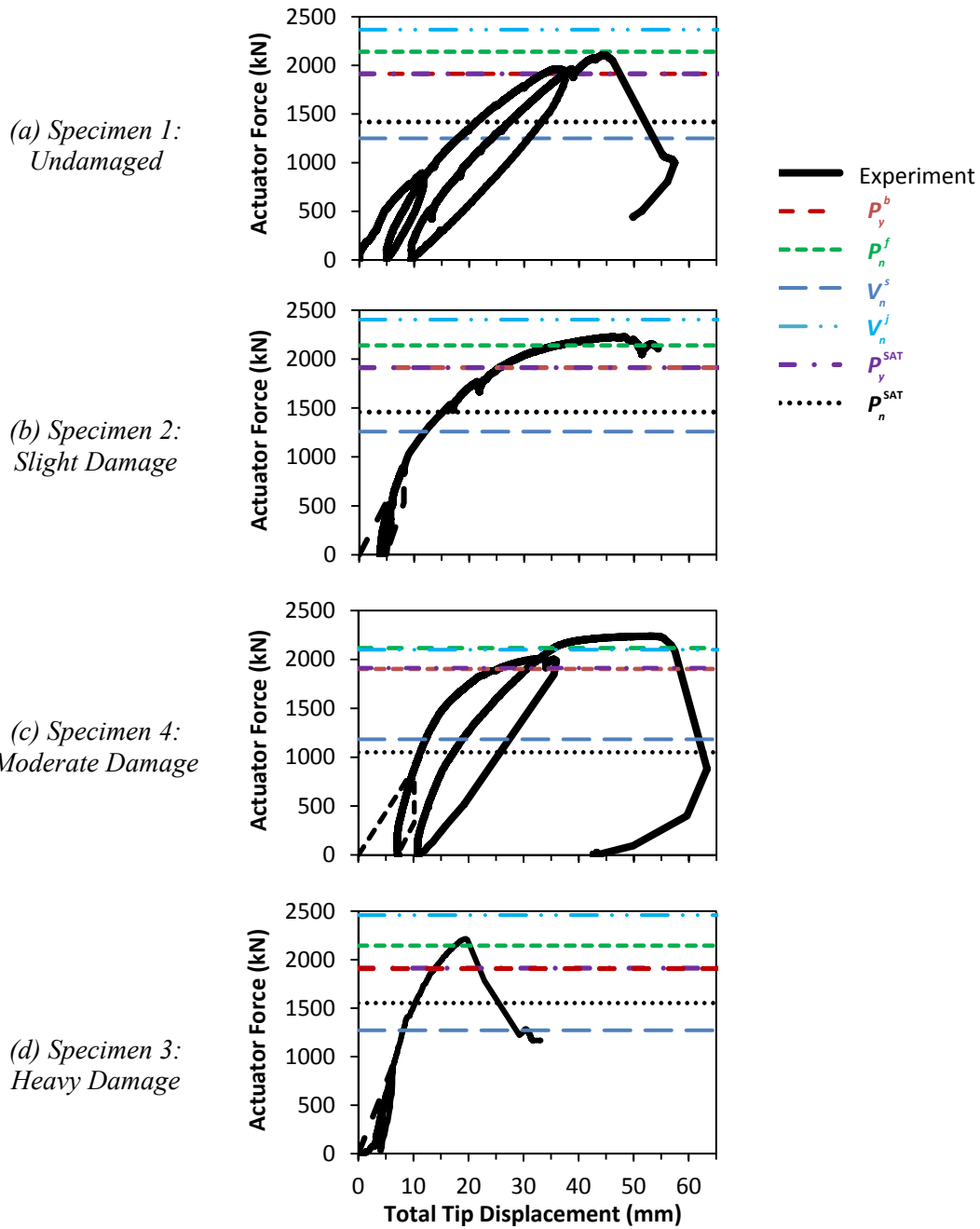
\*Expected critical failure mode capacity.

Superscript: *b*=beam; *f*=flexure; *s*=shear; *j*=joint; SAT=strut-and-tie; Expt=Experiment.

Notation for experimental results:







$P_y^b$  = External load causing flexural yield;  $P_n^f$  = External load causing beam flexure;  
 $V_n^s = V_s + V_c$  = Nominal beam shear;  $V_n^j = V_{truss} + V_{arch}$  = Joint shear;  $P_y^{SAT}$  = External load based on longitudinal steel yield from SAT;  $P_n^{SAT}$  = External load based on node capacity from SAT

Note: Experimental results of Specimens 1, 2, and 4 are from Mander et al. (2012).

**Figure A4-3: Experimental, Code Based Predictions and C-STM Results.**

However from the experimental results, it was observed that the load at failure for the four specimens was  $P_{\text{Failure}}^{\text{Expt}} = 2108 \text{ kN}$ ,  $2224 \text{ kN}$ ,  $2237 \text{ kN}$ , and  $2215 \text{ kN}$ , respectively. It is apparent from Stage 1 and Stage 2 of the analysis that they do not give a good prediction of the load carrying capacity of the specimens. Both methods (beam flexure and SAT) completely miss the actual failure mode (joint shear failure). The analysis results do not give any indication of the overall behavior of the structure.

From the above analyses, the externally applied load causing yielding based on beam flexure  $P_y^b$  and the SAT  $P_y^{\text{SAT}}$  methods agree well with the experimental observations. However, the sectional shear approach  $V_n^s$  had the largest discrepancy and did not accurately represent the specimen capacity. These predictions are unduly harsh because the shear capacity is calculated in a D-region where the sectional theory breaks down. It is for this reason a SAT analysis needs to be conducted. This analysis would imply that the beam-column joint would fail even before the beam yielded, thus suggesting that the structure fails in a very brittle manner. However, this is not the case as can be seen from the experimental results (Figure A4-3) and hence the SAT analysis predicts a somewhat faulty picture about the expected structural behavior. Moreover, it is not clear how the observed effects of ASR/DEF damage can be included in these simple methods.

It can be concluded from the analysis results that it is somewhat inconclusive as to what will be the failure mode of the specimen, as it is observed that the joint capacity is (theoretically) undependable. Additionally, the SAT analysis does not take into account the effects of ASR/DEF damage. To better understand the behavior of the structure and its final mode of failure, the C-STM analysis may be applied to evaluate the performance of the structure.

## **A5 COMPUTATIONS FOR STAGE 3 C-STM ANALYSIS FOR C-BEAM SPECIMENS**

In this appendix, the computation of concrete material properties to be used in the C-STM for C-beam specimen 1, 2 and 4 are presented first, followed by Specimen 3. Computation of prestrains to be applied to the C-STM model for Specimen 3 to simulate the effects of ASR/DEF into the analysis are also presented. This appendix supports material in Section 8.

### A5.1 Introduction

The computation of member and material properties of the C-STM model are presented below for Specimen 1 (control specimen) followed by Specimen 2 and 4 (with ASR/DEF damage). The computation of material properties for Specimen 3 is presented separate towards the end of this appendix. The computation of prestrains to be applied on C-beam Specimen 3 are also presented herein.

### A5.2 Computation for C-beam Specimen 1

A few section properties have to be determined beforehand to set up the C-STM geometry. These computations follow.

#### *Step 1: Calculate section properties*

The computation of the section properties including the steel area contribution to the compression and tension steel chords are presented in Table A5-1.

Determine the depth of compression zone  $kd$  of the singly and doubly reinforced beams and column using the equation:

$$k = \sqrt{\left(\rho_L + \rho'_L + \left(\frac{P}{f_c'bd}\right)\left(\frac{f_c'}{f_s}\right)\right)^2 n^2 + 2\left(\rho_L + \rho'_L\left(\frac{d'}{d}\right) + \left(\frac{P}{f_c'bd}\right)\left(\frac{f_c'}{f_s}\right)\right)n - \left(\rho_L + \rho'_L + \left(\frac{P}{f_c'bd}\right)\left(\frac{f_c'}{f_s}\right)\right)n}$$

For the beams the axial load  $P$  is zero. A summary of the computations is presented in Table A5-2.

**Table A5-1: Computation of Section Properties for C-STM.**

	Doubly Reinforced	Column	Singly Reinforced
<b>CROSS-SECTION</b>			
Compression Chord	8-#8 Bars	5-#8 Bars	2-#8 Bars
$h$ (mm)	914	914	914
$d'$ (mm)	57	57	57
$d$ (mm)	844	844	844
$A_s'$ (mm <sup>2</sup> )	4052	2535	1013
Steel contributing to tension chord	10 #8 Bars 2 sets of 2 #4	10 #8 Bars 2 sets of 2 #4	10 #8 Bars 2 sets of 2 #8
$A_{s(total)}$ (mm <sup>2</sup> )	5574	7097	5574
$\bar{y}$ (mm) (centroid of $A_{s(total)}$ )	96.0	123.4	96.0
$A_s$ (mm <sup>2</sup> ) $= A_{s(total)} \frac{h - d' - \bar{y}}{d - d'}$	5387	6613	5387
$jd = d - d'$ (mm)	787.4	787.4	787.4

**Table A5-2: Determining the Depth of the Compression Zone for Specimen 1.**

$f'_c =$ 37.2 MPa	Compression Steel		Tension Steel			Axial Load $P$ (kN)	Elastic Depth	
	$A_s'$ (mm <sup>2</sup> )	$(d'=57 \text{ mm})$ $\rho'$	$A_s$ (mm <sup>2</sup> )	$d$ (mm)	$(b=610 \text{ mm})$ $\rho$		$k$	$kd$ (mm)
Single Beam	1013	0.00197	5387	844	0.01046	-	0.307	258.8
Double Beam	4052	0.00787	5387	844	0.01046	-	0.283	239.3
Column	2529	0.00492	6613	844	0.01284	1912.7	0.394	332.7

***Step 2: Determine C-STM geometry based on Step 1***

The tension ties (AK and K1K2 in Figure A5-1) and compression chords (BH and L1L2 in Figure A5-1) in the beams and the column are placed along the centroids of the tension and compression steel determined in Table A5-1. The C-STM geometry is the same in both the singly and double reinforced beams. The overhang portion of the specimen is modeled using the single-point Gauss truss model as presented in Scott et al (2012a). The position of tie CB is determined based on the coefficients for the single point Gauss model. In the beam-column joint region, the ties GF and IH are placed along the position of the U-bars to better represent the specimen. All the dimensions of the C-STM are shown in Figure A5-1.

***Step 3: Determine axial rigidities***

The next step in the C-STM analysis is to determine the axial rigidities of each of the members constituting the C-STM model.

To model the combined response of steel and concrete in the compression chord members, the compatibility correction factor is calculated in Table A5-3. Based on these correction scalars, the modified stress-strain relation of the compression chord is determined.

The arch breadth scalar is calculated to determine the area that needs to be assigned to the inclined arch and the struts in the beam and the beam-column joints. The computations are presented in Table A5-4.

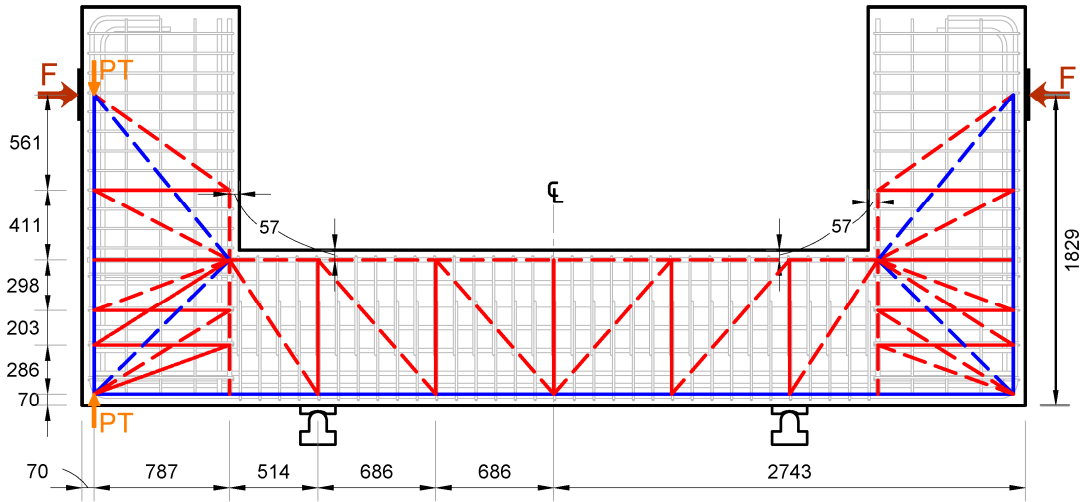
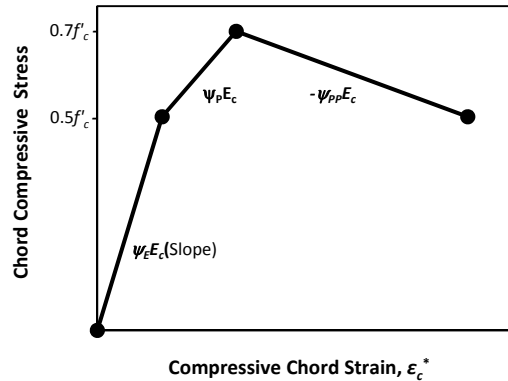


Figure A5-1: C-STM Model for C-beam Specimen 1.

Table A5-3: Computation of Compatibility Correction Scalar for Specimen 1.

	Singly Reinforced	Double Reinforced	Column
$d'$ (mm)	57	57	57
$kd$ (mm)	258.8	239.3	332.7
$f'_c$ (MPa)	37.2	37.2	37.2
$\psi_E = \frac{\sqrt{f'_c(\text{MPa})}}{14(1-d'/kd)}$	0.560	0.572	0.526
$\psi_P = \frac{\sqrt{f'_c(\text{MPa})}}{40(1-d'/kd)}$	0.196	0.200	0.184
$\psi_{PP} = -\frac{\sqrt{f'_c(\text{MPa})}}{125(1-d'/kd)}$	-0.063	-0.064	-0.059



**Table A5-4: Computing Arch Breadth Scalar.**

$\eta = \frac{V_{\text{arch}}}{V_{\text{arch}} + V_{\text{truss}}} = \frac{\rho_L f_y}{\rho_L f_y + \rho_T f_{yh} j \cot^2 \alpha}$			
	<b>Singly Reinforced</b>	<b>Double Reinforced</b>	<b>Column</b>
$d$ (mm)	844	844	844
$b$ (mm)	610	610	610
$s$ (mm)	114	114	203
$jd$ (mm)	787.4	787.4	787.4
$j$	0.93	0.93	0.93
$f_y = f_{yh}$ (MPa)	448	448	448
$A_y$ (mm <sup>2</sup> )	5387	5387	6613
$A_{sh}$ (mm <sup>2</sup> )	254	254	254
$\rho_T = A_{sh}/b_w s$	0.00364	0.00364	0.00205
$\rho_L = A_s/bd$	0.0105	0.0105	0.0128
$\alpha$ (degrees)	39.02	39.02	45
$\eta$	0.671	0.671	0.87 (0.75 used)

Based on the arch breadth scalars computed above and the theory presented in Scott et al (2012a), the axial rigidities are computed. The equations used to obtain the axial rigidities are also presented in Scott et al. (2012a). The axial rigidities for C-beam Specimen 1 are presented in Table A5-5.

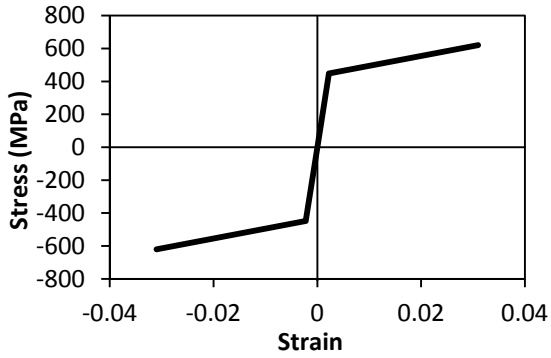
***Step 4: Determine constituent material properties***

The stress-strain models used for the members in Phase 1 of Specimen 1 are presented in Figure A5-2. The only difference for Phase 2 of the specimen is that the concrete tensile strength was reduced to 1.4 MPa to account for the minor concrete cracking that had occurred in Phase 1 of the experiment.

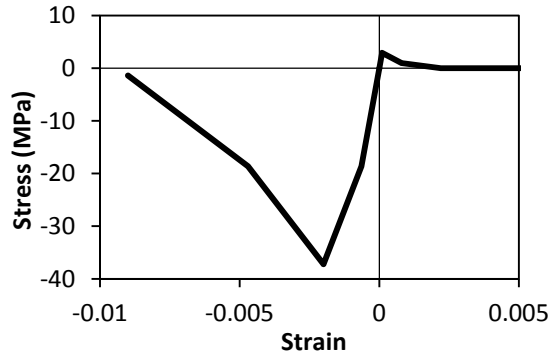


**Table A5-5: Axial Rigidities of C-STM Elements: Specimen 1.**

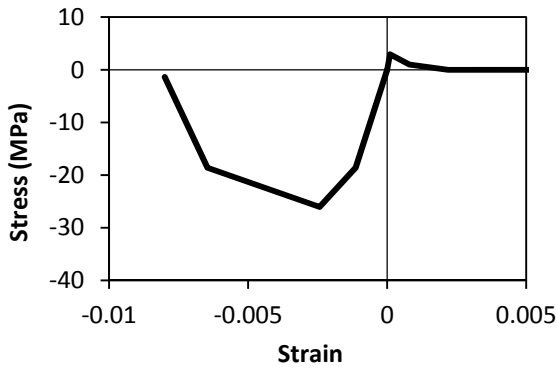
	MEMBER	Steel		Concrete		Comments
		$E$ (GPa)	$A$ (mm <sup>2</sup> )	$E$ (MPa)	$A$ (mm <sup>2</sup> )	
Beam	A-E (D)	200	5387	28890	157838	Tension Chord
	A-E (S)	200	5387	28890	157838	
	B-D (D)	200	4052	16596	47058	Compression Chord
	B-D (S)	200	1013	16210	50903	
	BC	200	1523	28890	104516	Transverse Steel
	AD	-	-	28890	156974	Concrete Arch
	AB	-	-	28890	74477	Concrete Truss
	CD	-	-	28890	69677	
Beam-Column Joint	E-K (D)	200	5387	28890	157838	Tension Chord
	E-K (S)	200	5387	28890	157838	
	D-H (D)	200	4052	16596	47058	Compression Chord
	D-H (S)	200	1013	16210	50903	
	FG&HI	200	252	28890	34839	Transverse Steel
	DK	-	-	28890	190916	Concrete Arch
	DG	-	-	28890	50619	Concrete Truss
	DI	-	-	28890	46277	
	FK	-	-	28890	52226	
	HK	-	-	28890	47581	
Column	JJ	200	6613	28890	203503	Tension Chord
	LL	200	2535	15245	203503	Compression Chord
Beam: $N_h = 6$ and beam-column joint: $N_h = 2$						
<i>(D) Doubly reinforced beam (S) Singly reinforced beam</i>						



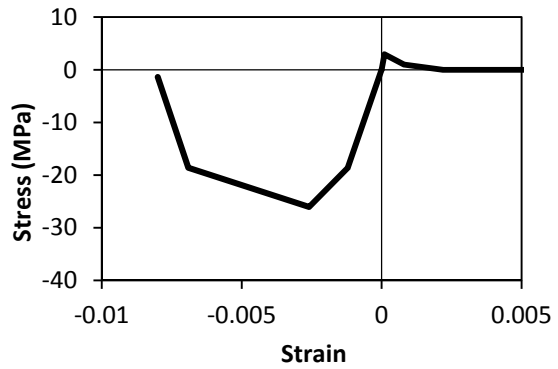
(a) All steel members.



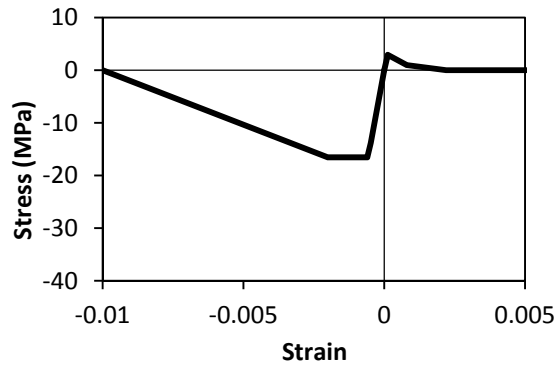
(b) All concrete members, except the beam and column compression chord members. AB, CD, GD, ID, FK, HK, AD, CB, GF, IH, J1J2, and AK.



(c) Beam compression chord BH



(d) Column compression chord. L1L2



(e) Softened concrete model for the beam-column joint concrete arch. DK (In Phase 2)

**Figure A5-2: Stress-Strain Models Used for C-STM Members: Phase 1 of Specimen 1.**

### **A5.3 Computation for C-beam Specimens 2 and 4**

C-beam Specimen 2 and 4 were subjected to *slight* and *moderate* amounts of ASR/DEF damage. While the procedure for calculating the member and material properties remains the same as in the case of Specimen 1, certain modifications are required to account for the effects of ASR/DEF in the specimens. The modifications are based on the recommendations made in Section 8.

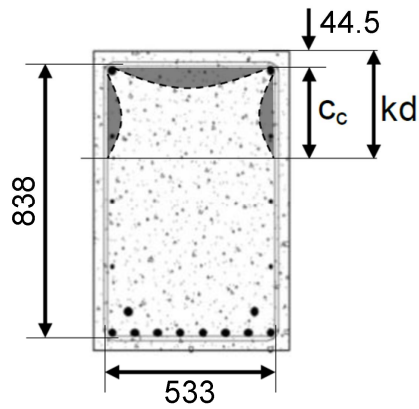
#### ***Step 1: Compute modified material properties to account for ASR/DEF***

To account for the effects of ASR/DEF on the C-beam specimens, modified material properties are calculated based on the theory presented in Section 8.

#### **Compute confinement ratio for the beam and the column:**

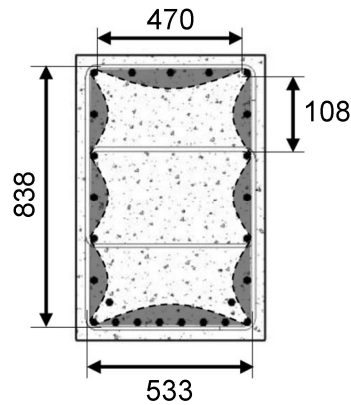
To account for the confinement caused by the swelling of core concrete, the confinement ratios are computed for the beam and the column. Table A5-6 and Table A5-7 respectively show the computation of the confinement ratios for the beam and the column for Specimens 2 and 4.

**Table A5-6: Calculating Confinement Ratio of the Beam for C-beam Specimens 2 and 4.**



	<b>Specimen 2</b>	<b>Specimen 4</b>
$f'_c$ (MPa)	38.6	27.6
$kd$ (mm)	260.4	284.5
$A_{cc}$ (mm <sup>2</sup> ) = $(c_c + d_s / 2) \times b_c$	118548	129484
$A_e$ (mm <sup>2</sup> ) = $(c_c + d_s / 2) \times b_c$ - area of shaded region	69651	79264
$k_e = A_e / A_{cc}$	0.5875	0.603
$f_{lx}$ (MPa)	1.31	1.21
$f_{ly}$ (MPa)	1.09	1.12
Smallest confining stress ratio $f_{ly} / f'_c$	0.028	0.041
Largest confining stress ratio $f_{lx} / f'_c$	0.034	0.44
$K = f'_{cc} / f'_c$	1.20	1.28
Confined concrete strength $Kf'_c$ (MPa)	46.3	35.3

**Table A5-7: Calculating Confinement Ratio of the Column for C-beam Specimens 2 and 4.**



	<b>Specimen 2</b>	<b>Specimen 4</b>
$f'_c$ (MPa)	38.6	27.6
$kd$ (mm)	260.4	284.5
$A_{cc}$ (mm <sup>2</sup> ) = $b_c d_c$	447096	
$A_e$ (mm <sup>2</sup> ) = $b_c d_c$ - area of shaded region	361838	
$k_e = A_e / A_{cc}$	0.81	
$f_{lx}$ (MPa)	1.92	
$f_{ly}$ (MPa)	1.51	
Smallest confining stress ratio $f_{ly} / f'_c$	0.039	0.055
Largest confining stress ratio $f_{lx} / f'_c$	0.049	0.069
$K = f'_{cc} / f'_c$	1.28	1.35
Confined concrete strength $Kf'_c$ (MPa)	49.4	37.2

Compute deteriorated cover concrete properties:

Based on the state of Specimen 2 and 4 at the end of the deterioration period, and the recommendations made in Section 8, the modified cover concrete strength were computed as presented in Table A5-8.

**Table A5-8: Modified Concrete Strength for Concrete Truss Members of the C-STM.**

	<b>Specimen 2</b>	<b>Specimen 4</b>
ASR/DEF damage level	Slight	Moderate
$f'_c$ (MPa)	38.6	27.6
$\lambda$	0.75	0.40
$f'_{cASR/DEF}$ (MPa) = $\lambda f'_c$	29	11.0

Compute effective concrete strength:

As both the cover and core concrete areas contribute to the area of the strut in the C-STM model, a weighted average value of concrete compressive strength is used in the C-STM model. A sample computation of effective concrete strength (for Specimen 3) is presented in Section A5.4. Adopting a similar procedure, the effective concrete strength  $f'_{eff}$  that was adopted for Specimens 2 and 4 respectively are shown in Table A5-9.

**Table A5-9: Effective Concrete Strength for C-STM Beam and Column Members for Specimens 2 and 4.**

	<b>Specimen 2</b>	<b>Specimen 4</b>
Beam elements $f'_{eff}$ (MPa)	35.5	27.3
Column elements $f'_{eff}$ (MPa)	27.9	29.5

Compute prestress in the beam and column ties:

The ASR/DEF model that was developed in Section 4 and applied to the C-beam specimens in Section 6, are used to compute the prestress in the various constituent members of the C-STM. A sample calculation for the computation of prestrains (in Specimen 3) is presented in Section A5.4 and a similar approach was used to obtain the prestress in Specimens 2 and 4. Knowing the prestress in the ties and the area of the tie, the prestress force to be applied in the C-STM model is computed.

***Step 2: Compute section properties***

The steel areas computed in Table A5-1 for Specimen 1 hold good for Specimen 2 and 4 as well. However, the depth of compression zone  $kd$  has to be recalculated to account for the prestress forces that are applied on the ties. The actual concrete strength is used in these computations.

**Table A5-10: Determining the Depth of the Compression Zone for Specimen 2 and 4 With ASR/DEF Damage.**

$d' = 57$ mm $d = 844$ mm $b = 610$ mm	Compression Steel		Tension Steel		Axial Load	Elastic Depth	
	$A_s'$ (mm <sup>2</sup> )	$\rho'$	$A_s$ (mm <sup>2</sup> )	$\rho$	$P$ (kN)	$k$	$kd$ (mm)
$f'_c = 38.6$ MPa		<b>Specimen 2</b>					
Single Beam	1013	0.00197	5387	0.01047	222.9	0.316	266.7
Double Beam	4052	0.00787	5387	0.01047	891.4	0.323	273.1
Column	2529	0.00492	6613	0.01284	2333.1	0.404	341.4
$f'_c = 27.6$ MPa		<b>Specimen 4</b>					
Single Beam	1013	0.00197	5387	0.01046	458.6	0.348	294.1
Double Beam	4052	0.00787	5387	0.01046	1835.3	0.379	320.3
Column	2529	0.00492	6613	0.01284	3045.7	0.448	378.5

***Step 3: Determine C-STM geometry***

The geometry of the C-STM remains the same as Specimen 1. However, axial loads are applied at the nodes to account for the ASR/DEF effects. The C-STM model for Specimen 2 and 4 is shown in Figure A5-3.

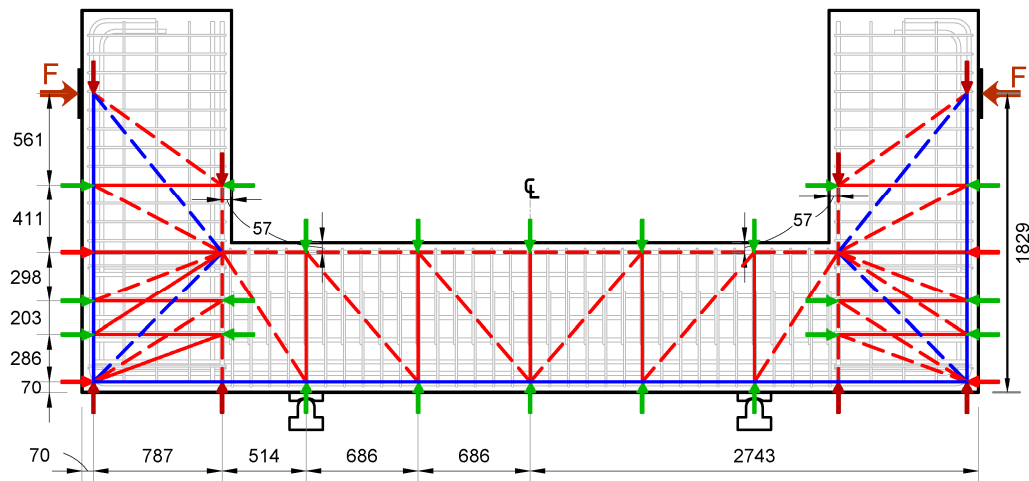


**Figure A5-3: C-STM Model for C-beam Specimen 2 and 4.**

***Step 4: Determine axial rigidities***

The computation for the compatibility correction factor for Specimens 2 and 4 are presented in Table A5-11 and Table A5-12. The arch-breadth scalar remains the same as in Table A5-4. The axial rigidities for Specimens 2 and 4 are recomputed based on the modified properties and presented in Table A5-13 and Table A5-14 respectively.

***Step 5: Determine constituent material properties***

The modified constituent material properties for Specimens 2 and 4 are presented in Figure A5-4 and Figure A5-5 respectively.



**Table A5-11: Computation of Compatibility Correction Scalar for Specimen 2.**

	<b>Singly Reinforced</b>	<b>Double Reinforced</b>	<b>Column</b>
$d'$ (mm)	57	57	57
$kd$ (mm)	263.1	260.4	352.8
$f'_c$ (MPa)	38.6	38.6	38.6
$\psi_E = \frac{\sqrt{f'_c \text{ (MPa)}}}{14(1-d'/kd)}$	0.567	0.568	0.530
$\psi_P = \frac{\sqrt{f'_c \text{ (MPa)}}}{40(1-d'/kd)}$	0.198	0.200	0.185
$\psi_{PP} = -\frac{\sqrt{f'_c \text{ (MPa)}}}{125(1-d'/kd)}$	-0.063	-0.064	-0.060

**Table A5-12: Computation of Compatibility Correction Scalar for Specimen 4.**

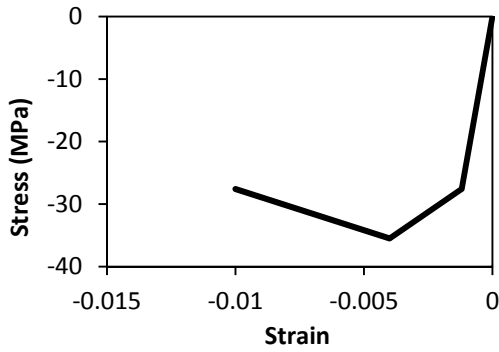
	<b>Singly Reinforced</b>	<b>Double Reinforced</b>	<b>Column</b>
$d'$ (mm)	57	57	57
$kd$ (mm)	284.7	289.6	386.6
$f'_c$ (MPa)	27.6	27.6	27.6
$\psi_E = \frac{\sqrt{f'_c \text{ (MPa)}}}{14(1-d'/kd)}$	0.470	0.467	0.440
$\psi_P = \frac{\sqrt{f'_c \text{ (MPa)}}}{40(1-d'/kd)}$	0.164	0.164	0.154
$\psi_{PP} = -\frac{\sqrt{f'_c \text{ (MPa)}}}{125(1-d'/kd)}$	-0.053	-0.052	-0.049

**Table A5-13: Axial Rigidities of C-STM Elements: Specimen 2.**

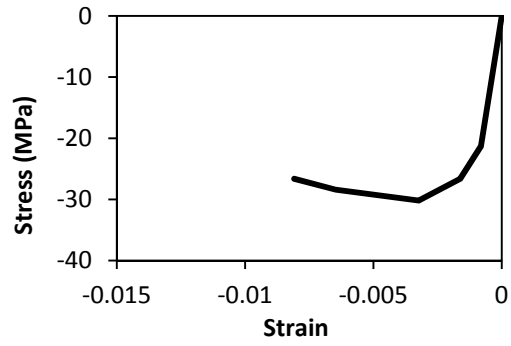
	MEMBER	Steel		Concrete		Comments
		$E$ (GPa)	$A$ (mm <sup>2</sup> )	$E$ (MPa)	$A$ (mm <sup>2</sup> )	
<b>Beam</b>	<b>A-E (D)</b>	200	5387	29407	159174	Tension Chord
	<b>A-E (S)</b>	200	5387	29407	159174	
	<b>B-D (D)</b>	200	4052	16865	49529	Compression Chord
	<b>B-D (S)</b>	200	1013	16700	51329	
	<b>BC</b>	200	1523	29407	104516	Transverse Steel
	<b>AD</b>	-	-	29407	156974	Concrete Arch
	<b>AB</b>	-	-	29407	74477	Concrete Truss
	<b>CD</b>	-	-	29407	69677	
<b>Beam-Column Joint</b>	<b>E-K (D)</b>	200	5387	29407	159174	Tension Chord
	<b>E-K (S)</b>	200	5387	29407	159174	
	<b>D-H (D)</b>	200	4052	16865	49529	Compression Chord
	<b>D-H (S)</b>	200	1013	16700	51329	
	<b>FG&amp;HI</b>	200	252	29407	34839	Transverse Steel
	<b>DK</b>	-	-	29407	190916	Concrete Arch
	<b>DG</b>	-	-	29407	50619	Concrete Truss
	<b>DI</b>	-	-	29407	46277	
	<b>FK</b>	-	-	29407	52226	
	<b>HK</b>	-	-	29407	47581	
<b>Column</b>	<b>JJ</b>	200	6613	29407	206561	Tension Chord
	<b>LL</b>	200	2535	15686	206561	Compression Chord
Beam: $N_h = 6$ and beam-column joint: $N_h = 2$						
<i>(D) Doubly reinforced beam (S) Singly reinforced beam</i>						

**Table A5-14: Axial Rigidities of C-STM Elements: Specimen 4.**

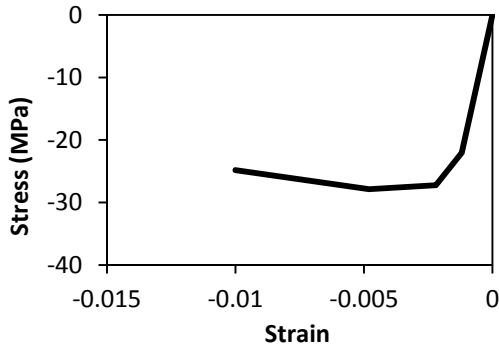
	MEMBER	Steel		Concrete		Comments
		$E$ (GPa)	$A$ (mm <sup>2</sup> )	$E$ (MPa)	$A$ (mm <sup>2</sup> )	
<b>Beam</b>	<b>A-E (D)</b>	200	5387	24856	179290	Tension Chord
	<b>A-E (S)</b>	200	5387	24856	179290	
	<b>B-D (D)</b>	200	4052	11432	62987	Compression Chord
	<b>B-D (S)</b>	200	1013	11659	57813	
	<b>BC</b>	200	1523	24856	104516	Transverse Steel
	<b>AD</b>	-	-	24856	156974	Concrete Arch
	<b>AB</b>	-	-	24856	74477	Concrete Truss
	<b>CD</b>	-	-	24856	69677	
<b>Beam-Column Joint</b>	<b>E-K (D)</b>	200	5387	24856	179290	Tension Chord
	<b>E-K (S)</b>	200	5387	24856	179290	
	<b>D-H (D)</b>	200	4052	11432	62987	Compression Chord
	<b>D-H (S)</b>	200	1013	11659	57813	
	<b>FG&amp;HI</b>	200	252	24856	34839	Transverse Steel
	<b>DK</b>	-	-	24856	190916	Concrete Arch
	<b>DG</b>	-	-	24856	50619	Concrete Truss
	<b>DI</b>	-	-	24856	46277	
	<b>FK</b>	-	-	24856	52226	
	<b>HK</b>	-	-	24856	47581	
<b>Column</b>	<b>JJ</b>	200	6613	24856	230058	Tension Chord
	<b>LL</b>	200	2535	11066	230058	Compression Chord
Beam: $N_h = 6$ and beam-column joint: $N_h = 2$						
<i>(D) Doubly reinforced beam (S) Singly reinforced beam</i>						



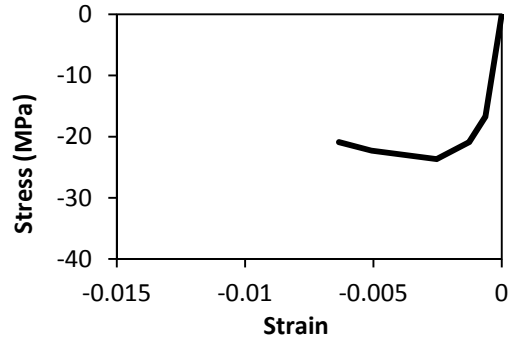
*All Beam elements excluding compression chords*



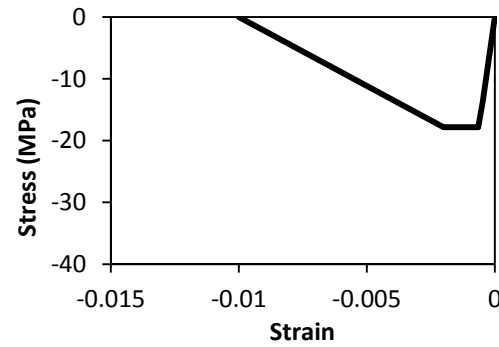
*Beam Compression Chord Members*



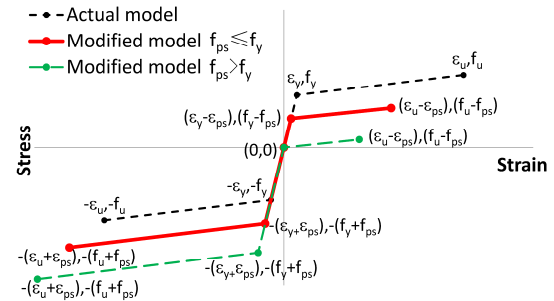
*All Column elements excluding compression chords*



*Column compression chord members*

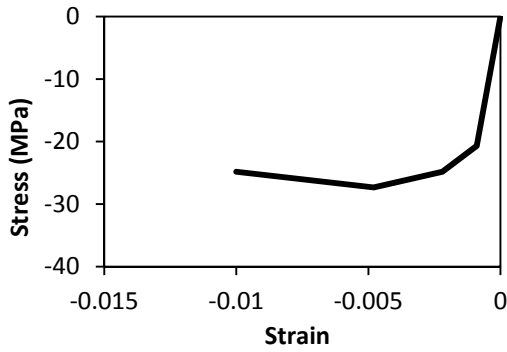


*Softened concrete model for diagonal arch member in the beam-column joint*

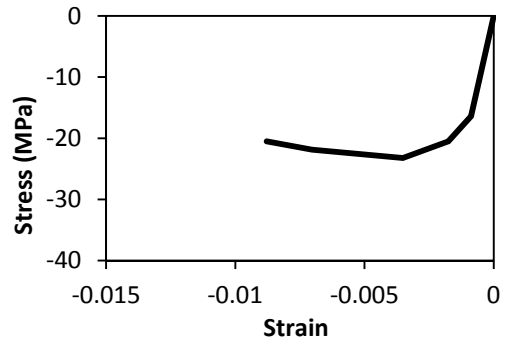


*All steel members.*

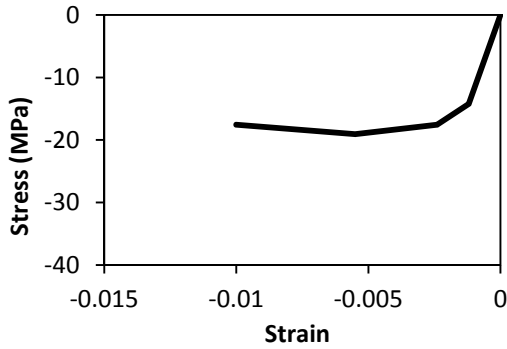
**Figure A5-4: Stress-Strain Models for the Elements of the C-STM Model: Specimen 2.**



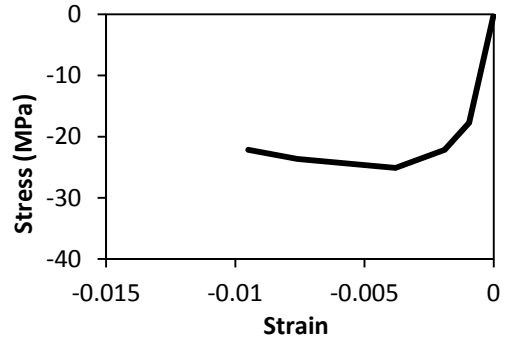
All Beam elements excluding compression chords



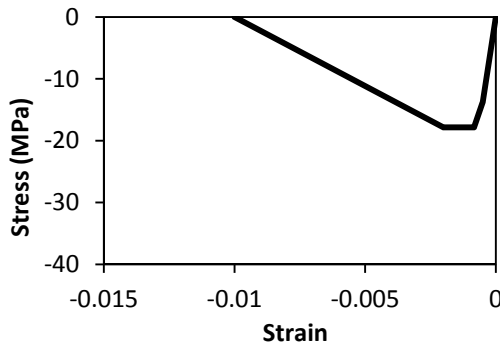
Beam Compression Chord Members



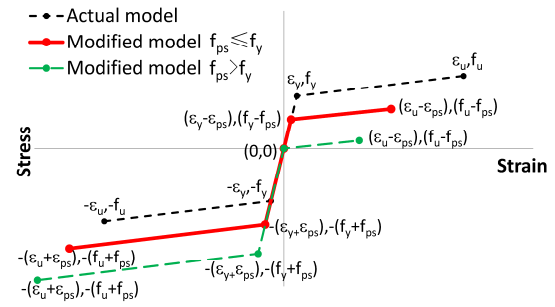
All Column elements excluding compression chords



Column compression chord members



Softened concrete model for diagonal arch member in the beam-column joint



All steel members.

**Figure A5-5: Stress-Strain Models for the Elements of the C-STM Model: Specimen 4.**

### A5.4 Computation of Material Properties and Prestrains for C-beam Specimen 3

COMPUTATION OF MATERIAL PROPERTIES TO PERFORM THE C-STM ANALYSIS FOR C-BEAM SPECIMEN 3		1 2
1. Computation of Confinement Ratio for Beam and Column		
Concrete compressive strength obtained experimentally from cylinder tests, $f'_c = 40.9$ MPa. As the strains in the steel were much higher than the yield strain, $f_y = 517$ MPa is considered for the following computations.		
<u>Computation of concrete confinement ratio: beam</u>		
$kd$ (mm)	287.3	
$A_{cc}$ (mm <sup>2</sup> ) = $(c_c + d_s / 2) \times b_c$	132903	
$A_e$ (mm <sup>2</sup> ) = $(c_c + d_s / 2) \times b_c$ - area of shaded region	80374	
$k_e = A_e / A_{cc}$	0.605	
$f_{lx}$ (MPa) = $k_e \frac{A_{str} f_y}{(c_c + d_{str}) s}$	1.39	
$f_{ly}$ (MPa) = $k_e \frac{2A_{str} f_y}{b_c s}$	1.30	
Smallest confining stress ratio $f_{ly} / f'_c$	0.032	
Largest confining stress ratio $f_{lx} / f'_c$	0.034	
$K$ (from chart)	1.21	
<u>Computation of concrete confinement ratio: column</u>		
$kd$ (mm)	355.1	
$A_{cc}$ (mm <sup>2</sup> ) = $(c_c + d_s / 2) \times b_c$	693	
$A_e$ (mm <sup>2</sup> ) = $(c_c + d_s / 2) \times b_c$ - area of shaded region	447096	
$k_e = A_e / A_{cc}$	0.81	
$f_{lx}$ (MPa) = $k_e \frac{(A_{str})_x f_y}{s d_c}$	2.21	
$f_{ly}$ (MPa) = $k_e \frac{(A_{str})_y f_y}{s b_c}$	1.74	
Smallest confining stress ratio $f_{ly} / f'_c$	0.042	
Largest confining stress ratio $f_{lx} / f'_c$	0.054	
$K$ (from chart)	1.31	

COMPUTATION OF MATERIAL PROPERTIES TO PERFORM THE C-STM ANALYSIS FOR C-BEAM SPECIMEN 3

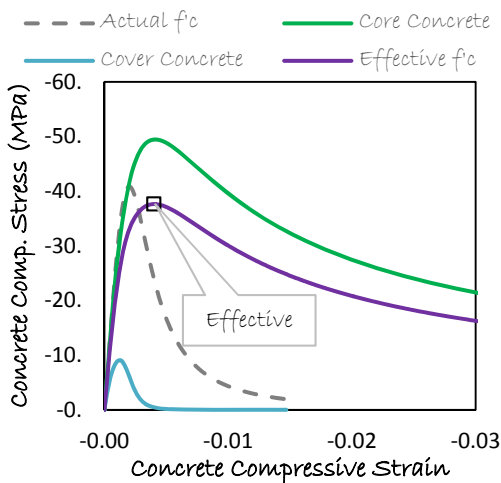
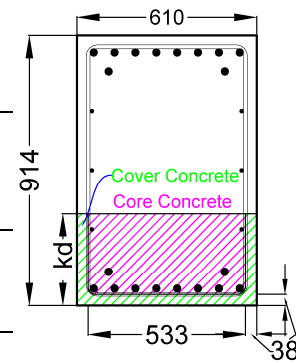
2  
2

2. Computation of effective concrete strength

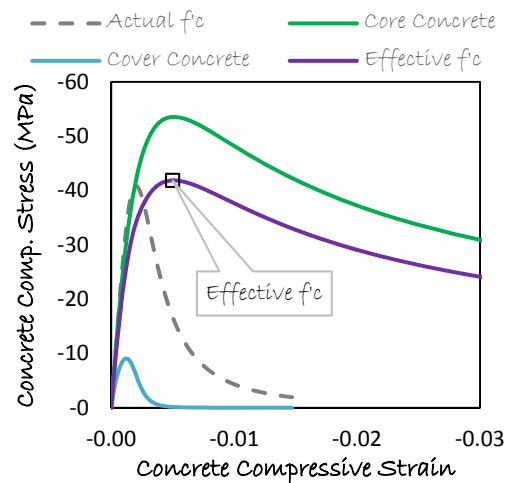
$kd$  = depth from the compression face to the neutral axis

Total area of concrete assigned to the chord members = breadth x depth to neutral axis from compression face,  $A_{total} = b \times kd = 610 \times kd$

	Beam	Column
$kd$ (mm)	287.3	355.1
Area of cover concrete (mm <sup>2</sup> )	42127	47280
$A_{cover} = 2(38) \times kd + [b - 2(38)]38$		
Area of core concrete (mm <sup>2</sup> )	133126	169331
$A_{core} = [610 - (2 \times 38)](kd - 38)$		
Contribution of cover concrete to the total area = $A_{cover}/A_{total}$	0.241	0.219
Contribution of core concrete to the total area = $A_{core}/A_{total}$	0.759	0.781
Effective $f'_c$ from graph (MPa)	37.6	41.9



Concrete Stress-Strain Relation for Beam



Concrete Stress-Strain Relation for Column

COMPUTATION OF PRESTRAINS IN THE VARIOUS MEMBERS OF THE C-STM MODEL FOR SPECIMEN 3

1  
5

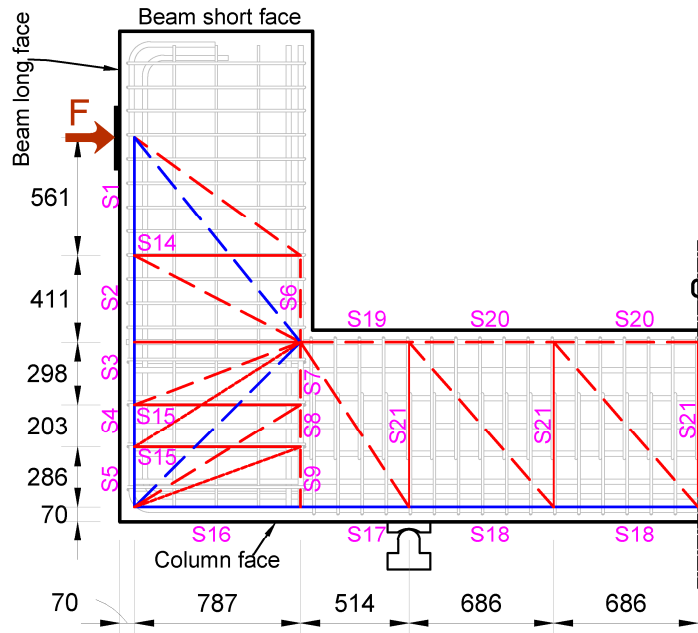
General notes

Development length for Specimen 3 #8 bars ( $DL$ ) = 1072 mm

Distance  $l$  to center of C-STM members

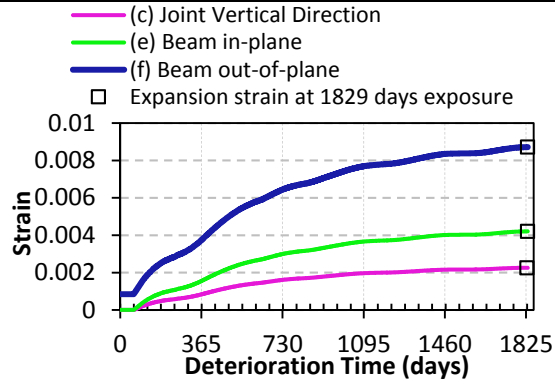
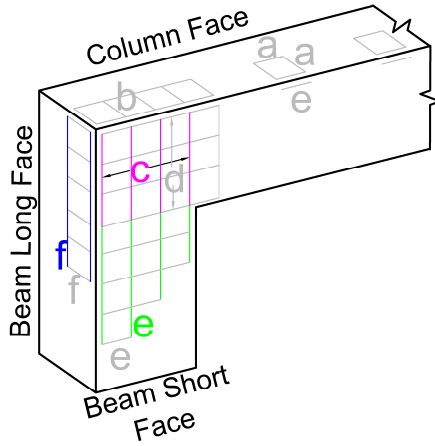
Member	from beam short face (mm)	from column face (mm)
S1	788.4	1478.8
S2/S6	1274.3	992.9
S3/S7	1629.0	638.2
S4/S8	1879.9	387.4
S5/S9	2124.3	142.9
	from beam long face (mm)	
S16	393.7	
S17/S19	1044.6	

Note: values in blue are less than the development length.





Longitudinal beam members (S1-S5)



Modeled Expansion Strains Outside Development Length Zone

The prestrains in the longitudinal beam members (S1-S5) are computed considering the average of modeled expansion strains at the end of the exposure period (1829 days) in the joint vertical direction (c presented as Case III in Appendix A3) or longitudinal beam in-plane direction (e presented as Case V in Appendix A3) and longitudinal beam out-of-plane direction (f presented as Case VII in Appendix A3).

Note:  $\rho_{eff} = (l/DL)\rho$  and  $\epsilon_{\rho^{(eff)}}^{1829}$  = expansion strain at 1829 days of exposure.

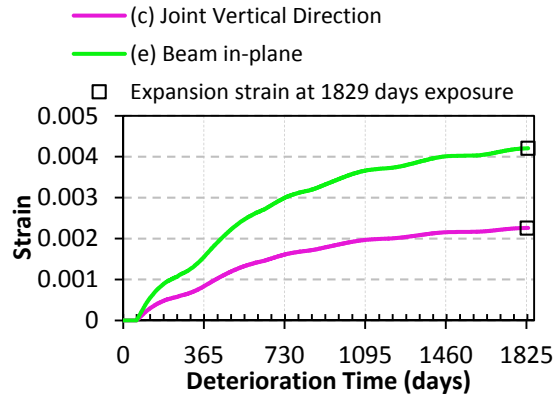
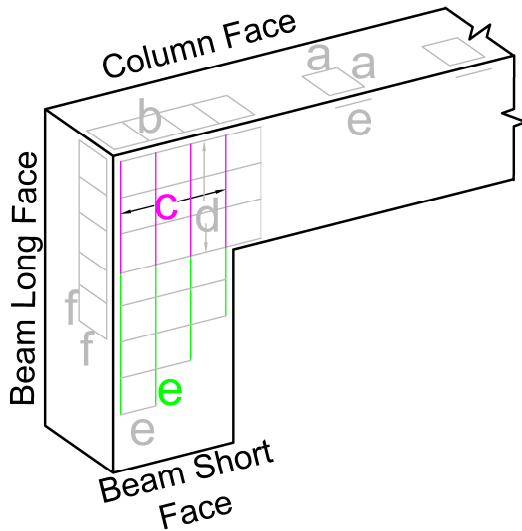
		Joint vertical direction c (Case III, Appendix A3)		Longitudinal beam out-of-plane direction f (Case VII, Appendix A3)		Average prestrain
Outside DL		$\rho = 0.0529$ $\epsilon_{\rho}^{1829} = 0.00226$		$\rho = 0.01428$ $\epsilon_{\rho}^{1829} = 0.00871$		
C-STM Member	l from column face (mm)	$\rho_{eff}$	$\epsilon_{\rho^{(eff)}}^{1829}$	$\rho_{eff}$	$\epsilon_{\rho^{(eff)}}^{1829}$	Average prestrain
S5	142.9	0.00705	0.00884	0.0019	0.0274	0.01812
S4	387.4	0.01912	0.00427	0.00516	0.01652	0.01040
S3	638.2	0.0315	0.00305	0.00850	0.01214	0.00759
S2	992.9	0.0490	0.00235	0.01323	0.00914	0.00575
		Longitudinal beam in-plane e (Case V, Appendix A3)		Longitudinal beam out-of-plane direction f (Case VII, Appendix A3)		Average prestrain
S2	Outside DL	$\rho = 0.01954$ $\epsilon_{\rho}^{1829} = 0.0042$		$\rho = 0.01428$ $\epsilon_{\rho}^{1829} = 0.00871$		0.00646
S1	788.4 mm	$\rho_{eff} = 0.01437$	$\epsilon_{\rho^{(eff)}}^{1829} = 0.00523$	$\rho_{eff} = 0.01050$	$\epsilon_{\rho^{(eff)}}^{1829} = 0.01060$	0.00792

Note: Prestrain values presented in blue are adopted for the corresponding C-STM member.

COMPUTATION OF PRESTRAINS IN THE VARIOUS MEMBERS OF THE C-STM MODEL FOR SPECIMEN 3

3  
5

Longitudinal Beam Members (S6-S9)



Modeled Expansion Strains Outside Development Length Zone

The prestraints in the longitudinal beam members (S6-S9) are computed considering the modeled expansion strains at the end of the exposure period in the joint vertical direction (c presented as Case III in Appendix A3) or longitudinal beam in-plane direction (e presented as Case V in Appendix A3).

		Joint vertical direction c (Case III, Appendix A3)	
Outside DL		$\rho = 0.0529 \quad \epsilon_p^{1829} = 0.00226$	
C-STM Member	l measured from column face (mm)	$\rho_{eff}$	$\epsilon_{p(eff)}^{1829}$
S9	142.9	0.00705	0.00884
S8	387.4	0.01912	0.00427
S7	638.2	0.0315	0.00305
S6	992.9	0.0490	0.00235
		Longitudinal beam in-plane e (Case V, Appendix A3)	
C-STM Member	l measured from beam short face	$\rho = 0.01954 \quad \epsilon_p^{1829} = 0.0042$	
S6	Outside DL		

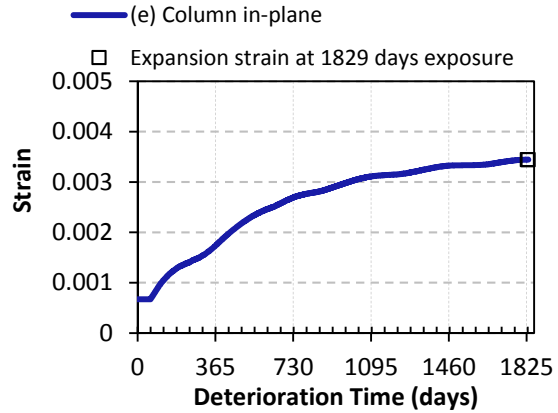
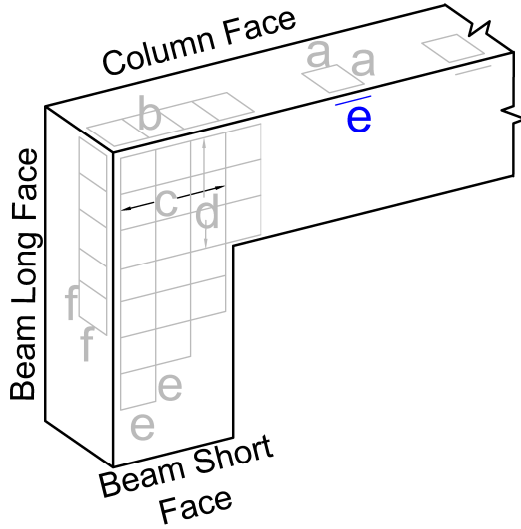
Note: Prestrain values presented in blue are adopted for the corresponding C-STM member.

COMPUTATION OF PRESTRAINS IN THE VARIOUS MEMBERS OF THE C-STM MODEL FOR SPECIMEN 3

4

5

Longitudinal column members (S16-S20)



Modeled Expansion Strains Outside Development Length Zone

The prestraints in the longitudinal column members (S16-S20) are computed considering the modeled expansion strains at the end of the exposure period (1829 days) in the column longitudinal face (e presented as Case VI in Appendix A3).

Note:  $\rho_{eff} = (l / DL) \rho$  and  $\epsilon_{\rho_{eff}}^{1829}$  = expansion strain at 1829 days of exposure.

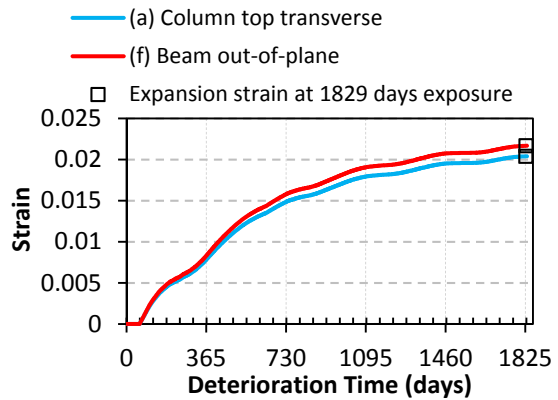
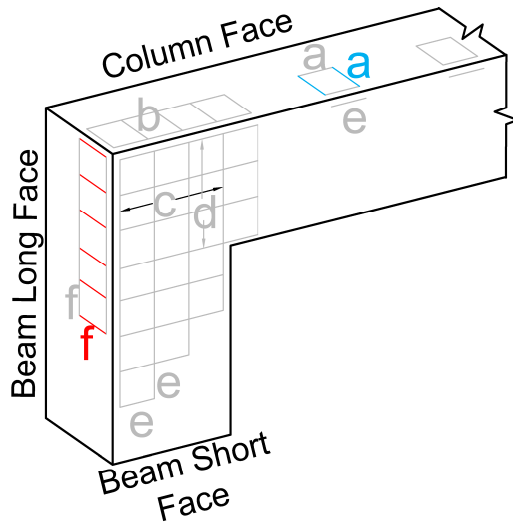
C-STM Member	$l$ measured from beam long face (mm)	Column longitudinal direction $e$ (Case VI, Appendix A3)	
S18/S20	Outside DL	$\rho = 0.0671 \epsilon_{\rho}^{1829} = 0.0034$	
		$\rho_{eff}$	$\epsilon_{\rho_{eff}}^{1829}$
S17/S19	1044.6	0.06539	0.0034
S16	393.7	0.02465	0.00565

Note: Prestrain values presented in blue are adopted for the corresponding C-STM member.

COMPUTATION OF PRESTRAINS IN THE VARIOUS MEMBERS OF THE C-STM MODEL FOR SPECIMEN 3

5  
5

Transverse members (S14, S15, S21)



Modeled Expansion Strains Outside Development Length Zone

The prestraints in the transverse members in the beam (S14) and the beam-column joint (S15) are computed considering the modeled expansion strains at the end of the exposure period (1829 days) in the beam out-of-plane region (f presented as Case I in Appendix A3). Similarly, the prestraints in the column transverse members (S21) are computed from the modeled expansion strains in the column top transverse region (a presented as Case II in Appendix A3).

Note:  $\rho_{eff} = (l / DL) \rho$  and  $\epsilon_{\rho}^{1829} =$  expansion strain at 1829 days of exposure.

C-STM Member	$\rho$	$\epsilon_{\rho}^{1829} =$
S14/S15	0.00177	0.02166
S21	0.00198	0.02038

Note: Prestrain values presented in blue are adopted for the corresponding C-STM member.